# FINAL REPORT

## On-Time 3D Time-Domain EMI and Tensor Magnetic Gradiometry for UXO Detection and Discrimination

## SERDP Project MM-1328

June 2008


Dr. David L. Wright
U.S. Geological Survey

Dr. David V. Smith
U.S. Geological Survey

Dr. Theodore H. Asch,
U.S. Geological Survey

Dr. Craig W. Moulton,
U.S. Geological Survey

Dr. Robert E. Bracken,
U.S. Geological Survey

Dr. Trevor P. Irons
U.S. Geological Survey

Dr. Yaoguo Li
Colorado School of Mines

Dr. Misac N. Nabighian
Colorado School of Mines



Strategic Environmental Research and Development Program

# REPORT DOCUMENTATION PAGE

*Form Approved*
*OMB No. 0704-0188*



**PLEASE DO NOT RETURN YOUR FORM TO THE ABOVE ORGANIZATION.**

| 1. REPORT DATE *(DD-MM-YYYY)* | 2. REPORT TYPE | 3. DATES COVERED *(From - To)* |
|---|---|---|
| 04-06-2008 | Final | July 1, 2002 - June 04, 2008 |

**4. TITLE AND SUBTITLE**

On-Time 3D Time-Domain EMI and Tensor Magnetic Gradiometry for UXO Detection and Discrimination

**5a. CONTRACT NUMBER**

**5b. GRANT NUMBER**

**5c. PROGRAM ELEMENT NUMBER**

**6. AUTHOR(S)**

David L. Wright, David vonG. Smith, Theodore H. Asch, Craig W. Moulton, Robert E. Bracken, Trevor P. Irons, Yaoguo Li, Misac N. Nabighian

**5d. PROJECT NUMBER**

MM-1328

**5e. TASK NUMBER**

**5f. WORK UNIT NUMBER**

**7. PERFORMING ORGANIZATION NAME(S) AND ADDRESS(ES)**

U.S. Geological Survey, M.S. 964, Box 25046, Federal Center, Denver, CO 80225
Colorado School of Mines, Department of Geophysics, Golden, CO 80401

**8. PERFORMING ORGANIZATION REPORT NUMBER**

**9. SPONSORING/MONITORING AGENCY NAME(S) AND ADDRESS(ES)**

Dr. Anne Andrews. Program Manager, Munitions Management
Strategic Environmental Research and Development Program
901 N. Stuart Street, Suite 303
Arlington, VA 22203-1853

**10. SPONSOR/MONITOR'S ACRONYM(S)**

SERDP

**11. SPONSOR/MONITOR'S REPORT NUMBER(S)**

**12. DISTRIBUTION/AVAILABILITY STATEMENT**

Approved for Public Release, Distribution is Unlimited

**13. SUPPLEMENTARY NOTES**

**14. ABSTRACT**

Project MM-1328 began as "Evaluation, Modification, and Testing of the Very Early Time Electromagnetic (VETEM) System, the High Frequency Sounder (HFS), and the Tensor Magnetic Gradiometer System (TMGS) for UXO Detection, Imaging, and Discrimination." We recommended that the TMGS be reconfigured and that a new multi-axis EMI system be developed. The new EMI system was named "ALLTEM" because it is a time domain electromagnetic induction (TEM) system whose triangle-wave excitation is on all the time. Project MM-1328 was continued with the revised project title, "On-Time 3D Time-Domain EMI and Tensor Magnetic Gradiometry for UXO Detection and Discrimination." Field tests of the revised TMGS and ALLTEM were carried out in October/November of 2005 and May of 2006. Colorado School of Mines and the USGS developed data inversion algorithms to solve for identifying target parameters. ALLTEM moving-platform survey-mode data are often of sufficient quality that reliable target parameters can be obtained to classify targets as likely UXO or non-UXO. This capability improves field efficiency.

**15. SUBJECT TERMS**

EMI, magnetics, UXO, sensor, Multi-axis, tensor, inversion, discrimination, ground-based, towed-system

| 16. SECURITY CLASSIFICATION OF: | | | 17. LIMITATION OF ABSTRACT | 18. NUMBER OF PAGES | 19a. NAME OF RESPONSIBLE PERSON |
|---|---|---|---|---|---|
| a. REPORT | b. ABSTRACT | c. THIS PAGE | | | David L. Wright |
| Unclassified | Unclassified | Unclassified | Unlimited | 277 | 19b. TELEPHONE NUMBER *(Include area code)* (303)236-1381 |

Reset

**Standard Form 298** (Rev. 8/98)
Prescribed by ANSI Std. Z39.18

# TABLE OF CONTENTS

# ABBREVIATIONS AND ACRONYMS

| | |
|---|---|
| **BTG** | **Blind Test Grid (at YPG)** |
| **Cal Grid** | **Calibration Grid (at YPG)** |
| **CoM** | **Center of Mass** |
| **CoR** | **Center of Rotation** |
| **CSM** | **Colorado School of Mines** |
| **DAS** | **Data Acquisition System** |
| **DFC** | **Denver Federal Center** |
| **DoD** | **Department of Defense** |
| **DOE** | **Department of Energy** |
| **EMI** | **Electromagnetic Induction** |
| **HFS** | **High-Frequency Sounder** |
| **HP** | **High-pass (filter description)** |
| **IDA** | **Institute for Defense Analysis** |
| **ISO 8601** | **International Organization for Standardization Date and Time Format** |
| **LP** | **Low-pass (filter description)** |
| **M1, M2, M3** | **Three Principal Orthogonal Polarizability Dipole Moments** |
| **MIU** | **Magnetometer Interface Unit** |
| **MSE** | **Mean Squared Error** |
| **NI** | **National Instruments** |
| **NLREG** | **Non-linear Regression program** |
| **PPS** | **Pulse Per Second** |
| **PXI** | **PCI eXtensions for Instrumentation - a modular instrumentation platform** |
| **RMS** | **Root Mean Squared** |
| **RTK** | **Real-Time Kinematic** |
| **RTK-GPS** | **Real-Time Kinematic Global Positioning System** |
| **Rx** | **Receiving Antenna** |
| **S/H** | **Sample and Hold** |
| **SERDP** | **Strategic Environmental Research and Development Program** |
| **SNR** | **Signal-to-Noise Ratio** |
| **SU** | **Seismic Unix data file format (not intrinsically related to seismic data)** |
| **TEM** | **Time Domain Electromagnetic** |
| **TMGS** | **Tensor Magnetic Gradiometer System** |
| **Tx** | **Transmitting Antenna** |
| **USGS** | **U.S. Geological Survey** |
| **UTC** | **Coordinated Universal Time** |
| **UXO** | **Unexploded Ordnance** |
| **VETEM** | **Very Early Time Electromagnetic** |
| **VLF** | **Very Low Frequency (3 kHz to 30 kHz)** |
| **YPG** | **Yuma Proving Ground** |

# LIST OF FIGURES

# LIST OF TABLES

# PREFACE

We initiated this project in order to determine whether USGS-developed geophysical prototype instruments could address the DoD need to detect and discriminate between UXO and harmless scrap metal. The prototype instruments had been designed and developed by the USGS Instrumentation Laboratory in the Crustal Imaging and Characterization Team in Denver for closely related shallow environmental geophysical applications such as waste pit mapping for the DOE. We thought that these prototype systems might be modified to make them effective for detection and discrimination of UXO. We are delighted that this project provided the resources needed to test that hypothesis and we think that the results of this project clearly demonstrate that at least one of our prototype instruments, ALLTEM, is a very strong performer. ALLTEM has now been moved to the demonstration/validation phase in a new ESTCP project.

In order to classify targets into likely UXO and non-UXO categories some kind of automated digital processing of the data is necessary. Classification algorithms can be "physics-based" in which case some identifiable target parameters are derived and used in classification. Alternatively, classification algorithms can look at "features" in the data without any attempt to relate these directly to physical parameters of targets. Perhaps as a consequence of the physics and geophysics backgrounds of many on our team we chose "physics-based" approaches. For ALLTEM the inversion algorithm solves for three time dependent magnetic principal orthogonal dipole moments. We plan to do classification using these target parameters that are directly related to target composition, size, and shape and are independent of burial depth or orientation.

This project included hardware development, data acquisition and processing software development, inversion algorithm development, field tests at both the Calibration Grid and Blind Test Grid at the Standardized UXO test facility at the Yuma Proving Ground (YPG), and the development and use of an automated test stand at the Denver Federal Center. Because this project initially involved two EMI prototype instruments and a tensor magnetic gradiometer, it has been a challenge to simultaneously move both EMI and magnetic systems and their unique data processing and inversion development forward, but we knew that we had a capable team and we think that the results justify the decision that SERDP made to allow us to proceed. Without our team the project could not have succeeded. Our team involved a collaborative effort between the USGS and the Colorado School of Mines, drawing on the strengths of each group. The combined geophysical experience and insights of Drs. Misac N. Nabighian and Yaoguo Li at the Colorado School of Mines, Department of Geophysics, has been critical to the success of this project. We also thank Mr. Vinicio Sanchez for his part in the development of the inversion algorithm developed at CSM for the TMGS.

At the end of the first phase of this project we saw that our VETEM system had produced interesting and hopeful results, but decided that we should design a new EMI system, retaining some features of VETEM. At this point, Dr. Nabighian advocated borrowing the triangle wave excitation, pioneered many years ago for minerals exploration, at the University of Toronto (West et al., 1984). We did adopt the triangle waveform and built the new ALLTEM system. After we found that in post-processing we could eliminate the initially unexpected response to ground magnetic susceptibility, ALLTEM has produced results with an excellent signal-to-noise

ratio. Triangle-wave excitation has proven to be very effective when the data are properly processed.

Conceptual elegance, however, cannot compensate for inadequate execution and the saying, "The rest is just engineering" puts a great deal of stress on the engineers. Fortunately, we had a very resourceful, ingenious, and determined engineering team consisting primarily of Craig Moulton and Raymond Hutton, with contributions from David Smith, Robert Bracken, and David Wright.

The "cart" was built by David Kibler, with important modifications by Paul Wigton to replace troublesome wheel ball-bearings with ceramic bushings and to redesign the front fork so that the cart tracks more accurately behind the towing vehicle.

Data acquisition systems and software for ALLTEM were designed by Craig Moulton. Raymond Hutton served in the same capacity for the TMGS. Craig Moulton has also written a great deal of post-processing software that prepares the ALLTEM data for the inversion algorithm.

An ALLTEM inversion algorithm was developed at the USGS by Charles Oden and extensively debugged by Craig Moulton. Ted Asch has removed the point dipole approximations for the receiving antennas and is continuing to improve the code.

CSM developed an inversion code for the TMGS and one was also developed at the USGS by Rob Bracken. Phil Brown also worked with TMGS and ALLTEM data.

Field personnel who went to YPG in one or more of our three deployments include Ted Asch, David Wright, David Smith, Craig Moulton, Philip Brown, Robert Bracken, Raymond Hutton, and Erin Wallin of the USGS and Yaoguo Li of CSM. We also acknowledge the considerable support we had from many at YPG and assistance from APG personnel as well.

The test stand was built by Craig Moulton and Paul Wigton with assistance from Trevor Irons. Data at the test stand have been acquired by Craig Moulton, Trevor Irons, David Smith, and Raymond Hutton with assistance from Chad Ailes, and Jonah Sullivan.

Finally, we acknowledge SERDP for supporting this project and thank SERDP program office personnel and the support staff at HydroGeologic for their encouragement and help along the way.

# DISCLAIMER

Any use of trade, product, or firm names in this report is for descriptive purposes only and does not imply endorsement by the U.S. Government.

# 1.0 Executive Summary

Project MM-1328 included two phases. The first phase began in July, 2002, with the title "Evaluation, Modification, and Testing of the Very Early Time Electromagnetic (VETEM) System, the High Frequency Sounder (HFS), and the Tensor Magnetic Gradiometer System (TMGS) for UXO Detection, Imaging, and Discrimination." The VETEM system is an electromagnetic induction (EMI) system that operates with pulses of only a few microseconds in length and therefore has an unusually high spectral content for a time domain EMI instrument. The High Frequency Sounder is a frequency domain instrument capable of operation over a broad frequency range, including that commonly used by commercial systems, but also reaching into the low megahertz range. The TMGS system is a passive magnetic gradiometer system using an array of four low noise, three-component, magnetometers. Some modifications were made to VETEM, the HFS and the TMGS so that continuous profiling incorporating real-time kinematic global positioning system (RTK-GPS) data could be accomplished with each of these instruments. In February and March of 2003, VETEM, the HFS, and the TMGS were demonstrated over the Calibration Grid at the Yuma Proving Ground (YPG). All three instruments performed well, considering that none of them was designed with UXO applications in mind. However, it was determined that significant modifications were necessary in order achieve a level of performance that could provide added benefit for UXO detection and discrimination. Specifically, we recommended that:

(1) The TMGS be retained, but with a new sensor configuration and

(2) VETEM and the HFS be merged into a single multi-axis time domain EMI system with a triangle-wave excitation advocated by Misac Nabighian and first used in minerals exploration by the UTEM system developed at the University of Toronto (West et al., 1984).

The new EMI system was named "ALLTEM" because it is a time domain electromagnetic induction (TEM) system whose excitation waveform is on all the time.

The second phase of MM-1328 was proposed and funded with the revised project title, "On-Time 3D Time-Domain EMI and Tensor Magnetic Gradiometry for UXO Detection and Discrimination." In the second phase three primary tasks were initially identified: (1) Development and testing of a new EMI system; (2) Modification and testing of the TMGS system; (3) Software development, including: (a) data acquisition and processing software and (b) inversion for physical parameters that are target identifiers. Late in the second phase another task was added: (4) Construction of a test stand and collection, evaluation, and distribution of ALLTEM and TMGS target data with high position accuracy (< 5 mm) over a suite of UXO and non-UXO targets as aids to both instrument evaluation and refinement, and testing and refinement of target discrimination and classification algorithms.

Field tests of the revised TMGS and ALLTEM were carried out in October/November of 2005 and May of 2006. Both the Colorado School of Mines and the USGS developed inversion algorithms for TMGS data. The USGS developed the inversion algorithm for ALLTEM data.

It was discovered that, although ALLTEM data show little response to soil conductivity, the system responds to soil magnetic susceptibility. However, the soil magnetic susceptibility response and residual system primary field leakage are both essentially square waves. Therefore, if data are examined only after the step response of the lowest frequency analog filter in the system has settled (about 280 μs) and we analyze data using only amplitude differences along the ALLTEM waveform, both the primary field leakage and the magnetic soil response are removed while responses to buried metal objects remain. Thus, after digital filtering and processing, ALLTEM data generally have a high signal-to-noise ratio (SNR). This fact, plus the fact that the polarity of the responses from ferrous and non-ferrous targets are opposite, provide advantages to ALLTEM data for inversion and classification of targets.

ALLTEM data have been compared to data acquired using an EM-62 MK2 when both were operated at similar speeds and identical line spacings over the Calibration Grid at YPG. The general conclusion is that ALLTEM provides a minor advantage over an EM-61 Mk2 in terms of target detection, but a major advantage in terms of inversion for target parameters because inclusion of horizontal field component data significantly improves inversions.

Another very important discovery was that Leica 1200 RTK-GPS data, acquired in 2006, were accurate enough that physically reasonable and repeatable inversions for target parameters for many of the Calibration Grid targets were obtained from moving platform survey mode ALLTEM data. We attribute this, in part, to the 20 Hz position update rate provided by the Leica 1200. We therefore conclude that it is possible to obtain accurate target inversions from data acquired in a moving platform survey mode without needing to stop to obtain stationary cued mode data, if the position data are sufficiently accurate. Random position noise was added to accurate test stand position data to test the effects of position errors on inversions for target parameters. Uniformly distributed position errors of up to 5 cm, and sometimes up to 10 cm, do not generally cause significant degradation of target inversions, at least when sensor SNRs are high. We also found that sensor SNRs as low as 18 dB often produce satisfactory inversions for target parameters. The effects of various combinations of position errors and sensor noise levels are still being examined.

We conclude that ALLTEM can provide survey-mode data from which reliable target parameters can be obtained in order to correctly classify targets as likely UXO or clutter. We think this ability may prove to be a significant benefit in many field applications.

## 2.0 Project Background

Detection and discrimination between buried unexploded ordnance (UXO) and harmless scrap metal are among the most urgent environmental needs for the Department of Defense (DoD). UXO of concern include items of widely varying size, from 20 mm projectiles to large bombs, varying depths, from the surface to many feet deep, and buried in unknown orientations in earth of varying electromagnetic and magnetic properties. Common systems for UXO applications use EMI or magnetometer sensors. While EMI and magnetometer sensors have demonstrated high detection rates under many conditions, the ability to discriminate between harmless buried metal objects and UXO using standard commercial benchmark systems is limited.

The USGS had previously developed three prototype systems for non-UXO, but closely related, geophysical applications. Two of these, the Very Early Time Electromagnetic (VETEM) System and the High Frequency Sounder (HFS), are active EMI systems. The third, the Tensor Magnetic Gradiometer System (TMGS) is a passive magnetic system. It was thought that with some modifications these prototype instruments could be tested and evaluated for their potential UXO applicability and the information derived from these tests and evaluations used to define and build EMI and magnetic systems optimized for UXO applications. As an integral part of the project, new interpretation algorithms would be developed that were appropriate for use with the new instruments.

## 3.0 Project Objective

The overall objective of this project was to demonstrate that improved discrimination between likely UXO targets and targets that are non-UXO is possible through a combination of modified instrumentation and appropriate inversion algorithms for EMI and magnetometer data.

## 4.0 Methods

The two methods that were used in this project are electromagnetic induction and magnetic gradiometry. EMI and magnetic methods are physically and theoretically well understood and are the two most commonly used techniques for UXO detection and discrimination. What distinguishes this work from most others is that: (a) ALLTEM uses multi-axis continuous triangle-wave excitation and corresponding multi-axis receiving sensors and (b) the TMGS records vector components of magnetic gradients rather than gradients of total fields. In the first phase of work the existing VETEM, HFS, and TMGS prototype systems were modified to make them more suitable for UXO application. Laboratory tests were conducted, and then all three systems were operated over the Calibration Area at the newly completed Standardized UXO Test

Area at the Yuma Proving Ground, Arizona, in 2003. The data were processed, and results evaluated to aid in the definition of new prototype instruments.

In the second phase of work, a new time-domain EMI system (ALLTEM) with triangle-wave excitation was built, tested, and evaluated, and modifications were made to the TMGS system to improve its performance for UXO applications. Inversion algorithms were developed for both TMGS data and ALLTEM data. The inversion algorithms are physics-based and solve for target parameters that are directly related to the size, shape, and material composition (ferrous versus non-ferrous metal) of buried objects (Oden, 2006; Oden and Moulton, 2006). In order to assess the performance of ALLTEM and the TMGS, both systems were operated at the Calibration Grid of the Standardized UXO Test Range at the Yuma Proving Ground, AZ, in 2005. In 2006 the TMGS was operated over the Blind Test Grid and ALLTEM over both the Calibration Grid and the Blind Test Grid. Finally, ALLTEM and TMGS data have been obtained on an automated test stand constructed of non metallic materials and with automated and accurate (~ +/- 3 mm) positioning.

# 5.0 Results and Accomplishments

In this section we discuss the early modification and testing of our existing magnetic and electromagnetic prototype instruments (section 5.1), the evolution of those instruments into the present ALLTEM and current configuration of the Tensor Magnetic Gradiometer System (TMGS) (section 5.2) and test results using these systems (section 5.3). We then discuss software for data acquisition, processing, and inversion for target parameters and classification in section 5.4. Late in this project a new task was added: acquisition of accurate test stand data for both the ALLTEM system and the TMGS. We discuss the test stand and test stand data in section 5.5. Woven through these sections are "lessons learned," but we also have summarized these in section 5.6 partly as a transition into the Conclusions of section 6 in which we include the hoped-for future for ALLTEM and the TMGS. A detailed list of test stand data is provided in Appendix A.

## 5.1 Pre-existing Prototype Systems

Over a period of several decades, the Instrumentation Laboratory at the USGS in Denver has developed a wide range of prototype instruments designed to make geophysical and geochemical measurements. Of these, it appeared to us that three had particular abilities that might lend themselves to the problem of UXO detection and to the discrimination of UXO from harmless scrap metal. Of these three, two were EMI instruments and one a passive magnetic system. The High Frequency Sounder (HFS) operates in the frequency domain and was designed for shallow environmental applications. The second, the Very Early Time ElectroMagnetic (VETEM) system, is a time domain electromagnetic (TEM) system designed for applications similar to those of the HFS. Of the two existing EMI prototypes the VETEM system was designed for and had been used for rapid profiling and subsequent mapping over waste pits at the Idaho National Laboratory (Abraham, Smith, and Wright, 2003). The HFS was originally seen as providing

detailed data more suitable for inversion, but the tradeoff was that originally the HFS was much slower than VETEM and could only operate while stationary. The passive magnetic Tensor Magnetic Gradiometer System (TMGS) was the third prototype system that we proposed be tested and evaluated for potential UXO applications.

### 5.1.1 The High Frequency Sounder

At the time of our first SERDP proposal in 2001, the HFS was capable of providing wide bandwidth information that we thought might prove beneficial in inverting for UXO target parameters. However, the HFS had never before been operated in a continuous profiling mode and for the sake of field efficiency, static-mode operation alone was insufficient.

#### 5.1.1.1 HFS Modifications

The HFS was furnished with a new antenna system, the same one used for VETEM and described below. In addition, new LabVIEW® data acquisition software, a new transmitting antenna driver, and new receiving loop amplifiers were designed and built. An Agilent 4395A Network/Spectrum Analyzer (10 Hz to 500 MHz frequency range) controlled by the LabVIEW® data acquisition software greatly speeded up HFS data acquisition and made it possible to take data continuously in profiling mode.

#### 5.1.1.2 HFS Laboratory and Field Tests

Laboratory tests at the USGS showed that the HFS was sensitive to metal objects, both ferrous and non-ferrous.

The HFS produced relatively good results over the Calibration Grid at the Yuma Proving Ground. We found that the data at frequencies over about 20 kHz included response to both the earth and the targets. Below 20 kHz the responses were due to the targets. Instrument shifts and drifts were evident in the data. Much of this was due to mechanical shifting in the closely coupled overlapped transmitting (Tx) and receiving (Rx) antennas. We found that a ratio of the quadrature (imaginary) to in-phase (real) data at 3 kHz did a good job of showing the targets after processing. An example of such HFS data is shown in figure 5.1.1.2.1.

VETEM and the HFS appear to have been approximately equal in target detection and both appear to have done about as well as some commercial instruments (EM-63 and GEM-3) in this regard, although we did not subject the data from the EM-63 or the GEM-3 to the same processing steps that we used for our prototype instruments. Since the HFS data rate was still not as high as that of the VETEM system, we elected to drop further development of the HFS in favor of the ALLTEM system. The results from the Calibration Grid can be compared to maps of the same area produced with VETEM, ALLTEM, and an EM-61 as shown in later sections.

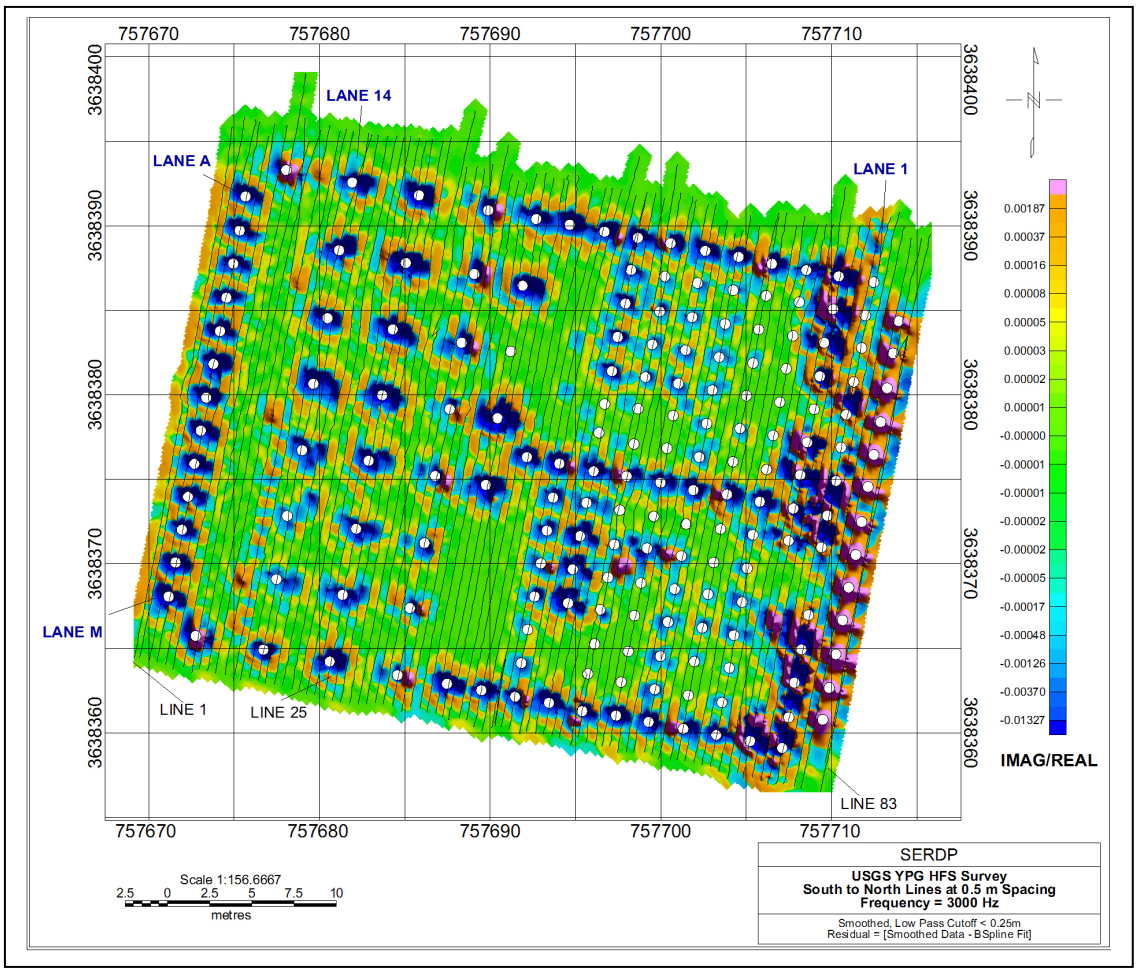


**Figure 5.1.1.2.1.** HFS 3 kHz surface map of the UXO Calibration Grid at YPG. The map shows the ratio of the imaginary to real components. Blue and pink areas represent targets that would be visible in the data. White dots show target locations and black lines show the locations of the data collection lines and are spaced approximately 0.5 m apart.

### 5.1.2 VETEM

Of the three existing prototypes, the VETEM system needed the least preparation for field tests because it had previously been operated in the field (Wright and Chew, 2000).

### 5.1.2.1 VETEM Modifications

The only significant modification that was made to the VETEM system was the development of an overlapping Tx-Rx loop pair with the amount of overlap finely adjustable to precisely null the primary field. This same antenna pair was also used for the HFS. Figure 5.1.2.1.1 shows the VETEM system in operation at YPG in 2003.


**Figure 5.1.2.1.1.** This photograph shows the VETEM system in operation at the YPG in 2003. The sub-compact tractor is advantageous because it is designed to operate at steady speeds.

### 5.1.2.2 VETEM Laboratory and Field Tests

Laboratory tests of the VETEM system showed good sensitivity to metal objects of both ferrous and non-ferrous types, as did the HFS (Wright et al., 2003). VETEM data collected over the Calibration Grid at YPG did exhibit sensitivity to targets, but target responses in the raw data were masked by both ground response and the effects of mechanical changes in the relationship between the Tx loop and the Rx loop. These competing effects are illustrated in figure 5.1.2.2.1. Figure 5.1.2.2.2 shows a map from processed data.

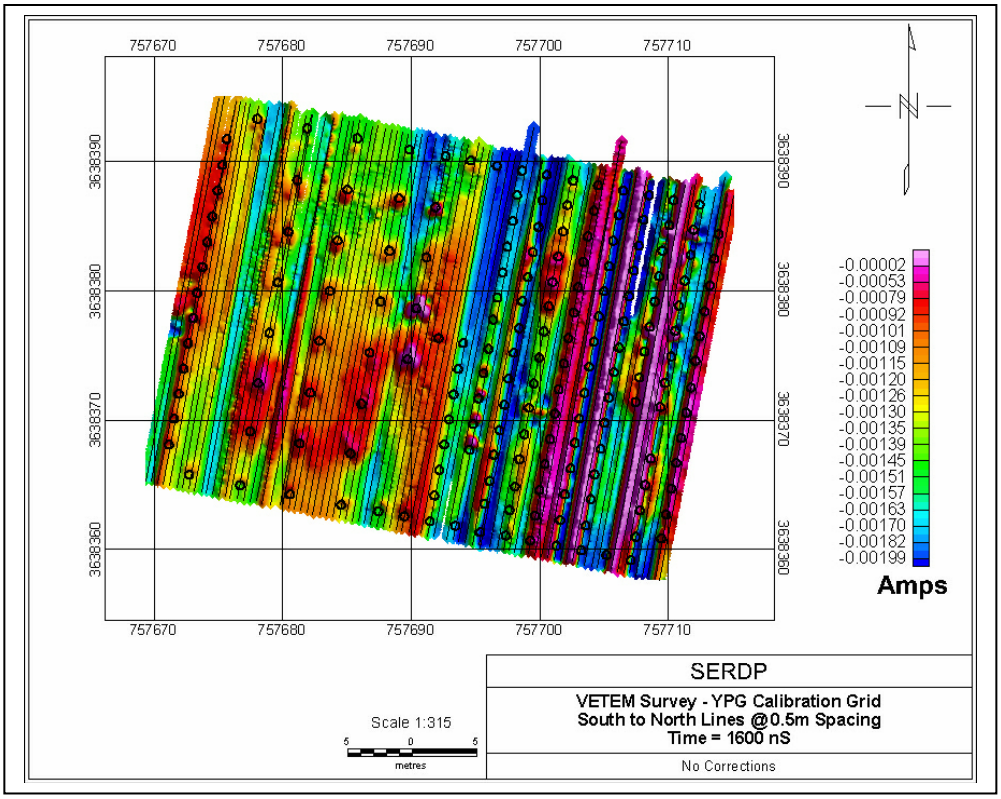


**Figure 5.1.2.2.1.** This figure shows raw VETEM data collected at the YPG Calibration Grid. Target responses are masked by both ground response and system level shifts.

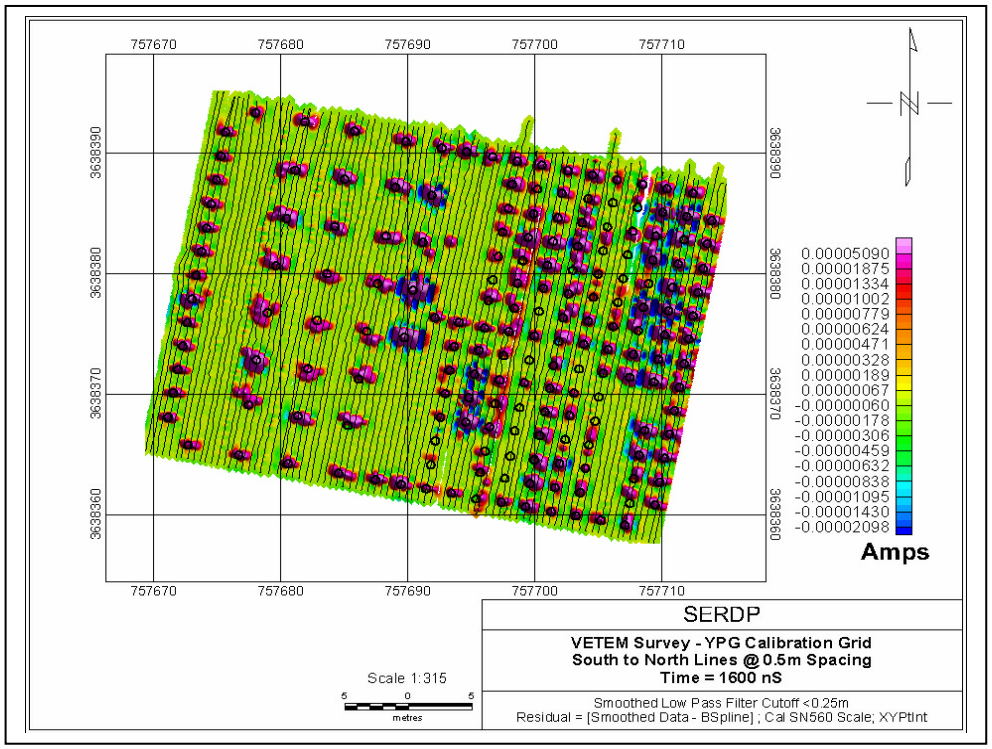


**Figure 5.1.2.2.2.** This VETEM map shows background removed data with good target sensitivity. Irregular target shapes are artifacts of GPS position errors.

By applying geophysical spatial filtering in which long wavelength changes are removed from the data we were able to produce a much improved map with the background removed as shown in figure 5.1.2.2.2. Although the map of figure 5.1.2.2.2 is a vast improvement over figure 5.1.2.2.1, the amount of post-processing to get from raw data to the background removed data is considerable. In addition, VETEM provides only single polarization data. Another problem is highlighted by the map of figure 5.1.2.2.2. Our position data were not sufficiently accurate to prevent noticeable distortion in the target patterns. The distortion is more than enough to defeat any attempt to invert or classify the data. The problem was caused by a combination of a slow GPS update rate and a software problem. Both the update rate and the software problem were solved before the 2006 tests discussed below.

### 5.1.3 The TMGS

The original TMGS used four three-axis fluxgate magnetometers mounted on a tetrahedral structure as shown in figure 5.1.3.1. TMGS was intended to measure gradients of vector components of magnetic fields. Like the HFS, the TMGS had only been used in static data acquisition mode when this project began. Magnetic vector gradient measurements have advantages over total field measurements including reduced motion noise sensitivity.

**Figure 5.1.3.1.** This figure shows the TMGS in its original tetrahedral configuration at YPG. The tow bar is 7 m long to reduce the effect of the tractor signature on the data.

## 5.2 ALLTEM and the Modified TMGS

### 5.2.1 ALLTEM

The ALLTEM system is unusual in that the Tx loops are driven by a continuous triangle current waveform and the resulting electromagnetically induced target responses are treated in the time domain. The measured quantity is the voltage in Rx induction loops. This is theoretically equivalent to an integration of the voltage measured by a conventional EMI system that relies on a rapid current turn-off in a Tx loop. Practically, the use of a triangle wave results in much smaller early-time voltages induced in the Rx loops, reducing dynamic range demands on the receiver. Another useful consequence is that ferrous and non-ferrous targets show distinctly different waveforms (figure 5.2.1.1 and Wright et al., 2005). The UTEM system developed at the University of Toronto some years ago was a pioneer in the use of a triangle waveform in EMI systems (West et al., 1984) and has a theoretical advantage of emphasizing highly conducting targets buried in a less conductive host (Smith and Annan, 1998). ALLTEM is intended to obtain the advantages of triangle wave excitation in a system whose dimensions, characteristics, and geometry are appropriate to UXO applications.

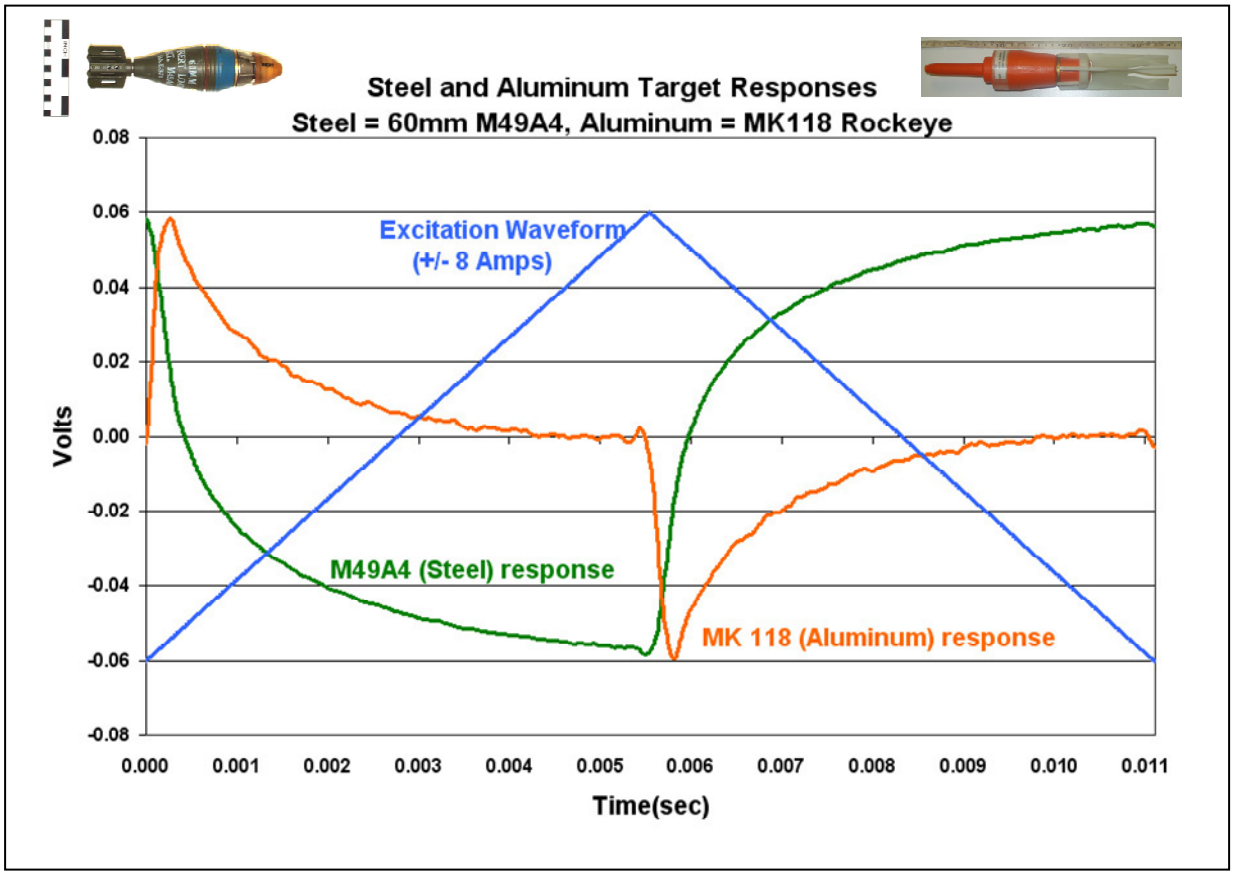


**Figure 5.2.1.1.** This figure shows a scaled Tx loop current waveform (blue) and Rx response waveforms from a mostly steel 60 mm M49A4, (green) and a mostly aluminum MK118 Rockeye (orange)

Beyond detection of metal objects, the ability to discriminate between UXO and non-UXO targets is a highly prized goal, because in many cases more than 70 percent of range clearance costs are attributed to digging up harmless scrap metal that could have been left in the ground. An ideal UXO EMI system would not only have a 100 percent probability of detection, but also the ability to perfectly discriminate between scrap metal and UXO. ALLTEM and other EMI systems distinguish between scrap and UXO based on size, shape, and material composition that determine the target responses. We have developed an algorithm to solve for three time-varying principal components of a target's "polarizability." These polarizability moments are characteristics of the target and if the data are of good quality and the inversion algorithm is adequate, these calculated parameters should be independent of the target's depth and orientation. Many UXO items are composites of ferrous and non-ferrous parts, but, unlike landmines, there is little incentive to eliminate ferrous materials, thus the great majority of UXO items have significant ferrous metal content. As we have already mentioned, a very useful consequence of the triangle waveform is an ability to distinguish between ferrous and non-ferrous metals in many cases. As a further aid to discrimination, we have designed ALLTEM with a multi-axis capability. There are three orthogonal Tx loops, an array of five Rx loops on the top and bottom of a 1-m cube, and Rx loops on each of the four vertical sides of the cube as shown in Figure 5.2.1.2. Voltage outputs of loops on opposite sides of the cube are subtracted to remove the large primary field response. Thus, the system measures secondary field differences.

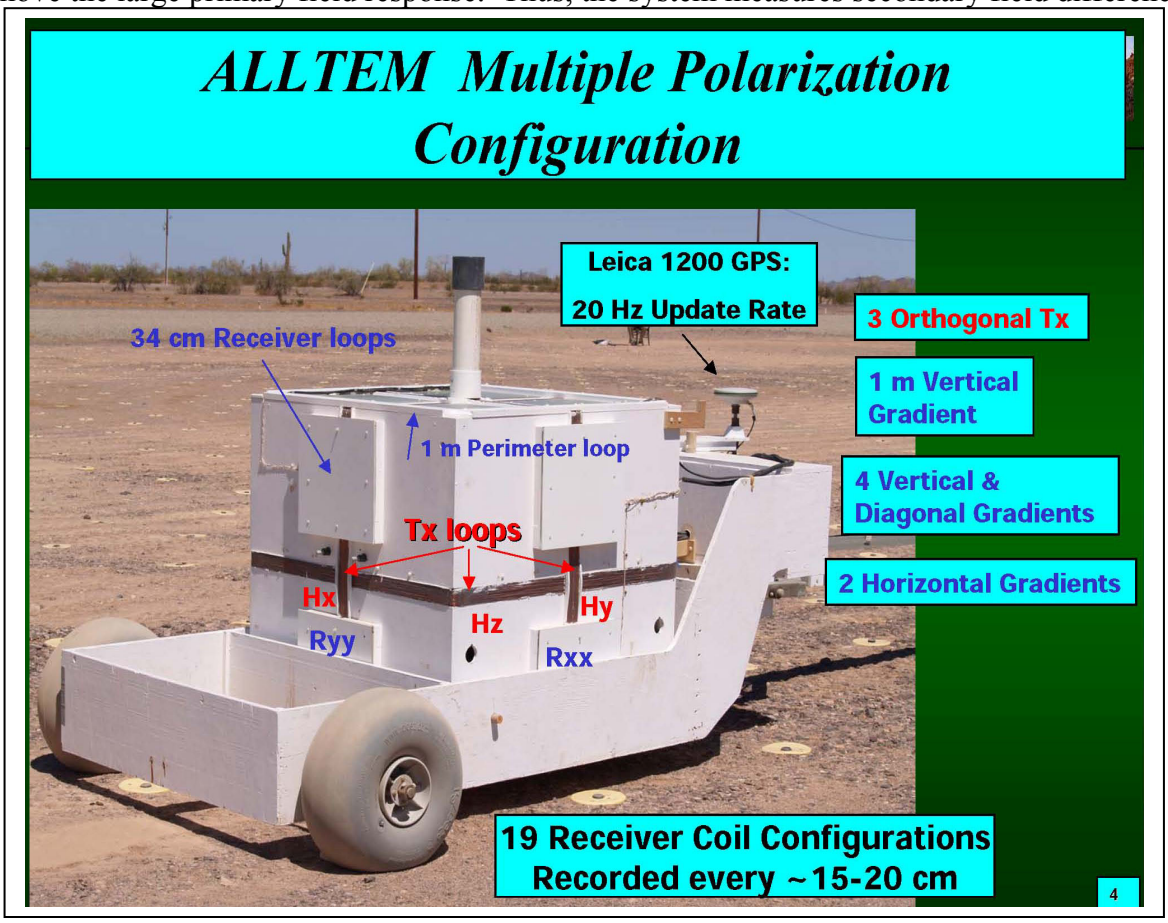


**Figure 5.2.1.2.** This annotated photograph of the ALLTEM system shows the three orthogonal square Tx loops and the square Rx loops of 1-m and 34-cm size.

Given the large number of possible transmitting and receiving coil pairs that can be combined, we developed a file naming convention that identifies which transmitting and receiving coils were used for a given data set. Figure 5.2.1.3 graphically illustrates the file-naming convention used for the ALLTEM YPG tests. Front, back, left and right are as viewed along the direction of cube motion (Y-axis). Each file had a unique file-name extension based on the following:

*First letter*: Direction of H field produced by drive coils:

X is perpendicular to the cube motion
Y is in the direction of the cube motion
Z is vertical, positive pointing up from the ground

*Second letter*: Axis that gradiometer Rx coils are measuring:

X field (gradiometer Rx coils on Left-Right (LR) sides of cube)
Y field (gradiometer Rx coils on Front-Back (FB) sides of cube)
Z field (gradiometer Rx coils on Top-Bottom (TB) sides of cube)

*Third letter or number*: Orientation of gradiometer Rx coils:

For small (34 cm) Rx coils measuring Z-axis fields:

Straight-Down Gradiometer:
1 = 1st quad of XY plane (Front Right (FR) position) FR top – FR bottom
2 = 2nd quad of XY plane (Front Left (FL) position) FL top – FL bottom
3 = 3rd quad of XY plane (Back Left (BL) position) BL top – BL bottom
4 = 4th quad of XY plane (Back Right (BR) position) BR top – BR bottom

Front-Back Gradiometer:
A = 1st quad of XY plane (FR position) FR top – BR bottom
B = 2nd quad of XY plane (FL position) FL top – BL bottom
C = 3rd quad of XY plane (BL position) BL top – FL bottom
D = 4th quad of XY plane (BR position) BR top – FR bottom

Diagonal Gradiometer :
E = 1st quad of XY plane (FR position) FR top – BL bottom
F = 2nd quad of XY plane (FL position) FL top – BR bottom
G = 3rd quad of XY plane (BL position) BL top – FR bottom
H = 4th quad of XY plane (BR position) BR top – FL bottom

Left-Right Gradiometer:
I = 1st quad of XY plane (FR position) FR top – FL bottom
J = 2nd quad of XY plane (FL position) FL top – FR bottom
K = 3rd quad of XY plane (BL position) BL top – BR bottom
L = 4th quad of XY plane (BR position) BR top – BL bottom

For large (1 m) Rx coils measuring Z-axis fields:

M = 1 meter coil

For Rx coils measuring X- and Y- axis fields (not illustrated in figure 5.2.1.3):

1= gradiometer across cube (small (34 cm) Rx coils)

Examples:

ZZM = Z-axis H field, Z-axis Rx gradiometer coils, 1m Rx coils
ZX1 = Z-axis H field, X-axis Rx gradiometer coils, 0.34 m Rx coils
ZXE = Z-axis H field, X-axis Rx gradiometer coils, 0.34 m Rx coils
diagonal gradiometer, 1st quadrant
XZM = X-axis H field, Z axis Rx gradiometer coils, 1 m Rx coils
XX1 = X-axis H field, X axis Rx gradiometer coils, 0.34 m Rx coils

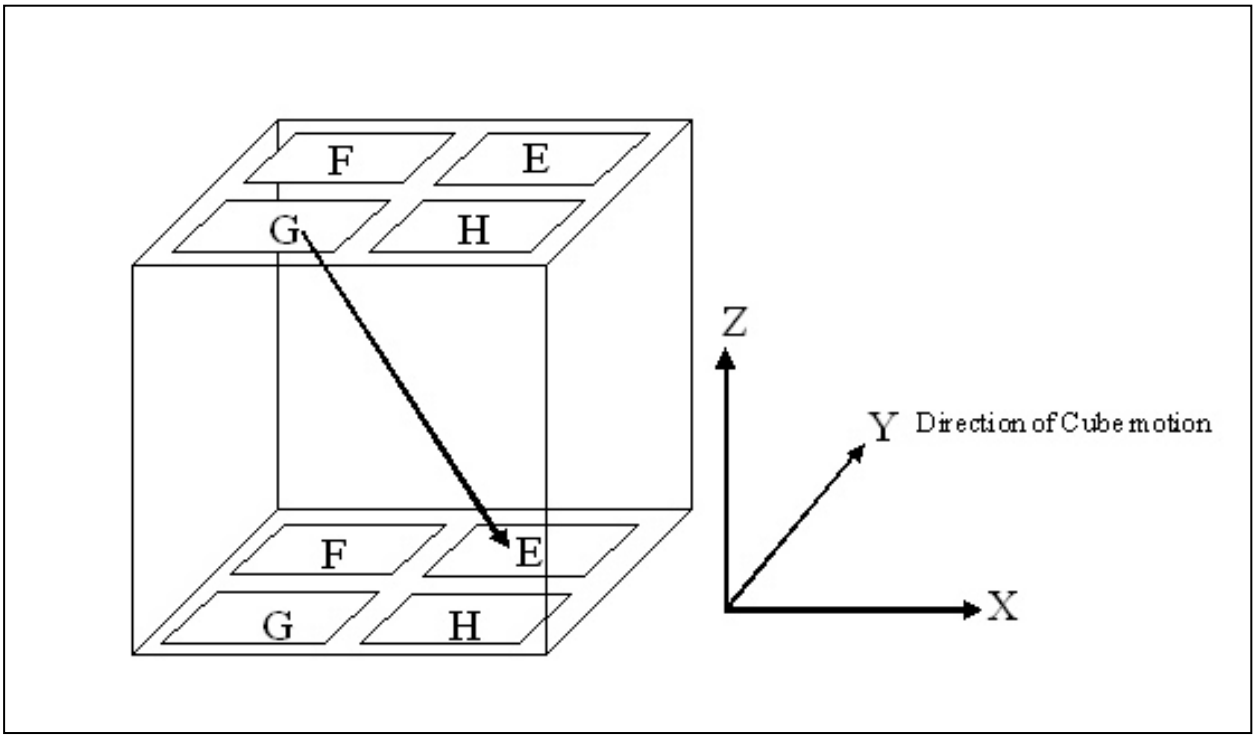


**Figure 5.2.1.3.** The arrow in this figure illustrates one possible diagonal gradiometer configuration with the small Rx coils. Files are named according to the location of the top antenna (e.g. ZZG file is the top (G) antenna minus the bottom (E) antenna).

At YPG, 19 of the possible configurations were recorded. These were XZE, XZF, XZG, XZH, YZE, YZF, YZG, YZH, ZZE, ZZF, ZZG, ZZH, ZX1, ZY1, XX1, YY1, XZM, YZM and ZZM. Some of these had better SNR than others.

The triangle waveform frequency can be varied, within limits, under software control, but for several reasons we settled on 90 Hz for field work. First, a half-period at 90 Hz is long enough to derive time decays for most UXO objects. Second, higher frequencies require higher driving voltages to maintain the same current amplitude. Third, averaging waveforms over three cycles at 90 Hz greatly reduces 60 Hz interference. To minimize 60 Hz interference, the triangle wave frequency should be $(n+1/2)\cdot 60$ Hz where "n" is an integer, for example: 30 Hz, 90 Hz, 150 Hz, and so forth. Finally, 90 Hz allows us to do some waveform averaging before recording, yet retain good spatial data density while moving at speeds up to or slightly faster than 1 m/s.

The Tx loops are each 63 turns and the current waveform that we apply to these loops is symmetric about zero amperes. The amplitude is variable under software control, but we generally run using a peak amplitude of 8 A. The peak Tx loop moment in this case is thus about 500 $A\cdot m^2$. Each Rx loop has 200 turns. A higher voltage gain is applied to the 34-cm Rx loop outputs than to the 1-m Rx loops so that the voltage inputs to the digitizer for the same target are comparable.

The digitizer has eight simultaneous channels digitizing to 24 bits at a rate of 100 kilo samples/s. The 90 Hz triangle wave frequency is derived from the digitizer clock frequency to keep everything phase locked. The three-cycle averaged data may be further averaged under software control from one to 10 times before recording. A spatial data interval of 20 cm or less is used for each recorded channel along a line to ensure that each Rx gradiometer loop pair has more than one "look" at even the smallest and shallowest target it may pass over.

The data acquisition software, written in National Instruments LabVIEW®, allows the operator to select the receiver channel(s) to display in real time and view raw waveforms of any polarity and/or a strip-chart style display of sums and differences between amplitudes near the beginning and end of the waveforms. The latter style can be useful for ferrous/non-ferrous target discrimination. All viewing options are also available when playing back recorded data. Figure 5.2.1.4 shows one of the many possible displays.

It is common for TEM systems to implement one or several "time-gates" with digital or analog signal averaging to improve the SNR in each time gate. However, we have chosen to record all the points along the waveforms at the full 10 μs/sample rate. This is possible because mass storage has become inexpensive and the data rates can be managed. After waveforms are recorded, any desirable form of digital data processing can subsequently be implemented. To improve SNR we may average waveform groups, while retaining all the points along the waveforms, provided that we retain adequate spatial data density while doing so. Summation averaging of waveforms before writing to mass storage also reduces file sizes.

In order to most faithfully preserve waveform shapes it would be ideal to dispense with all analog hardware filters, but in most environments, especially the noisy Denver metropolitan area, we find that we cannot remove all filters. Three types of hardware filters exist in the system. A high-pass filter, not used when multiplexing, with a cut-off at 0.1 Hz may be used to block any amplifier DC offsets. A Bessel two-pole low-pass filter, designed for little or no overshoot when a voltage step is applied, and whose cutoff frequency is selectable at approximately 5, 7, 17, or 90 kHz, limits high-frequency noise.

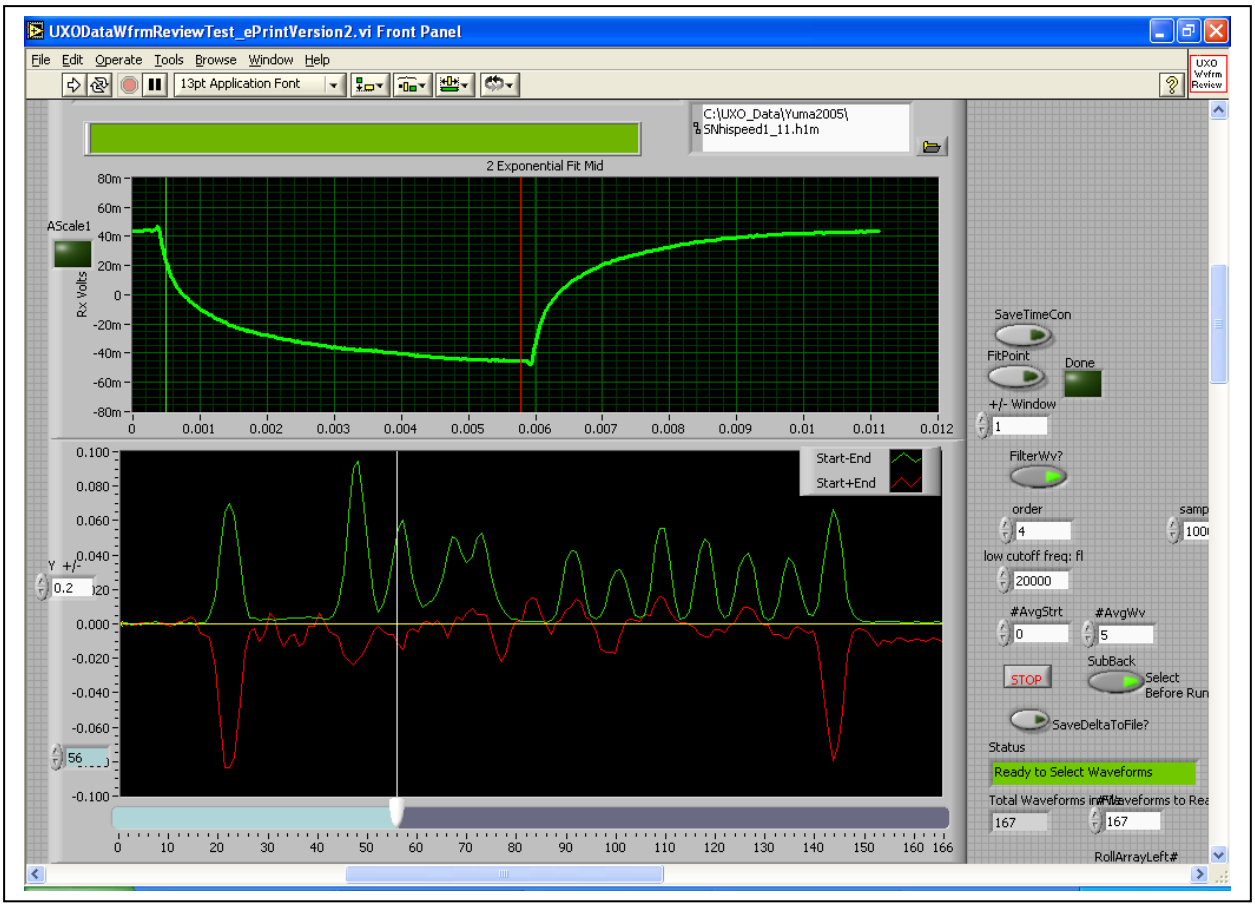


**Figure 5.2.1.4.** This figure shows one example display screen available in the LabVIEW® data acquisition and processing software. One waveform from a profile (line) is shown in the top panel with two cursors set, one near the beginning of the waveform (green) and one near the end (red). The bottom channel shows the result of plotting the difference (green curve) and the sum (red curve) along the entire line of data. When red and green lines move with opposite polarities this typically indicates a ferrous target. When the curves do not move in opposition this typically indicates a non ferrous or mixed composition object although this indicator can be influenced by target shape and orientation.

We almost always use 5, 7, or 17 kHz to reduce radio interference, including Very Low Frequency (VLF) stations in the 20+ kHz range. There is also a 60 Hz hardware notch filter to further reduce 60 Hz interference. When possible, we avoid using the 60 Hz filter because it introduces significant distortion "droop" on the recorded waveforms. The digitizer we are using has a powerful 50 kHz low-pass 8th order "brick wall" filter to prevent any possible aliasing. Some researchers have noted that this brick wall filter distorts fast time-domain transients. We have not encountered this because with our triangle wave and our low-pass hardware filters, we have almost no spectral content exceeding 50 kHz. Figure 5.2.1.5 illustrates the hardware and software filtering and processing steps. Several of these steps are done in real time prior to digital recording. At least once a day and perhaps more often we back up the data recorded on the ALLTEM system computer and transfer that data to a second computer for post-processing and inversion as will discussed more thoroughly in section 5.4.

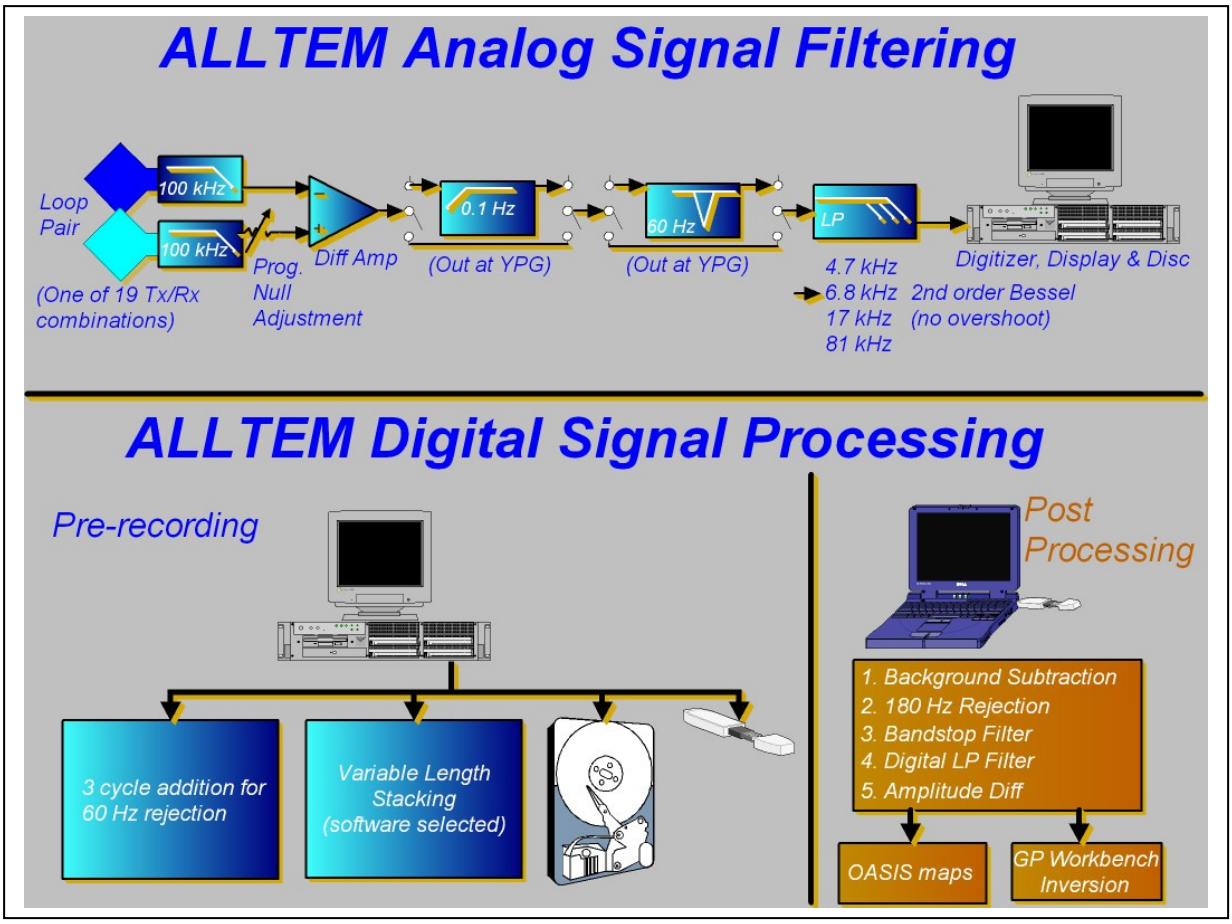


**Figure 5.2.1.5**. This schematic shows analog signal filters and digital processing steps. We typically average waveforms prior to recording, both to improve the SNR and to reduce the volume of recorded data. However, there is a trade-off between real time signal averaging and spatial data density. Our practice has been to maintain a spatial data interval for each recorded Tx-Rx combination that does not exceed about 20 cm. This specification is being examined using test stand data discussed in section 5.5 and in appendix A of this report.

### 5.2.2 TMGS

The original tetrahedral geometry, suitable for stationary geomagnetic observations, was not optimal for UXO surveys on a towed platform. Following computer simulations of possible array geometries, we settled on a planar array with the fluxgate heads positioned in a cross-array. This simple arrangement makes calculation of the gradients straightforward (divide the measured field values of diametrically opposed components by their separation distance), and places the calculated gradients in the plane of the array, approximately co-located at the array center. Experimental data in a magnetically shielded quiet room determined that the sensors could be operated as close as 0.25 m without uncompensatable cross-talk and interference. In order to keep the sensor geometry in a fixed frame of reference, the sensor heads were affixed to a 0.5-m diameter, 5-cm thick vitreous-ceramic base-plate which has a very high modulus (72 GPa) and a very low thermal expansion coefficient ($2.8 \times 10^{-6}$ per degree F). The base plate was mounted on a fiberglass honeycomb panel with an intervening pad of viscoelastic material (Sorbothane). This

arrangement distributed supporting stresses uniformly and relieved (decoupled) mechanical strains from the underlying platform, which, being made of wood, tended to flex. The array assembly is shown being centered and aligned in the cargo bay of the platform in figure 5.2.2.1.

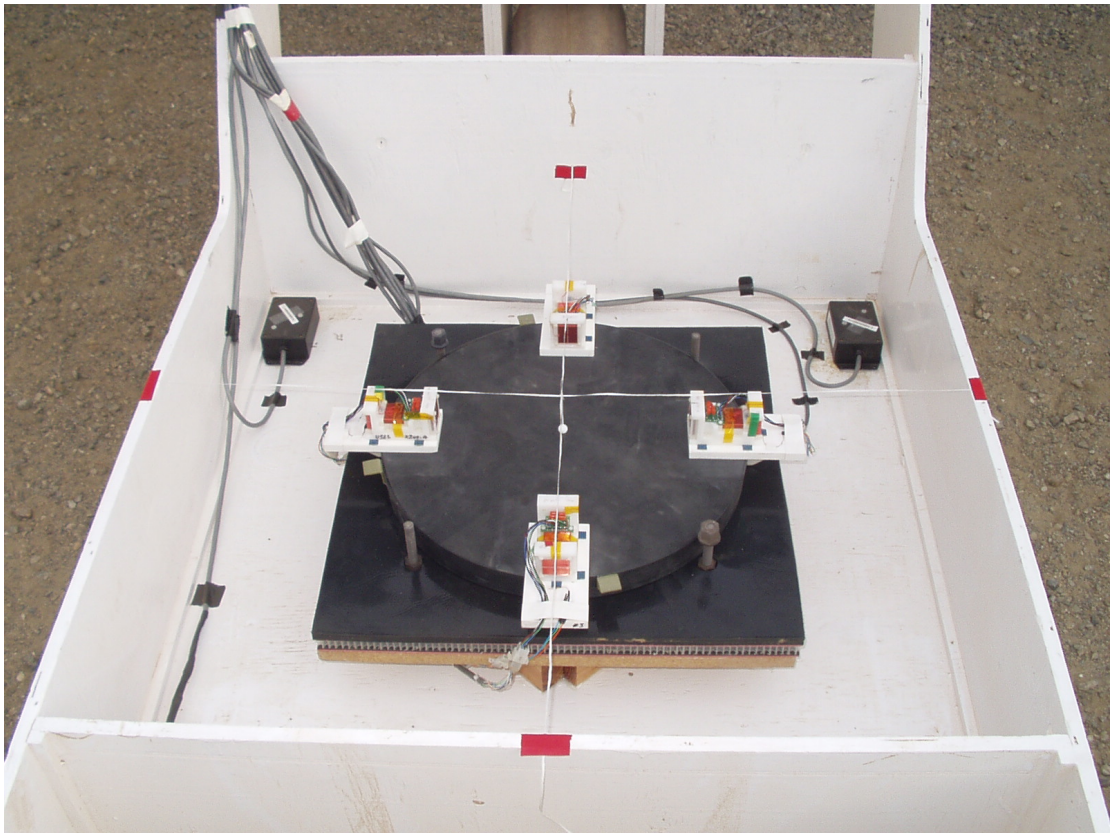

**Figure 5.2.2.1.** The magnetometer array mounted in the towed platform during alignment. The magnetometer heads are (clockwise from top): Head 1, Head 2, Head 3, and Head 4.

Two solid-state three-axis accelerometers were installed in the cargo bay forward of the array (black boxes in figure 5.2.2.1). This was to provide data on platform shocks and vibrations which could be used to correlate with, and thus identify, any motion-induced noise in the magnetometer channels.

A two-axis inclinometer was installed in the cargo bay aft of the array. This unit measured the roll and pitch angles during the survey. Because the GPS receiving antenna was mounted over the front wheel of the platform, about 1.4 m forward of the array and about 1.4 m above the ground, tilting of the platform would cause the position of the antenna to change. Recorded GPS positions would therefore differ from the true position of the sensor array, which would sway less than the Rx antenna because of its closeness to the ground (0.67 m). Given the fixed array-Rx geometry of the platform, inclination data would provide precise positions for the array itself.

Because the GPS and the data acquisition system operated asynchronously, we recorded separate GPS and magnetometer data files. The records in each file were time-tagged to allow synchronization of the two data sets in post-processing.

The data acquisition system was upgraded to a National Instruments (NI) PXI chassis which holds a computer motherboard, sample-and-hold (S/H) boards, and a 40 channel 24-bit digitizer board. Data acquisition was controlled by LabVIEW® software. Data were acquired at 1,000 samples per second, as this was the lowest rate provided by the S/H clock. A system block diagram of the complete modified TMGS is shown in figure 5.2.2.2.

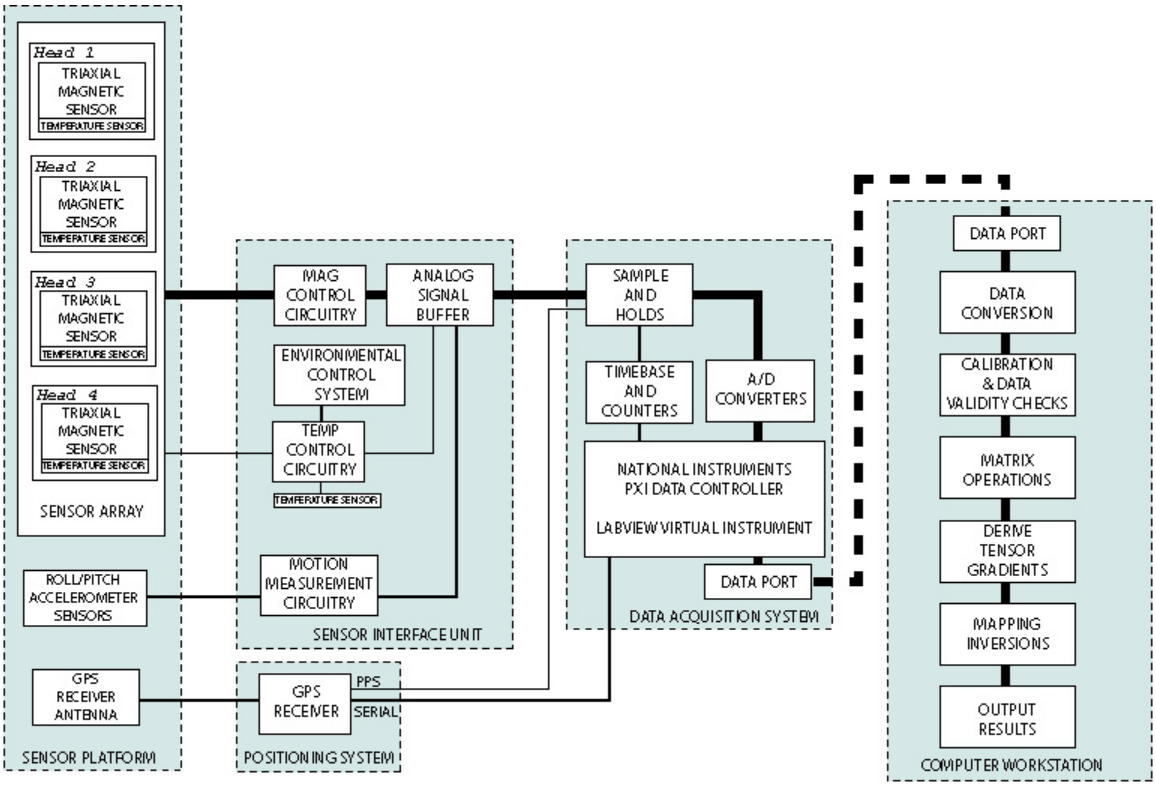


**Figure 5.2.2.2**. Modified TMGS System Block Diagram showing the five major components (dashed, shaded boxes). Major and minor data paths are indicated by thick and thin lines, respectively. The computer workstation (on right) is independent of the other components, which operate together in real time. Data are transferred to the computer workstation using portable storage media, such as an external hard disk drive. A TMGS data file contains the following data channels:

**Table 5.2.2.1**. TMGS data file header

| NI Channel Number | Channel Name | Description |
|---|---|---|
| 1 | UTC-Time | Julian seconds |
| 2 | Head4-Z | Bin Number |
| 3 | Head4-Z | Error Signal |
| 4 | Head4-Y | Bin Number |
| 5 | Head4-Y | Error Signal |
| 6 | Head4-X | Bin Number |
| 7 | Head4-X | Error Signal |
| 8 | Head3-Z | Bin Number |
| 9 | Head3-Z | Error Signal |

| | | |
|---|---|---|
| 10 | Head3-Y | Bin Number |
| 11 | Head3-Y | Error Signal |
| 12 | Head3-X | Bin Number |
| 13 | Head3-X | Error Signal |
| 14 | Head2-Z | Bin Number |
| 15 | Head2-Z | Error Signal |
| 16 | Head2-Y | Bin Number |
| 17 | Head2-Y | Error Signal |
| 18 | Head2-X | Bin Number |
| 19 | Head2-X | Error Signal |
| 20 | Head1-Z | Bin Number |
| 21 | Head1-Z | Error Signal |
| 22 | Head1-Y | Bin Number |
| 23 | Head1-Y | Error Signal |
| 24 | Head1-X | Bin Number |
| 25 | Head1-X | Error Signal |
| 26 | N/A | Broken pin |
| 27 | Temperature | Head-3 |
| 28 | Temperature | Head-2 |
| 29 | Temperature | Head-1 |
| 30 | Temperature | Internal |
| 31 | Temperature | Ambient |
| 32 | Tilt | Pitch |
| 33 | Tilt | Roll |
| 34 | Accelerometer 1 | X |
| 35 | Accelerometer 1 | Y |
| 36 | Accelerometer 1 | Z |
| 37 | Accelerometer 2 | X |
| 38 | Accelerometer 2 | Y |
| 39 | Accelerometer 2 | Z |
| 40 | PPS | Waveform |
| 41 | Temperature | Head-4 |

Note that each magnetic component has two channels: Bin Number and Error Signal. In order to maximize sensitivity over a limited dynamic range of output voltage, a bucking current is used to partially cancel the magnetic field inside the fluxgate core. This current is applied in steps, with each step corresponding to a discrete interval of magnetic field strength. For example, if each step represents 500 nT, then Bin Step 21 equals a bucking field of 21 times 500, or 10,500 nT. Thus, Bin Step 21 can measure between 10,500 and 11,000 nT, outside of which it switches to a different (either higher or lower) Bin Step. On top of the bucking field is the residual (un-bucked) magnetic field in the core. This Error Signal is proportional to this uncancelled field, nominally 1 volt per 100 nT. Following this scheme, a Bin Step of 21 and Error Signal of 1.37 volts equals a magnetic field value of 10,637 nT. A magnetic field slightly greater than 11,000 nT, say 11,003.1 nT, would trigger a switch to Bin Step 22 and an Error Signal of 0.031 volt. The determining formula is:

$$B(nT) = (nT / Bin\_Step) \times Bin\_Step + (nT / volt) \times Error\_Signal \qquad (5.2.2.1)$$

where the value for the coefficient (nT/Bin Step) is specified by the manufacturer for each magnetometer interface circuit board. The coefficient (nT/volt) we used for the Error Signal was *not* based on the specifications, but rather was determined empirically from spin calibration data.

### 5.3 Tests at YPG

We tested both ALLTEM and the TMGS in 2005 and 2006 at YPG. In 2005 we tested over the Calibration Grid only. In 2006 we again ran ALLTEM at the Calibration Grid and ran both ALLTEM and the TMGS over the Blind Test Grid. A map of the targets in the Calibration Grid as of 2005 is in figure 5.3.1.

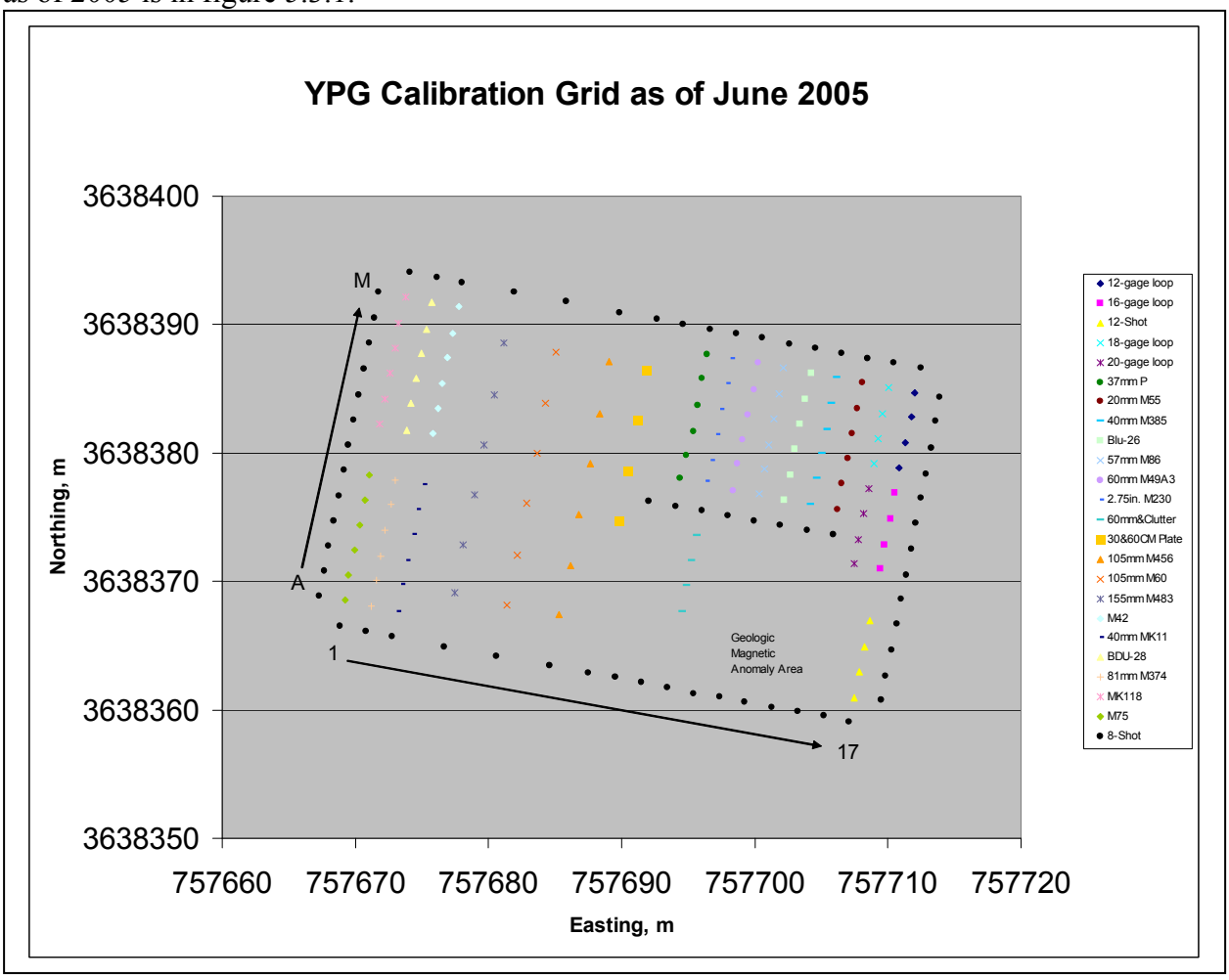


**Figure 5.3.1.** This map shows the targets buried in the YPG Calibration Grid as of 2005. Figure courtesy of the U.S. Army.

### 5.3.1 ALLTEM at YPG

In 2005 we operated ALLTEM over the Calibration Grid and recorded data with several of the possible Tx-Rx combinations. An example amplitude map for the vertical excitation and observation polarization (ZZM) case is shown in figure 5.3.1.1. Although almost all of the targets are detected, many of the target spatial response shapes are distorted. This is due to GPS positioning errors from two sources: (a) a software error involving an improper data buffer clear operation, and (b) a relatively low update rate (1 per second) on the GPS. We did notice and call to the attention of the Army an anomaly near cell D4. It can be seen more distinctly in one of the horizontal polarizations as shown in figure 5.3.1.2.

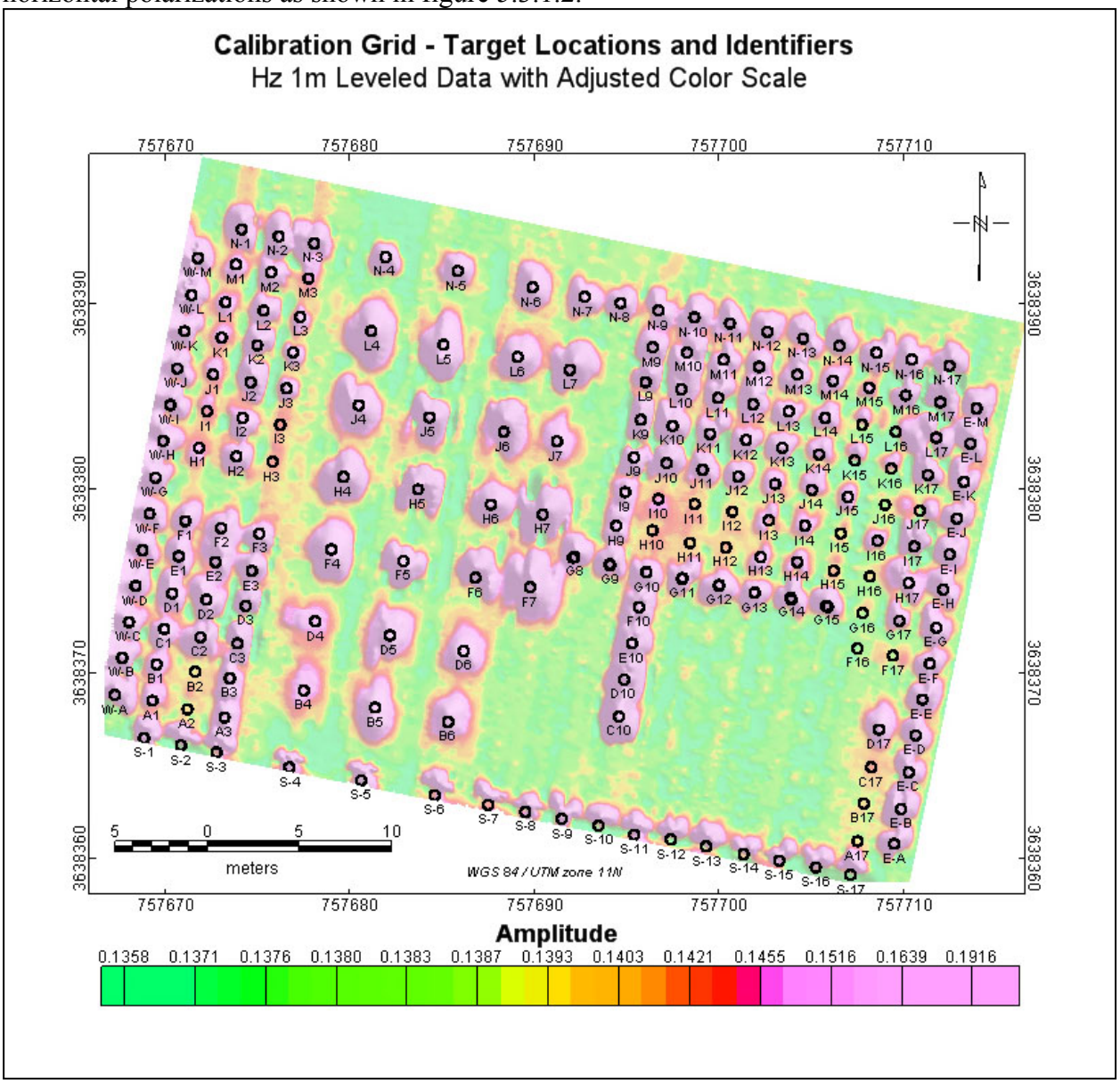


**Figure 5.3.1.1.** This map is a leveled data amplitude map overlaid with the Calibration Grid cell designations provided by the U.S. Army. All but a few of the targets are clearly detected.

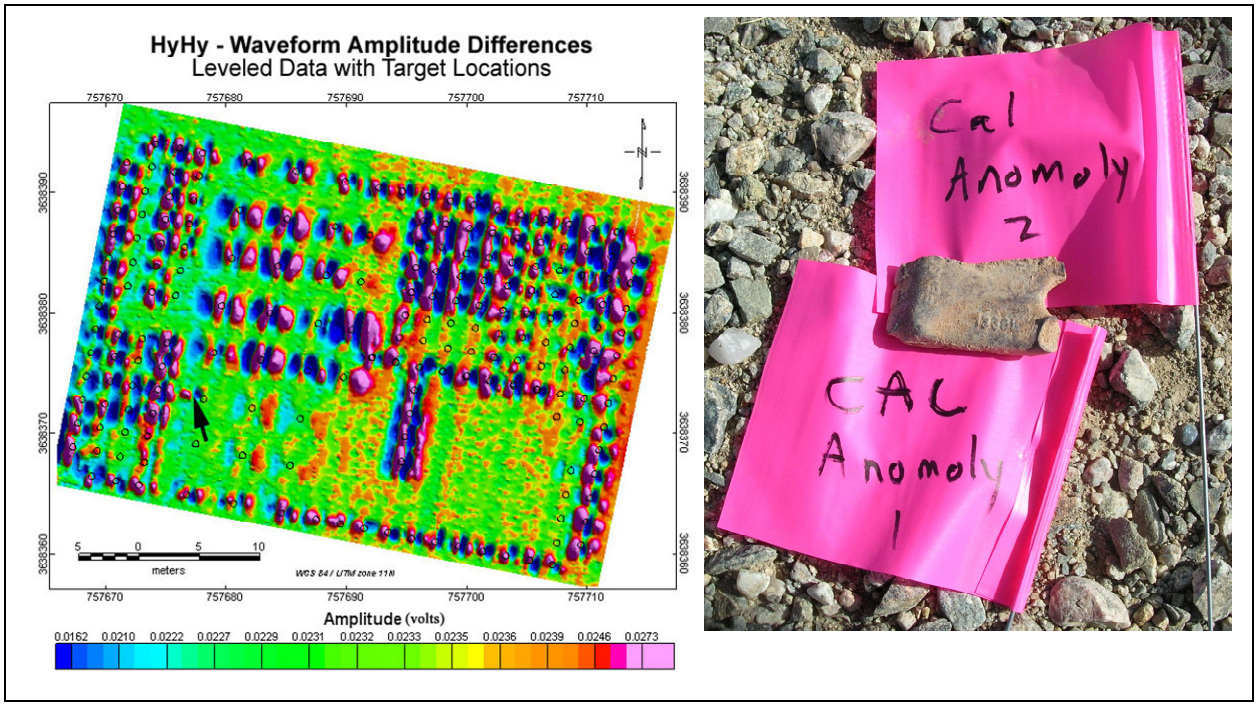


**Figure 5.3.1.2.** The amplitude map on the left is from y-component horizontal data. The arrow indicates the location of an undocumented anomaly near cell D4 (figure 5.3.1.1). The anomaly was later verified by the Army and turned out to be a broken tooth from a backhoe used to dig the hole for burying the intended target. The broken tooth is shown in the photograph on the right.

The ragged shapes of the target responses due to the position errors in the data stream are not serious enough to materially degrade detection, but they are large enough to cause serious problems with attempts to invert the data.

Between 2005 and 2006 the Crustal Imaging and Characterization Team of the USGS invested in a new Leica 1200 RTK-GPS system that has a 20 Hz position update rate, as opposed to the 1 Hz update rate of the Javad RTK-GPS that we used in 2005. We switched to the Leica 1200 system and determined that the Leica positions were accurate to within 2 cm, even in profiling mode, when the "fixed" data quality was achieved. However, in ALLTEM tests just prior to our scheduled visit to the YPG in 2006 we ran some final shakedown tests and discovered that we still had significant position errors when running the full data acquisition software. We postponed our trip and traded a week of time with the Lawrence Berkeley Laboratory group. We also changed our initial plan to deploy ALLTEM prior to the TMGS and did the reverse, deploying TMGS first. We discovered that a position data buffer "clear" operation, that should have happened only at the start of each recorded file, was improperly continuing throughout data acquisition with the consequence that some position data were lost and the asynchronous position data were not always associated with the correct sensor data. This was quickly fixed and we then deployed ALLTEM to YPG.

In addition to the RTK-GPS upgrade and acquisition software fix noted above, we added four Rx coils to the sensor cube, replaced troublesome wheel bearings with ceramic bushings, modified

the cart towing yoke assembly, and abandoned solid foam-filled tires. The latter two changes were adopted because we had noted that the cart would not pull in a very straight line behind the tractor so that the line coverage was not very uniform. The coverage in 2006 was much better than in 2005. Figure 5.3.1.3 shows ALLTEM in operation at YPG in May, 2006. The mid-day temperatures sometimes reached 106$^{o}$ F. The tractor was newly equipped with a sun shade and a canvas tarp was draped over the electronics racks and periodically wetted to gain some evaporative cooling. When these measures were taken we were able to operate even in the mid-day heat. We also found it necessary to add air to the cart's very low pressure tires (2 – 4 psi above ambient) in the morning and bleed the tires later in the day as they heated.

**Figure 5.3.1.3.** The ALLTEM system in operation at YPG in May, 2006.

### 5.3.1.1 Comparisons of ALLTEM Data to EM61-MK2 Data

As an action item, we had been requested to provide comparisons between ALLTEM and EM61-MK2 data. Figures 5.3.1.1.1, 5.3.1.1.2, 5.3.1.1.3, and 5.3.1.1.4 show example amplitude maps from EM61-MK2 data and ALLTEM data collected in May 2006 at the Calibration Grid at YPG. Figure 5.3.1.1.1 shows a raw data map of EM-61 data. Figure 5.3.1.1.2 shows a similar raw data map of ALLTEM data using the ZZM (vertical component, 1 m coils). Figures 5.2.1.1.3 and 5.3.1.1.4 show the best processed data acquired for the EM-61 and ALLTEM ZZM component.

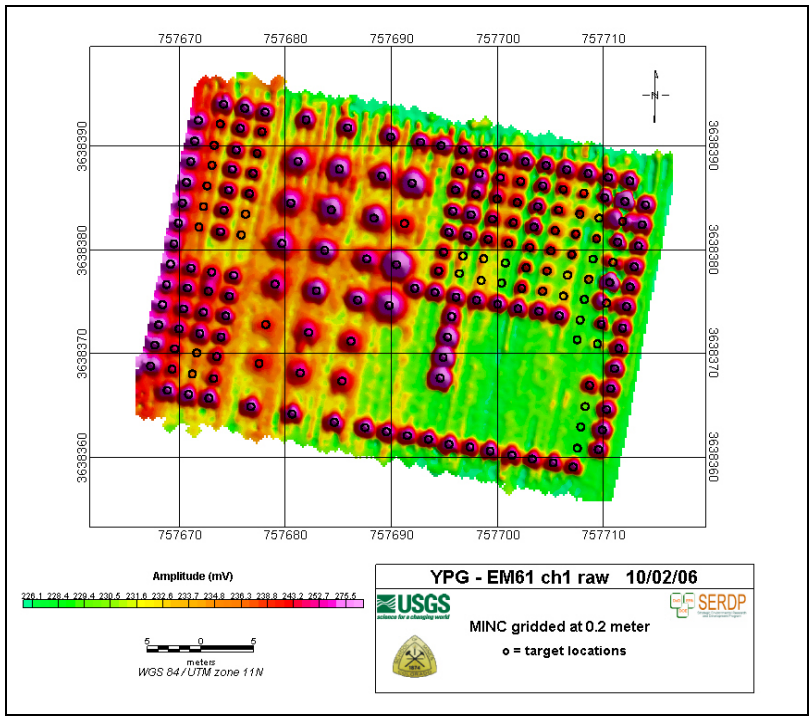


**Figure 5.3.1.1.1**. EM61-MK2 channel 1 raw data map of the Calibration Grid. EM61 data are mapped using the same minimum curvature and 0.2 m gridding as was applied to the ALLTEM data. Open circles indicate target locations supplied by the Army.

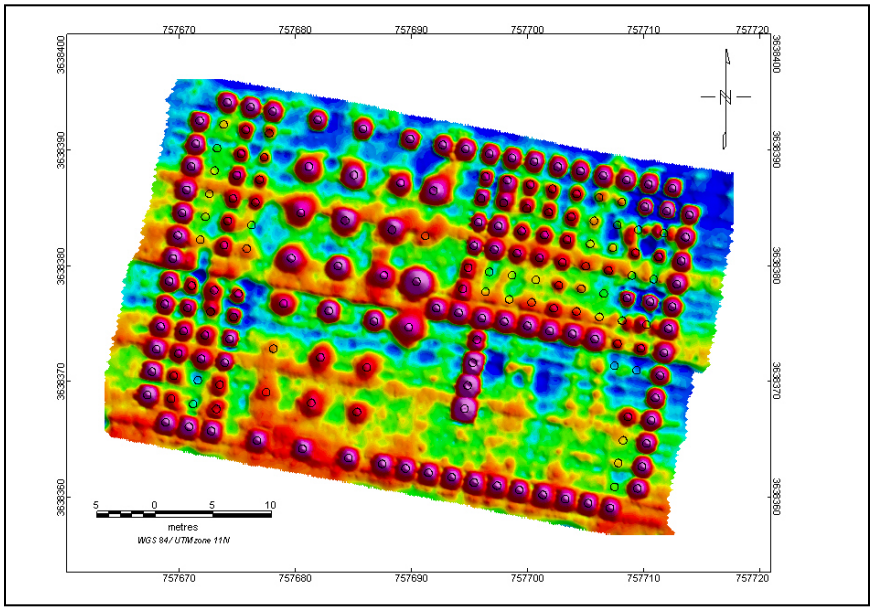


**Figure 5.3.1.1.2**. ZZM component raw ALLTEM data map analogous to the previous figure for the EM61. The lines were run orthogonal to those used for the EM61, but the line spacings were both 0.5 m and the operating speeds were similar.

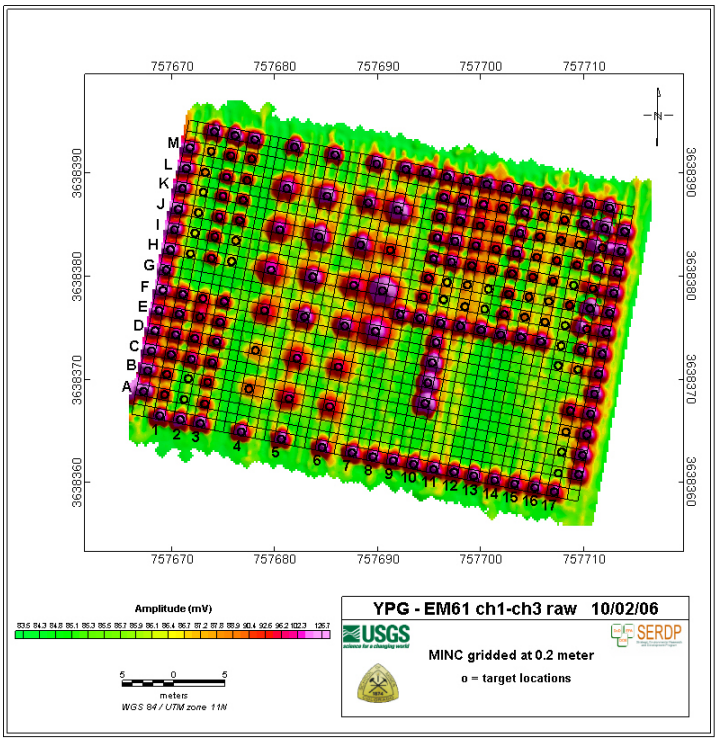


**Figure 5.3.1.1.3**. This figure shows the best EM61-MK2 processed data that we obtained. Differencing the channel 1 and channel 3 data effectively removed the system drift.

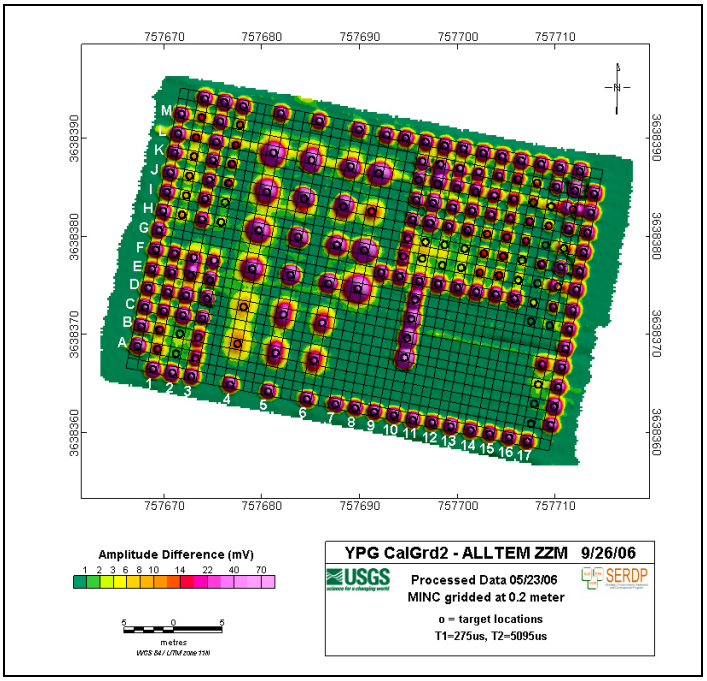


**Figure 5.3.1.1.4**. This amplitude difference map of the ZZM component of ALLTEM data reveals a level of target detection that is at least equal to that of the EM61-MK2 shown in the previous figure.

### 5.3.1.2 Selected ALLTEM Data Maps

Here we show a few maps of selected polarizations collected over the Calibration Grid and over the Blind Test Grid in May, 2006. The full set of data maps is included in our 2006 YPG report (Wright et al., 2006, http://www.serdp.org/Research/upload/MM-1328-IR-YPG-2006.pdf).

Figure 5.3.1.2.1 shows the ZZM data over the Calibration Grid. This is the same map as figure 5.3.1.1.3 without the cell grids and with the line trajectories shown. The coverage is good. The minor deviations of the lines are mostly from the slight unevenness of the ground.

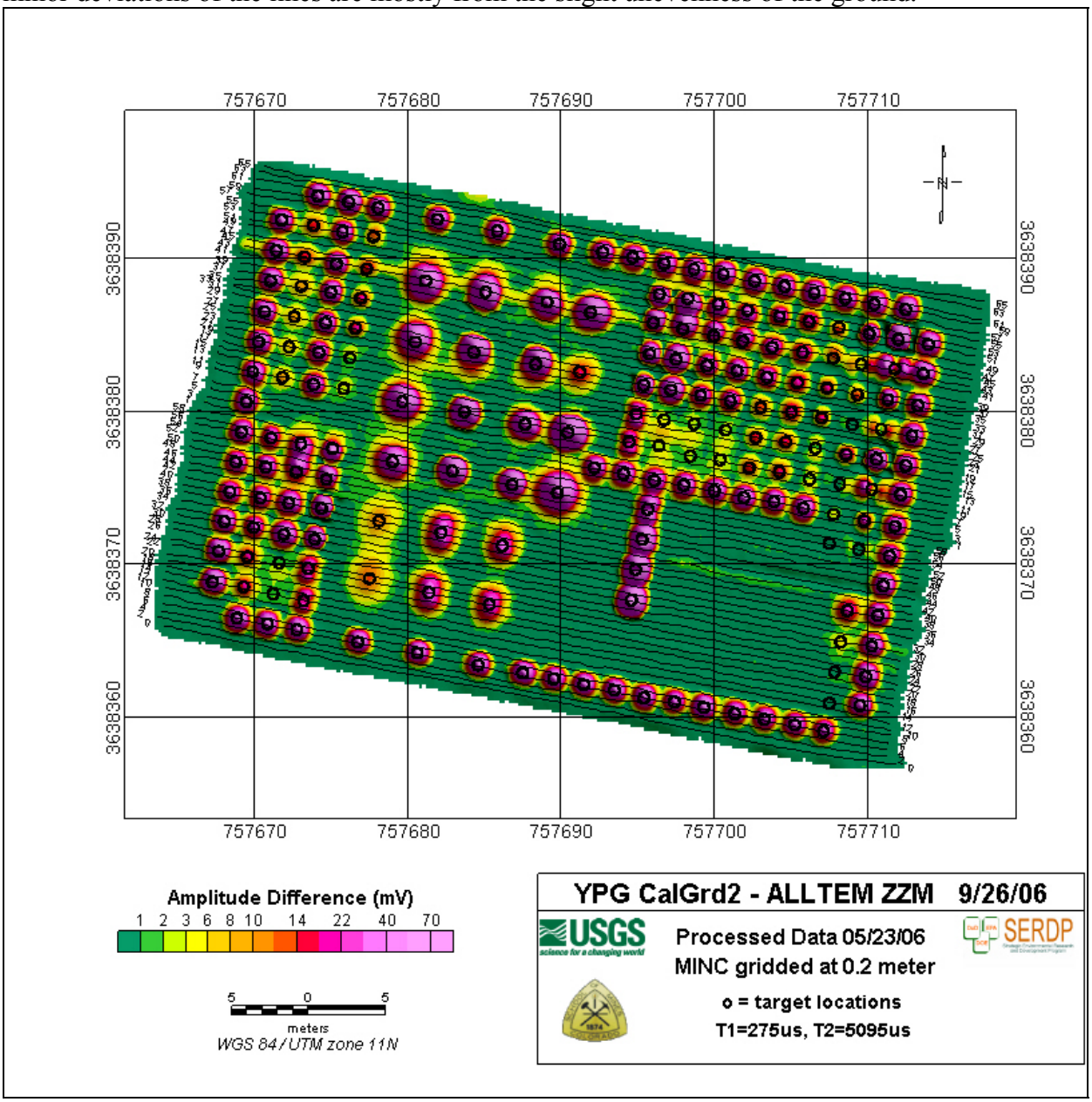


**Figure 5.3.1.2.1.** This figure shows the line trajectories overlaid on the ZZM component amplitude difference map. The cart was tracking well behind the tractor. Minor wiggles in the lines are mostly from some small topography variations on the Calibration Grid.

Figure 5.3.1.2.2 shows the ZZG polarization map. This map uses the same Z-axis excitation as in the previous figure, but instead of using the large 1-m perimeter Rx loop receiver, it uses one of the 34 cm diagonal Rx loop combinations as shown in figure 5.2.1.2 above and discussed in the text near that figure.

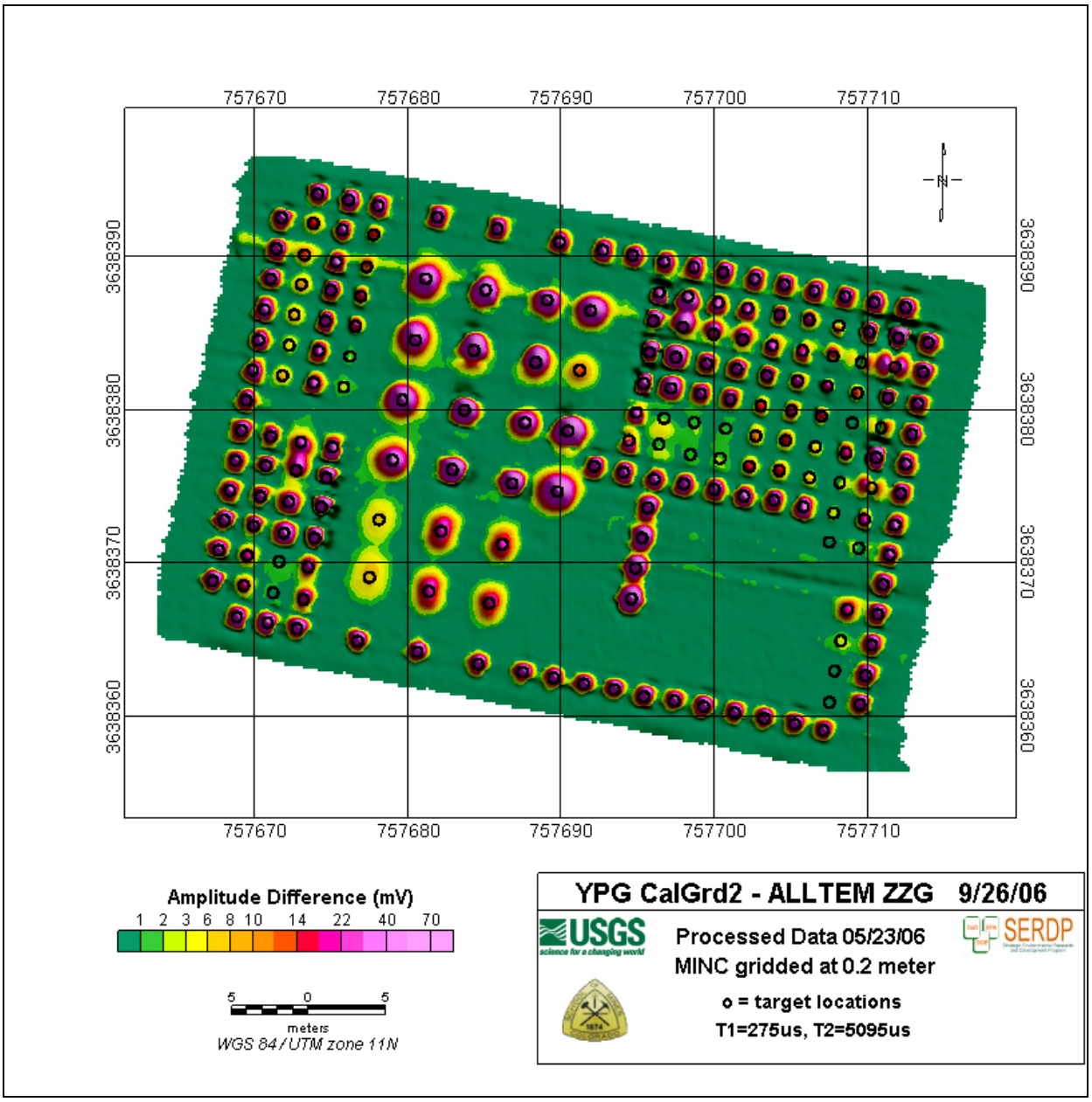


**Figure 5.3.1.2.2**. The map in this figure is very similar to that of the previous figure except that the use of one of the smaller Rx loops sharpens some of the shallower target patterns. In a few instances there is a slight loss of signal amplitude with the smaller coils, although the electronic gain applied to them is greater than for the large 1-m coils, but for most targets the SNR is still very good.

Figure 5.3.1.2.3 shows the XX1 polarization that uses the X-directed magnetic field excitation and observes the X-directed received secondary field component. Note that there are two targets highlighted with ellipses and arrows. The target indicated by the black arrow is a boundary marker sphere that has a vertical rotational axis of symmetry (for a sphere, every axis passing through the center is an axis of rotational symmetry).

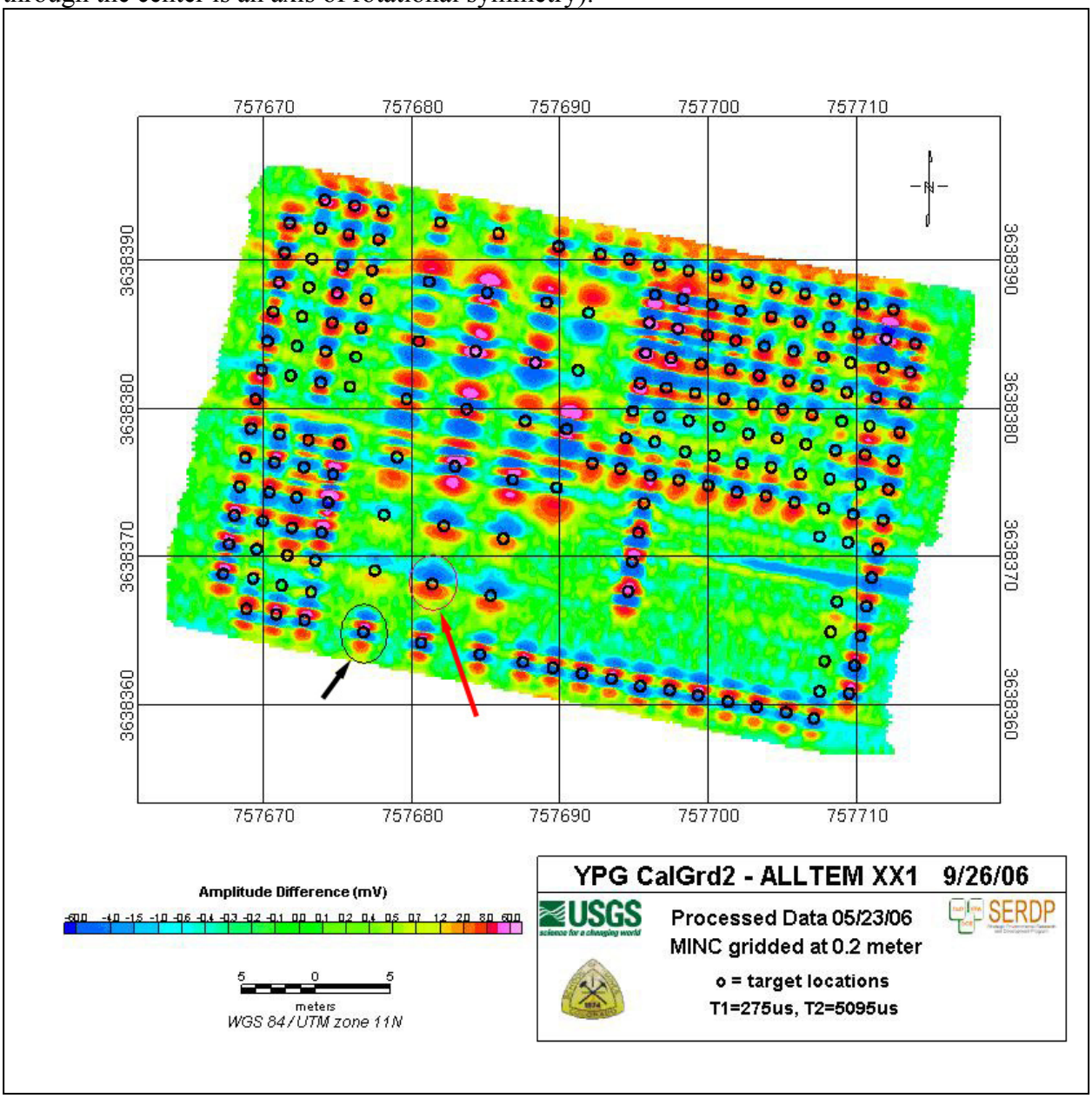


**Figure 5.3.1.2.3**. This map of the XX1 data recorded over the Calibration Grid has two targets highlighted with red and black ellipses and arrows. These may be compared to the YY1 component in the following figure.

Figure 5.3.1.2.4 shows the YY1 map, again with two targets highlighted. Note that for the boundary marker sphere the pattern is the same except rotated counterclockwise by 90 degrees. However the target highlighted by the red arrow is a 105 mm projectile that is buried horizontally. Since the axis of rotational symmetry of the projectile is not vertically oriented, the pattern is not a rotated version of the XX1 field component.

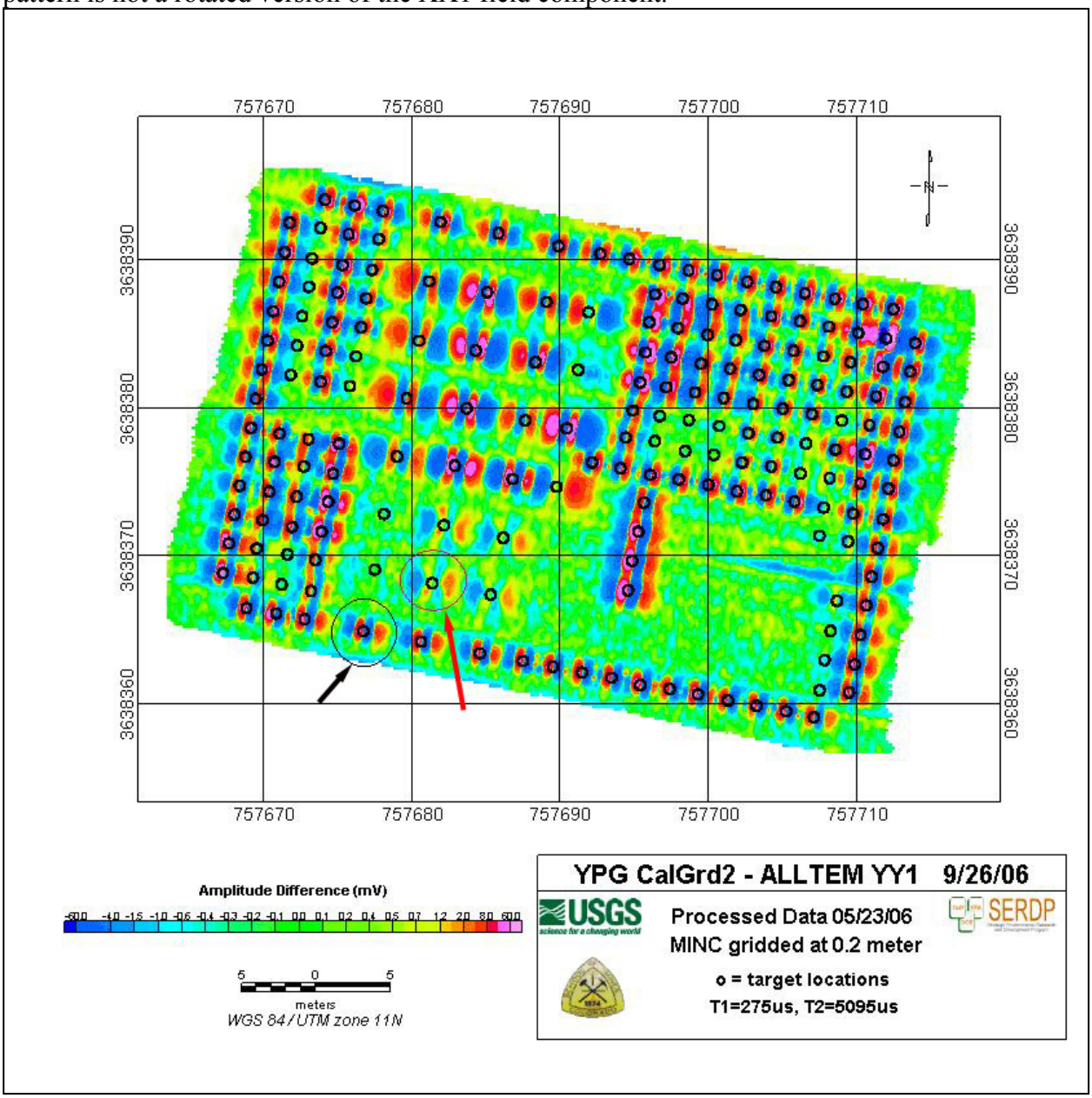


**Figure 5.3.1.2.4**. This YY1 field component highlights the same two targets as in the XX1 map. The boundary marker ball (black arrow) pattern is a 90º rotated version of the XX1 pattern, but the target highlighted by the red arrow has a pattern that is not a simple rotation from that of the previous figure. These differences are used by the inversion algorithm, discussed later, to derive a target's shape and orientation in the ground.

Figure 5.3.1.2.5 shows the XZM combination in which the excitation is horizontal, X-direction, but the vertical, Z-component is being observed. The comments for the previous two figures regarding axes of symmetry apply to this figure and the following figure as well.

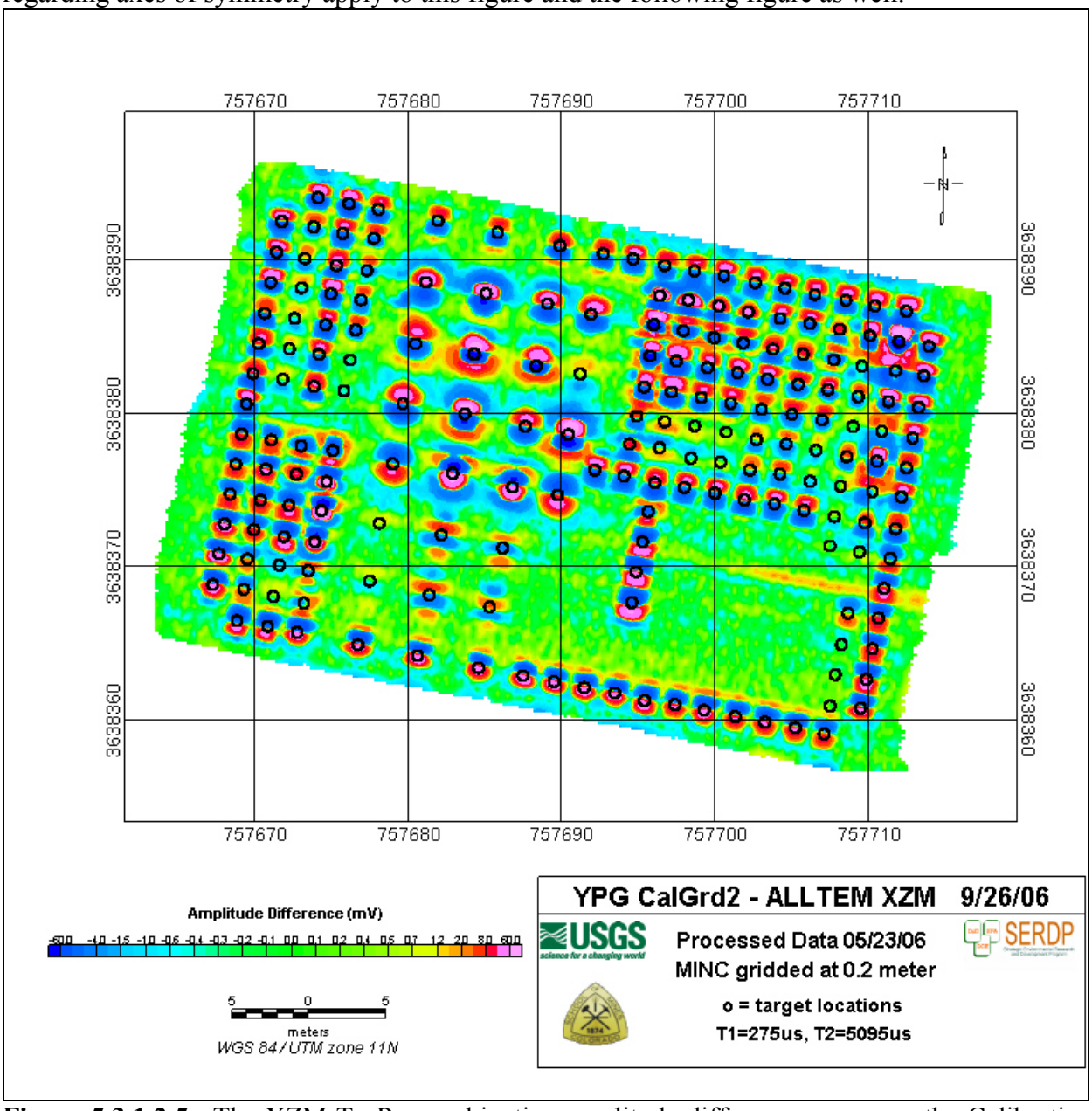


**Figure 5.3.1.2.5.** The XZM Tx-Rx combination amplitude difference map over the Calibration Grid.

Figure 5.3.1.2.6 shows the YZM combination. The SNRs for this case and for ZZM are relatively high.

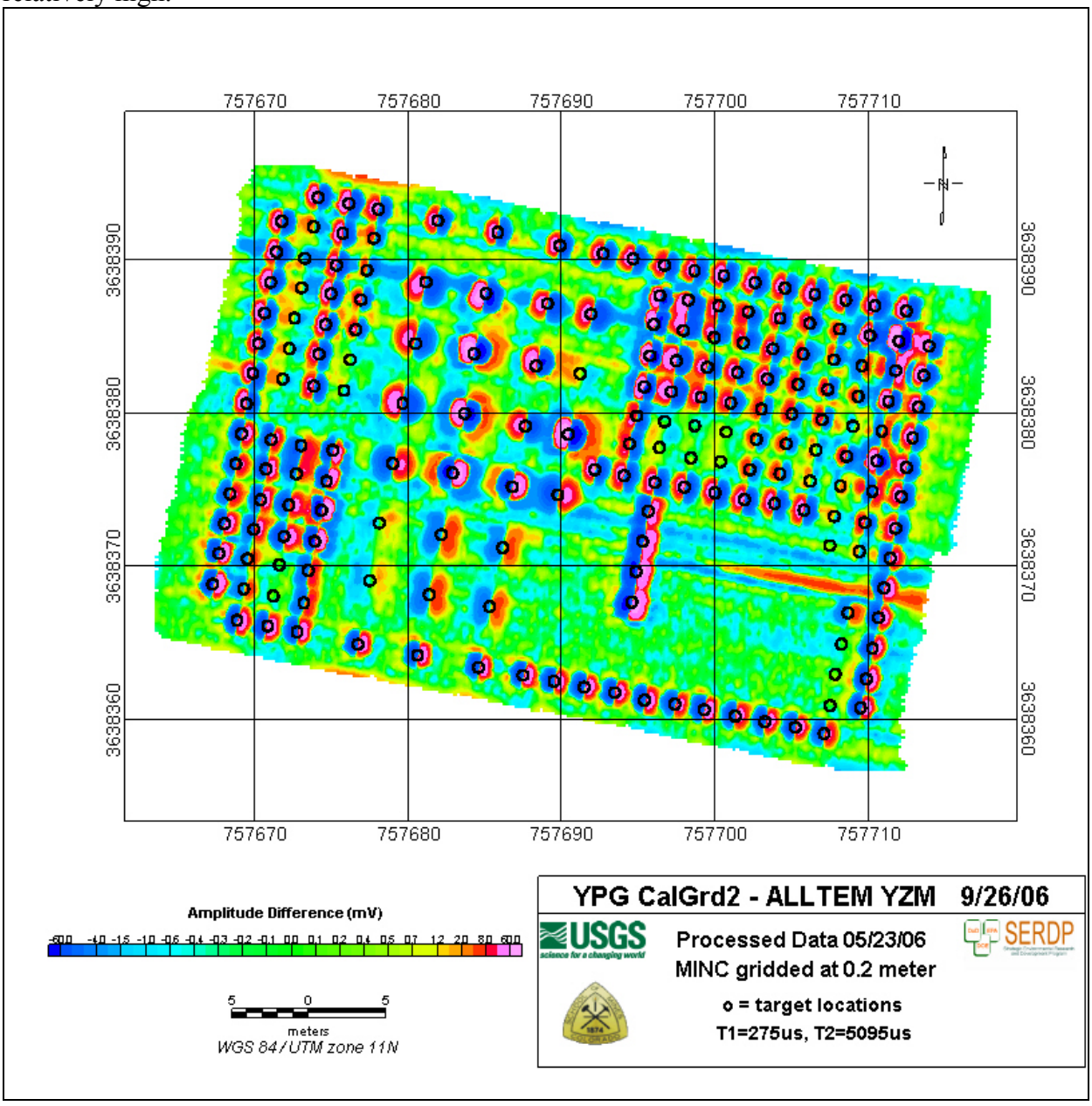


**Figure 5.3.1.2.6.** The YZM Tx-Rx amplitude difference map over the Calibration Grid.

Some of the Tx-Rx field component combinations that theoretically should have had the same SNR did not. We have determined the reason for this. The correction will require some additions to the electronics and possibly additional fine mechanical adjustments in the positions of our 34 cm Rx loops. All 19 recorded Tx-Rx combinations over the Calibration Grid are included in an appendix in Wright et al., 2006, http://www.serdp.org/Research/upload/MM-1328-IR-YPG-2006.pdf.

Figure 5.3.1.2.7 shows a ZZM component raw data map over the Blind Test Grid (BTG). The spreadsheet we supplied to the Army for scoring was based on a geophysicist's assessment of probable target locations and identifications based on this map plus two other polarizations. At that time our inversion algorithm was not reliable. The data had not been processed in all the ways that we later discovered were needed. Subsequent to reprocessing and to corrections to our inversion code, discussed in section 5.4.3 of this report, we submitted another spreadsheet to the Institute for Defense Analysis (IDA). The scoring results were much better and are discussed in section 5.4.3.4 of this report.

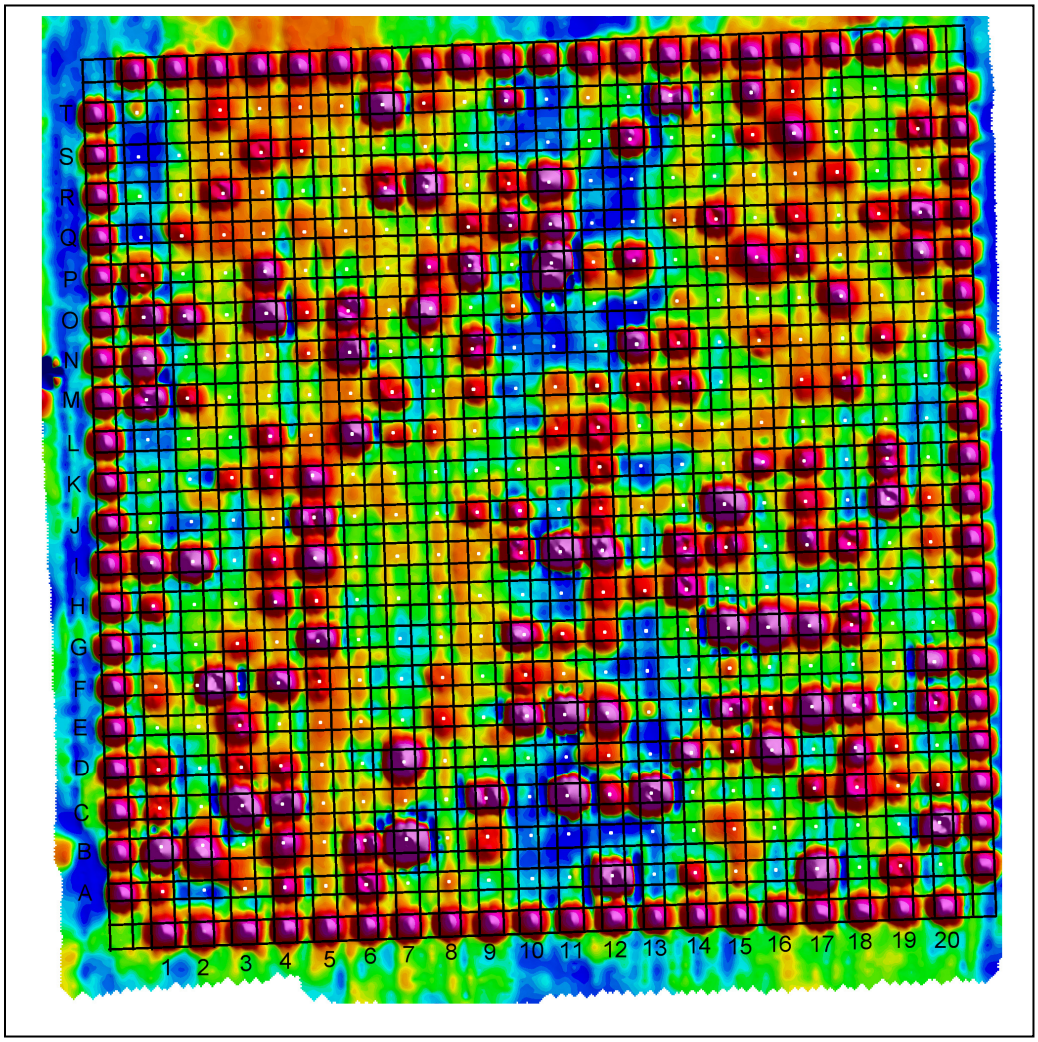


**Figure 5.3.1.2.7.** This ZZM component ALLTEM raw data map over the Blind Test Grid at YPG is of relatively high quality, but far inferior to later maps from processed data. The black grid overlay has 1-m cells. The white dots indicate the centers of the 2-m target cells for the BTG that may, or may not, have targets in them.

Figure 5.3.1.2.8 shows a ZZM map made from processed data over the BTG. Several additional targets, annotated by "x" are evident in this map. Note also that there is a target at location F-2.5 where there should be no target. All targets were supposed to be at the cell centers (white dots).

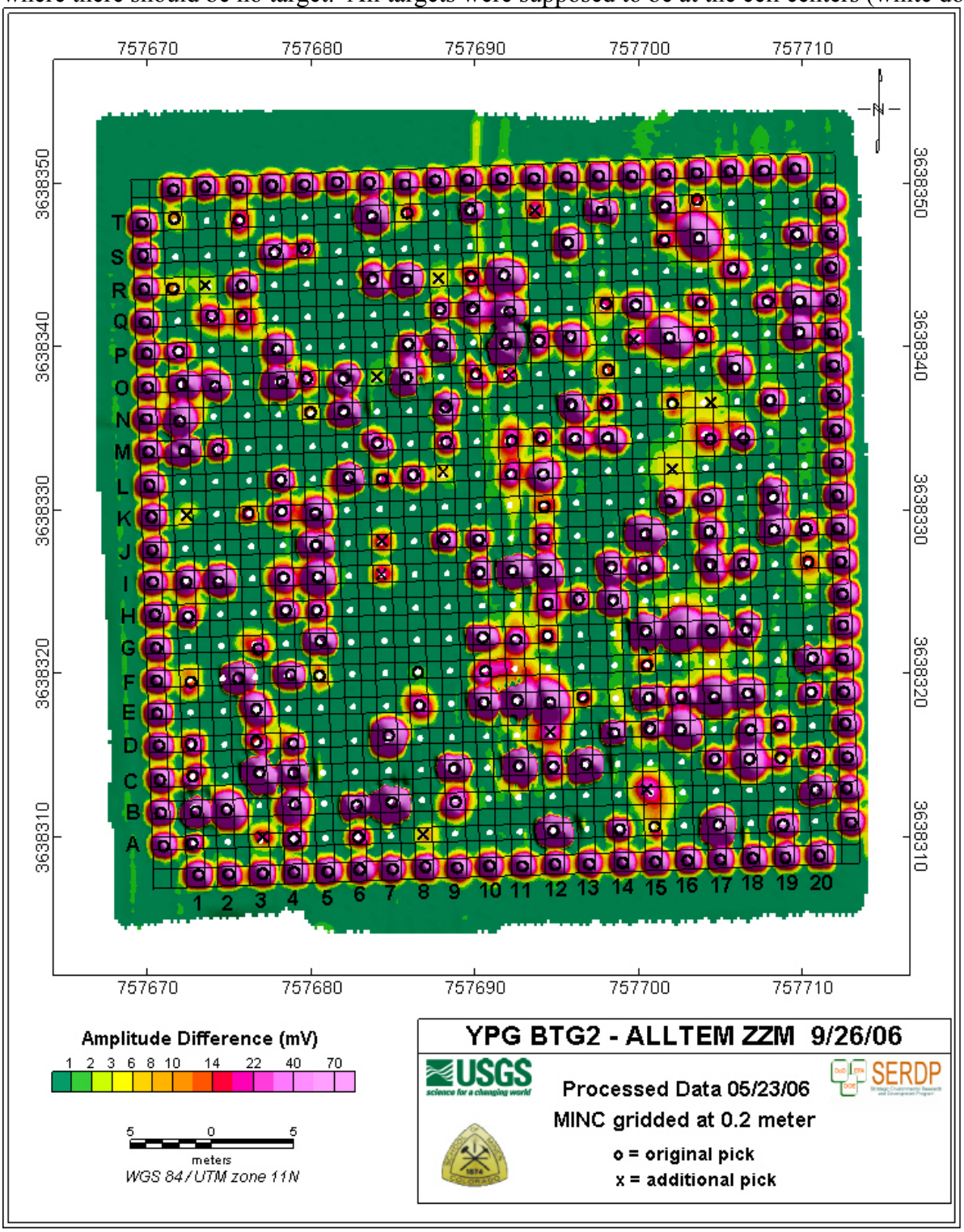


**Figure 5.3.1.2.8.** This ZZM BTG map is overlaid with a 1 m by 1 m grid. Cell center locations are noted with white dots. Original "o" and 16 additional "x" target picks are annotated.

Figure 5.3.1.2.9 is the same as the previous figure except that survey lines instead of cells are shown.

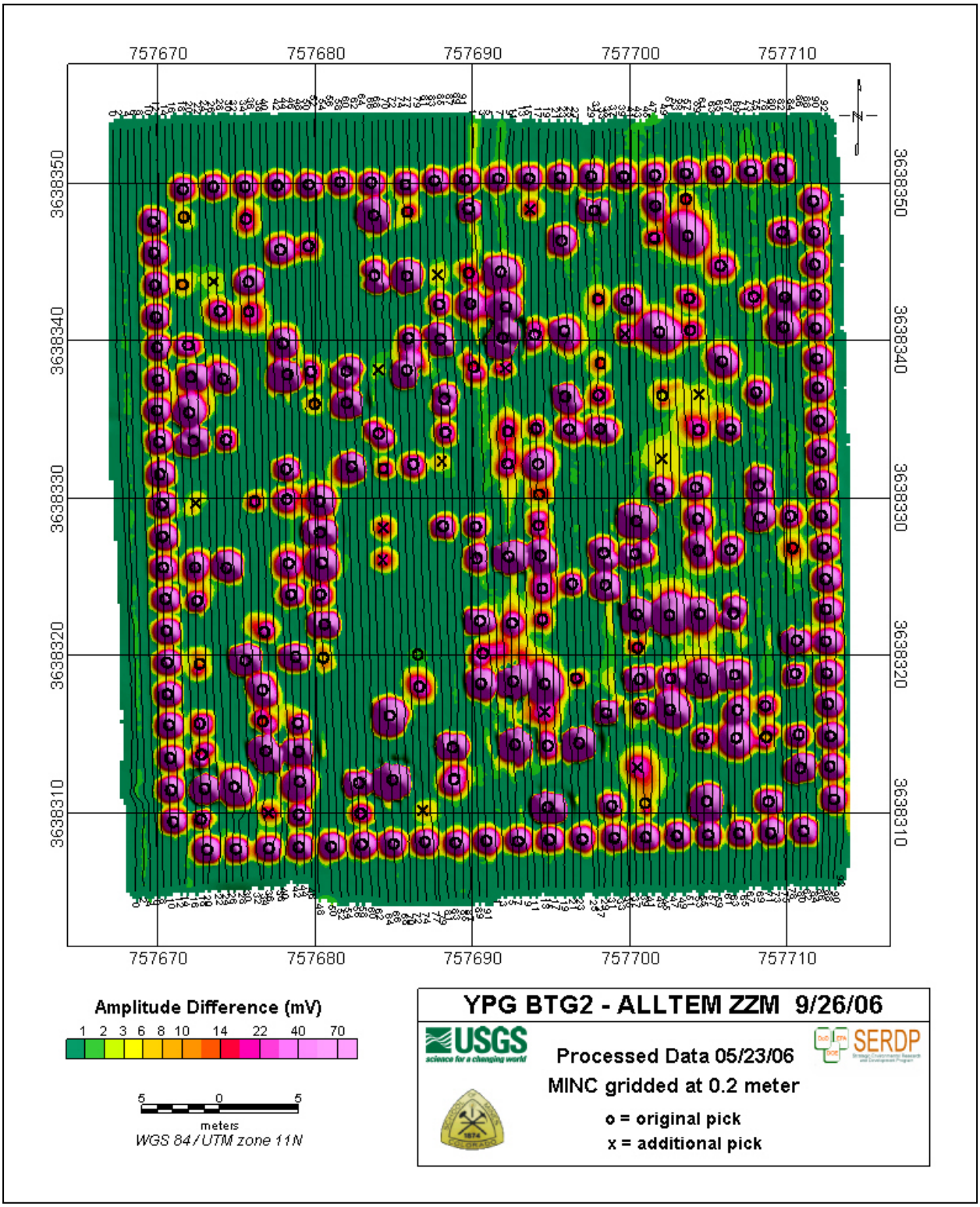


**Figure 5.3.1.2.9.** The survey line paths show good coverage and relatively straight lines except for a westerly "bulge" from a topographic mound just west and slightly north of the southwest corner of the grid.

Figure 5.3.1.2.10 shows the ZZE component map that has slightly higher spatial resolution for shallow targets than the ZZM map that uses the larger 1-m Rx loops.

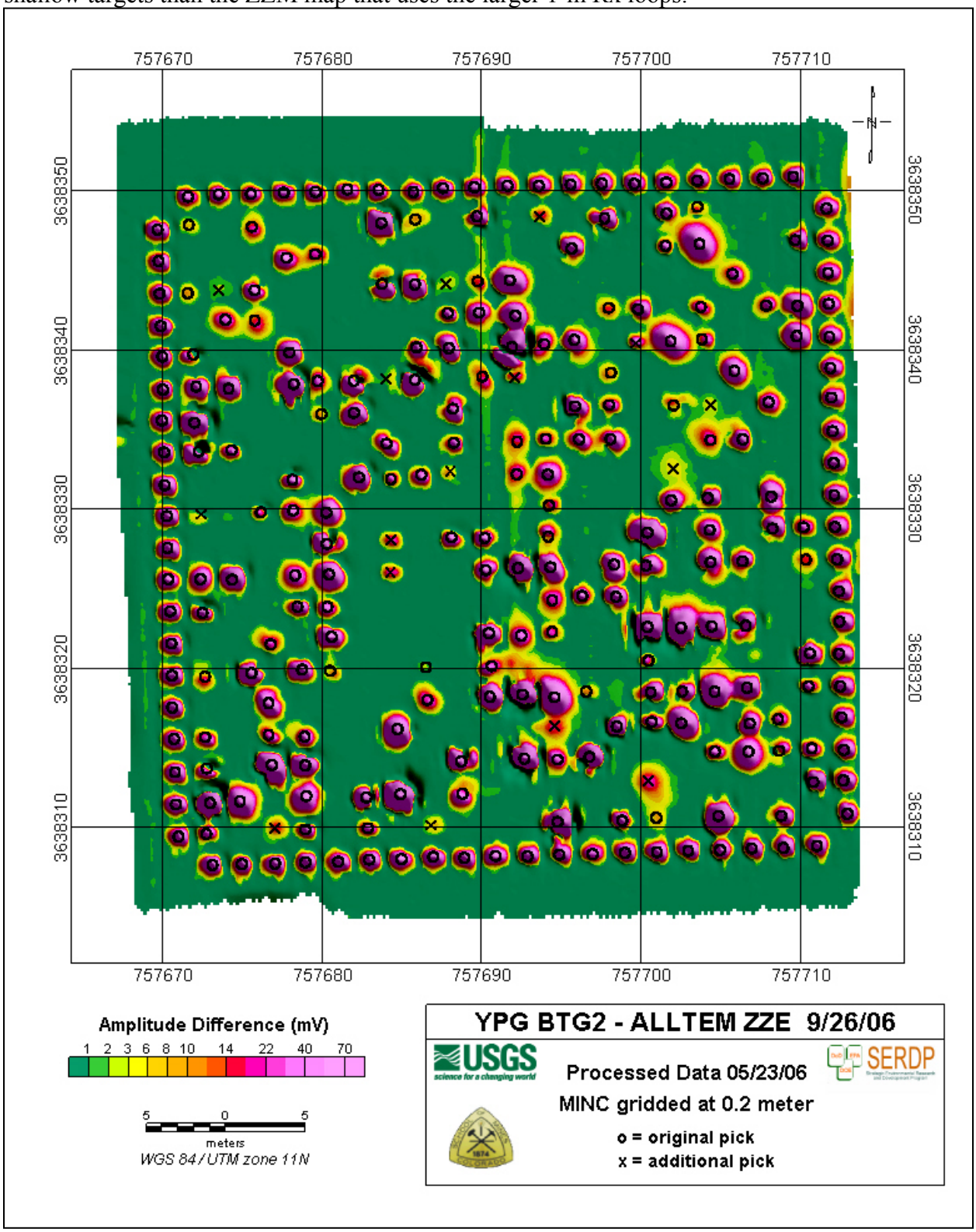


**Figure 5.3.1.2.10.** This figure shows the ZZE combination that uses 34-cm Rx loops.

Figure 5.3.1.2.11 shows the ZX1 component.

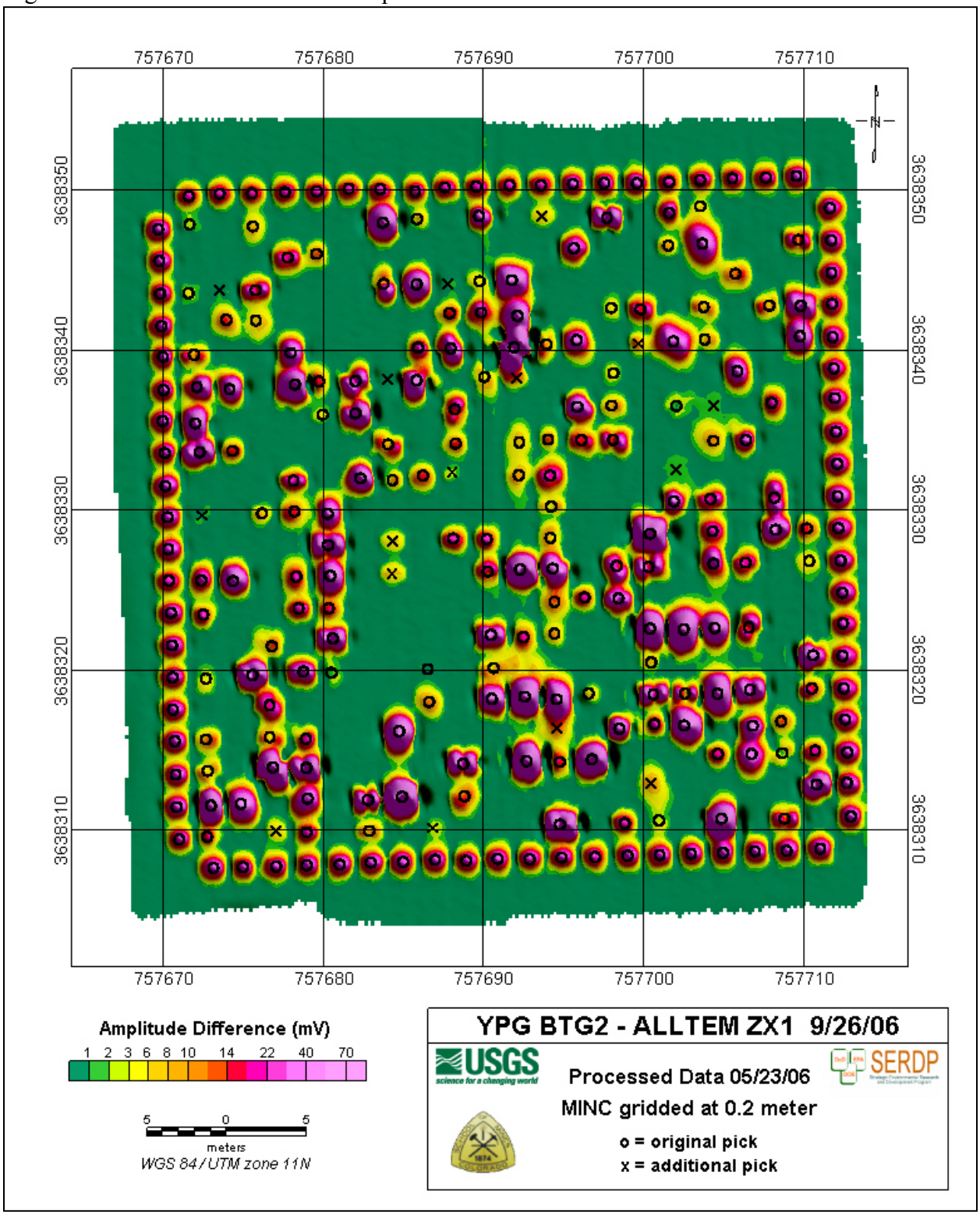


**Figure 5.3.1.2.11.** This ZX1 cross-polarized case shows a BTG map where the excitation was vertical and the received component was in the x direction.

Figure 5.3.1.2.12 shows the ZY1 component.

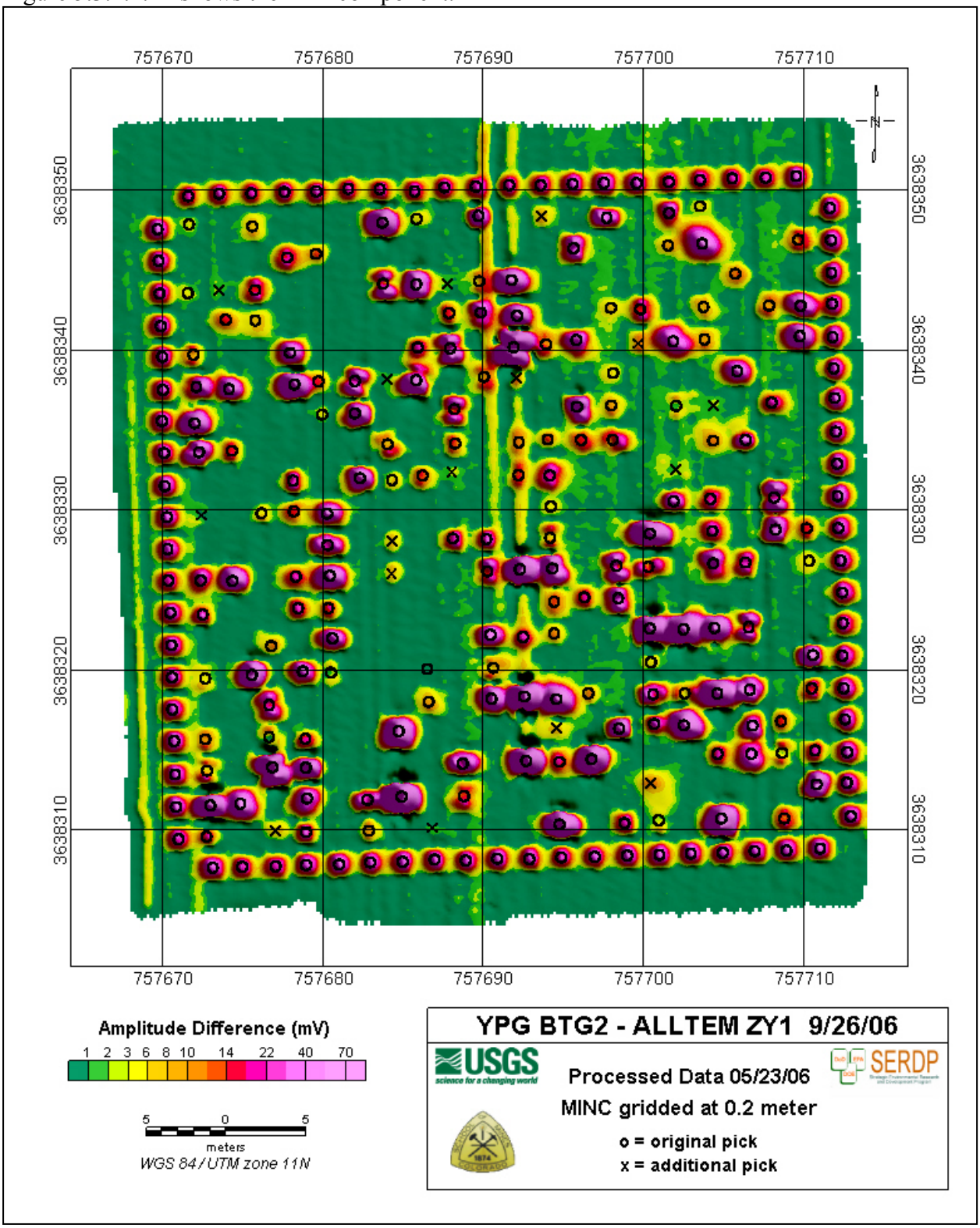


**Figure 5.3.1.2.12.** The ZY1 component has a slightly lower SNR than ZX1. This indicates that mechanical and/or electronic adjustments to improve the nulling of the primary field are needed for this case. A remaining puzzle is why the right half of the map is nosier than the left half.

Figure 5.3.1.2.13 shows the XZM Tx-Rx cross-polarized case.

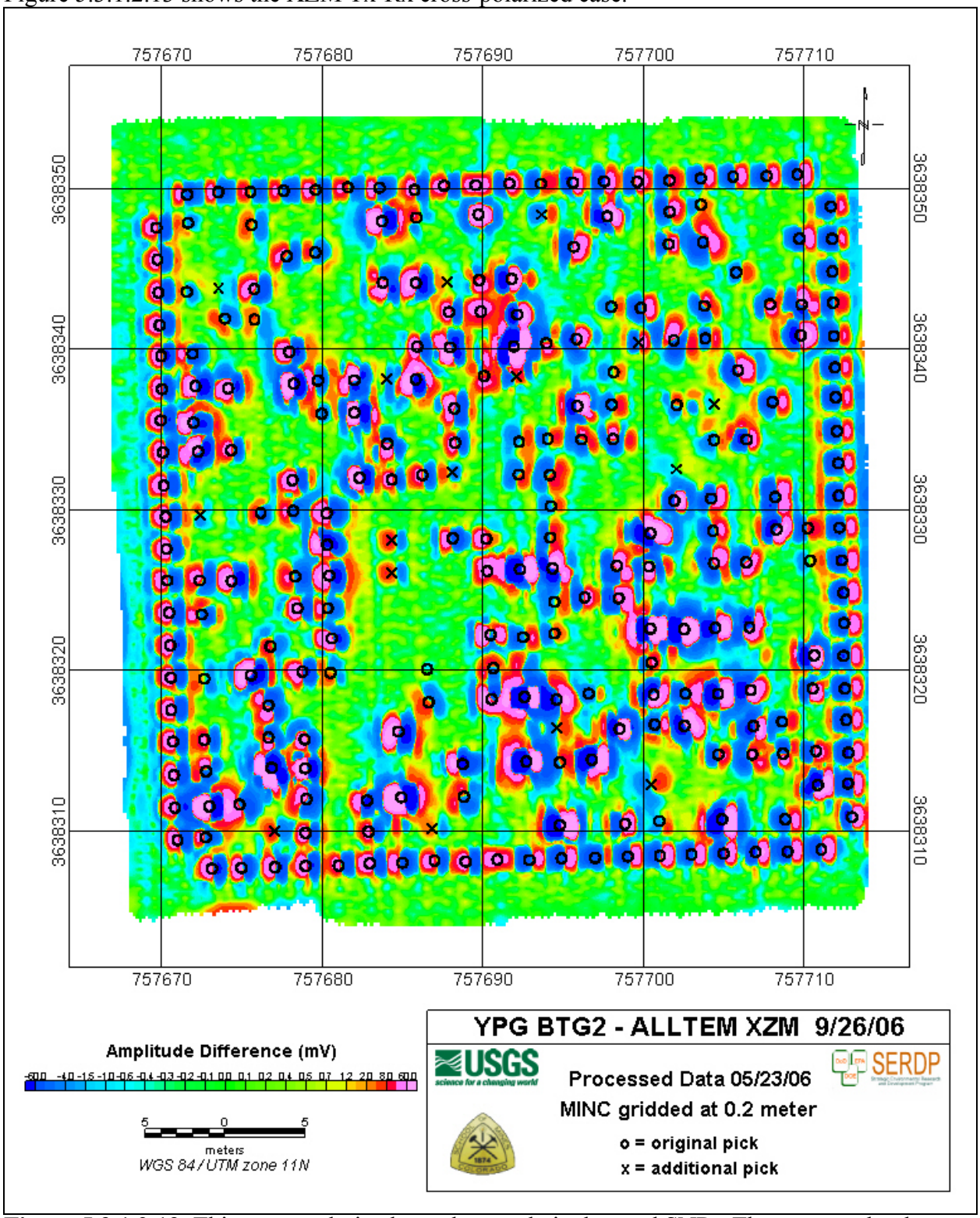


**Figure 5.3.1.2.13**. This cross-polarized case has a relatively good SNR. The measured voltages for this component can swing both negative and positive as shown on the color bar.

Figure 5.3.1.2.14 shows the YZM cross-polarized case.

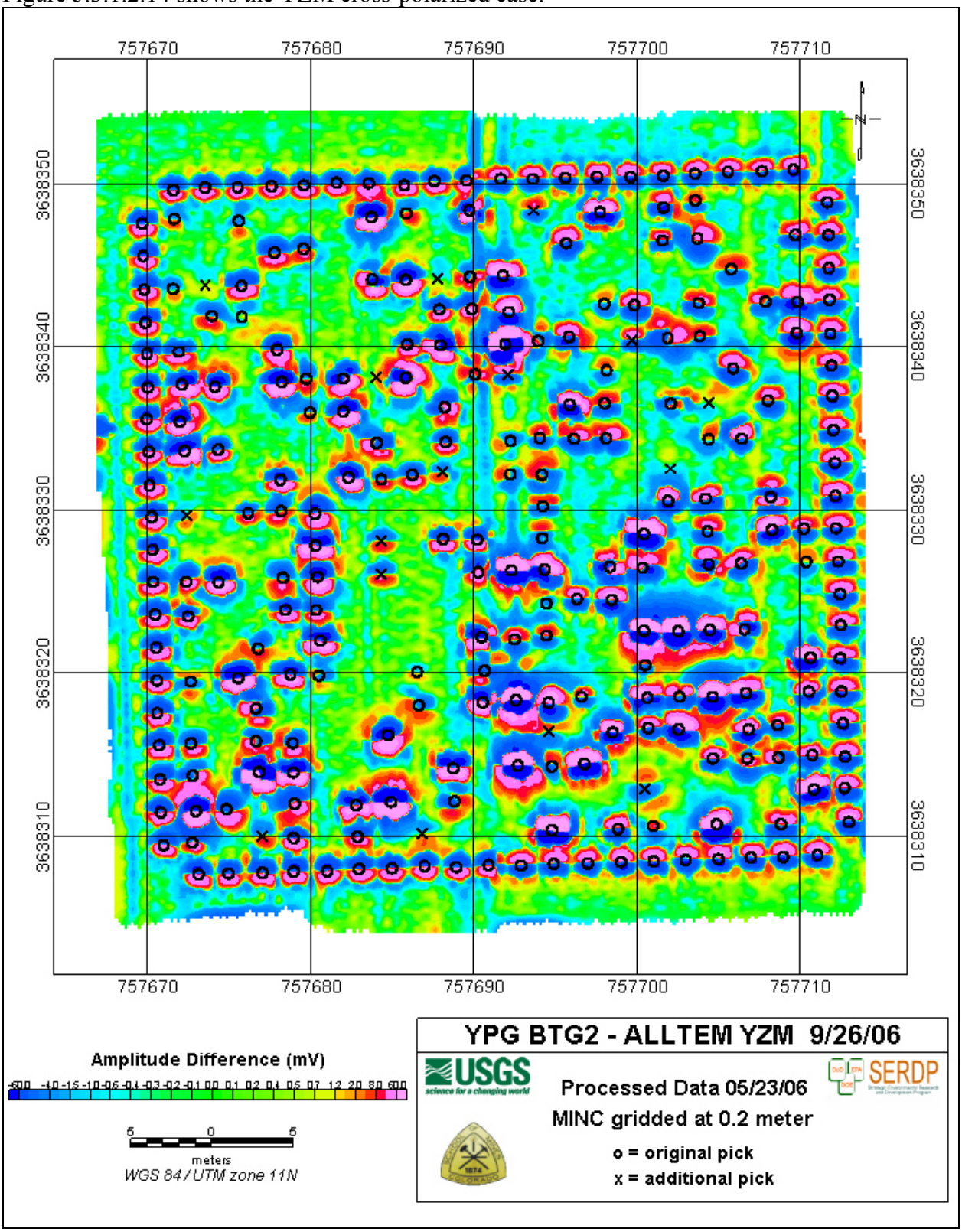


**Figure 5.3.1.2.14.** The YZM case also has a relatively good SNR.

The data maps shown in the previous figures are of relatively high quality, but processing in specific ways is necessary in order to achieve a high SNR and there were some instances in which certain Tx-Rx combinations had a lower SNR than other channels that theoretically should have had equal SNRs. As we mentioned earlier, all 19 Tx-Rx combinations are included in an appendix in (Wright et al., 2006, http://www.serdp.org/Research/upload/MM-1328-IR-YPG-2006.pdf). Inadequate primary nulling for some Tx-Rx cases appears to be the culprit. In the current implementation of the ALLTEM electronics each pair of Rx gradiometer coils are nulled only with respect to the vertical, Z-component, Tx coil. Thus when the X- or Y- component Tx coils are active, those coils are, in general, not as well nulled. For cases where they are not, a large primary signal is present that degrades the overall SNR for that case, and post-processing removal of the primary is not fully successful at removing noise in the presence of a very large primary component. In our next ESTCP phase we plan to (a) test to see whether fine position adjustments of the Rx loop positions can help reduce the unwanted primary signal, and (b) add more electronic differential gain circuits so that each selected Rx coil pair can be electronically nulled separately for each of the three Tx polarizations. In addition, in order to achieve a high SNR ALLTEM data must be preprocessed in certain ways. The necessary data processing steps and our ALLTEM inversion algorithm are discussed in sections 5.4.1 and 5.4.2.

### 5.3.2 TMGS at YPG

Tests with the modified TMGS were conducted at YPG in November, 2005, and in May, 2006. The 2005 tests concentrated on the Calibration Grid, whereas in 2006 we operated the TMGS over the BTG. Each time, the logistics for deploying the TMGS were very similar:

1. Erect the spin calibration apparatus in a magnetically clean area,
2. Acquire spin calibration data with the array in various orientations,
3. Outfit and configure the tractor and platform for field data acquisition,
4. Acquire field data,
5. Acquire lag-line data,
6. Dismount TMGS electronics off the tractor,
7. Acquire spin calibration data with the array in various orientations, and
8. Stow equipment for return to depot.

*Spin Calibrations*

First, a reconnaissance survey was completed over possible magnetically clean and quiet areas of the Standardized Test Site. An operator packing the Leica GPS system walked the areas with the G-858 cesium magnetometer in gradiometer mode. These data were downloaded and processed in the command trailer. Three locations were identified on the resulting maps which displayed very small horizontal and vertical magnetic gradients. These locations were re-surveyed with the G-858 on a high-resolution 20 by 20 m grid. A prime location for the spin calibration experiments was found approximately 100 m south of the BTG. This location was also suitable for the magnetic reference base station. The reference base station consisted of a G-858 automatically recording total field readings at one measurement per second. These reference

values were tied to the total magnetic field at the location of the turntable. Therefore, the total magnetic field being measured by the sensor array as it spun around was accurately known.

The spin calibration apparatus consists of four main components:

1. A motor drive assembly, in which a small, high-torque, gear head dc-motor transmits power through a 50:1 gear box to a V-belt pulley;
2. An intermediate stage of ganged V-belt pulleys, which reduces the rotation by a factor of 6;
3. A pulley-driven turntable mounted on a sturdy base that has 3-point leveling; and
4. A lectern on which the magnetometer array is mounted.

The entire apparatus is shown in figure 5.3.2.1 as it was set up for a calibration run. Except for the dc motor and gear box on the stand farthest away from the array, all materials are nonmagnetic. Magnetic signature tests with a G-858 magnetometer verified that at the separation distance (greater than 3 m), no magnetic noise was detectable at the array location. A close-up photograph of the lectern is shown in figure 5.3.2.2. The data acquisition system was stationed about 10 m away (figure 5.3.2.3), where the operator directed operations and continuously monitored in-coming data. In addition to the NI data acquisition system, a portable laptop computer simultaneously recorded serial data sent by the magnetometer interface unit.

A variety of experiments were conducted: normal (array facing up on lectern), inverted (array facing down on lectern), heads removed in sequence, heads remounted in sequence, array vertical (on edge), and array horizontal (facing up). The normal spin rate was one revolution in 13 minutes. Some experiments were repeated at a slower spin rate (one revolution in 26 minutes) to establish the fact that magnetometer slew rates were not adversely affecting the spin calibration accuracy. Final spin calibrations on November 5, 2005, had the array on the lectern in normal and inverted aspects. These data are used for all subsequent data corrections because the heads remained fixed afterwards without further adjustments.

**Figure 5.3.2.1**. The spin calibration apparatus set up at a magnetically clean location for a calibration run. The electric motor drive assembly (left) transmits power through a set of tandem pulleys (center) to the rotating platen on the turntable assembly (right). The magnetometer array is mounted on a lectern which rests on the turntable platen. The array is shielded from direct sunlight in order to minimize large, rapid temperature variations.

**Figure 5.3.2.2.** The magnetometer array mounted on the lectern (brown material) at a 57-degree inclination. The clamping bar and stops around the perimeter of the array prevented it from shifting while the array was manipulated for various experiments.

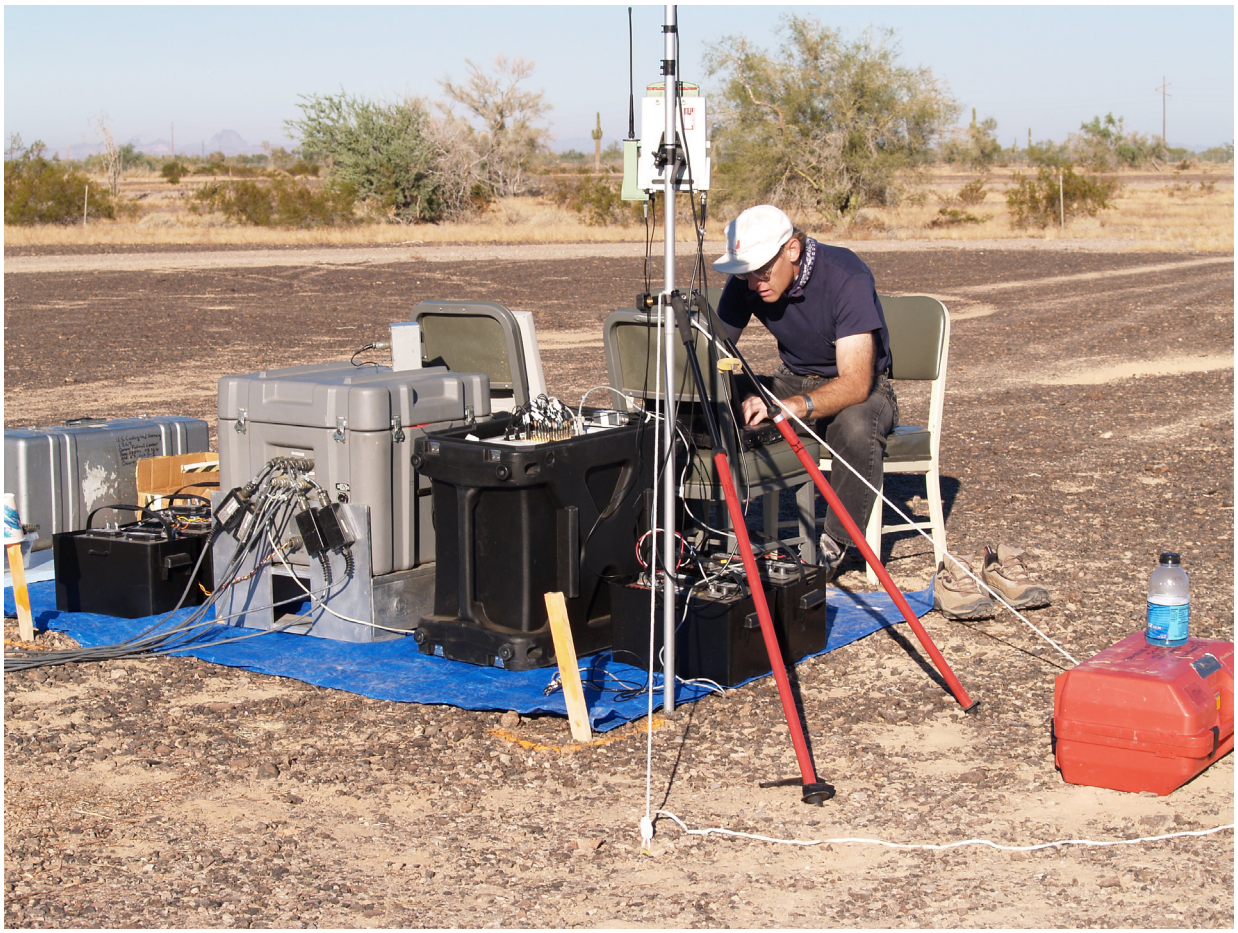

**Figure 5.3.2.3.** The TMGS data acquisition system was stationed about 10 m away from the magnetometer array. The magnetometer interface unit (square grey case on left) and the NI computer (tall black case) are flanked by lead acid batteries. The GPS receiver (top center, on the pole) supplied PPS timing pulses.

Raw data from a single sensor head from a single spin are plotted in figure 5.3.2.4, in which the array was tilted at 57 degrees from horizontal. Note the stationary data at the beginning and end of the rotation. These stationary data were used to characterize the noise levels of the fluxgate axes. We discovered that signal transitions on the Bin_Step channels were correlated with transients on the Error_Signal channels (figure 5.3.2.5). This noise was ubiquitous, in that a Bin_Step on any axis of any head caused simultaneous transient spikes (of various amplitudes) on all 12 Error_Signal channels. The effect this has on any one moving magnetometer channel is illustrated in figure 5.3.2.6, where it can be seen that transient noise is greater where the rate of change of the magnetic field is high. The data were denoised by deleting 15 samples from all the Error_Signal channels at the occurrence of each Bin_Step, after we determined that the settling time of each spike was 15 ms. Denoised spin datasets were aggregated into a single dataset for regression analysis. Processing of the spin calibration data to derive calibration coefficients is discussed in section 5.4.2.

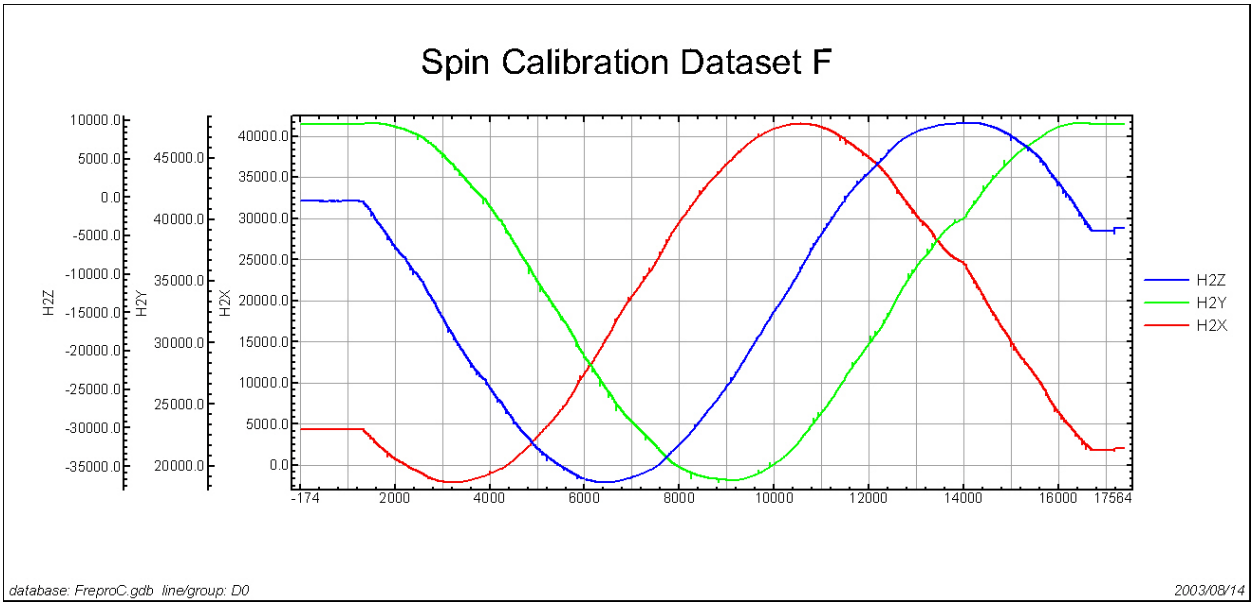


**Figure 5.3.2.4.** Example of raw spin calibration data from a single magnetometer (Head 2) for a single spin. The three vector components X, Y, and Z are plotted in red, green, and blue, respectively.

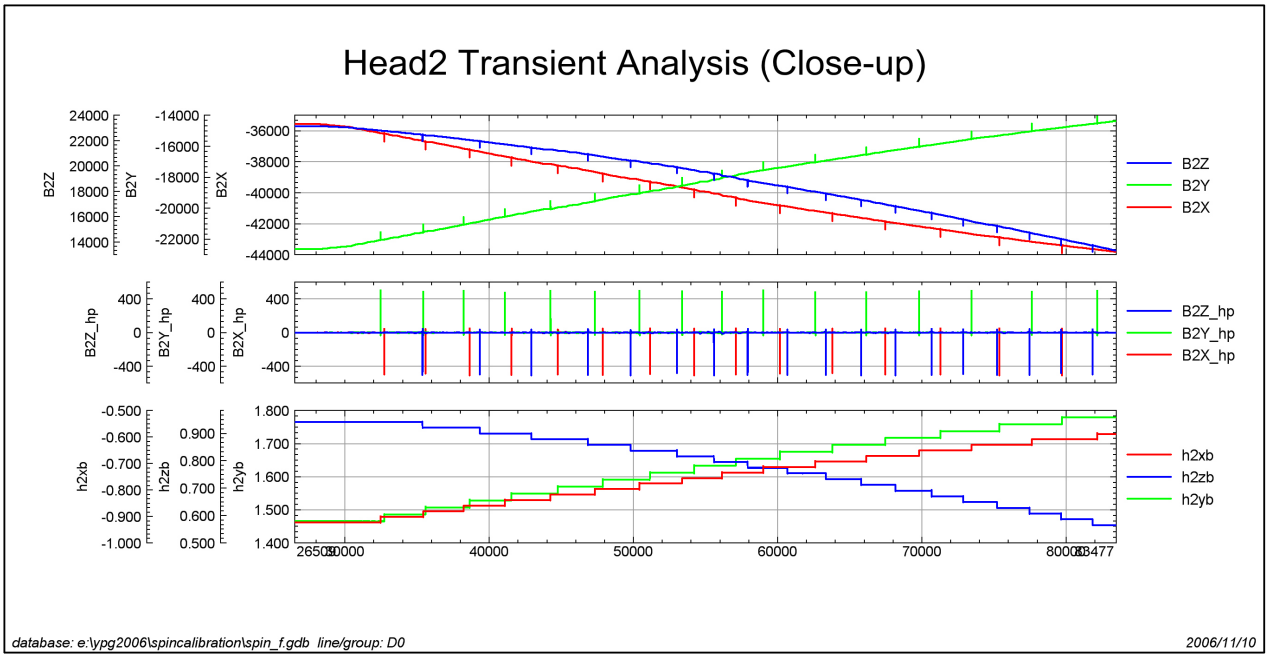


**Figure 5.3.2.5.** Close-up of raw spin calibration data showing systematic noise. The top graph plots the raw B-field values (volts converted to nanotesla). The transient spikes, obtained by high-pass filtering the B-field data, are plotted in the middle graph. The bottom graph plots the Bin_Step levels, and illustrates that binning causes the transient spikes observed in the B-field data.

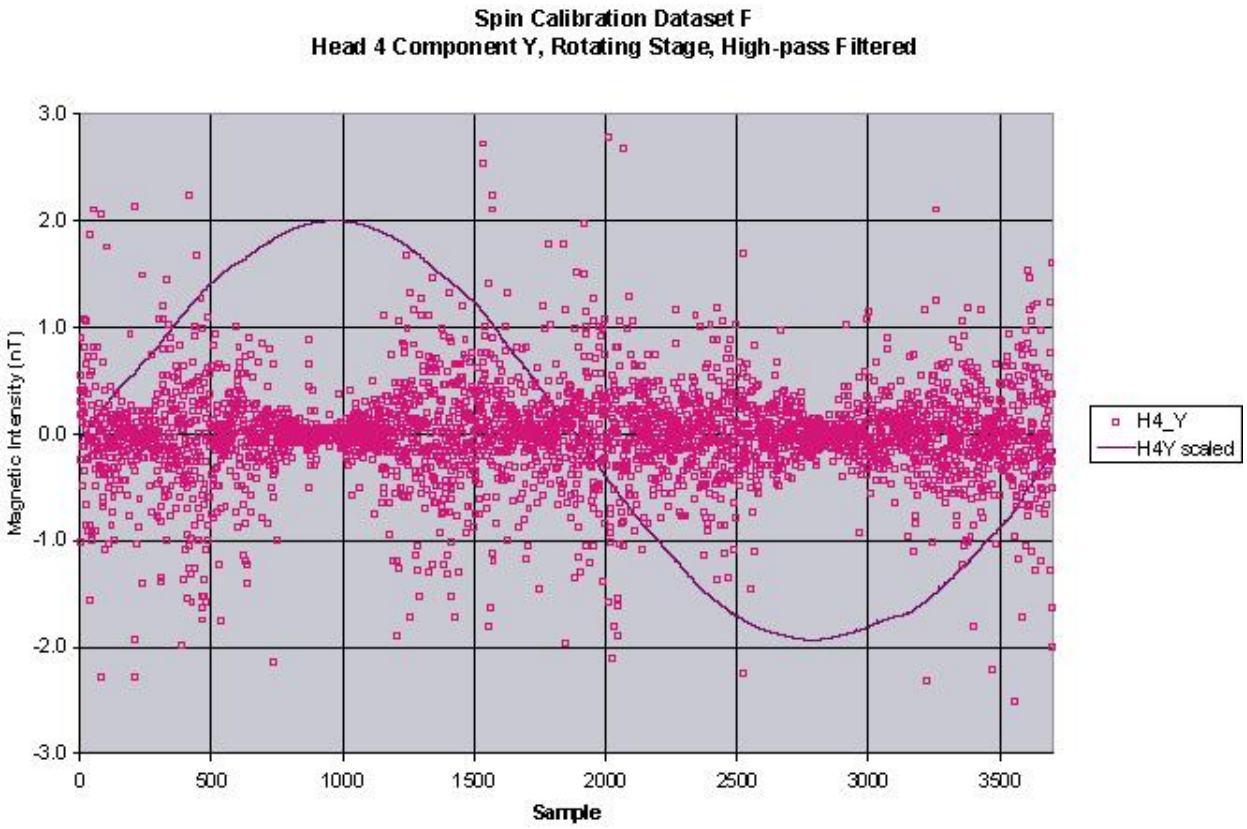


**Figure 5.3.2.6.** The effect of binning noise on dynamic magnetometer data. The spin calibration data set was high-pass filtered (square symbols) to remove the long period sinusoidal variation (solid line). These plots reveal a relationship between the noise and rate of change of the magnetic field.

*Outfitting and Configuring the Tractor and Platform*

A shelf at the rear of the tractor held the magnetometer interface unit, the data acquisition system (DAS), and the power distribution box. The GPS receiver and telemetry antenna were affixed to the roll-bar. A dashboard shelf supported a keyboard, touchpad, and video monitor, all connected to the DAS via conduit-routed cables. Main power came from four 12 volt deep-cycle lead-acid batteries strapped to a shelf forward of the engine shroud. The entire tractor configuration, as it was deployed at YPG, is illustrated in figure 5.3.2.7.

The magnetometer array was carefully centered and aligned in the cargo bay of the platform with sensor heads 1 through 4 oriented at 12 o'clock (fore), 3 o'clock, 6 o'clock (aft), and 9 o'clock positions, respectively. The magnetometer heads were then thermally insulated with foam boxes (figure 5.3.2.8). Note that, because heads 2, 3, and 4 are physically rotated relative to the leading sensor (head 1), the axes primarily sensing north- and east-components of the magnetic field are likewise changed. For example, if the platform heading is north, the north component of the magnetic field is measured by the middle coil of head 1, the inner coil of head 2 (negative polarity), the middle coil of head 3 (negative polarity), and the inner coil of head 4 (figure 5.3.2.9). These changes in sense axis and polarity, as well as coil separation distances, are reconciled for all field components during post processing, when spin-calibration coefficients are used to un-rotate the sensor heads mathematically, and gradients are calculated.

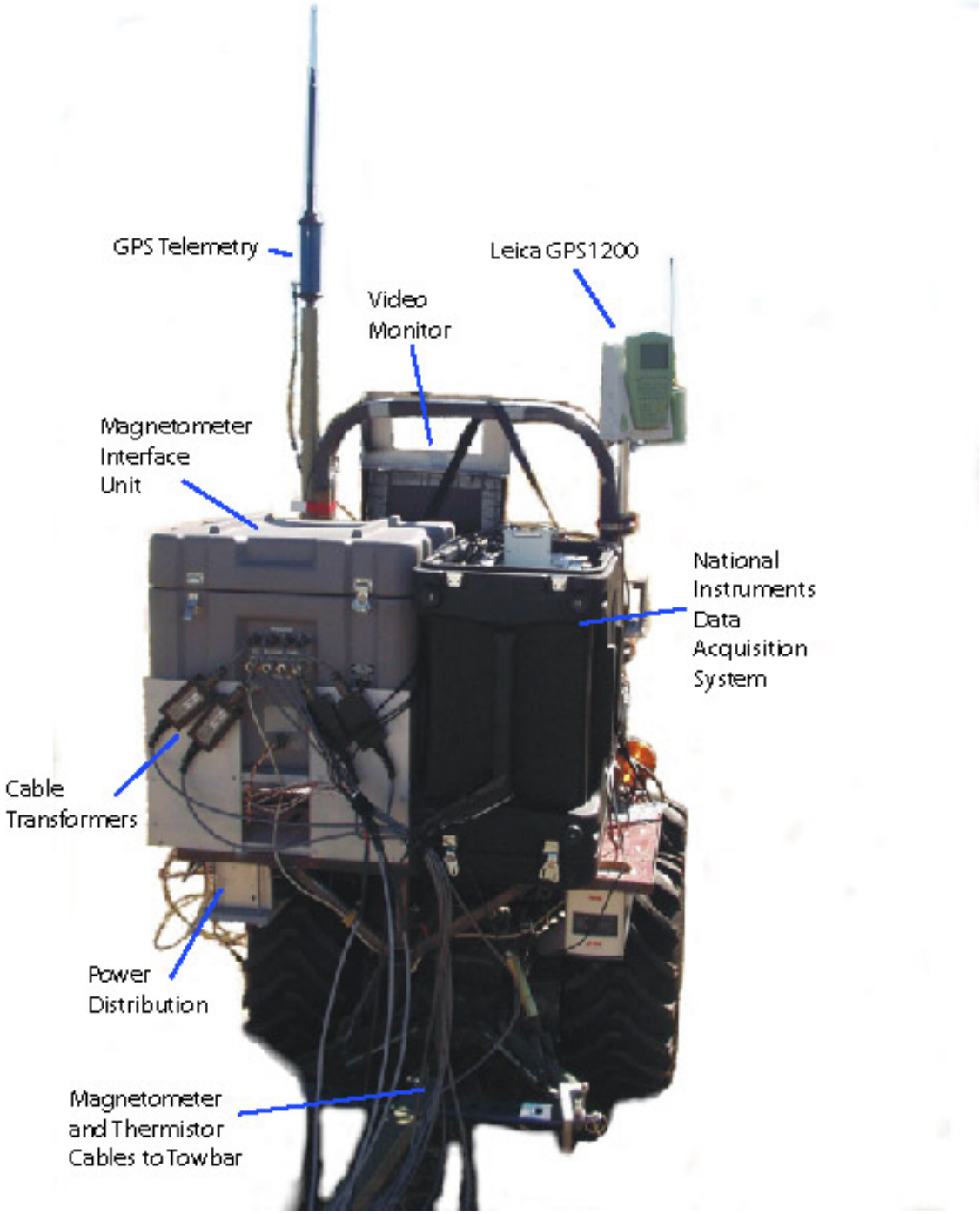


**Figure 5.3.2.7.** The TMGS electronics are shown mounted on the prime mover, a Kubota tractor. The Magnetometer Interface Unit (MIU) (grey case on left) is the only original piece of TMGS equipment still being used. The computer-controlled data acquisition system (black case on right) receives analog signals from the MIU and ancillary sensors, along with serial data from the GPS receiver mounted on a short mast. A keyboard, monitor, and mouse face the driver/operator. Not shown is a bank of four 12 volt lead acid batteries mounted on a shelf over the front bumper of the tractor.

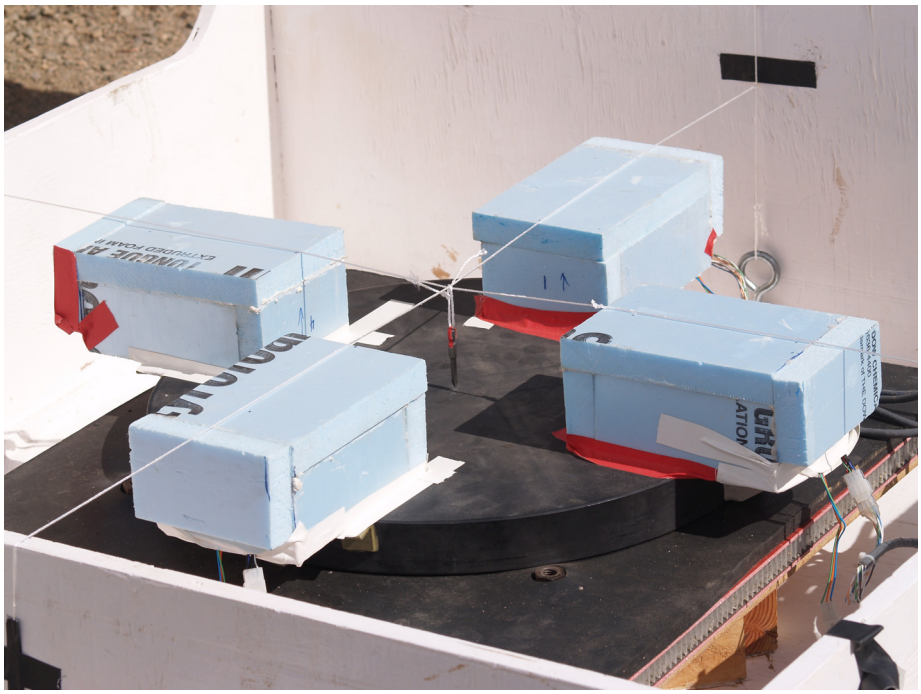

**Figure 5.3.2.8.** Centered and aligned array on the platform with magnetometer heads covered by thermally insulating boxes.

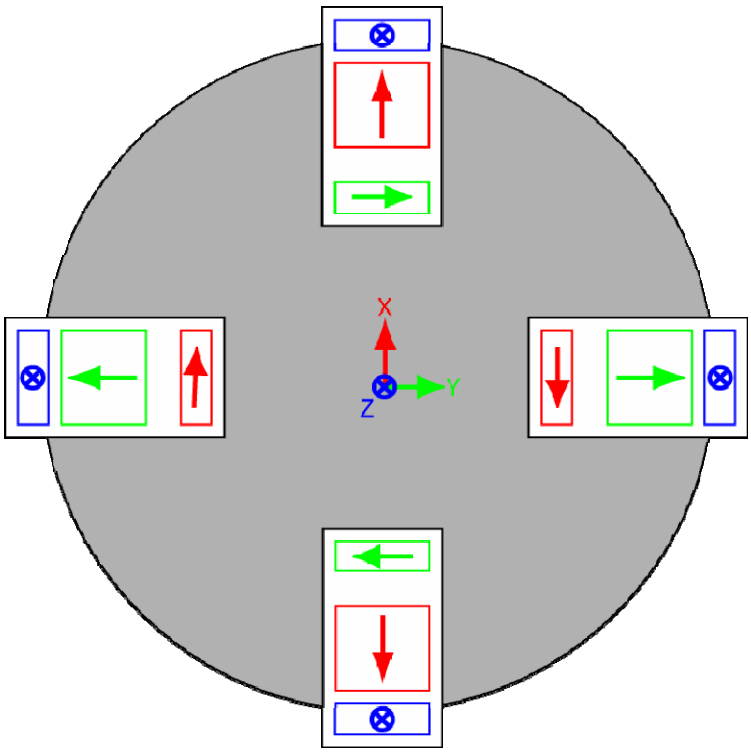


**Figure 5.3.2.9**. Vector convention in the frame of reference of the magnetometer array is borrowed from geodetic coordinates (X (red) is north, Y (green) is east, Z (blue) is positive down).

*Lag-line Experiments*

We checked system performance after the tractor and platform had been fully configured. On a level stretch of the gravel access road just to the west of the Calibration Grid, we buried a permanent bar magnet vertically in a shallow, marked hole. We then drove the tractor-platform assembly along straight lines over the magnet, following a rosette pattern (figure 5.3.2.10). The gridded and mapped data revealed velocity-dependent offsets of peak magnetic field and the magnet location (figure 5.3.2.11). The magnitude of the lag was fixed for any given data run, but differed between separate runs (a "run" is defined as data collected between the time the NI is turned on and off). We determined that the lag was caused by the initialization process between the system clock and the LabVIEW® software – that it was software dependent. This problem could not be fixed in the field during the 2005 survey, but we engineered a solution prior to the 2006 tests. We added a circuit to output an inverse-exponential decay (saw tooth) waveform triggered by the pulse-per-second (PPS) output of the GPS. The PPS is extremely precise, and allowed us to determine sample times to within 10 microseconds of absolute. The lag-line experiment in 2006 (figure 5.3.2.12) confirmed that the latency had been eliminated (figure 5.3.2.13). The magnet was located to within 1.7 cm, which is well within the specification for the GPS in differential RTK mode.

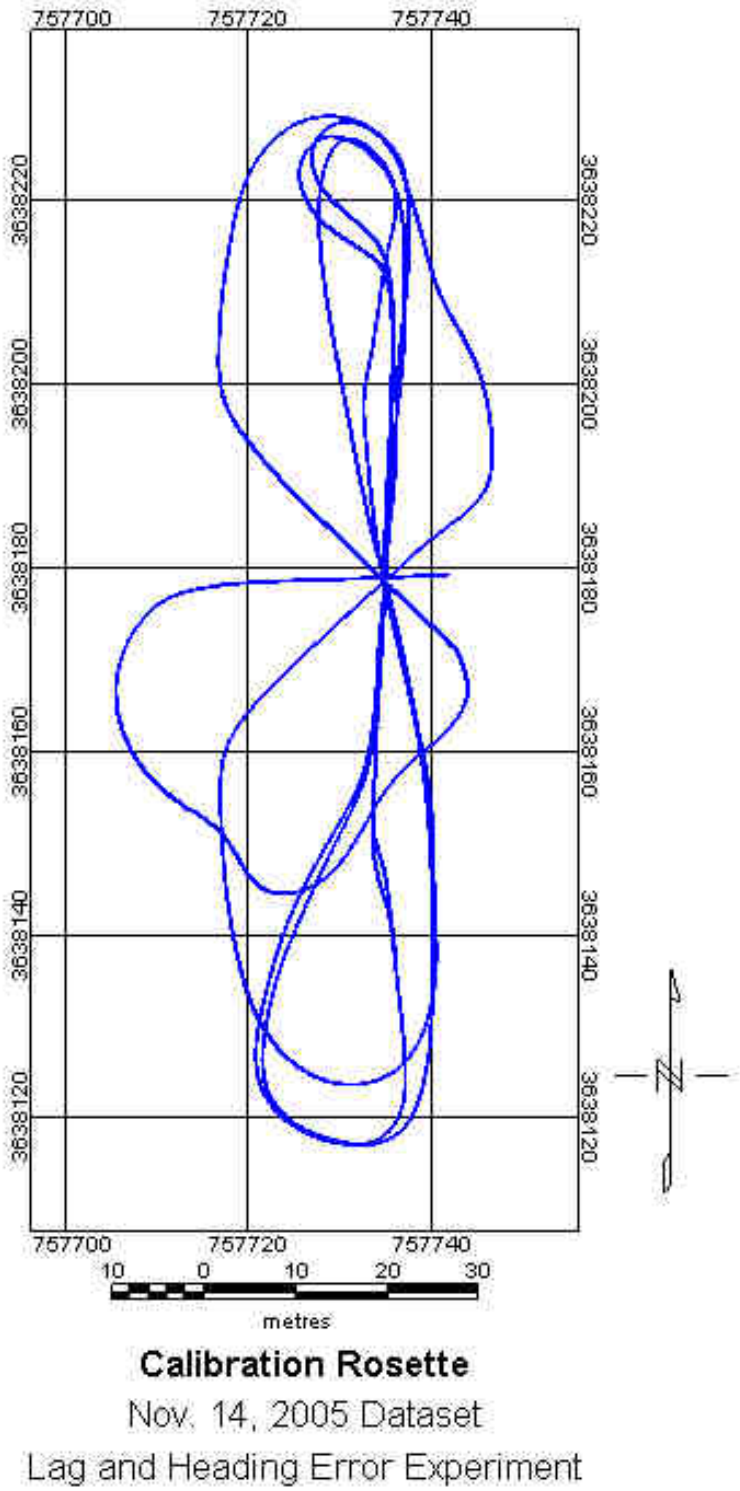


**Figure 5.3.2.10.** Lag-line experiment in 2005 over a buried bar magnet, which was located at the intersection of the path taken by the platform.

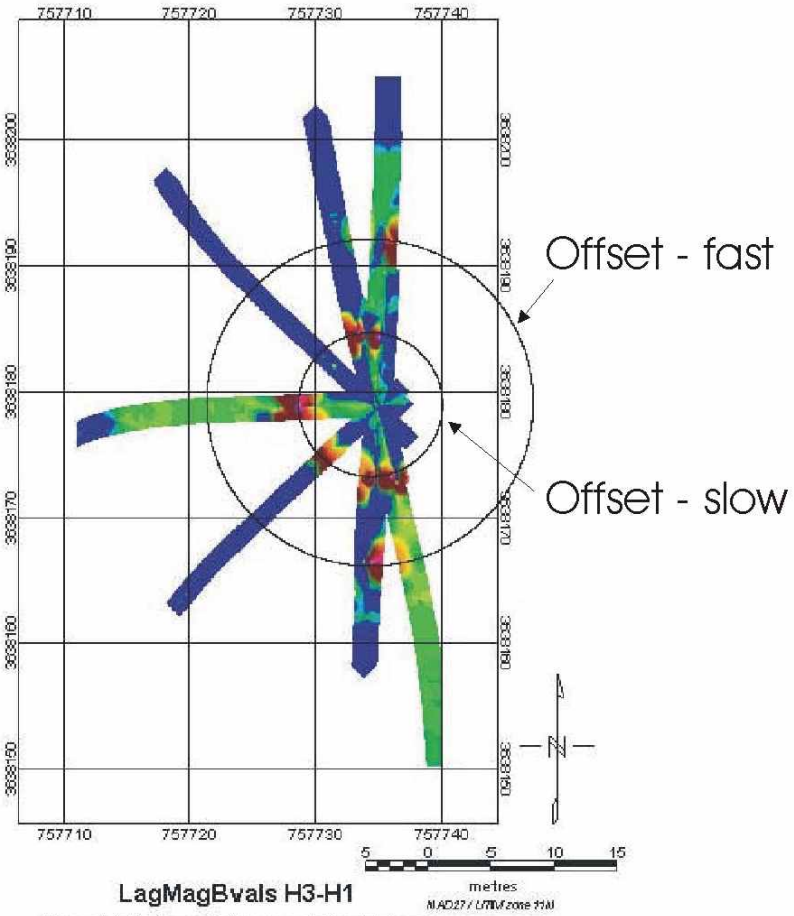


| UTM E (peak anomaly) (m) | UTM N (peak anomaly) (m) | DESC. | AVG VEL (cm/s) | L (m) | delT (s) |
|---|---|---|---|---|---|
| 757734.220 | 3638166.392 | fast S-N | 151.5 | 12.534 | 8.273 |
| 757735.372 | 3638191.888 | fast N-S | 157.5 | 12.988 | 8.246 |
| 757734.332 | 3638173.192 | slow S-N | 77.9 | 5.739 | 7.368 |
| 757734.906 | 3638184.262 | slow N-S | 72.8 | 5.350 | 7.354 |

757656.648 3638374.911 center (WGS84)
-114:14:48.565310 E2:51:11.591860 N center (Lon/Lat)
757734.791 3638178.913 center (NAD27)

**Figure 5.3.2.11.** Magnetic anomalies (red) due to the magnet at the intersection of the lag lines did not coincide at the center, as had been expected. Timing delays caused an apparent spatial offset, the size of which was a function of the velocity of the platform.

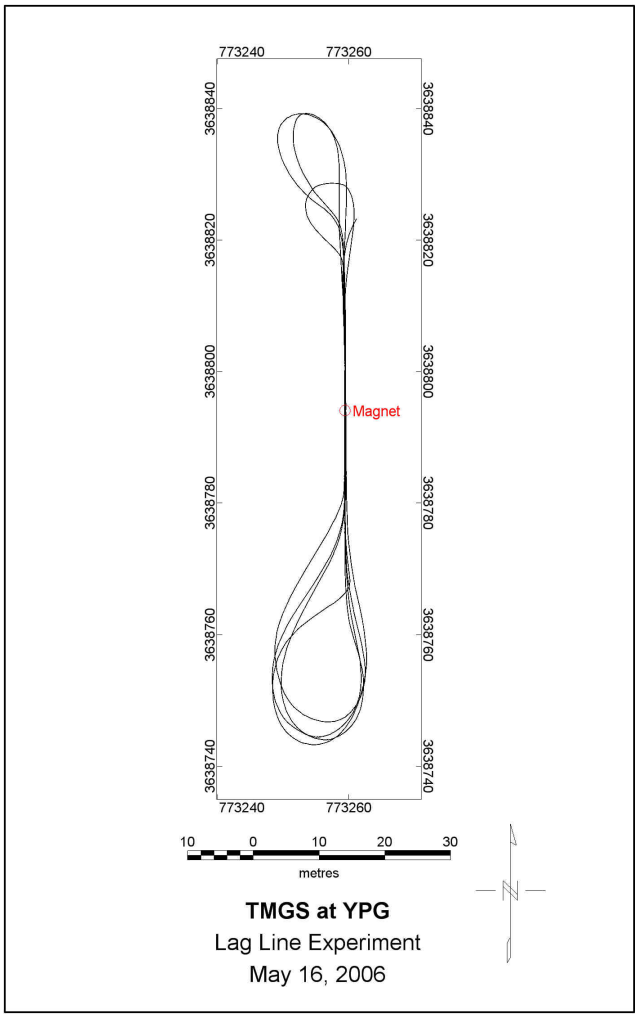


**Figure 5.3.2.12.** The lag-line experiment in 2006 was run along a single marked lane over a buried permanent magnet at the center, over which the cart was towed at different speeds.

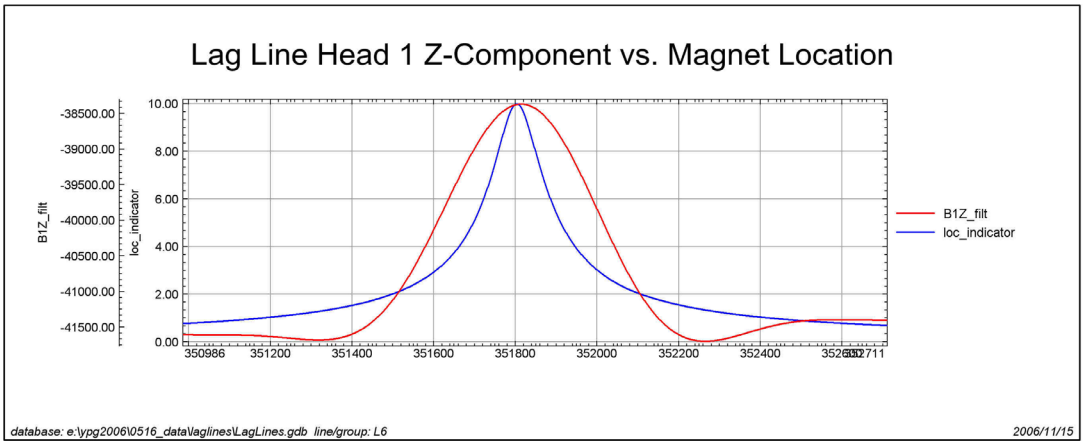


**Figure 5.3.2.13.** Lag-line experiments in 2006 confirmed that the PPS-timing circuit eliminated latency between the GPS and the DAS. The magnet location (blue line peak) coincides with its magnetic anomaly (red line). Abscissa is in sample number.

*Tractor Self-signature Experiment*

An important consideration with any towed platform system is the effect, if any, of the prime mover on data quality. While at YPG in March, 2003, we conducted an experiment to determine the magnetic self-signature of the Kubota tractor. The cart was unhitched from the tractor and data were acquired as the tractor drove slowly away to the limit of the cables. The largest anomaly was seen in the north-going data. Data from Head 2 (the head on the tetrahedron closest to the tractor) were converted to total field measurements, as shown in figure 5.3.2.14. The data (blue symbol) consisted of two components: (1) a large anomaly due to the tractor's engine and frame (red line) and (2) a varying signal (green) due to magnetization of the large rear tire rims. Using a regression procedure, we derived a tractor moment of approximately 450 A-m$^2$, and a (combined) wheel-rims moment of approximately 150 A-m$^2$. With a 7.1 m tow bar, the leading sensor of the magnetometer array would be 8.1 m away from the hitch. At this distance, the contribution from the tractor would be 2.2 nT, whereas the wheels would cause an alternating signal of ± 0.85 nT. In practice, the tractor signature would vary as a function of heading, causing a classic heading error. The rims would cause an oscillating signal with a spatial frequency of about 2 m. Because each rim has a separate magnetization, the amplitude of the oscillation could change with differential rotation of the wheels. In principle, permanent magnets can be affixed to the tractor to cancel the remanent magnetization and much of the induced magnetization. This method of passive compensation was not attempted.

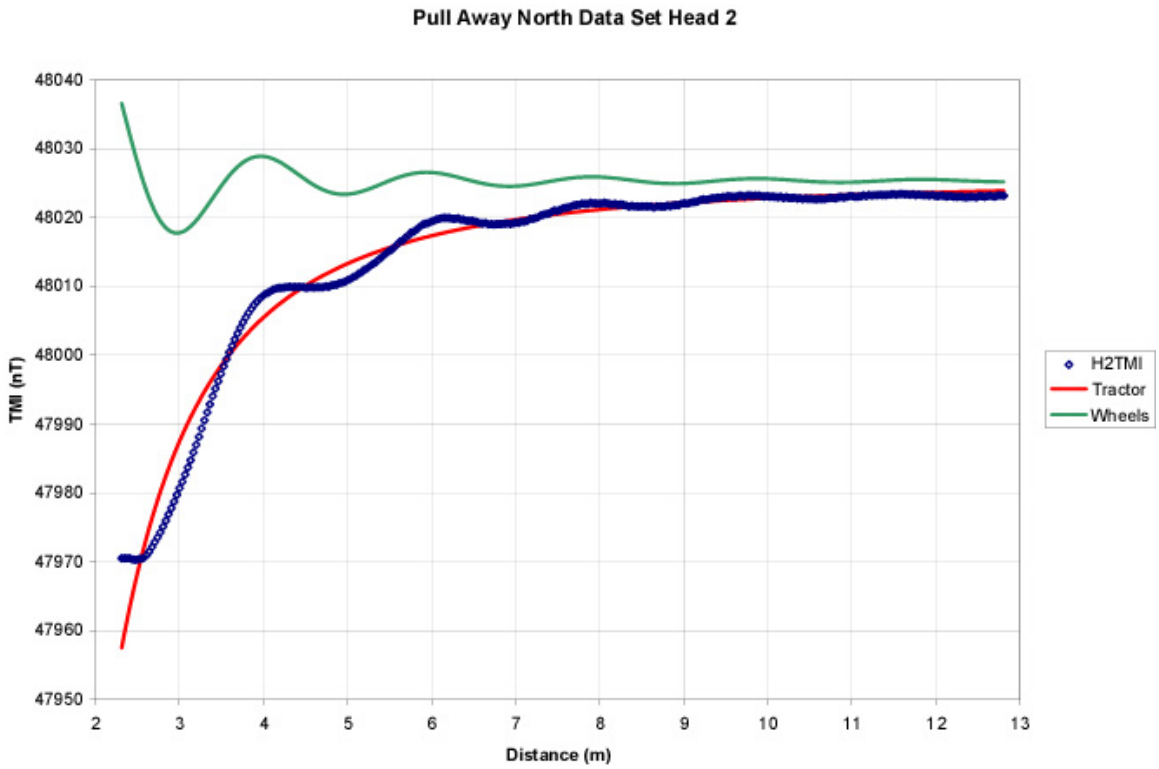


**Figure 5.3.2.14.** Tractor pull-away data from 2003 experiments.

*Calibration Grid and Blind Test Grid Surveys*

In November, 2005, we operated the modified TMGS solely over the Calibration Grid. Leica GPS provided position updates at 20 per second. As discussed in the preceding section, spatial

offsets (lags) were observed in the lag-line data and field data. These spatial tears were removed using lag-correction routines. Two complete surveys were made over each grid with the tractor-platform moving in "racetrack" mode, which proceeded in a continuous loop. The lines in the western half of the grid were taken in a south-to-north direction. The ones in the eastern half were taken in a north-to-south direction. Wide turnarounds were made beyond the northern and southern borders. Array trajectories for the November, 2005 tests are shown in figure 5.3.2.15. Figure 5.3.2.16 shows a photograph of the tractor-platform during data acquisition. Array trajectories over the BTG in May, 2006 are displayed in figure 5.3.2.17. Note that the Calibration Grid is aligned with magnetic north, whereas the BTG is aligned with geographic north.

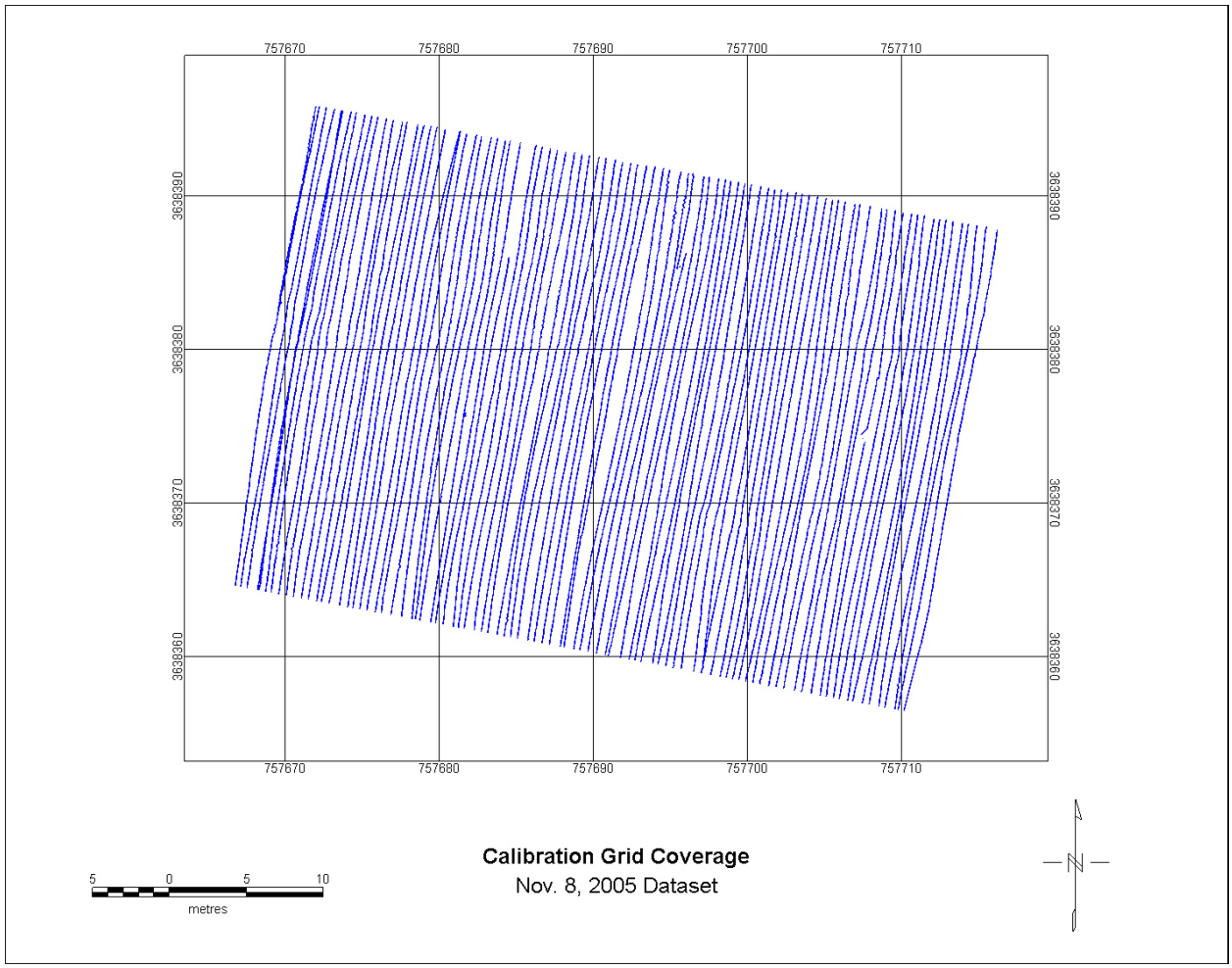


**Figure 5.3.2.15.** The Calibration Grid was surveyed along lines spaced 0.5 m apart. A few lines are truncated because GPS position quality changed from fix (acceptable) to float (unacceptable).

**Figure 5.3.2.16.** The TMGS in operation over the Calibration Grid. The operator used a simple outrigger pointer to guide the tractor between large red disks that marked the corners of individual cells.

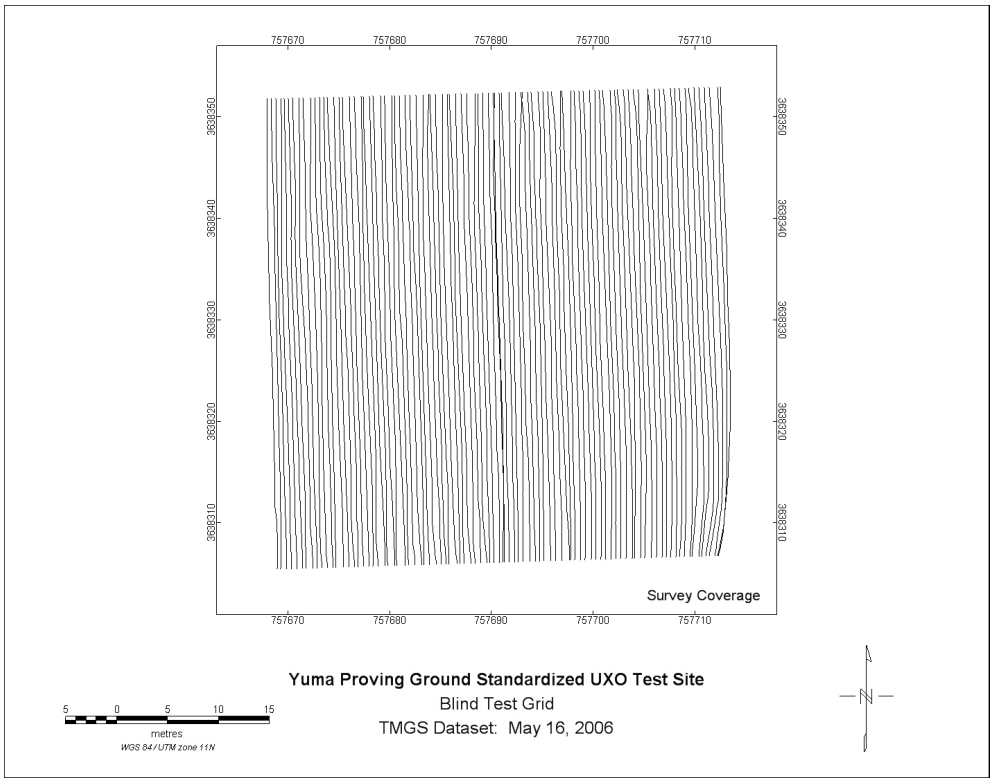


**Figure 5.3.2.17.** Array trajectories over the BTG in May, 2006. Lines are 0.5 m apart.

*Accelerometer Performance*

Two three-axis accelerometer units were affixed to the floor of the equipment bay on the cart. The main purpose of these accelerometers was to record large amplitude shocks and vibrations that could be correlated with sensor noise, if any deleterious effects were observed. As a test, one wheel of the cart was raised 10 cm and then released. The units easily measured moderate to large accelerations, as the data from this cart drop-test (figure 5.3.2.18) and the low-pass filtered data from the Blind Test Grid survey in 2006 (figure 5.3.2.19) show. The difference in amplitude of the signals in the drop-test was due to the different moment arm from each accelerometer unit to the pivot of rotation. The strip of large acceleration values bordering the grid on the north were caused when the cart rolled up and over PVC pipes protruding out of the ground. Other features were due to uneven terrain. The instantaneous values of acceleration were too contaminated by system noise to use in post-processing. We suspect the noise was caused by a faulty, floating ground between the units and the NI sample-and-hold card.

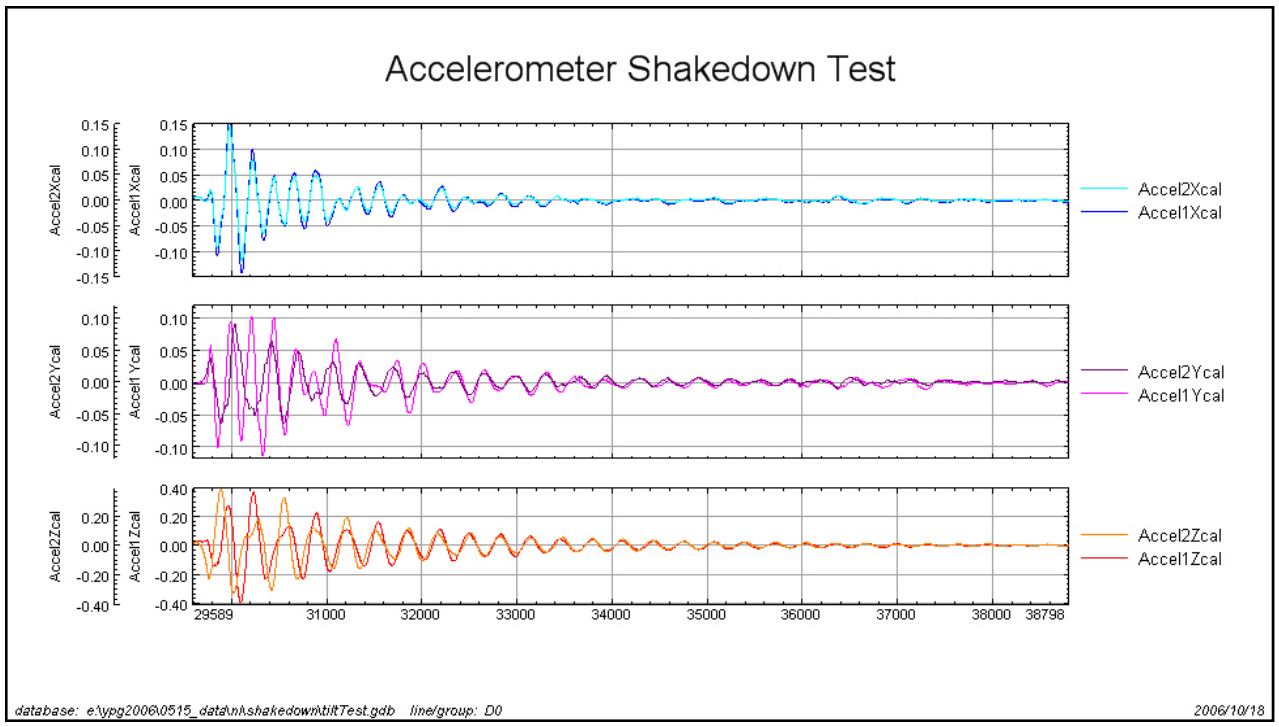


**Figure 5.3.2.18.** Accelerometer data from cart drop-test.

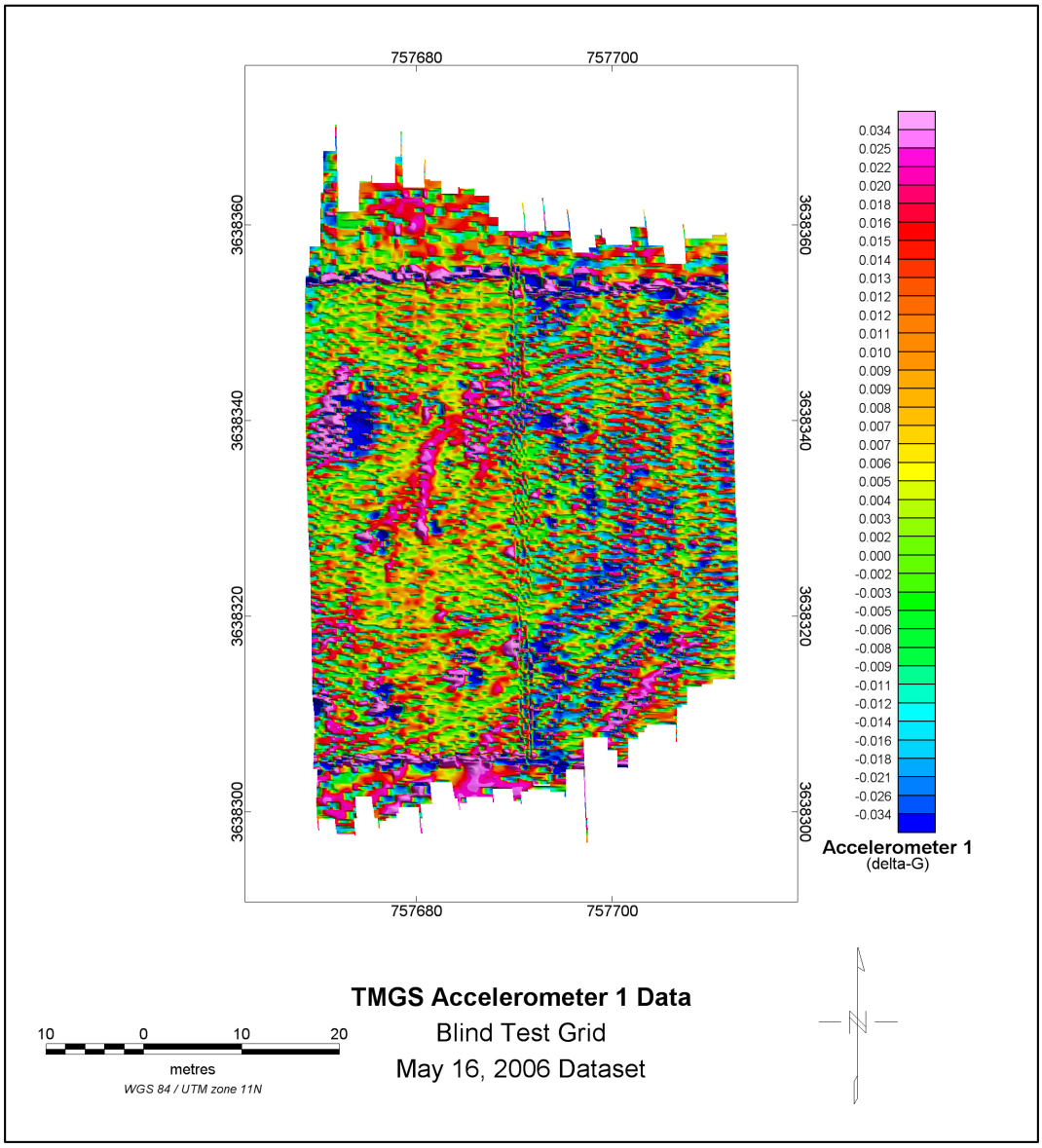


**Figure 5.3.2.19.** Map of accelerometer data over the Blind Test Grid after low-pass filtering.

*Inclinometer Performance*

A two-axis inclinometer unit was affixed to the bottom of the equipment bay of the cart. The purpose of this unit was to measure roll and pitch of the cart as it moved across the survey area. Roll and pitch angles can be used to correct a magnetic gradient tensor for rotations. The unit easily measured angle data, as the data from the cart drop-test (figure 5.3.2.20) and the low-pass filtered data from the Blind Test Grid survey in 2006 (figure 5.3.2.21) show. The strip of large pitch values bordering the grid on the north were caused when the cart rolled up and over PVC pipes protruding out of the ground. Other features were due to uneven terrain. The instantaneous values of roll and pitch were too contaminated by noise to use in post-processing. We suspect the noise was caused by high frequency, erratic sloshing of the electrolytic fluid in the sensing transducer. A different type of inclinometer sensor would solve this problem.

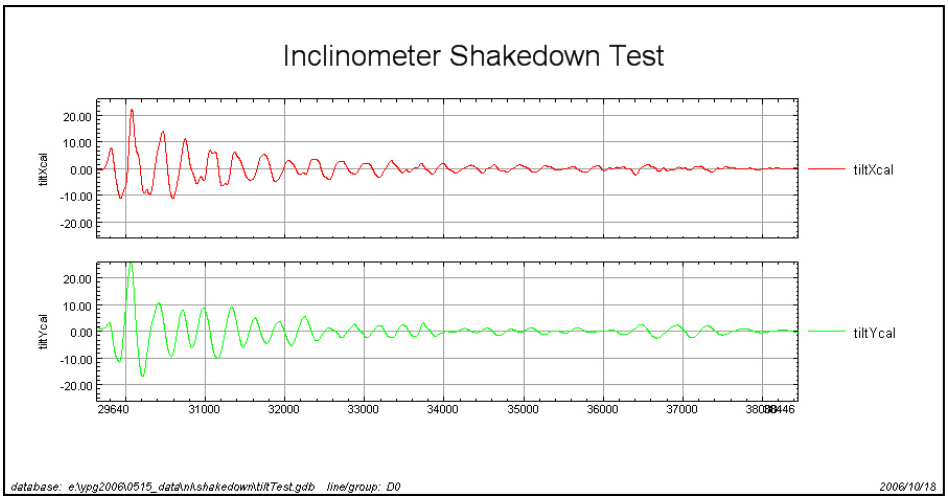


**Figure 5.3.2.20.** Inclinometer data from a cart drop-test.

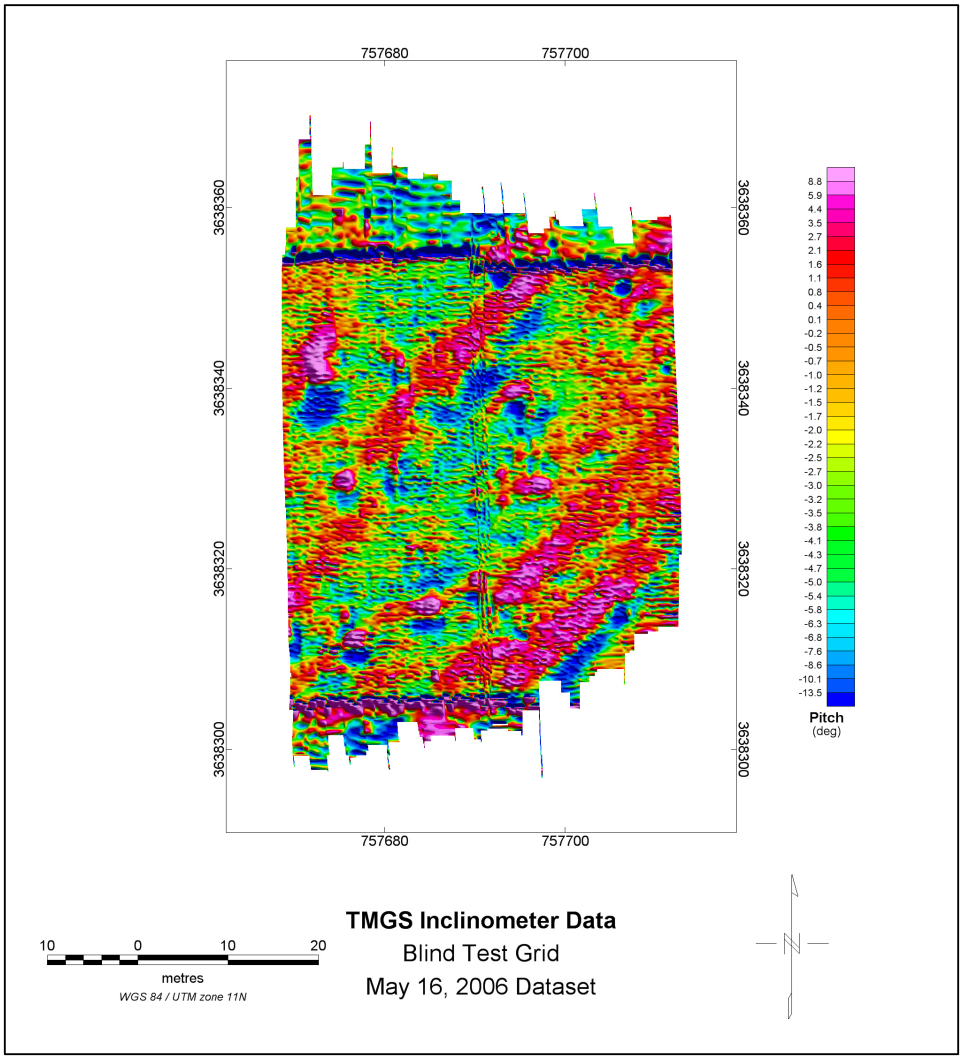


**Figure 5.3.2.21.** Inclinometer (pitch) data over the Blind Test Grid after low-pass filtering.

*GPS Performance*

Positioning information was obtained using a Leica GPS1200 system, operating in differential real-time kinematic (RTK) mode. New position updates were recorded in a separate data file at 20 updates per second. The accuracy of the positions was checked in an experiment where the antenna was moved in different directions at about 1 m/s over a microswitch located at a pre-surveyed location. The result of this experiment is shown in figure 5.3.2.22. The inset box compares the locations of the GPS antenna when the microswitch was tripped, compared to the true location (blue cross). Data clustered into two groups: the SW-NE paths and the NW-SE paths. The centroid of each group is within 4 cm of absolute. A map of the GPS elevation data from 2005 gives a representation of the topography over the Calibration Grid (figure 5.3.2.23), which shows a relative accuracy in *Z* in the order of 1 cm.

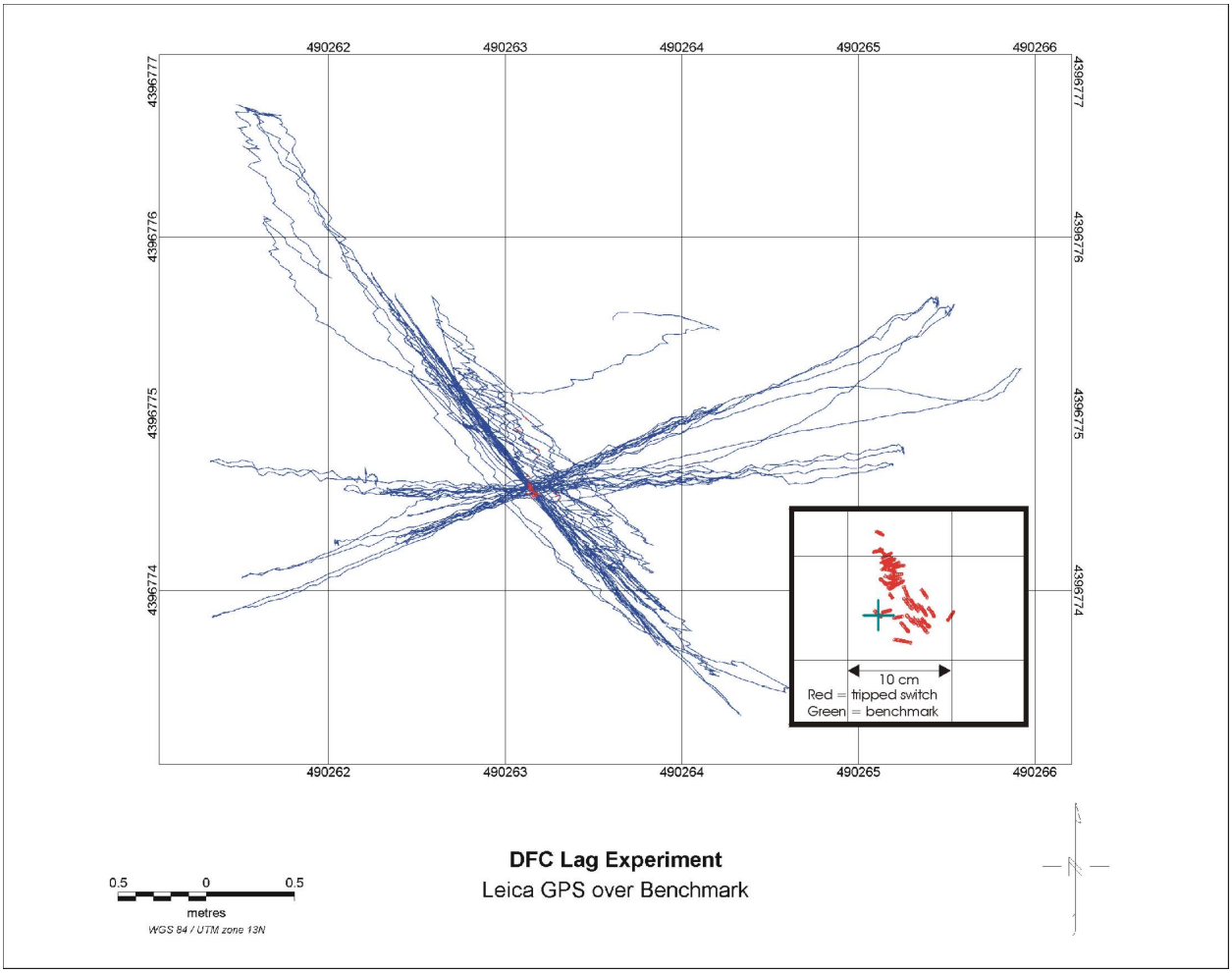


**Figure 5.3.2.22.** GPS accuracy experiment with Leica GPS1200 in RTK mode. A close-up of the data at the intersection over the microswitch is given in the inset box. Position errors include both GPS accuracy and system latency components.

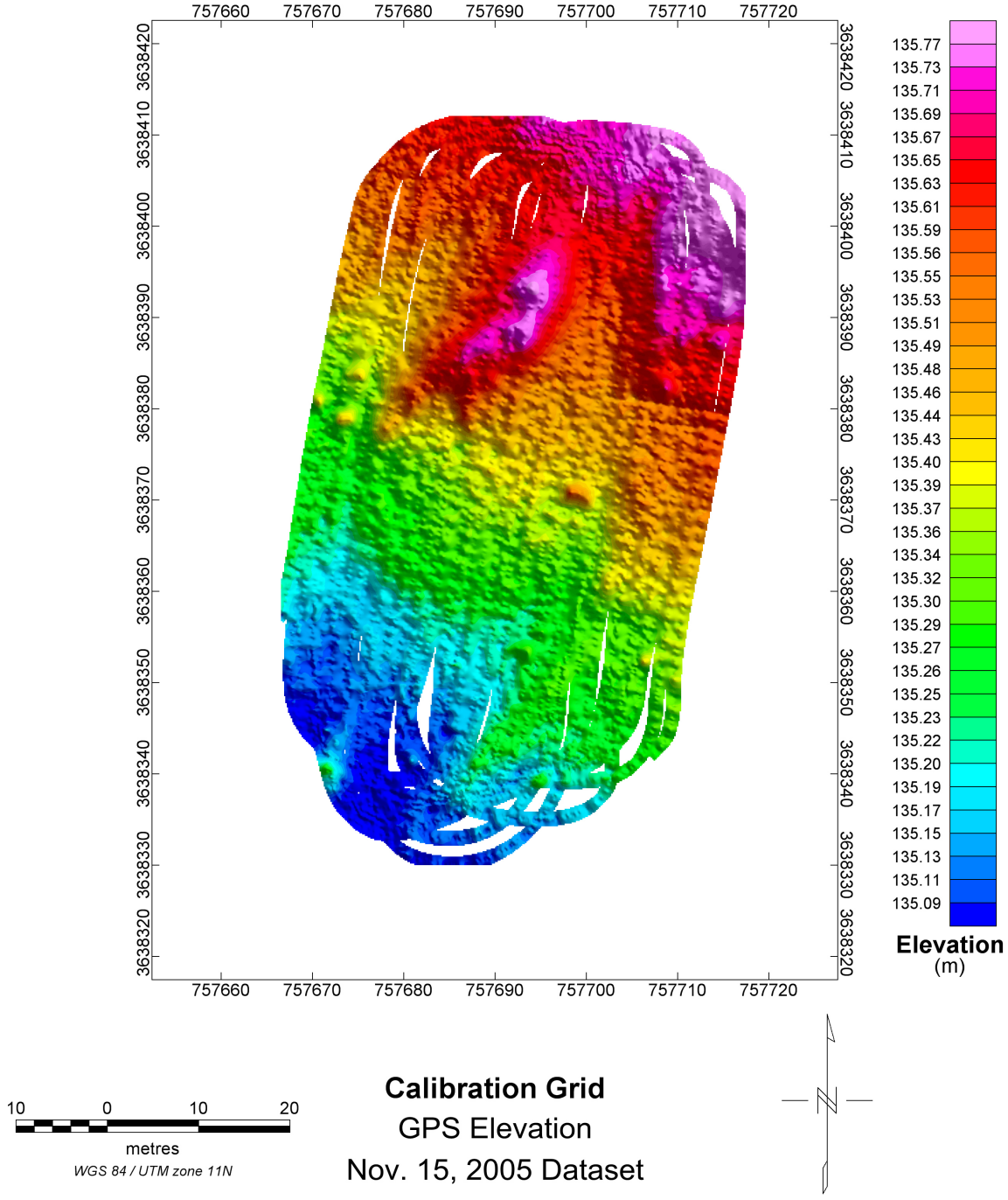


**Figure 5.3.2.23.** Map of GPS elevation data from tests in 2005 over the Calibration Grid.

Figure 5.2.2.24 shows a similar map over the BTG from 2006 data.

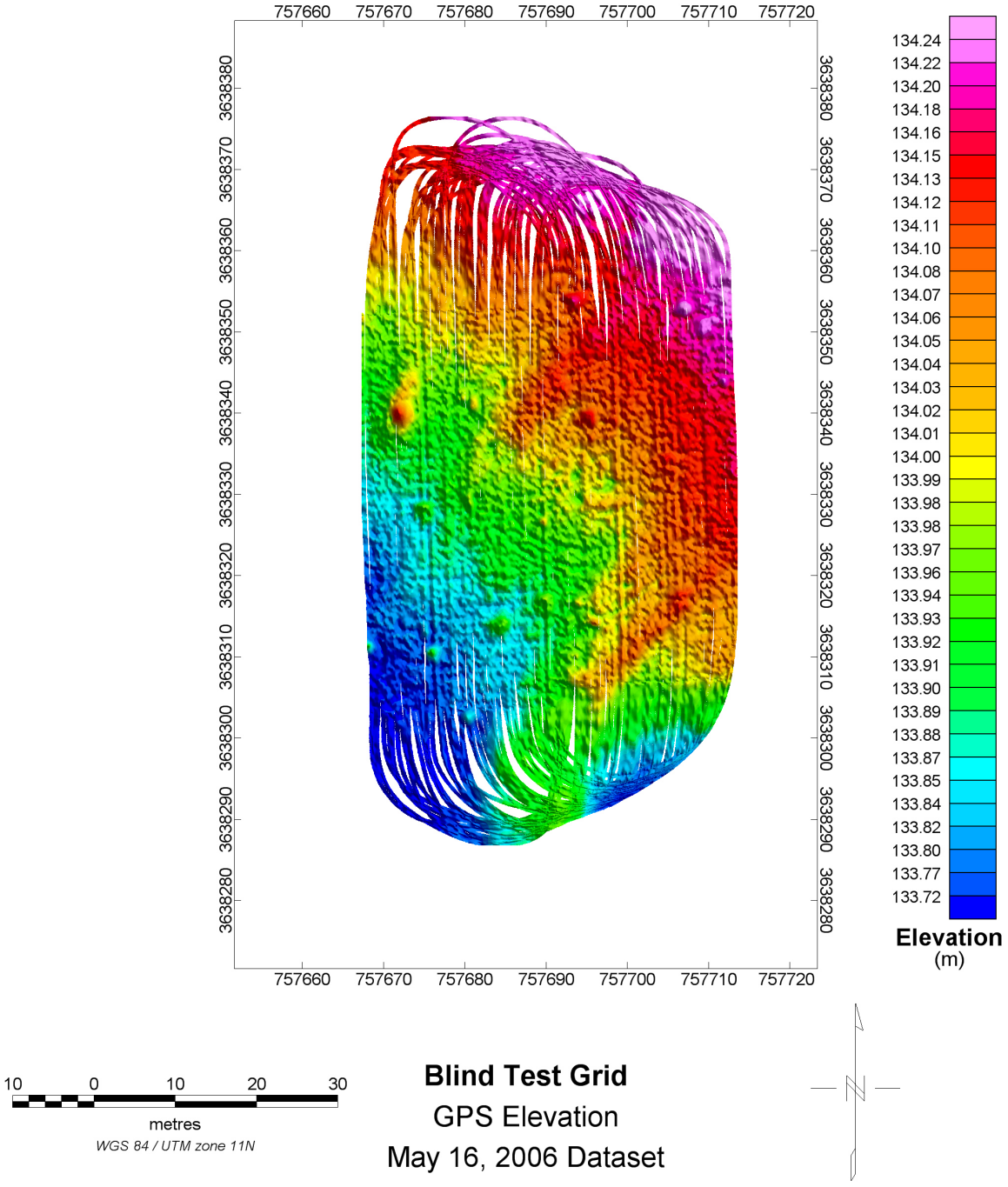


**Figure 5.3.2.24.** Map of GPS elevation data from tests in 2006 over the Blind Test Grid.

*Sensor Noise*

Along with position error (discussed in the preceding section *Lag Line Experiments*), sensor noise fundamentally limits ultimate performance, as the achievable signal-to-noise ratio determines both detection and discrimination capabilities. In this discussion, "sensor noise" refers to noise seen at the analog-to-digital inputs of the Error Signal of the magnetometer

channels. The manufacturer of the fluxgate magnetometers supplied specifications for each of the triaxial sensors (figure 5.3.2.25).

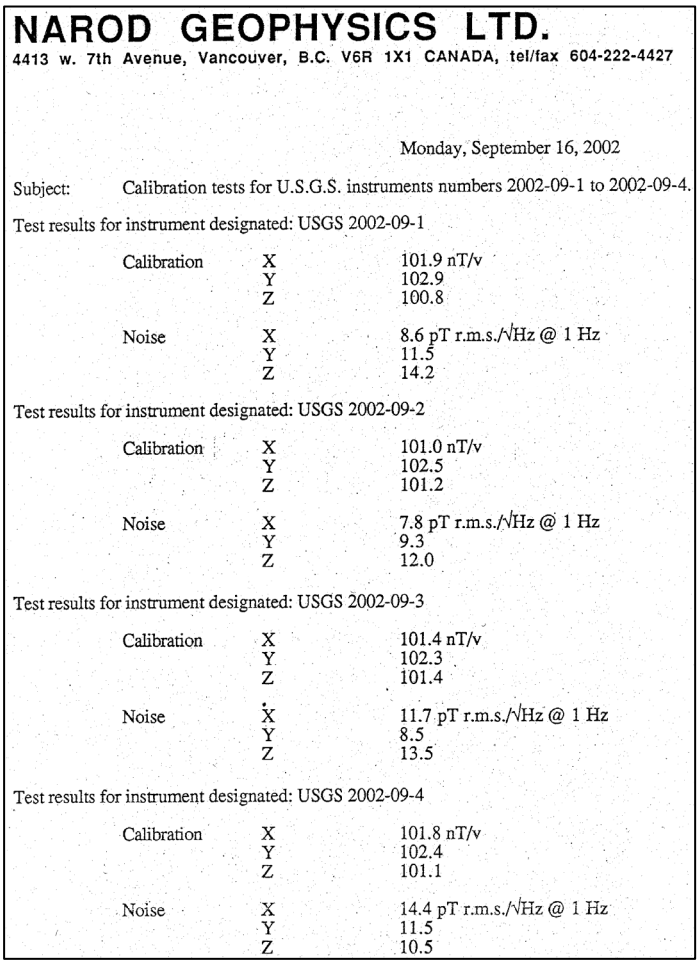

**NAROD GEOPHYSICS LTD.**

4413 w. 7th Avenue, Vancouver, B.C. V6R 1X1 CANADA, tel/fax 604-222-4427

Monday, September 16, 2002

Subject: Calibration tests for U.S.G.S. instruments numbers 2002-09-1 to 2002-09-4.

Test results for instrument designated: USGS 2002-09-1

| | | |
|---|---|---|
| Calibration | X | 101.9 nT/v |
| | Y | 102.9 |
| | Z | 100.8 |
| Noise | X | 8.6 pT r.m.s./√Hz @ 1 Hz |
| | Y | 11.5 |
| | Z | 14.2 |

Test results for instrument designated: USGS 2002-09-2

| | | |
|---|---|---|
| Calibration | X | 101.0 nT/v |
| | Y | 102.5 |
| | Z | 101.2 |
| Noise | X | 7.8 pT r.m.s./√Hz @ 1 Hz |
| | Y | 9.3 |
| | Z | 12.0 |

Test results for instrument designated: USGS 2002-09-3

| | | |
|---|---|---|
| Calibration | X | 101.4 nT/v |
| | Y | 102.3 |
| | Z | 101.4 |
| Noise | X | 11.7 pT r.m.s./√Hz @ 1 Hz |
| | Y | 8.5 |
| | Z | 13.5 |

Test results for instrument designated: USGS 2002-09-4

| | | |
|---|---|---|
| Calibration | X | 101.8 nT/v |
| | Y | 102.4 |
| | Z | 101.1 |
| Noise | X | 14.4 pT r.m.s./√Hz @ 1 Hz |
| | Y | 11.5 |
| | Z | 10.5 |

**Figure 5.3.2.25.** Manufacturer's specifications for the four triaxial fluxgate magnetometers used in the TMGS planar array.

As shown previously in figure 5.3.2.4, stationary data were acquired before and after spin calibration rotation. These data were excerpted and statistically analyzed for what they could tell us about actual sensor baseline noise. An example of the data is given in figure 5.3.2.26, with its continuous summary statistics given in figure 5.3.2.27. Comparative statistics for all 12 axes are presented in figure 5.3.2.28.

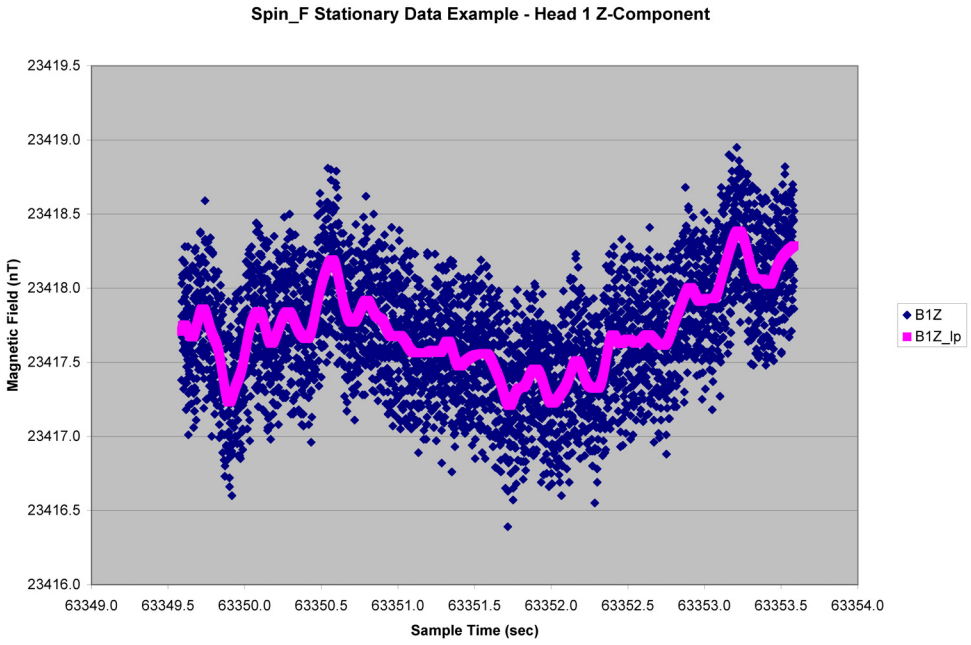


**Figure 5.3.2.26.** Example of raw (dark blue) and low-pass filtered (magenta) stationary data. High frequency noise rides on low frequency drift.

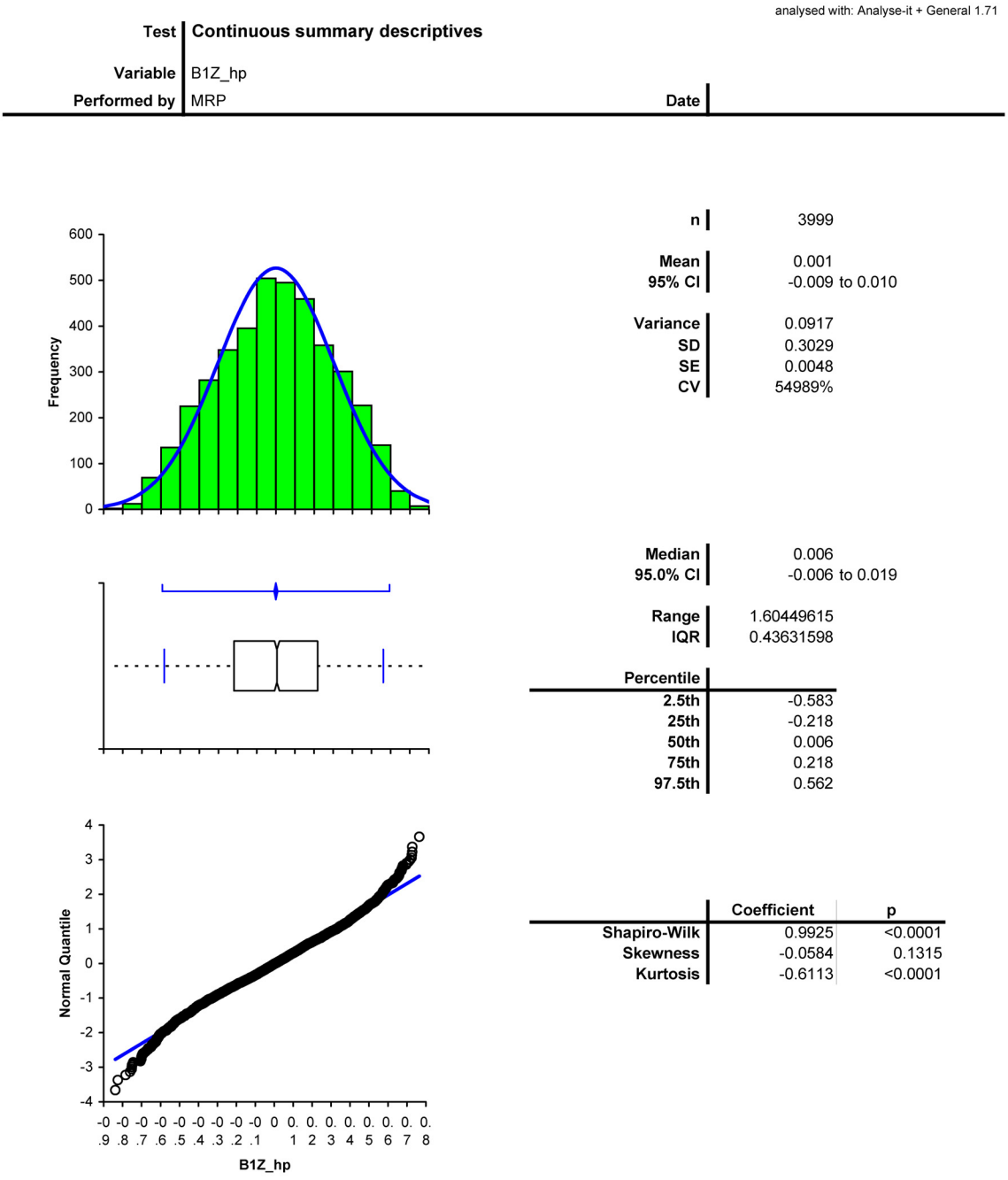


**Figure 5.3.2.27.** Continuous summary descriptive statistics for a single magnetometer axis (Head 1, Z-component, high-pass filtered) showing a normal distribution.

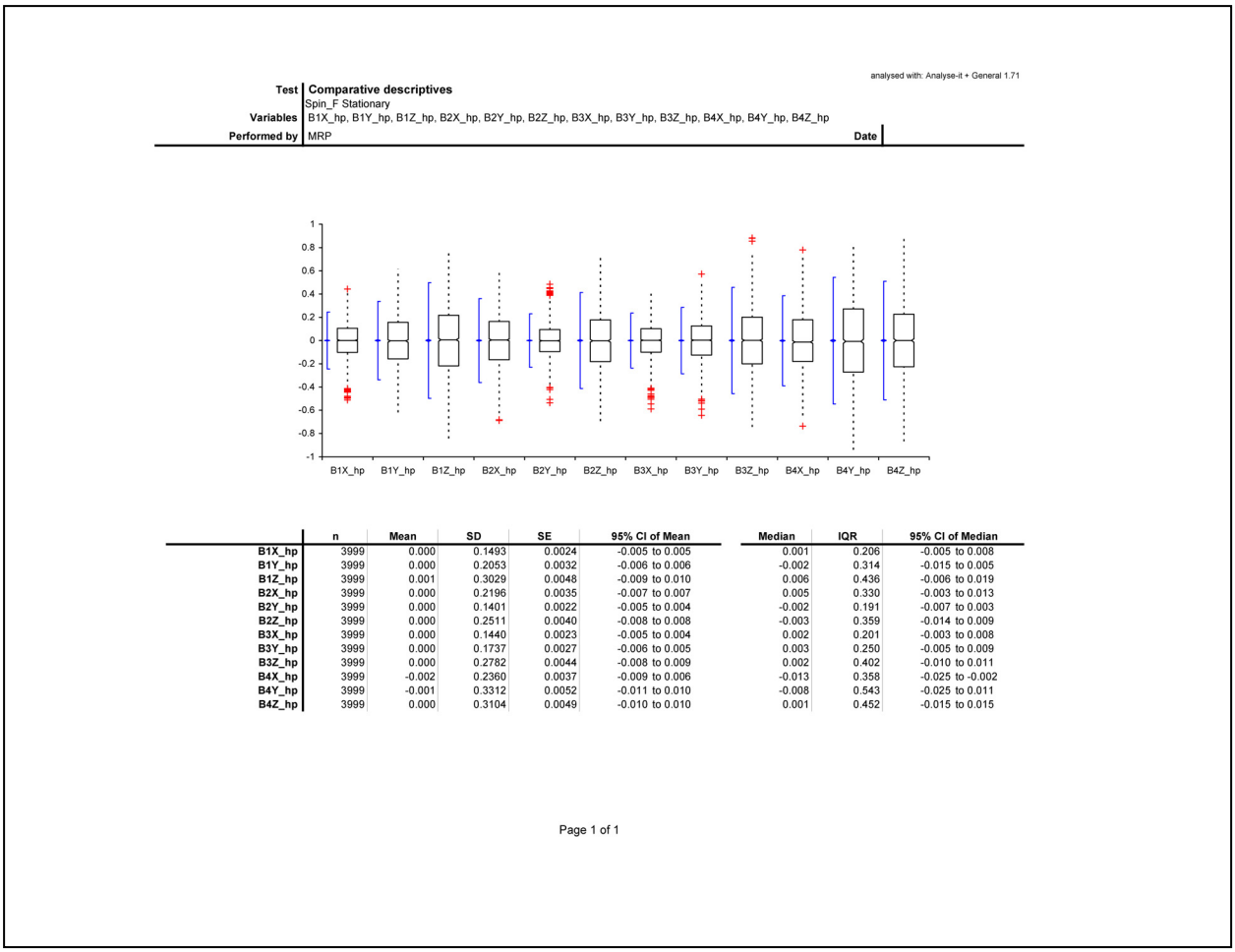

analysed with: Analyse-it + General 1.71

| | |
|---|---|
| Test | Comparative descriptives |
| | Spin_F Stationary |
| Variables | B1X_hp, B1Y_hp, B1Z_hp, B2X_hp, B2Y_hp, B2Z_hp, B3X_hp, B3Y_hp, B3Z_hp, B4X_hp, B4Y_hp, B4Z_hp |
| Performed by | MRP |
| Date | |



| | n | Mean | SD | SE | 95% CI of Mean | Median | IQR | 95% CI of Median |
|---|---|---|---|---|---|---|---|---|
| B1X_hp | 3999 | 0.000 | 0.1493 | 0.0024 | -0.005 to 0.005 | 0.001 | 0.206 | -0.005 to 0.008 |
| B1Y_hp | 3999 | 0.000 | 0.2053 | 0.0032 | -0.006 to 0.006 | -0.002 | 0.314 | -0.015 to 0.005 |
| B1Z_hp | 3999 | 0.001 | 0.3029 | 0.0048 | -0.009 to 0.010 | 0.006 | 0.436 | -0.006 to 0.019 |
| B2X_hp | 3999 | 0.000 | 0.2196 | 0.0035 | -0.007 to 0.007 | 0.005 | 0.330 | -0.003 to 0.013 |
| B2Y_hp | 3999 | 0.000 | 0.1401 | 0.0022 | -0.005 to 0.004 | -0.002 | 0.191 | -0.007 to 0.003 |
| B2Z_hp | 3999 | 0.000 | 0.2511 | 0.0040 | -0.008 to 0.008 | -0.003 | 0.359 | -0.014 to 0.009 |
| B3X_hp | 3999 | 0.000 | 0.1440 | 0.0023 | -0.005 to 0.004 | 0.002 | 0.201 | -0.003 to 0.008 |
| B3Y_hp | 3999 | 0.000 | 0.1737 | 0.0027 | -0.006 to 0.005 | 0.003 | 0.250 | -0.005 to 0.009 |
| B3Z_hp | 3999 | 0.000 | 0.2782 | 0.0044 | -0.008 to 0.009 | 0.002 | 0.402 | -0.010 to 0.011 |
| B4X_hp | 3999 | -0.002 | 0.2360 | 0.0037 | -0.009 to 0.006 | -0.013 | 0.358 | -0.025 to -0.002 |
| B4Y_hp | 3999 | -0.001 | 0.3312 | 0.0052 | -0.011 to 0.010 | -0.008 | 0.543 | -0.025 to 0.011 |
| B4Z_hp | 3999 | 0.000 | 0.3104 | 0.0049 | -0.010 to 0.010 | 0.001 | 0.452 | -0.015 to 0.015 |

Page 1 of 1

**Figure 5.3.2.28.** Comparative descriptive statistics for all 12 magnetometer axes, derived from 4 seconds (4,000 samples per axis) of simultaneous stationary array data. The standard deviation ranged from 0.1401 to 0.3312 nT, which is also equivalent to the root-mean-squared (RMS) value.

*Platform Motion Noise*

The fluxgate axes are exquisitely sensitive to motion noise. Take the extreme case where an axis is perpendicular to the main magnetic field, which has a magnitude of about 50,000 nT. Being perpendicular, the measured field is zero. If the axis deviates the slightest bit, then a large component will be measured as a function of the sine of the angle to the main field. Thus, a mere 0.01 degree change away from perpendicular results in a reading of 8.7 nT. Clearly, the slightest motion will cause significant changes in the measured magnetic components. This is shown in figure 5.3.2.29, in which the cart was given a slight push at about T = 53635.5 sec. The cart oscillated on its balloon tires with a frequency of about 2.9 Hz, causing the Head 1 X-component to register amplitude swings of between 2-3 nT. The effects of roll and pitch over uneven terrain are much more severe. No commercial attitude and heading measuring instrument is accurate and stable enough to correct for this motion noise, therefore the individual 12 magnetic components can not be used directly. Rather, parallel and diametrically opposite magnetic components must be differenced. When normalized by their separation distance, these gradients are free of motion noise (figure 5.3.2.30).

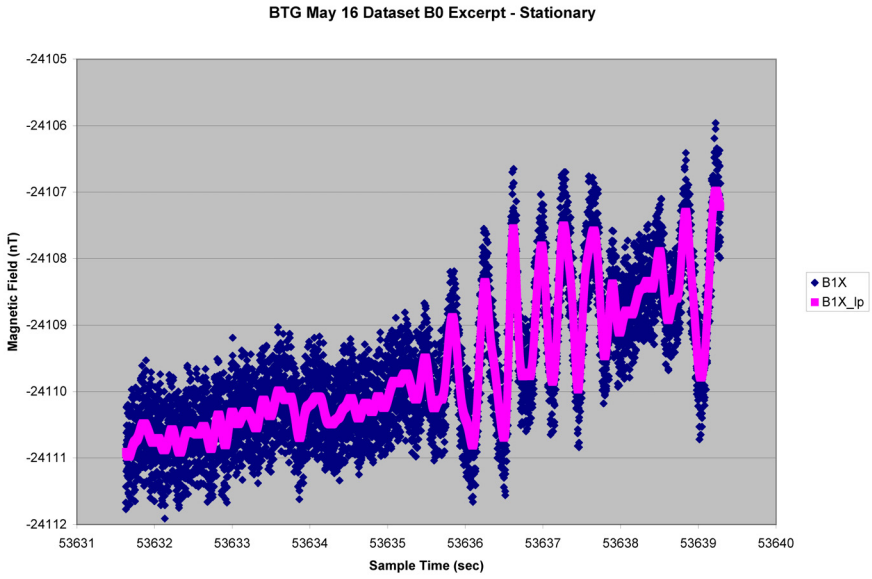


**Figure 5.3.2.29.** Raw (dark blue) and low-pass filtered (magenta) motion-induced noise commencing after T = 53635 seconds.

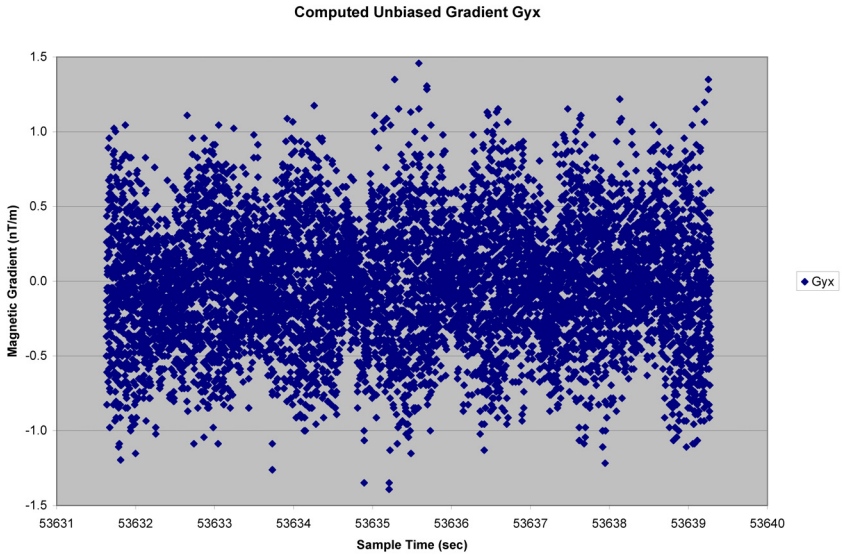

**Figure 5.3.2.30.** Calculated Gyx gradient demonstrating elimination of motion-induced noise. Uncorrelated high frequency noise remains.

*Thermal Drift Experiment*

Fluxgate magnetometers are inherently prone to thermal drift as a consequence of the ferromagnetic properties of the metallic alloys used in the cores and dimensional changes of the drive and sense coils. Either the array can be placed in a thermally controlled, constant temperature environment, or the thermal drift can be measured and removed in post-processing as a step in system calibration. To minimize the complexity of the cart, we chose the latter approach. Field conditions in the 2006 survey gave us an excellent opportunity to conduct a thermal drift experiment, with cool temperatures in the morning steadily increasing to hot in the afternoon. We parked the cart at a magnetically clean location and, using wooden blocks, tilted the cart with the top of the array facing northeast. In this attitude all 12 magnetometer axes were exposed to large vector components of the Earth's magnetic field. Any thermally induced changes in fluxgate responses would have operated on large measured values, thus magnifying the effects.

Each magnetometer head had a thermistor affixed to the head's plastic coil-mounting block. The temperature measured by any one of these thermistors is the sum of the outside ambient temperature filtering in through the sensor head's insulation, and a slow build-up of excess heat inside the insulation due to the very small currents running in the fluxgate coils. Temperature changes are buffered by the heat capacities of the sensor's mounting block and coils, so that all head temperatures change slowly in order to minimize thermal gradients. The result is that a repeatable correction, as a function of head temperature, can be applied to the field measurements of each axis. A thermistor in the temperature-stabilized magnetometer interface unit recorded the temperature of the electronic circuits. The active thermal control has been designed to maintain a constant temperature for the circuit board environment to within ±0.5° C, once stabilized. Pre-construction testing of the circuit boards indicated that these temperature limits were sufficient to limit circuit-temperature-related magnetic variation to within ±0.1 nT per axis. A temperature sensor affixed to the mechanical support structure of the array measured the ambient temperature in the cargo bay of the platform.

Data were collected from 53300 to 70400 UTC (0748 to 1233 local time). As figure 5.3.2.31 shows, the ambient temperature (orange line) had already begun rising because of solar loading. The temperatures of the heads (green, blue, magenta, purple) started rising a while later due primarily to current-related heat buildup, and secondarily to the rise in ambient temperature filtering through the thermal insulating boxes. The temperature spread between heads was probably due to slight variations from head to head in the amount of insulation. The electronics interface unit took about 1.3 hours to stabilize to within 0.1° C of 33.9° C in a range of 33.0-34.0° C, which is normal and well within design specifications. At about 67000 UTC, the internal temperature started to decrease and stabilized at about 33.6° C. This behavior is also normal, well within specifications, and probably results from subtle interactions between the active stabilization program and turbulent flow of internal fan-forced air over the thermistor. Nevertheless, to eliminate the possibility of electronic thermal drift as a forcing function, we analyzed only the data from 60000 to 67000 UTC (nearly 2 hours), when the internal temperature was most stable. The temperature and magnetic field data used in the regression

analysis are shown in figures 5.3.2.32 and 5.3.2.33. Linear regression solutions are shown in figure 5.3.2.34.

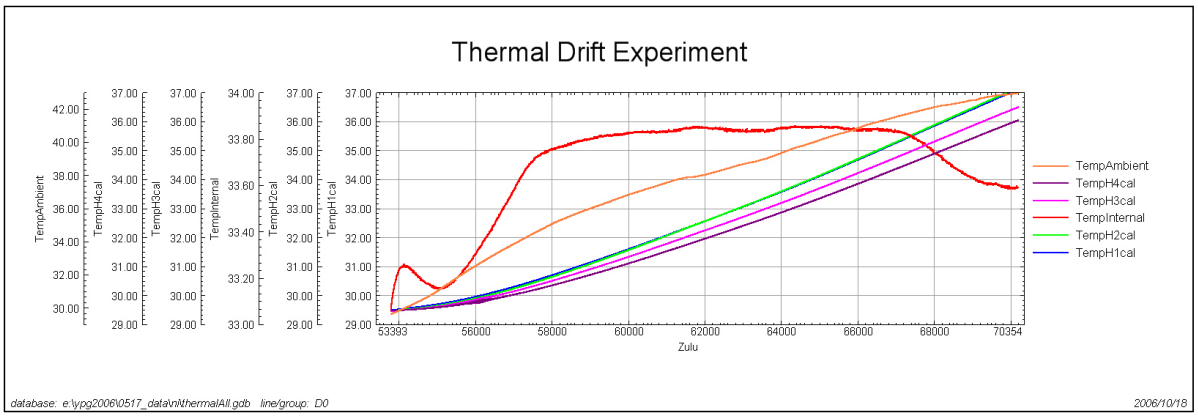


**Figure 5.3.2.31.** Thermal drift data showing ambient, internal, and heads H1, H2, H3, and H4 temperatures from system turn-on to turn-off.

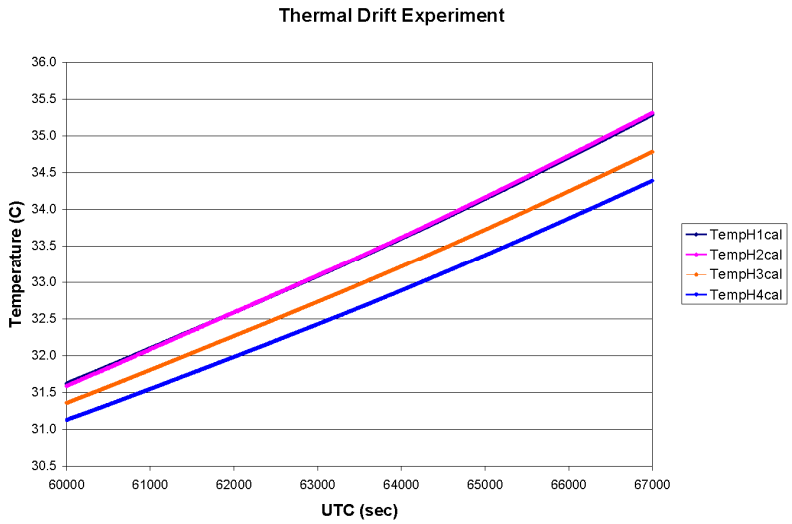


**Figure 5.3.2.32.** Four head temperatures used for regression analysis.

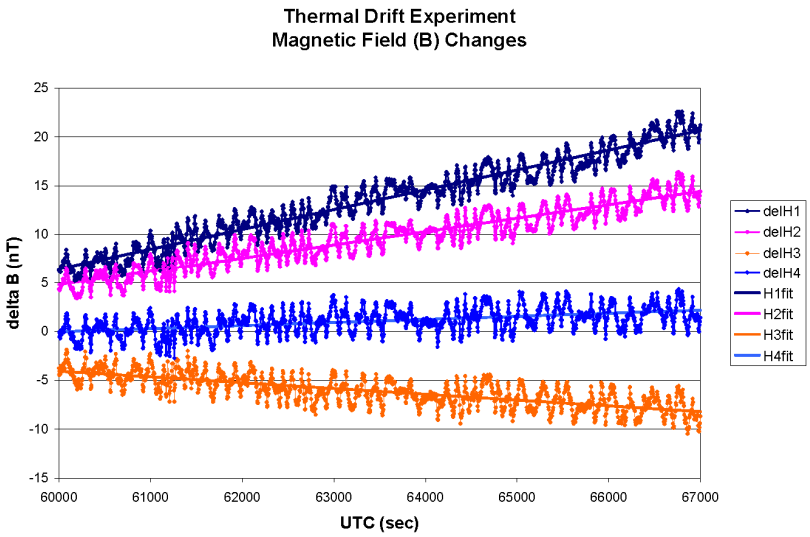


**Figure 5.3.2.33.** Magnetic field data (line with symbol) and linear fitted trend (solid line) for the four heads.

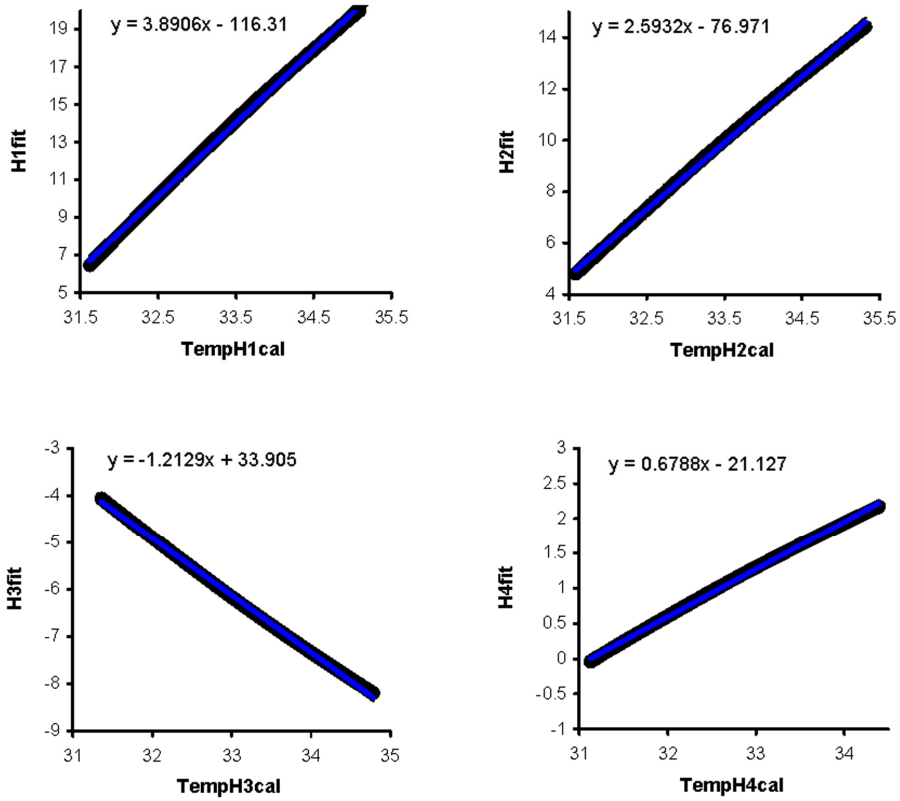


**Figure 5.3.2.34.** Linear regression solutions of magnetic field trend (dependent variable) versus temperature (independent variable)

Results of the thermal drift experiment verify the suspected sensitivity of the fluxgate magnetometers to temperature. Each fluxgate behaved differently, with a range of –1.21 to 3.89 nT/°C. If the relationships are fixed and linear, then temperature measurements can be used to compensate the magnetic field measurements. If not, then the sensor array will have to be enclosed in a temperature-stabilized (± 0.1°C) environment - a range not even achieved with the sophisticated and cumbersome electronics interface unit.

#### 5.3.2.1 Comparisons of TMGS data to G-858 data

In March, 2003, the original, tetrahedral TMGS was operated over the Calibration Grid at the Standardized Test Site at Yuma Proving Ground in proof-of-principle tests. The Calibration Grid is a flat, rectangular area divided into 1 m by 1 m grid cells. The cells were seeded with degaussed inert ordnance items, clutter items, or no item. The layout of the Calibration Grid is displayed in figure 5.3.2.1.1. Note that the grid is aligned with magnetic north, rather than geographic north. This favored the creation of nearly ideal magnetic anomalies along the principal axes of axisymmetric bodies. If, instead, the grid and targets had been aligned with true north, then the Earth's magnetic field, expressed in geomagnetic convention as *HDZ* (horizontal, declination, and vertical down), would have had a large transverse field component, *D*, at each target location, where *D* is the geomagnetic declination component. A large *D* would induce a significant transverse magnetization, thereby skewing the magnetic anomalies from the grid's orientation. Aligning the grid with magnetic north eliminates transverse components, leaving only horizontal and vertical components of the Earth's field (in the grid's frame of reference).

For experimental control, a dual-head cesium vapor magnetometer was mounted on the towed platform (figure 5.3.2.1.2). The top head was at the same height as the top sensor (Head 1) on the tetrahedron. The bottom head was at the same height as the leading sensor (Head 2). Both datasets were filtered, diurnal corrected (using base station data), denoised, spline-fitted, and trend removed. To facilitate comparison of total field data, the vector resultant of the axial components of Head 2 was calculated. The processed datasets can be seen in figures 5.3.2.1.3 and 5.3.2.1.4. Based upon these data, the fluxgate sensor head was deemed to be as accurate, if not more accurate, than the cesium vapor sensor when operating on a moving platform.

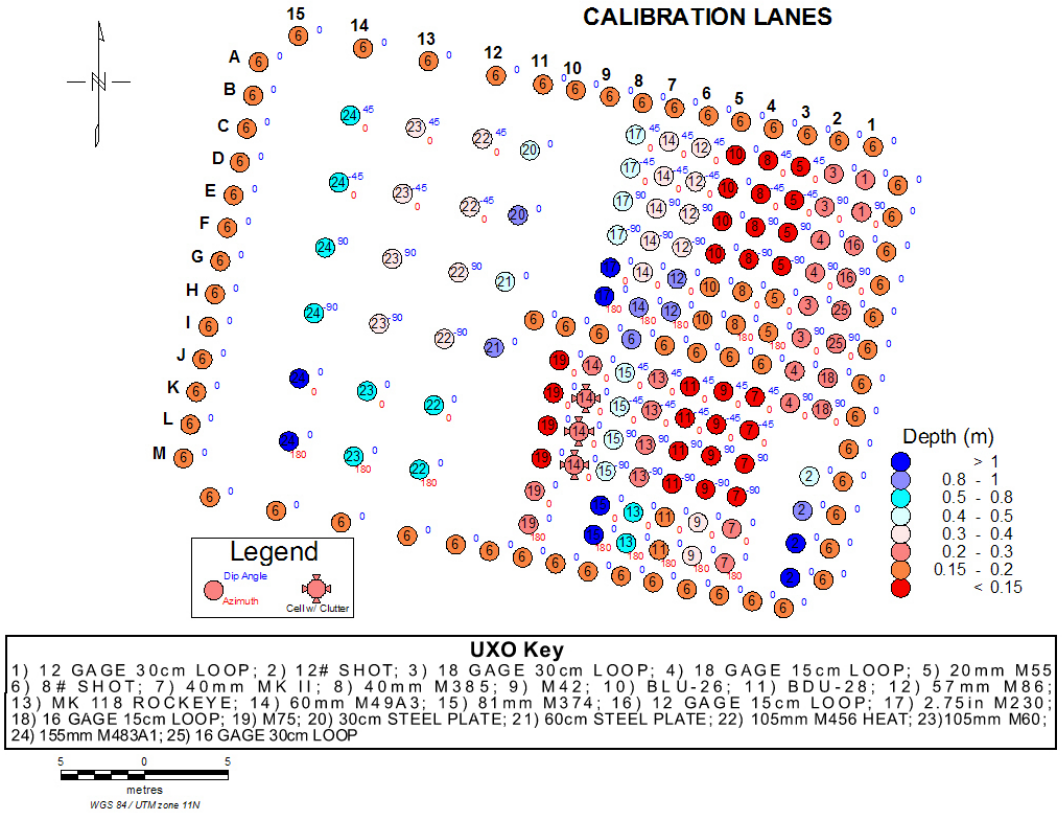


**Figure 5.3.2.1.1.** Calibration Grid map and target key for the March, 2003, field tests.

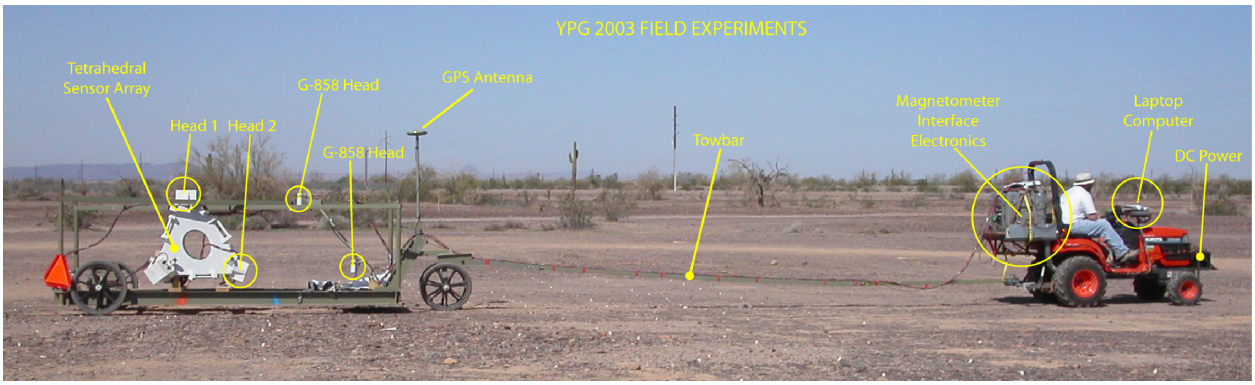


**Figure 5.3.2.1.2.** Field experiments at YPG in 2003 with the original tetrahedral array and G-858 magnetometers.

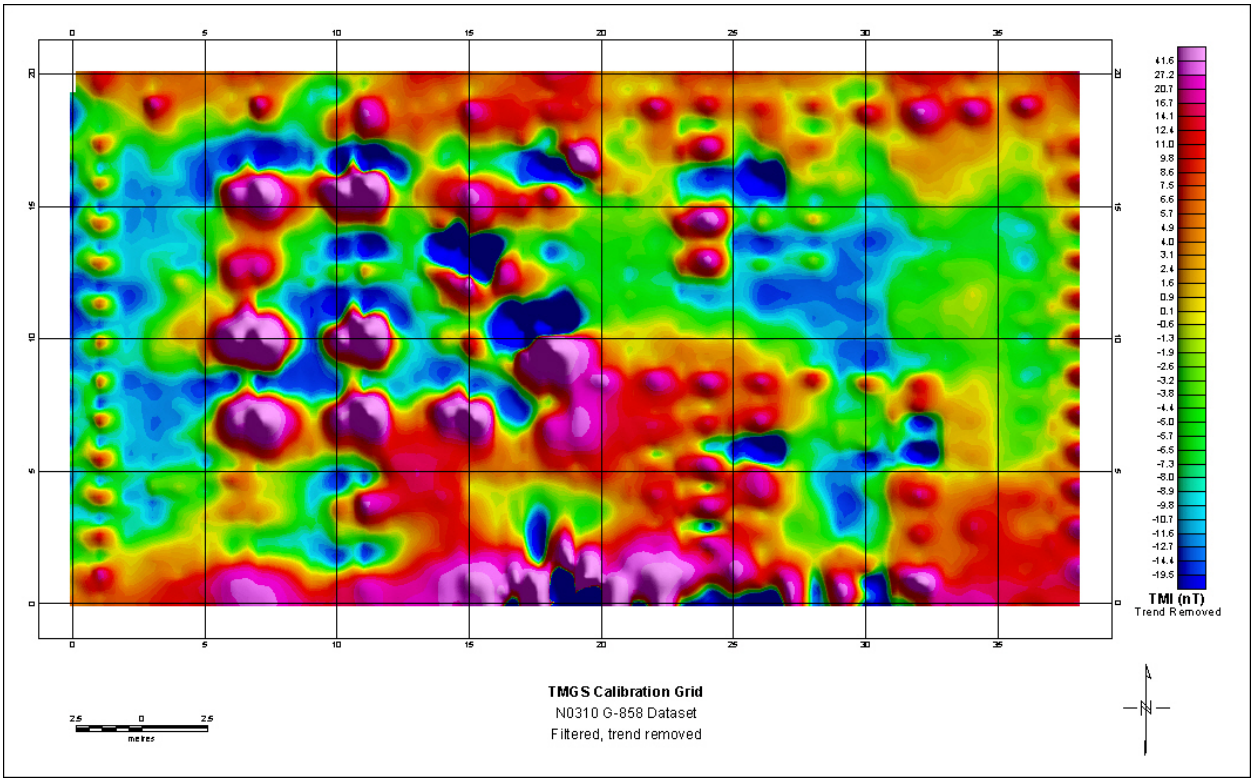


**Figure 5.3.2.1.3.** G-858 data collected over the Calibration Grid in 2003.

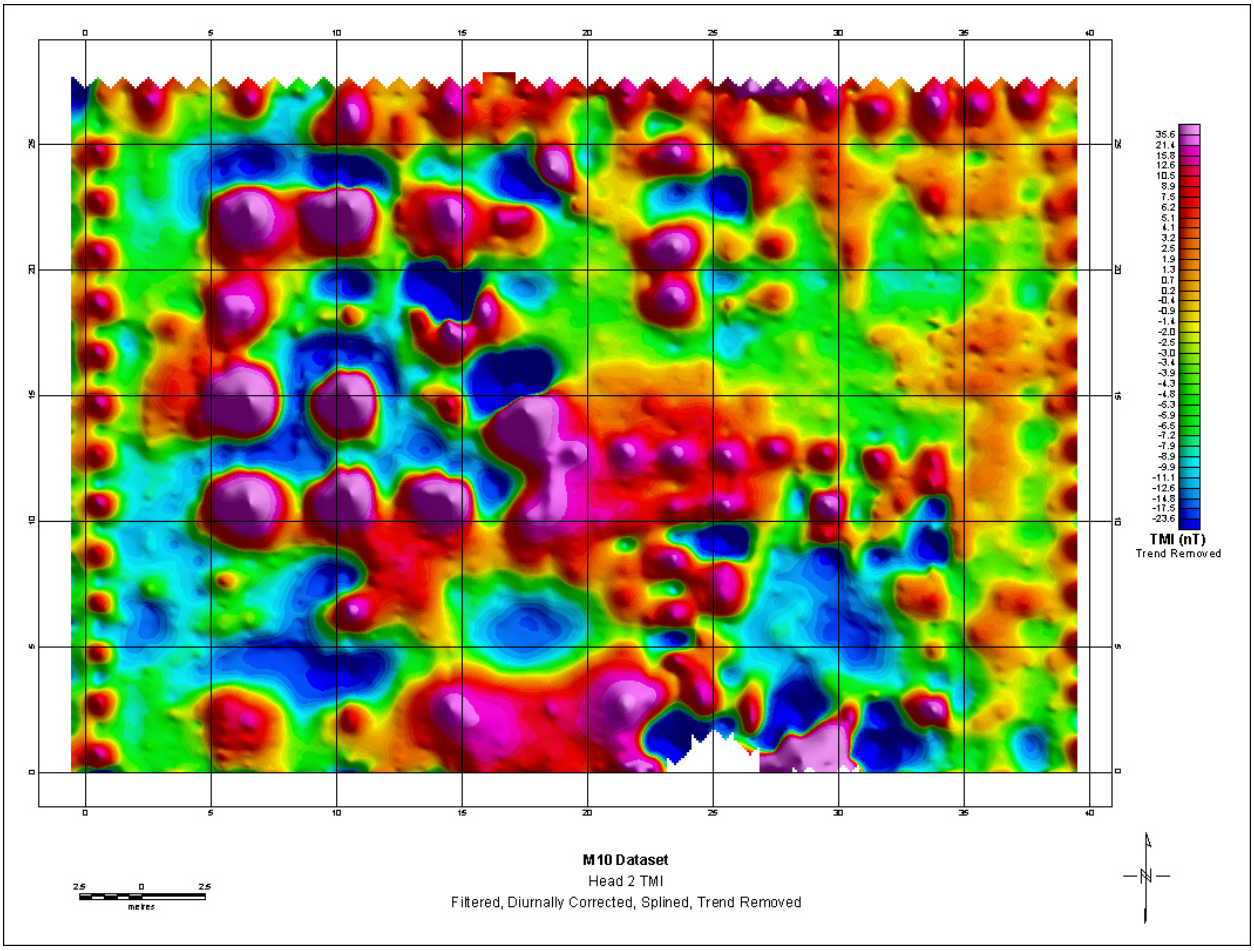


**Figure 5.3.2.1.4**. TMGS data in 2003 using the tetrahedral array over the Calibration Grid (Head 2 total magnetic field equivalent)

A map of total field equivalent data for Head 1, collected over the Calibration Grid with the planar array in 2005, is shown in figure 5.3.2.1.5. Note the prominent baseline shift due to heading error in magnetic field values on the west and east halves of the area. Comparisons of TMGS planar-array data acquired in 2005 and 2006 to G-858 data is not possible because hardware breakdowns, combined with inexperienced personnel, confounded our attempts to re-survey the Calibration Grid with a G-858 magnetometer system.

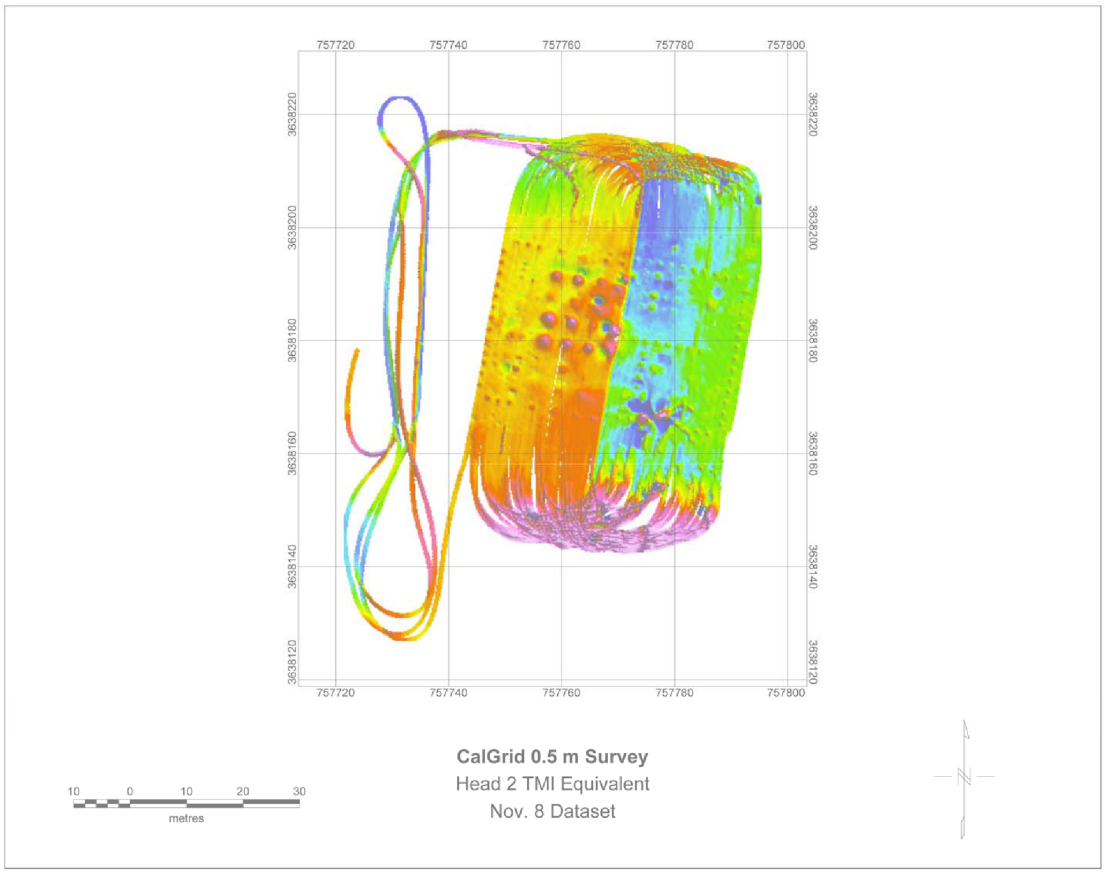


**Figure 5.3.2.1.5.** Map of Head 2 total field equivalent data from 2005.

### 5.3.2.2 Selected TMGS data maps

As in figure 5.3.2.1.4 above, total magnetic field equivalent maps were made by vector summing the data from each magnetometer head. These maps are shown in figure 5.3.2.2.1, where an apparent heading error of approximately 30 nT is evident as an intensity shift (higher values on the west half, lower values on the east half). As discussed in section 5.3.2 above under Tractor Self-Signature Experiments, a small part of the heading error can be attributed to a change in the magnetic moment of the tractor as it travels along different bearings (discussed in section 5.4.2 below). Maps of each of the magnetic gradient components (G*xx*, G*xy*, G*xz*, G*yy*, G*yz*, G*zz*) over the BTG are shown in figure 5.3.2.2.2. In this nomenclature, G*xy* means "gradient of the X-component in the Y-direction", for example. Although gradients were not directly measured in the Z-direction (no sensor above or below the plane of the array), the symmetry of the gradient tensor makes G*xz* = G*zx*, and G*yz* = G*zy*. Also, G*zz* is derived from the trace: G*zz* = -( G*xx*+ G*yy*). These represent the individual gradient components comprising a magnetic tensor. Note that the strong heading error present in the total field maps is missing in the gradient maps, as are anomalies caused by changes in the cart's attitude.

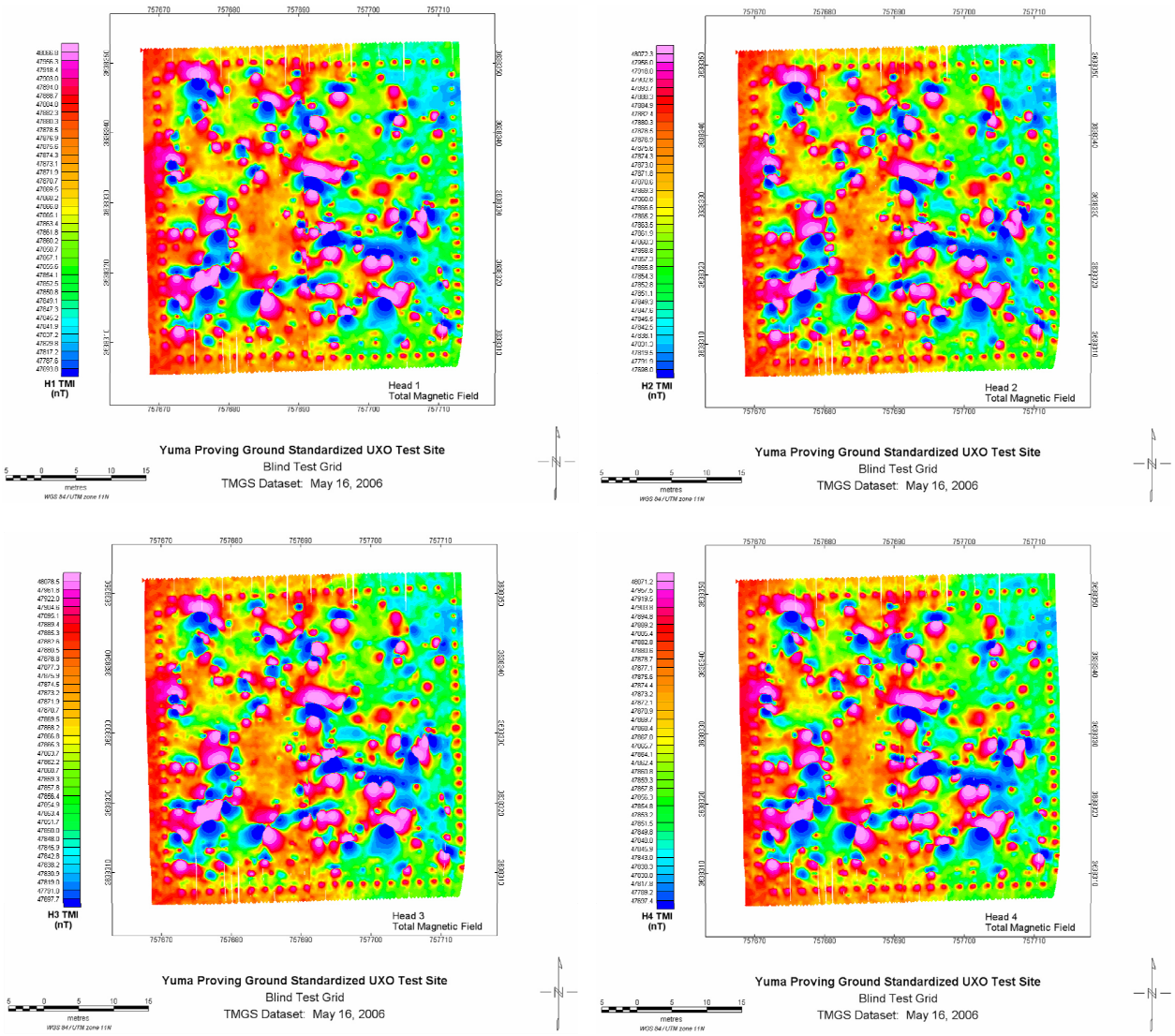


**Figure 5.3.2.2.1.** Total field equivalent maps of Head 1, Head 2, Head 3, and Head 4, in order from left to right, starting at top row.

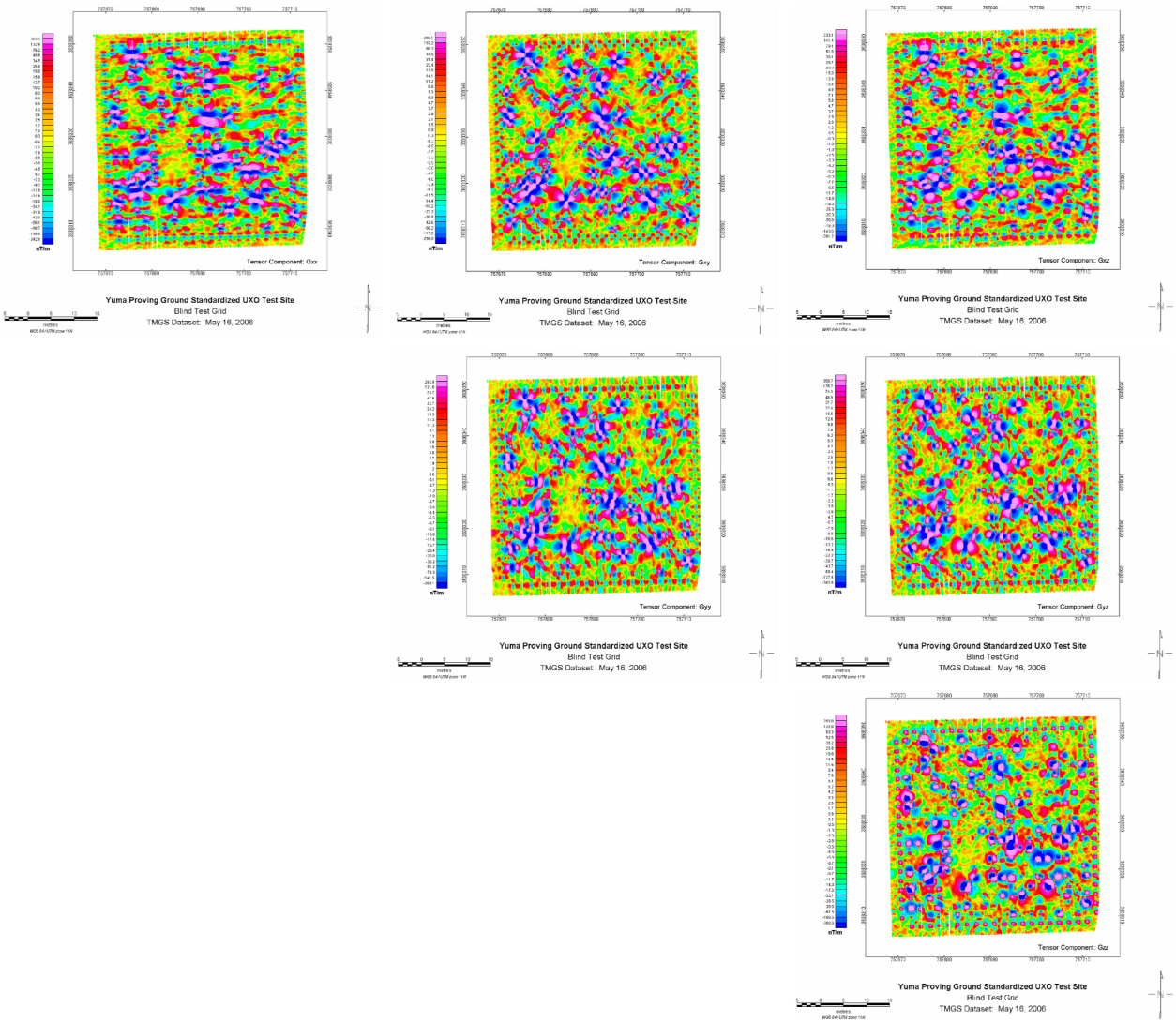


**Figure 5.3.2.2.2.** Maps of each of the magnetic gradient components (G*xx*, G*xy*, G*xz*, G*yy*, G*yz*, G*zz*) over the BTG, shown in order from left to right, starting at the top row.

Seeing that a set of gradient component maps is cumbersome and difficult to interpret, we turn toward an effective method of displaying all the information in a single dataset, in which the components of the magnetic gradient tensor are reduced to a single scalar quantity called a tensor invariant. A tensor invariant is, by definition, a quantity that remains constant regardless of how the tensor has been rotated. It is therefore independent of the TMGS array's attitude, much the same way that a value of total field is independent of the total-field sensor's attitude. Consequently, we can produce an anomaly map directly from the TMGS data – not as a derivative – that is completely analogous to a total field map, except that instead of field magnitude, it shows gradient magnitude.

There are three tensor invariants, commonly called: $I_0$, $I_1$, and $I_2$. They may also be designated with the Roman numerals, I, II, III. The direct formulas for each are shown here:

$$I_0 = G_{XX} + G_{YY} + G_{ZZ} = 0. \qquad (5.3.2.2.1)$$

$$I_1 = G_{XX}G_{YY} + G_{YY}G_{ZZ} + G_{XX}G_{ZZ} - (G_{XY})^2 - (G_{YZ})^2 - (G_{XZ})^2 \quad (5.3.2.2.2)$$

$$I_2 = G_{XX}(G_{YY}G_{ZZ} - G_{YZGZY}) - G_{XY}(G_{YX}G_{ZZ} - G_{YZGZX}) + G_{XZ}(G_{YX}G_{ZY} - G_{YY}G_{ZX}). \quad (5.3.2.2.3)$$

Invariant $I_0$ is simply the trace of the tensor, which vanishes because the divergence of a magnetostatic field is zero; and it is therefore not directly useful. Invariant $I_2$ is found by taking the determinant of the matrix; which is of cubic form, potentially taking on extreme positive and negative values, and making it difficult to reduce the $I_2$ invariant to a physically meaningful value. However, the $I_1$ invariant is always negative, and taking advantage of the vanishing trace, can be easily converted to the always-positive Frobenius norm:

$$(\|G\|_F)^2 = (G_{XX})^2 + (G_{YY})^2 + (G_{ZZ})^2 + 2(G_{XY})^2 + 2(G_{YZ})^2 + 2(G_{XZ})^2 = -2I_1 \quad (5.3.2.2.4)$$

If we then rotate the tensor into its principal coordinate system, the trace components become the eigenvalues, $G_X$ , $G_Y$ , $G_Z$ , and the cross components vanish. By taking the square root of both sides, a physically meaningful quantity results, which we call the Tensor Magnitude ($T_m$):

$$T_m = (\|G\|_F) = \sqrt{(G_X)^2 + (G_Y)^2 + (G_Z)^2} = \sqrt{-2I_1} \quad (5.3.2.2.5)$$

The tensor magnitude is simply the length of the vector whose components are the eigenvalues of the tensor. In other words, the tensor magnitude is the intensity of the magnetic gradient in units of nT/m.

Before we returned to YPG in 2005 to continue testing, the Calibration Grid was reconfigured in order to mitigate the effects of a large natural anomaly. The original grid (figure 5.3.2.1.1) changed to the layout shown in figure 5.3.2.2.3. A tensor magnitude map of the Calibration Grid is given in figure 5.3.2.2.4. A tensor magnitude map of the Blind Test Grid is shown in figure 5.3.2.2.5.

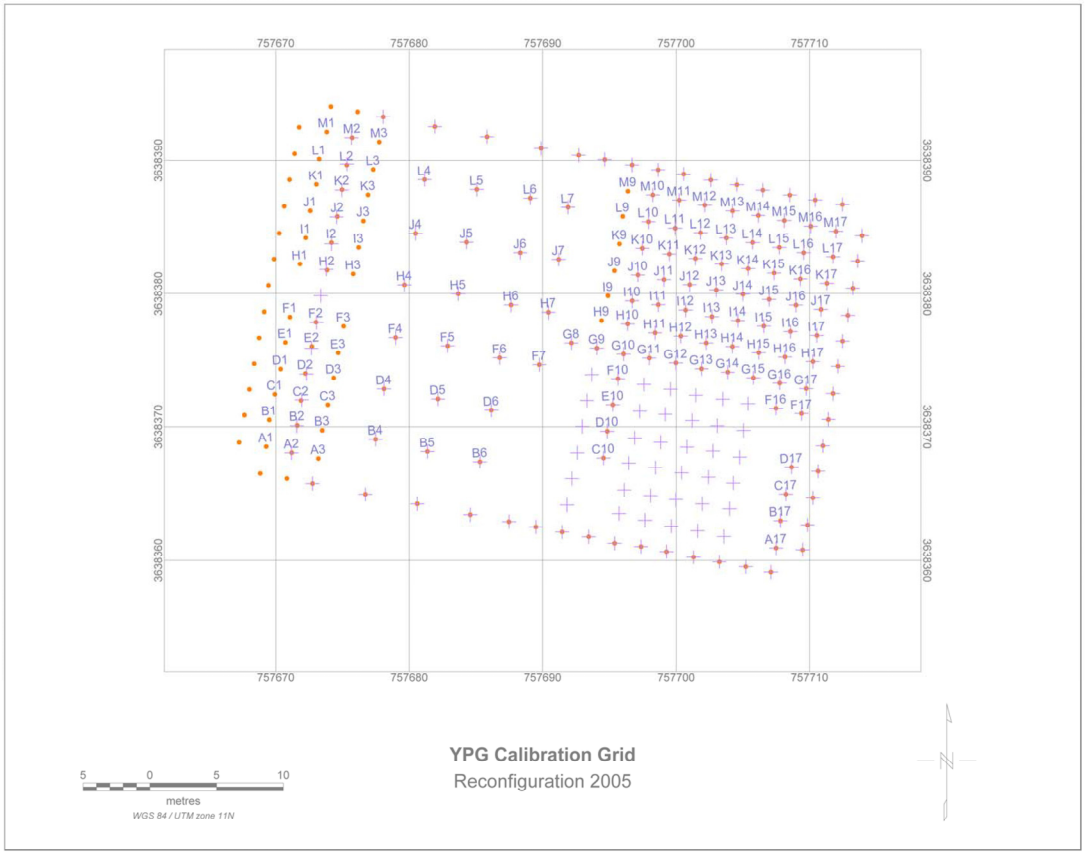


**Figure 5.3.2.2.3.** Calibration Grid layout in 2005 after reconfiguration.

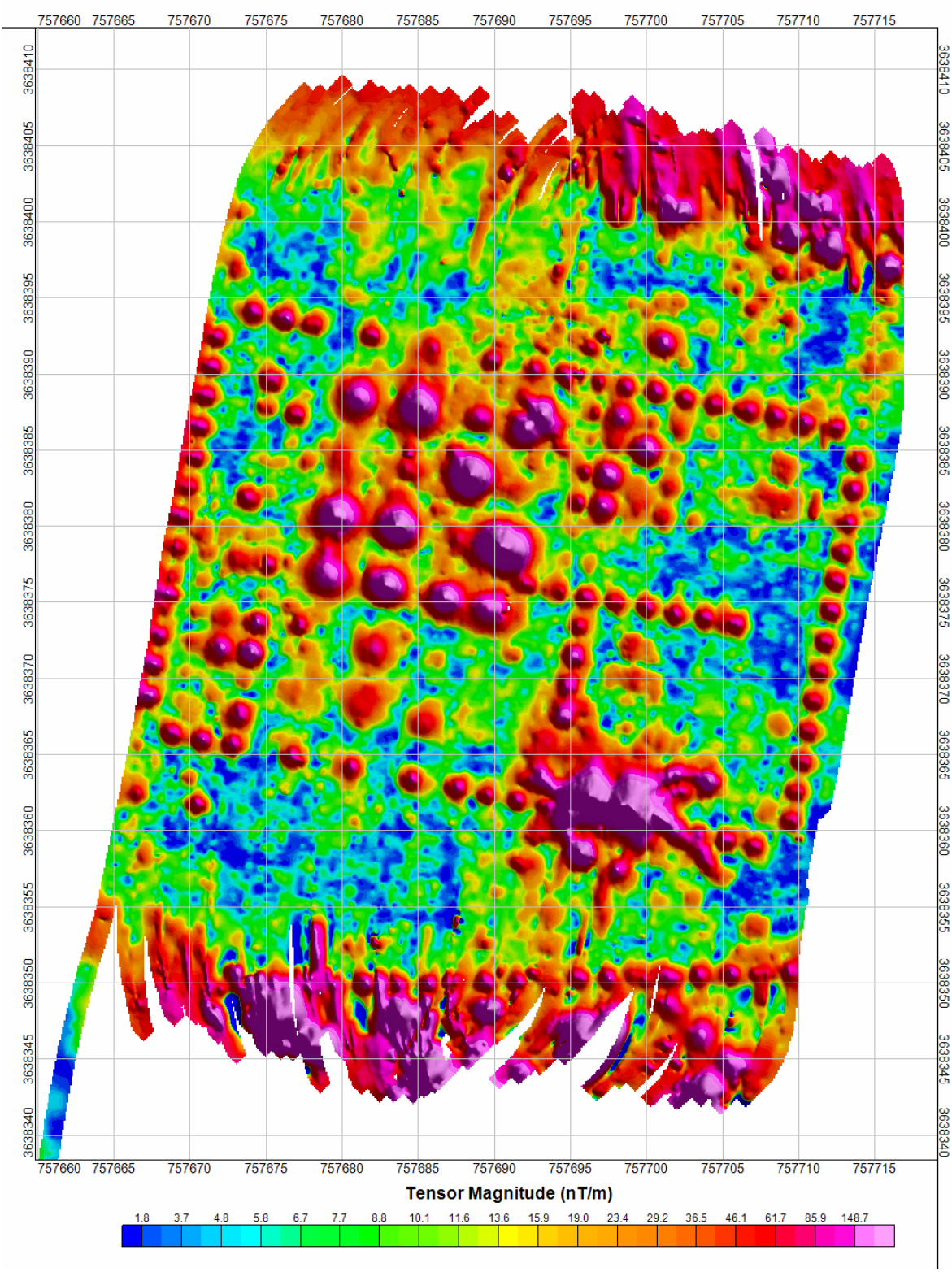


**Figure 5.3.2.2.4.** Calibration Grid tensor magnitude map from 2005 data.

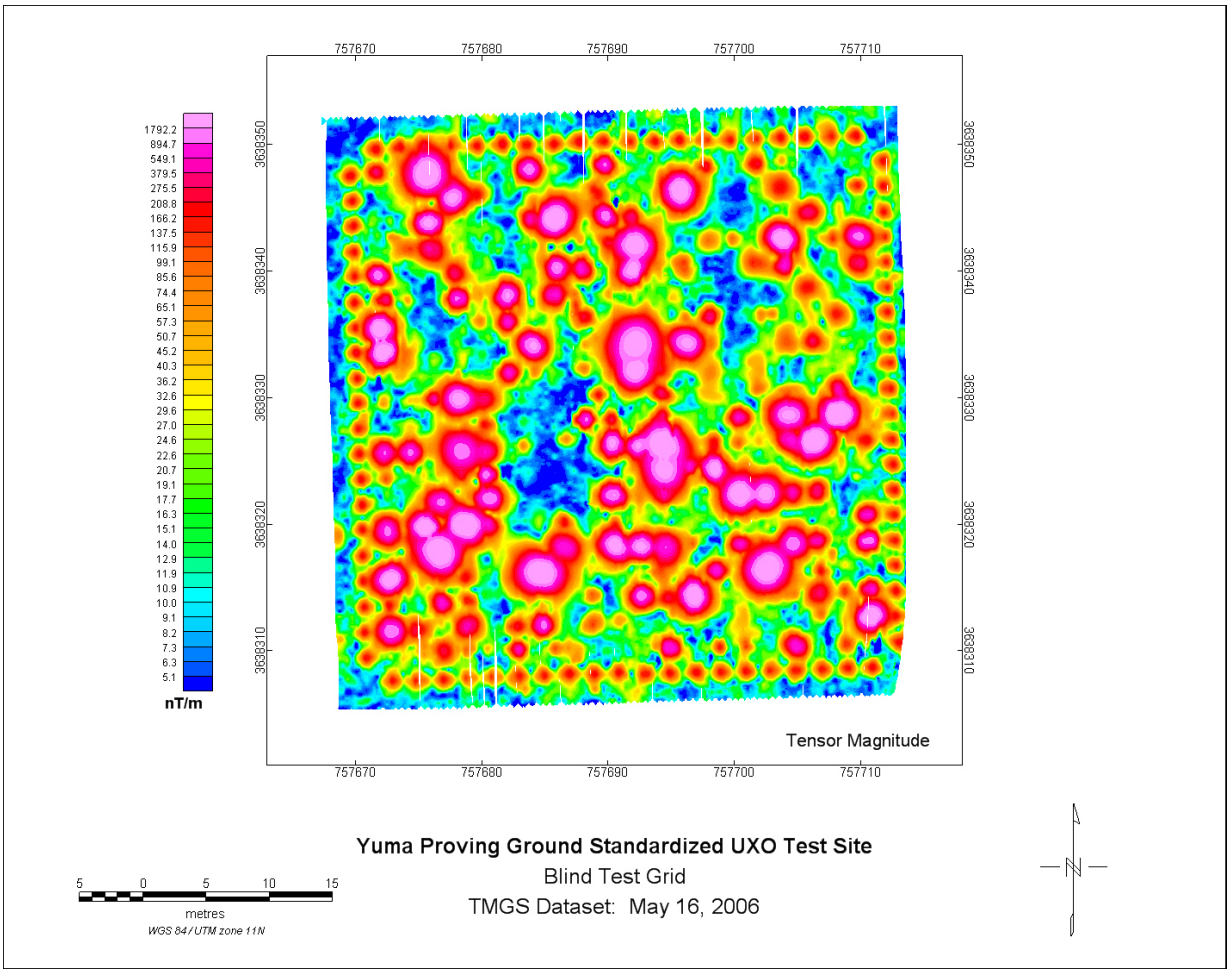


**Figure 5.3.2.2.5.** TMGS tensor magnitude map of the Blind Test Grid data from 2006.

## 5.4 Data Processing and Inversion - Algorithms and Results

Raw data may be useful for target detection, but to produce high quality maps and especially for the critical problem of target identification or classification it is necessary to process our data in certain ways. In this section we discuss data processing and data inversion for ALLTEM and then for the TMGS.

### 5.4.1 ALLTEM Data Processing

In this section we discuss system electronic filtering and subsequent digital data processing of ALLTEM data that produced the markedly superior maps shown in section 5.3.1.2. The most significant finding is that earth and system response can be greatly reduced by working only with data beginning at about 275 μs as discussed below. We begin by showing some typical raw waveforms in figure 5.4.1.1.

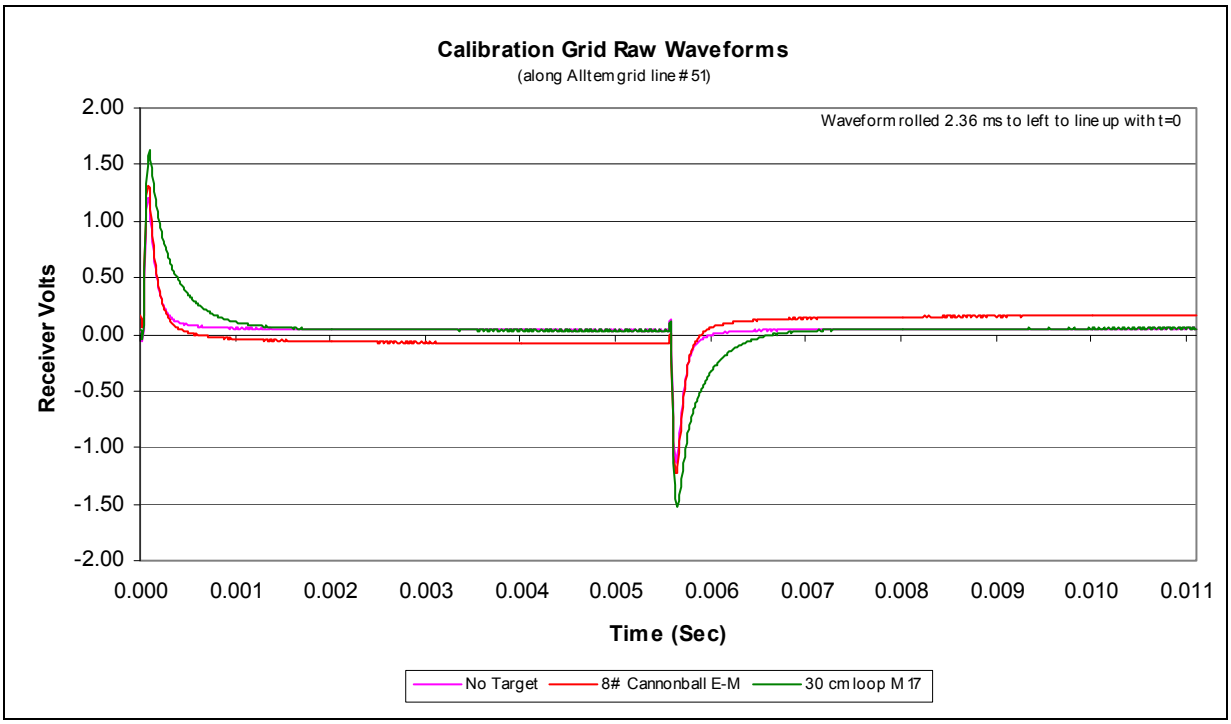


**Figure 5.4.1.1**. This figure illustrates some raw ALLTEM waveforms recorded over the Calibration Grid. The samples in these waveform arrays have been circularly rotated 2.36 ms (236 samples) so that the response to the triangle corner occurs near t=0. For an example of the unrotated waveform, see figure 5.4.1.5.

*Hardware Analog Filtering (prior to data digitizing and recording – also see figure 5.2.1.5)*

The signals from the gradiometer pairs of receiving antennas were low-pass (LP) filtered at ~100 kHz before being electronically subtracted. This removed most high frequency communication-type noise. The subtracted signal can then be high-pass (HP) filtered (at ~ 0.1 Hz), 60 Hz notch filtered, and low-pass filtered (2nd order, selectable frequency). At YPG in 2006, only the final LP filter was used. The LP filter corner frequency was set at 6.8 kHz (3dB down) and 9.85 kHz (6dB down). The HP filter caused problems when switching between the 3 drive polarities because its settling time was too long to allow the output to reach a new stable dc value in the allowed dead-band time (~33 ms) between drive polarities. Without the dc-blocking HP filter, any dc drifts in the amplifiers downstream are not removed. Since the inversion algorithm works on voltage differences between points along the waveform, this was not a serious problem. Because the 60 Hz notch filter causes a slight droop on the waveforms and the 60 Hz interference at the YPG UXO site was not severe, the 60 Hz notch filter was not used.

*Software Processing and Filtering*

A total of three groups of three waveforms were digitized during the on time of each drive polarity. These waveforms were then added in software and divided by 3 before saving. This helps remove any 60 Hz interference on the waveforms and reduces data file sizes. Figure 5.4.1.2 shows some data after processing using all the filters discussed below.

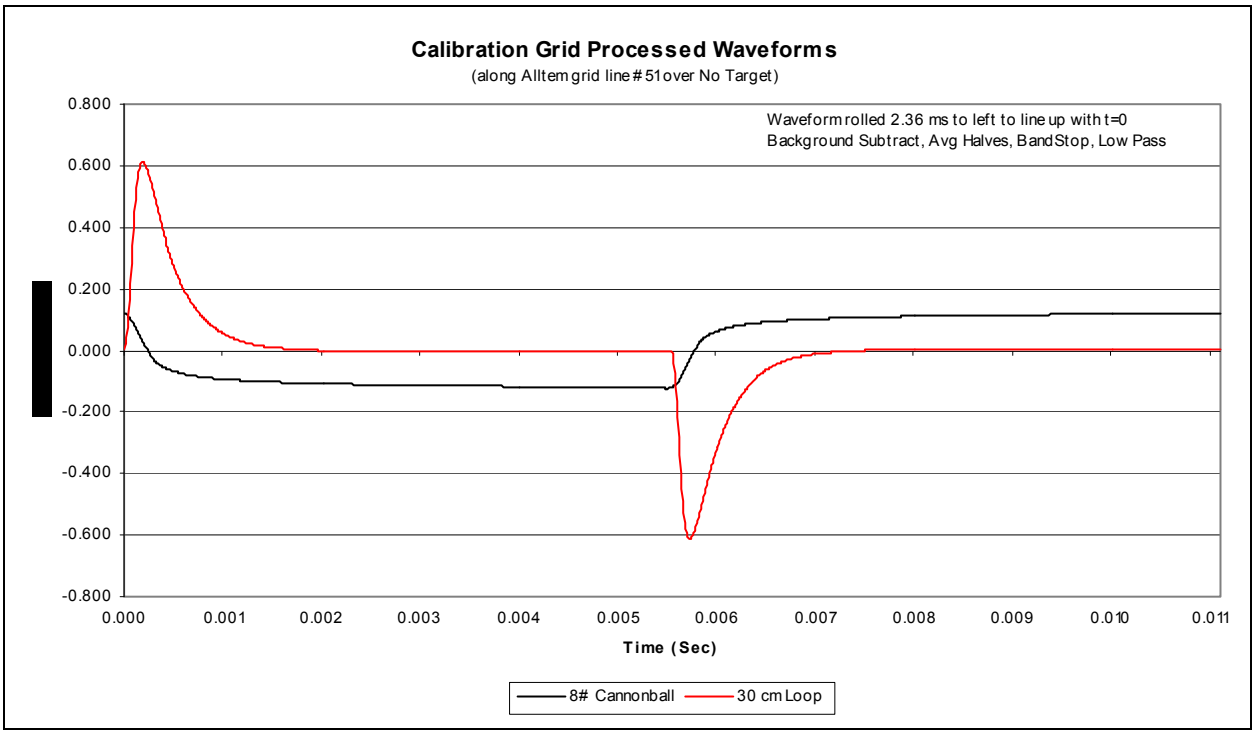


**Figure 5.4.1.2** shows waveforms over an 8-pound shot and a 30-cm loop after background subtraction, waveform halves averaging, band-stop and low-pass filters have been applied.

*Background Subtraction*

Normally, the first few waveforms along a line are recorded with the cart stationary over an area outside the grid where it is known that there are no targets. Typically, an average of the first four waveforms is subtracted from all the waveforms along the line. Performing this task before a digital band-stop filter is applied helps minimize Gibbs effects (ringing artifacts) because the large transitions at the triangle corners are reduced. A later modification to the LabVIEW® data processing program allows a user-selected number of waveforms at a second section of the line (usually at the end, and usually three) to be averaged. The end-of-line average is then subtracted from the beginning-of-line average and this new average waveform is then linearly apportioned along the line and added or subtracted from the beginning average. This removes linear drift in the system along a given line. Drift along a single line is normally negligible except at the beginning of a day when the system is not fully warmed up. However, this feature also anticipates operation where line lengths might be much greater than they were over the Calibration Grid and Blind Test Grid. This additional refinement was only employed for lines that had an observed drift problem.

*Waveform-Halves Averaging*

The recorded waveforms from YPG had a component of 180 Hz, synchronous, "system noise" that was relatively small, but for small targets could reduce the SNR appreciably. Each waveform of 1111 samples contains two complete, but opposite polarity, responses beginning at each inflection point in the triangle current waveform that drives the Tx coil. By splitting the

1111 samples in half, inverting the second half opposite polarity response, adding it to the first half, and dividing the sum by 2, the 180 Hz component is significantly reduced. To reconstruct an entire 1111 sample waveform, the half-waveform produced by the averaging was inverted and added to the end of the previous half-waveform. Non-synchronous noise is also further reduced by the waveform halves averaging. Figure 5.4.1.3 illustrates the improvement provided by waveform halves averaging after background subtraction.

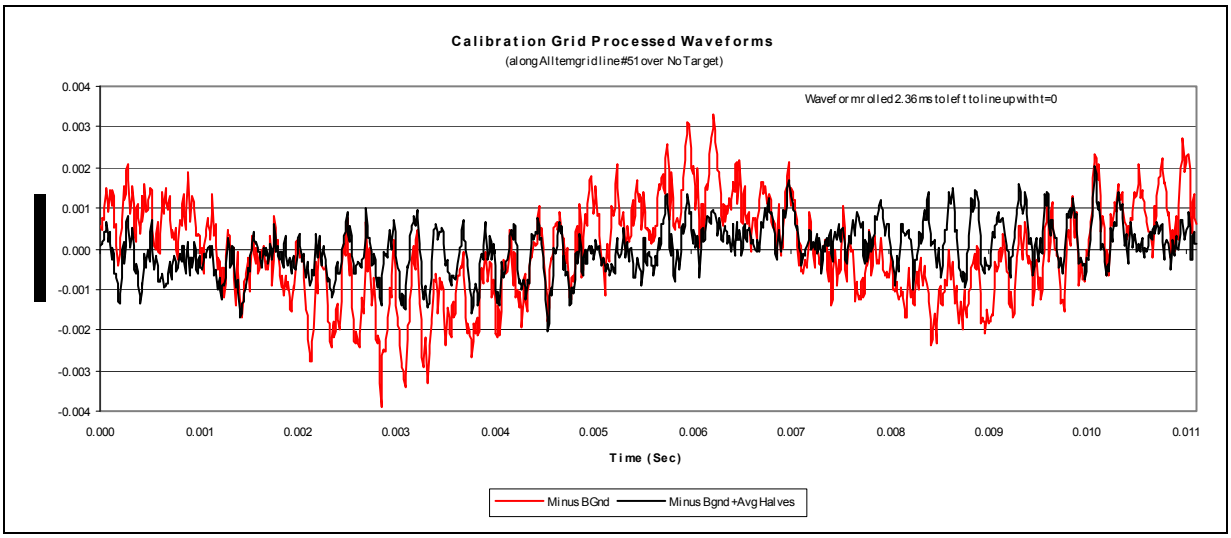


**Figure 5.4.1.3**. This figure shows the noise level reduction obtained from waveform halves averaging after background removal.

*Band-Stop Filter*

A component of noise was visible in all the waveforms at around 4.3 kHz. By applying a LabVIEW® zero-phase, band-stop filter, with low-stop = 3.3 kHz and high-stop = 5.3 kHz, the 4.3 kHz component was somewhat reduced. Filter orders higher than two introduce excessive Gibbs peaking around large transitions in the waveforms. This peaking could affect the accuracy of "sample picking" near the transitions for determining the responses. Figure 5.4.1.4 shows the reduction in noise when the digital 2nd order band-stop filter is applied to a waveform with little or no target response. The great majority of the noise is below 1 mV.

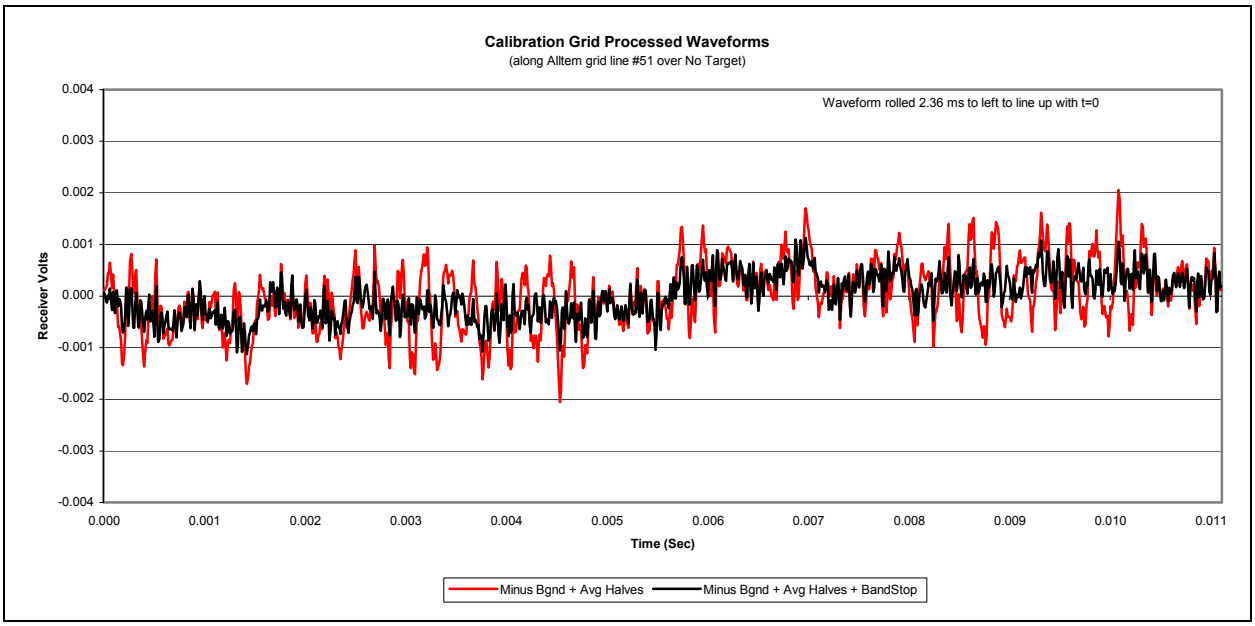


**Figure 5.4.1.4.** This figure shows the noise reduction achieved using the band-stop filter described above (black curve).

Figure 5.4.1.5 illustrates the Gibbs phenomenon (overshoot at a transition that results when the spectrum of the signal is truncated) caused by the 2nd order digital filter and especially noticeable when there is a strong target response resulting in large amplitude transitions. A higher order filter would further reduce the noise shown in figure 5.4.1.4 above, but increase the Gibbs overshoot to an unacceptable level.

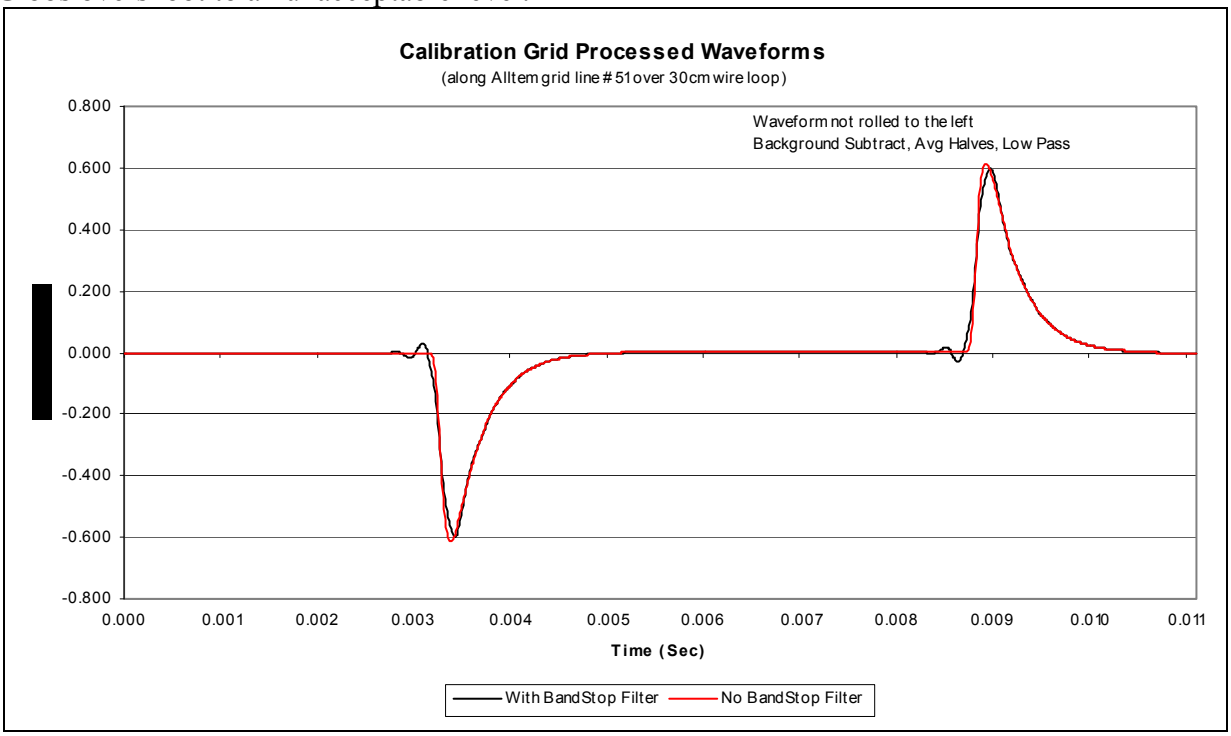


**Figure 5.4.1.5**. This figure illustrates the Gibbs phenomenon (overshoot and undershoot and precursor at the transitions) that results from the use of the 2nd order band-stop digital filter.

*Low-Pass Filter*

The final digital filter that we discuss is a LabVIEW®, zero-phase, eight-order, low-pass filter that was applied to roll off any higher frequency noise that might be in the recorded data from Very Low Frequency (VLF) radio stations. The filter was placed at 15 kHz, which was far enough from any target frequencies of interest, that any Gibbs effects were not significant. Figure 5.4.1.6 shows an example of the noise reduction due to use of this filter.

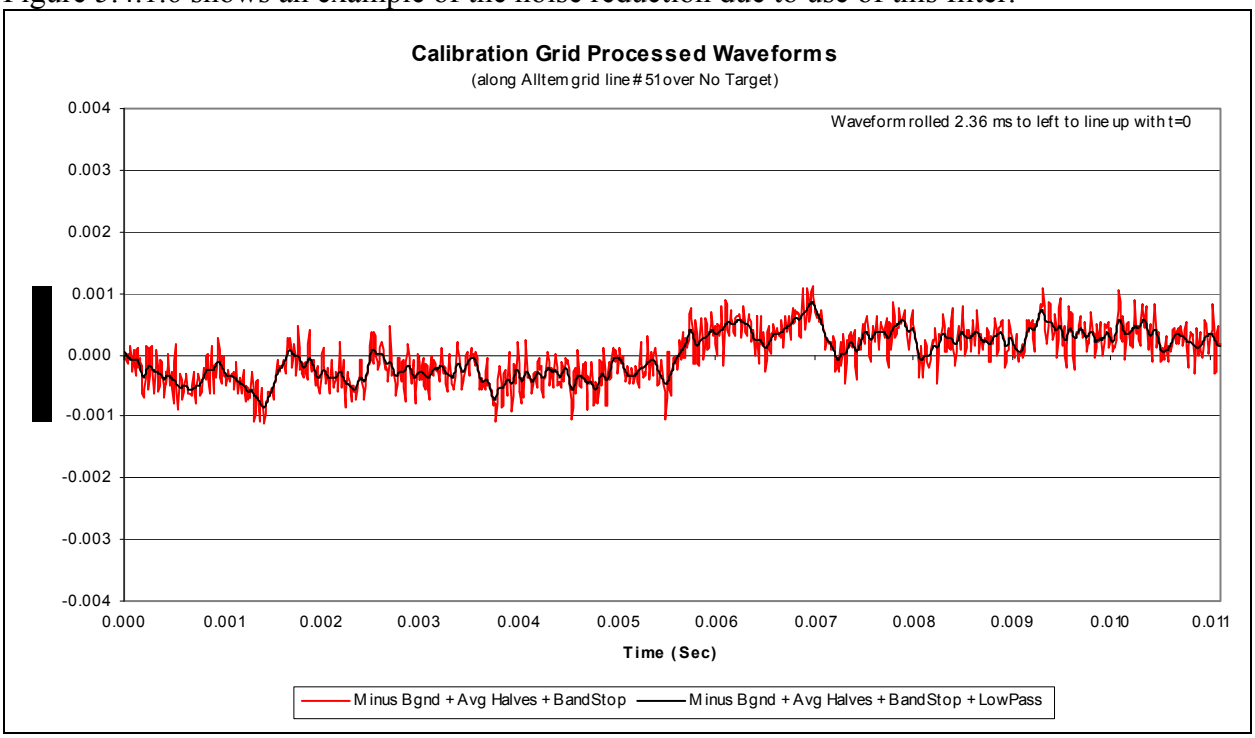


**Figure 5.4.1.6**. This figure illustrates the reduction in high frequency noise obtained when the digital low-pass filter described in the text is applied to ALLTEM data.

Figure 5.4.1.7 is an example of raw (except for background removal) and fully filtered data. A noise level of 1 mV corresponds to a dB/dt noise level of about 90 nT /s or a dH/dt noise level of 0.072 amp · turn/(m · s) for the 1-m Rx coil and a dB/dt noise level of about 200 nT/s or a dH/dt noise level of about 0.16 amp · turn/(m · sec) for the 0.35-cm Rx coils using the gain conversion factors given in appendix A for those coils.

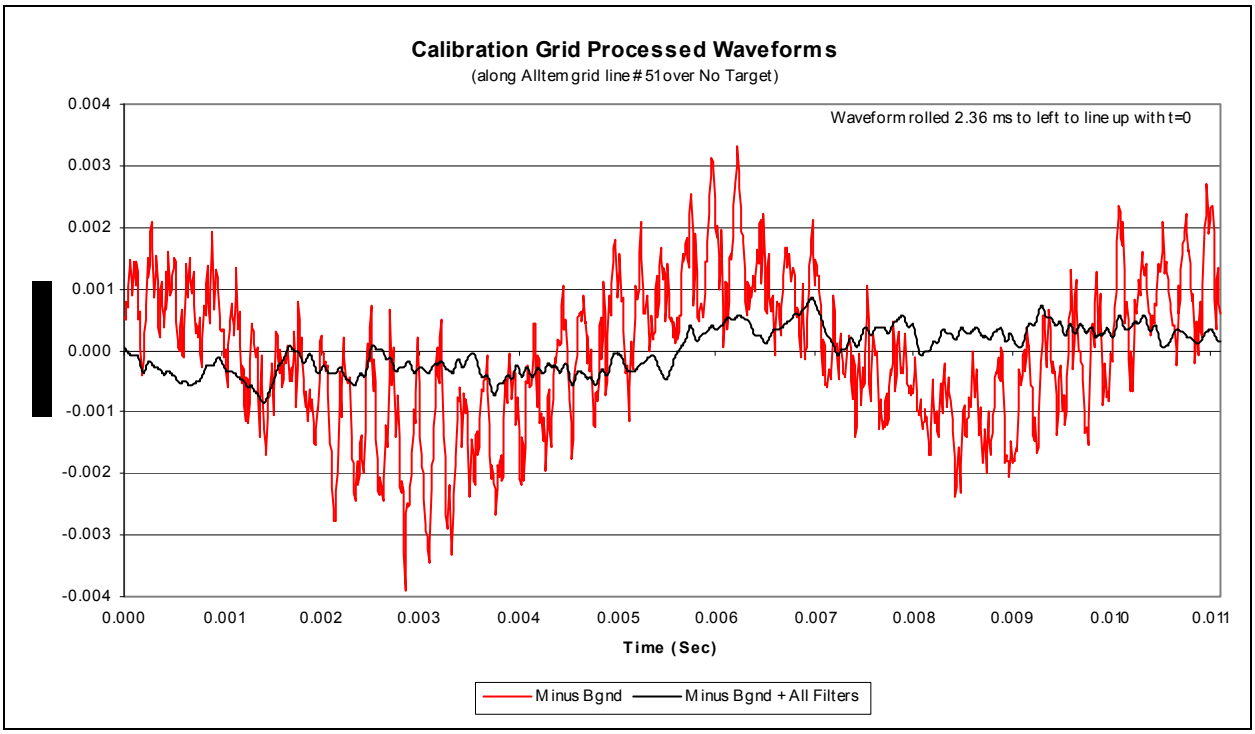


**Figure 5.4.1.7**. This figure illustrates the improvement obtained by application of all the filters described above. The filtered data noise level is less than +/- 1 mV.

*Time Picks – The 200 μs Difference*

Picking a later early sample for target analysis has a huge impact on system and earth response "noise" and is more significant than all the filters discussed above. When we made the first amplitude difference maps the early sample time pick was 75 μs from t = 0 where zero time is defined as the time of an inflection point (corner) on the ALLTEM triangle current excitation waveform. The second (later) time was chosen at 5095 μs. Small differences in the choice of the late time sample make little difference, as expected, but the choice for the early time turned out to have a huge impact as we describe below. Figure 5.4.1.8 shows one (ZZM) waveform obtained when ALLTEM was over one of the boundary marker spheres.

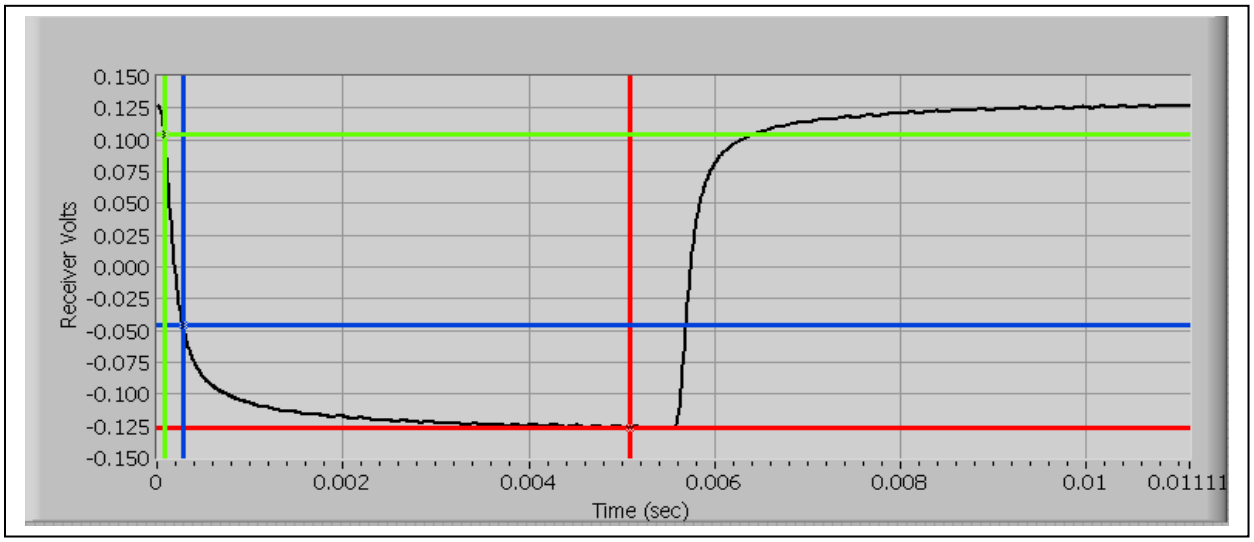


**Figure 5.4.1.8.** A waveform (black trace) from the ZZM data channel when ALLTEM was over one of the boundary marker shots. The green vertical cursor shows the location of the original 75 μs time pick. The blue vertical cursor is the location of the 275 μs pick. Amplitude differences between late time value (horizontal red cursor) and either the green horizontal cursor amplitude or the blue horizontal cursor amplitude are the quantities that are mapped.

The amplitude difference map shown in figure 5.3.1.1.2 was made using the 75 μs early time pick (green cursor location) for the amplitude differences on the raw or unfiltered data.

The amplitude difference maps shown in section 5.3.1.2 were produced using filtered data and using a first time pick of 275 μs (blue cursor), that is, 200 μs later than our original time pick (green cursor). The original earlier time of 75 μs was chosen because this earlier time captures nearly the full amplitude of the target signatures. Unfortunately, it also captures ground response and system drift. By moving the first time to 275 μs we moved far enough out that the step response of our low-pass (6.8 kHz) hardware filter has essentially reached its final value. The earth step response is a much faster transient than the response of the metallic targets and also shorter than the step response of the LP filter. Since even the smallest (20 mm) targets have not fully reached their late-time asymptotic value by 275 μs, their signatures are still detectable with the 275 μs time pick, although it was not intuitively obvious that the later first time pick could be advantageous. However, even though the amplitudes of the target responses are reduced by moving the time pick to 275 μs, the trade-off is a favorable one because we have reduced noise proportionally far more than we have reduced target amplitude responses. Therefore, we have significantly improved the SNR for all targets. This makes a huge difference for targets that were marginally detectable or undetectable in the original maps. We added 16 probable new detected targets to our initial target picks for the Blind Test Grid list and several to the Calibration Grid maps as can be seen by inspection of the "before" and "after" maps (compare figures 5.3.1.2.7 and 5.3.1.2.8, for example).

As an aside, we had intended to operate ALLTEM with a hardware LP filter corner frequency (3 dB down) appreciably higher than the 6.8 kHz that we actually used. We lowered the corner

frequency because of noise that may have been induced, at least in part, by damage to the electronics in transport. Conventional wisdom has been that spectral content to at least 30 kHz was needed for target characterization. However, because ALLTEM measures step response, as opposed to impulse response (late time values do not go to zero for ferrous targets), it seems that with ALLTEM a narrower bandwidth (~7 kHz) is sufficient. A narrow bandwidth certainly yields a lower noise figure.

Figure 5.4.1.9 shows results of a test we made with a 20 mm M55 projectile using four different low-pass filters. Only the lowest frequency (4.7 kHz) filter induced a noticeable change in the response other than progressively reducing noise as the pass-band was reduced.

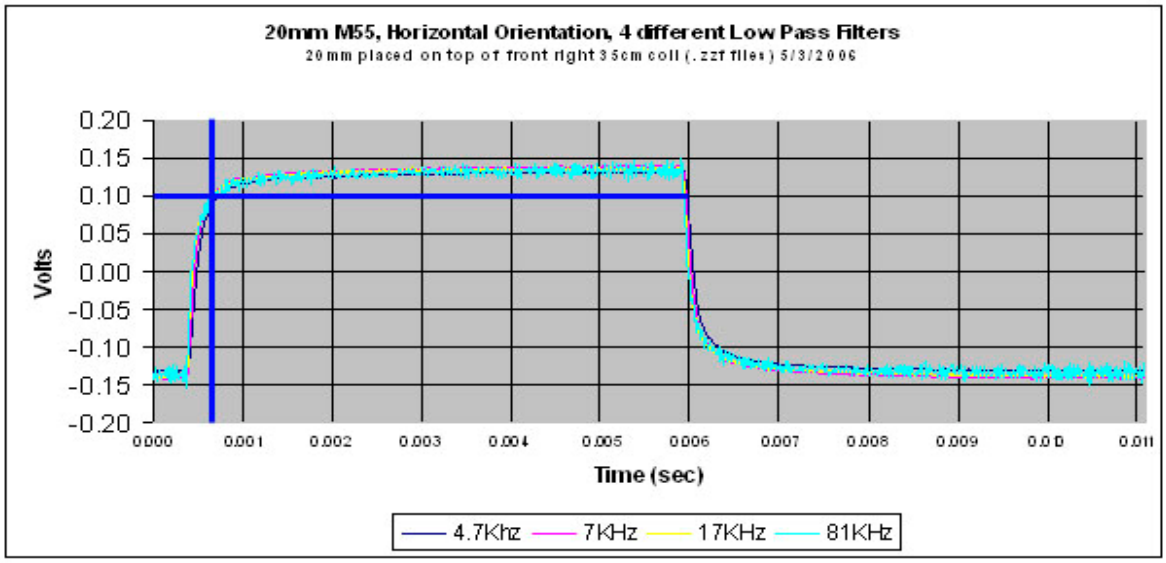


**Figure 5.4.1.9**. This figure shows that low-pass filters down to 7 kHz have little effect on the step response of a horizontally oriented 20 mm M55. Noise from external sources, however, is substantially reduced as the corner frequency of the low-pass filter is reduced. The location of the 275 μs early time pick is shown by the blue cursor. In this small-signal case we have sacrificed about 86 percent of the target signal amplitude in favor of reduced ground and system response. Even so, the trade-off is a good one. ALLTEM detected all 20 mm targets on the Calibration Grid (Lane 15 in figure 5.3.1.1.4). Larger targets have longer time constants, so the percentage amplitude loss is less.

### 5.4.2 TMGS Data Processing

Processing TMGS data involved a complex series of steps using routines written and executed in several programming languages. Figure 5.4.2.1 illustrates the data flow. This complexity results from the need to efficiently convert, validate, calibrate, index, and interpolate large volumes of data on different hardware platforms.

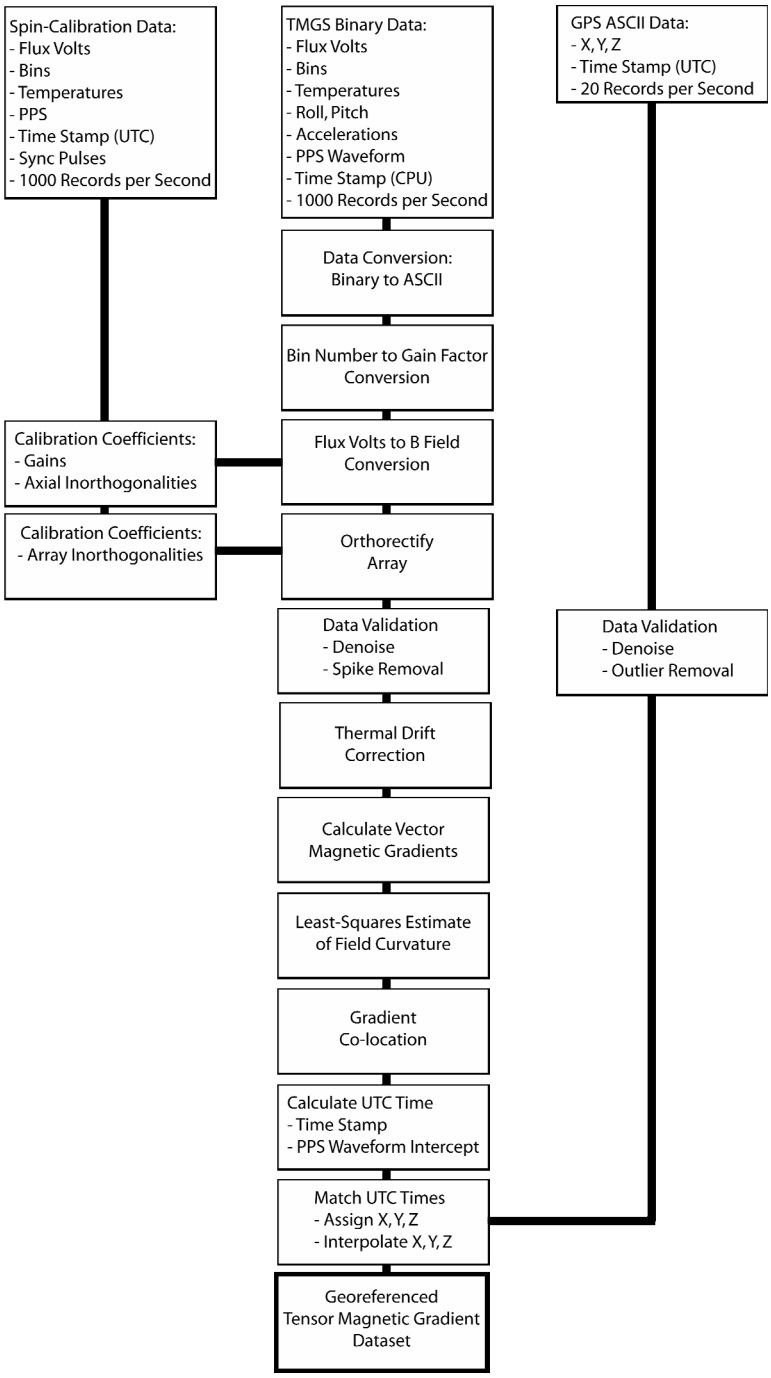


**Figure 5.4.2.1**. Data flow diagram originating from three separate datasets and resulting in a final georeferenced magnetic gradient tensor dataset.

*Spin-Calibration Regression Analysis*

The following program, using the nonlinear regression program NLREG (available at http://www.nlreg.com), was used to estimate the calibration coefficients for each individual triaxial magnetometer. The input variables are:

- T1 = the instantaneous observed total field as measured by a reference base station magnetometer

- V1 = the measured voltage for magnetic flux component 1
- V2 = the measured voltage for magnetic flux component 2
- V3 = the measured voltage for magnetic flux component 3

The parameters (set to their starting values) to estimate are:

- a = third order coefficient
- b = second order coefficient
- c = first order coefficient
- d = dc offset
- alpha = angle of y-axis to x-axis
- beta = angle of y-axis to z-axis
- gamma = angle of z-axis to x-axis

The NLREG program minimized the difference between the observed total field and the total field calculated using measured voltages.

```
 1: VARIABLE T1, V1,V2,V3 ;
 2: PARAMETER  a1=0,b1=0,c1=100.d0,d1=0,
 3:           a2=0,b2=0,c2=100.d0,d2=0,
 4:           a3=0,b3=0,c3=100.d0,d3=0,
 5:           alpha=90, beta=90, gamma=90 ;
 6:
 7: FUNCTION T1 = SQRT(
 8: +(
 9:   +(a1*V1^3+b1*V1^2+c1*V1+d1)
10: )^2
11: +( (
12:   -(a1*V1^3+b1*V1^2+c1*V1+d1) * COSD(alpha)
13:   +(a2*V2^3+b2*V2^2+c2*V2+d2))/ SIND(alpha)
14: )^2
15: +(
16:   +(a1*V1^3+b1*V1^2+c1*V1+d1) * (COSD(beta)*COSD(alpha)/SIND(alpha)-COSD(gamma))
17:   -(a2*V2^3+b2*V2^2+c2*V2+d2) * (COSD(beta)/SIND(alpha))
18:   +(a3*V3^3+b3*V3^2+c3*V3+d3)
19: )^2
20:                          / (1.d0-COSD(beta)**2-COSD(gamma)**2)
21: ) ;
22:
23: TOLERANCE  1.e-5 ;
24: DATA "spin_all_m1.asc";
```

The parenthetical group ($a_n$*$V_n$^3 + $b_n$*$V_n$^2 + $c_n$*$V_n$ + $d_n$) is the cubic transfer function for converting volts to nanotesla, with the indices (n = 1, 2, 3) designating different axial components. A cubic form was chosen because it can best describe a hysteresis response of a hard magnetic material. The trigonometric formulation derives from orthogonalization equations. In the case where alpha, beta, and gamma are 90, the equation collapses to the vector resultant, total field value (square root of the sum of the squares). Final results of a nonlinear regression run are given below.

---- Final Results ----

NLREG version 5.4


Number of observations = 3870
Maximum allowed number of iterations = 500
Convergence tolerance factor = 1.000000E-005
Stopped due to: Relative function convergence.
Number of iterations performed = 4
Final sum of squared deviations = 5.0303208E-002
Final sum of deviations = 2.2893633E-004
Standard error of estimate = 0.00361232
Average deviation = 0.00288423
Maximum deviation for any observation = 0.0137279
Proportion of variance explained (R^2) = 0.9109 (91.09%)
Adjusted coefficient of multiple determination (Ra^2) = 0.9106 (91.06%)
Durbin-Watson test for autocorrelation = 0.070
This Durbin-Watson value indicates autocorrelation or inappropriate function.
Analysis completed 24-Apr-2006 11:00. Runtime = 2.90 seconds.

---- Descriptive Statistics for Variables ----

| Variable | Minimum value | Maximum value | Mean value | Standard dev. |
|---|---|---|---|---|
| T1 | 174.2122 | 174.2614 | 174.2422 | 0.0120797 |
| V1 | -1.495562 | 1.511552 | -0.01718138 | 1.135718 |
| V2 | -1.474014 | 1.486727 | 0.01753284 | 1.136482 |
| V3 | -0.9329526 | 0.9203768 | -0.006232078 | 0.6441766 |

---- Calculated Parameter Values ----

| Parameter | Initial guess | Final estimate | Standard error | t | Prob(t) |
|---|---|---|---|---|---|
| a1 | 0 | -0.0663136169 | 0.001596759 | -41.53 | 0.00001 |
| b1 | 0 | 0.00843040117 | 0.00018073 | 46.65 | 0.00001 |
| c1 | 100 | 100.382575 | 0.002949577 | 34032.88 | 0.00001 |
| d1 | 0 | -0.191374465 | 0.000369839 | 517.45 | 0.00001 |
| a2 | 0 | -0.0789559855 | 0.001661117 | -47.53 | 0.00001 |
| b2 | 0 | -0.00715293666 | 0.0001800509 | -39.73 | 0.00001 |
| c2 | 100 | 101.614217 | 0.003004824 | 33817.03 | 0.00001 |
| d2 | 0 | -0.118200893 | 0.0003844281 | -307.47 | 0.00001 |
| a3 | 0 | 0.0579488577 | 0.002294676 | 25.25 | 0.00001 |
| b3 | 0 | 0.00243374269 | 0.0007613215 | 3.20 | 0.00140 |
| c3 | 100 | 99.4253149 | 0.001430871 | 69485.86 | 0.00001 |
| d3 | 0 | -0.178534301 | 0.0005033608 | -354.68 | 0.00001 |
| alp | 90 | 89.9245933 | 6.531504E-005 | 1.4E+006 | 0.00001 |
| bet | 90 | 90.7817341 | 8.572799E-005 | 1.1E+006 | 0.00001 |
| gam | 90 | 89.6882855 | 9.405177E-005 | 953605.49 | 0.00001 |

The accuracy of the calibration coefficients was checked by using them to convert raw spin calibration data into B-field values, and looking for discrepancies between individual heads. If the calibration procedure were perfect, then each head in a full spin would look exactly like every other head (perfectly calibrated heads would behave identically). Differencing Heads 2, 3, and 4 with Head 1, for example, should give zero residual. Although on the full scale (bottom plot, purple) all four x-components appeared identical, significant residuals (hundreds of nanotesla) were revealed when Head 1 values were subtracted from the other heads (figure 5.4.2.2).

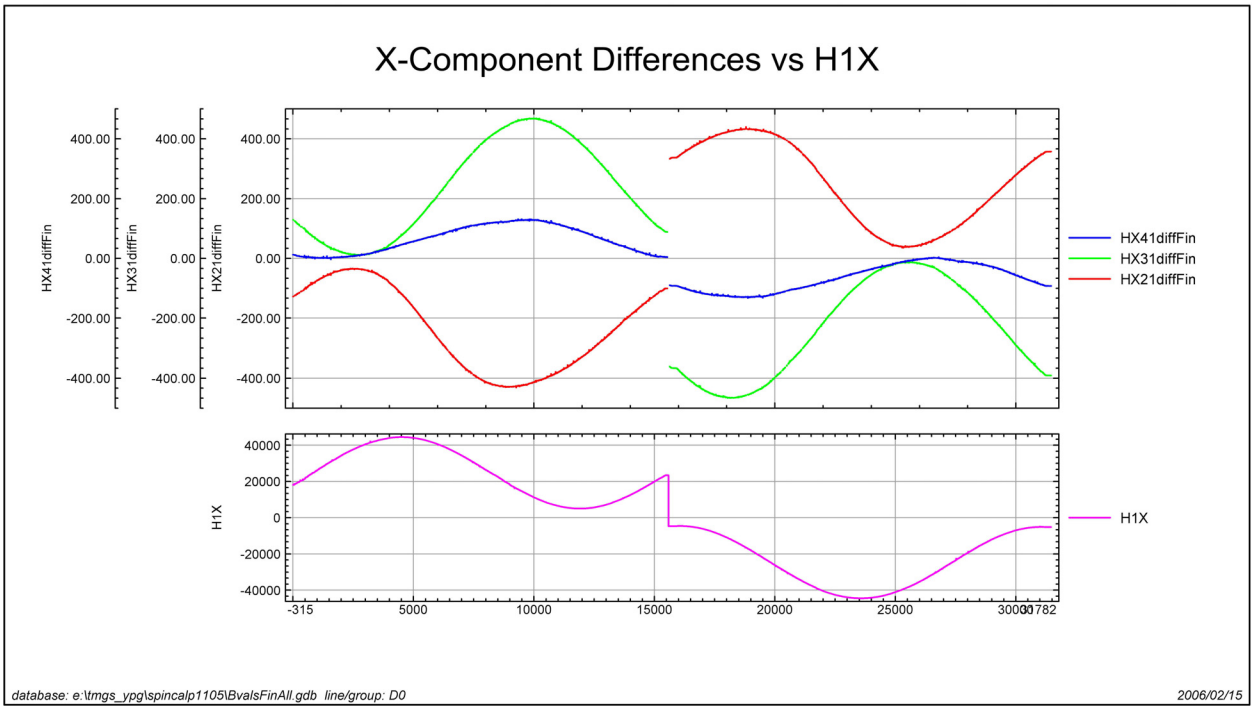


**Figure 5.4.2.2.** After full calibration, significant residual errors remained. The top plot shows H2X minus H1X (red), H3X minus H1X (green), and H4X minus H1X (blue). The bottom plot shows H1X at full scale.

The error (residual) waveforms are sinusoidal and out of phase with the principal waveforms, indicating that there is an angular dependence neither explained by the cubic transfer function nor by the orthogonalization angles. A possible explanation for the error is cross-axis sensitivity, whereby the measured flux value is not simply the dot product of the sensing axis and the B-field vector (proportional to the cosine of their inner angle). Rather, it is a more complex functional relationship, like a classical B-H ferromagnetic hysteresis curve. Instead of a straight line (or mild cubic function) through the origin, the curve passes around the origin depending on the history of magnetic exposure. The error magnitude, then, is a function of the bearing of the sensor array in the ambient magnetic field, much akin to the heading error experienced in airborne magnetic surveys. Over a full 360 degree swing, the error can swing up to 400 nT. However, if the bearing of the array is restricted to a very narrow range, the error swing can be minimized to a few nanotesla. In surveys of the Calibration Grid and the Blind Test Grid (BTG),

the platform was moved over the area in straight lines as uniformly as possible. This greatly minimized along-line error. However, north-going lines showed a significant offset from their south-going counterparts. This apparent heading error was removed in post-processing using conventional processing tools originally developed for airborne magnetic data.

A further source of error lies in the instability of the fluxgate transfer function, both in short term and over long periods of time. Subtle changes in circuit gain, for example, are expected with discrete analog circuitry. We compared the first-order gain coefficients (nominally 100 nT/V) obtained with calibration data taken six months apart (figure 5.4.2.3). Some coefficients changed hardly at all (H3X) while others changed more than 1 percent (H2Z). These variations might be due to changes over time of the fluxgate responses or of their interface electronics. If so, then on-site spin calibrations will account for the instrument drift. Alternatively, the variations may be due, in part, to sensitivities in the regression procedure used to determine the parameter values. A sensitivity analysis of the regression procedure can be done to identify which parameters may be modeling noise in the calibration data, and therefore passing noise into the final estimations. If it is found that the existing regression procedure models noise excessively, then this can be mitigated by either reformulating the objective function or preconditioning the input calibration data, or both.

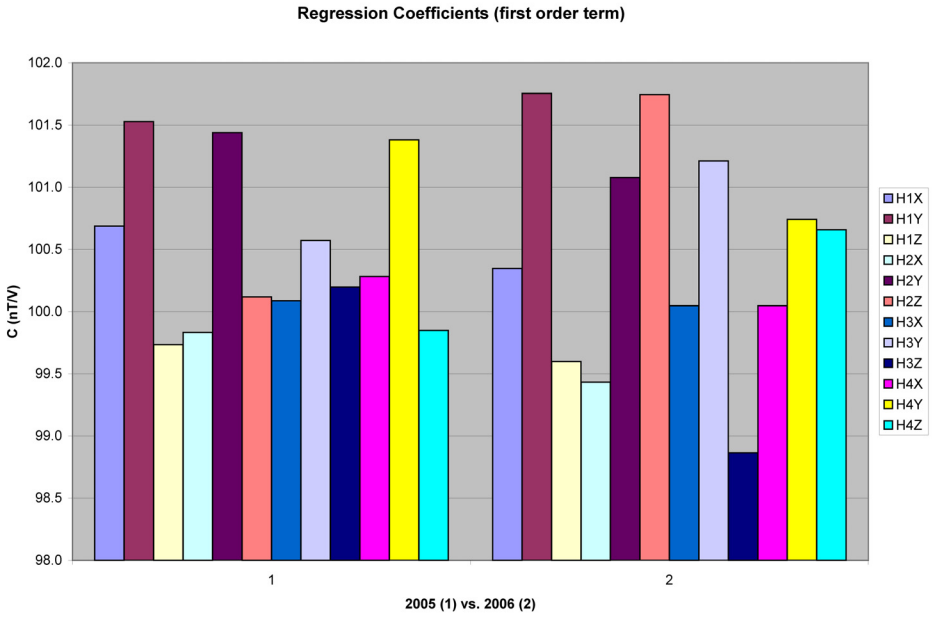


**Figure 5.4.2.3**. Comparison of two sets of regression coefficients obtained six months apart at YPG. Bars of the same color correspond to the same sensor axis.

### 5.4.3 ALLTEM Target Modeling and Inversion

This section describes the data forward modeling and inversion algorithm that have been developed for ALLTEM at the USGS to estimate UXO parameters such as depth, attitude, shape, size and composition. Although the text discusses both magnetostatic and electrodynamic cases, in practice we run only the magnetostatic case of the inversion, either at a single time difference or for a series of time differences to produce decay curves for three orthogonal polarizability dipole moments.

#### 5.4.3.1 Forward Model

A forward operator has been developed to approximate the response of a subsurface UXO. This operator describes the induced magnetic fields in the UXO in terms of three orthogonal magnetic dipole moments. A set of dipole moments is used to describe the induced magnetostatic response, and another set is used to describe the induced electrodynamic response. The forward operator $A$ used in the inversion has the form

$$A([\mathbf{r}_{cart},\mathbf{r}_{Tx},\mathbf{r}_{Rx1},\mathbf{r}_{Rx2}\mathbf{P}_{Tx},\mathbf{P}_{Rx},t],[\mathbf{r}_{s,uxo},\phi_s,\theta_s,m_{s,1},m_{s,2},m_{s,3},\mathbf{r}_{t,uxo},\phi_t,\theta_t,m_{t,1},m_{t,2},m_{t,3},\tau_1,\tau_2,\tau_3]) = y([\mathbf{r}_{cart},\mathbf{r}_{Tx},\mathbf{r}R_{Rx1},\mathbf{r}R_{Rx2},\mathbf{P}_{Tx},\mathbf{P}_{Rx},t]) \quad (5.4.3.1.1)$$

where $\mathbf{r}_{\text{cart}}$ is the location of the center of the ALLTEM cart, $\mathbf{r}_{\text{Tx}}$, $\mathbf{r}_{\text{Rx1}}$, and $\mathbf{r}_{\text{Rx2}}$ are the locations of the transmitting and receiving loops, $\mathbf{P}_{\text{Tx}}$ and $\mathbf{P}_{\text{Rx}}$ are the polarizations of the transmitting and receiving coils, $t$ is time, and $y$ are the simulated data. The UXO parameter set is listed in the second set of square brackets in the argument list of the forward operator, where $\mathbf{r}_{\text{s,uxo}}$ is the location of the UXO, $m_{\text{s,1}}$-$m_{\text{s,3}}$ are the magnitude of the three orthogonal induced magneto-static dipole moments, $\phi_s$ and $\theta_s$ are the azimuth and inclination of the $m_1$ component, $\mathbf{r}_{\text{t,uxo}}$, $m_{\text{t,1}}$-$m_{\text{t,3}}$, $\phi_t$ and $\theta_t$ are the analogous parameters for the transient electro-dynamic response, and $\tau_1$-$\tau_3$ are the late time decay constants for the transient dipole moments. Separate sets of UXO parameters are used for the static and transient response to provide more information to better facilitate discrimination. This parameter set will be estimated by the inverse algorithm discussed below.

The forward model includes both the induced magnetostatic response, and the electrodynamic response from induced transient eddy currents. The magnetostatic UXO response is modeled as three orthogonal magnetic dipoles, and the electrodynamic response is modeled as three orthogonal exponentially decaying magnetic dipoles. It is assumed that the target and the ALLTEM cart are in a non-magnetic, non-conducting whole space. The modeled magnetostatic induction at a receiver coil $\mathbf{B_s}(\mathbf{r})$ is calculated using

$$\mathbf{B_s}(\mathbf{r}) = \vec{\mathbf{k}} \cdot \left[ \frac{3\hat{\mathbf{R}}(\mathbf{m}_s \cdot \hat{\mathbf{R}}) - \mathbf{m}_s}{R^3} \right] \quad (5.4.3.1.2)$$

where $\vec{\mathbf{k}}$ is a calibration matrix, $\mathbf{r}$ is the location of the receiver, $\mathbf{r}'$ is the UXO location, $\mathbf{R} = \mathbf{r} - \mathbf{r}'$, $R = |\mathbf{R}|$, $\hat{\mathbf{R}} = \mathbf{R}/R$, and $\mathbf{m}_s$ is the static induced dipole moment. The static induced dipole moment is given by

$$\mathbf{m}_s = \begin{bmatrix} \mathbf{m}_{s,1}\hat{\mathbf{m}}_{s,1} & \mathbf{m}_{s,1}\hat{\mathbf{m}}_{s,2} & \mathbf{m}_{s,1}\hat{\mathbf{m}}_{s,3} \\ \mathbf{m}_{s,2}\hat{\mathbf{m}}_{s,1} & \mathbf{m}_{s,2}\hat{\mathbf{m}}_{s,2} & \mathbf{m}_{s,2}\hat{\mathbf{m}}_{s,3} \\ \mathbf{m}_{s,3}\hat{\mathbf{m}}_{s,1} & \mathbf{m}_{s,3}\hat{\mathbf{m}}_{s,2} & \mathbf{m}_{s,3}\hat{\mathbf{m}}_{s,3} \end{bmatrix} \cdot \mathbf{H_p}(\mathbf{r}') \qquad (5.4.3.1.3)$$

where $\mathbf{H_p}(\mathbf{r}')$ is the primary magnetic field, and the three induced magnetic moments are related by

$$\hat{\mathbf{m}}_2 = \hat{\mathbf{m}}_1 \times \hat{\mathbf{z}} \text{ and } \hat{\mathbf{m}}_3 = \hat{\mathbf{m}}_1 \times \hat{\mathbf{m}}_2 \qquad (5.4.3.1.4)$$

The primary field $\mathbf{H_p}(\mathbf{r}')$ at the UXO location is calculated using the Biot-Savart law (Jackson, 1999) for the 1-meter square loop transmitting coils. Similar relationships are used to model the electro-dynamic induction at a receiving coil,

$$\mathbf{B_t}(\mathbf{r}) = \vec{\mathbf{k}} \cdot \left[ \frac{3\hat{\mathbf{R}}(\mathbf{m}_t(t) \cdot \hat{\mathbf{R}}) - \mathbf{m}_t(t)}{R^3} \right] \qquad (5.4.3.1.5)$$

$$\mathbf{m}_t(t) = \begin{bmatrix} \mathbf{m}_{t,1}\hat{\mathbf{m}}_{t,1}e^{-t/\tau_1} & \mathbf{m}_{t,1}\hat{\mathbf{m}}_{t,2}e^{-t/\tau_1} & \mathbf{m}_{t,1}\hat{\mathbf{m}}_{t,3}e^{-t/\tau_1} \\ \mathbf{m}_{t,2}\hat{\mathbf{m}}_{t,1}e^{-t/\tau_2} & \mathbf{m}_{t,2}\hat{\mathbf{m}}_{t,2}e^{-t/\tau_2} & \mathbf{m}_{t,2}\hat{\mathbf{m}}_{t,3}e^{-t/\tau_2} \\ \mathbf{m}_{t,3}\hat{\mathbf{m}}_{t,1}e^{-t/\tau_3} & \mathbf{m}_{t,3}\hat{\mathbf{m}}_{t,2}e^{-t/\tau_3} & \mathbf{m}_{t,3}\hat{\mathbf{m}}_{t,3}e^{-t/\tau_3} \end{bmatrix} \cdot \mathbf{H_p}(\mathbf{r}') \qquad (5.4.3.1.6)$$

where $\tau_1$-$\tau_3$ are the late time decay constants. To calculate the ALLTEM response to a UXO target using a given loop polarization, the primary field $\mathbf{H_p}(\mathbf{r}')$ is calculated at the UXO location for the relevant transmitting loop and the *B* fields at the relevant receiving loop locations are calculated. Each transmitting coil is modeled as a 1-meter square loop. For a given measurement, ALLTEM uses two receiving coils to make a differential measurement. The *B* fields at each coil location are subtracted to model the differential measurement. Originally each receiving coil was approximated as an ideal small dipole located at the center of the actual coil, however we have now revised the forward model and use the Biot-Savart law and reciprocity to fully model the Rx loops to improve accuracy when a target is close to a receiver coil.

Using this forward operator, the fields for various UXO targets can be simulated. For example, Figures 5.4.3.1.1-5.4.3.1.6 show the magneto-static fields simulated for targets listed in table 5.4.3.1.1. To generate these figures, data were calculated for cart positions located on a grid two meters on each side and a simulated UXO target located beneath the center of the grid. The aspect ratios listed in table 5.4.3.1.1 compare the length of the target to its width. Note that the synthetic data shown in these plots have a zero noise level.

**Table 5.4.3.1.1.** List of UXO attributes used to generate synthetic data shown in figures 5.4.3.1.1-5.4.3.1.6. Azimuth and inclination are in degrees, and depth is in cm.

| Description | Aspect ratio | Azimuth | Inclination | Depth | Figure |
|---|---|---|---|---|---|
| Vertical rod | 5:1 | 0 | 90 | 25 | 5.4.3.1.1 |
| Horizontal rod | 5:1 | 45 | 0 | 25 | 5.4.3.1.2 |
| Oblique rod | 5:1 | 10 | 10 | 25 | 5.4.3.1.3 |
| Oblique rod | 5:1 | 45 | 45 | 25 | 5.4.3.1.4 |

| | | | | | |
|---|---|---|---|---|---|
| Ball | 1:1 | 0 | 0 | 25 | 5.4.3.1.5 |
| Horizontal disk | 1:5 | 45 | 0 | 25 | 5.4.3.1.6 |

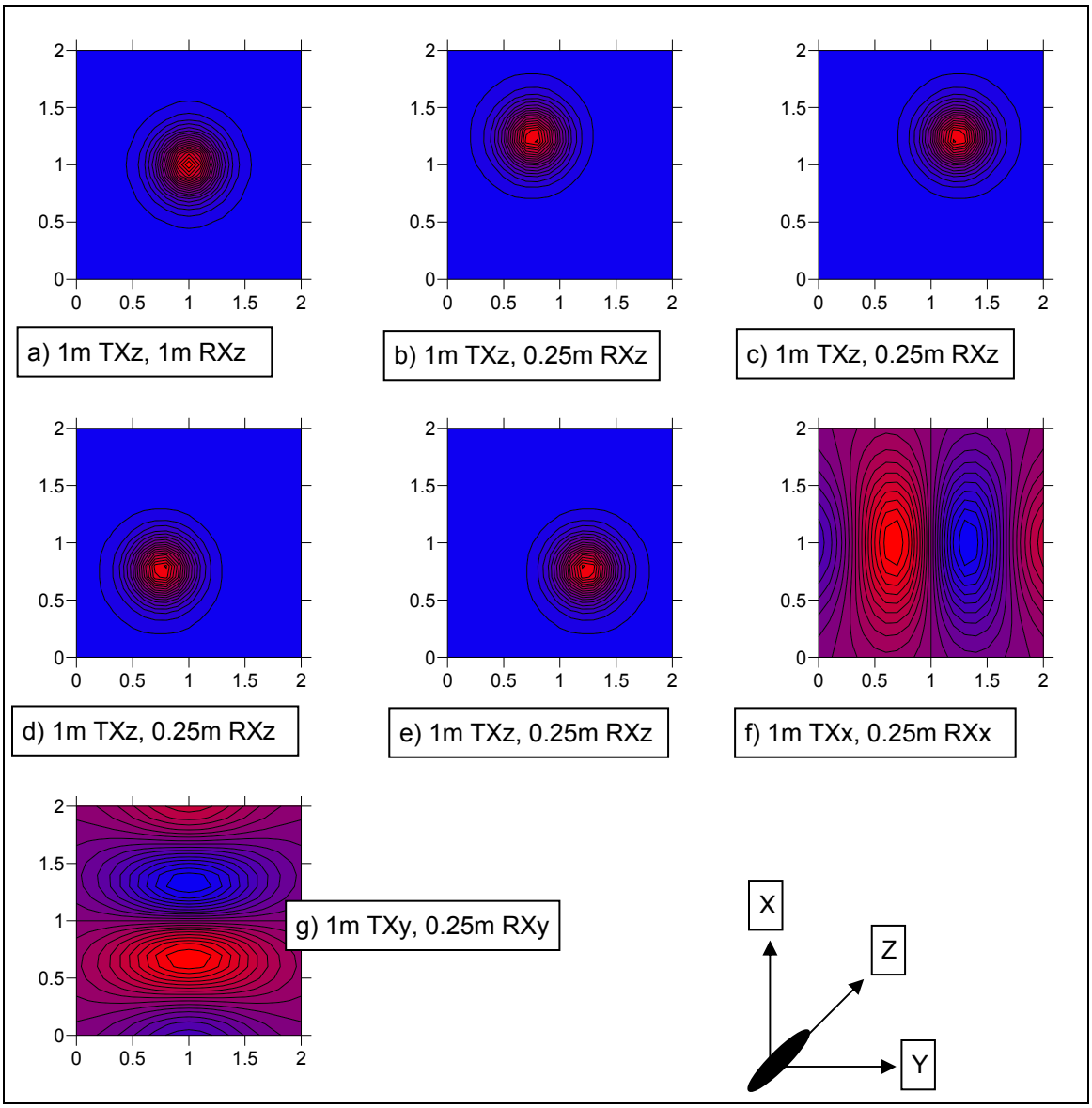


**Figure 5.4.3.1.1**. Simulated ALLTEM magnetostatic response for a vertical rod-like structure. The length of the rod is five times its width. The response is shown for five different vertically polarized coil sets, and two different horizontal sets. Note the symmetric response by the different components. The response of the 1-m vertical gradient receiver is truly symmetric to the system whereas the 0.25-m vertical gradients are slightly offset according to their respective locations.

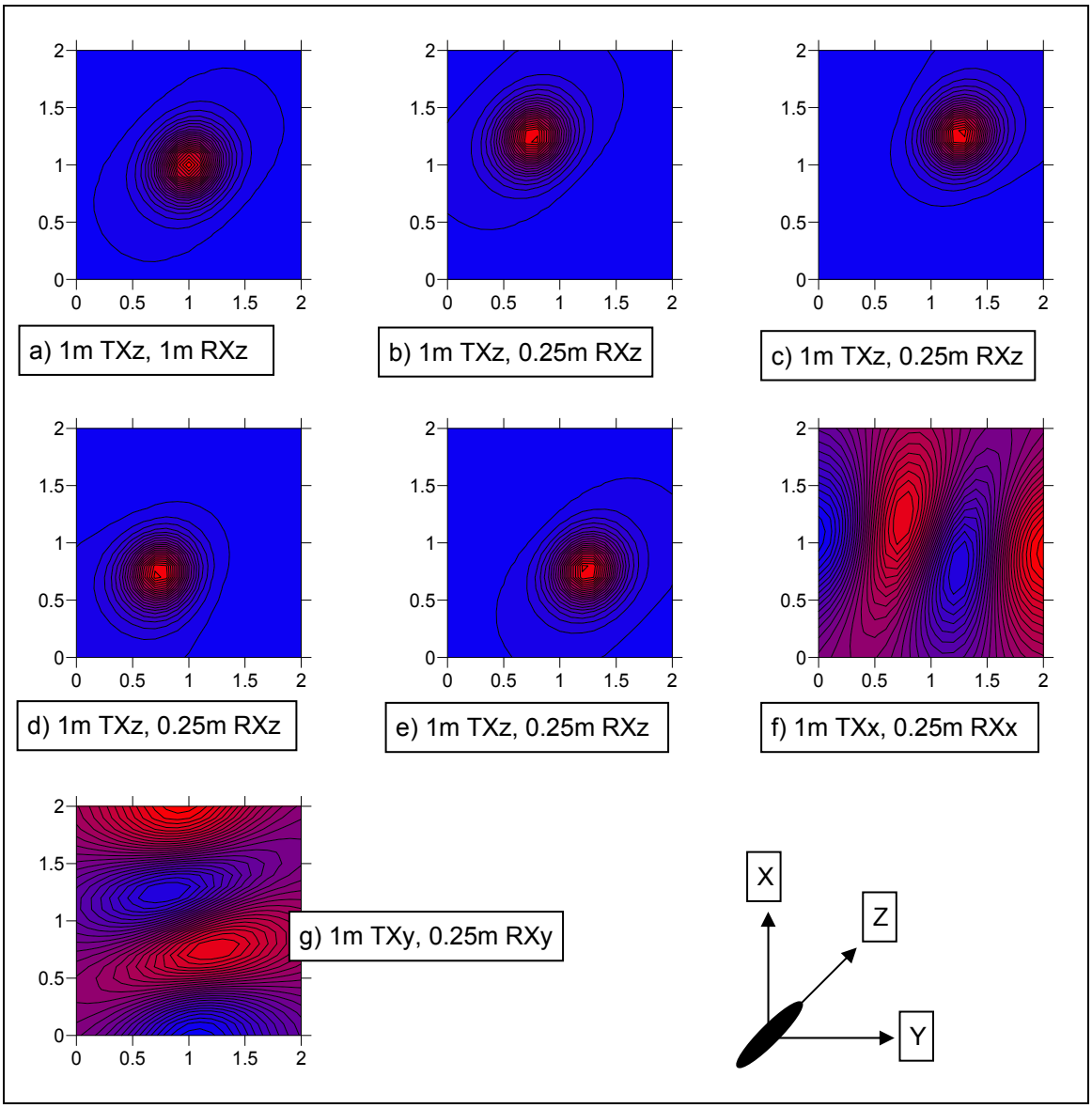


**Figure 5.4.3.1.2**. Simulated ALLTEM magnetostatic response for a horizontal rod-like structure at an azimuth of 45 degrees. The length of the rod is five times its width. The response is shown for five different vertically polarized coil sets, and two different horizontal sets. Note the oriented response in both the vertical and horizontal components.

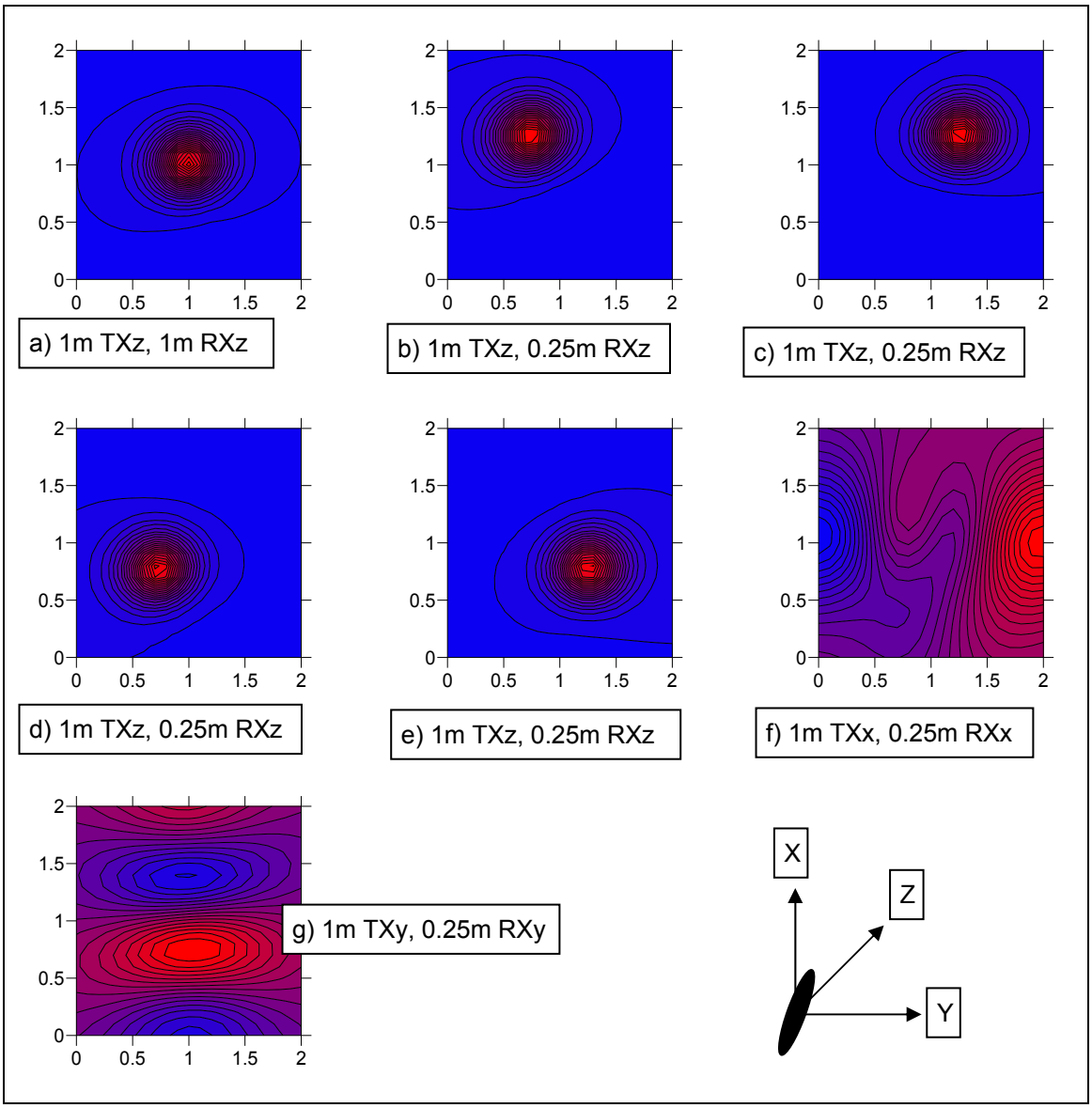


**Figure 5.4.3.1.3**. Simulated ALLTEM magnetostatic response for a rod-like structure at an inclination of 10 degrees and at an azimuth of 10 degrees. The length of the rod is five times its width. The response is shown for five different vertically polarized coil sets, and two different horizontal sets. Note the oriented response in both the vertical and horizontal components.

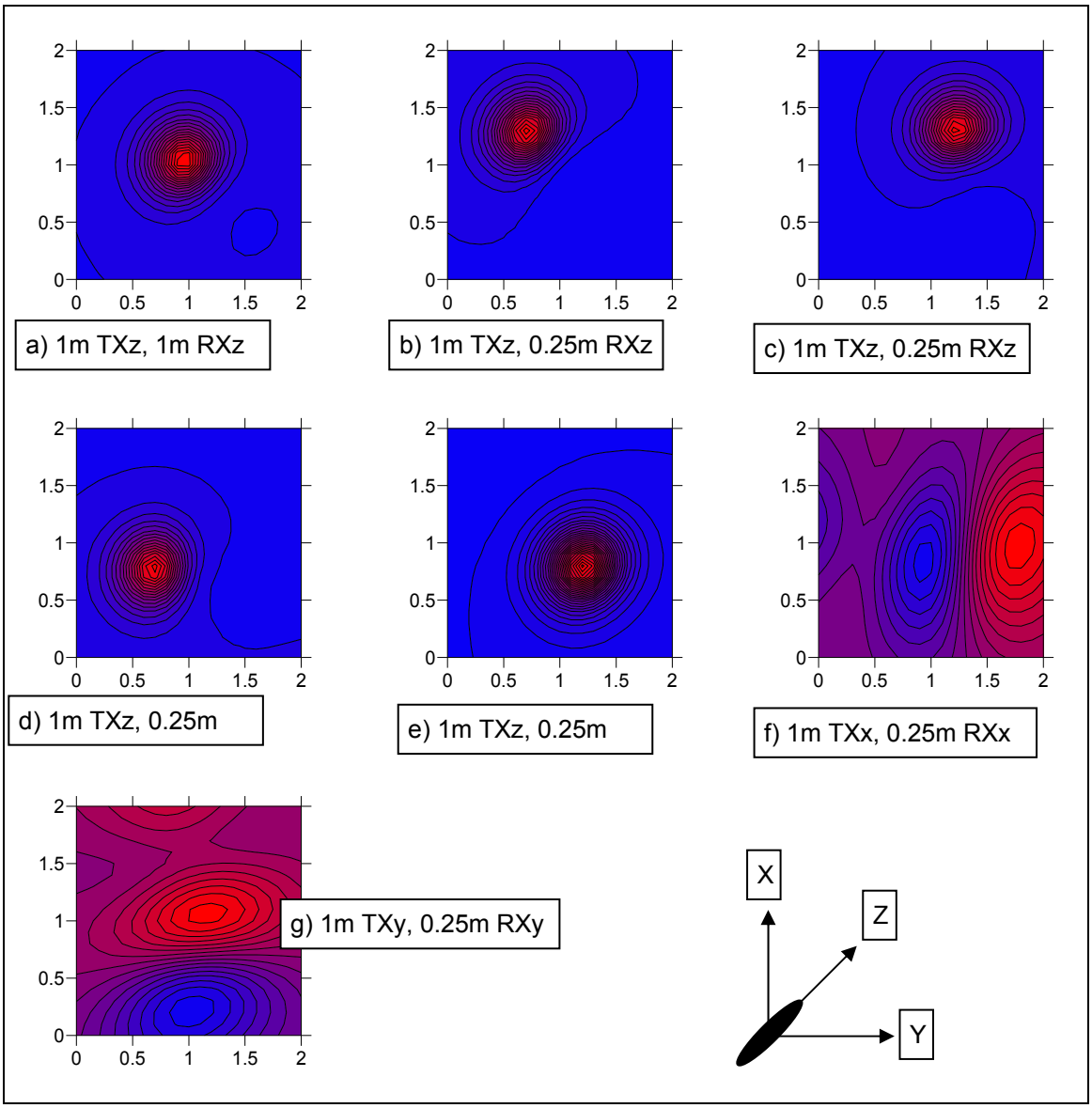


**Figure 5.4.3.1.4**. Simulated ALLTEM magnetostatic response for a rod-like structure at an inclination of 45 degrees and at an azimuth of 45 degrees. The length of the rod is five times its width. The response is shown for five different vertically polarized coil sets, and two different horizontal sets. Note the oriented response in both the vertical and horizontal components.

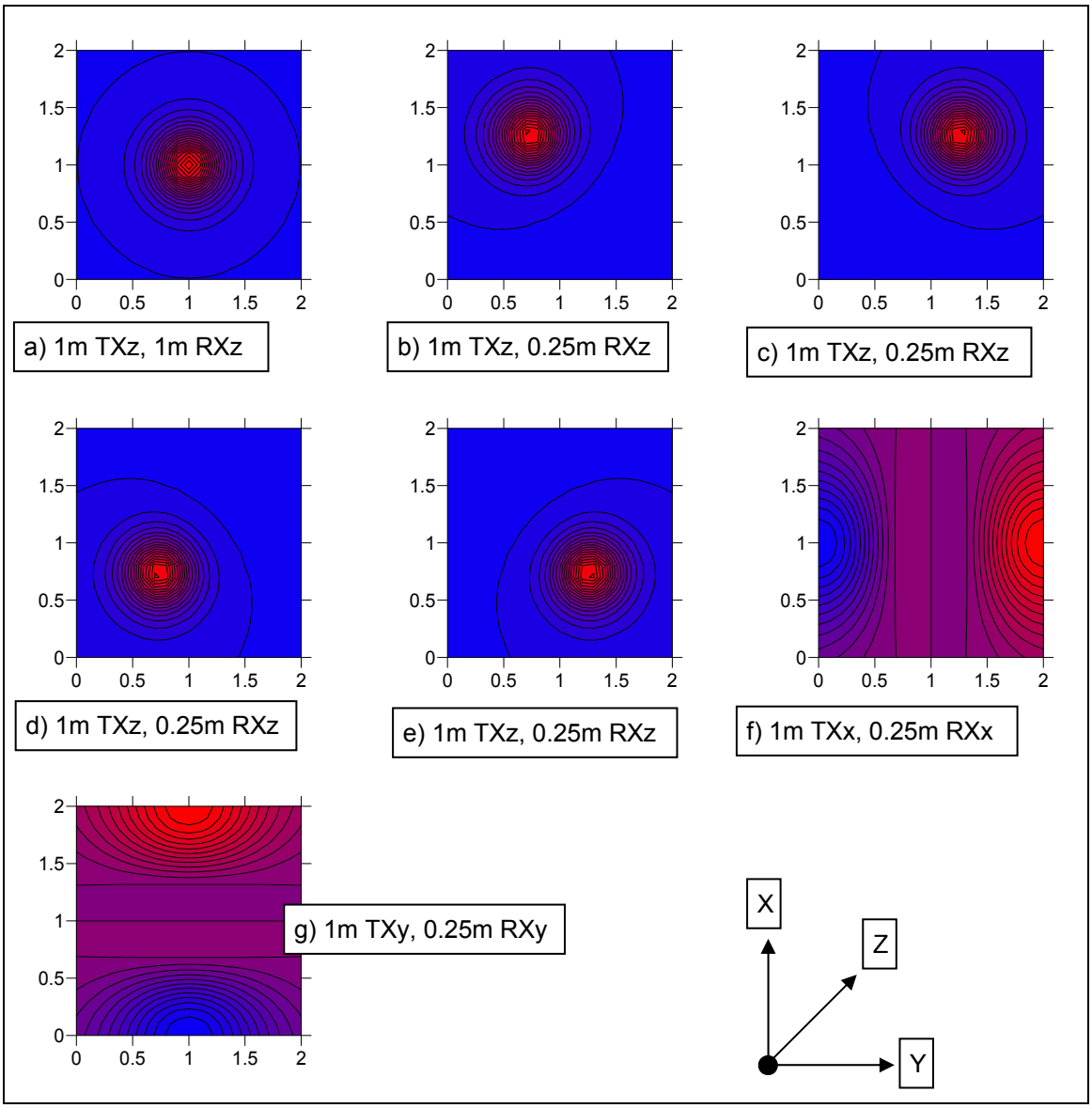


**Figure 5.4.3.1.5**. Simulated ALLTEM magnetostatic response for a ball-like target. The response is shown for five different vertically polarized coil sets, and two different horizontal sets. Note the symmetric responses for the horizontal components and the vertical 1-m loop receiver and the slightly offset responses for the small vertical loop receivers.

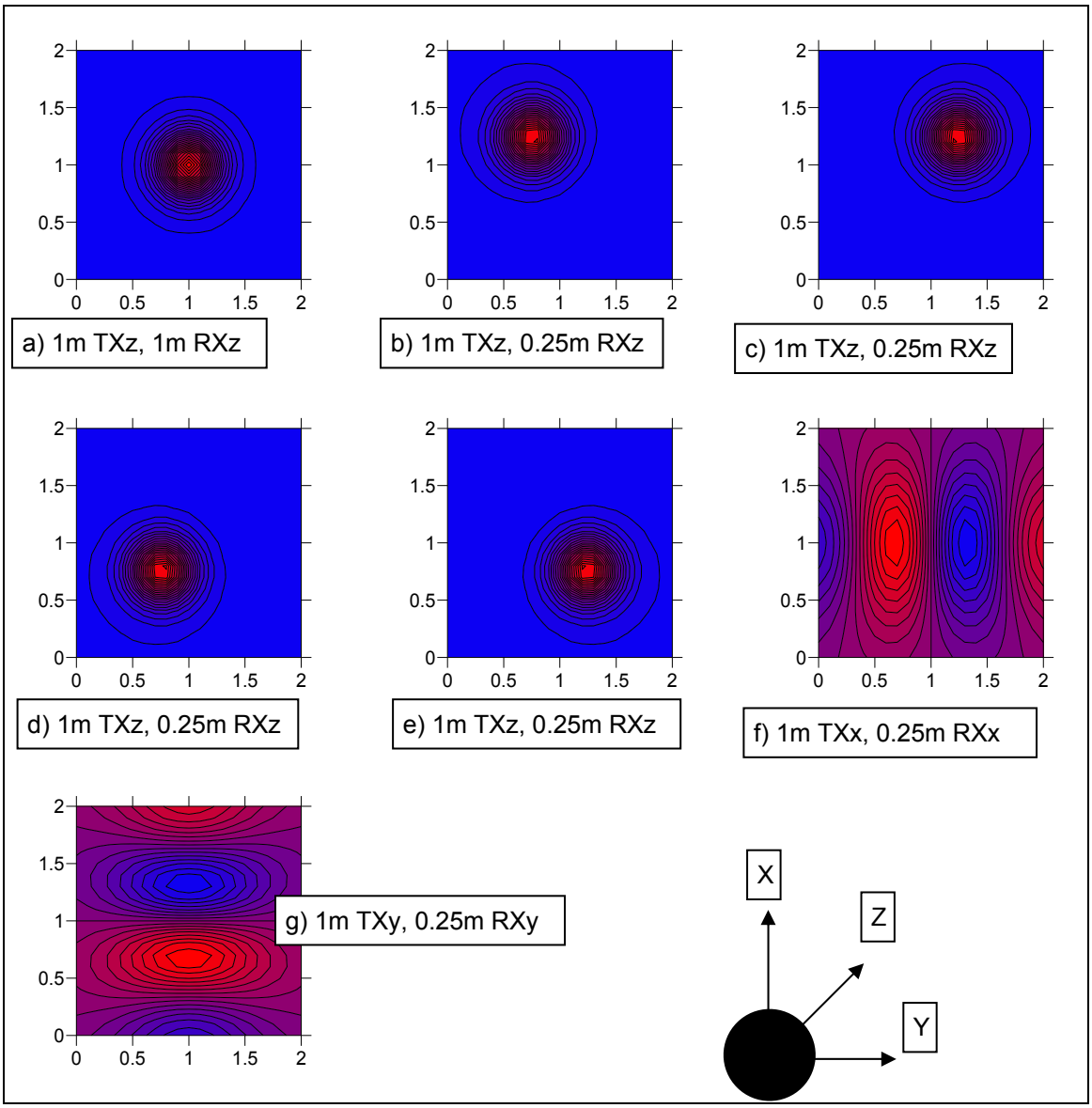


**Figure 5.4.3.1.6**. Simulated ALLTEM magnetostatic response for a horizontal disk-like target. The width of the disk is five times its height. The response is shown for five different vertically polarized coil sets, and two different horizontal sets. Note the difference between the 1-m vertical gradient response in figure 5.4.3.5.1a and 5.4.3.6a above.

### 5.4.3.2 Inversion Algorithm

The forward operator generates a data set that can be compared to survey data to invert for UXO parameter estimates. For a given UXO target, a small data set is extracted from the field data set for use in the inversion. During a survey, the ALLTEM system records the response of various transmitting and receiving loop combinations at successive positions along a survey line. A survey generally consists of a collection of survey lines. A small data set for an individual target is made by extracting received waveforms with locations inside a window over the target as shown in figure 5.4.3.2.1. For each waveform, three data points are extracted. One

point is extracted for the static response, and two points are extracted for the transient response (see figure 5.4.3.2.2). The transient points are taken at 10 percent and 25 percent of the peak value so that late time decays are measured. The resulting data set for a given target is made up of the three waveform points extracted from waveforms recorded at various ALLTEM cart locations using various coil polarizations. For a standard survey, using 50 cm line spacing, 20 cm between each record along each line, and seven different polarization combinations of the transmitting and receiving loops, there will be about 350 waveforms and 1050 data points that can be used to estimate 19 parameters.

During the early-time transient response, the induced dipole moments are oriented parallel to the primary magnetic field. The induced eddy currents will attenuate quickly if the cross-sectional area of the currents in the target is small. Conversely, the induced currents will decay slowly if the cross-sectional area containing the currents is large. Therefore, the late-time transient data contains information about the orientation of the large area conductive planes in the target, and the targets aspect ratio (length to width ratio). For these reasons, late-time data are used in the forward model and inversion, and early-time data are not processed.

The inverse algorithm uses the Gauss-Newton (Gill et al., 1996; Zhdanov, 2002) method to reduce the RMS difference between the predicted data and the measured data. This RMS difference is referred to as the objective function. The predicted data are calculated using the forward operator with an initial set of UXO parameters, and the value of the objective function is calculated. The inversion algorithm then chooses a new set of UXO parameters by moving in the down-gradient direction of the objective function. The value of the objective function using the new parameter set will (usually) be less than the value using the initial parameter set. This process is repeated until the objective function is minimized. An acceptable solution (a UXO parameter set) to the inverse problem is reached when the RMS difference between the predicted data and the actual data is less than the RMS noise level in the data. Since this is a non-linear problem, it is possible that the UXO parameter set determined by the inversion algorithm is located at a local minimum of the objective function rather than a global minimum. The parameter set at a local minimum may not be an acceptable solution to the inverse problem, and may have markedly different values than the parameter set at the global minimum. To solve this problem, the inversion is performed with many initial parameter sets starting at different locations in parameter space. An attempt is made with each initial model to obtain an acceptable solution to the inverse problem. In general, an acceptable solution cannot always be found for each initial model. Given a suitable number of initial models, and a noise level that is above some portions of the objective function topography, some acceptable solutions will be found.

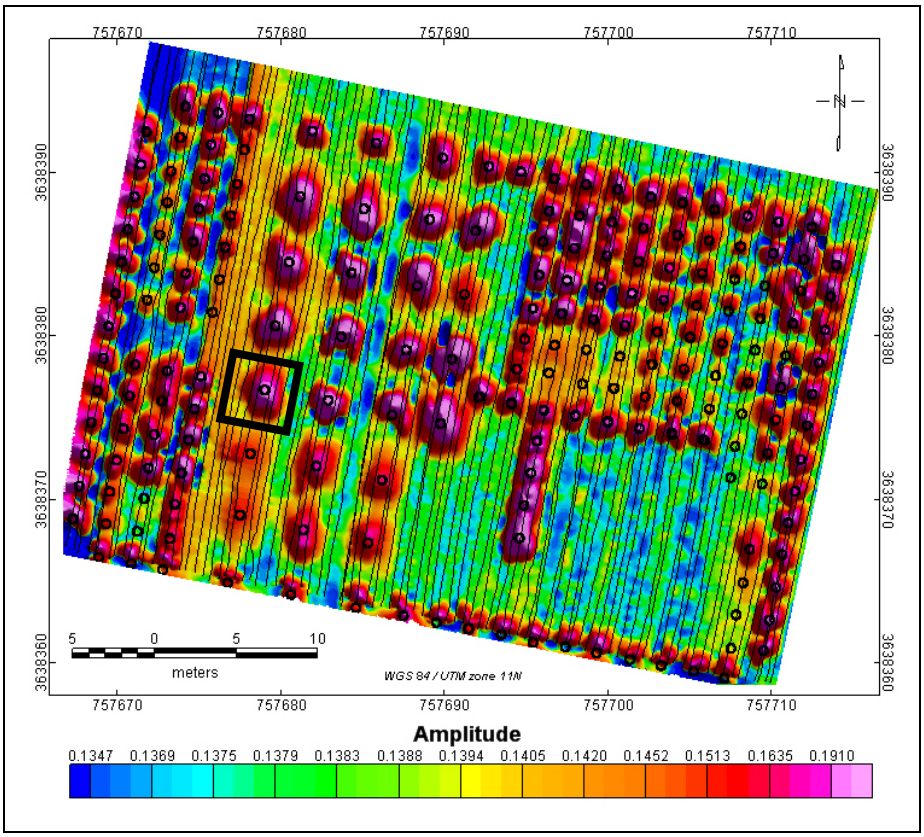


**Figure 5.4.3.2.1**. ALLTEM data from the YPG UXO Calibration Grid. Data are for 1-meter square vertically polarized transmitting and receiving coils. A data set for an individual target is made by extracting received waveforms with locations inside a window over the target as shown.

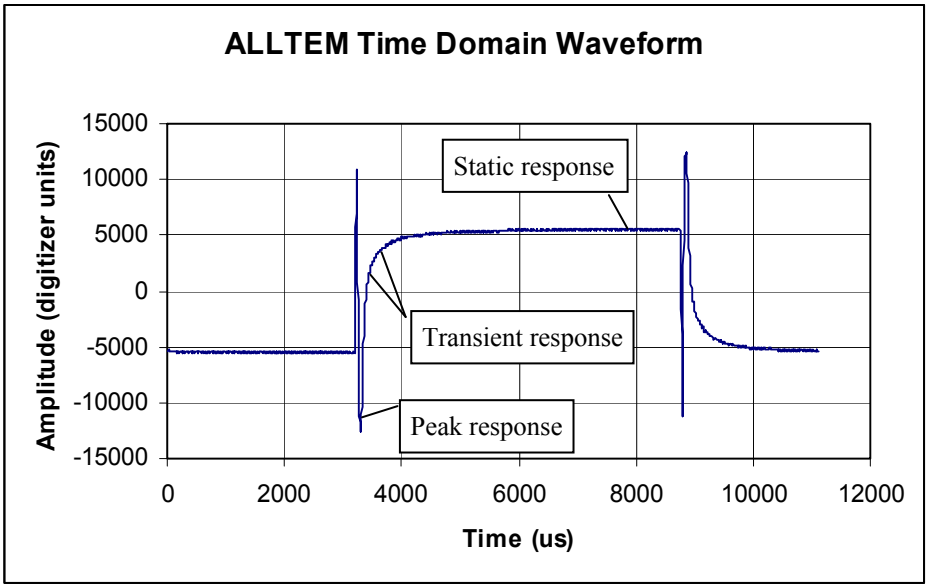


**Figure 5.4.3.2.2**. ALLTEM time domain waveform.

The final solution is calculated by averaging the results from the set of acceptable solutions. This inversion scheme has been used successfully for other non-linear problems (Oden, 2006; Oden et al. 2006).

The RMS noise in the data has several components. They are system noise from the electronics and sensors, electromagnetic interference, the response from varying electromagnetic properties of the soil, the response to topography, and the response due to changing attitude of the cart. Before inverting the extracted target data set, data points are removed from the set if their amplitude is less than the noise level. This makes the inversion less susceptible to noisy data. We chose not to weight data according to their SNR, because this would possibly de-weight some data points that contain valuable information about the targets.

#### 5.4.3.3 Target Classification

The inversion algorithm provides estimates of the UXO parameter set described in section 5.4.3.2 above on the forward model. The inversion algorithm does not directly identify specific targets. A library can be compiled that maps specific UXO types to the UXO parameter set estimated by the inversion. Some of the data needed for such a library has been obtained using the test stand, discussed later, and more data can be obtained. The aspect ratio of a target is determined from the three components of the induced magnetic moment. If one component is significantly larger than the others, then the target is rod-like. If one component is significantly smaller than the others, then the target is disk-like. If all components have similar magnitudes, then the target is ball-like. A target classifier is being developed under a follow-on ESTCP project MM-200809. The classifier will use target SNR and principal polarizability moment information, with or without the associated time constants, generated by the inversion discussed here.

#### 5.4.3.4 Parameter Sensitivity Analysis

A preliminary sensitivity analysis was made to estimate the performance of the inversion algorithm for the magneto-static response. Synthetic data generated by forward modeling were used to estimate the sensitivity of various model parameters to noise and measurement uncertainties. Data were generated for a 2-meter square grid using a 20 cm interval in the $x$ direction (along survey lines), and a 50 cm interval in the $y$ direction. The location of the survey positions is shown in figure 5.4.3.3.1 for a typical target. Tables 5.4.3.4.1 and 5.4.3.4.2 list locations in UXO parameters space where the sensitivities were determined. The simulated data with a 1:1 aspect ratio are representative of a steel shot with a diameter of 8.9 cm like those buried at the YPG. The data with an aspect ratio of 5:1 are representative of an 81 mm M374 ordnance.

These preliminary theoretical parameter sensitivity analyses have been supplemented by sensitivity analyses using actual system data recorded at the test stand. The test stand results are discussed in section 5.5.1 of this report. Additional systematic parameter sensitivity analyses are being performed under ESTCP sponsorship and these could lead to some modifications to the sensor cube geometry and/or changes in the particular Rx-Tx polarization combinations that are recorded and used in the target inversions.

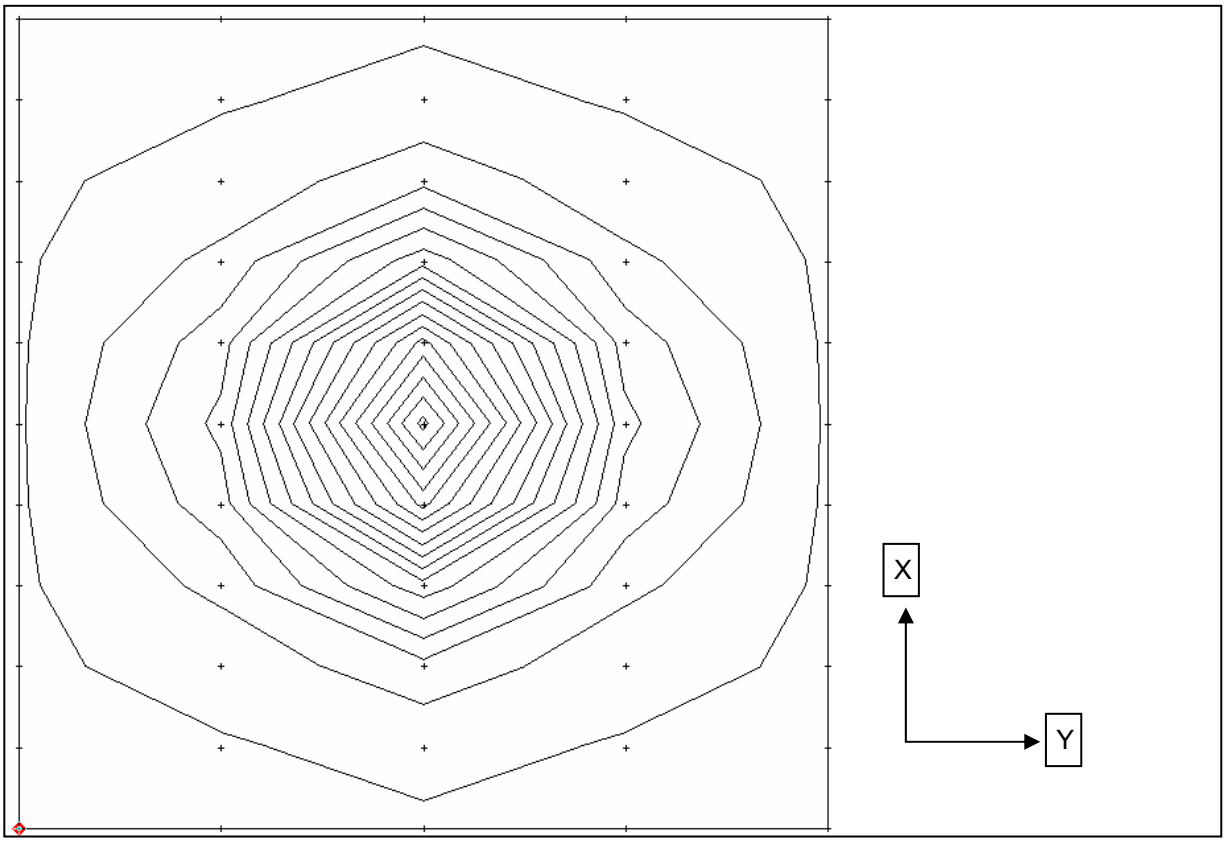


**Figure 5.4.3.4.1**. Cart locations used to generate synthetic data. Contours show a typical response to a vertical target under the center of the survey grid measured by the 1-m vertical gradient receiver. These simulated locations represent five survey lines along the *x* direction.

**Table 5.4.3.4.1**. Parameter sensitivities using only the vertical polarizations. Depth is in cm, and azimuth and inclination are in degrees.

| Target Parameters | | | | Parameter Uncertainty (+/-) | | | |
|---|---|---|---|---|---|---|---|
| Depth | Aspect ratio | Az./Inc. | Comment | Depth | Aspect ratio | Az./Inc. | Num. data |
| 10 | 5:1 | 0/90 | vert. rod | 0.06 | ? | 10.6/23.0 | 166 |
| 10 | 5:1 | 45/0 | hor. rod | 0.02 | 0.07 | 7.4/8.7 | 251 |
| 10 | 5:1 | 10/10 | oblique rod | 0.21 | 0.08 | 5.8/11.9 | 248 |
| 10 | 5:1 | 45/45 | oblique rod | 0.88 | 0.21 | 13.7/7.9 | 161 |
| 10 | 1:1 | 0/0 | ball | 0.09 | 0.08 | ?/14.6 | 107 |
| 10 | 1:5 | 45/0 | hor. disk | 0.18 | 0.07 | ?/8.8 | 257 |
| 25 | 5:1 | 0/90 | vert. rod | 1.3 | ? | 60.3/79.2 | 113 |
| 25 | 5:1 | 45/0 | hor. rod | 5.6 | 0.42 | 24.4/34.0 | 201 |
| 25 | 5:1 | 10/10 | oblique rod | 5.5 | 0.48 | 26.3/28.5 | 199 |
| 25 | 5:1 | 45/45 | oblique rod | 30.1 | 1.1 | 78.7/12.5 | 120 |
| 25 | 1:1 | 0/0 | ball | 16.4 | 0.23 | ?/? | 81 |
| 25 | 1:5 | 45/0 | hor. disk | 0.18 | 0.51 | ?/39.4 | 237 |
| 50 | 5:1 | 0/90 | vert. rod | 5.0 | ? | ?/35.6 | 47 |
| 50 | 5:1 | 45/0 | hor. rod | 18.7 | 2.0 | 27.7/38.2 | 141 |
| 50 | 5:1 | 10/10 | oblique rod | 85.4 | 3.4 | 32.7/34.0 | 140 |
| 50 | 5:1 | 45/45 | oblique rod | 145 | 6.3 | ?/24.7 | 131 |
| 50 | 1:1 | 0/0 | ball | 70.0 | ? | ?/? | 99 |
| 50 | 1:5 | 45/0 | hor. disk | 6.7 | 1.4 | ?/41.4 | 129 |

**Table 5.4.3.4.2**. Parameter sensitivities using both vertical and horizontal polarizations.

| Target Parameters | | | | Parameter Uncertainty (+/-) | | | |
|---|---|---|---|---|---|---|---|
| Depth | Aspect ratio | Az./Inc. | Comment | Depth | Aspect ratio | Az./Inc. | Num. data |
| 10 | 5:1 | 0/90 | vert. rod | 0.31 | ? | 9.0/19.5 | 261 |
| 10 | 5:1 | 45/0 | hor. rod | 0.07 | 0.06 | 6.2/7.4 | 359 |
| 10 | 5:1 | 10/10 | oblique rod | 0.19 | 0.07 | 4.9/10.1 | 358 |
| 10 | 5:1 | 45/45 | oblique rod | 0.77 | 0.18 | 11.6/6.7 | 270 |
| 10 | 1:1 | 0/0 | ball | 0.32 | 0.07 | ?/12.3 | 197 |
| 10 | 1:5 | 45/0 | hor. disk | 0.16 | 0.06 | ?/7.4 | 351 |
| 25 | 5:1 | 0/90 | vert. rod | 1.4 | ? | 50.9/67.0 | 210 |
| 25 | 5:1 | 45/0 | hor. rod | 4.7 | 0.35 | 20.6/28.7 | 309 |
| 25 | 5:1 | 10/10 | oblique rod | 4.7 | 0.41 | 22.3/24.1 | 308 |
| 25 | 5:1 | 45/45 | oblique rod | 25.4 | 0.91 | 66.5/10.6 | 229 |
| 25 | 1:1 | 0/0 | ball | 13.9 | 0.16 | ?/? | 167 |
| 25 | 1:5 | 45/0 | hor. disk | 0.33 | 0.43 | ?/33.3 | 331 |
| 50 | 5:1 | 0/90 | vert. rod | 5.3 | ? | ?/31.1 | 134 |
| 50 | 5:1 | 45/0 | hor. rod | 15.9 | 1.7 | 23.5/32.3 | 249 |
| 50 | 5:1 | 10/10 | oblique rod | 72.2 | 2.9 | 27.7/28.7 | 249 |
| 50 | 5:1 | 45/45 | oblique rod | 123 | 5.3 | ?/21.0 | 236 |
| 50 | 1:1 | 0/0 | ball | 59.2 | 3.1 | ?/? | 179 |
| 50 | 1:5 | 45/0 | hor. disk | 5.7 | 1.1 | ?/35.0 | 223 |

Note: In the above table a "?" indicates that the parameter is not meaningful or cannot be determined.

The resolution of the inversion algorithm is estimated as follows. For a given datum $y_i$, the sensitivity to the UXO parameters $x$ at a specified location in UXO parameter space is given by

$$\Delta y_i = \sum_j J_{i,j} \Delta x_j \qquad (5.4.3.4.1)$$

where $J_{i,j} = \partial y_i / \partial x_j$ is the Jacobian. Similarly, the sensitivity of each UXO parameter to the data is

$$\Delta x_j = \sum_i S_{j,i} \Delta y_i \,. \qquad (5.4.3.4.2)$$

where $S_{j,i} = \partial x_j / \partial y_i$ (to first order). An estimate of the UXO parameter resolution is given by

$$\sigma_{x,j}^2 = \frac{1}{N_i} \sum_i \left( S_{j,i} \sigma_{y,i} \right)^2 \,, \qquad (5.4.3.4.3)$$

where $\sigma_{y,i}$ is the RMS noise of the $i$th datum $y_i$, and $\sigma_{x,j}$ is the RMS uncertainty in the $j$th UXO parameter estimate $x_j$. The Jacobian $J_{i,j}$ and sensitivity $S_{j,i}$ parameters are calculated numerically from the forward model. This simple formulation assumes that the noise in the data is uncorrelated, which is almost certainly not the case for some noise components such as topography.

To estimate the RMS noise level in a typical data set, the YPG data collected in October, 2005 were examined. ALLTEM measurements of buried steel shots were made near lane one of the YPG Calibration grid. These shots were buried at a depth of 20 cm and have a radius of 8.9 cm. The noise level due to electronic noise, electromagnetic interference, topography, and the changing electromagnetic properties of the soil was estimated to be two percent of the peak

signal level measured above the steel shots. An RMS noise level for synthetic data was estimated as two percent of the peak signal level of the simulated data for a spherical target (i.e. an aspect ratio of 1:1) at a depth of 20 cm. When calculating the uncertainty values listed in Tables 5.4.3.4.1 and 5.4.3.4.2, any synthetic data values with a magnitude less than the synthetic RMS noise level were removed before applying equation 5.4.3.4.3.

Some generalizations can be made based on the results shown in tables 5.4.3.4.1 and 5.4.3.4.2, from the forward operator relationships, and from the mechanisms used in the inverse algorithm.

1. Deeper targets produce fewer data points above the noise level. The RMS uncertainties for the UXO parameter estimates are larger for deeper targets. The UXO parameters for targets on the order of 9 by 40 cm that are deeper than 50 cm are not resolvable at the noise levels observed in the data examined for this analysis. Deeper targets can be located, but the data quality is insufficient to facilitate inversion for parameter estimates.

2. Under the assumption that all sensitivity $S_{j,i}$ parameters have similar values, the RMS uncertainty in the UXO parameter estimates will decrease as $1/\sqrt{N_i}$ where $N_i$ is the number of data points collected. The number of data points can be increased by using a more dense survey grid, and/or collecting data using more polarization combinations from the ALLTEM coils. Collecting more data on a more dense survey grid increases survey time. In practice, the $S_{j,i}$ parameters do not all have similar values, but the inverse square root relationship does provide useful insight.

3. Reducing the RMS noise level and increasing the signal level can increase the depth to which useful UXO parameter estimates can be obtained. The signal level could be increased with more primary field energy, but significant increases in driving current would be difficult to achieve from an engineering standpoint. A somewhat larger vertical axis transmitting coil might be worthwhile and possible. Non-coherent system noise and electromagnetic interference can be reduced by increasing the number of stacks used when acquiring data, but this slows data acquisition and additional stacking is thus practical only in cued mode. It is likely that the response due to changes in topography, cart attitude, and variations in the electromagnetic properties of the soil can be reduced by adding additional sensors to the cart to record topography and cart attitude. The SNR could also be increased by placing the cart closer to the ground, but we are already near a practical minimum on all but the smoothest ground. For some of our data, digital filtering to remove some high frequency coherent system noise and external VLF radio station noise considerably improves the SNR.

4. Figures 5.4.3.1.1-5.4.3.1.6 indicate that the horizontal components contain valuable information regarding target attitude. Unfortunately, the signals from horizontal component coils at depth are weaker than the vertical components, and have a smaller SNR. Tables 5.4.3.4.1 and 5.4.3.4.2 show that adding these components reduces uncertainty in the UXO parameter estimates, but not markedly. It is anticipated that adding more measurements using different coil polarizations will incrementally reduce the uncertainty.

5. Target azimuth can not be estimated when the target has radial symmetry such as a vertical rod-like structure or a horizontal disk-like structure. It is only possible to determine a target's azimuth over a range of 0-180 degrees, and inclination over 0-90 degrees. It is not possible, for instance, to determine whether the tail of a target is pointing up or down. By having some prior knowledge about the targets, it may be possible to better estimate the attitude of some targets.

6. The uncertainty in the estimated aspect ratios increases when the induced dipole moments are aligned with the polarizations of the ALLTEM coils.

7. The uncertainties listed in tables 5.4.3.4.1 and 5.4.3.4.2 assume a locally linear forward operator. The actual forward operator is non-linear, which may pose difficulty in finding a solution(s). The character of the objective function (RMS difference between the predicted data and the actual data) has not been studied. The objective function may have several or many local minima. The nature of the objective function will determine how difficult it is and how much searching in UXO parameter space is needed to find an acceptable solution set. It is possible that a solution set may extend across multiple basins of attraction, leading to a less-unique solution.

8. Positional errors will detract from the accuracy and increase uncertainty associated with the inverse solution. These have recently been studied by adding simulated position errors to real test stand data as discussed in section 5.5.1. If the target SNR is high it appears that positional errors of up to +/- 5 cm can be tolerated without a great increase in uncertainty in the inverse solutions for target parameters.

### 5.4.3.5 Inversion Results from the YPG Calibration Grid and Blind Test Grid

At the time of our May, 2006 YPG deployment we were still in the process of debugging our inversion algorithm software. After we thought we had identified and fixed the major bugs in the inversion software, we ran inversions on many of the targets in the Calibration Grid where we knew the ground truth. We found that inversions over different size targets were yielding polarizability moments that were consistent with the relative target sizes and that inversions over more than one 60 mm mortar round of the same type, but different depths and orientations were producing relatively consistent polarizability moments. We began to gain confidence in the inversion algorithm and in the possibility of reliably inverting data acquired from a moving platform. We realized that a necessary condition for a good inversion was that measured field data and the corresponding patterns produced by the forward modeler, discussed in section 5.4.3.1 above, should closely match. Figures 5.4.3.5.1 and 5.4.3.5.2 below show a comparison for a subset of 6 of the 19 recorded Tx-Rx combinations of the measured data and the corresponding patterns produced by the forward modeler at the last iteration. The dots in the measured "ZZF" panels of each figure show the locations at which the data used in the inversion were located. The two figures show results over the same target, but with lines run in orthogonal directions. The field patterns should be different for the two cases, as indeed they are, but the calculated target parameters should ideally be exactly the same. Tables 5.4.3.5.1, 5.4.3.5.2, and 5.4.3.4.3 show inversion results for three cases of data over a 60 mm mortar round.

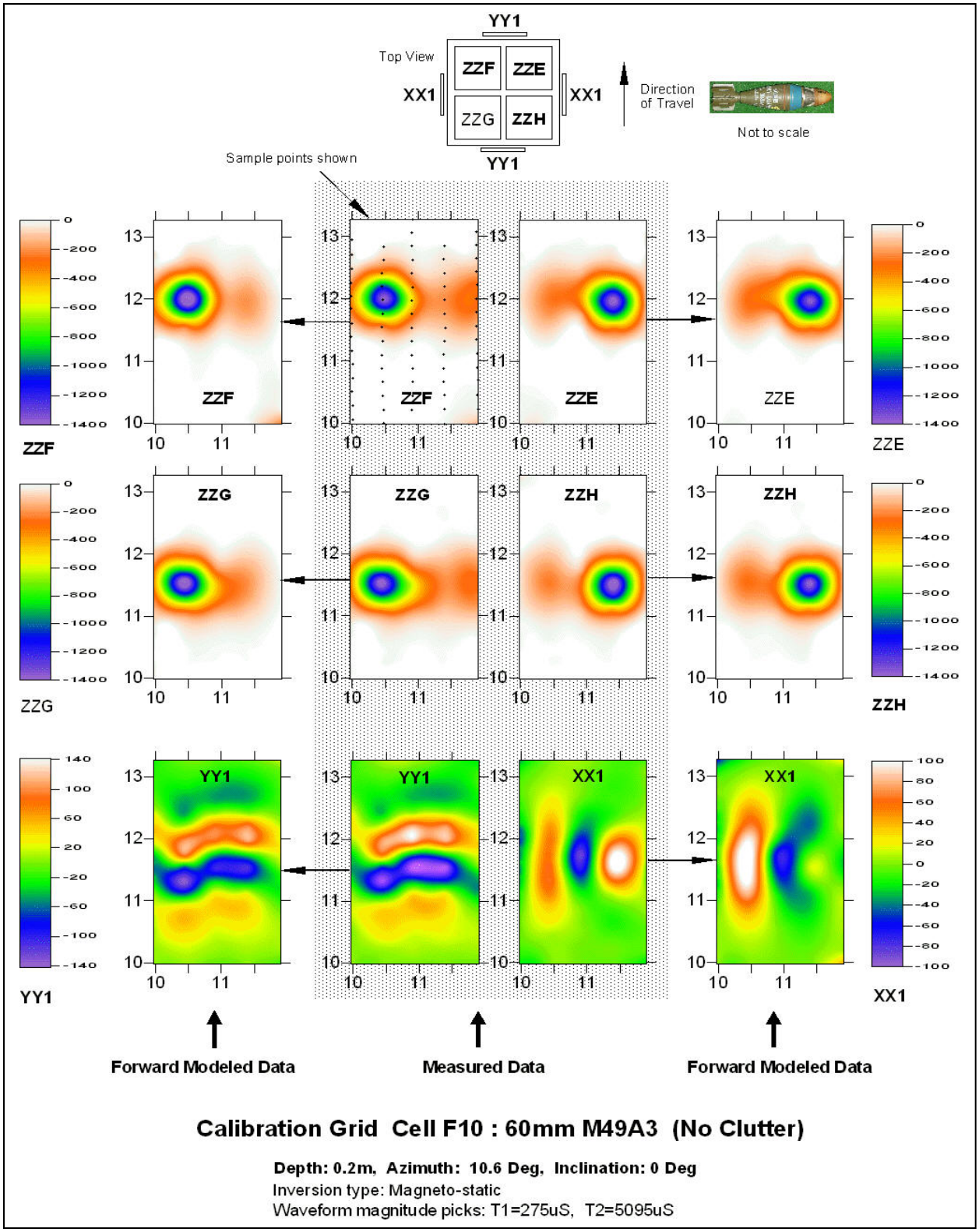


**Figure 5.4.3.5.1.** Measured and forward modeled data for six Rx-Tx combinations over a 60 mm mortar round in Cell number F10 in the Calibration Grid at YPG. The measured data are in the six interior maps. The corresponding forward modeled maps are on the outside.

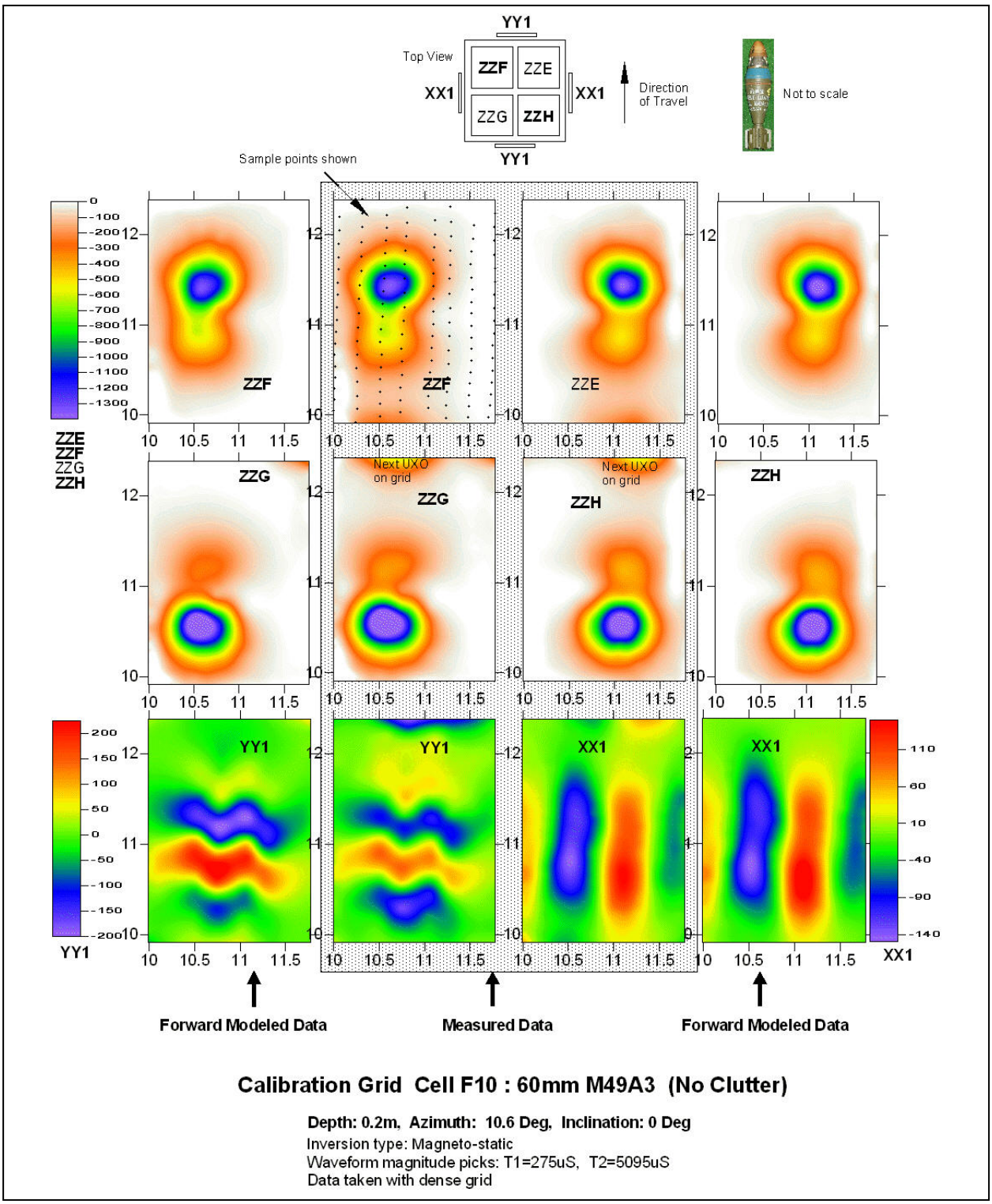


**Figure 5.4.3.5.2.** This comparison of measured field data and forward modeled data is similar to that of the previous figure except that the data were acquired along lines run parallel to the long axis of the target. The horizontal polarization field patterns "YY1" and "XX1" differ from those of the previous figure, as expected, but for each case the measured and modeled data agree.

**Table 5.4.3.5.1.** Inversion over 60 mm M49A3 at grid location F10 with lines run east to west.

| X (m) | Y (m) | Depth (m) | Azimuth (degrees) | Inclination (degrees) | M1 | M2 | M3 | MSE |
|---|---|---|---|---|---|---|---|---|
| 695.636 | 373.609 | -0.25 | 10.60 | 0.0 | * | * | * | * |
| 695.387 | 373.766 | -0.27 | 15.75 | 0.0 | 2.19 | 0.38 | 0.39 | 0.035 |

**Table 5.4.3.5.2.** Inversion over 60 mm M49A3 at grid location F10 with lines run south to north.

| X (m) | Y (m) | Depth (m) | Azimuth (degrees) | Inclination (degrees) | M1 | M2 | M3 | MSE |
|---|---|---|---|---|---|---|---|---|
| 695.636 | 373.609 | -0.25 | 10.60 | 0.0 | * | * | * | * |
| 695.636 | 373.543 | -0.26 | 16.80 | 2.9 | 1.99 | 0.43 | 0.35 | 0.026 |

**Table 5.4.5.3.** Inversion over 60 mm M49A3 at grid location M11.

| X (m) | Y (m) | Depth (m) | Azimuth (degrees) | Inclination (degrees) | M1 (m3) | M2 (m3) | M3 (m3) | MSE |
|---|---|---|---|---|---|---|---|---|
| 700.225 | 387.001 | -0.48 | 10.60 | 45.0 | * | * | * | * |
| 700.225 | 386.877 | -0.47 | 2.88 | 49.8 | 1.98 | 0.42 | 0.31 | 0.045 |

In each of the three tables the first row of data is the ground truth. The asterisks in the M1, M2, and M3 polarizability columns indicate that although the target type is given, the moments associated with that type of target are not given. What is known is that there should be a dominant moment, M1, and that M2 and M3 should be smaller and equal. The first two tables are over the same target, but the inverted values come from two different data sets acquired with lines run first east to west and then south to north and with differing data densities. We find that the computed values for M1, M2, and M3, while not precisely the same, are close together. The third table shows results of an inversion over the same kind of 60 mm mortar round buried deeper and at an inclination of 45 degrees. Note that the inversions in both cases got the depths correct to within 2 cm and the azimuths and inclinations are correct to within 7 degrees in every case. $\|Yp-Y\|/\|Y\|$, where Yp is the predicted data vector and Y is the measured data, is the normalized mean squared error (MSE) and measures the difference between the final forward model and the data. ALLTEM inversions are not overly sensitive to noise and in our experience an MSE below 0.1 suggests a good inversion. Failed inversions typically have an MSE well above 0.2, but there can be exceptions and it should be cautioned that a low MSE is a suggestive, but not definitive criterion for a good inversion.

In these tables we give a single number for the polarizability moments, but in reality these parameters are functions of time and the time "decay" provides another parameter for identification and classification of targets. Figures 5.4.5.3.3, 5.4.5.3.4, and 5.4.5.3.5 show examples of calculated time dependent magnetic polarizability moments.

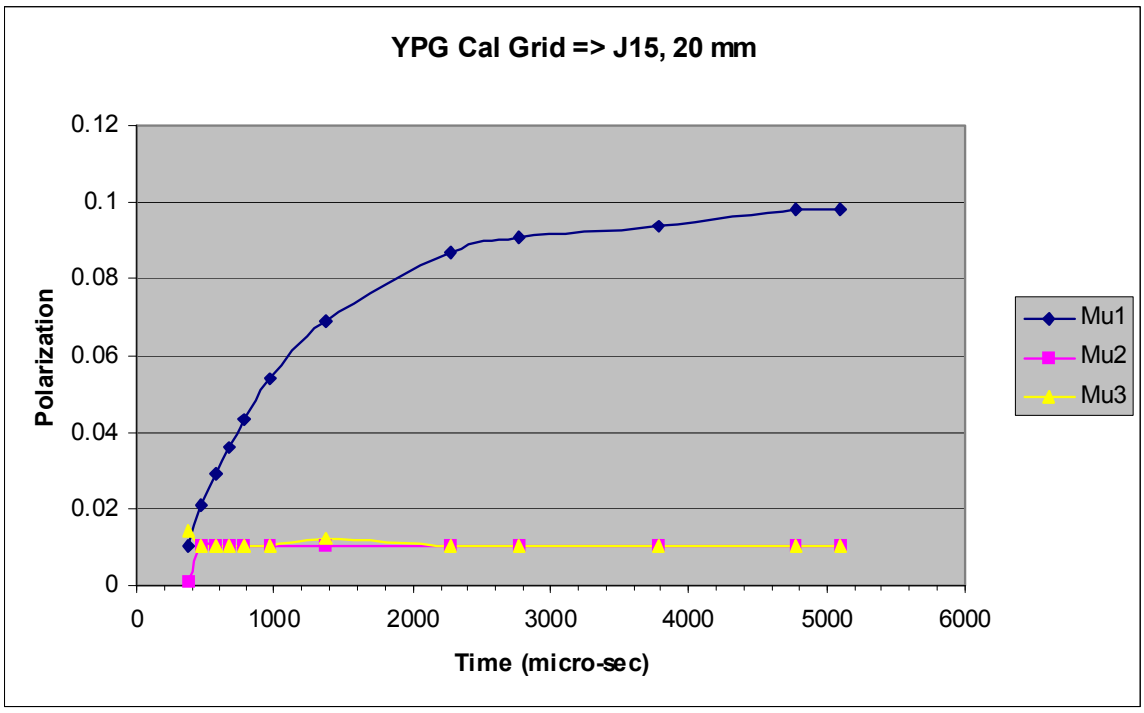


**Figure 5.4.3.5.3.** This figure shows inversion results at a series of times for a 20 mm round at cell J15 in the YPG Calibration Grid. The results are consistent with a small axi-symmetric target.

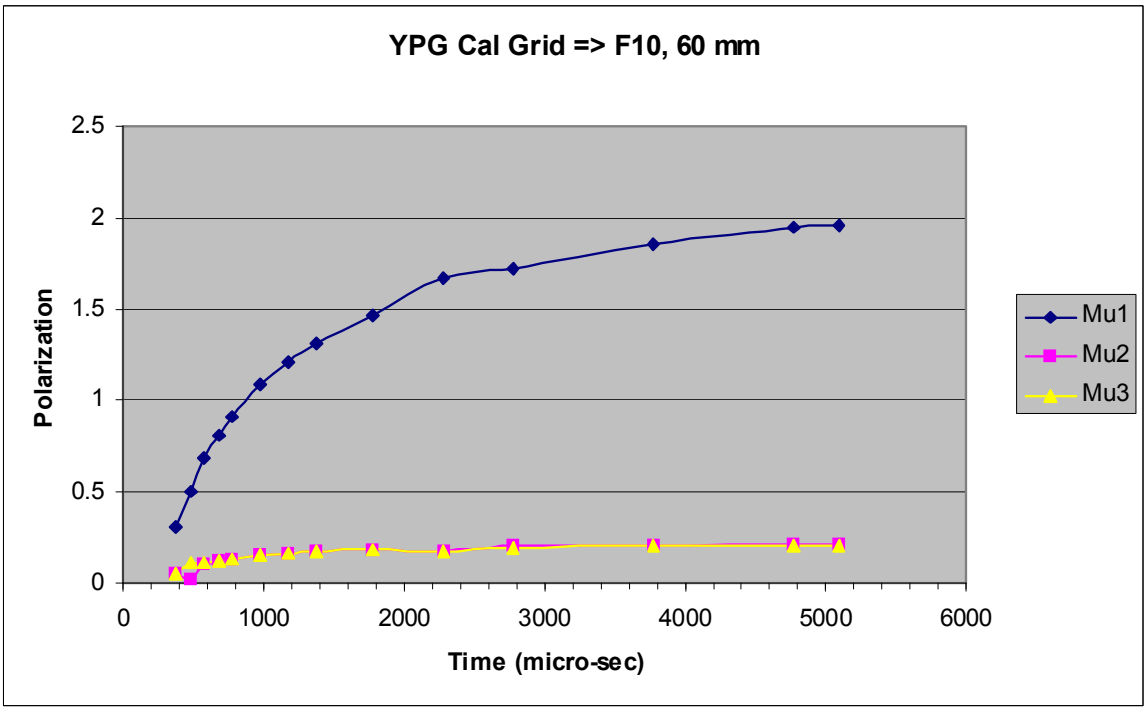


**Figure 5.4.3.5.4.** This is similar to the previous figure, but over a 60 mm mortar round at cell F10 in the Calibration Grid. Note the much larger values for the polarizability moments.

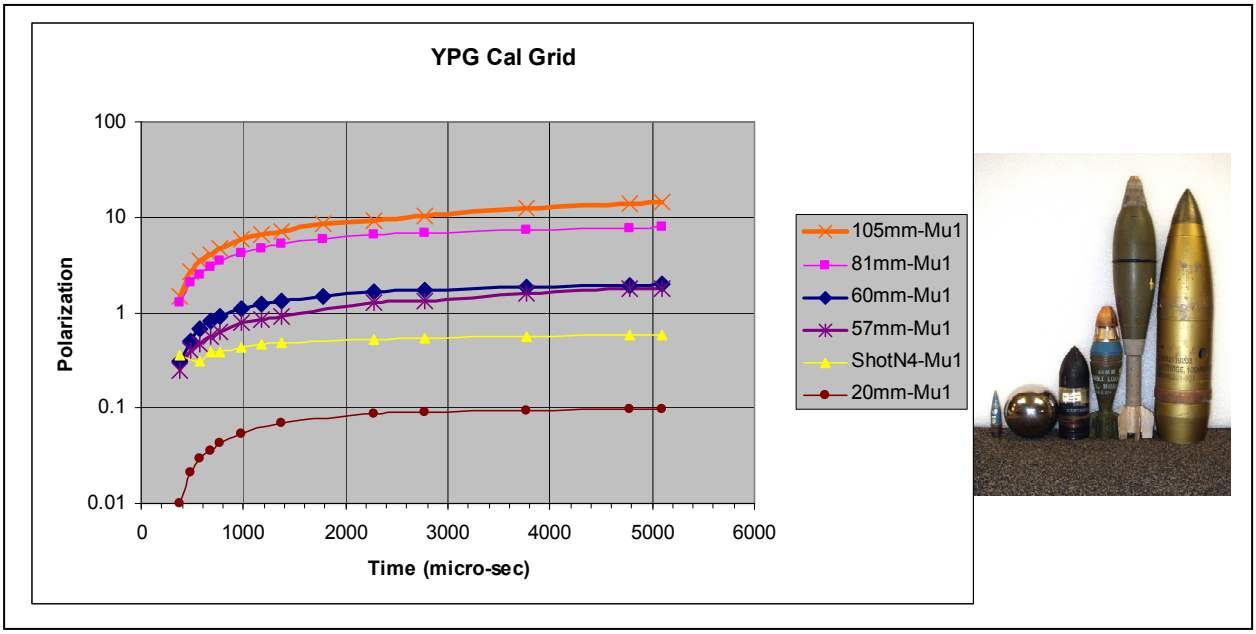


**Figure 5.4.3.5.5.** This figure shows the time history of the largest polarizability moment for the six targets shown at the right.

In figure 5.4.3.5.5, the vertical axis is plotted on a logarithmic scale so that the time variations can be seen for this wide range of targets that span more than two orders of magnitude in calculated polarizability moments. These targets also span a range of 120:1 in mass from the 105 mm to the 20 mm. Polarizability moments are functions of mass, shape, and composition and form the basis around which our automated target classifier will be developed.

Shortly after the May 2006 YPG deployment we submitted a target spreadsheet for evaluation to the Army. At that time we had not realized the importance of the time picks nor was our inversion algorithm debugged. Thus our scores for target identification and discrimination were low. Later, when the inversion algorithm was debugged and trusted, we were asked to generate a new target spreadsheet and submit this spreadsheet to the Institute for Defense Analysis (IDA) for scoring. Feedback from IDA, with results rounded to the nearest 5 percent to protect the integrity of the BTG, included the following:

*Pd-res = (O or C calls on cells containing O)/(total # of O) = 100%*
*Pba-res = (O or C calls on cells containing B)/(total # of B) = 0%*
*Pd-disc = (O calls on cells containing O)/(total # of O) = 90%*
*Pfp-disc = (O calls on cells containing C)/(total # of C) = 0%*
*Pba-disc = (O calls on cells containing B)/(total # of B) = 0%*
*where "O" indicates a cell containing ordnance, "C" indicates a cell containing clutter, and "B" indicates a blank (empty) cell.*

*The UXO items you incorrectly classified as clutter ranged from small to large, with no particular preference on size. You correctly identified the type of UXO (e.g., 37mm, 105mm, etc.) for about 90% of the items you correctly classified as UXO.*

Although there is still room for improvement, these results were quite encouraging to us.

To improve field efficiency and reduce human subjectivity, an automated classifier is being developed, as discussed in section 5.3.4.4 above.

### 5.4.4 TMGS Inversion Algorithms

Two independent efforts were undertaken to develop inversion algorithms for TMGS data. One, led by Dr. Yaoguo Li of the Geophysics Department at the Colorado School of Mines (CSM), focused on a traditional approach, namely an iterative nonlinear least-squares fit of a windowed subset of field observations to the classical magnetostatic field equations. The other, led by Robert Bracken of the USGS, aimed at a fully automatic process based on field equations of separated monopoles.

#### 5.4.4.1 Colorado School of Mines TMGS inversion algorithm

CSM implemented tensor inversion code in MatLab. Input can be a random, sparse dataset of X-coordinate, Y-coordinate, G*xx*, G*xy*, G*xz*, G*yy*, and G*yz* in tabulated text format. The code offers the option of inverting for dipole and quadrupole moments. It uses a nonlinear least squares fitting function, and iterates until either convergence criteria are met, or the iteration count is exceeded.

Six discrete targets and seven steel balls (lane markers) on the eastern boundary were excerpted from BTG tensor dataset. The targets were selected because they promised to yield good inversion results from the corresponding ALLTEM data. The balls were selected because, as ferromagnetic spheres, they may serve as canonical targets – each should have a simple dipole magnetic moment. Representative target anomalies (the G*xy* component only) are pictured in figure 5.4.4.1.1. Each target box is approximately 8 m on a side. The center of the target's grid cell is indicated with a white dot. Because of the large area of the boxes, some small anomalies, such as target 02 and 04, are difficult to discern. Thin black lines mark the path of the array, white streaks occur where interpolation failed to fill in between lines.

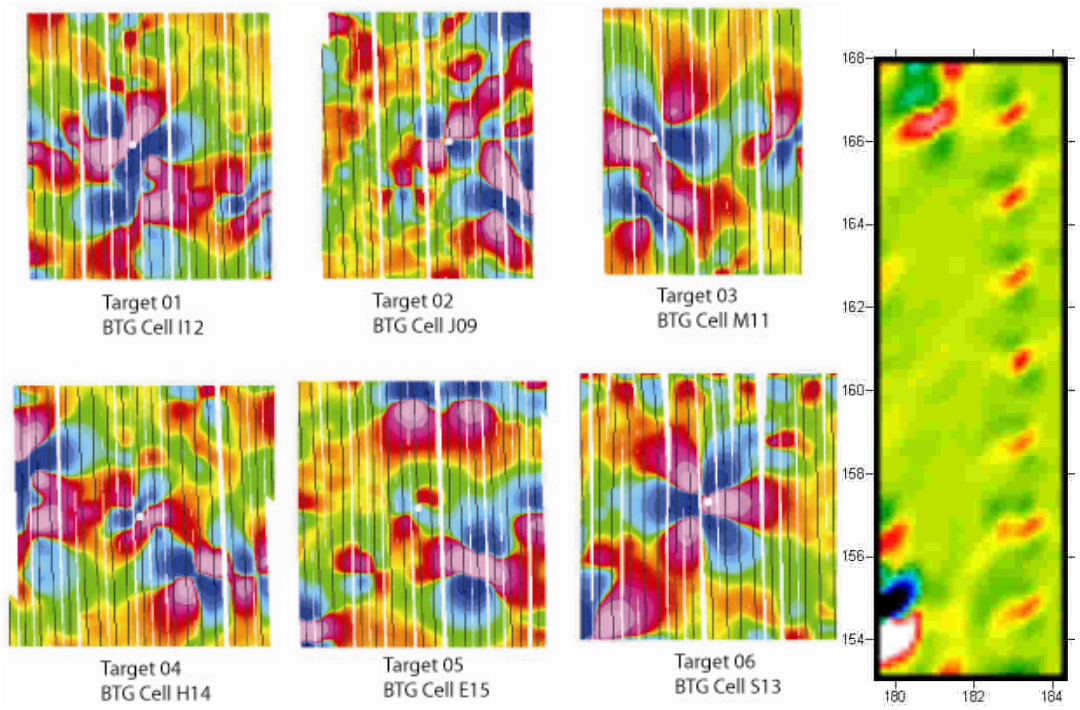


**Figure 5.4.4.1.1.** Target anomalies excerpted for CSM inversions. Six targets were excerpted from the BTG (left) and seven steel balls on the periphery (right). Only the G*xy* tensor component is shown.

The CSM inversion results are given in table 5.4.4.1.1. The inversion succeeded for four of the six targets (targets 1, 3, 4, and 5) and failed for two (targets 2 and 6). The eastings and northings are in excellent agreement. We lack ground truth for the BTG and therefore cannot judge the accuracy of the estimated depths. The estimated depths to the centers of the steel marker balls appear reasonable, though the actuals are not known.

**Table 5.4.4.1.1**. CSM tensor inversion results for selected targets

| ID | BTG Cell | Easting (True) | Northing (True) | Easting (Estimated) | Northing (Estimated) | Depth (m) |
|---|---|---|---|---|---|---|
| T_01 | I12 | 757694.30 | 3638326.28 | 757694.28 | 3638326.21 | 0.261 |
| T_02 | J09 | 757708.23 | 3638328.81 | N/A | N/A | N/A |
| T_03 | M11 | 757692.00 | 3638334.26 | 757692.03 | 3638334.16 | 0.644 |
| T_04 | H14 | 757698.39 | 3638324.38 | 757698.37 | 3638324.36 | 0.155 |
| T_05 | E15 | 757700.56 | 3638318.53 | 757700.44 | 3638318.42 | 0.108 |
| T_06 | S13 | 757695.65 | 3638346.36 | N/A | N/A | N/A |
| | | | | | | |
| Ball_01 | * | * | * | * | * | 0.271 |
| Ball_02 | * | * | * | * | * | 0.221 |
| Ball_03 | * | * | * | * | * | 0.240 |
| Ball_04 | * | * | * | * | * | 0.173 |
| Ball_05 | * | * | * | * | * | 0.242 |
| Ball_06 | * | * | * | * | * | 0.175 |
| Ball_07 | * | * | * | * | * | 0.164 |

Notes: N/A denotes inversion failed. * denotes not attempted.

| Target | Mx | My | Mz | invertE | InvertN | InvertZ | trueE | trueN |
|---|---|---|---|---|---|---|---|---|
| t01 | -11.0 | 6.8 | -0.3 | 350.63 | 346.25 | 0.64 | 350.64 | 346.32 |
| t04 | 1.3 | -0.3 | -0.1 | 724.98 | 609.63 | 0.53 | 725 | 609.66 |
| t05 | -8.6 | -5.9 | -1.6 | 374.78 | 461.73 | 0.71 | 372.82 | 463.75 |
| t06 | 3.5 | -0.1 | -0.4 | 651.50 | 198.10 | 0.57 | 651.64 | 198.16 |

### 5.4.4.2 USGS TMGS inversion algorithm

We developed an automated method to locate and characterize buried discrete magnetic sources using the TMGS. This method is automated in the sense that human intervention and tedious extraction of individual anomalies are not required. It operates directly on TMGS data collected along one-dimensional profile lines, as is the usual data collection mode, and does not require interpolation between parallel lines onto a two-dimensional surface. Although they may help to improve some solutions, parallel data collection lines are not necessary. In fact, if adequate position and attitude recovery are provided, the data collection path need not be linear. Because the TMGS can "see" typical anomalies in a 2-m swath (1 m either side of the sensor array), it is conceivable that this process can be applied to difficult terrains where obstacles impose erratic data collection paths. This initial study concentrates the parallel lanes of the BTG at YPG. Because a given target may be visible to the instrument from multiple lines, multiple calculations of the solution may be possible, which ultimately provides a greater level of confidence in the final result.

The core components of the algorithm have been implemented, but some peripheral functions remain conceptual. These distinctions will be made during the ensuing discussions.

*Overview of the Inversion Process*

TMGS data are collected with the sensor platform in any orientation and along any kind of smooth path, straight or otherwise. Primary data collected include: TMGS magnetic field components, attitude-sensor data, positioning data, and temperature data. Secondary data collected on-site include: scalar and vector base magnetometer data. Auxiliary data collected either on-site or in the laboratory include: spin-calibration data, bin-step data, and axis-tracking data.

All of the various data channels are combined in a reduction process to produce the following calibrated data channels on a per-gather basis: 12-component magnetic field data, 3-axis sensor-platform attitude data, and 3-coordinate sensor-platform location data.

Ideally, the spin calibration and data reduction processes would have yielded perfectly accurate tensors. However, an unexpected systematic error has caused tensor errors that had to be remediated before proceeding. We removed heading and attitude errors out of each gradient using the inverse of the $I_1$ tensor invariant as a weighting factor in a running window, the width of which was adjusted to be slightly greater than the width of the flanks of the larger tensor magnitude anomalies in the BTG. The running window was applied non-causally to each

gradient in the tensor, and the resultant profile subtracted from its gradient. Areas in the BTG that had the lowest gradients then approached zero and the anomalies were largely unaffected except for the removal of fictitious heading related gradients. Figure 5.4.4.2.1 is the resultant tensor magnitude anomaly map.

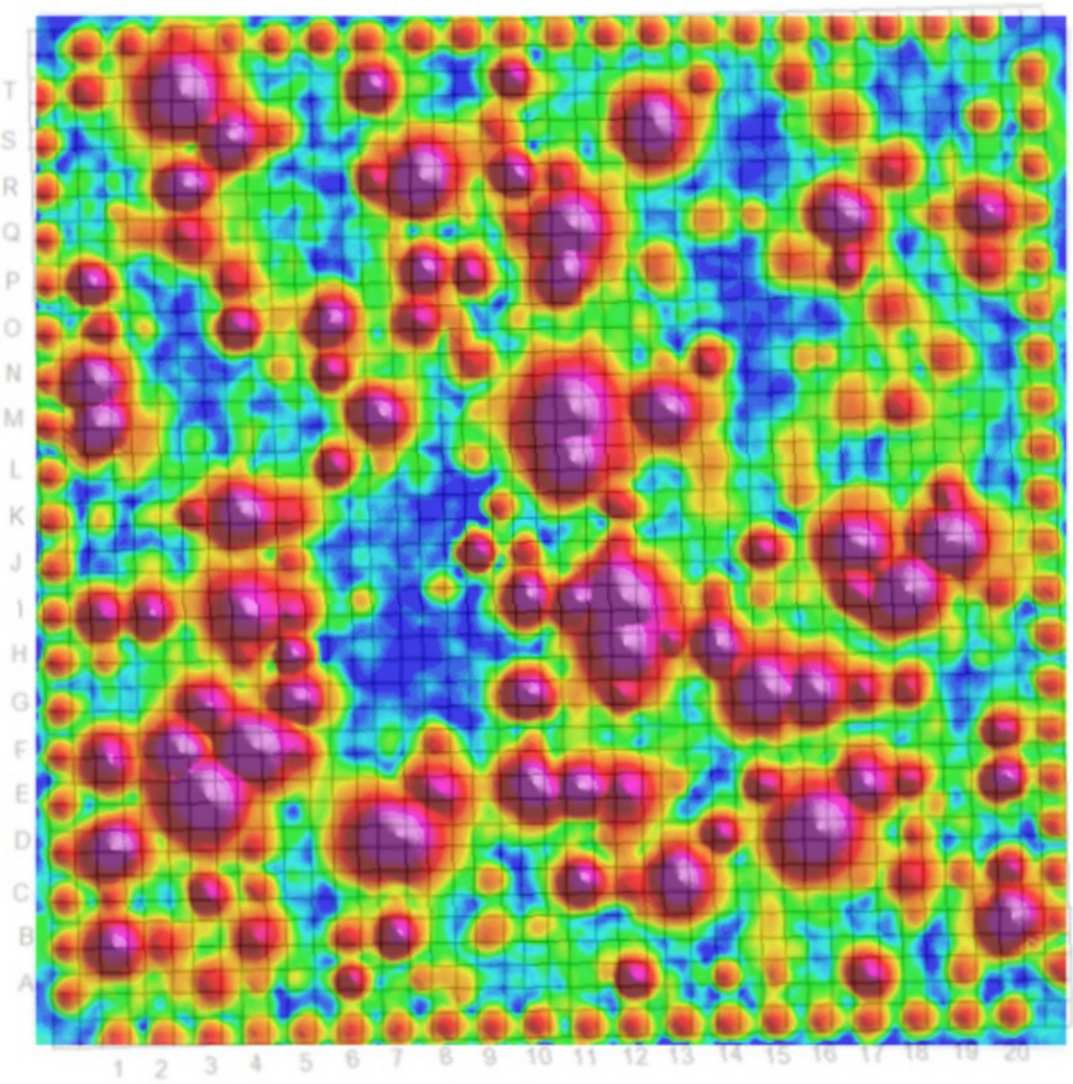


**Figure 5.4.4.2.1**. Tensor magnitude target location map of the BTG with an approximate overlay of the 2-m grid cells. Data collection lines were spaced at 0.5 m with a south heading in the west half and a north heading the east half of the mapped area.

*First Inversion Step – Anomaly Selection*

The tensor magnitude is used in profile as the basis for an automatic anomaly picker. A quartic function is fitted to the tensor magnitude within a 0.5-meter running window. The 0th order coefficient is then a slightly filtered version of the tensor magnitude profile, the 1st order term is the first derivative, and so forth. Essentially, an anomaly peak is selected wherever the first derivative crosses from positive to negative. Higher order terms are used in a similar way to select anomaly half-point and anomaly base-point locations. The anomaly is accepted for inversion if the peak value at the first-derivative crossing minus the base value is greater than a

user-selected threshold. Necessary anomaly information is then passed on to the next step of the inversion process. Figure 5.4.4.2.2 shows anomaly picks in the BTG.

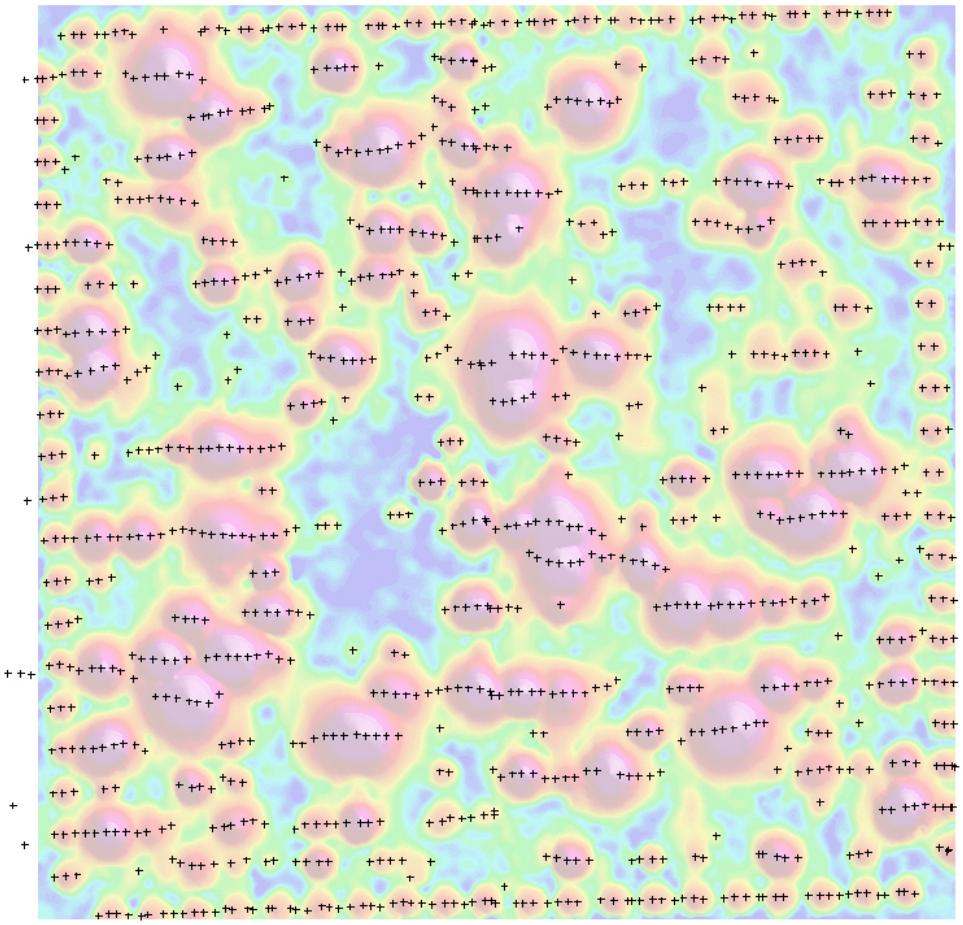

**Figure 5.4.4.2.2.** Locations where the data collection lines cross tensor magnitude anomalies, marked with plus (+) signs, selected by the automatic anomaly picker using a peak-to-base magnitude threshold of 20 nT/m.

*Second Inversion Step – Invert each Gather Discretely*

One data gather from the anomaly peak is used for inversion. As will be explained in detail below, the underlying viewpoint of this inversion is that the least amount of noise and error will be introduced into the inversion process if all inverted data were obtained simultaneously, during one gather, with no mixing of sensor platform attitudes. A solution will then consist of the following quantities, initially given in the sensor platform's instantaneous frame of reference:

1) Along track distance (m = x-distance to source)
2) Across track distance (m = y-distance to source)
3) Depth (m = z-distance to source)
4) Dipolar moment magnitude (A-$m^2$)
5) Moment azimuth (degrees clockwise from north)
6) Moment dip (degrees down from horizontal)
7) Monopole separation distance (m)

The initial solution is then rotated and transformed into the geographic frame of reference using the sensor-platform attitude and location data associated with the inverted gather.

In the current implementation only one gather from the automatically picked anomaly is fed into the inversion. However, there is the possibility that the particular gather selected could contain random noise that could throw the solution off. Therefore, future implementations will invert each of several gathers, probably selected from between the anomaly half points and pass each solution on to the third inversion step.

This inversion handles issues of anomaly identification and separation using the tensor magnitude as a guide. The tensor magnitude will reach its peak value almost directly over the target; or in profile, the greatest anomaly flank value will be very near the closest approach to the target. This peak value location is where the gradients are more purely originating from that target. As the location recedes from its peak, the gradients will have increasing mixtures of gradients from other targets. Consequently, the best gathers to use for a given target are those nearest the tensor-magnitude peak (figure 5.4.4.2.3).

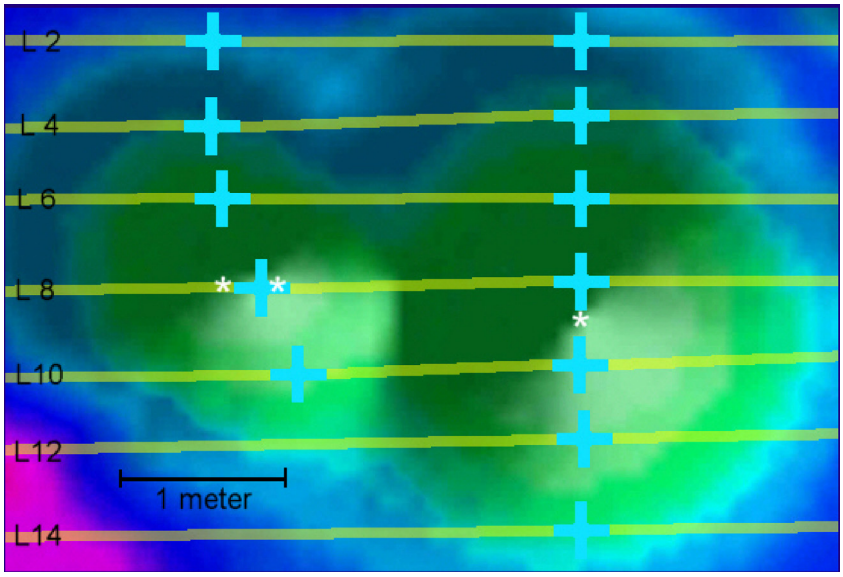


**Figure 5.4.4.2.3.** Peak values (blue plus-sign) automatically picked from tensor magnitude profiles.

For the peaks that exceed a threshold value that is proportional to the interpolated maxima (white stars in figure 5.4.4.2.3), inversions are performed. Results are shown as red dots and arrows in figure 5.4.4.2.4.

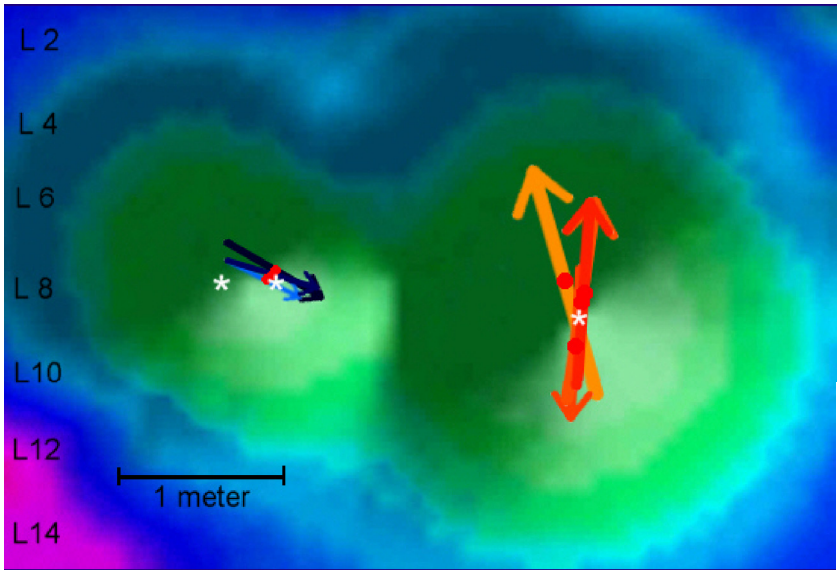


**Figure 5.4.4.2.4.** Inversions (red dots and associated vectors) for peaks exceeding a threshold value.

Solution clusters are averaged to determine the best estimated solution for a single anomaly, as shown in figure 5.4.4.2.5. These best solutions are tabulated in a final dig list.

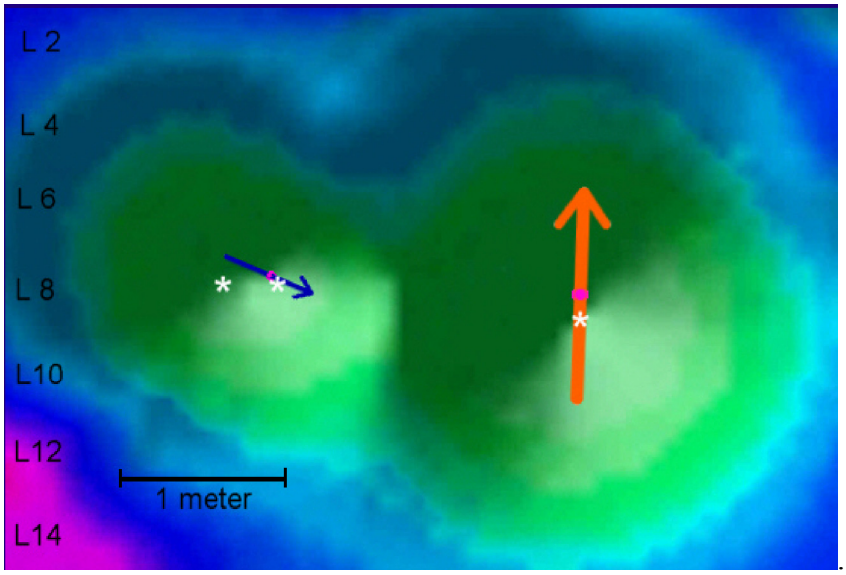


**Figure 5.4.4.2.5.** Best estimated solutions (red dots and associated vectors).

To illustrate how the inversion procedure worked on the entire BTG, figures 5.4.4.2.6-5.4.4.2.11 show each (non-averaged) solution as a colored circle in map view over the tensor magnitude map. The colors represent target parameters in their respective figures: depth, moment magnitude, moment azimuth, moment dip, monopole separation distance, and the convergence parameter chi.

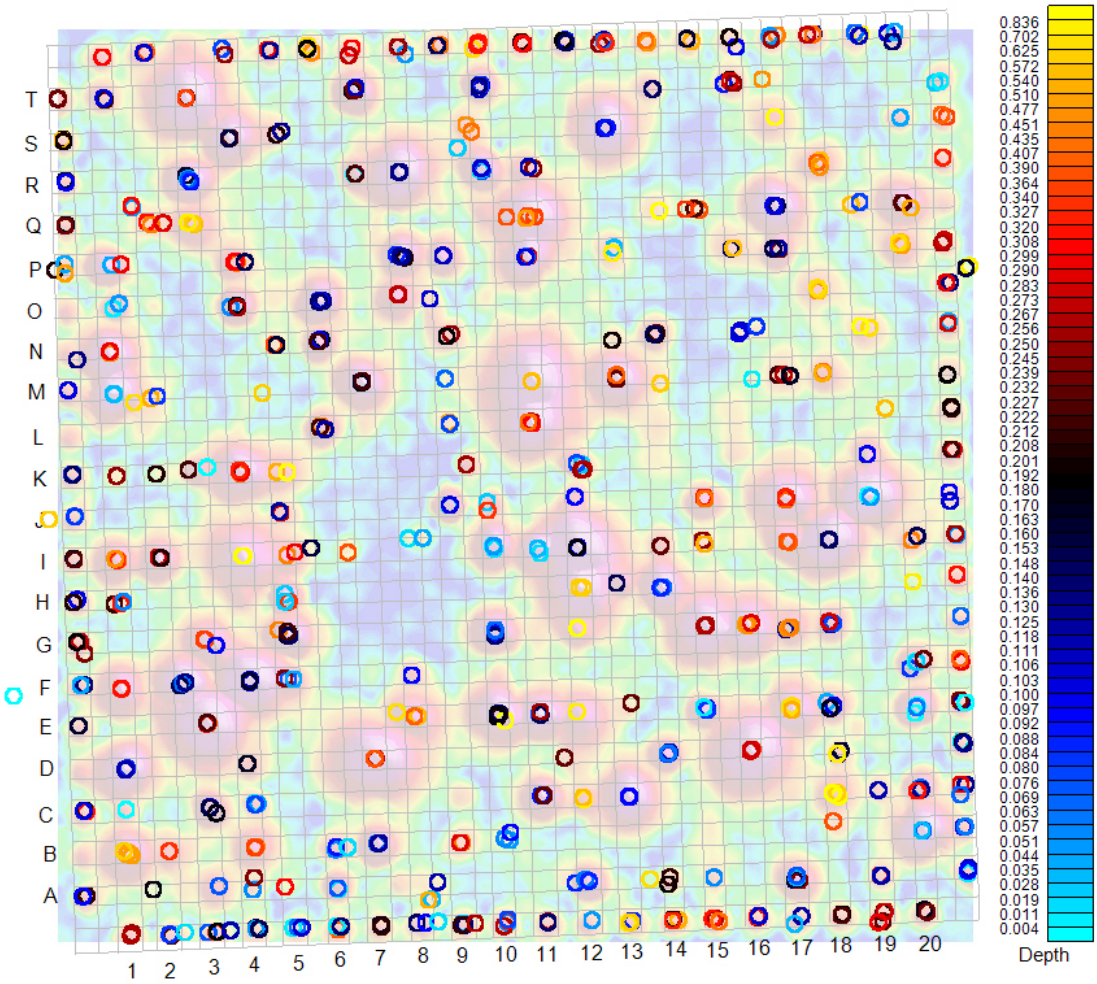


**Figure 5.4.4.2.6.** Solution clusters with estimated depth below ground (meters) shown in color.

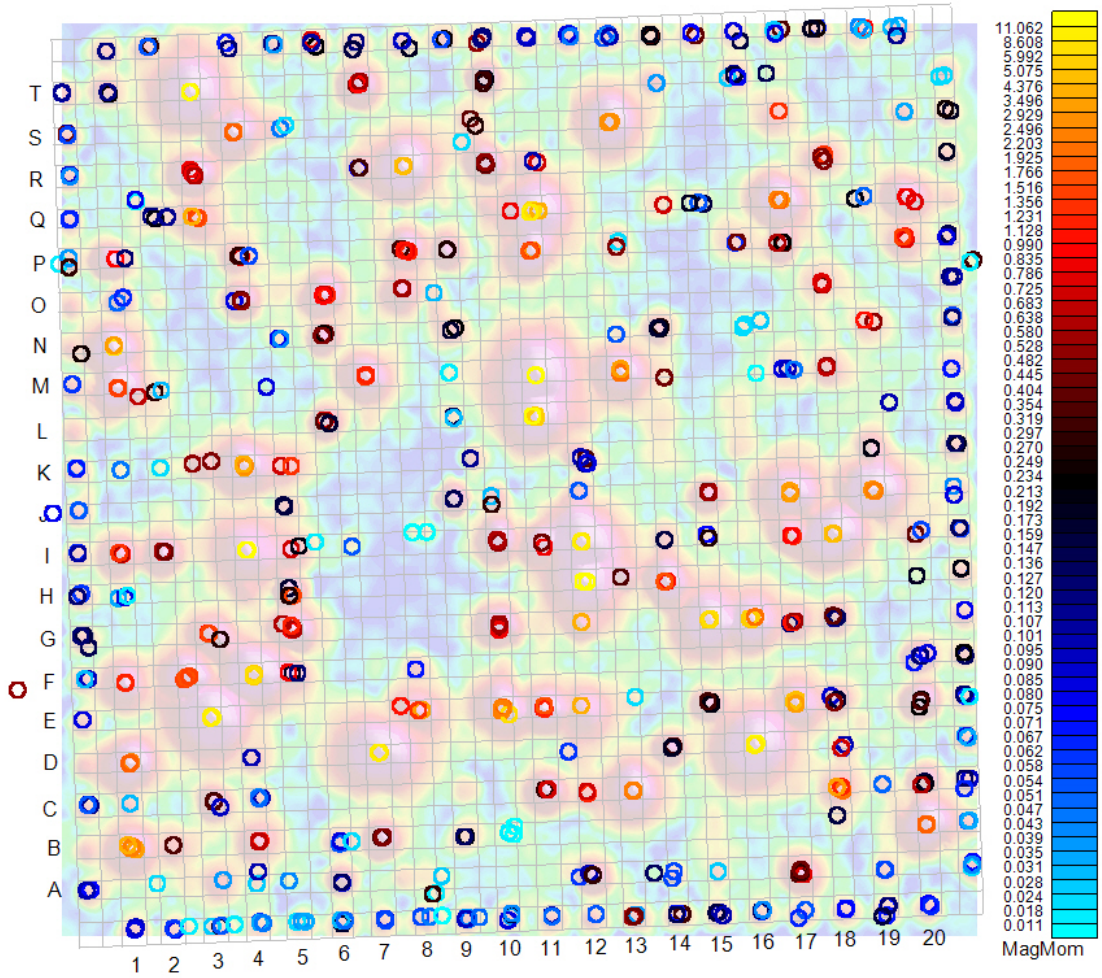


**Figure 5.4.4.2.7.** Solution clusters with estimated magnetic moment (A-m$^2$) shown in color.

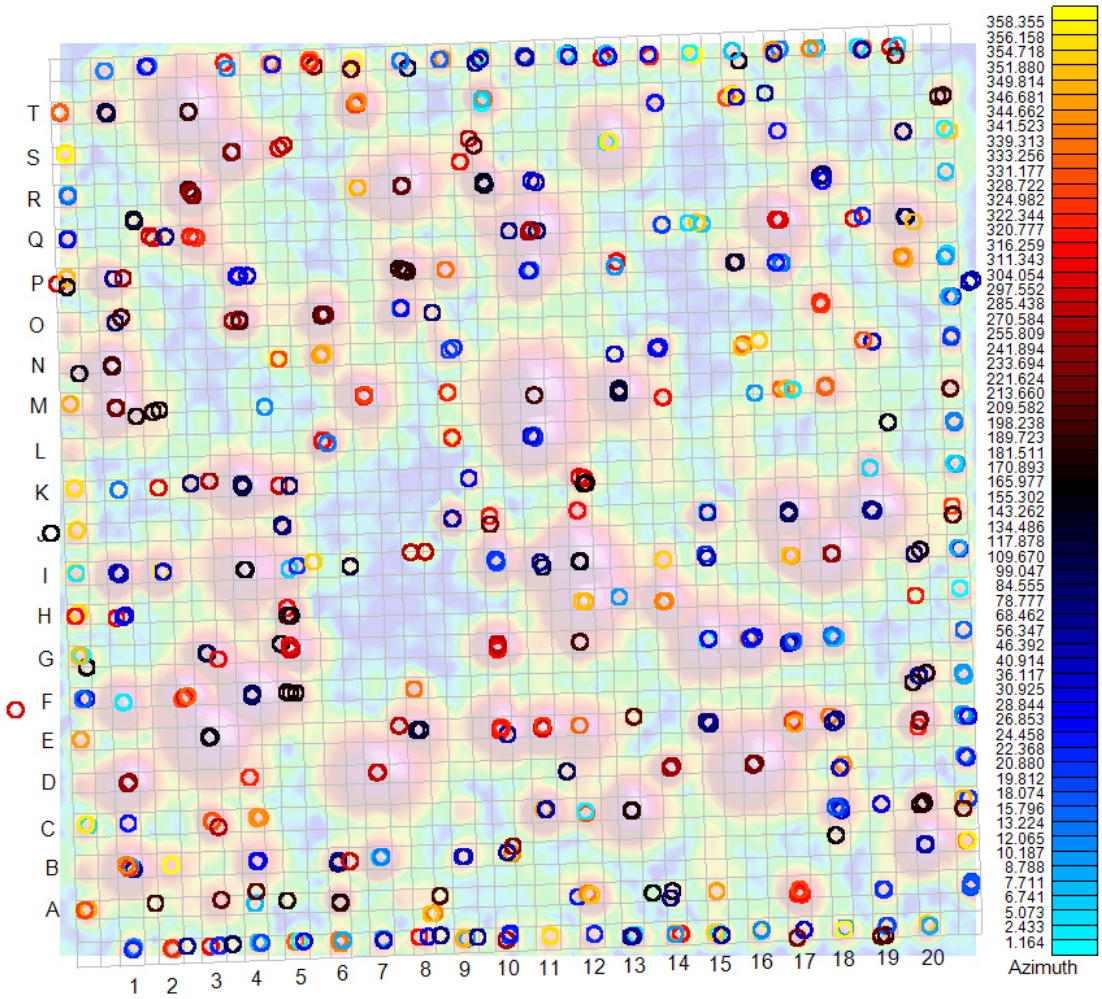


**Figure 5.4.4.2.8.** Solution clusters with estimated target azimuth (degrees clockwise from north) shown in color.

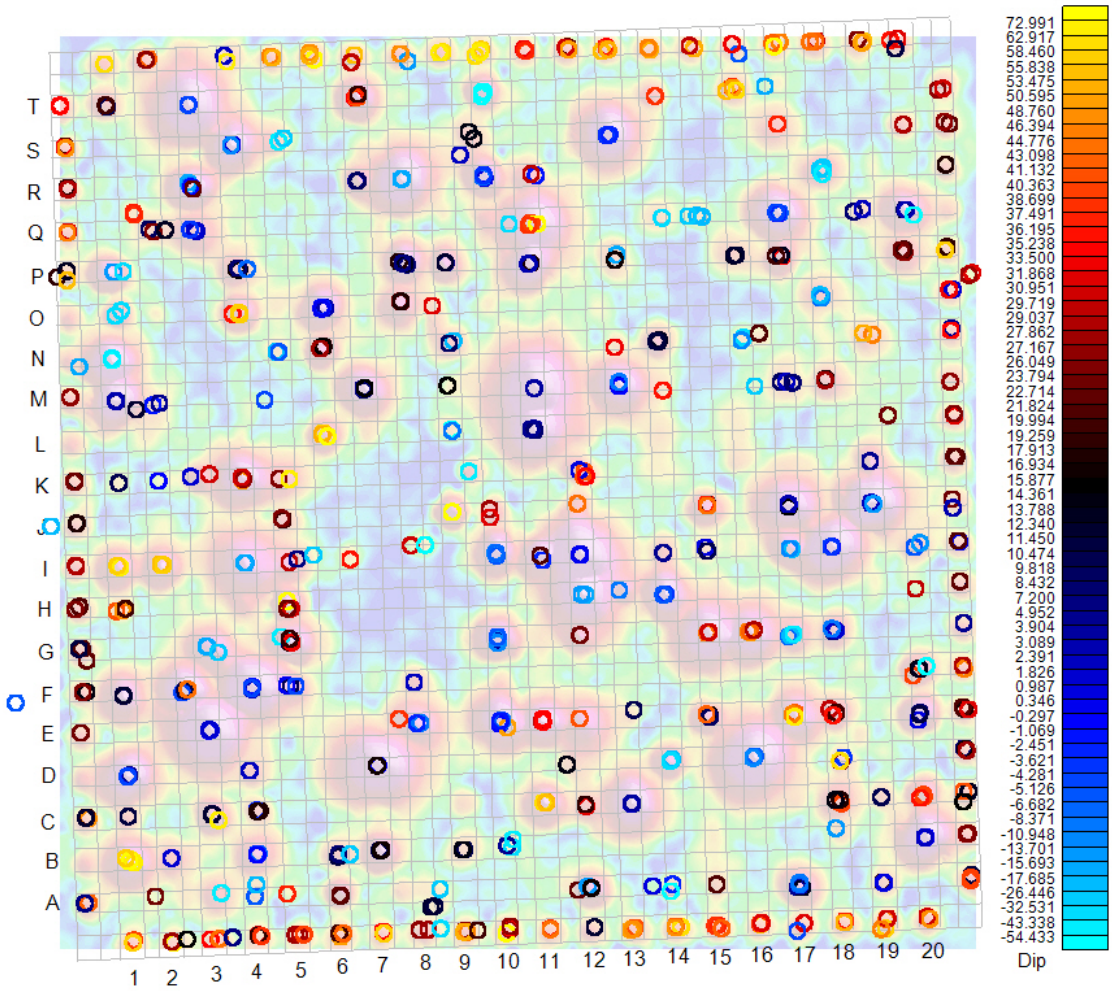


**Figure 5.4.4.2.9.** Solution clusters with estimated target dip (degrees below horizontal) shown in color.

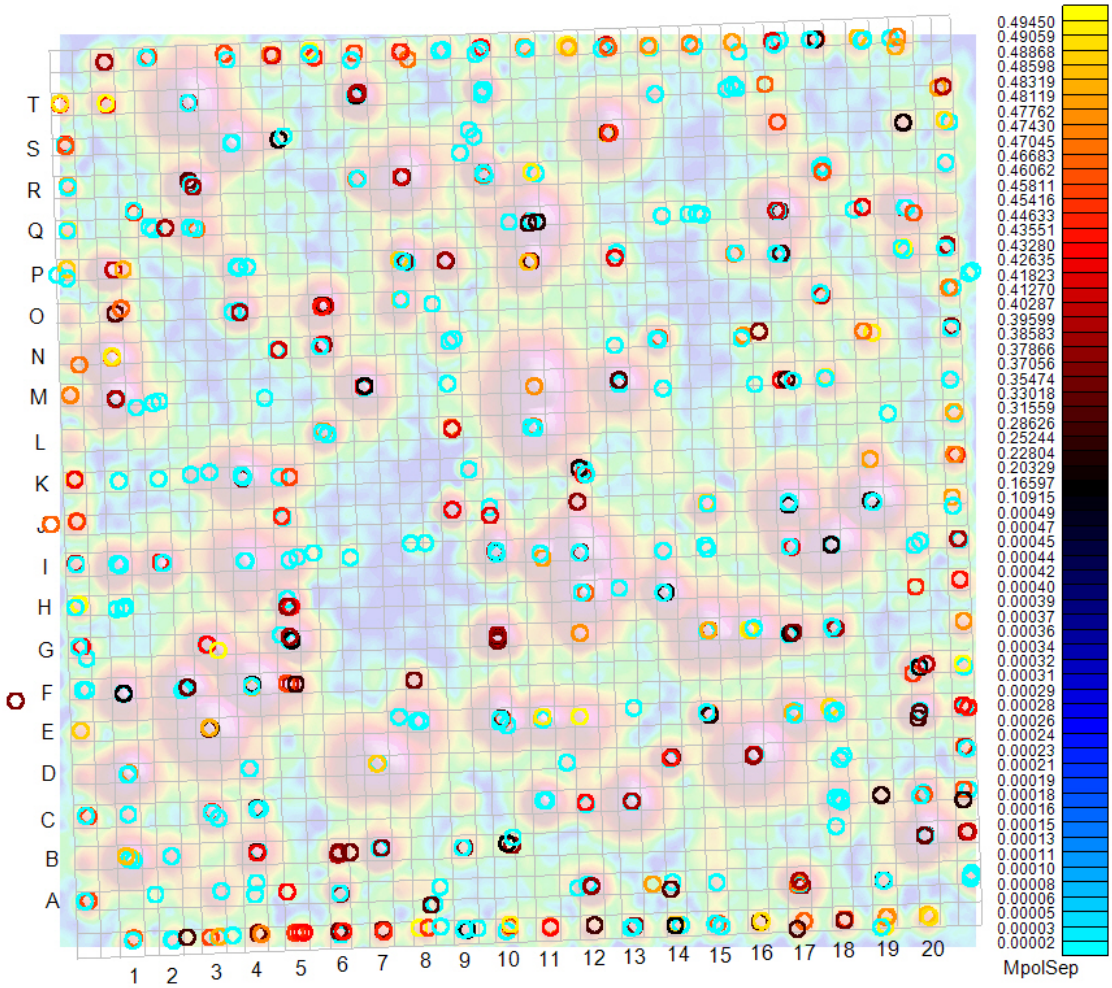


**Figure 5.4.4.2.10**. Solution clusters with estimated target monopole separations (meters) shown in color.

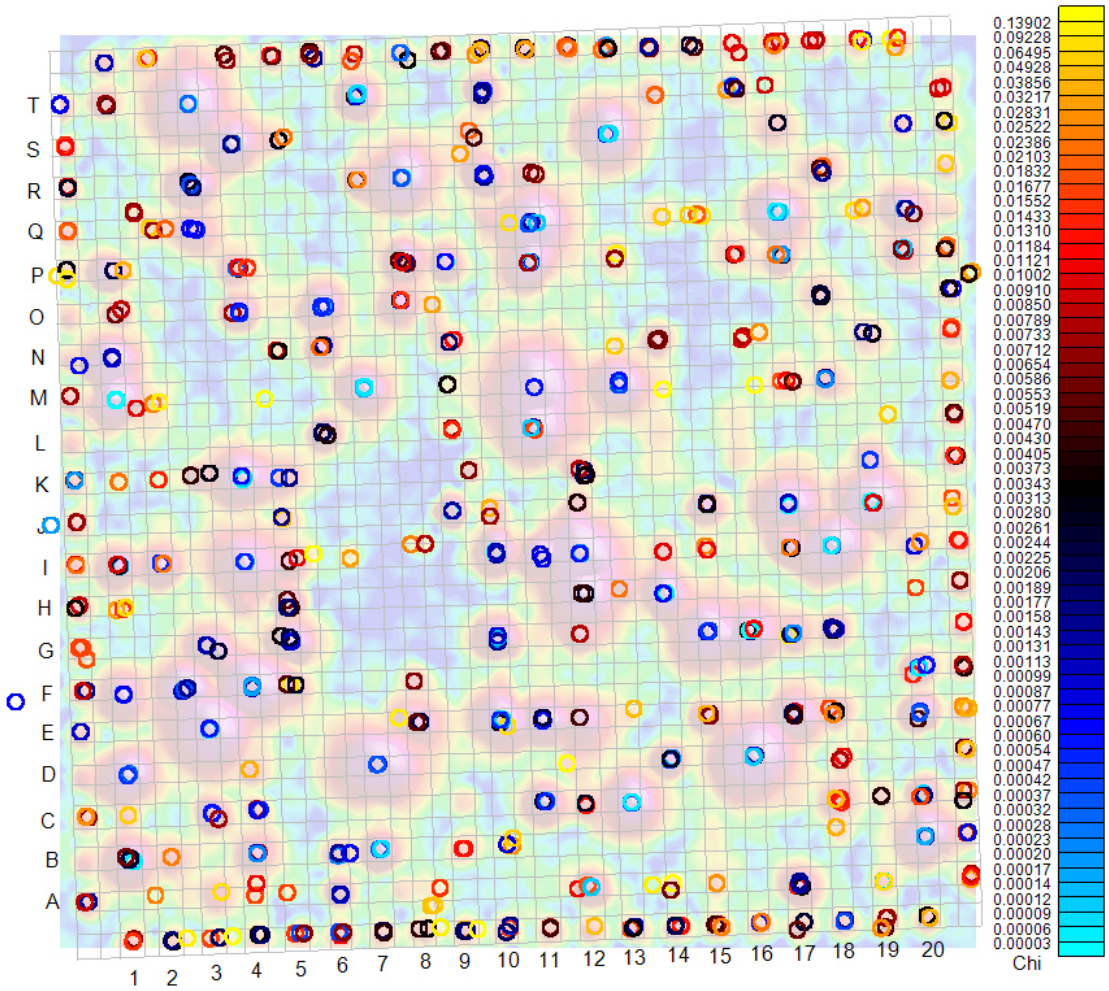


**Figure 5.4.4.2.11.** Solution clusters with solution convergence parameter, chi, shown in color.

*Third Inversion Step – Solution Windowing, Weighting, and Averaging:*
Weighting and averaging of solutions and their characteristics are performed during this step on the solutions after all solutions from the project area have been accumulated. The current process passes a small three-dimensional box through the project area and uses a clumping algorithm together with solution confidence levels passed from the inverter to arrive at a best possible solution for a given target. A preliminary, trial version of this has been written but plots were not generated.

Inversion results for six selected targets (see figure 5.4.4.1.1 above) are given in table 5.4.4.2.1. These six targets were chosen because they promised to be good candidates for both the ALLTEM inversion and for the CSM inversion discussed in the preceding section. Because ground truth is not available for the BTG, the accuracy of the results is unknown.

**Table 5.4.4.2.1.** USGS inversion results for selected targets

| Cell ID | Line# | Fid | Easting (m) | Northing (m) | Depth (m) | Moment ($A\text{-}m^2$) | Azimuth (deg) | Dip (deg) |
|---|---|---|---|---|---|---|---|---|
| I12 | 14 | 1292 | 757694.30 | 3638326.22 | 0.11 | 8.48 | 150.22 | -0.84 |
| J09 | 81 | 1431 | 757688.16 | 3638328.26 | 0.02 | 0.12 | 321.60 | 85.69 |
| M11 | 8 | 1532 | 757692.09 | 3638334.19 | 0.55 | 18.09 | 192.22 | 3.65 |
| H14 | 30 | 1160 | 757698.36 | 3638324.35 | 0.08 | 1.09 | 346.21 | -7.31 |
| E15 | 38 | 914 | 757700.47 | 3638318.59 | 0.09 | 0.22 | 40.50 | 16.90 |
| S13 | 20 | 2123 | 757695.55 | 3638346.27 | 0.11 | 2.81 | 4.97 | -3.58 |

*Fundamental Concepts of this Inversion*

After appropriate data reduction, using spin calibration coefficients and other calibration procedures, the data produced by the TMGS consist of 12 magnetic field components, four in each of three orthogonal directions referenced to the sensor array. The X-components always point toward the "front" of the sensor array regardless of its attitude in space; the Y-components always point to the right; and the direction of the Z-components is determined by the right-hand orthogonal rule. For example, if the array is level and pointing east, the four X-components will be pointing east, the four Y-components south, and the four Z-components vertically down. Each of the 12 components has a unique measurement location relative to the others, falling at various radial distances on cardinal lines. For example, all of the Z-components are at a radius of about a quarter meter and arranged on the 12, 3, 6, and 9 o'clock radials of the sensor array, corresponding respectively to magnetometer head numbers 1, 2, 3, and 4. The X- and Y-components fall on the same radials but closer to the center. This is illustrated in figure 5.3.2.9. Each group of 12 magnetic field components is sampled simultaneously and referred to as a "gather". Gathers are obtained at a rate of 1,000 per second.

As was discussed in section *Platform Motion Noise* above, the magnetic field components are extremely sensitive to changes in the platform's attitude with respect to the earth's main field. Thus, they cannot be used for nearby source characterization. However, in a properly calibrated instrument, the field components may be differenced, and these differences are insensitive to rotations relative the earth's main field. When normalized by the sensor separation distance, the differences become gradients. We can then use them to characterize nearby sources, without any interference from the main field.

Attitude changes between gathers, however, still affect the gradients, but only in an unamplified manner. As an illustration, variations in the gradients from a nearby source, as seen by the TMGS when it tilts to the right, for example, are equivalent to the way scenery changes, as viewed by an airline passenger when the right wing dips. It then stands to reason, that if the source can be fully characterized from a single gather, relative to the sensor platform, much as a camera captures its subject with a single snapshot, the absolute position and depth of the source can be found by performing a simple rotation into the geographic reference frame, and then adding the absolute location of the sensor array to the relative location of the source. If on the other hand, the source cannot be fully characterized from a single gather, then a myriad of attitude corrections based on a local-field model must be applied; and this could bring in a host

of errors and biases that otherwise would not exist. Consequently, it benefits us to search for a process to serve as a basic foundation of our method, by which the desired source can be fully characterized from each gather.

With the planar geometry, two independent gradient baselines are established in the X- and Y-directions, and they cross at the center of the array. If the magnetic gradient is effectively constant over the dimensions of the array, then the three gradients measured on each of the two baselines will be coincident at the center, yielding six gradient measurements and having five degrees of freedom ($\partial B_x/\partial y = \partial B_y/\partial x$). The gradients on the Z-baseline, which are not directly measured, are calculated from tensor characteristics.

However, if the gradient tensor changes over the dimensions of the array, meaning that field curvature is present, then the gradients calculated on the X- and Y-baselines will not necessarily be coincident. Each of the three gradients calculated on the X-baseline will be offset an unknown amount from the center, in the –X or +X direction; similarly with the Y-baseline gradients, only in the –Y or +Y direction. This occurs because the mean value theorem establishes that, while a gradient calculated by differencing exists between the two bounding points, its exact location cannot be known. Therefore, each of the six measured gradients could conceivably be part of a proper tensor that is not seen by the other gradients. Consequently, with curvature present, an additional degree of freedom is added to the system, and all six gradient measurements become independent.

The curvature effect is a problem when it comes to calculating a proper tensor at an infinitesimal point, but for establishing the largest possible set of independent variables for signal input to a multi-dimensional parameter space, curvature is needed. We can actually find three more independent variables by calculating the differences between the three gradients in the X-baseline direction and the three gradients in the Y-baseline direction. Now if the distance to the source is large compared to the dimensions of the array, no measurable field curvature will be present, and only five independent variables will be available, but then, no inversion will be attempted on that target anyway – not until it is closer. (The peak-to-base threshold in the automatic anomaly picker will exclude the distant anomaly). However, if the source is nearby, field curvature will always be present, and the TMGS will return nine independent gradient variables. This concept is foundational to this method because, for each gather with a proximate UXO target, it becomes theoretically possible to calculate a complete solution having up to nine source parameters. Whether or not it is actually practical to use all nine parameters is another matter. Noise and inaccuracies tax the system as the number of parameters grows, and this tends to limit the number of parameters. Therefore, we constrain both the number of parameters and the values of the parameters as much as possible. In the current implementation, there are seven parameters or degrees of freedom, as well as an obvious set of constraints on their values.

*A Forward Model of the Source*

Boundary condition requirements for external and internal B and H fields of a high-permeability material are such that the magnetic flux lines will tend to enter and exit at sharp bends in the

material, such as the tail and the nose of an intact UXO. Therefore, the pole separations will be similar to the length of a UXO – not infinitesimal, as is implicit to the multipole expansion.

Consequently, the most likely simple model of a UXO would be a long, thin solenoid, which can be approximated as a pair of equally charged, oppositely signed electric monopoles separated by a distance and scaled into units of magnetism. The equation of the forward model currently implemented is:

$$[B] = (\mu/2a)\{[R1]/(r1^3)-[R2]/(r2^3)\}k$$

where:

$\mu$ = magnetic moment in <ampere*m*m>
2a = separation between the two monopoles <m>
k = $1/(4\pi(e0)cc)$ = 1.0e-7 exactly
= $\mu_o/4\pi$ <henry/m> = <kg*m/(q*q)>
if the desired units are nanotesla (nT), then
multiply k by 1.e+9:
k = 100 <kg*m/(q*q)><nT/T>
[R1]= Vector from positive end to measurement point <m>.
r1 = Magnitude of [R1] <m>.
[R2]= Vector from negative end to measurement point <m>.
r2 = Magnitude of [R2] <m>.

This two-pole equation perhaps should be replaced with an equation for a long, thin solenoid, because there may be some unrealistic spurious field components coming from the unshielded space between the monopoles.

In either case, we can derive seven parameters that must be simultaneously solved:

1) Along track distance (m = *x*-distance to source)
2) Across track distance (m = *y*-distance to source)
3) Depth (m = *z*-distance to source)
4) Dipolar moment magnitude (A-$m^2$)
5) Moment azimuth (degrees clockwise from north)
6) Moment dip (degrees down from horizontal)
7) Monopole separation (m)

Therefore, the complete forward model inputs values for these seven parameters into the forward equation and calculates field components at the 12 locations of the TMGS sensor components. From these 12 calculated field values, calculated gradients are derived in the manner already described.

*The Inversion Regressions*

The inversion is a two-stage, non-linear regression in which the first stage uses a Monte Carlo initial-value selector and an infinitesimal dipole assumption with five parameters to arrive at a preliminary solution.

The solution from the first stage is then inputted to the second stage as a set of initial values, and the second stage adds the monopole separation to regress six parameters. The moment magnitude is not a regressed parameter because its value can always be directly calculated from the result of either the five or six parameter regression.

It has been found that the monopole separation distance is highly susceptible to noise in the data, and usually tends to lengthen as the noise level is increased. If allowed to increase too far, the other parameters can become significantly compromised. Therefore, for the initial test on BTG data (figure 5.4.4.2.1), a limit of 0.5 m was placed on the monopole separation. If the regression went beyond that limit, its results were rejected and the final solution reverted to the first-stage preliminary solution.

Comprehensive tests of the inversion regressions were performed using model data with no noise. Hypothetical targets were generated having parameters selected by a Monte Carlo method, with parameters limited as follows:

1) along track: ±1 meter
2) across track: ±2 meters
3) depth: 0 to 2 meters
4) magnetic moment: (normalized)
5) target azimuth: 0 to 360 degrees
6) target dip: ±90 degrees
7) monopole separation: 0 to 1 meter

This test generated over 1,000 noiseless hypothetical targets, and without exception, all of them converged to the exact target parameters. We can conclude from this test that the method is theoretically sound.

Another set of tests involved the injection of Gaussian noise into the test data. When the RMS value of this noise exceeded 5 nT/m, about 50 percent of the second-stage separations converged to values in error by more than 15 cm. At 15 nT/m none converged to better than 15 cm. However, the first-stage parameters remained fairly reliable (locations and depths to within ±2 cm) to even higher noise levels. In observing the large number of solutions from the BTG inversion that reverted to the first-stage solutions, we can surmise that the noise or error levels of the TMGS were probably between 5 and 10 nT/m.

## 5.5 Test Stand Data

Figures 5.5.1 and 5.5.2 show the automated test stand that the USGS built at the DFC.


**Figure 5.5.1.** The ALLTEM cube is mounted under a cover on the test stand deck. Ordnance and clutter items are moved underneath the deck by computer-controlled stepper motors. Positions are measured by a combination of a string potentiometer and lasers and are accurate to within +/- 3 mm.

The test stand proper is constructed of treated wood and uses no metal fasteners. Ordnance and clutter items are transported on the "shuttle" shown in figure 5.5.2 that simulates running ALLTEM along a line. After completion of each line the shuttle resets and the "trolley" beam moves to a new line position. Dynamic positions are measured with a Celesco "cable-extension position transducer" that uses an incremental encoder. We commonly refer to this device as a "string potentiometer." Lasers are used to measure static positions and initialize the string potentiometer readings prior to running a line and to verify the ending position of the shuttle along each line.

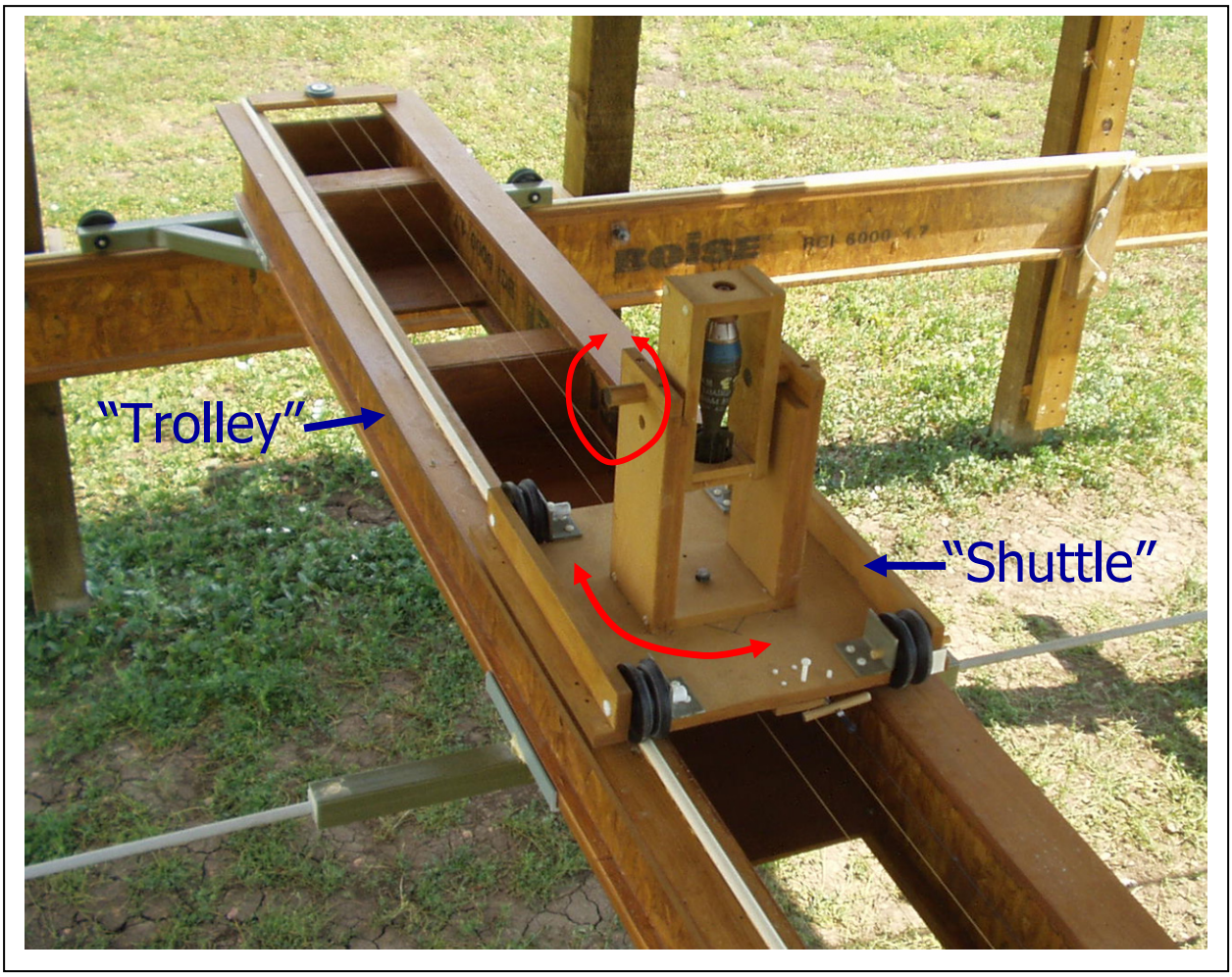


**Figure 5.5.2.** This view shows a 60 mm mortar round in a holder that can be rotated 360 degrees in two axes. The shuttle is pulled by a Kevlar string and the trolley is moved by a rotating threaded fiberglass rod.

### 5.5.1 ALLTEM Test Stand Data

ALLTEM data have been acquired for a number of ordnance and non-ordnance items. These data have been filtered and preprocessed and are being used both to study and evaluate our own inversion algorithm and have been distributed to some other SERDP/ESTCP investigators.

Amplitude difference maps analogous to the one shown in figure 5.3.1.2.8 may be made for any or all of the 19 Tx-Rx combinations that were recorded. Figure 5.5.1.1 shows a schematic of the top view of the ALLTEM sensor cube. In the figures that follow, a subset of the 19 possible maps is shown for a selection of the vertical, diagonal, and horizontal polarizations. Figures 5.5.1.2, 5.5.1.3 and 5.5.1.4 are maps made over the 60 mm mortar round shown in figure 5.5.2 when the round is vertical. Figure 5.5.1.2 shows the Z-component 1-m loop response when the excitation is also in the Z direction. Figures 5.5.1.3 and 5.5.1.4 show results from X- and Y-oriented excitation and responses. Note that the X and Y responses match except for a 90 degree pattern rotation.

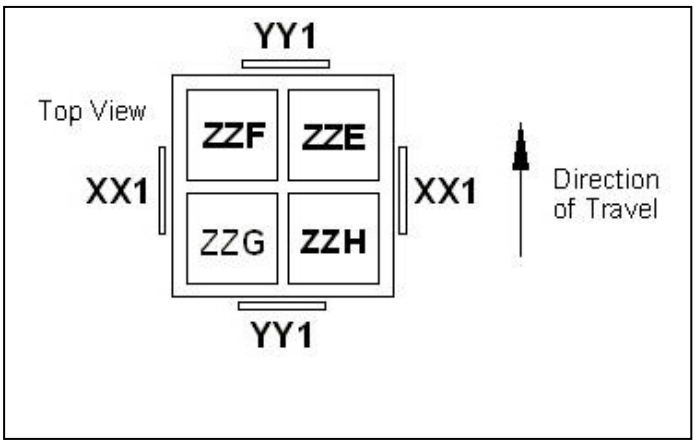


**Figure 5.5.1.1.** Schematic top view of ALLTEM cube

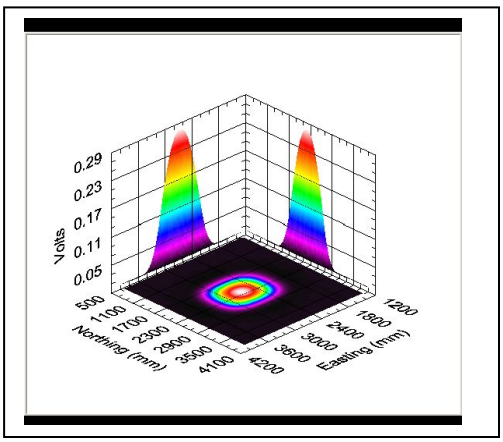


**Figure 5.5.1.2.** ZZM amplitude map.

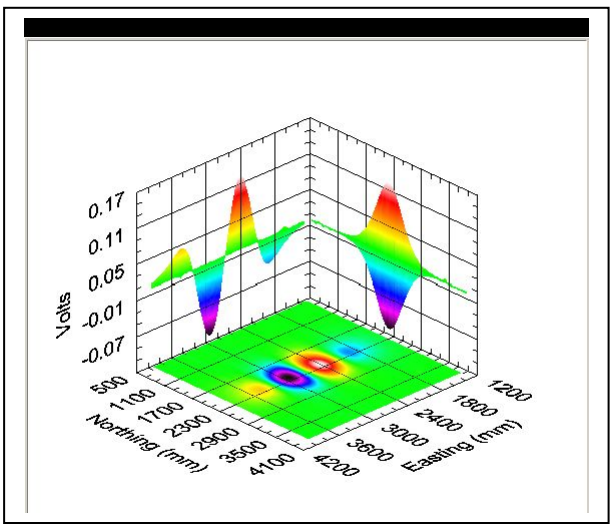


**Figure 5.5.1.3.** The XX1 amplitude pattern.

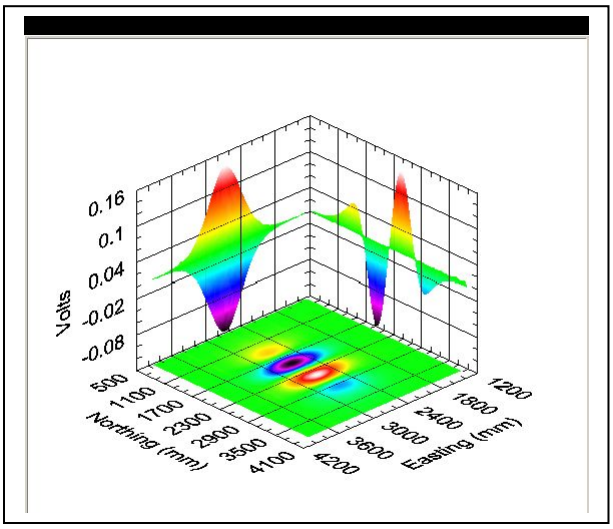


**Figure 5.5.1.4.** The YY1 amplitude pattern

Figures 5.5.1.5 through 5.5.1.8 show responses to a horizontal 81 mm mortar round.

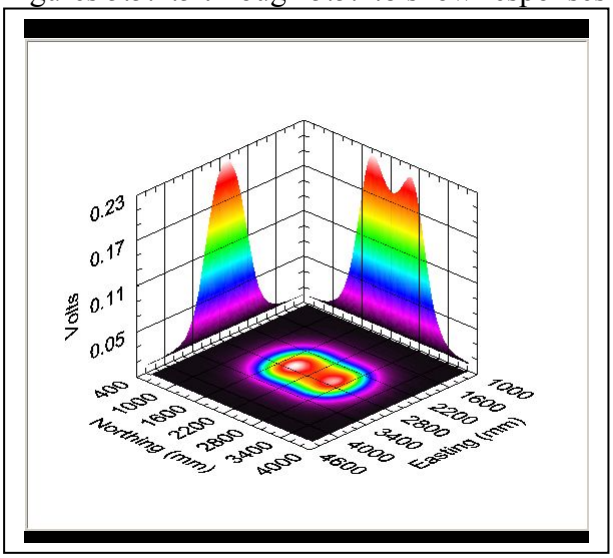


**Figure 5.5.1.5.** Vertical large loop (ZZM) response.

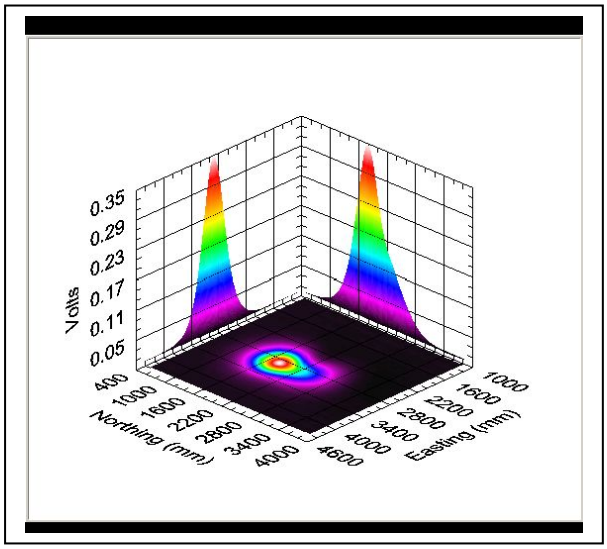


**Figure 5.5.1.6.** Small loop (ZZE) response.

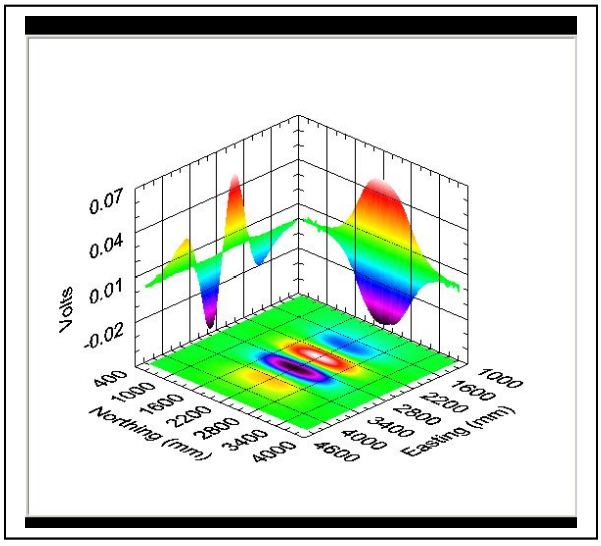


**Figure 5.5.1.7.** XX1 pattern for horizontal 81 mm.

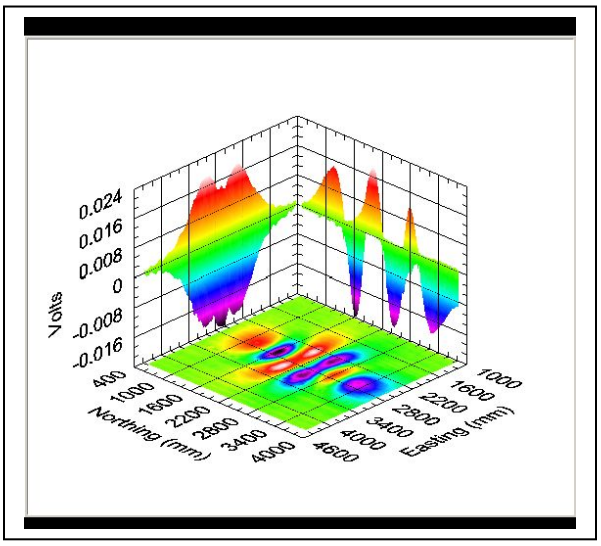


**Figure 5.5.1.8.** YY1 pattern.

Note that the horizontal spatial patterns of figures 5.5.1.7 and 5.5.1.8 do not match when rotated. The YY1 pattern is considerably more complex than XX1. The target is oriented parallel to the northing (Y) direction. These pattern differences are data used by the inversion algorithm to solve for target parameters.

The full suite of ALLTEM test stand data is described in appendix A of this report.

*Target Parameter Inversion Sensitivities to Sensor Noise and Position Error*

Figure 5.5.1.9 shows inversions for the three principal polarizability moments, M1, M2, and M3 with added uniformly distributed random position error. M1, M2, and M3 are actually functions of time, but we show the values at a single time.

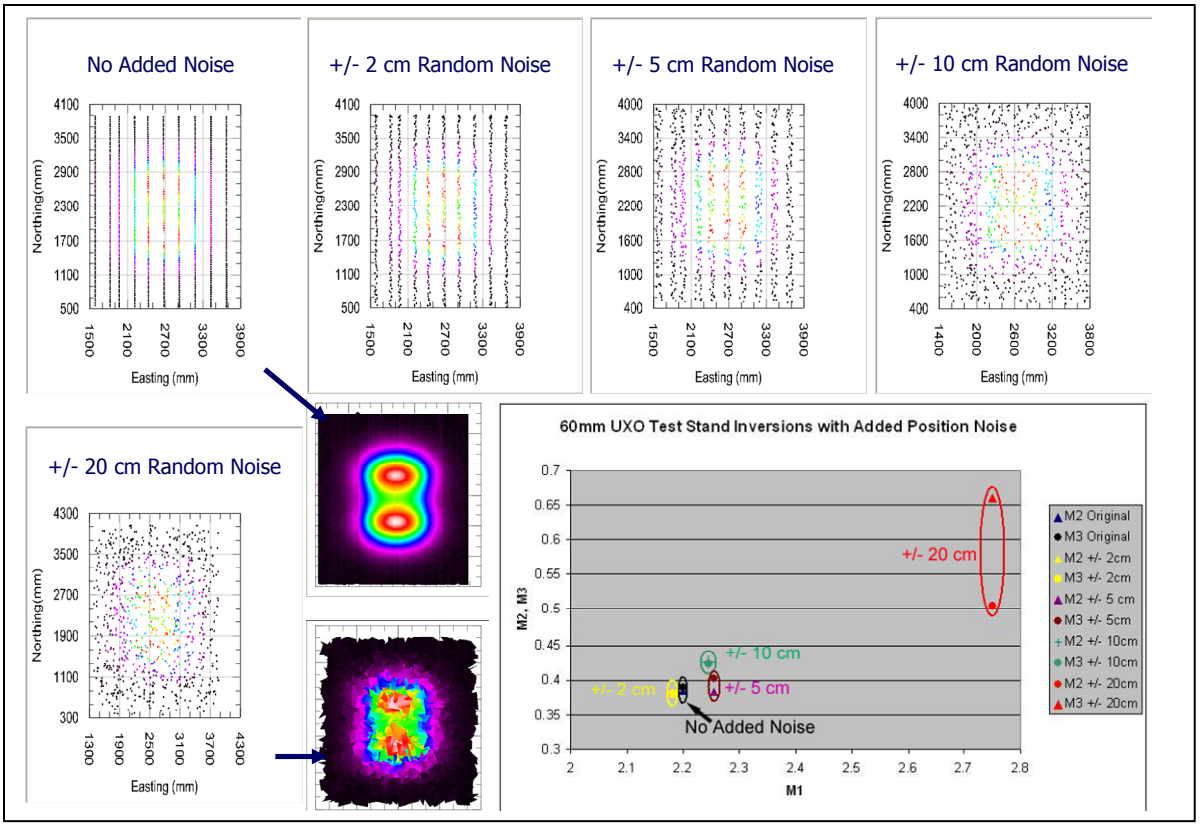


**Figure 5.5.1.9.** Variations in M1, M2, and M3 for a 60 mm UXO with added position noise. We find that the values of the principal polarizabilities, M1, M2 and M3 were relatively unchanged until the random position noise range reached +/- 20 cm.

Figure 5.5.1.10 shows how M1, M2, and M3 varied as random sensor noise was added to the inversions. The inversions were relatively robust against this added noise. This result and the previous one probably reflect benefit from spatial averaging of the data that go into the inversion.

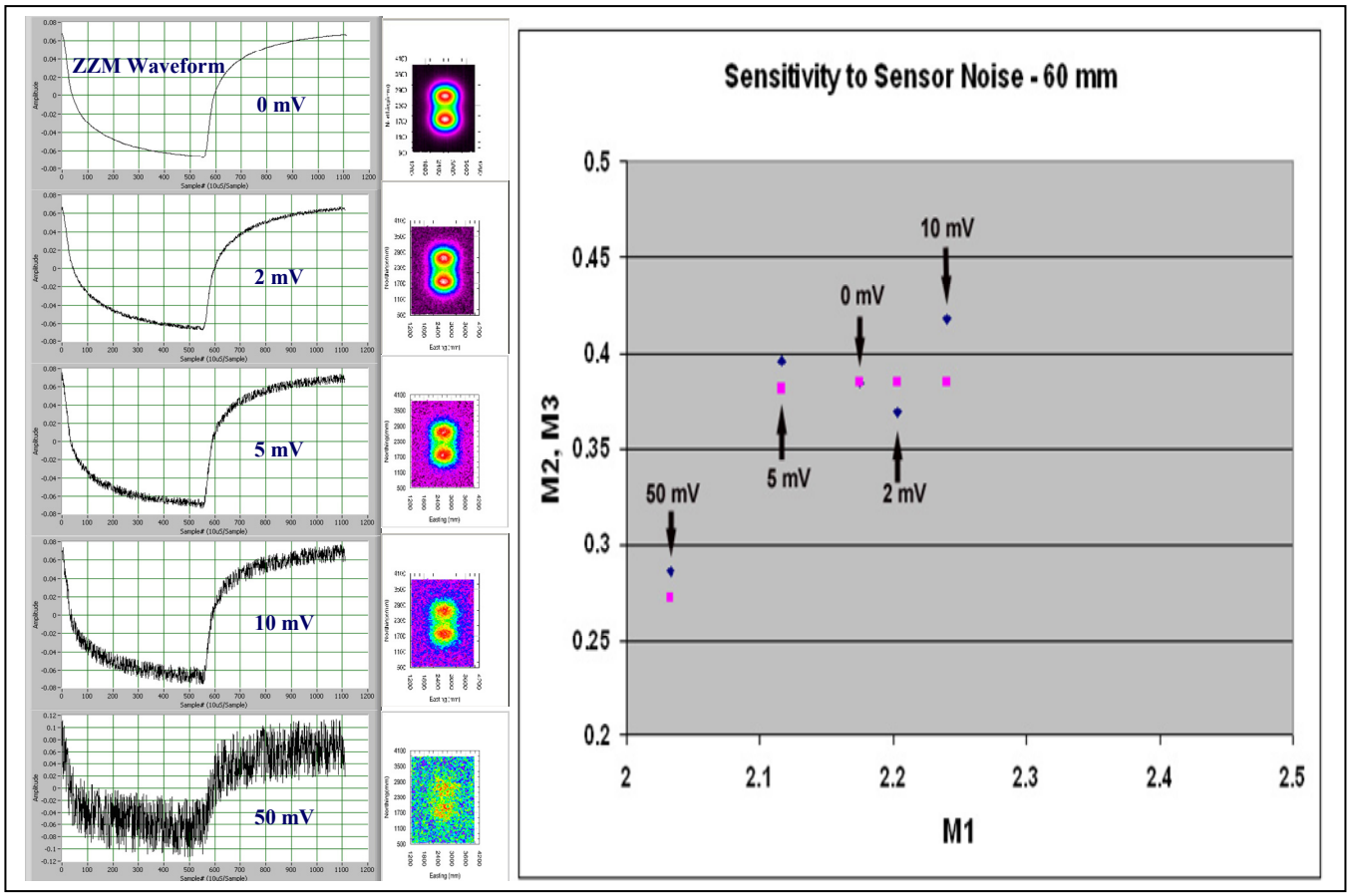


**Figure 5.5.1.10.** This figure shows a waveform for the large receiving loop vertical component polarization (ZZM) with no added noise, and added noise levels of 2 mV, 5 mV, 10 mV, and 50 mV. All of the inverted values are relatively close together and M2 and M3 are nearly the same as they should be. Even for the 50 mV added noise case the target would be identified as a probable UXO because of the indicated rotational symmetry. The second column of thumbnails shows what amplitude maps would look like with the added noise level shown in the waveforms in the first column.

For every run a different set of random numbers was generated and each set of random numbers impacts the inverted values of M1, M2, and M3 in a unique way. Therefore the observed changes with increasing random error are not monotonic for either added position noise or added sensor noise.

Another test examined how inversions vary as the spatial data density is changed. Figure 5.5.1.11 shows inversions at four densities. Case 1 is for data taken at 0.25 m line spacing and 0.12 m density along the line. Case 2 is 0.5 m line spacing and 0.20 m along the line. Case 2 corresponds to the density of data we took in the field at YPG in 2006. Case 3 spatial density is reduced to 1.0 m line spacing and 0.4 m along the line, and Case 4 is a 1 m line spacing and 1 m data along the line. Although this test needs to be run for more cases, the preliminary conclusion is that the inversions are being varied by only modest amounts by the density and the particular lines chosen. That there is any variation at all may indicate that we have not done a perfect job of calibrating the system. This possibility is being investigated. Another possibility is that the

single dipole target approximation is not adequate because the target was too close to the sensors. This is also being examined.

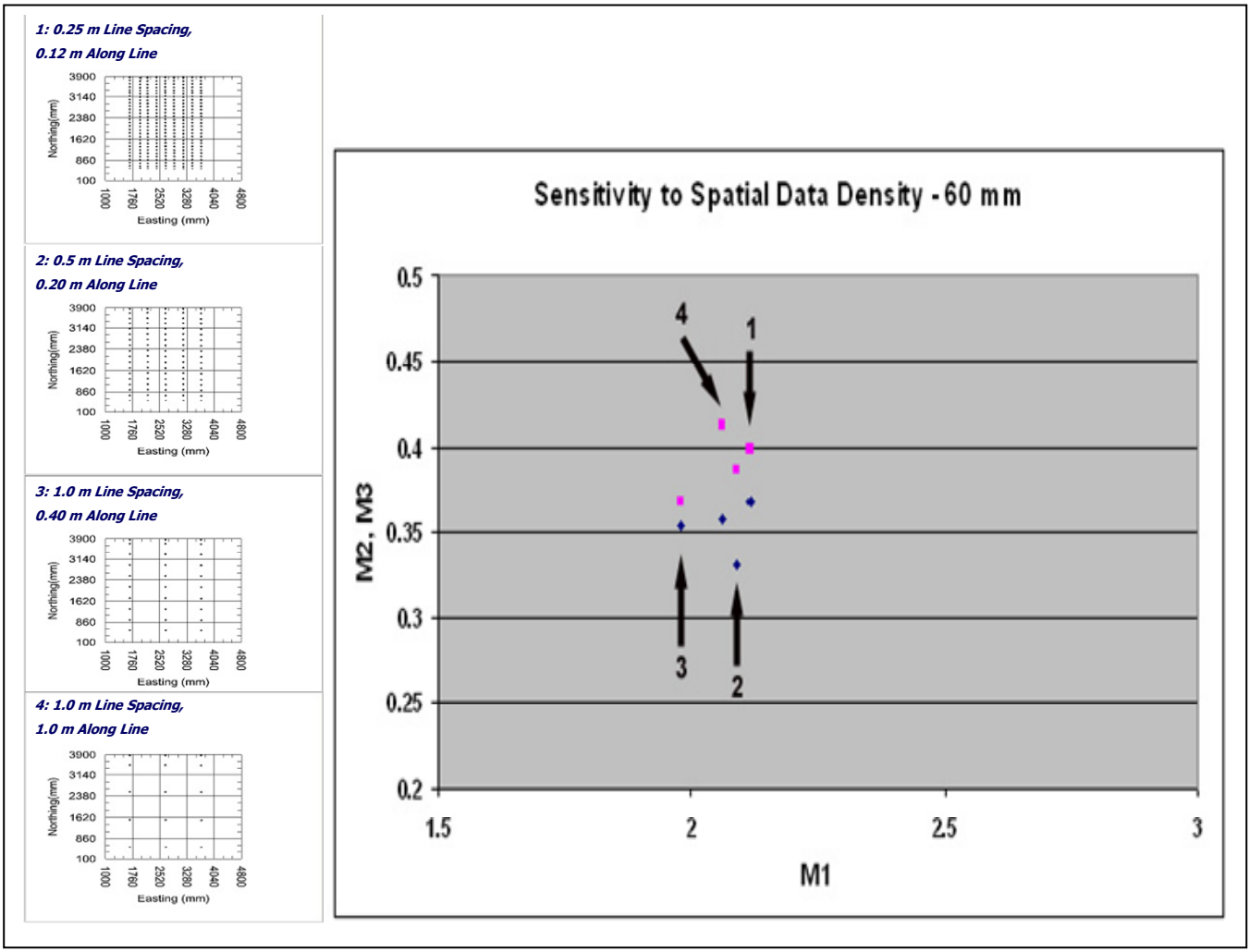


**Figure 5.5.1.11.** This figure shows how inversions for M1, M2, and M3 vary with the spatial density of data used in the inversion. Although there is some variation, the 60 mm would be flagged as likely UXO for all cases shown here.

As a final example, we show a comparison of inversions for a 20 mm, 60 mm, 105 mm, and the clutter item shown in figure 5.5.1.12. For these cases each of the UXO plot with a dominant M1 and two smaller and nearly equal moments, M2 and M3, and would be identified as a "rod-like" target and likely UXO even if the type of ordnance was not correctly identified. In contrast, the non-UXO clutter item is calculated to have three distinct M's no two of which are close together. This is diagnostic of a non-symmetric item.

*Inversion Conclusions*

From both field data and test stand studies it appears possible to invert for target principal polarizability moments with a high degree of confidence when the data have a high SNR and

position errors are not too high. Inversions have shown a gratifying robustness to both position errors and sensor noise. Continuing examination of test stand data will lend a greater degree of understanding of limits for confident inversion and therefore classification. It appears that it is possible to acquire data in a survey mode that can be inverted with a high degree of confidence without needing to stop to acquire cued-mode data.

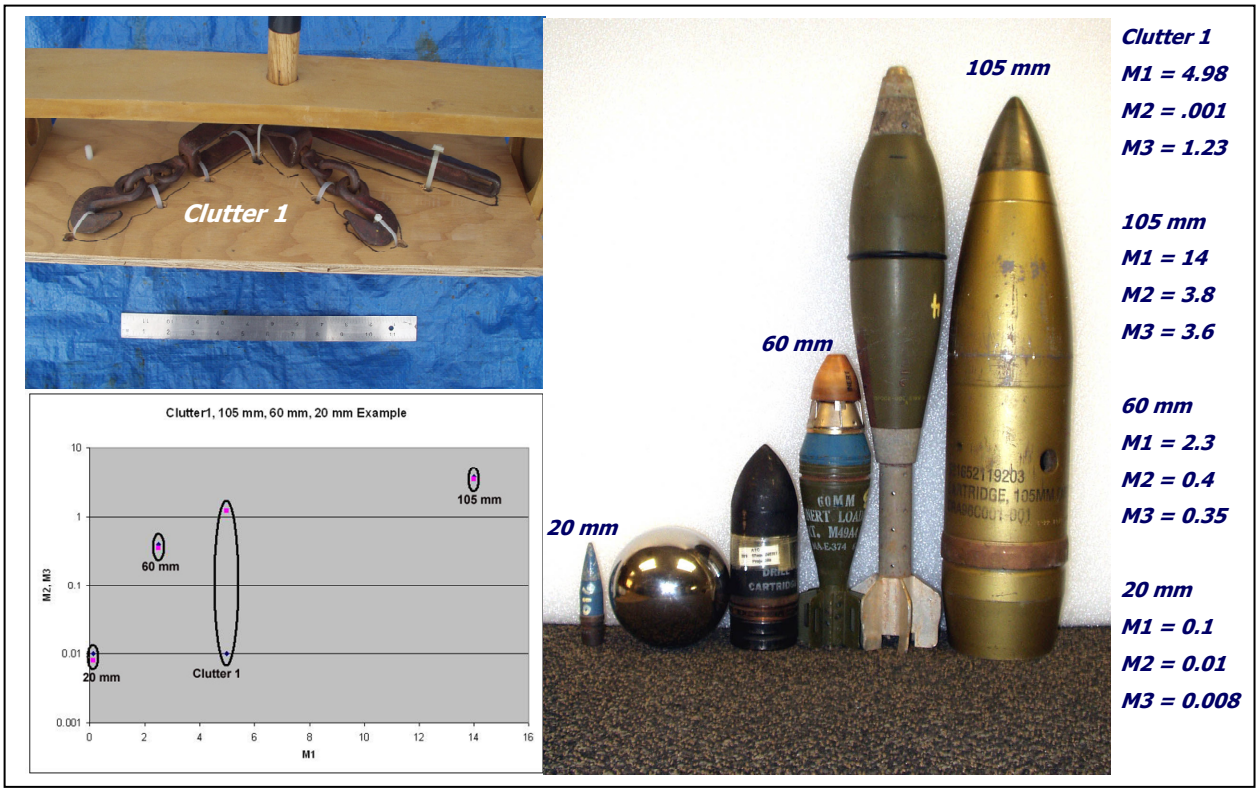


**Figure 5.5.1.12.** This figure shows inversions for M1, M2, and M3 for 20 mm, 60 mm, and 105 mm UXO items and for the clutter item shown. For the UXO items the calculated M2 and M3 are close together which is an indication of rotational symmetry and therefore likely UXO. For the clutter item no two of the three M's are close together, indicating a non-symmetric shape.

### 5.5.2 TMGS Test Stand Data

The TMGS was used from October 2 through October 11, 2007 to collect magnetic anomaly data over eight inert UXO, six clutter items, one 4-in steel ball, one bar magnet, and a blank run with no item. We followed the same experimental procedures as in the ALLTEM test stand measurements. Because we wanted to concentrate on the smaller ordnance types, we did not include the large items, nor all of the clutter types. The items and orientations are given in table 5.5.2.1.

**Table 5.5.2.1**. Test items and their orientations.

| Item | Az:0, Dip:0 | Az:90, Dip:0 | Dip:90 | Az:45, Dip:45 | Az:0, Dip:45 |
|---|---|---|---|---|---|
| 40 mm | Yes | Yes | Yes | Yes | Yes |
| 57 mm | Yes | Yes | Yes | Yes | Yes |
| 60 mm | Yes | Yes | Yes | Yes | Yes |
| 81mm mortar | Yes | Yes | Yes | Yes | Yes |
| M42 | Yes | Yes | Yes | Yes | Yes |
| BLU-26 | Yes | Yes | Yes | Yes | Yes |
| BDU-28 | Yes | Yes | Yes | Yes | Yes |
| 2.75” rocket | Yes | Yes | Yes | Yes | Yes |
| Clutter #1 | Yes | Yes | Yes | Yes | Yes |
| Clutter #2 | Yes | Yes | Yes | Yes | Yes |
| Clutter #4 | Yes | Yes | Yes | Yes | Yes |
| Clutter #6 | Yes | Yes | Yes | Yes | Yes |
| Clutter #7 | Yes | No | Yes | No | No |
| Clutter #8 | Yes | No | Yes | No | No |
| Steel ball | Yes* | N/A | N/A | N/A | N/A |
| Magnet | Yes | Yes | Yes | No | No |
| Blank Run | Yes* | N/A | N/A | N/A | N/A |

Note: Yes means dataset acquired, No means no dataset acquired, * means orientation does not matter, and N/A means “not applicable.”

The magnetometer array was placed in the recessed compartment at the center of the test stand deck, with Head 1 north, Head 2 east, Head 3 south, and Head 4 west. The cables from the array hung over the edge of the deck and were routed to the data acquisition systems set up as far away as possible from the southeast corner (figure 5.5.2.1). The TMGS data acquisition system acquired magnetometer data, and a separate laptop computer (controlling the stepper motors) acquired target position data from the string-pot and the laser distance meters. Thus, each TMGS data file is associated with a position data file.

After acquiring data with items at the approximately 0.8 m separation distance (plane of target centroid to plane of array centroid), we raised the rails 0.3 m for a 0.5 m separation distance. Seasonal cold weather settled in, and we had to suspend operations pending warmer weather in the spring of 2008.

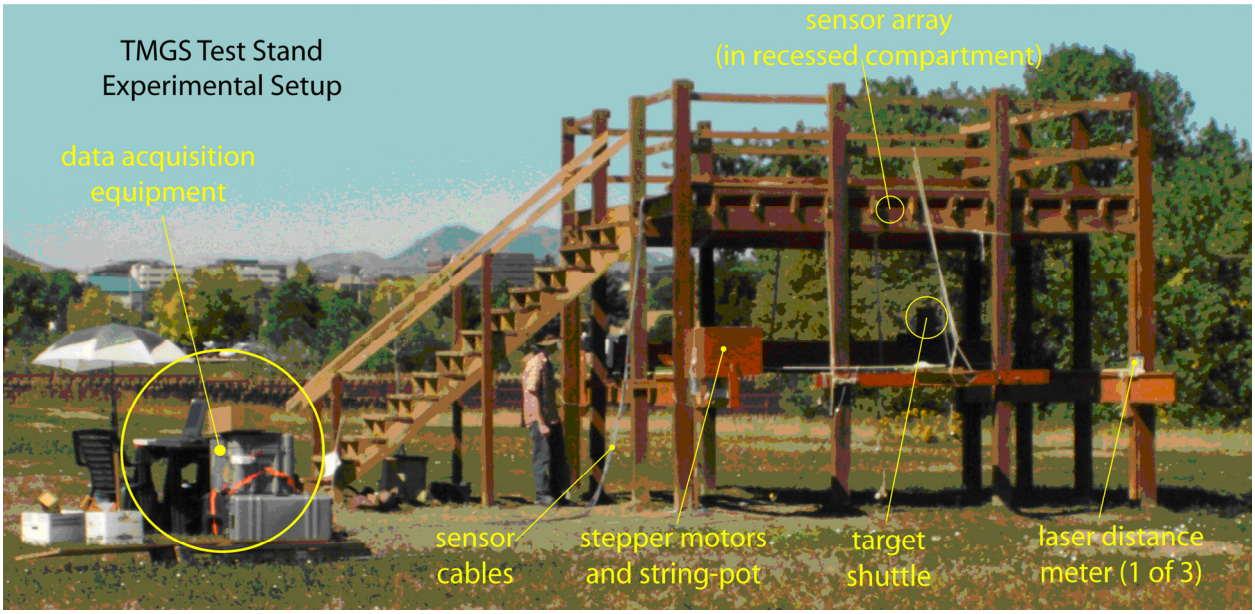


**Figure 5.5.2.1**. TMGS target anomaly test stand setup in October, 2007.

### 5.6 Some Lessons Learned

Some of the lessons learned are not unexpected to experienced field personnel. One is that full "dry runs" before any major deployment are necessary, especially with prototype systems like ALLTEM and the TMGS. Had we not done a final full ALLTEM test at the Denver Federal Center we would not have discovered that we still had an unsolved, seemingly random, positioning error even after upgrading to a Leica 1200 GPS that has a fast 20 Hz update rate.

A closely related lesson is, "When you know you have a problem, fix it before deployment." It was difficult and embarrassing to postpone the ALLTEM field deployment to YPG in 2006 at the last minute, yet had we not done so, the position data would have been no better than in 2005 and the errors would have large enough that inversions for target parameters would not have been possible.

In general it is necessary to "sweat the details" if the results from a field deployment are going to be fully successful. We had a couple of incidents of equipment damaged in transit because an equipment rack bracket was not adequate for the job and broke under the stress induced by many miles on a bumpy road, and have seen instances where fasteners loosened because they were installed without lock washers or a thread locking compound. Most of the lost time in the field had to do with mechanical issues such as transportation damage, failed wheel bearings, and punctured tires.

We expected that at the low 90 Hz base triangle wave frequency ALLTEM would show little or no response to earth conductivity, and that has proven to be accurate in all cases we have encountered to date. What we did not anticipate, however, was that ALLTEM would respond to soil magnetic susceptibility. That response initially caused us great concern, but we found that

we can circumvent the effects of that response by analyzing amplitude differences along waveforms rather than the amplitudes themselves.

We have great respect for baseline commercial instruments such as the Geonics EM61-MK2 and the Geometrics G-858 and find that it is a considerable challenge to build a system that will equal or better them at what they do best, namely, detection. Detection of metal targets is largely governed by sensor geometry and SNR and the baseline instruments generally do a fine job at detection, although even time-tested commercial systems have some quirks and could be improved. Nevertheless they are fine instruments. In a direct field comparison between ALLTEM and the EM61-MK2 we find that raw ALLTEM data do not have a better SNR that raw EM61-MK2 data, but digitally filtered and processed ALLTEM data appear, in general, to have a slightly better SNR than the EM61-MK2. The more important advantage is the benefit of multi-axis data for inversions.

When we elected to design and build what became ALLTEM around the triangle wave excitation we realized that we were buying all the challenges that come with any system that attempts to detect a very small signal in the presence of a very large signal. We realized at the outset that we would never be able to totally eliminate the very large primary signal by very precise location of Rx antennas used in gradiometer fashion, so we elected to supplement mechanical positioning with programmable electronic differential gain adjustment. This was a good choice.

Even with precise positioning and rigid mounting of the Rx loops on a cube made from a material with a low coefficient of thermal expansion and supplemented by electronic "nulling" we realized that there would inevitably be some thermal "creep" and that has been shown to be the case. A strong benefit of the triangle wave excitation is that when there is leakage of the primary signal into the receiving circuits due to thermal deformation, the dB/dt induction loops produce a square wave and the same amplitude differencing discussed in section 5.4.1 of this report, that we use to eliminate response to soil magnetic susceptibility also removes any primary signal leakage.

Another decision that we made early in the ALLTEM development was to digitize at a high and constant rate along our received waveforms rather than to filter and save the signal at a small number of "time gates" as is customary in TEM equipment. We are satisfied with this decision as it allows us considerably more flexibility in post-processing the data at the penalty of high data volume. With modern mass storage capabilities growing all the time we think we made the right decision, although we plan to move to a faster data transfer method to speed up data dumps and backups.

The previous comments apply equally well to the TMGS. Early on, we decided to build the data acquisition system around the National Instruments (NI) PXI-bus standard. As it turned out, the slowest the sample-and-holds could run was 1 kHz, which is an excessively high sample rate for this application. Rather than decimate the incoming data to something like 100 samples/second, we opted to keep all the measurements. These time-series data came in very handy when we started to look at calibration data and baseline noise.

Although we knew that system calibration was the key to deriving valid magnetic gradient tensors from the individual vector field measurements, we learned that estimating the calibration coefficients using 81 parameters has its pitfalls. The values for the coefficients changed from calibration run to calibration run, and it became apparent that before we could attribute these changes to variations in hardware, it would be necessary to perform a thorough sensitivity analysis of our regression procedure. Furthermore, there appears to be a significant angularly-dependent error that is not modeled by the objective function we used. These two issues remain unsettled.

We learned, as well as with ALLTEM, that post-processing involves putting large volumes of data through many steps. With the TMGS it was necessary to invoke Fortran programs to convert the proprietary NI binary data files to a more generally readable format. Much of the post-processing was performed using the IDL programming language, whereas graphs and maps were generated using Geosoft Oasis montaj. The nonlinear regressions were done using NLREG, a utility available on the Internet. Obviously, the best situation would be to have all data processing routines handled by a single application, such as Oasis montaj, which is the software environment chosen by the Army for UXO investigations. To do this would require a full-time programmer proficient in writing Geosoft executables (GXs) and associated math and script files.

Perhaps most important, we believe the TMGS project suffered from the push to mobilize to YPG in May, 2006, before having processed (at least partially) the Calibration Grid data from YPG in November, 2005. We certainly had hardware and software changes to make, especially with tying the data files to the GPS pulse-per-second timing in order to eliminate the erratic latency we saw. However, by not calibrating and processing the data from the Calibration Grid, we were left in the dark regarding ground truth and target signatures as we proceeded to process the Blind Test Grid data to submit for scoring. In hindsight, it would have been better to have dealt with the Calibration Grid data before committing to further deployments.

We think that we had a good mix of backgrounds on our team. We had both geophysicists and electronics engineers. Our backgrounds influenced the way we approached issues and the back-and-forth between the geophysicists and engineers improved our results. We think that designers of electronic systems should be required to go to the field and use their own equipment in the field as we have done.

We have made great strides in the area of post-processing and inverting data quickly, efficiently, and automatically, but there will always remain room for improvement.

# 6.0 Conclusions

We have developed two prototype multi-axis systems, ALLTEM and the TMGS. ALLTEM is an active EMI system and has an ability to detect and, in many cases, to distinguish between ferrous and non-ferrous targets. The TMGS is a passive tensor magnetic system that uses magnetic gradients to greatly reduce noise effects from the Earth's field including motion-induced noise. For both systems we have developed methods for data processing and inversion for target parameters. Multiple polarization data have advantages for target parameter inversion and therefore for target classification.

We conclude that it is possible to collect survey-mode (moving platform) data with a multi-axis system such as ALLTEM with position errors and sensor noise levels sufficiently low that dependable inversions for target parameters can be obtained. Therefore target classification with a high level of confidence can be done in many cases without having to stop and collect data at a fixed location. We conclude this based on data gathered at YPG over the Calibration Grid and Blind Test Grid, as well as from subsequent test stand data studies. This conclusion is supported by the results from IDA's analysis of our revised dig list.

A key to the success of accurate target classification from moving platform data is accurate position data either integrated in real time into the main data stream as we have done with ALLTEM or time-tagged for post-processing as we have done for the TMGS. Our studies indicate that on flat ground the present generation of RTK-GPS units provides sufficient accuracy when the "fixed" data quality is achieved. A laser total station such as the Leica would be even more accurate, and we think the cost of these units will decrease and their use will increase. We are adding a roll, pitch, and yaw orientation sensor to ALLTEM to handle cases where the ground is not flat. These additional data will improve results from our classification algorithm.

# 7.0 References


Abraham, J.A., Smith, D. vonG., Wright, D.L., VETEM (Very Early Time Electromagnetic) System final report survey of Pit 4 and Pit 10 subsurface disposal radioactive waste management complex, Idaho Falls, ID: U.S. Geological Survey Open-File Report 03-0140. Available on-line at http://pubs.usgs.gov/of/2003/ofr-03-140/

Barrowes, B., O'Neill, K., Snyder, D.D., George, D.C., Shubitidze, F., 2006, New man-portable vector time domain EMI sensor and discrimination processing, *in* Proc. of the UXO-Countermine-Range Forum, July 10-13, 2006, Las Vegas, NV, (Power Point presentation, 18 slides).

Collins, L.M., 2006, Statistical and adaptive signal processing for UXO discrimination for next-generation sensor data: SERDP Project MM-1442 In-Progress Review, Feb. 22, 2006, (Power Point presentation, 49 slides)

Gill, P.E., Murry, W., and Wright, M.H., 1986, Practical optimization: Amsterdam, Elsevier, 401 p.

Jackson, J.D., 1999, Classical Electrodynamincs, 3rd Edition, Wiley and Sons: Hoboken, NJ, 808 p.

Oden, C.P., 2006, Calibration and Data Processing Techniques for Ground Penetrating Radar Systems with Applications in Dispersive Ground: Ph.D. Dissertation, Dept. of Geophysics, Colorado School of Mines, Golden, CO, 249 p.

Oden, C.P., and Moulton, C.W., 2006, GP Workbench Manual: Technical Manual, User's Guide, and Software Guide: U. S. Geological Survey Open-File Report 2006-1365. (available on line at: http://pubs.usgs.gov/of/2006/1365.)

Smith, R., and Annan, P., 1998, The use of B-field measurements in an airborne time-domain system: Part I. Benefits of B-field versus dB/dt data: Exploration Geophysics, vol. 29, p. 24-29.

West, G.F., Macnae, J.C., and Lamontagne, Y., 1984, A time-domain electromagnetic system measuring the step response of the ground: Geophysics, vol. 49, p. 1010.

Wright, D.L., and Chew, W.C., 2000, Enhancements to and characterization of the very early time electromagnetic (VETEM) prototype instrument and applications to shallow subsurface imaging at sites in the DOE complex, Final Report. (http://www. osti.gov/em52/final_reports/60162.pdf.).

Wright, D.L., Smith, D. vonG., Moulton, C.W., Hutton, S.R., Bracken, R.E., Wallin, E.L., Brown, P.J., Stoddard, C.E., Kibler, J.D., Nabighian, M.N., and Li, Y., 2003, Laboratory evaluation of three prototype geophysical instruments for UXO applications: : Symposium on the Application of Geophysics to Engineering and Environmental Problems (SAGEEP 2003), Proceedings CD, p. 1431-1444, San Antonio, TX, 05/06/2003.

Wright, D.L., Moulton, C.W., Asch, T.H., Hutton, S.R., Brown, P.J., Nabighian. M.N. and Li, Y., 2005, ALLTEM, a triangle wave on-time time-domain system for UXO applications: Proceedings of the 18th Annual Symposium on the Application of Geophysics to Engineering and Environmental Problems, 04/05/2005, Atlanta, GA, p. 1357-1367.

Wright, D.L., Smith, D.vonG., Moulton, C.W., Asch, T. H., Brown, P.J., Hutton, S.R., Bracken, R.E., Li, Y., Nabighian, M.N., and Sanchez, V., 2006, ALLTEM and TMGS May, 2006 Tests at the Standardized UXO Test Area at the Yuma Proving Ground, November 17, 2007, 238 pp. (http://www.serdp.org/Research/upload/MM-1328-IR-YPG-2006.pdf)

Zhdanov, M.S., 2002, Geophysical Theory and Regularization Problems, Elsevier: Amsterdam, 628 p.

# 8.0 Appendices

## Appendix A. Supporting Data – ALLTEM Test Stand Data

Raw or processed digital data sets produced by both the TMGS and ALLTEM are too large to include here or maintain long term on a USGS server. However, processed ALLTEM YPG Calibration Grid data can be supplied on DVD. In addition, we have processed most of the Test Stand ALLTEM data. Upon request, these data are available to other interested SERDP/ESTCP researchers.

This appendix includes documentation of available ALLTEM Test Stand Data.



### A.1 - Introduction

A non-metallic test stand (figure A.1.1) was constructed at the Denver Federal Center for use in benchmarking UXO instruments. The test stand features an automated ordnance positioning system capable of precisely placing items within a roughly 4 m by 4 m area with an accuracy of ± 5 mm. Position data were collected using a combination of laser distance meters and a linear position sensor (string pot). ALLTEM test stand data were collected in July and August of 2007.

Section A.2 outlines the file organization of this data release. In section A.3 specifics about each included survey are outlined, as well as surface plots of each dataset [1].

Several sub-appendices have been included in this appendix to assist those who have not worked with ALLTEM data. These documents are provided as a convenience and reviewing them may not be necessary for all parties. General geometrical information about ALLTEM can be found in sub-appendix AA. Sub-appendix AB describes the binary file format used to store the data. In sub-appendix AC the preprocessing that has already been applied to the data is discussed. Details on the transfer function between the sense coils and digitizer can be found in sub-appendix AD. A key to the file naming convention used is outlined in sub-appendix AE. Details of the positioning system and general test stand information are available in sub-appendix AF.

(a) (b) (c)

**Figure A.1.1.** A non-metallic test stand was built (a) housing the ALLTEM instrument (b) in a fixed location. A shuttle and trolley (c) moved the targets around. Position data were taken with a combination of lasers and string-pots and held to better than +/- 5 mm accuracy.

### A.1.1 General information

The test stand displayed in Figure A.1.1 featured an automated 'trolley' and 'shuttle' system (figure.A.1.1.1). By convention, the shuttle moved the target (ordnance or clutter item) along a line running from north to south. Data were recorded while the shuttle was in motion at a fixed velocity. Between lines the trolley moved the shuttle and target to the next line. Line spacing was usually 5 or 10 cm. For a few of the larger targets the line spacing was increased.

[1]These surface plots were generated using the difference between two time picks (31 and 513) on decay curves. Released datasets contain complete decay curves. These plots are provided as a convenience for first-look only.

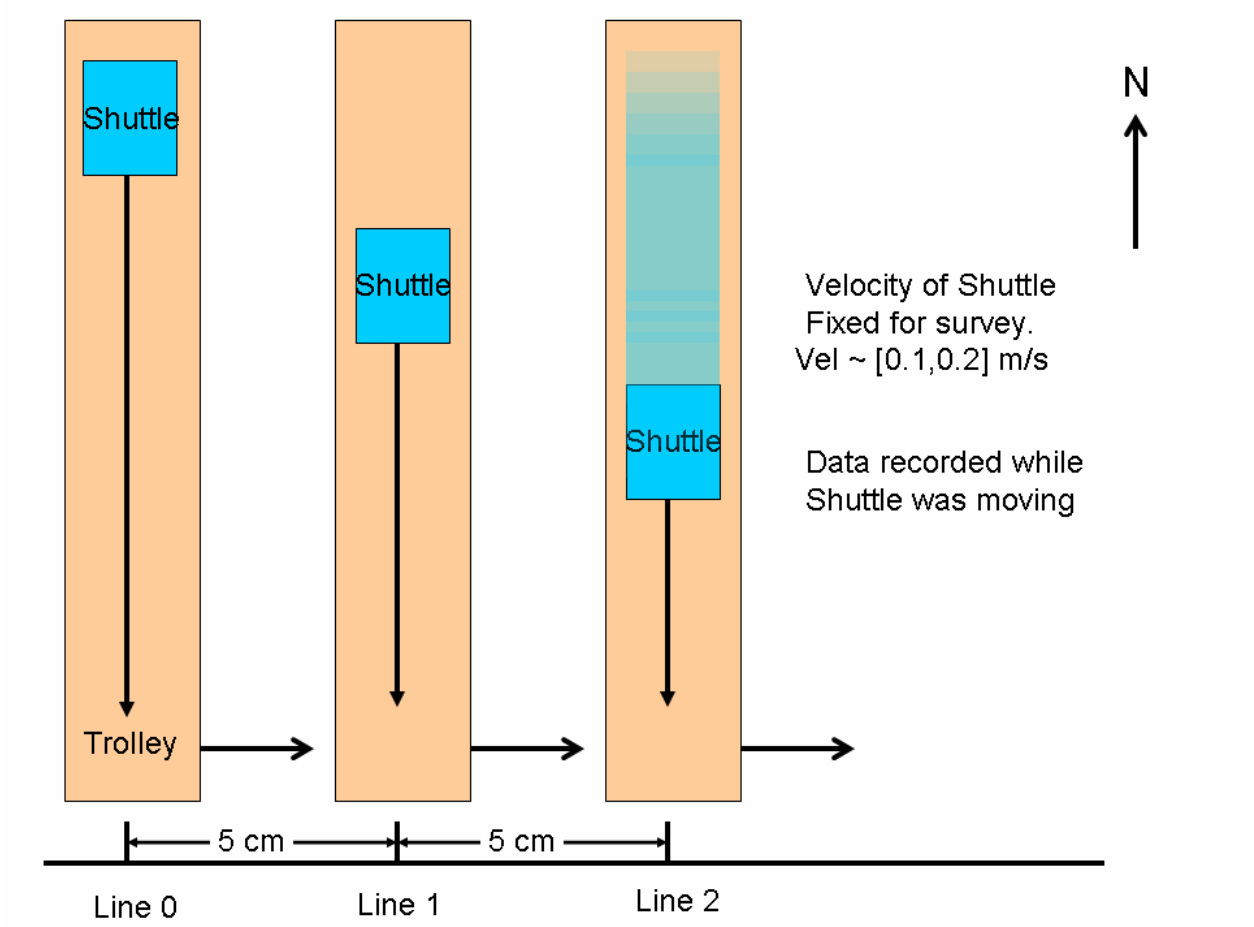


**Figure A.1.1.1.** This is a simplified map view of the test stand looking directly down from the ALLTEM cube's perspective. The area in the figure is the area directly under the ALLTEM cube. The test stand features a moving trolley and shuttle system. The shuttle held a target and moved it along the survey lines. Survey lines were run north to south. The trolley moved the shuttle (and target) to new lines. Line spacing was consistent within a survey and was generally either 5 or 10 cm. For some of the larger targets line spacing was 20 or 25 cm. No data were recorded while the trolley was moving.

Due to the nature of the test stand, these data require pre-processing to convert data from a fixed instrument frame of reference to a fixed target frame. This has been done. All of the data included in this distribution have been converted to a moving instrument frame. Additionally, several filters were applied to the data. These filters include despiking (median), low-pass, and band-stop. Also waveform stacking (summation averaging) was applied for noise reduction. Details of the preprocessing filters may be found in sub-appendix AC. Each survey may be analysed as a traditional but densely sampled dataset. Lines were run north to south and spacing between lines was either 5 or 10 cm. Most of the lines were sampled at a velocity of 0.1 or 0.2 m/s. A few were run a 0.5 m/s. The 0.1 and 0.2 m/s correspond to a data sampling density of 0.04 m/sample or 0.08 m/sample, respectively.

### A.1.2 Ordnance Targets

A total of 12 ordnance items were surveyed. These are outlined and named in figure A.1.2.1. Table A.1.1 gives the full U.S. Military description of each ordnance type along with the shortened names you will find in the data release files.

**Table A.1.1.** Data file names. These are shortened versions of the full ordnance item name. Note that when present, decimal points in ordnance names have been replaced with the character 'p' to avoid confusion with the conventional file extension character '.' Ordnance names were provided using ORDATA II Version 1.0

| Shortened Names in Files | Full U.S Military Description |
|---|---|
| 60mm | U.S. PROJECTILE, 60-MM, HE, M49A4 (M49A2E2) |
| 81mm | U.S. PROJECTILE, 81-MM, HE, M889A1 |
| 40mm | U.S. PROJECTILE, 40-MM, PRACTICE, M385 |
| 20mm | U.S. 20-MM PROJECTILE |
| 2p75 | U.S. ROCKET WARHEAD, 2.75-INCH, PRACTICE, M230 |
| MK118Rockeye | U.S. BOMB, AT, MK 118 (Bomblet from Rockeye guided dispenser) |
| BLU-26 | U.S. BOMB UNIT, FRAG, BLU-26/B |
| BDU-28 | U.S. BOMB UNIT, BDU28/B |
| 105mm | U.S. CARTRIDGE, 105-MM (M494E3) |
| 57mm | U.S. CARTRIDGE, 57-MM M22 DRILL CARTRIDGE |
| M42 | U.S. GRENADE, M42 |
| 75mm | U.S. 75-MM ANTI-TANK |

81mm

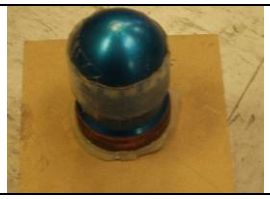

40mm

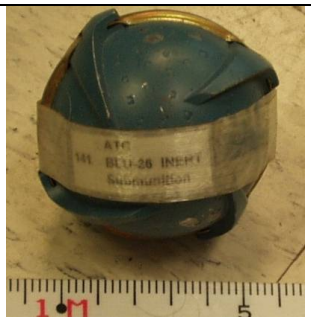

BLU-26

20mm

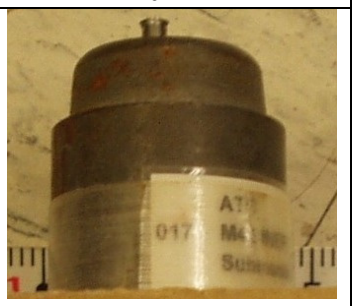

M42

2.75" Rocket

MK118 Rockeye

75mm

57mm

60mm

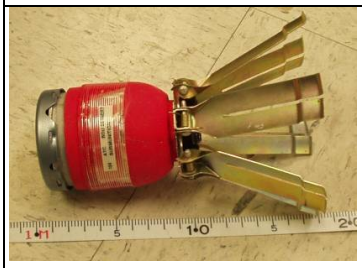

BDU-28

105mm

**Figure A.1.2.1**. The surveyed ordnance items are displayed above as well as the names used to describe them.

### A.1.3 Clutter Targets

Ten pieces of clutter were also surveyed. Some items of clutter display symmetry similar to a UXO ordnance (e.g. rod-like or circular-shaped) while others are more irregular (e.g. a piece of chain). Figure A.1.3.1 outlines each of these items and the naming convention used to distinguish them. Details of the clutter items are outlined below:

- Clutter_DiskLarge:
  Material: Steel
  Diameter: ≈ 320 mm
  Thickness: 6.5 mm
- Clutter_DiskSmall:
  Material: Steel
  Diameter: ≈ 190 mm
  Thickness: 6.5 mm
- Clutter_Ring:
  Material: Steel
  Diameter: ≈ 250 mm (outer), 200 mm (inner)
  Thickness: 6.5 mm
- Clutter_PlateAlum:
  Material: Aluminum
  Dimensions: Irregular, ≈ two joined rectangles, 85mm×250mm and 94mm×91mm
  Thickness: 19.2 mm
- Clutter_Rod:
  Material: Steel
  Diameter: 47.5 mm
  Length: 210mm
- Clutter_AngleLong:
  Material: Steel
  Length: 305 mm
  Width: 32 mm
  Shape: Extruded ‘U’ shaped channel, web width ≈ 4mm
- Clutter_AngleShrt:
  Material: Steel
  Length: 136 mm
  Width: 51 mm
  Shape: Extruded ‘U’ shaped channel, web width ≈ 3.5mm
- Clutter_BallStainless:
  Material: StainlessSteel
  Diameter: 102mm
- Clutter_BallBrass:
  Material: Brass
  Diameter: 102mm
- Clutter_Chain:
  Material: Steel
  Shape: Irregular, chain, chain and hook, and extruded bar.

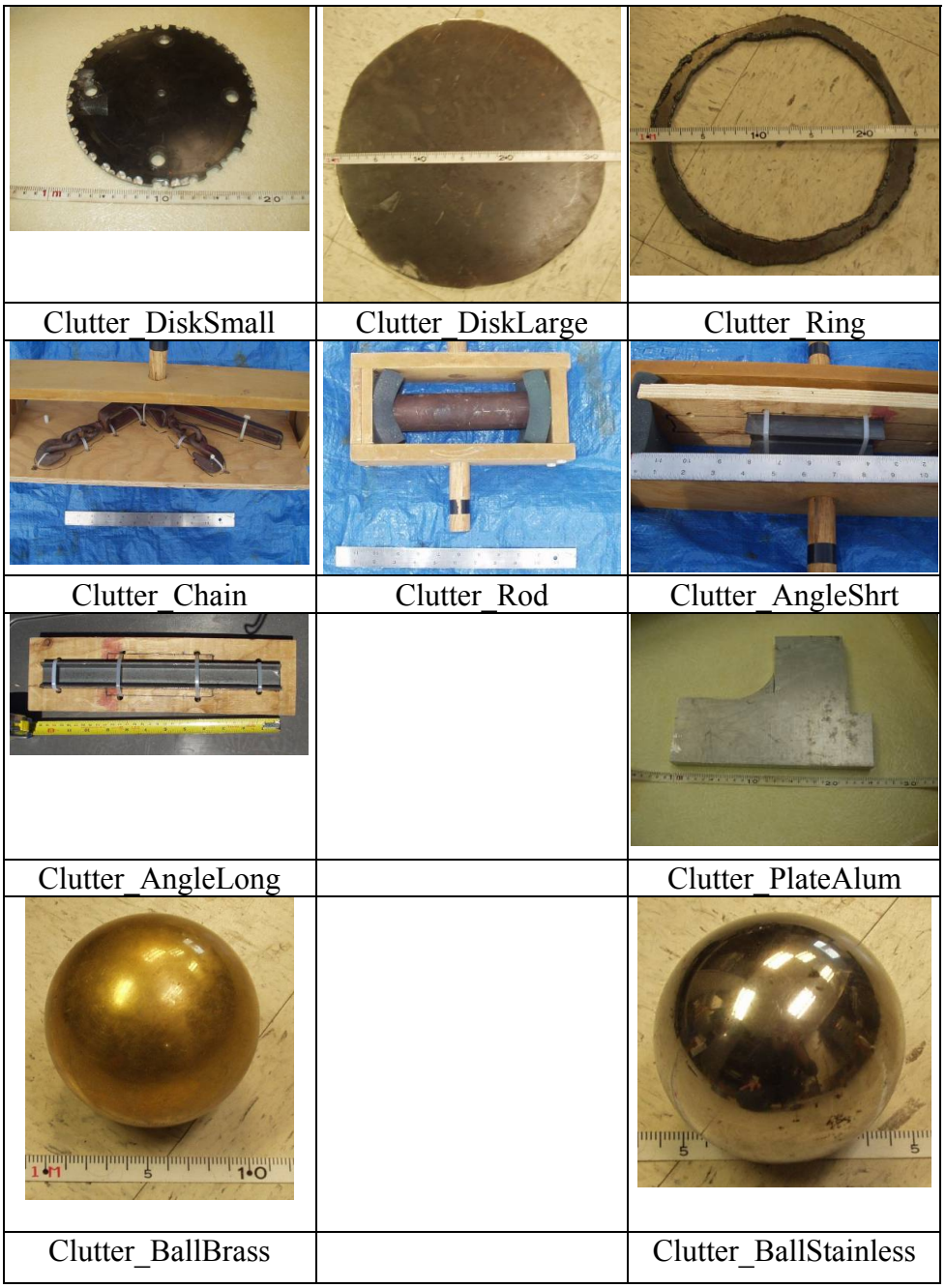


**Figure A.1.3.1.** Several items of clutter were surveyed including a steel chain, a rusted steel rod, a short piece of angle iron, a longer piece of angle iron, a steel ring, and an irregular aluminum plate. The names below the pictures are the naming conventions used in data files.

## A.2 Data Release Conventions

### A.2.1 Coordinates

The global coordinates of the surveys are referenced to the SE corner of the test stand. The center of the ALLTEM cube was at 2066 mm northing and 2677 mm easting. This is roughly the location of the center of mass of each of the targets, after the transformation between a moving target to a moving ALLTEM cube reference frame has been performed.

### A.2.2 Target Position

All target positions were referenced from the center of mass of an ordnance or clutter item.

#### *A.2.2.1 Azimuth and inclination*

Inclination, in degrees, was referenced from a level plane parallel to the surface of the Earth. By convention items dipping downward towards the ground were assigned positive inclination values. An item whose nose was pointed directly towards the ground was therefore given an inclination value of 90°.

Azimuth is referenced from north in degrees. An item with nose pointed due north was given an Azimuth value of 0. Values increase clockwise. An azimuth value of 90°refers to due east and a value of 180°, south. Figure A.2.2.1.1 gives a schematic of the azimuth and inclination naming convention and figure A.2.2.1.2 shows the 60mm ordnance in the five most common orientations.

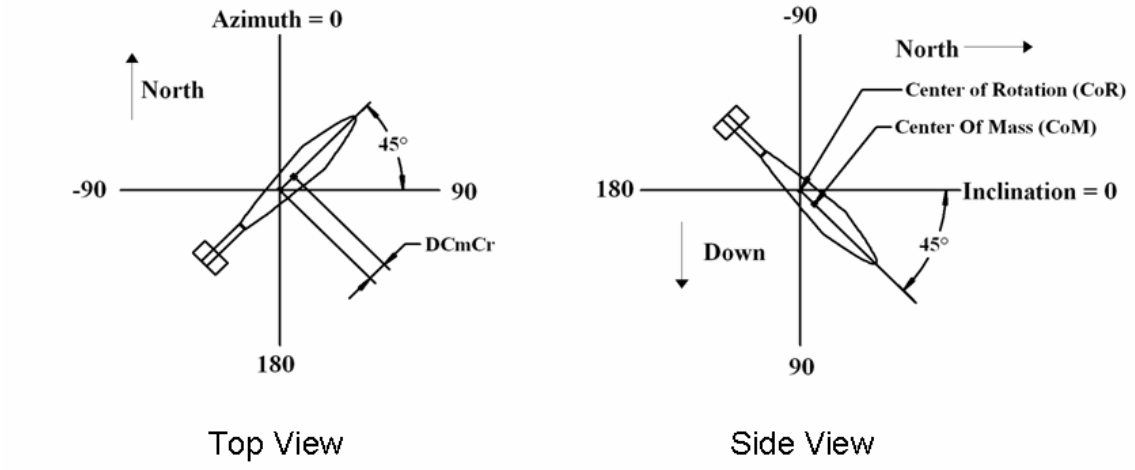


**Figure A.2.2.1.1**. Ordnance azimuth values were referenced to north. Values were measured in degrees and increased in the usual clockwise convention. Inclination values were referenced to a level surface parallel to the ground and increased as the nose of the ordnance dipped further downward.

Az0Inc0

Az0Inc45

Az0Inc90

Az45Inc45

Az90Inc0

**Figure A.2.2.1.2.** The five most common ordnance orientations. A 60 mm ordnance is shown here. The labels "Az0Inc0" etc. are from file names and indicate azimuth and inclination.

*Azimuth and inclination correction*

A decision was made to use the center of mass of the ordnance for its location. Due to the design of the fixtures used to hold the various ordnance items during the surveys on the test stand, the center of mass was not always at the center of rotation when the ordnance was placed at the various azimuths and inclinations. For each ordnance, the distance from the center of mass to the center of rotation was measured ($D_{CmCr}$). The distance was considered positive if it placed the center of mass (CoM) further north of the center of rotation (CoR), when the ordnance was oriented with azimuth=0, inclination=0. These offsets are given for reference in table A.2.2.2.1. However, corrections have been made so that all measurements are given from the ordnance center of mass.

The $D_{CmCr}$ distance, along with the particular Az and Inc settings, were used to modify the reported Northing and Easting values according to the formulas:

$$Easting\ \ Correction \quad = \quad \sin(Az)\times\cos(Inc)\times D_{CmCr} \qquad (A.2.1)$$

$$Northing\ \ Correction \quad = \quad \cos(Az)\times\cos(Inc)\times D_{CmCr} \qquad (A.2.2)$$

### *A.2.2.2 Trolley Depth*

The survey file names have a field that indicates the depth of the 'trolley' that the ordnance shuttle was travelling on as it traversed its lines. This is the value 'Td73' or 'Td103' which appears after the Azimuth (Az) and Inclination (Inc) in the filenames. 'Td' stands for 'TrolleyDepth'. The actual depth recorded in the file names was measured from the top surface of the ordnance shuttle to the bottom of the ALLTEM Cube. This is the 0.73 meter (or 73cm) value shown in the figure A.2.2.2.1. Since all of the receiver antenna positions are referenced to the center of the ALLTEM cube, the distance 0.923 m in the figure A.2.2.2.1 is important because it represents the ordnance center of mass to the cube center. For the case where Td103 is in the filename, the 0.923 m value will be 30 cm larger, or 1.223 m.

Also, a positive Inc value increases the depth of the center of mass of the ordnance, below the ALLTEM cube, according to the formula:

$$Depth\ \ Inc\ \ Correction = Depth\ \ to\ \ Ordnance\ \ CoR + \sin(Inc) * D_{CmCr} \qquad (A.2.3)$$

This calculation (equation A.2.3) has been applied to the depths listed in table A.2.2.2.1.

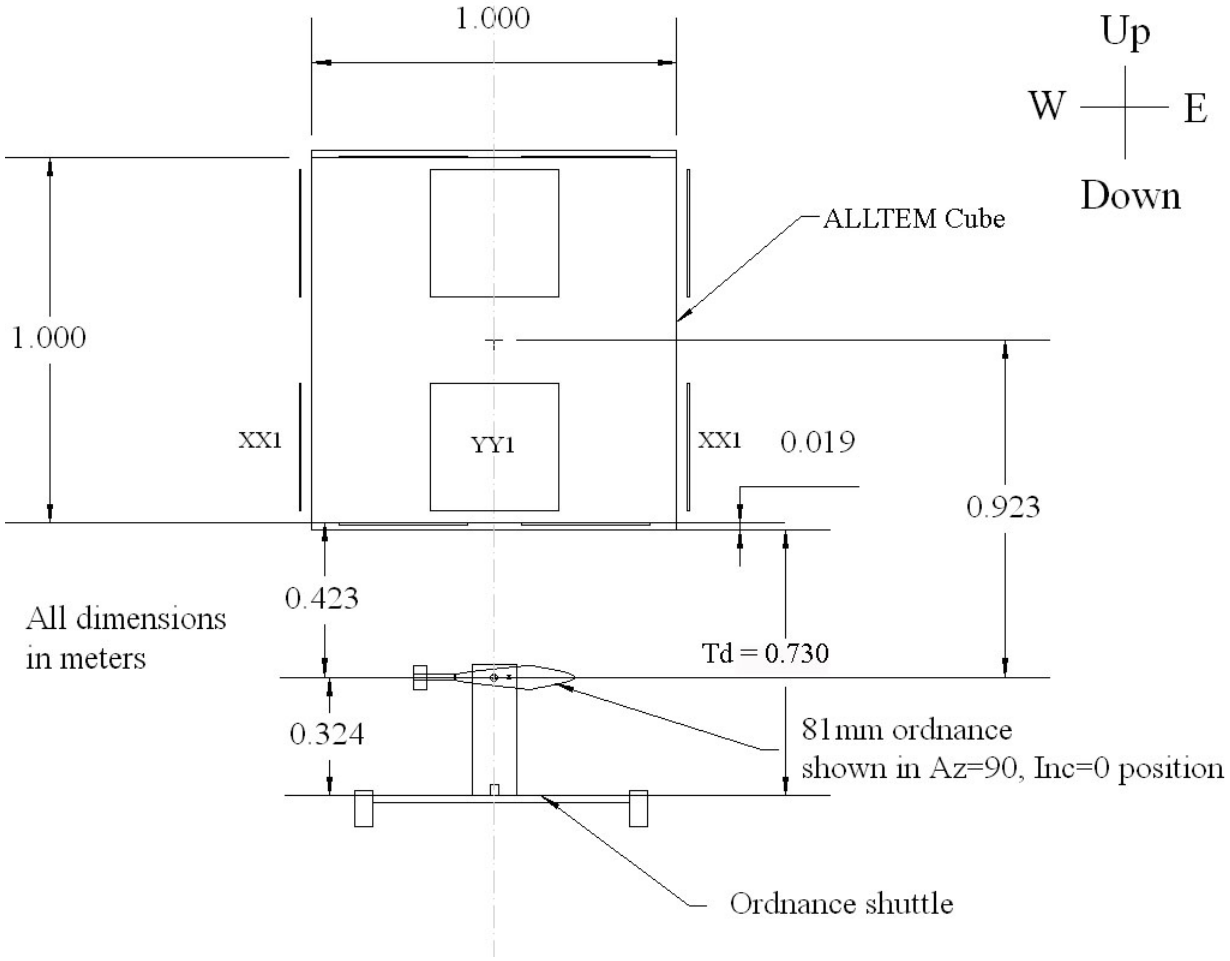


**Figure A.2.2.2.1.** The 'Td' measurement that is shown in the data release files corresponds to the distance from the top surface of the shuttle platform to the bottom face of the ALLTEM cube, measured 0.73 above. The actual target depth is listed in table A.2.2.2.1.

**Table A.2.2.2.1.** Corrected ordnance positions.

| | | | | | Td 73 | Td 103 | |
|---|---|---|---|---|---|---|---|
| Target | Azimuth | Inclination | Northing | Easting | Depth | Depth | CoR-CoM |
| | (deg) | (deg) | (mm) | (mm) | (mm) | (mm) | (mm) |
| 105mm | 0 | 0 | 2066 | 2677 | 923 | 1223 | 0 |
| | 0 | 45 | 2066 | 2677 | 923 | 1223 | 0 |
| | 0 | 90 | 2066 | 2677 | 923 | 1223 | 0 |
| | 45 | 45 | 2066 | 2677 | 923 | 1223 | 0 |
| | 90 | 0 | 2066 | 2677 | 923 | 1223 | 0 |
| | | | | | | | |
| 20mm | 0 | 0 | 2066 | 2677 | 923 | 1223 | 0 |
| | 0 | 45 | 2066 | 2677 | 923 | 1223 | 0 |
| | 0 | 90 | 2066 | 2677 | 923 | 1223 | 0 |
| | 45 | 45 | 2066 | 2677 | 923 | 1223 | 0 |
| | 90 | 0 | 2066 | 2677 | 923 | 1223 | 0 |
| | | | | | | | |
| 2p75 | 0 | 0 | 2066 | 2677 | 923 | 1223 | -33.6 |
| | 0 | 45 | 2066 | 2677 | 894 | 1194 | -33.6 |
| | 0 | 90 | 2066 | 2677 | 893 | 1193 | -33.6 |
| | 45 | 45 | 2066 | 2677 | 894 | 1194 | -33.6 |
| | 90 | 0 | 2066 | 2677 | 923 | 1223 | -33.6 |
| | | | | | | | |
| 57mm | 0 | 0 | 2066 | 2677 | 923 | 1223 | -12.5 |
| | 0 | 45 | 2066 | 2677 | 912 | 1212 | -12.5 |
| | 0 | 90 | 2066 | 2677 | 912 | 1212 | -12.5 |
| | 45 | 45 | 2066 | 2677 | 912 | 1212 | -12.5 |
| | 90 | 0 | 2066 | 2677 | 923 | 1223 | -12.5 |
| | | | | | | | |
| 60mm | 0 | 0 | 2066 | 2677 | 923 | 1223 | 7 |
| | 0 | 45 | 2066 | 2677 | 929 | 1229 | 7 |
| | 0 | 90 | 2066 | 2677 | 929 | 1229 | 7 |
| | 45 | 45 | 2066 | 2677 | 929 | 1229 | 7 |
| | 90 | 0 | 2066 | 2677 | 923 | 1223 | 7 |
| | | | | | | | |
| 75mm | 0 | 0 | 2066 | 2677 | 923 | 1223 | -11.1 |
| | 0 | 45 | 2066 | 2677 | 914 | 1214 | -11.1 |
| | 0 | 90 | 2066 | 2677 | 913 | 1213 | -11.1 |
| | 45 | 45 | 2066 | 2677 | 914 | 1214 | -11.1 |
| | 90 | 0 | 2066 | 2677 | 923 | 1223 | -11.1 |
| | | | | | | | |
| 81mm | 0 | 0 | 2066 | 2677 | 923 | 1223 | 47.6 |
| | 0 | 45 | 2066 | 2677 | 964 | 1264 | 47.6 |
| | 0 | 90 | 2066 | 2677 | 966 | 1266 | 47.6 |
| | 45 | 45 | 2066 | 2677 | 964 | 1264 | 47.6 |
| | 90 | 0 | 2066 | 2677 | 923 | 1223 | 47.6 |
| | | | | | | | |
| BDU-28 | 0 | 0 | 2066 | 2677 | 923 | 1223 | -27.6 |
| | 0 | 45 | 2066 | 2677 | 900 | 1200 | -27.6 |
| | 0 | 90 | 2066 | 2677 | 898 | 1198 | -27.6 |
| | 45 | 45 | 2066 | 2677 | 900 | 1200 | -27.6 |
| | 90 | 0 | 2066 | 2677 | 923 | 1223 | -27.6 |
| | | | | | | | |

| | | | | | | | |
|---|---|---|---|---|---|---|---|
| BLU-26 | 0 | 0 | 2066 | 2677 | 923 | 1223 | 0 |
| | 0 | 45 | 2066 | 2677 | 923 | 1223 | 0 |
| | 0 | 90 | 2066 | 2677 | 923 | 1223 | 0 |
| | 45 | 45 | 2066 | 2677 | 923 | 1223 | 0 |
| | 90 | 0 | 2066 | 2677 | 923 | 1223 | 0 |
| | | | | | | | |
| M42 | 0 | 0 | 2066 | 2677 | 923 | 1223 | 0 |
| | 0 | 45 | 2066 | 2677 | 923 | 1223 | 0 |
| | 0 | 90 | 2066 | 2677 | 923 | 1223 | 0 |
| | 45 | 45 | 2066 | 2677 | 923 | 1223 | 0 |
| | 90 | 0 | 2066 | 2677 | 923 | 1223 | 0 |
| | | | | | | | |
| MK118Rockeye | 0 | 0 | 2066 | 2677 | 923 | 1223 | 84.4 |
| | 0 | 45 | 2066 | 2677 | 995 | 1295 | 84.4 |
| | 0 | 90 | 2066 | 2677 | 998 | 1298 | 84.4 |
| | 45 | 45 | 2066 | 2677 | 995 | 1295 | 84.4 |
| | 90 | 0 | 2066 | 2677 | 923 | 1223 | 84.4 |
| | | | | | | | |
| AngleLong | 0 | 0 | 2066 | 2677 | 923 | 1223 | 0 |
| | 0 | 45 | 2066 | 2677 | 923 | 1223 | 0 |
| | 0 | 90 | 2066 | 2677 | 923 | 1223 | 0 |
| | 45 | 45 | 2066 | 2677 | 923 | 1223 | 0 |
| | | | | | | | |
| AngleShrt | 0 | 0 | 2066 | 2677 | 923 | 1223 | 0 |
| | 0 | 45 | 2066 | 2677 | 923 | 1223 | 0 |
| | 0 | 90 | 2066 | 2677 | 923 | 1223 | 0 |
| | 45 | 45 | 2066 | 2677 | 923 | 1223 | 0 |
| | 90 | 0 | 2066 | 2677 | 923 | 1223 | 0 |
| | | | | | | | |
| BallBrass | ----- | ----- | 2066 | 2677 | 877 | 1177 | 0 |
| | | | | | | | |
| BallStainless | ----- | ----- | 2066 | 2677 | 877 | 1177 | 0 |
| | | | | | | | |
| Chain | 0 | 0 | 2066 | 2677 | 923 | 1223 | 0 |
| | 0 | 45 | 2066 | 2677 | 923 | 1223 | 0 |
| | 0 | 90 | 2066 | 2677 | 923 | 1223 | 0 |
| | 45 | 45 | 2066 | 2677 | 923 | 1223 | 0 |
| | 90 | 0 | 2066 | 2677 | 923 | 1223 | 0 |
| | | | | | | | |
| DiskLarge | Vert | Disk Plane N-S | 2066 | 2677 | 923 | 1223 | 0 |
| | Horz | ----- | 2066 | 2677 | 923 | 1217 | 0 |
| | | | | | | | |
| DiskSmall | Vert | Disk Plane N-S | 2066 | 2677 | 923 | 1223 | 0 |
| | Horz | ----- | 2066 | 2677 | 923 | 1223 | 0 |
| | | | | | | | |
| PlateAlum | Vert | Plate Plane N-S | 2066 | 2677 | 923 | 1223 | 0 |
| | Horz | ----- | 2066 | 2677 | 923 | 1223 | 0 |
| | | | | | | | |
| Ring | Vert | Disk Plane N-S | 2066 | 2677 | 923 | 1223 | 0 |
| | Horz | ----- | 2066 | 2677 | 923 | 1223 | 0 |
| | | | | | | | |
| Rod | 0 | 0 | 2066 | 2677 | 923 | 1223 | 0 |

| | | | | | | | |
|---|---|---|---|---|---|---|---|
| | 0 | 45 | 2066 | 2677 | 923 | 1223 | 0 |
| | 0 | 90 | 2066 | 2677 | 923 | 1223 | 0 |
| | 5 | 45 | 2066 | 2677 | 923 | 1223 | 0 |
| | 90 | 0 | 2066 | 2677 | 923 | 1223 | 0 |
| | | | | | | | |

Note: "-------" indicates that the parameter is not meaningful for the target shape.

### A.2.3 File Names

Datasets are arranged by ordnance. Within a given ordnance directory surveys are arranged by date taken as well as ordnance position. tables A.2.3.1 and A.2.3.2 outline the file and directory hierarchy.
Each data file name contains:

- The name of the ordnance surveyed.
- The spatial position of the ordnance (azimuth and inclination).
- The survey date [2].
- Depth of the trolley.
- On occasion other notes about the survey such as survey velocity or filter settings if these were different than the usual settings.

While this results in lengthy filenames, most pertinent information is available without relying on the file's metadata.

Each data file's name is organized as:
*ASCII-DATE_Ordnance-Info_Preprocessing-settings_Line-number_.polarization.SU*

For example:

*2007–08–17_60mmAz0Inc45Td103_STDc_Ln0.xx1.SU* (A.2.3.1)

#### *A.2.3.1 Ordnance Information*

Ordnance information uses the following convention:
OrdNameAz#Inc#Td#Notes
Ordnance name is one of the names outlined in either section A.1.2 or A.1.3 depending on whether it was an ordnance or clutter item. In example A.2.3.1 the ordnance surveyed was the 60 mm.

***Ordnance Position***

The ordnance position convention was discussed in detail in section A.2.2. The filename contains the string *Az#Inc#Td#*. The # symbols represent values that describe the position of the ordnance for a given file. In example A.2.3.1 the ordnance surveyed was at an azimuth of $0^{O}$ (north facing) and an inclination of $45^{O}$ (nose dipping down $45^{O}$).

#### *A.2.3.2 Preprocessing settings*

Preprocessing settings identify the various settings used in the preprocessing step. This was discussed in section A.1.1. All datasets in this release have a *STDc* marker here stating that the standard preprocessing steps were taken.

#### *A.2.3.3 Line number*

[2]The ISO 8601 date convention (yyyy-mm-dd) was adopted.

The line number within a survey is recorded in each file. Lines ran north-to-south. Along a line easting positions within the header will be *nearly* constant. Survey lines were sequenced either east-to-west or west-to-east. Lines were generally spaced either 5cm or 10 cm apart. Line number 0 is normally the first line in a survey and therefore has the greatest or smallest easting value. In a few cases Line 0 may have been aborted or incomplete and was therefore not included in the release. In this case the lowest numbered line will be the beginning of the survey. Line 0 was being surveyed in Example A.2.3.1.

**Table A.2.3.1**. Directories and files are organized as shown.

- OrdnanceName
  - (ISO 8601 Date)_(OrdnanceNameOrdPositionTrolleyDepth)_(Preprocessing Standard)
    - ReadMe.Txt
    - (Preprocessing Standard)_(Polarity)_SurveySurfacePlot.jpg
    - ...
    - (Preprocessing Standard)_LargestZZMWaveform.jpg
    - (Date)_(Ordnance Info)_(Preprocessing Std)_(Line).(Polarity).SU
    - ...

**Table A.2.3.2**. On Disk One 60mm data is contained in the files shown.

- *60mm*
  - *2007-07-16_60mmAz0Inc0Td73_STDc*
  - *2007-07-17_60mmAz0Inc45Td73_STDc*
  - *2007-07-17_60mmAz0Inc90Td73_STDc*
  - ...
  - *2007-08-17_60mmAz0Inc45Td103_STDc*
    - *STDc_LargestZZMWaveform.jpg*
    - *STDc_XX1SurveySurfacePlot.jpg*
    - *STDc_XZESurveySurfacePlot.jpg*
    - *... (All 19 Polarities)*
    - *2007-08-17_60mmAz0Inc45Td103_STDc_Ln0.XX1.SU*
    - *2007-08-17_60mmAz0Inc45Td103_STDc_Ln0.XZE.SU*
    - *... (All 19 Polarities for line 0)*
    - *2007-08-17_60mmAz0Inc45Td103_STDc_Ln1.XX1.SU*
    - *... (All 19 Polarities for line 1)*
    - *... (All 33 Lines)*

## A.3 - Data Sets

### 105 mm

Due to the size of the 105 mm projectile, data were collected only at the lower depth and for a limited number of orientations. Nineteen thumbnail amplitude patterns and a ZZM waveform are shown.

Table A.3.1. DiskOne 2007-08-22 105mmAz0Inc45Td103Two

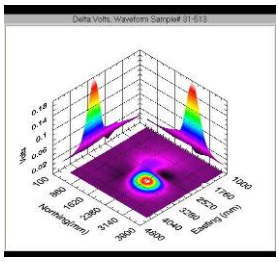
XZE

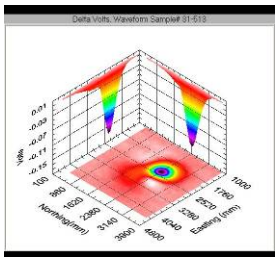
XZF

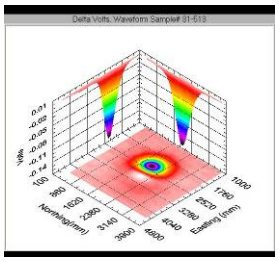
XZG

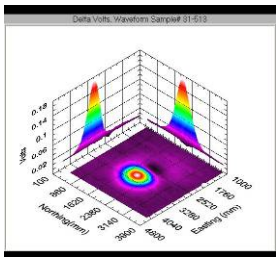
XZH

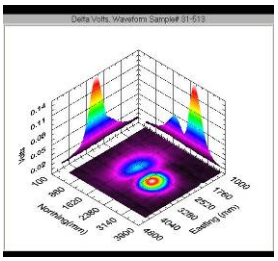
YZE

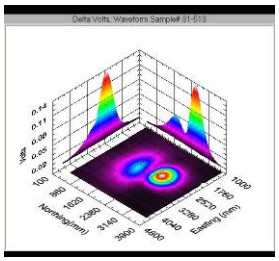
YZF

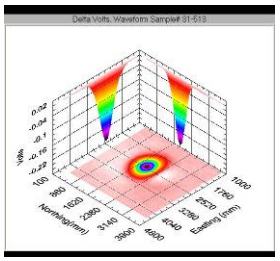
YZG

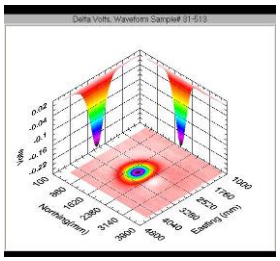
YZH

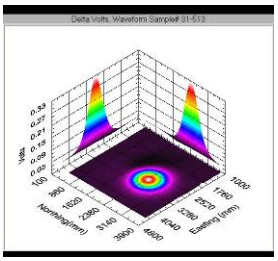
ZZE

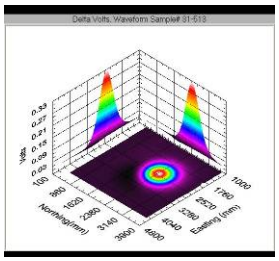
ZZF

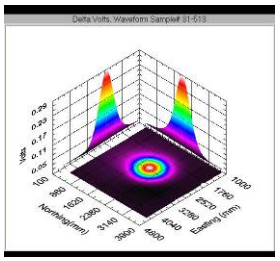
ZZG

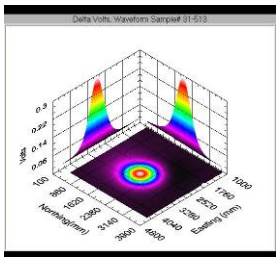
ZZH

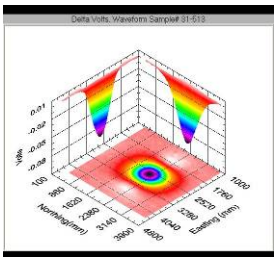
ZX1

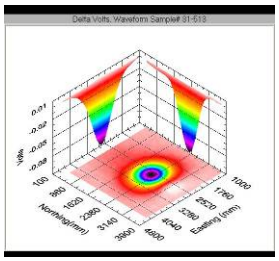
ZY1

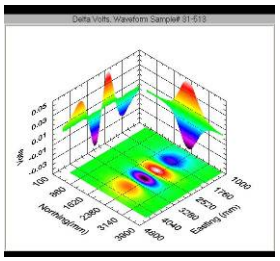
XX1

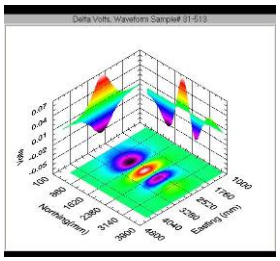
YY1

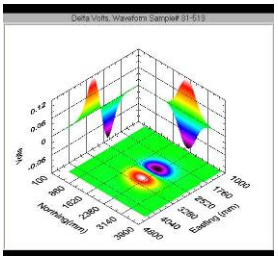
XZM

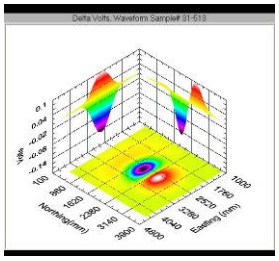
YZM

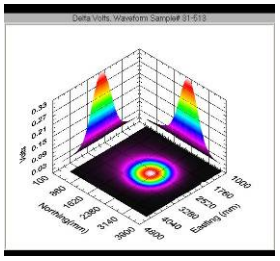
ZZM

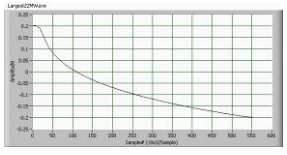
Largest ZZM waveform

Table A.3.2. DiskOne 2007-08-23 105mmAz0Inc0Td103Two

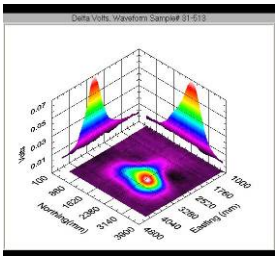
XZE

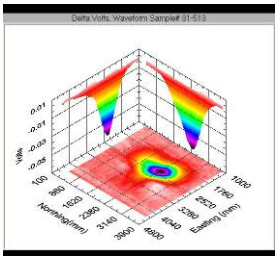
XZF

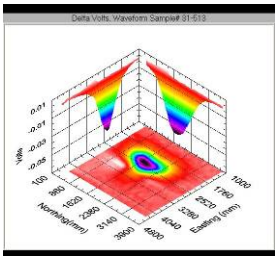
XZG

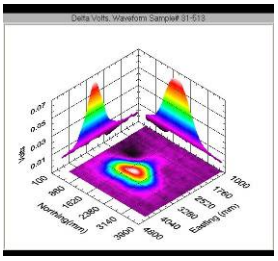
XZH

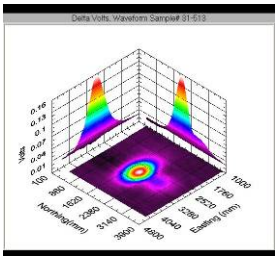
YZE

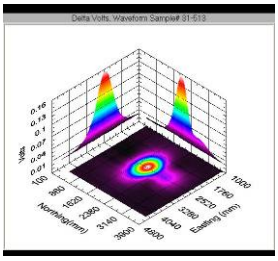
YZF

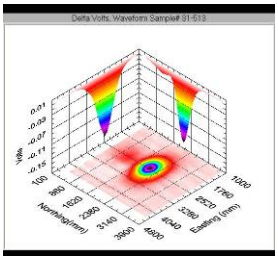
YZG

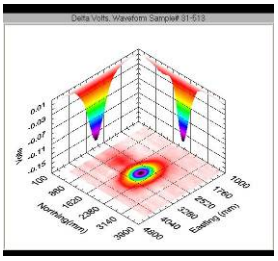
YZH

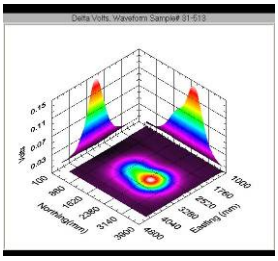
ZZE

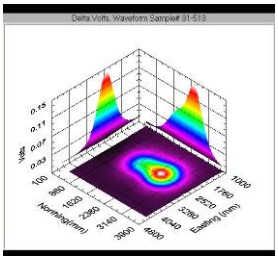
ZZF

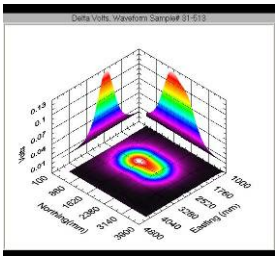
ZZG

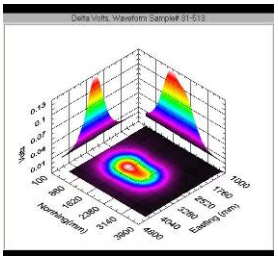
ZZH

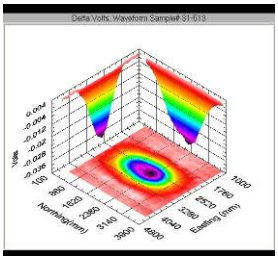
ZX1

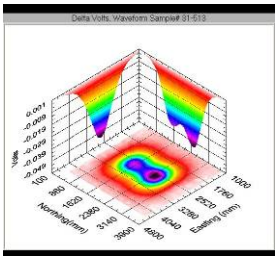
ZY1

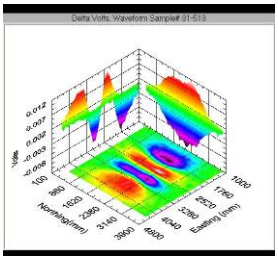
XX1

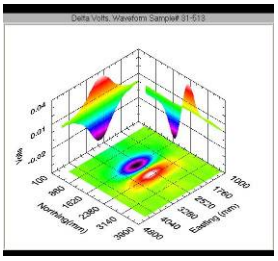
YY1

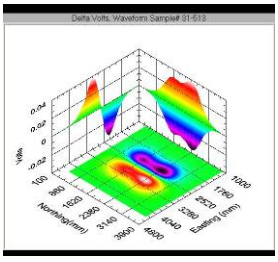
XZM

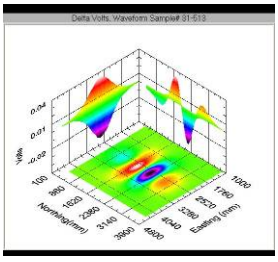
YZM

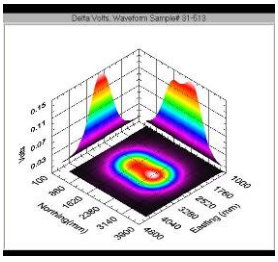
ZZM

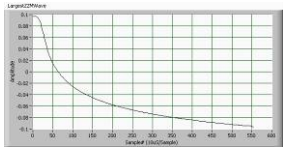
Largest ZZM waveform

Table A.3.3. DiskOne 2007-08-23 105mmAz90Inc0Td103Three

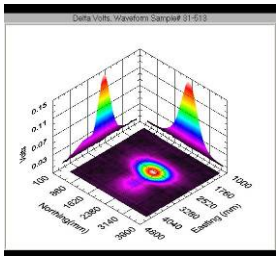
XZE

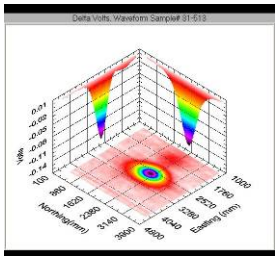
XZF

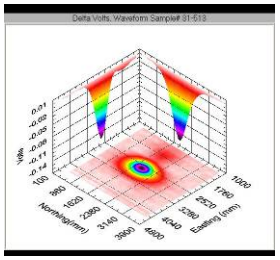
XZG

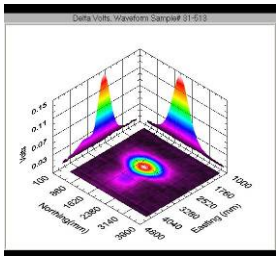
XZH

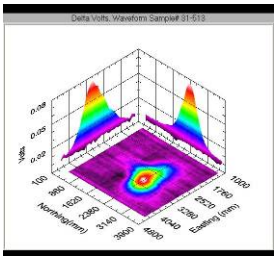
YZE

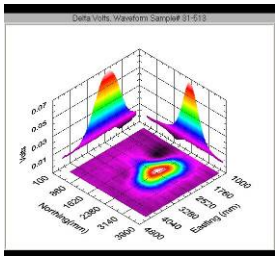
YZF

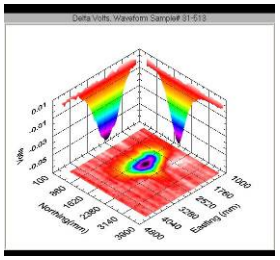
YZG

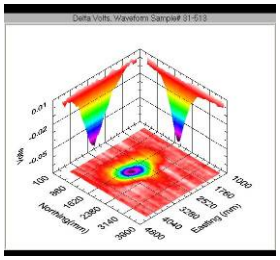
YZH

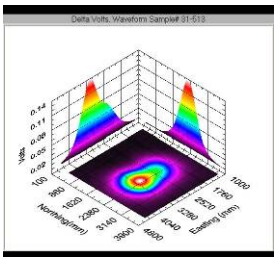
ZZE

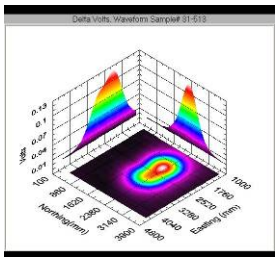
ZZF

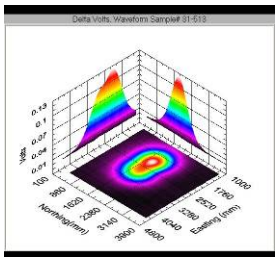
ZZG

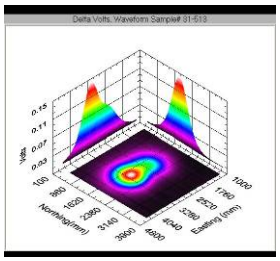
ZZH

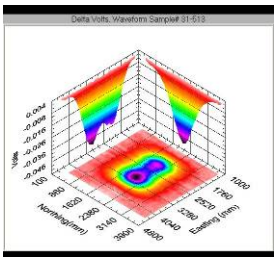
ZX1

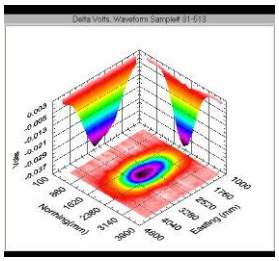
ZY1

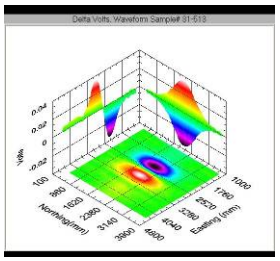
XX1

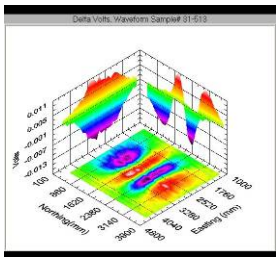
YY1

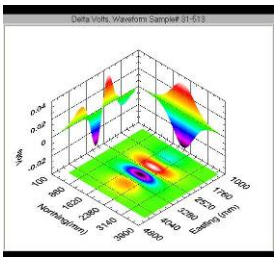
XZM

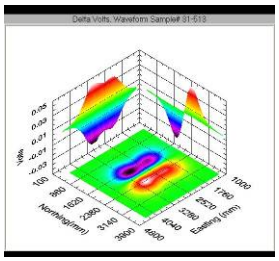
YZM

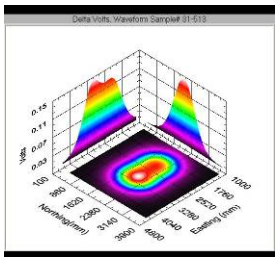
ZZM

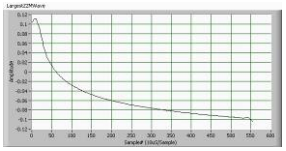
Largest ZZM waveform

## 20 mm

Due to the small size of the 20 mm ordnance these data were only taken at the shallow depth.
The *Lp17kHz* dataset was taken with the ALLTEM's analog low-pass filter set at 17 kHz rather than the usual 7 kHz.

Table A.3.4: DiskOne 2007-08-15 20mmAz0Inc45Td73Lp17kHz

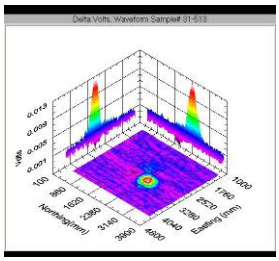
XZE

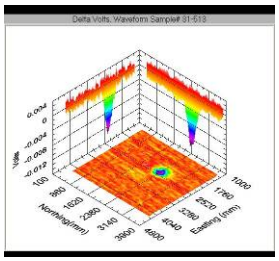
XZF

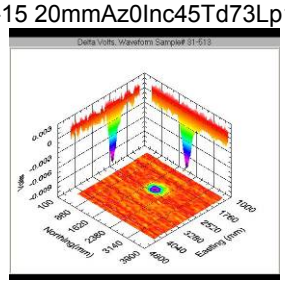
XZG

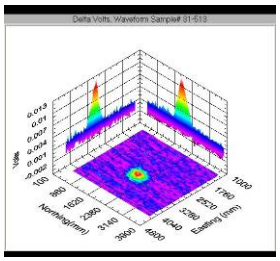
XZH

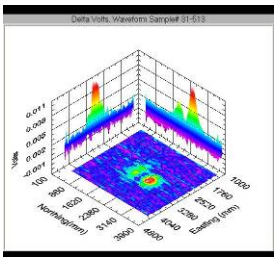
YZE

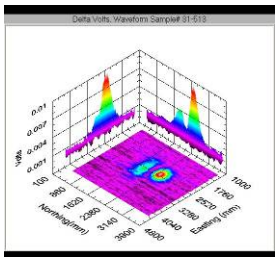
YZF

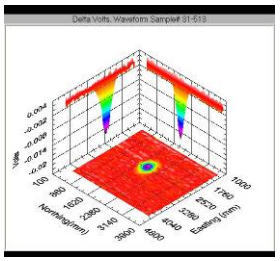
YZG

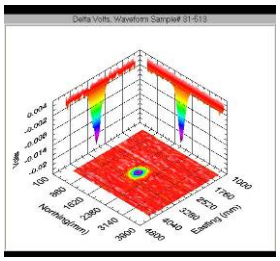
YZH

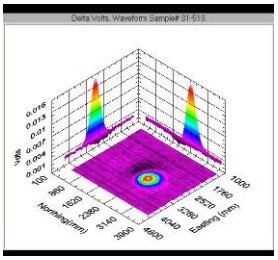
ZZE

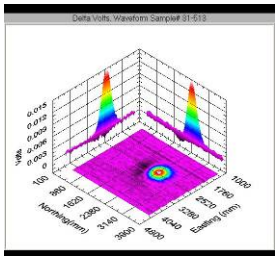
ZZF

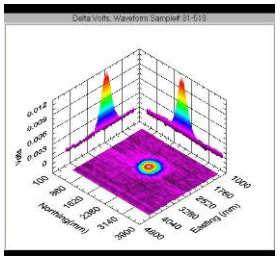
ZZG

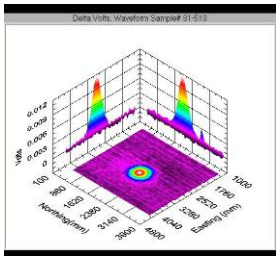
ZZH

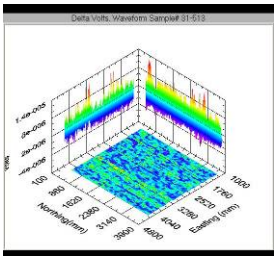
ZX1

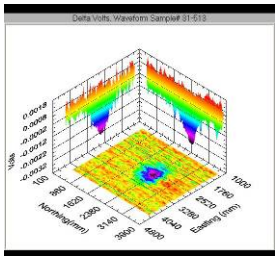
ZY1

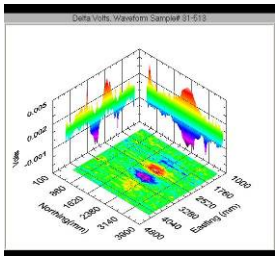
XX1

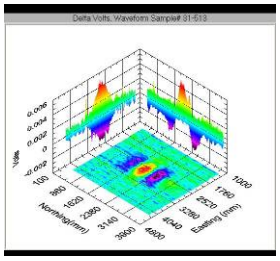
YY1

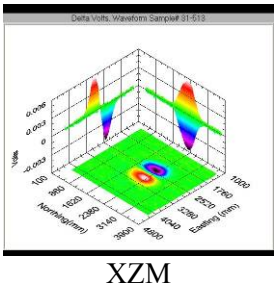
XZM

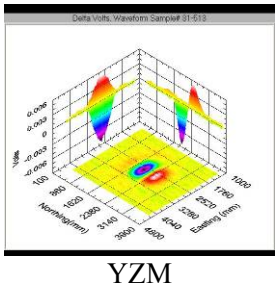
YZM

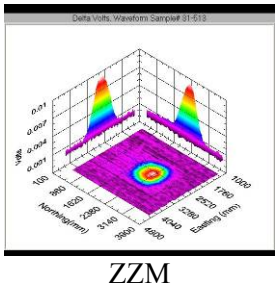
ZZM

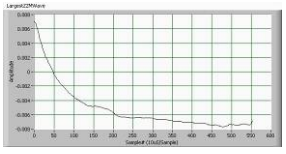
Largest ZZM waveform

# 75 mm

Table A.3.5. DiskOne 2007-08-14 75mmAz0Inc45Td73

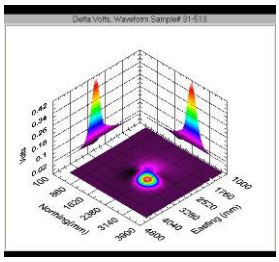
XZE

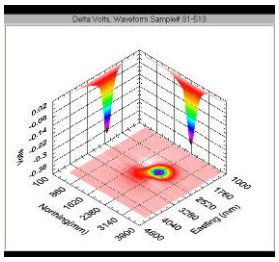
XZF

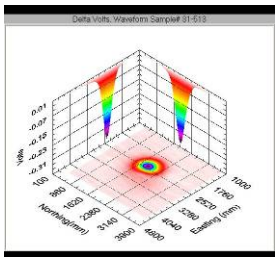
XZG

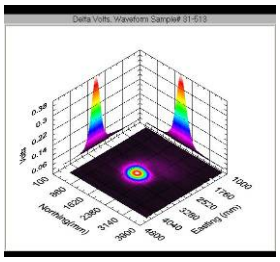
XZH

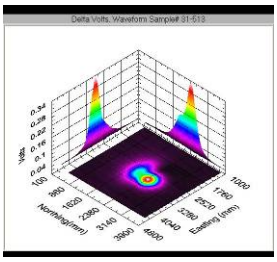
YZE

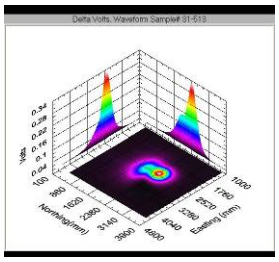
YZF

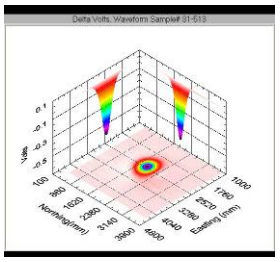
YZG

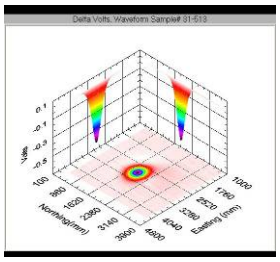
YZH

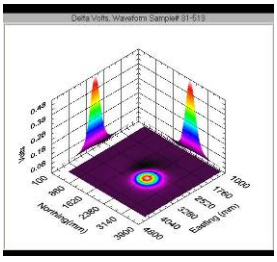
ZZE

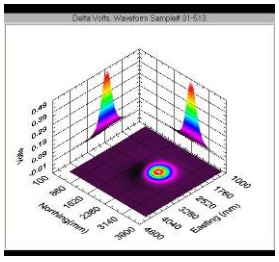
ZZF

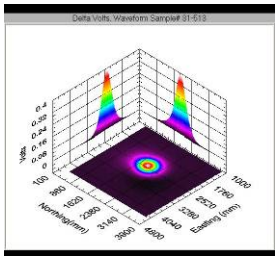
ZZG

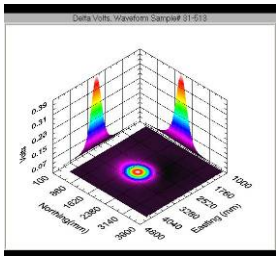
ZZH

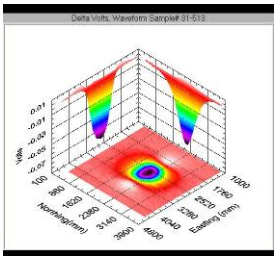
ZX1

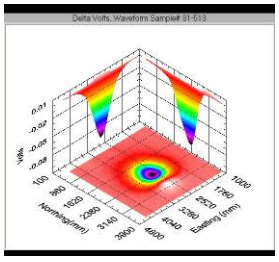
ZY1

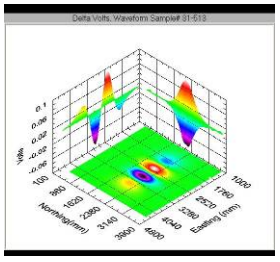
XX1

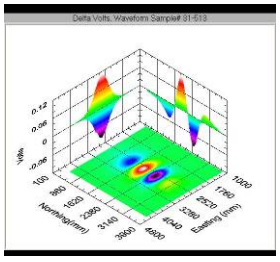
YY1

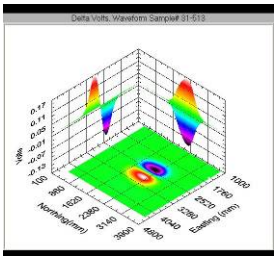
XZM

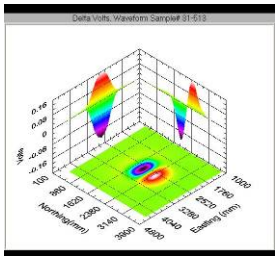
YZM

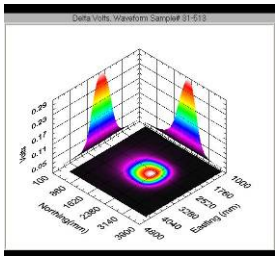
ZZM

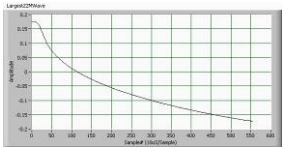
Largest ZZM waveform

Table A.3.6. DiskOne 2007-08-14 75mmAz0Inc90Td73

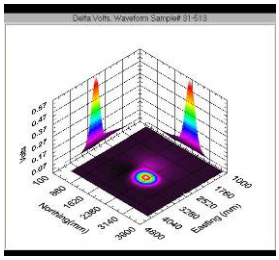
XZE

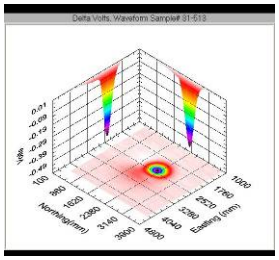
XZF

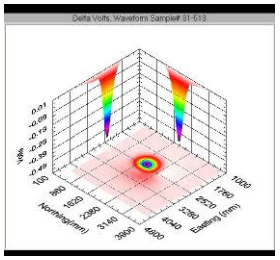
XZG

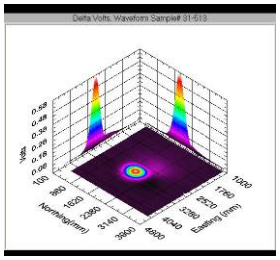
XZH

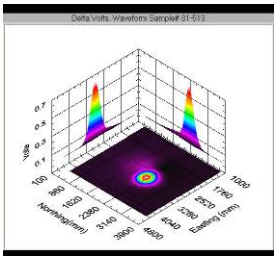
YZE

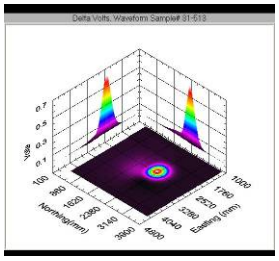
YZF

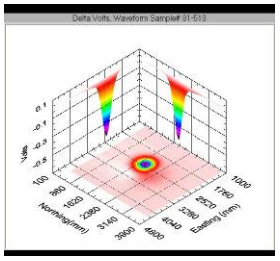
YZG

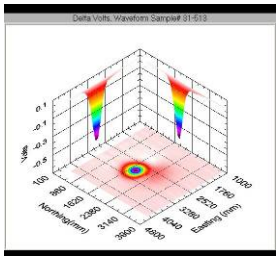
YZH

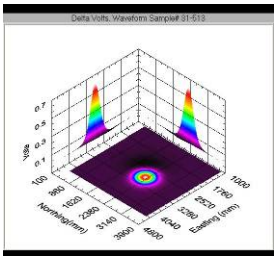
ZZE

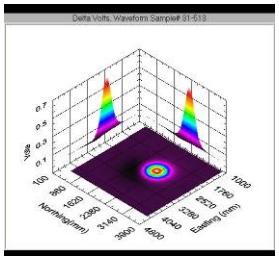
ZZF

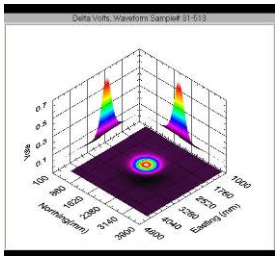
ZZG

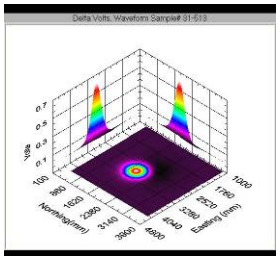
ZZH

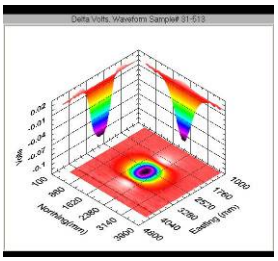
ZX1

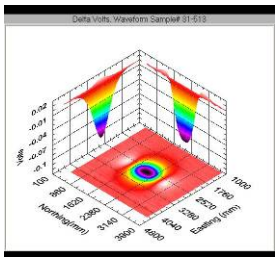
ZY1

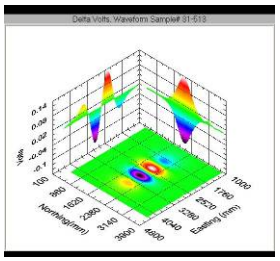
XX1

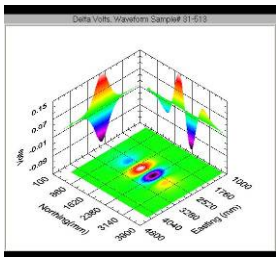
YY1

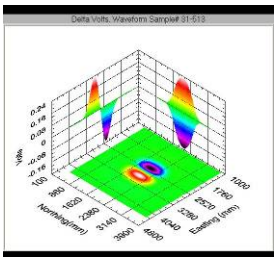
XZM

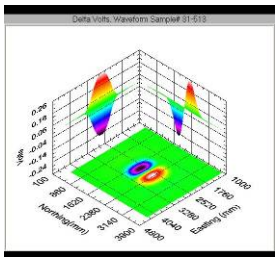
YZM

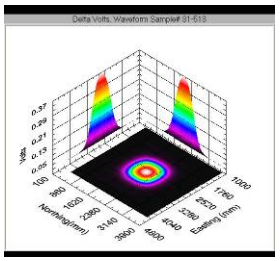
ZZM

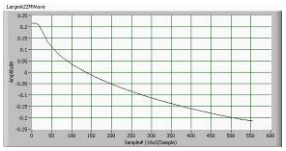
Largest ZZM waveform

Table A.3.7. DiskOne 2007-08-14 75mmAz45Inc45Td73

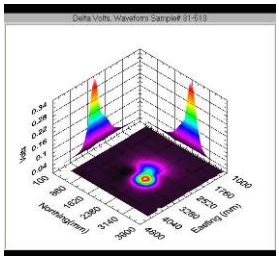
XZE

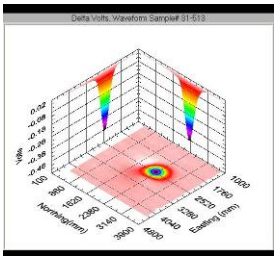
XZF

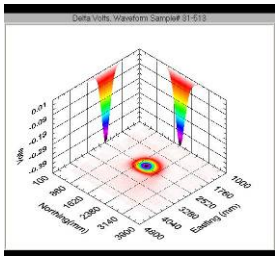
XZG

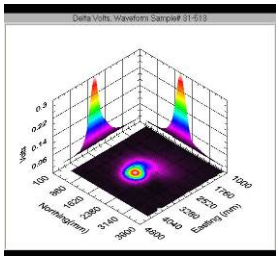
XZH

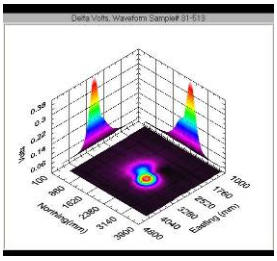
YZE

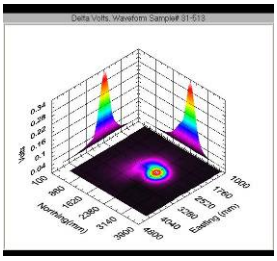
YZF

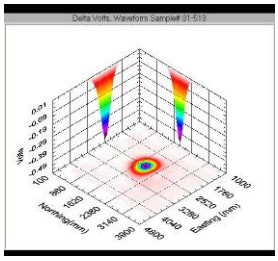
YZG

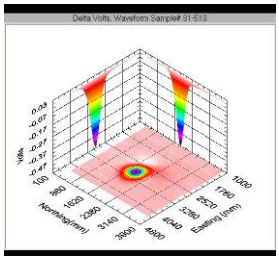
YZH

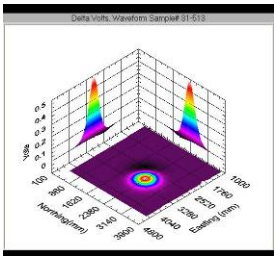
ZZE

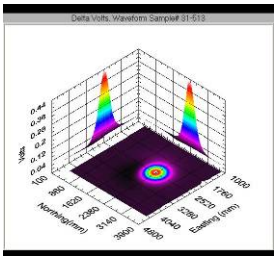
ZZF

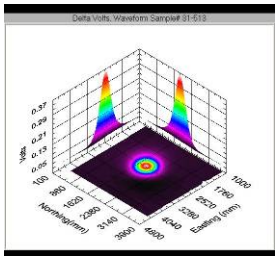
ZZG

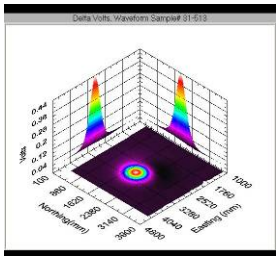
ZZH

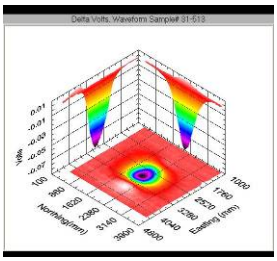
ZX1

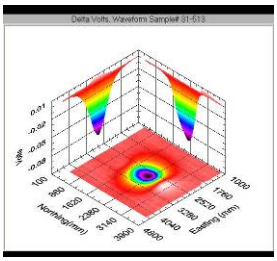
ZY1

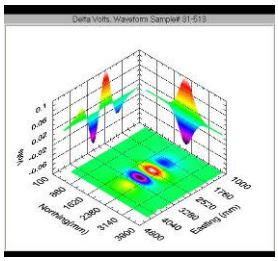
XX1

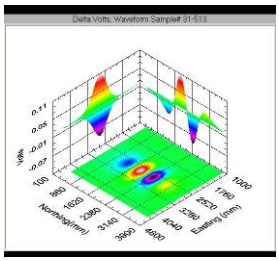
YY1

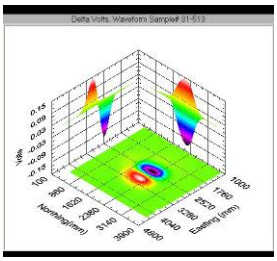
XZM

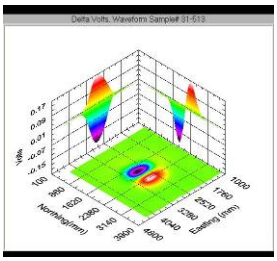
YZM

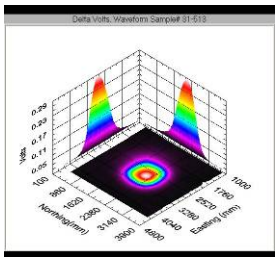
ZZM

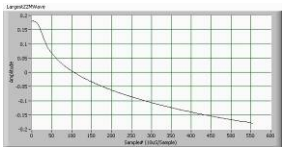
Largest ZZM waveform

Table A.3.8. DiskOne 2007-08-14 75mmAz90Inc0Td73

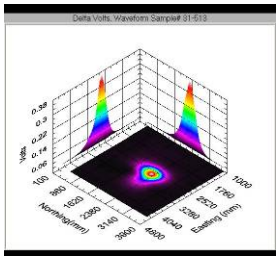
XZE

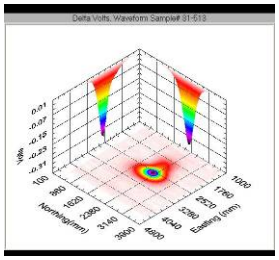
XZF

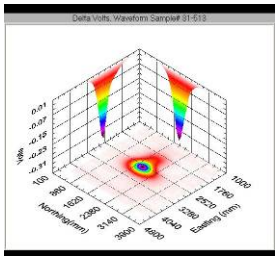
XZG

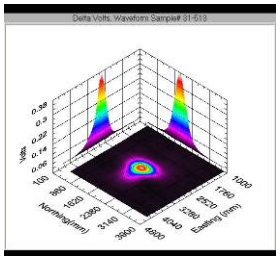
XZH

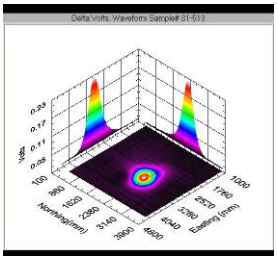
YZE

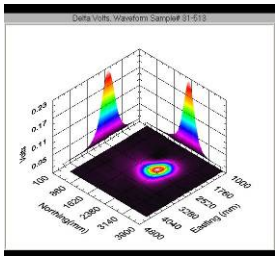
YZF

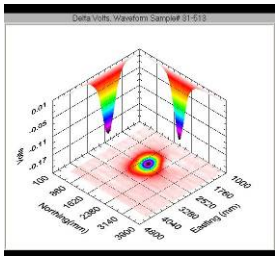
YZG

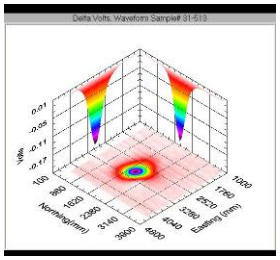
YZH

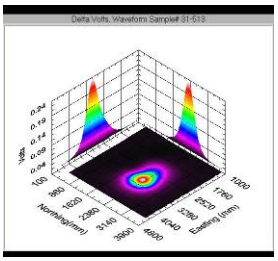
ZZE

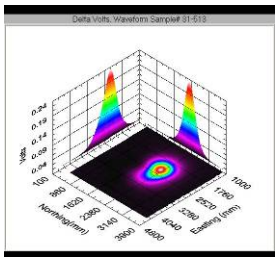
ZZF

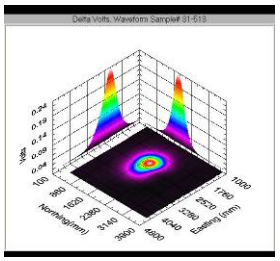
ZZG

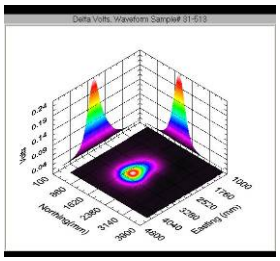
ZZH

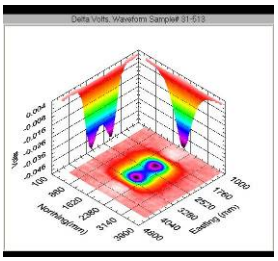
ZX1

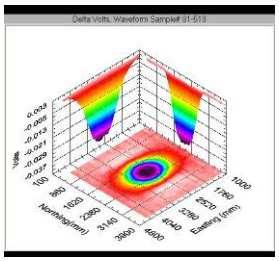
ZY1

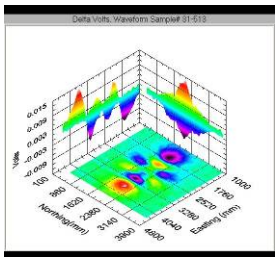
XX1

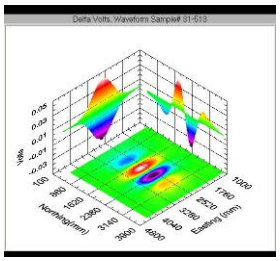
YY1

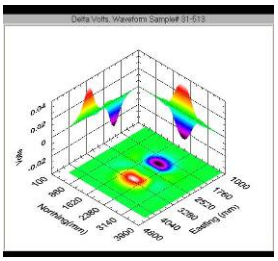
XZM

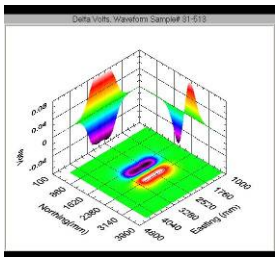
YZM

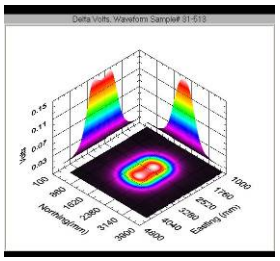
ZZM

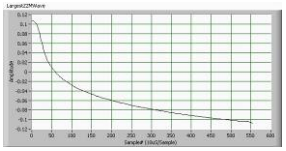
Largest ZZM waveform

Table A.3.9. DiskOne 2007-08-23 75mmAz0Inc0Td103

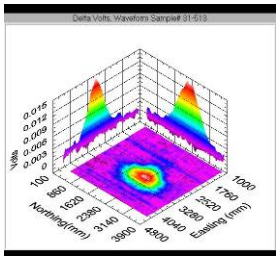
XZE

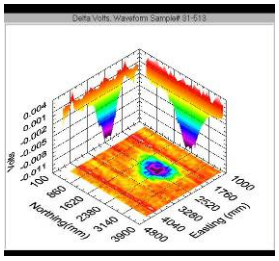
XZF

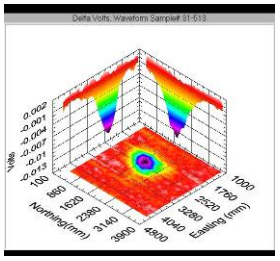
XZG

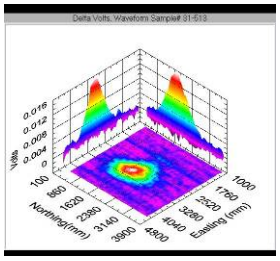
XZH

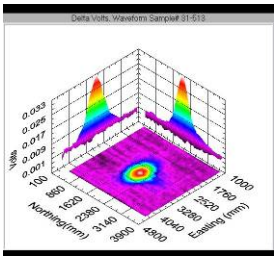
YZE

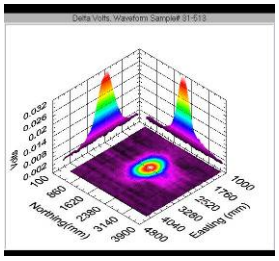
YZF

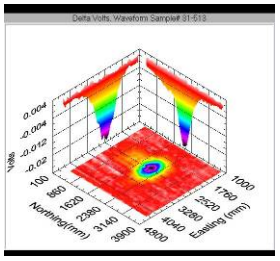
YZG

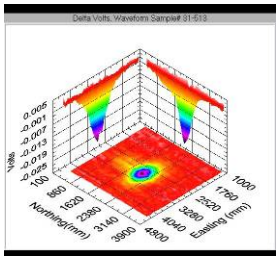
YZH

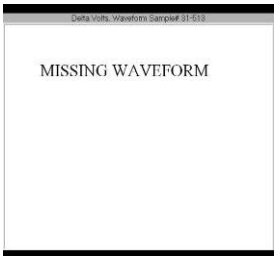

ZZE

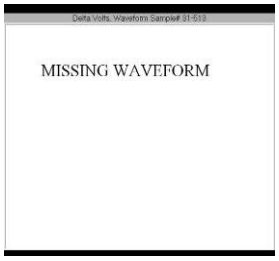

ZZF

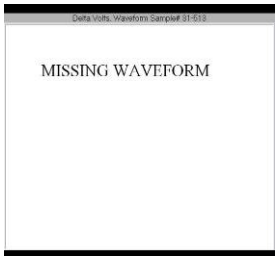

ZZG

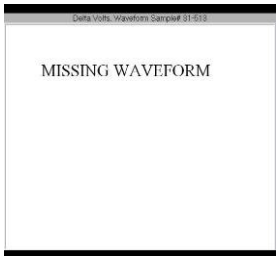

ZZH

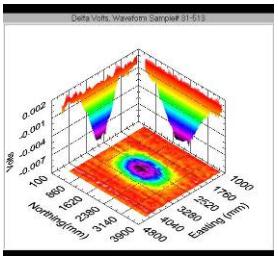
ZX1

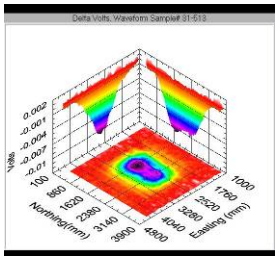
ZY1

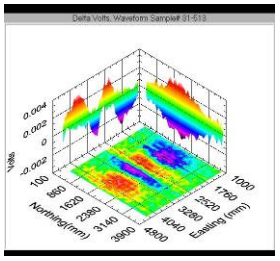
XX1

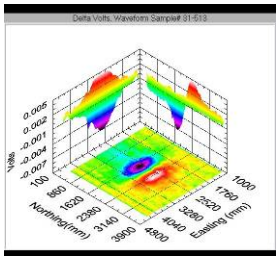
YY1

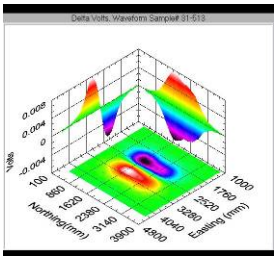
XZM

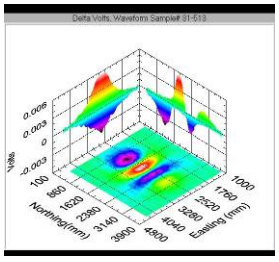
YZM

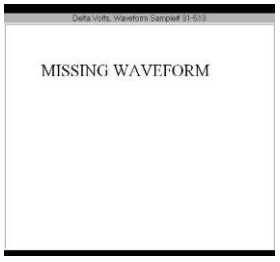

ZZM

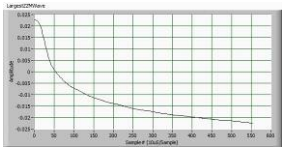
Largest ZZM waveform

Table A.3.10. DiskOne 2007-08-23 75mmAz0Inc45Td103

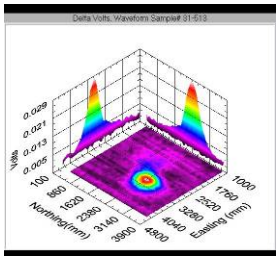
XZE

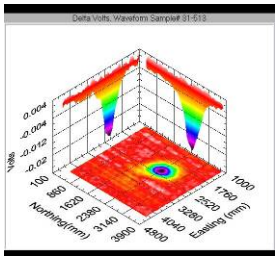
XZF

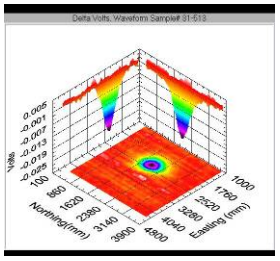
XZG

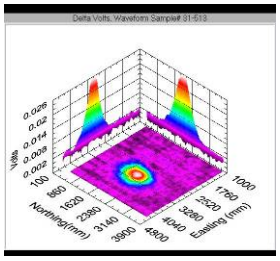
XZH

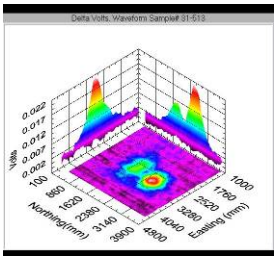
YZE

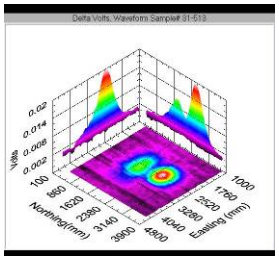
YZF

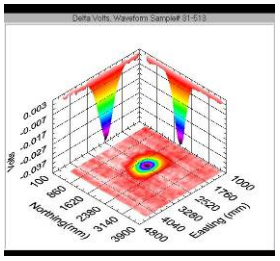
YZG

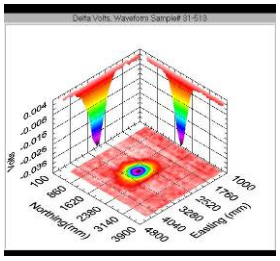
YZH

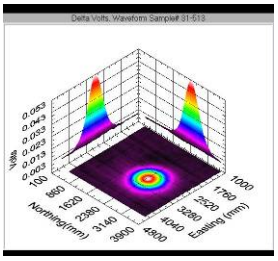
ZZE

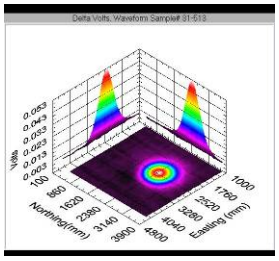
ZZF

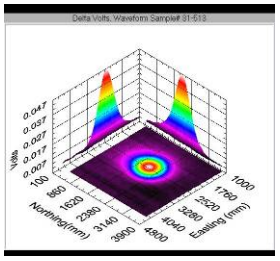
ZZG

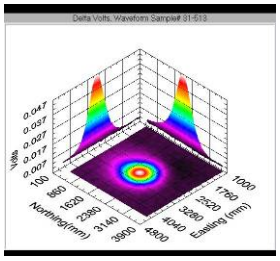
ZZH

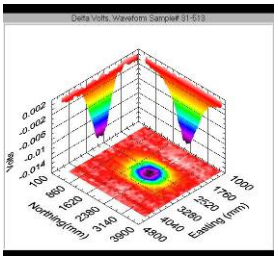
ZX1

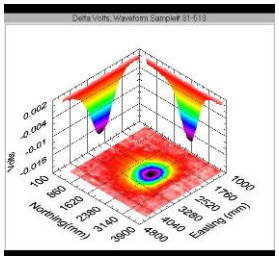
ZY1

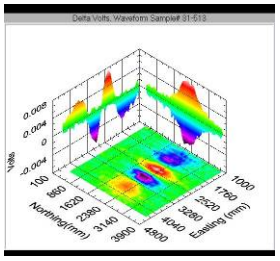
XX1

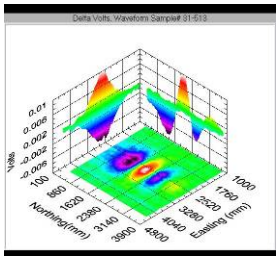
YY1

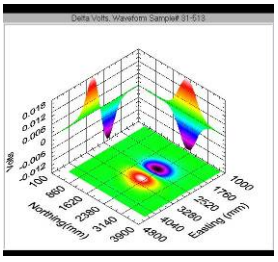
XZM

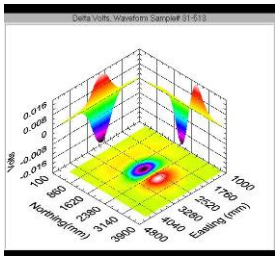
YZM

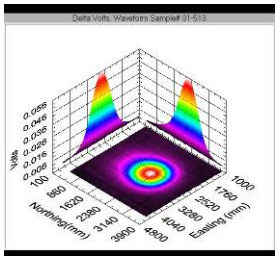
ZZM

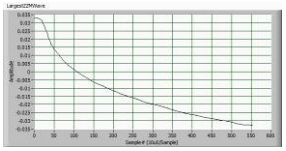
Largest ZZM waveform

Table A.3.11. DiskOne 2007-08-23 75mmAz45Inc45Td103

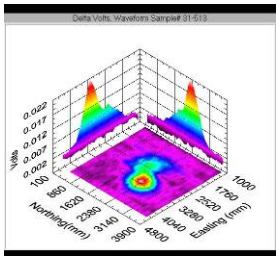
XZE

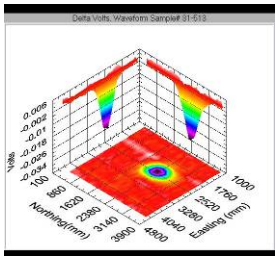
XZF

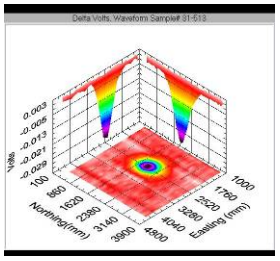
XZG

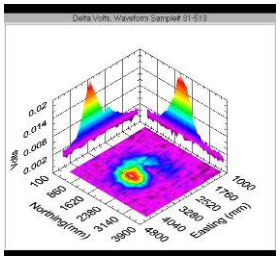
XZH

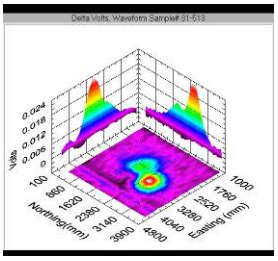
YZE

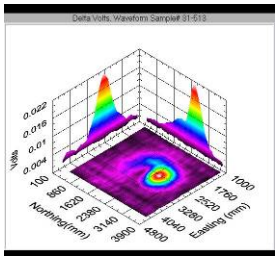
YZF

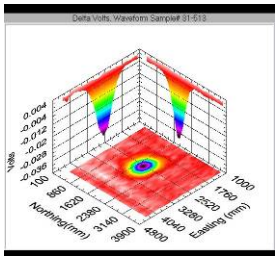
YZG

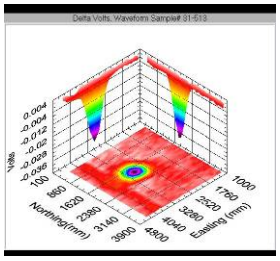
YZH

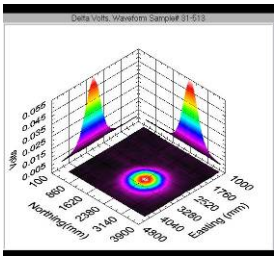
ZZE

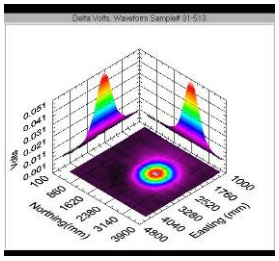
ZZF

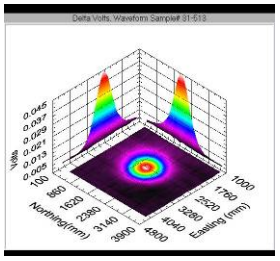
ZZG

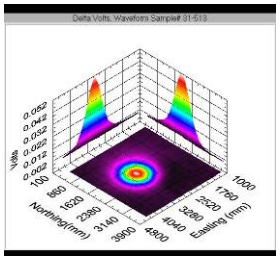
ZZH

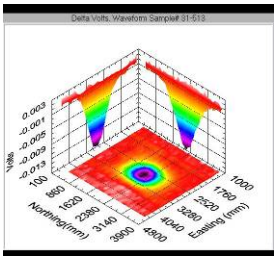
ZX1

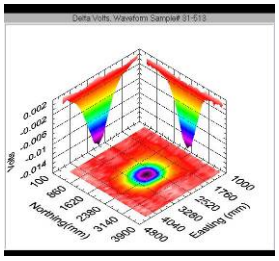
ZY1

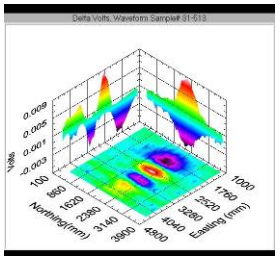
XX1

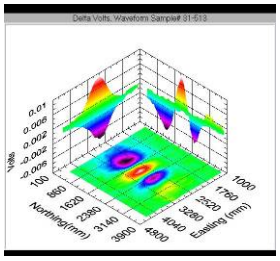
YY1

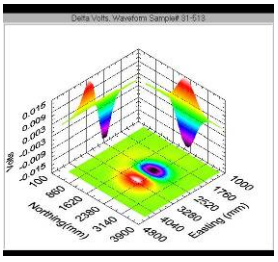
XZM

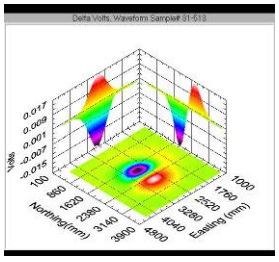
YZM

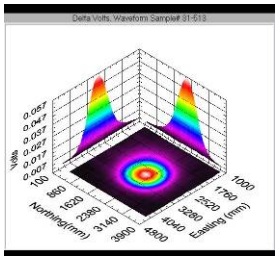
ZZM

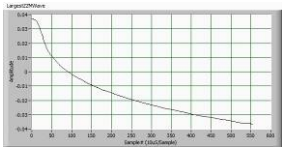
Largest ZZM waveform

# 40 mm

Table A.3.12. DiskOne 2007-08-03 40mmAz0Inc0Td73

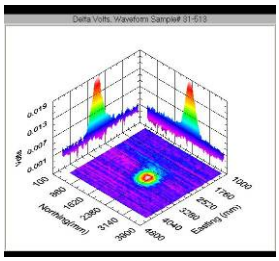
XZE

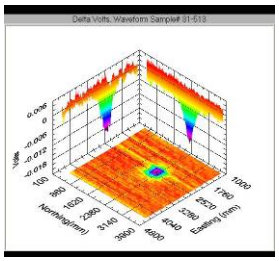
XZF

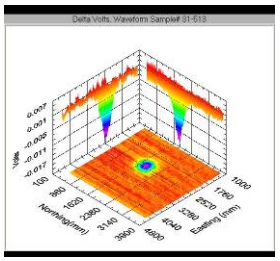
XZG

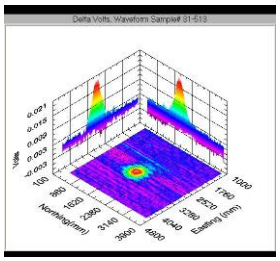
XZH

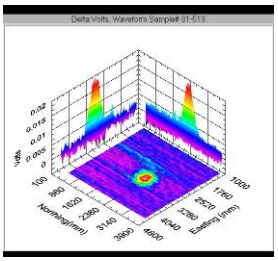
YZE

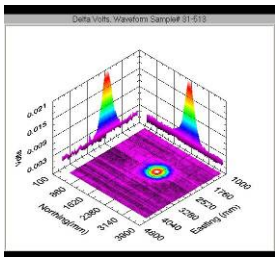
YZF

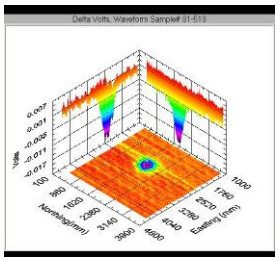
YZG

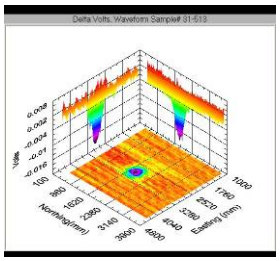
YZH

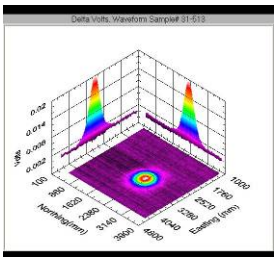
ZZE

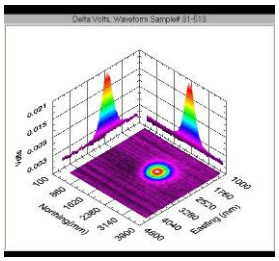
ZZF

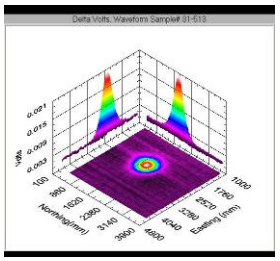
ZZG

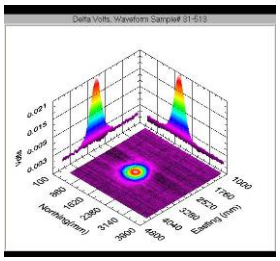
ZZH

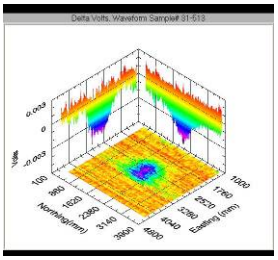
ZX1

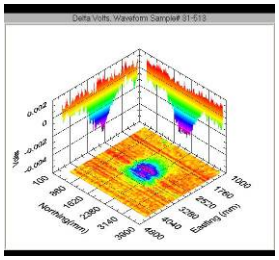
ZY1

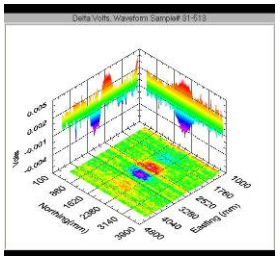
XX1

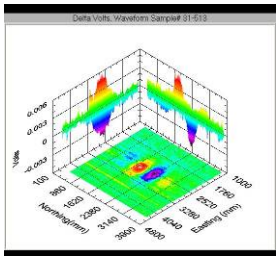
YY1

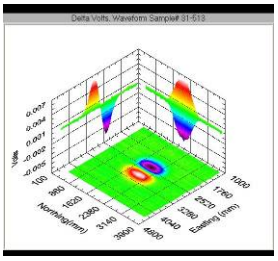
XZM

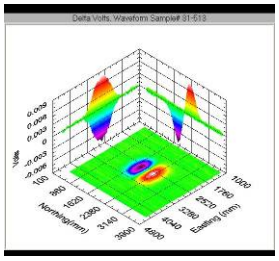
YZM

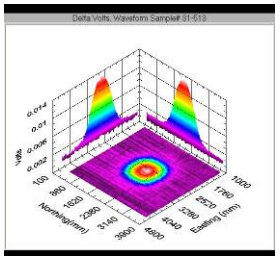
ZZM

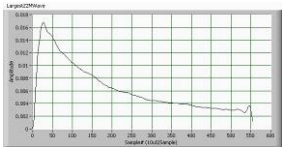
Largest ZZM waveform

# 60 mm (M49A4)

Table A.3.13. DiskOne 2007-07-16 60mmAz0Inc0Td73

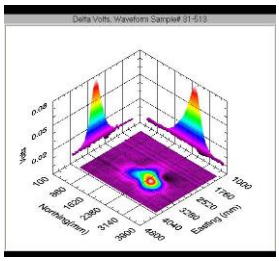
XZE

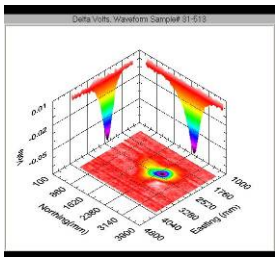
XZF

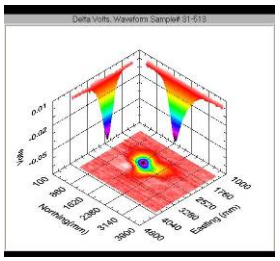
XZG

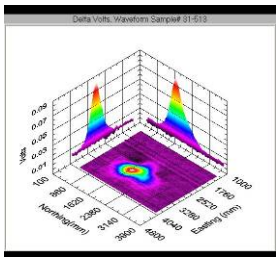
XZH

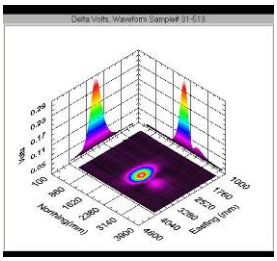
YZE

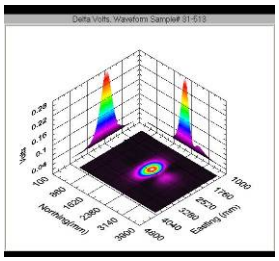
YZF

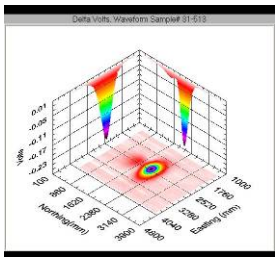
YZG

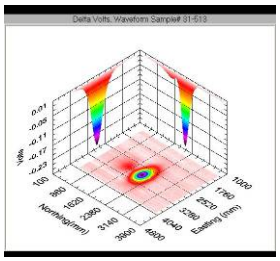
YZH

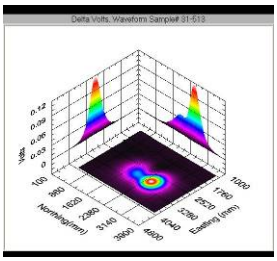
ZZE

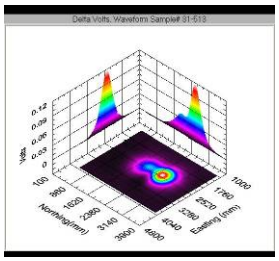
ZZF

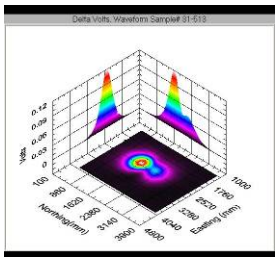
ZZG

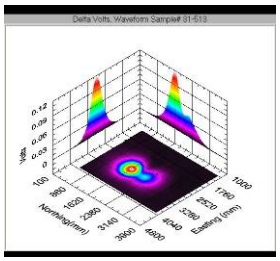
ZZH

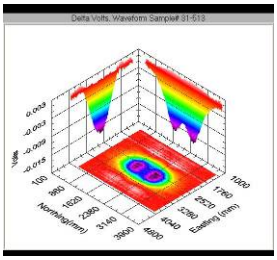
ZX1

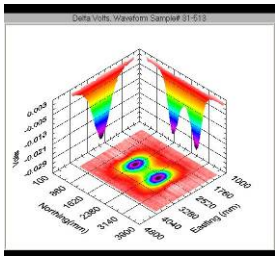
ZY1

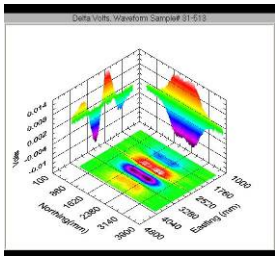
XX1

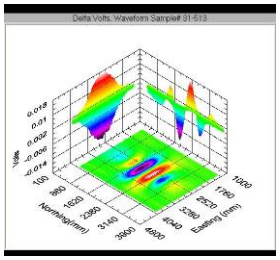
YY1

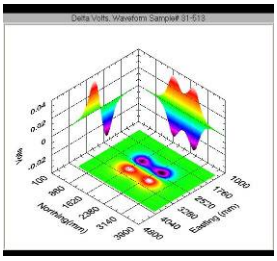
XZM

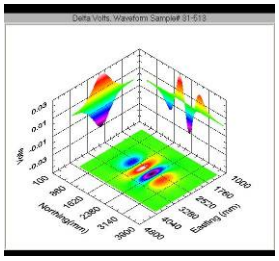
YZM

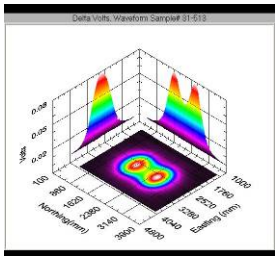
ZZM

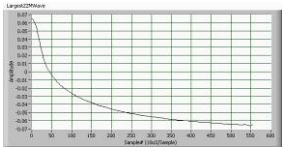
Largest ZZM waveform

Table A.3.14. DiskOne 2007-07-17 60mmAz0Inc90Td73

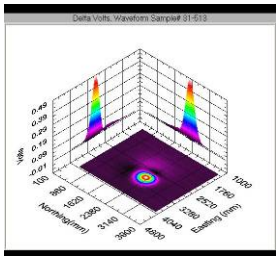
XZE

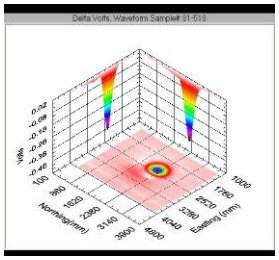
XZF

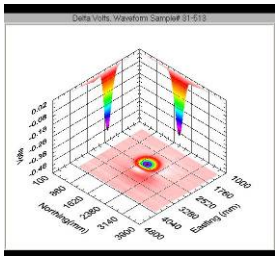
XZG

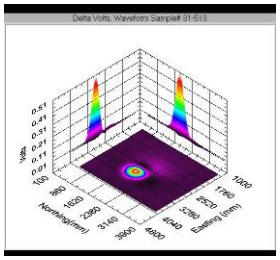
XZH

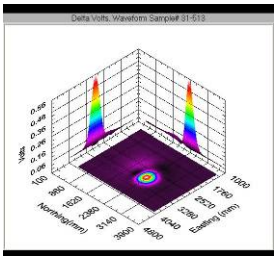
YZE

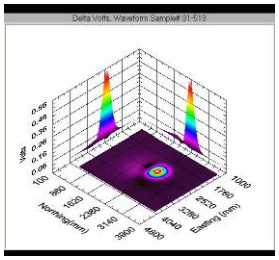
YZF

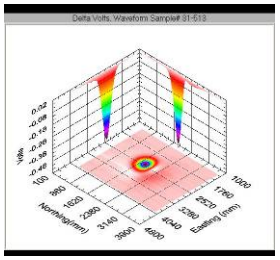
YZG

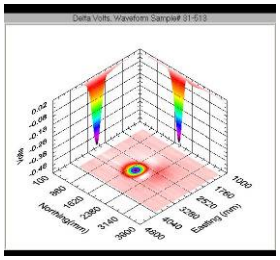
YZH

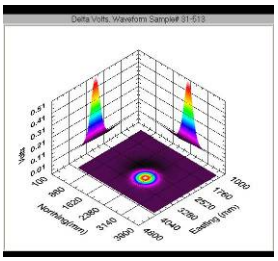
ZZE

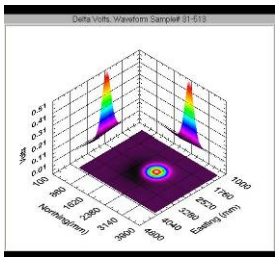
ZZF

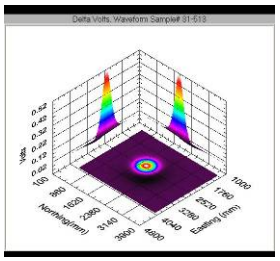
ZZG

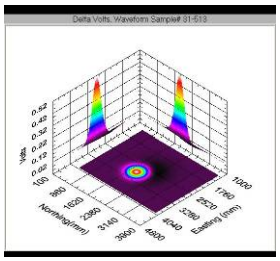
ZZH

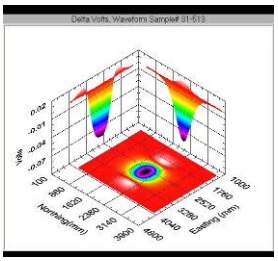
ZX1

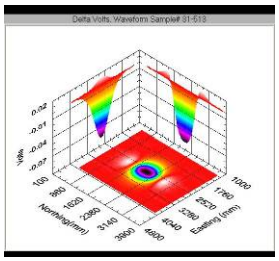
ZY1

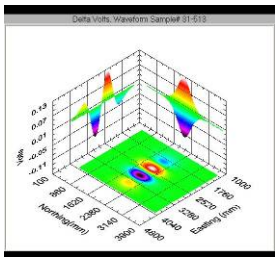
XX1

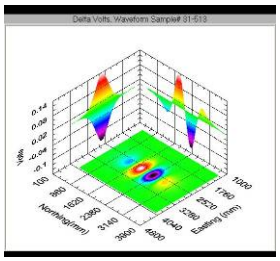
YY1

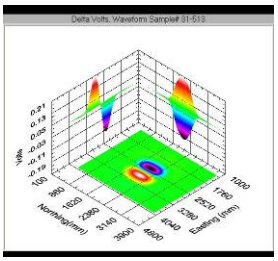
XZM

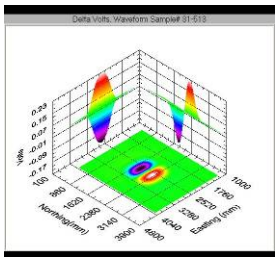
YZM

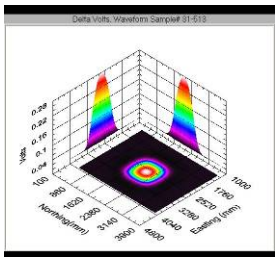
ZZM

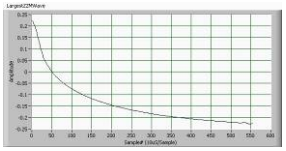
Largest ZZM waveform

Table A.3.15. DiskOne 2007-08-17 60mmAz0Inc45Td103

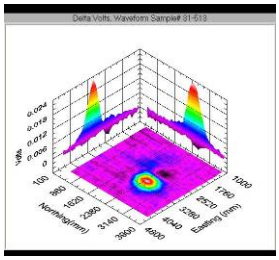
XZE

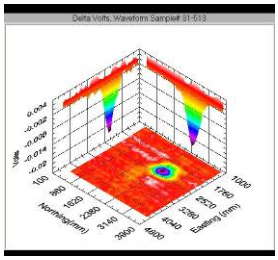
XZF

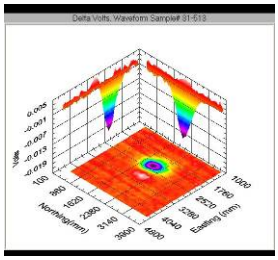
XZG

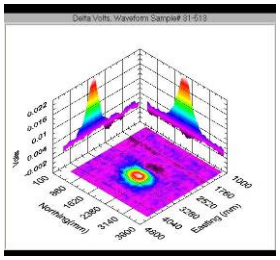
XZH

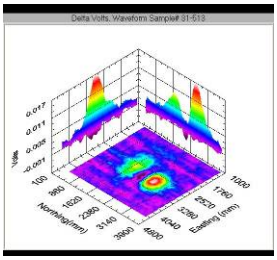
YZE

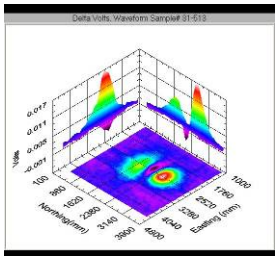
YZF

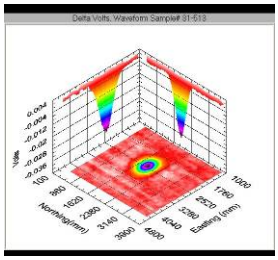
YZG

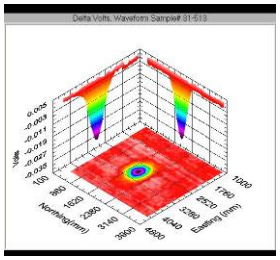
YZH

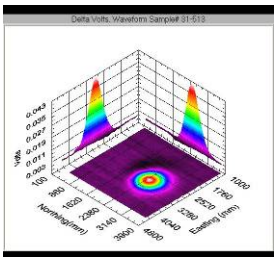
ZZE

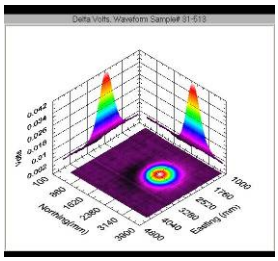
ZZF

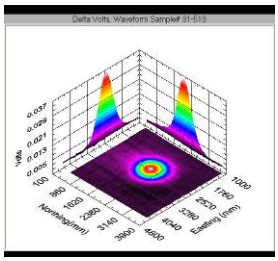
ZZG

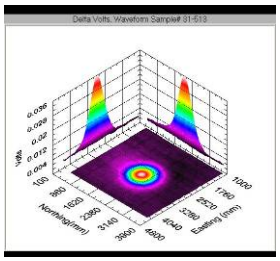
ZZH

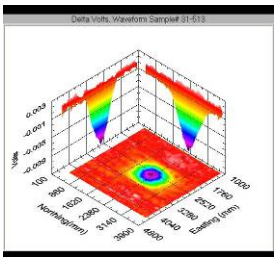
ZX1

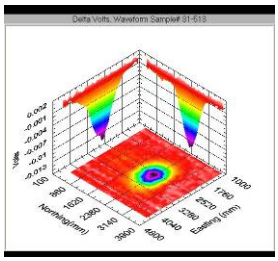
ZY1

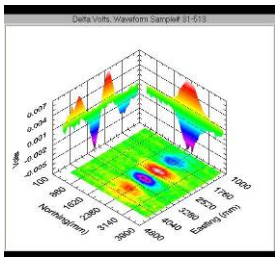
XX1

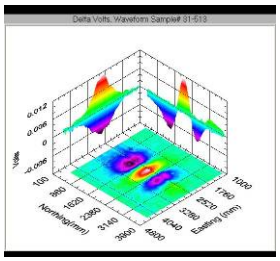
YY1

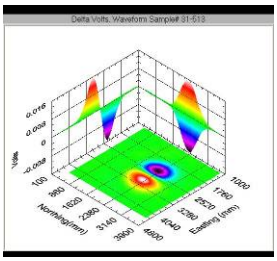
XZM

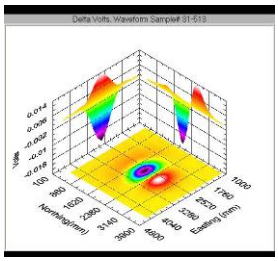
YZM

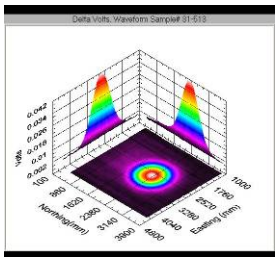
ZZM

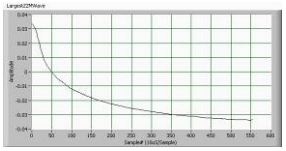
Largest ZZM waveform

# 2.75 Inch Rocket

Recalling the naming convention outlined in table A.1.1, files named '2p75' reference datasets taken from a 2.75 inch rocket ordnance. The decimal point has been replaced with the character 'p'.

Table A.3.16. DiskOne 2007-07-20 2p75Az0Inc45Td73

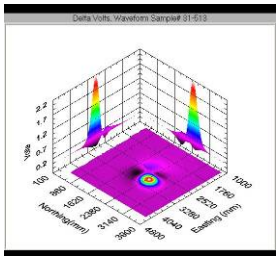
XZE

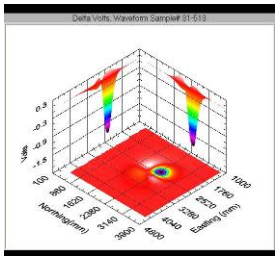
XZF

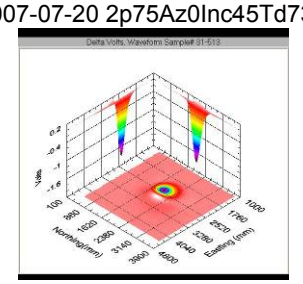
XZG

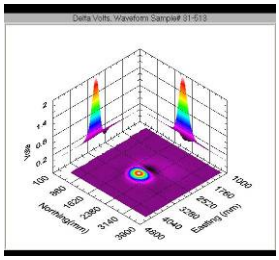
XZH

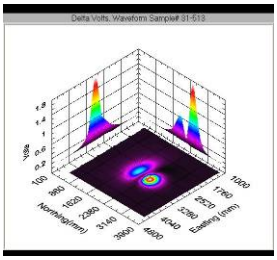
YZE

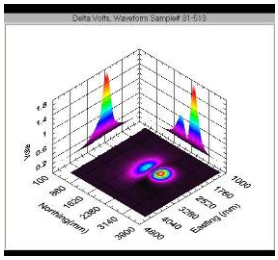
YZF

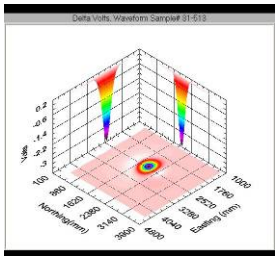
YZG

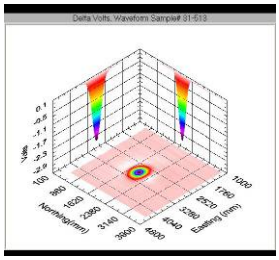
YZH

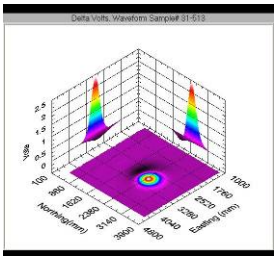
ZZE

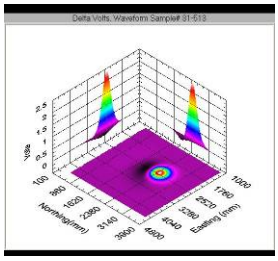
ZZF

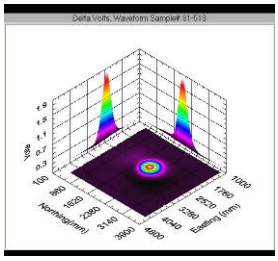
ZZG

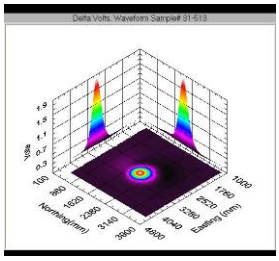
ZZH

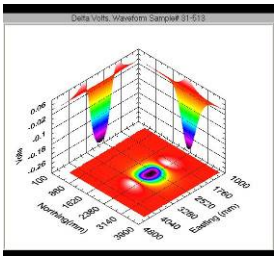
ZX1

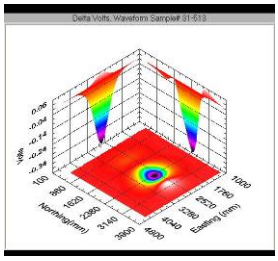
ZY1

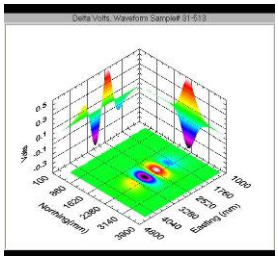
XX1

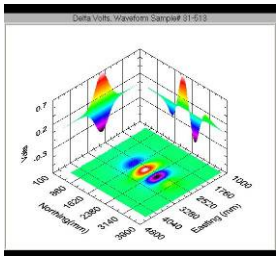
YY1

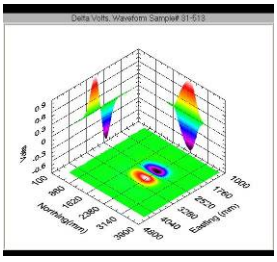
XZM

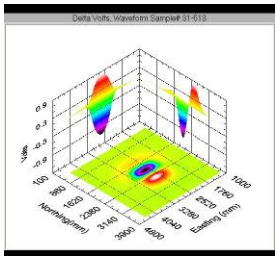
YZM

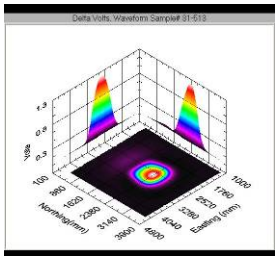
ZZM

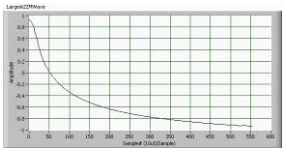
Largest ZZM waveform

Table A.3.17. DiskOne 2007-07-20 2p75Az90Inc0Td73

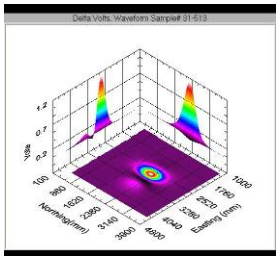
XZE

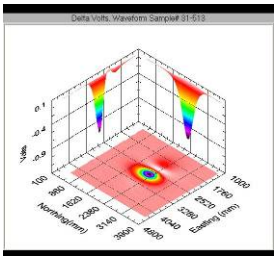
XZF

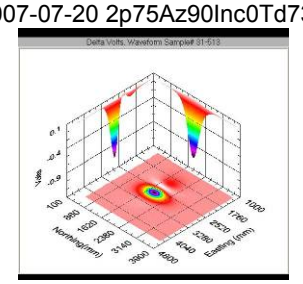
XZG

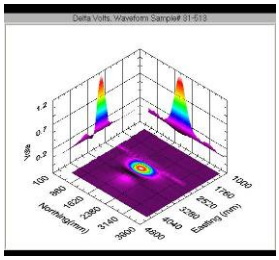
XZH

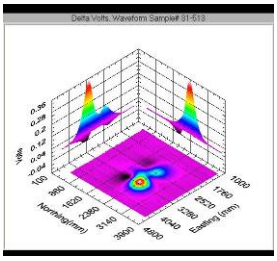
YZE

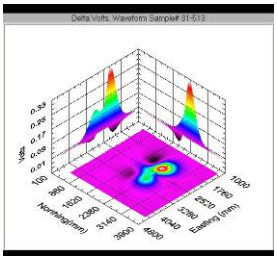
YZF

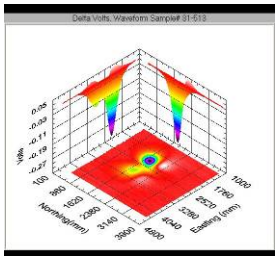
YZG

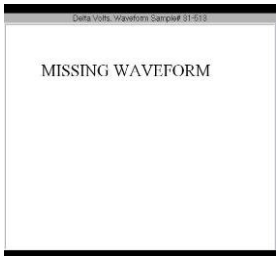

YZH

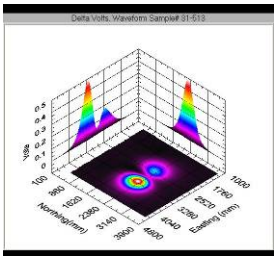
ZZE

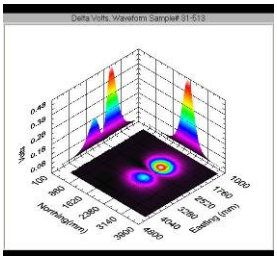
ZZF

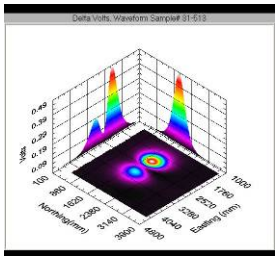
ZZG

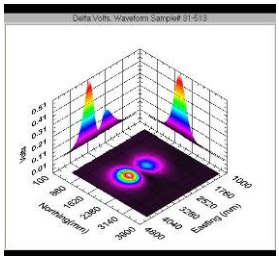
ZZH

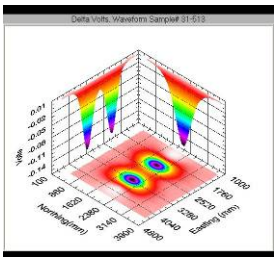
ZX1

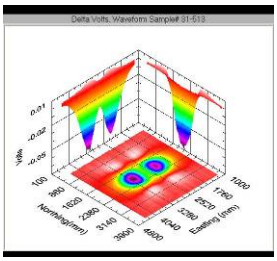
ZY1

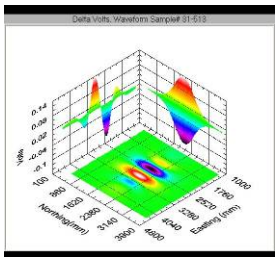
XX1

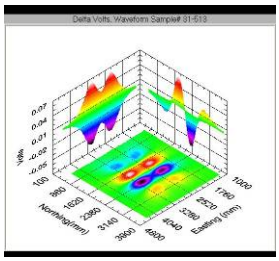
YY1

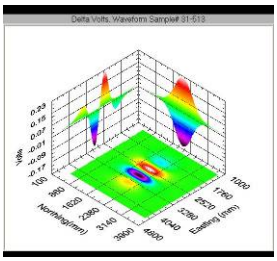
XZM

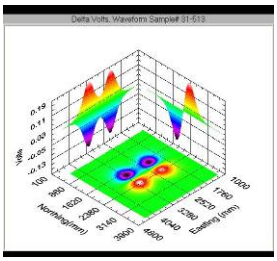
YZM

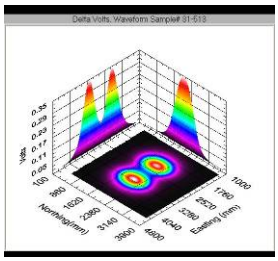
ZZM

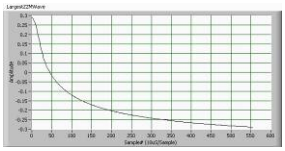
Largest ZZM waveform

Table A.3.18. DiskOne 2007-08-17 2p75Az0Inc45Td103

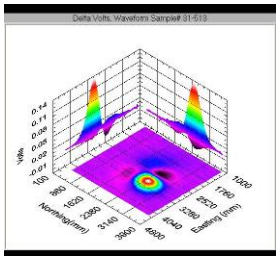
XZE

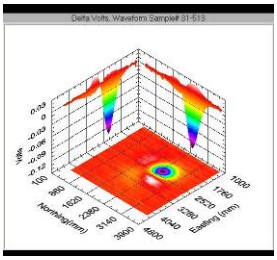
XZF

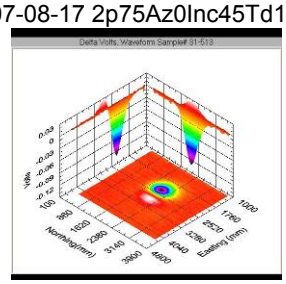
XZG

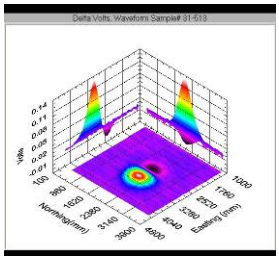
XZH

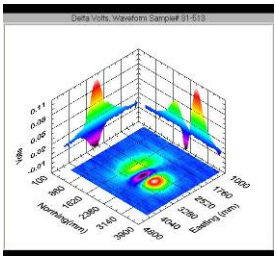
YZE

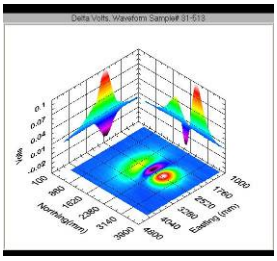
YZF

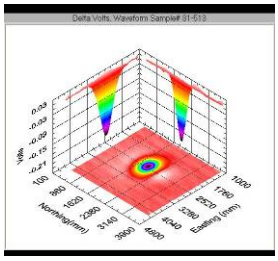
YZG

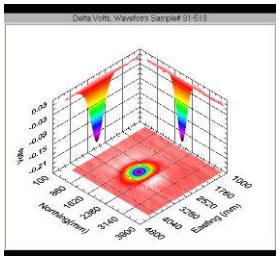
YZH

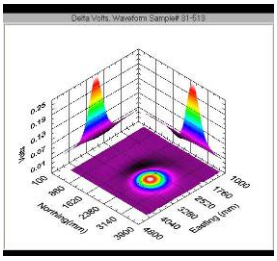
ZZE

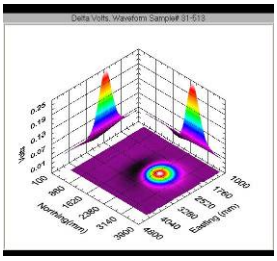
ZZF

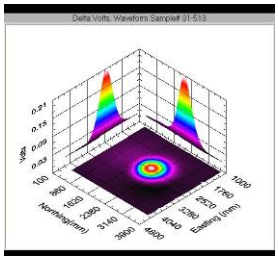
ZZG

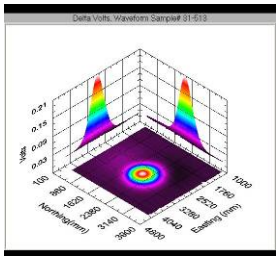
ZZH

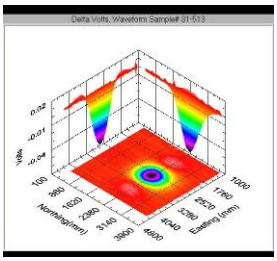
ZX1

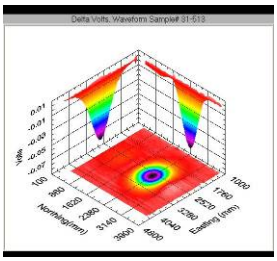
ZY1

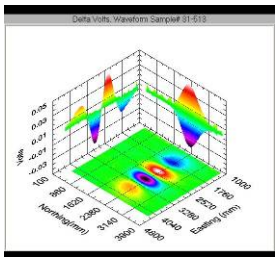
XX1

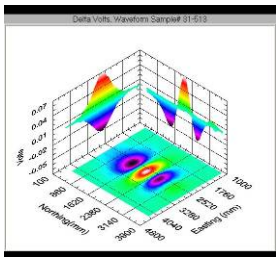
YY1

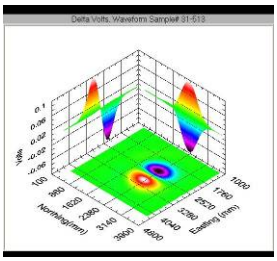
XZM

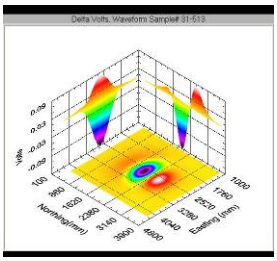
YZM

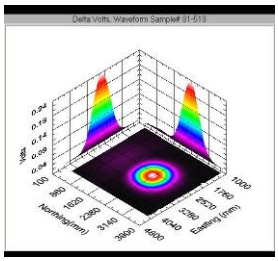
ZZM

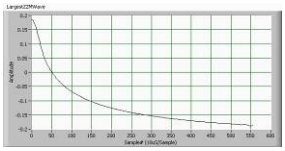
Largest ZZM waveform

Table A.3.19. DiskOne 2007-08-20 2p75Az0Inc90Td103

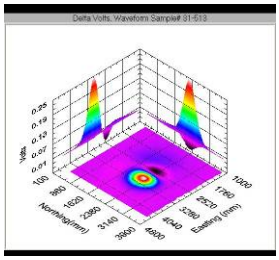
XZE

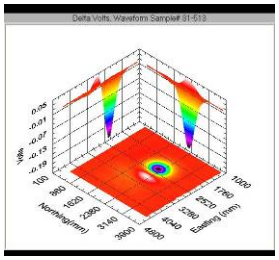
XZF

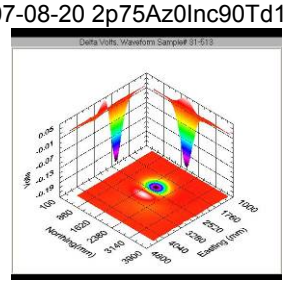
XZG

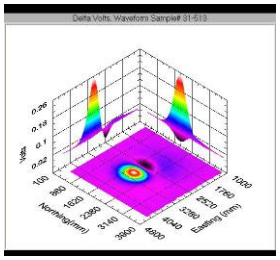
XZH

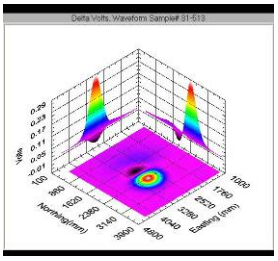
YZE

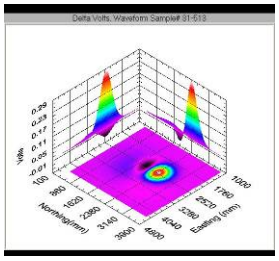
YZF

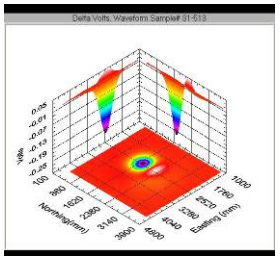
YZG

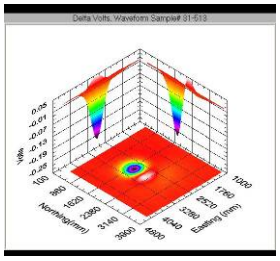
YZH

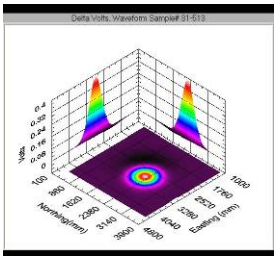
ZZE

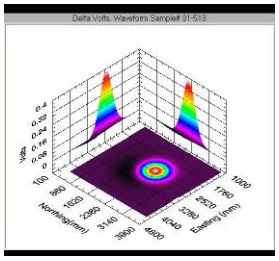
ZZF

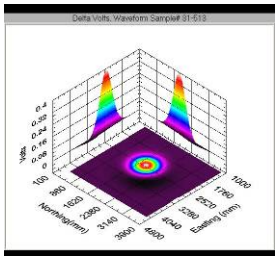
ZZG

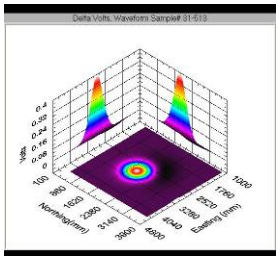
ZZH

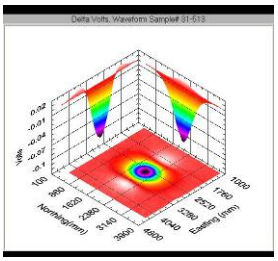
ZX1

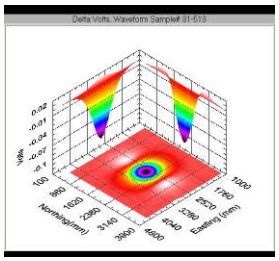
ZY1

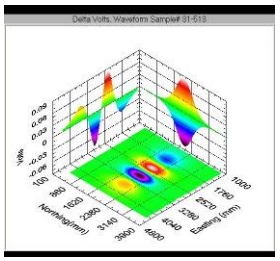
XX1

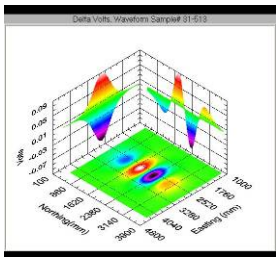
YY1

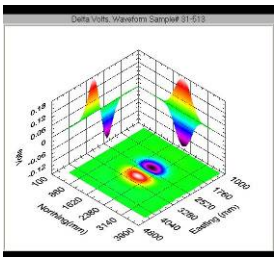
XZM

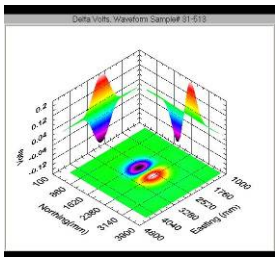
YZM

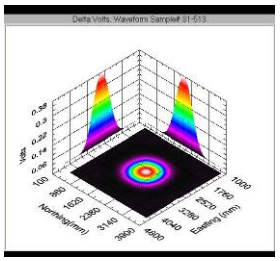
ZZM

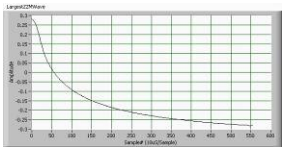
Largest ZZM waveform

Table A.3.20. DiskOne 2007-08-20 2p75Az45Inc45Td103Two

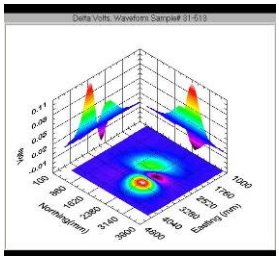
XZE

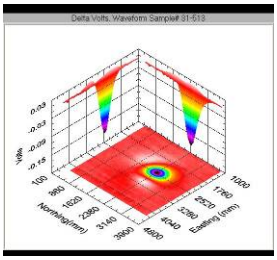
XZF

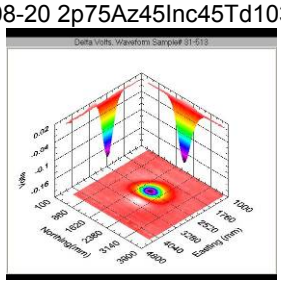
XZG

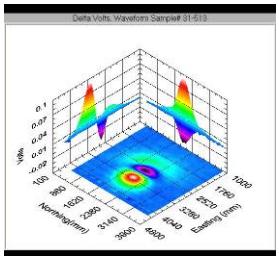
XZH

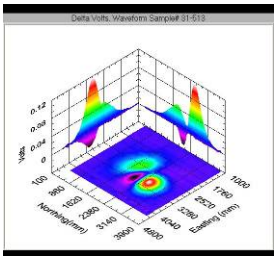
YZE

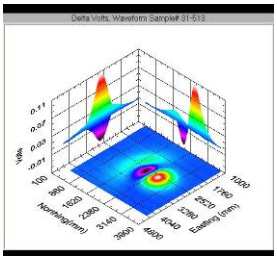
YZF

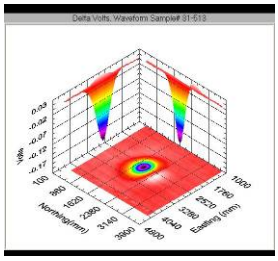
YZG

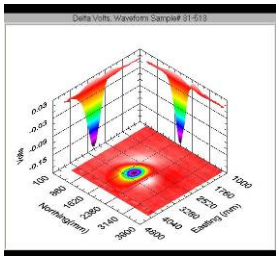
YZH

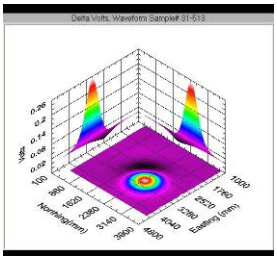
ZZE

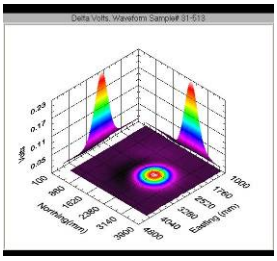
ZZF

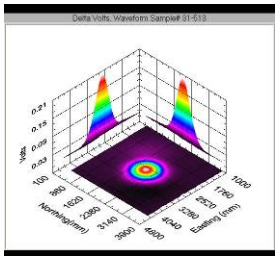
ZZG

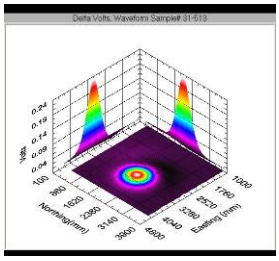
ZZH

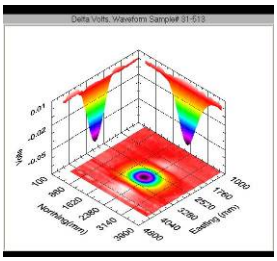
ZX1

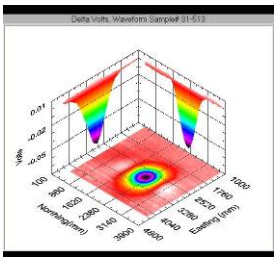
ZY1

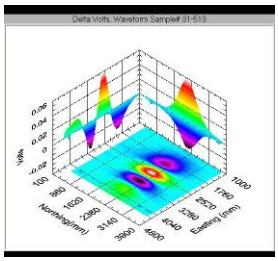
XX1

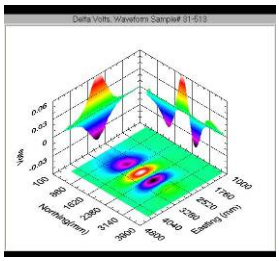
YY1

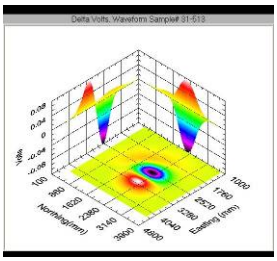
XZM

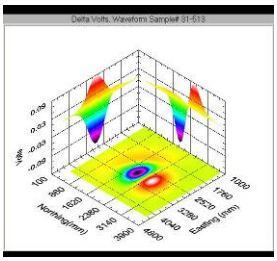
YZM

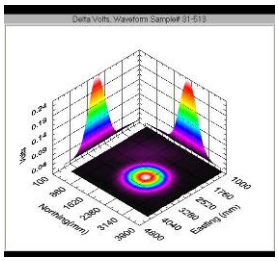
ZZM

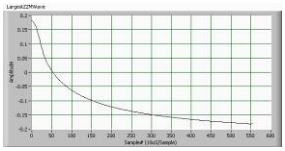
Largest ZZM waveform

# 57 mm

Table A.3.21. DiskOne 2007-07-26 57mmAz45Inc45Td73

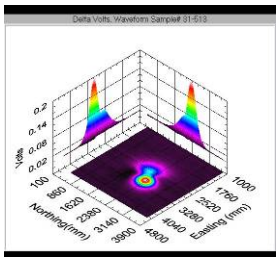
XZE

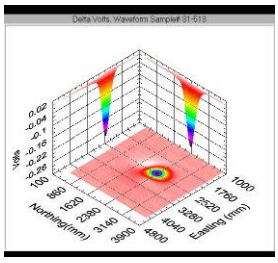
XZF

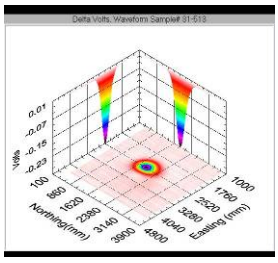
XZG

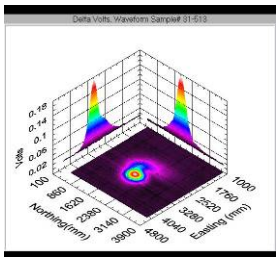
XZH

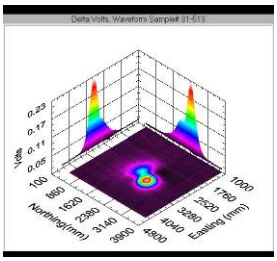
YZE

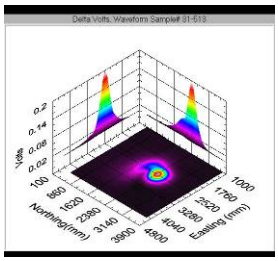
YZF

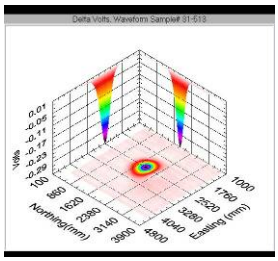
YZG

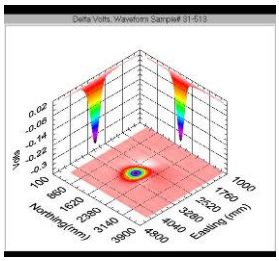
YZH

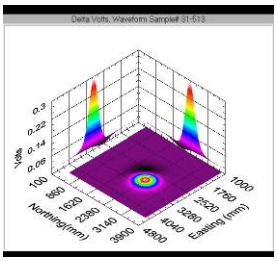
ZZE

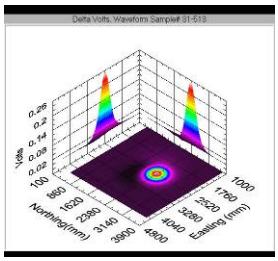
ZZF

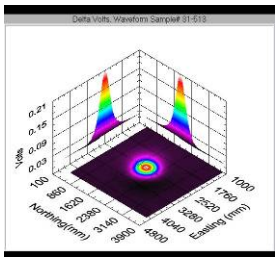
ZZG

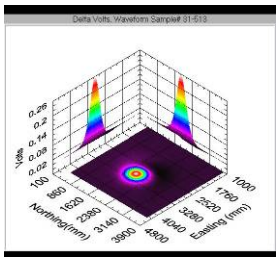
ZZH

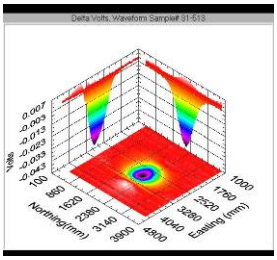
ZX1

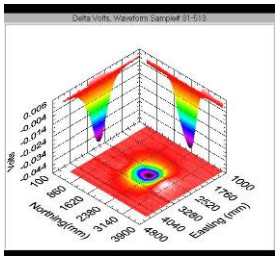
ZY1

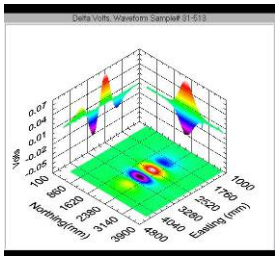
XX1

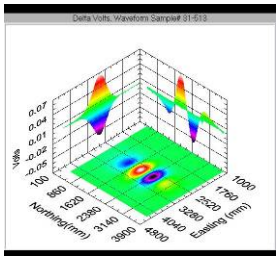
YY1

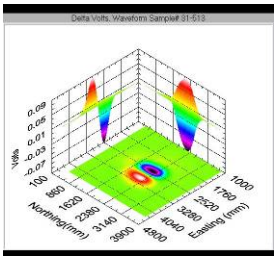
XZM

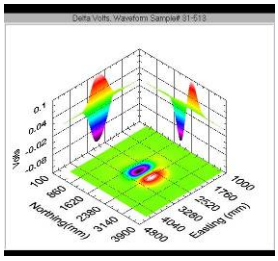
YZM

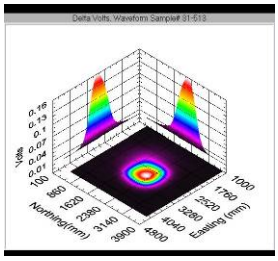
ZZM

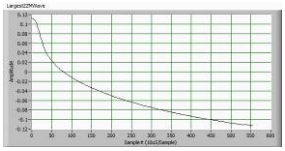
Largest ZZM waveform

# BDU-28

Due to its folding fins, the BDU-28 may be oriented with any numbers of fins tucked in or out. Unless otherwise noted the ordnance was surveyed with its fins out.

The dataset *2007-08-22_BDU-28Az0Inc90Td013* was named incorrectly. A typographical error occurred, the depth was really 103, not 013.

Table A.3.22. DiskOne 2007-08-08 BDU-28Az0Inc90Td73

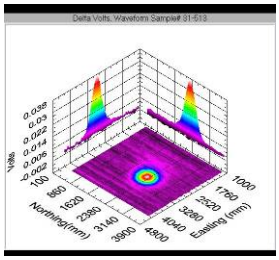
XZE

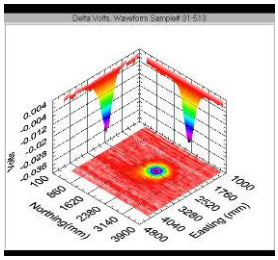
XZF

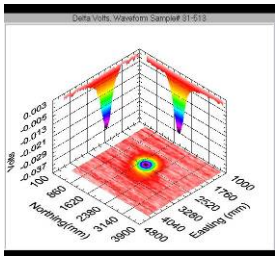
XZG

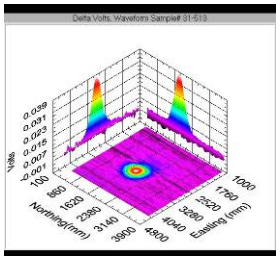
XZH

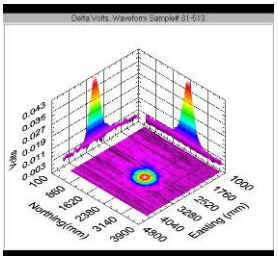
YZE

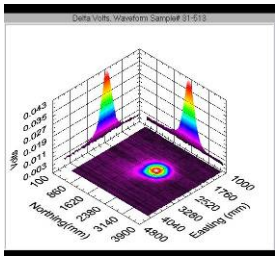
YZF

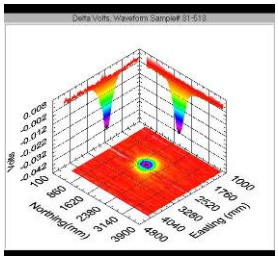
YZG

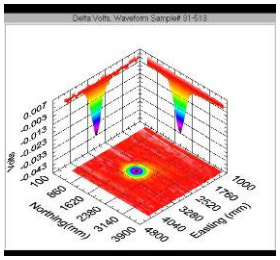
YZH

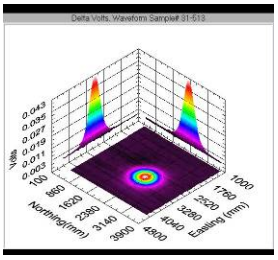
ZZE

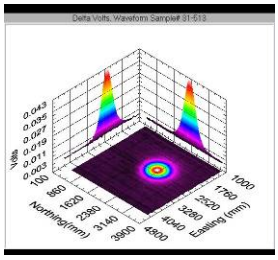
ZZF

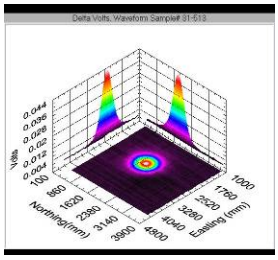
ZZG

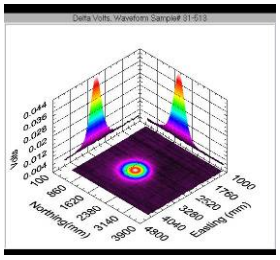
ZZH

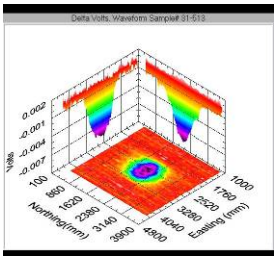
ZX1

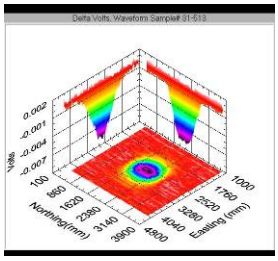
ZY1

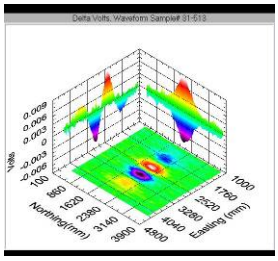
XX1

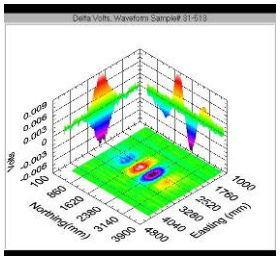
YY1

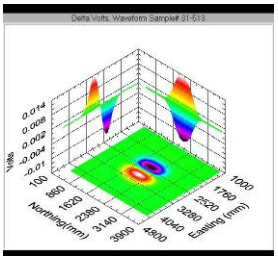
XZM

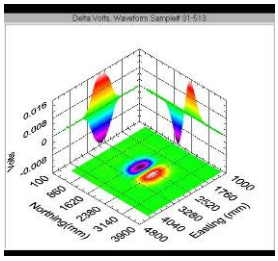
YZM

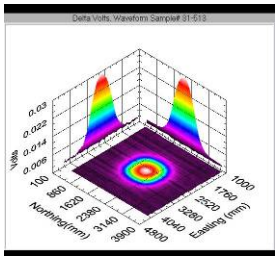
ZZM

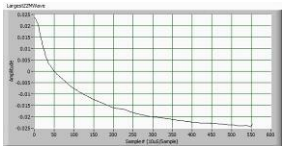
Largest ZZM waveform

Table A.3.23. DiskOne 2007-08-14 BDU-28Az0Inc0FinsInTd73

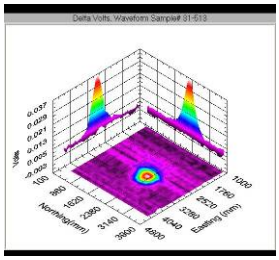
XZE

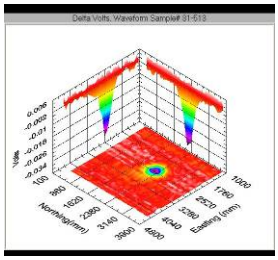
XZF

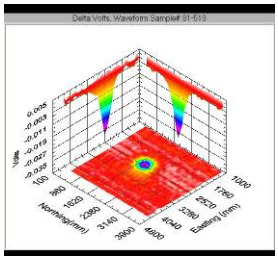
XZG

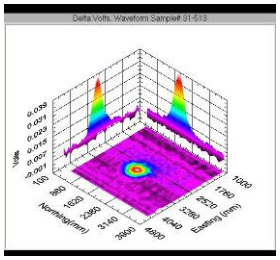
XZH

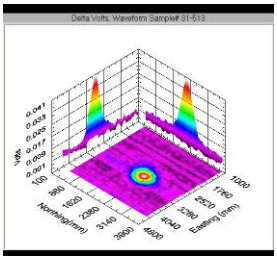
YZE

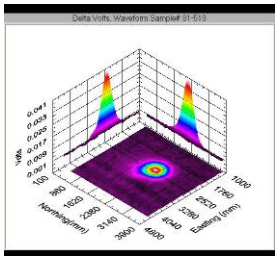
YZF

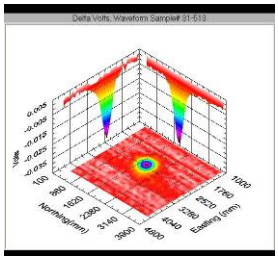
YZG

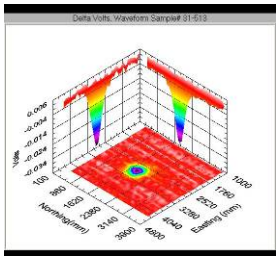
YZH

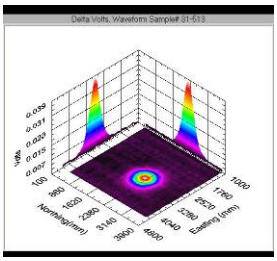
ZZE

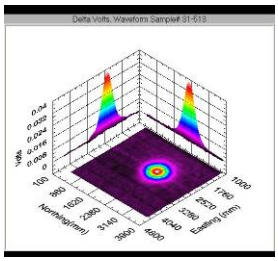
ZZF

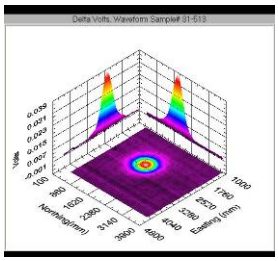
ZZG

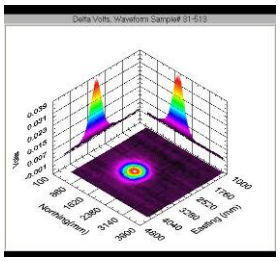
ZZH

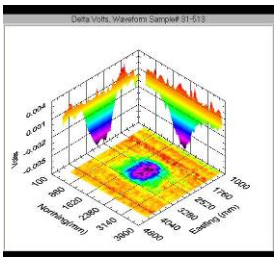
ZX1

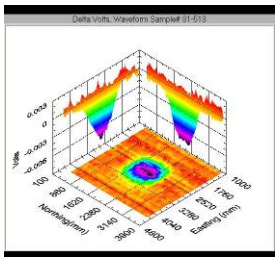
ZY1

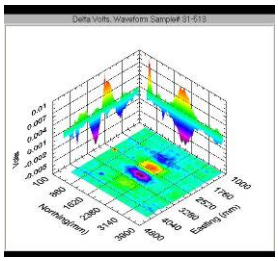
XX1

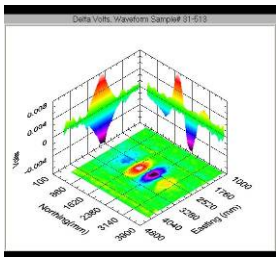
YY1

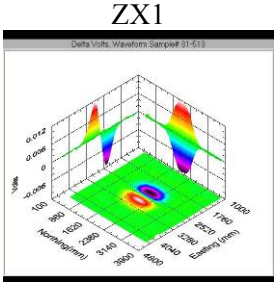
XZM

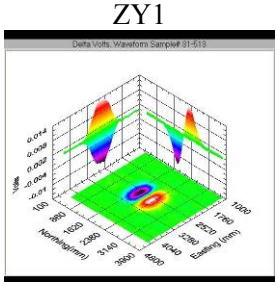
YZM

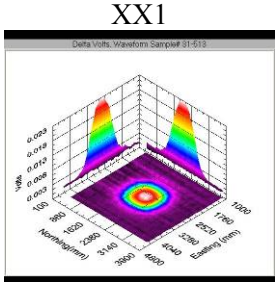
ZZM

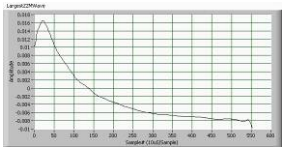
Largest ZZM waveform

Table A.3.24. DiskOne 2007-08-14 BDU-28Az90Inc0FinsInTd73

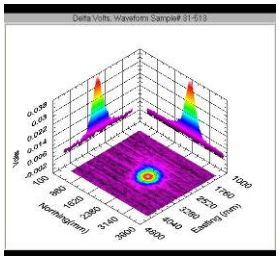
XZE

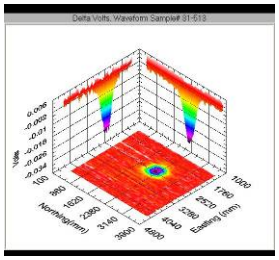
XZF

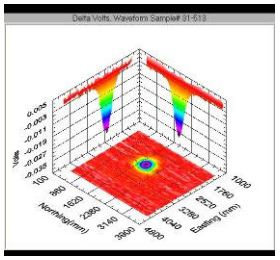
XZG

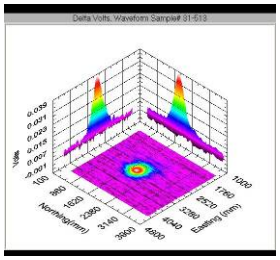
XZH

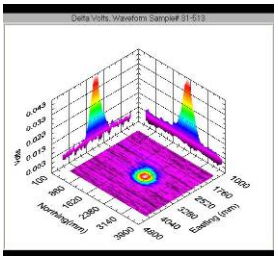
YZE

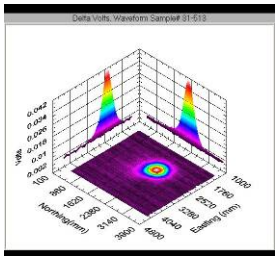
YZF

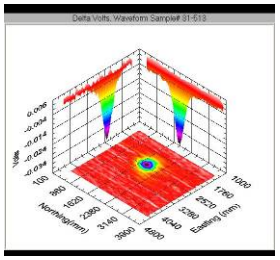
YZG

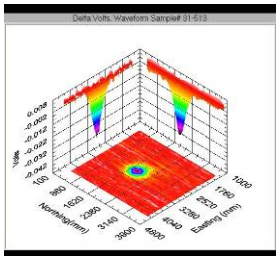
YZH

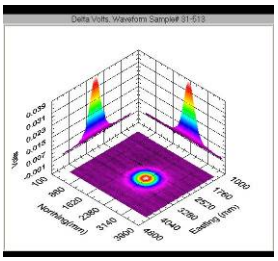
ZZE

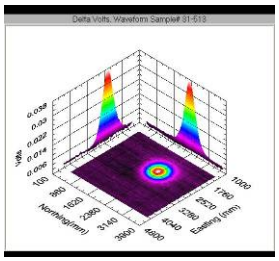
ZZF

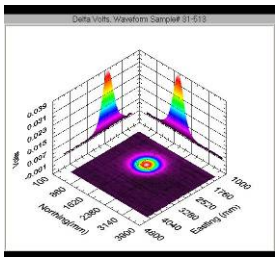
ZZG

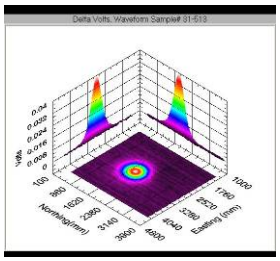
ZZH

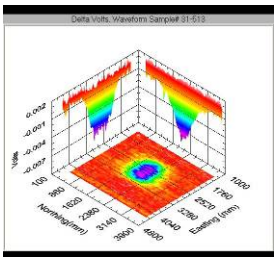
ZX1

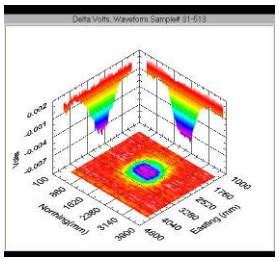
ZY1

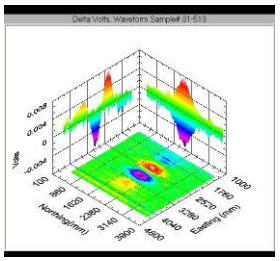
XX1

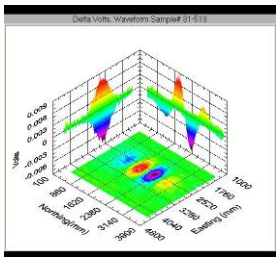
YY1

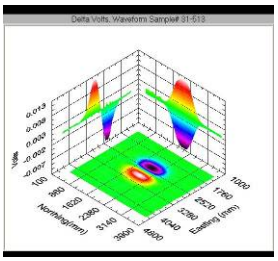
XZM

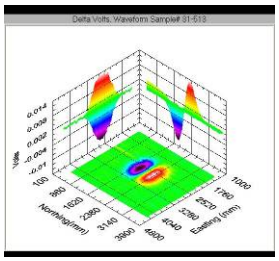
YZM

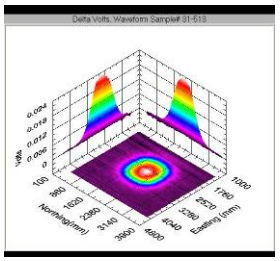
ZZM

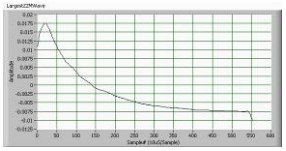
Largest ZZM waveform

Table A.3.25. DiskOne 2007-08-15 BDU-28Az45Inc45FinsInTd73

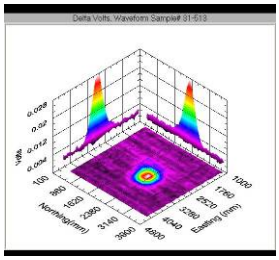
XZE

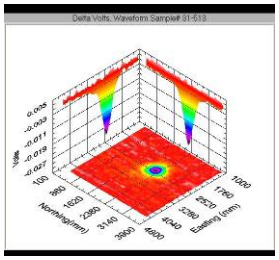
XZF

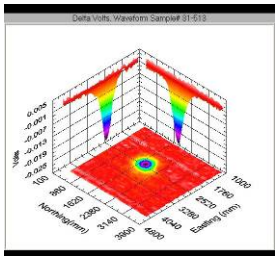
XZG

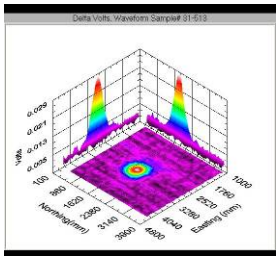
XZH

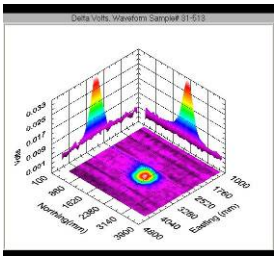
YZE

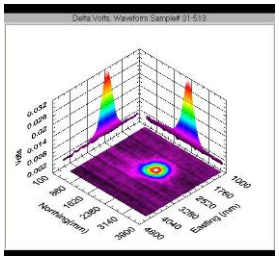
YZF

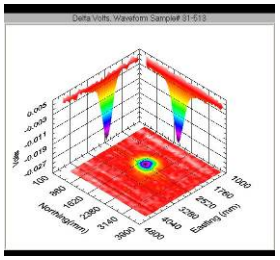
YZG

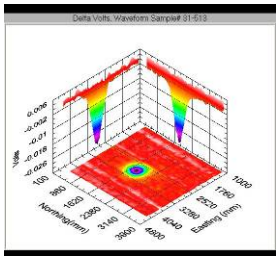
YZH

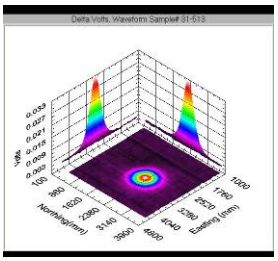
ZZE

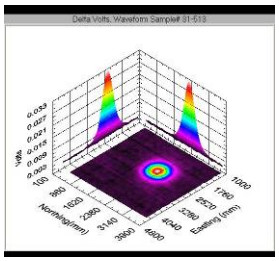
ZZF

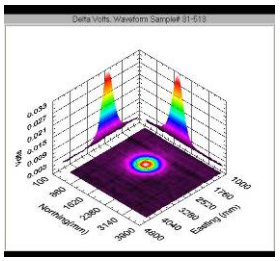
ZZG

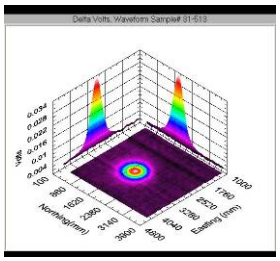
ZZH

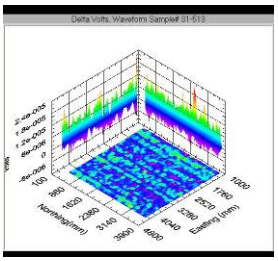
ZX1

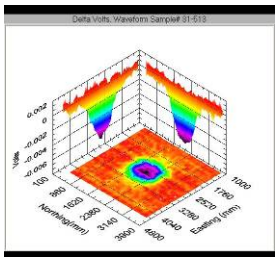
ZY1

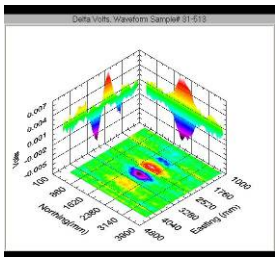
XX1

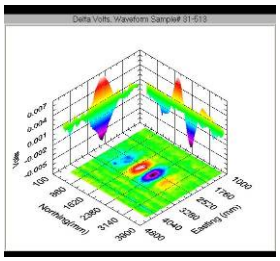
YY1

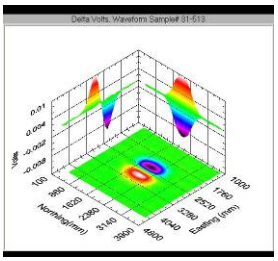
XZM

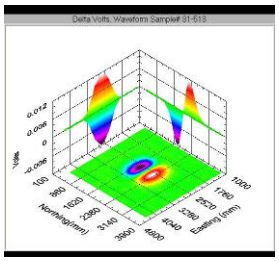
YZM

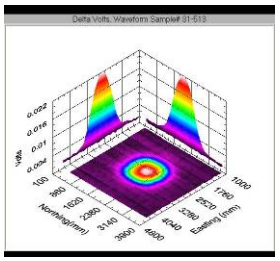
ZZM

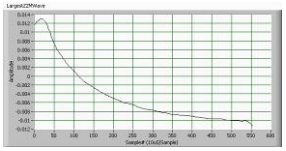
Largest ZZM waveform

Table A.3.26. DiskOne 2007-08-22 BDU-28Az0Inc90Td013Two

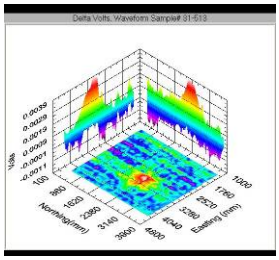
XZE

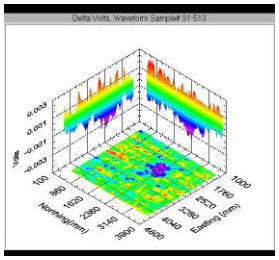
XZF

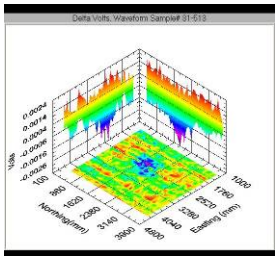
XZG

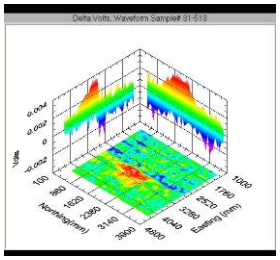
XZH

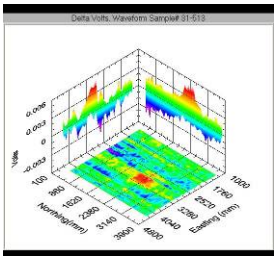
YZE

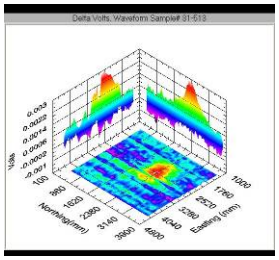
YZF

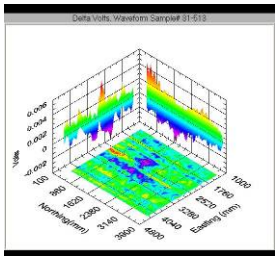
YZG

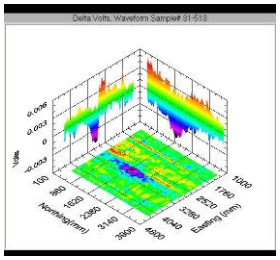
YZH

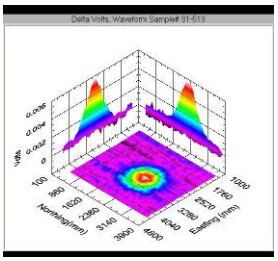
ZZE

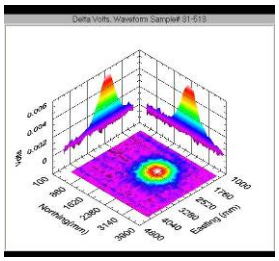
ZZF

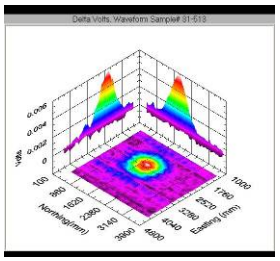
ZZG

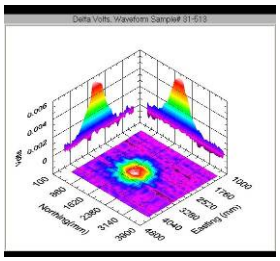
ZZH

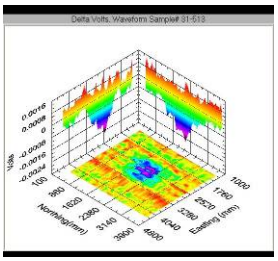
ZX1

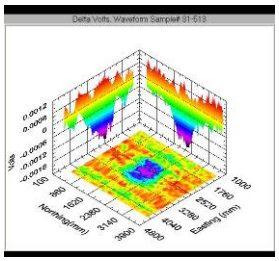
ZY1

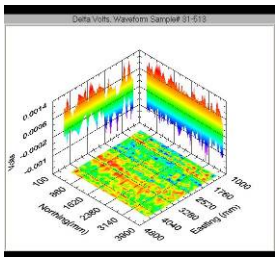
XX1

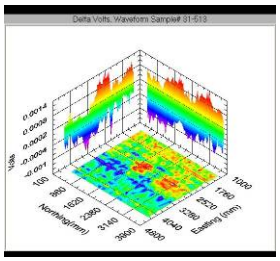
YY1

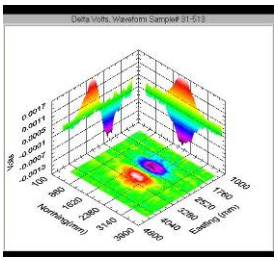
XZM

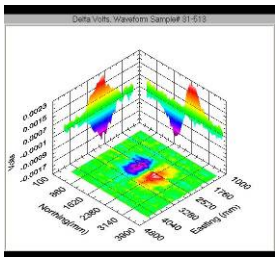
YZM

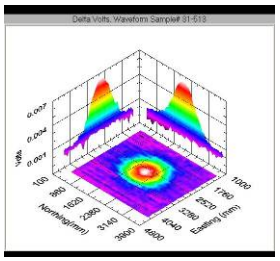
ZZM

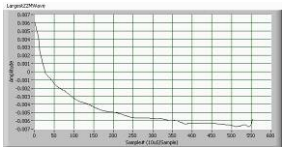
Largest ZZM waveform

Table A.3.27. DiskOne 2007-08-22 BDU-28Az45Inc45Td103

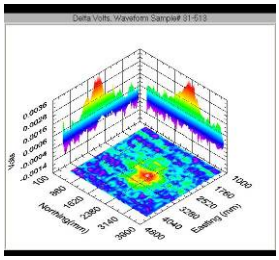
XZE

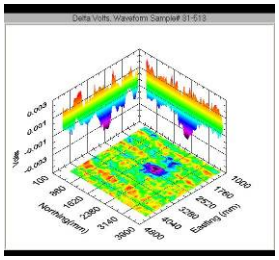
XZF

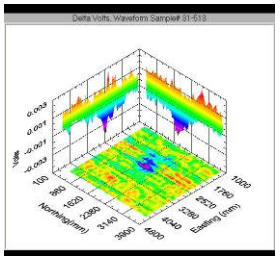
XZG

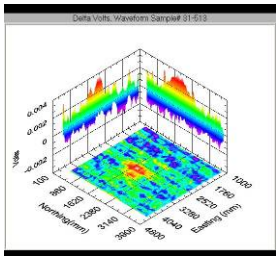
XZH

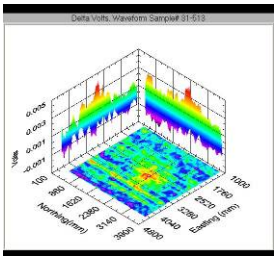
YZE

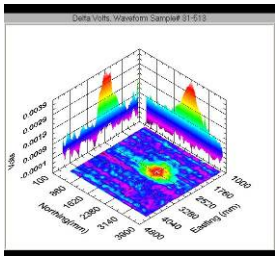
YZF

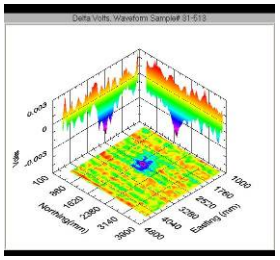
YZG

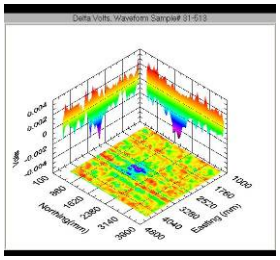
YZH

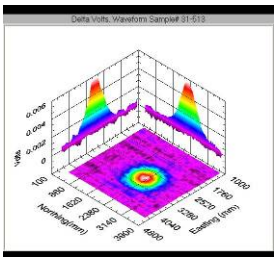
ZZE

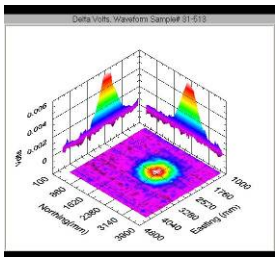
ZZF

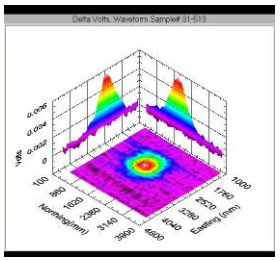
ZZG

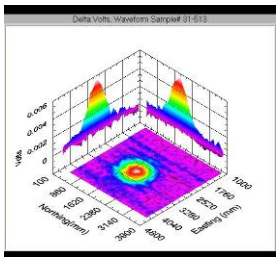
ZZH

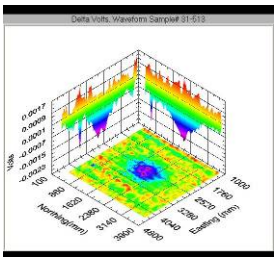
ZX1

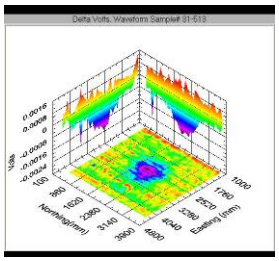
ZY1

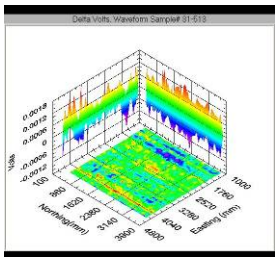
XX1

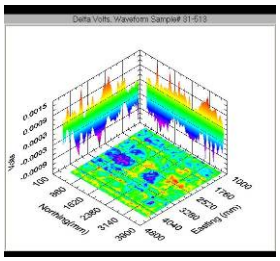
YY1

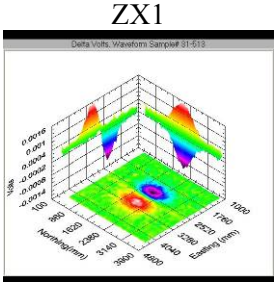
XZM

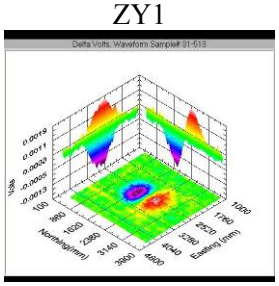
YZM

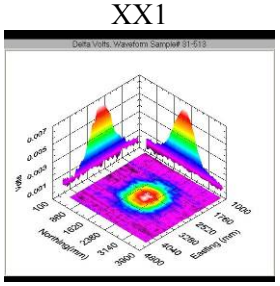
ZZM

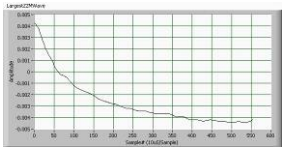
Largest ZZM waveform

# BLU-26

The BLU-26 is spherical in shape (figure A.1.2.1). Due to its symmetry it was only run with its outer ring oriented either vertically or horizontally.

Table A.3.28. DiskOne 2007-07-31 BLU-26RingHorzTd73

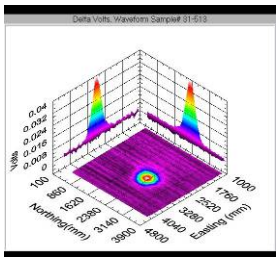
XZE

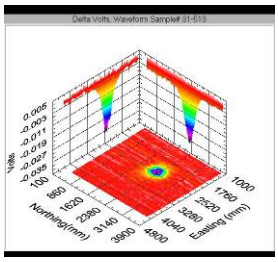
XZF

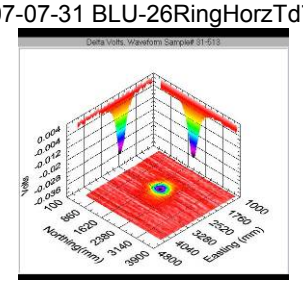
XZG

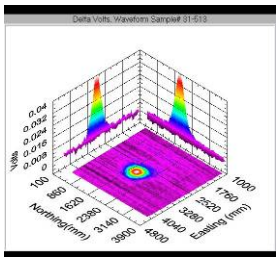
XZH

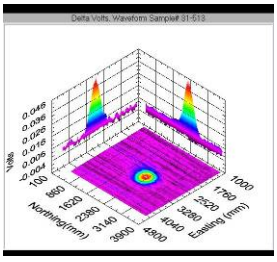
YZE

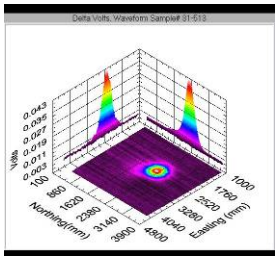
YZF

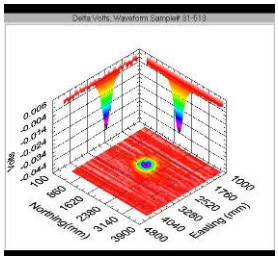
YZG

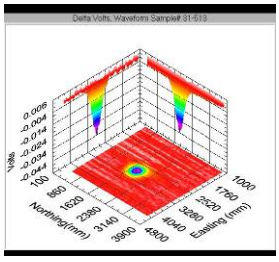
YZH

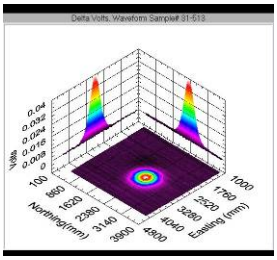
ZZE

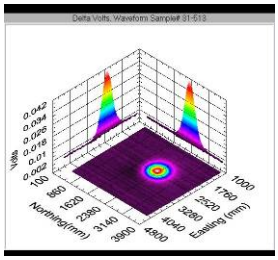
ZZF

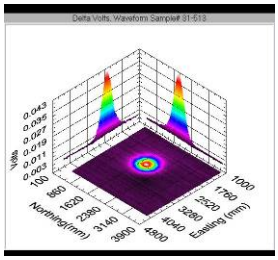
ZZG

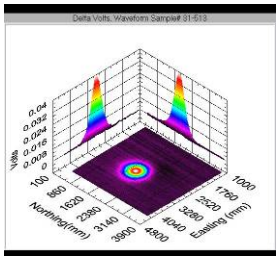
ZZH

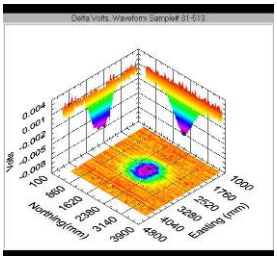
ZX1

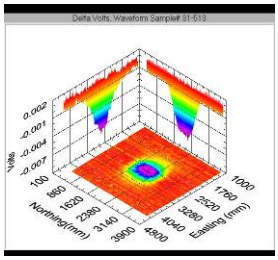
ZY1

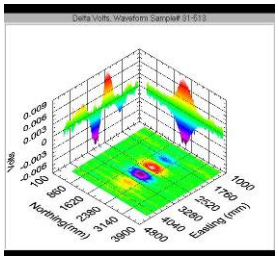
XX1

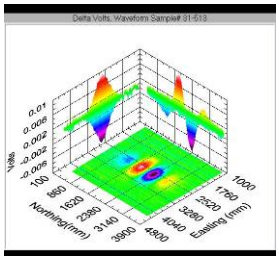
YY1

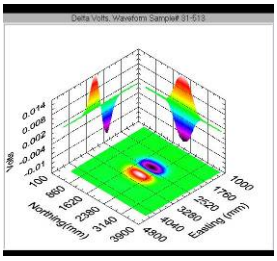
XZM

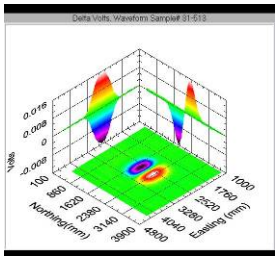
YZM

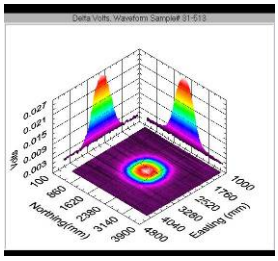
ZZM

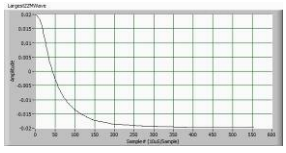
Largest ZZM waveform

## M42

Due to its small size, the M42 surveys were run only at the shallow depth.

Table A.3.29. DiskOne 2007-08-08 M42Az0Inc45Td73

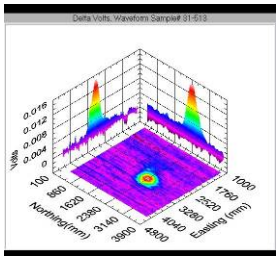
XZE

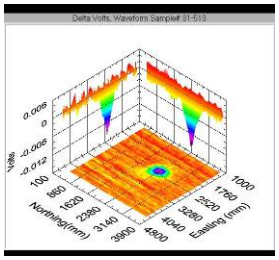
XZF

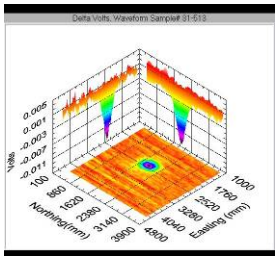
XZG

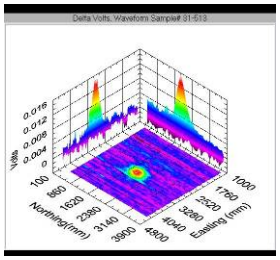
XZH

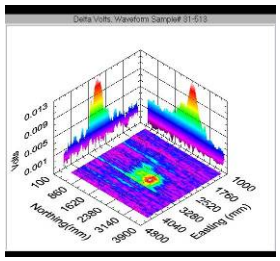
YZE

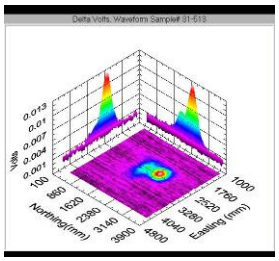
YZF

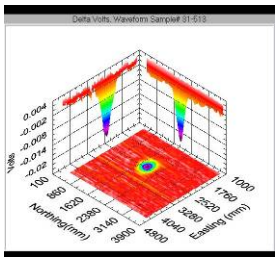
YZG

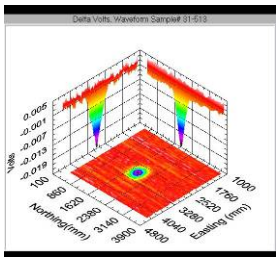
YZH

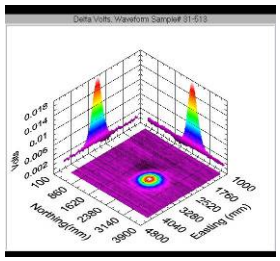
ZZE

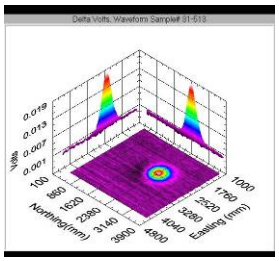
ZZF

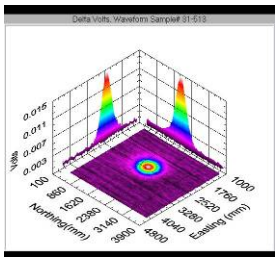
ZZG

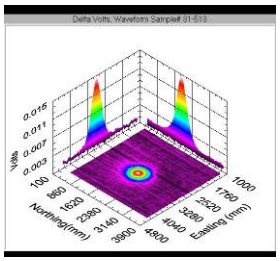
ZZH

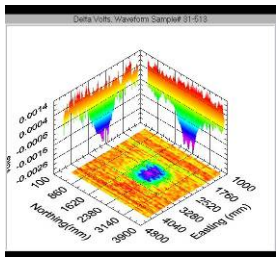
ZX1

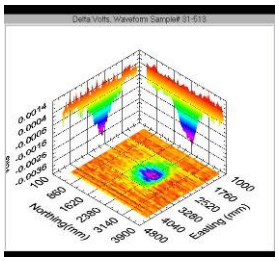
ZY1

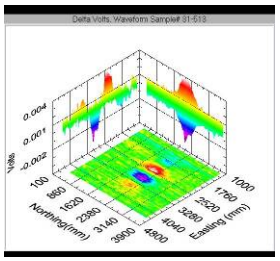
XX1

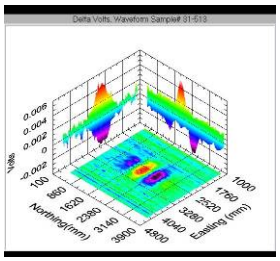
YY1

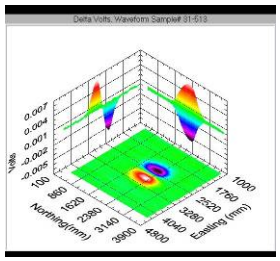
XZM

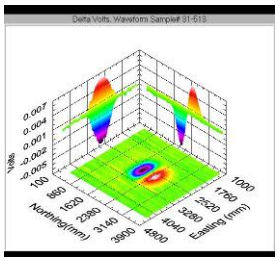
YZM

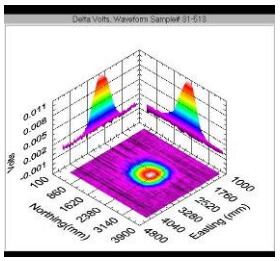
ZZM

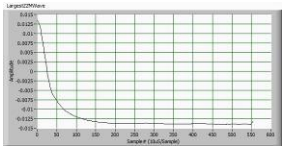
Largest ZZM waveform

Table A.3.30. DiskOne 2007-08-08 M42Az0Inc90Td73

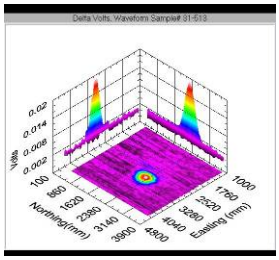
XZE

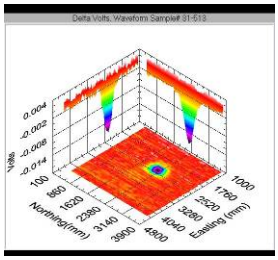
XZF

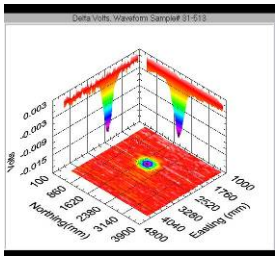
XZG

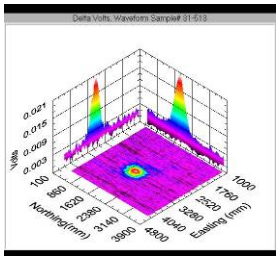
XZH

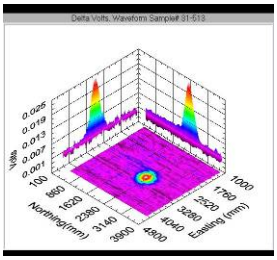
YZE

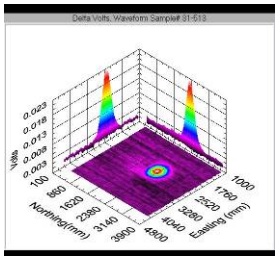
YZF

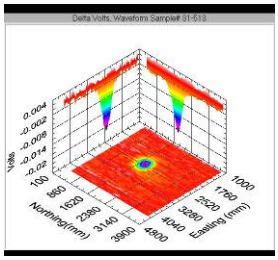
YZG

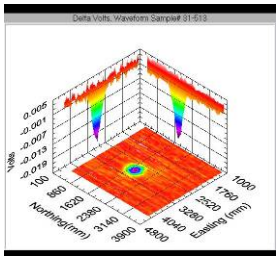
YZH

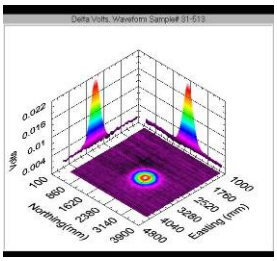
ZZE

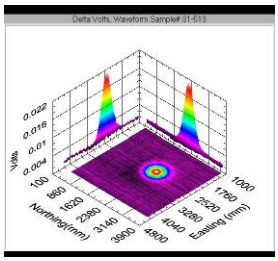
ZZF

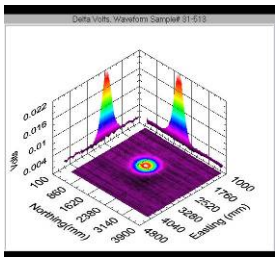
ZZG

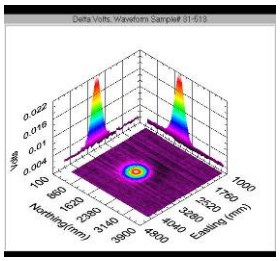
ZZH

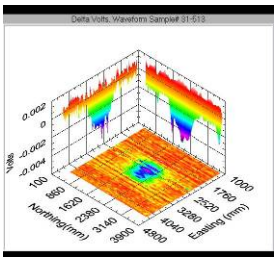
ZX1

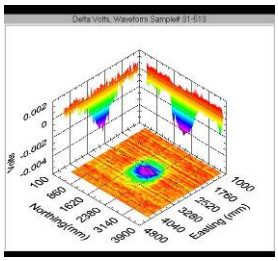
ZY1

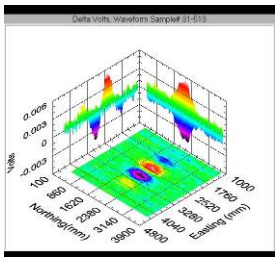
XX1

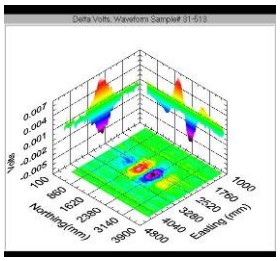
YY1

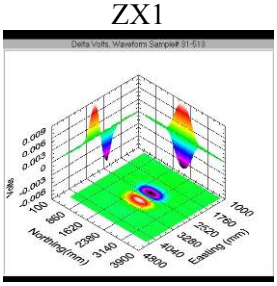
XZM

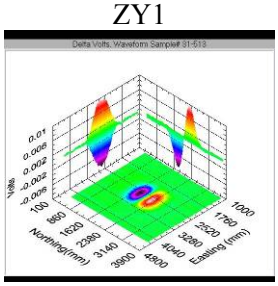
YZM

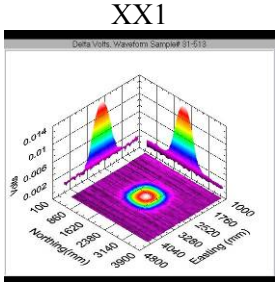
ZZM

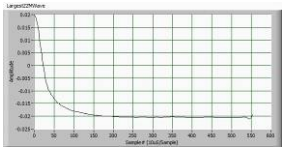
Largest ZZM waveform

Table A.3.31. DiskOne 2007-08-08 M42Az45Inc45Td73

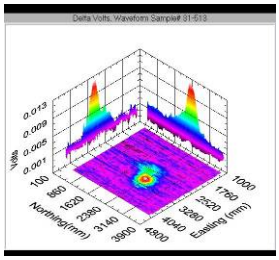
XZE

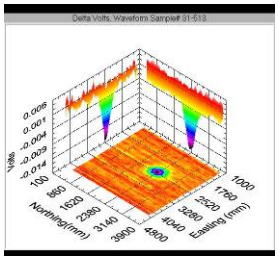
XZF

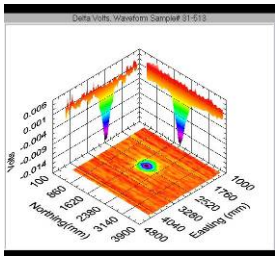
XZG

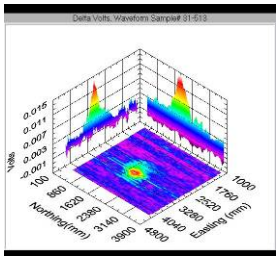
XZH

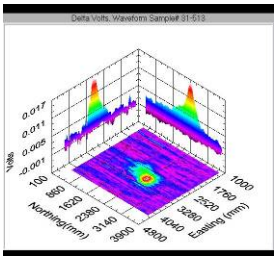
YZE

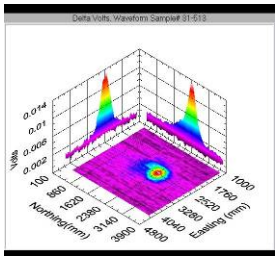
YZF

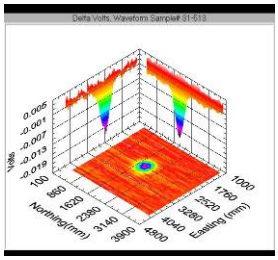
YZG

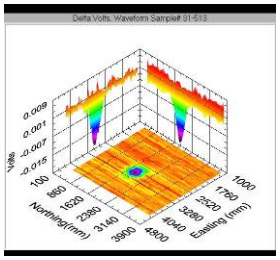
YZH

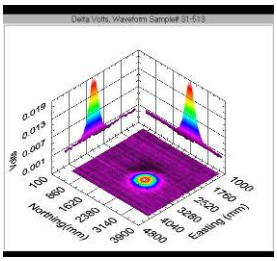
ZZE

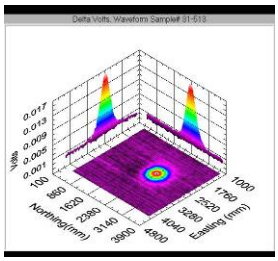
ZZF

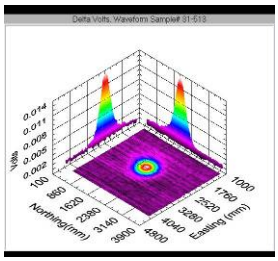
ZZG

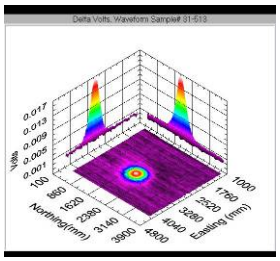
ZZH

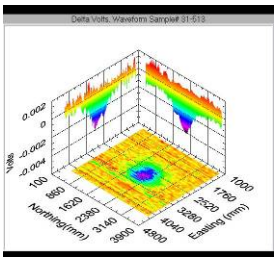
ZX1

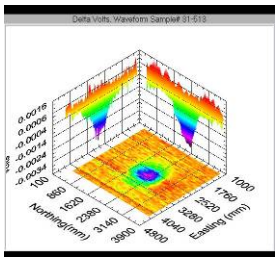
ZY1

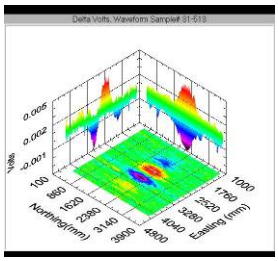
XX1

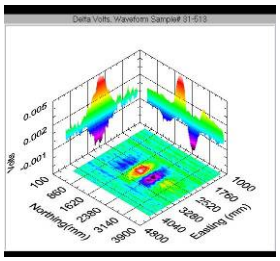
YY1

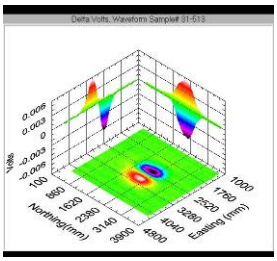
XZM

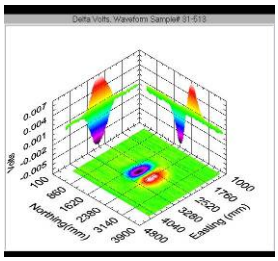
YZM

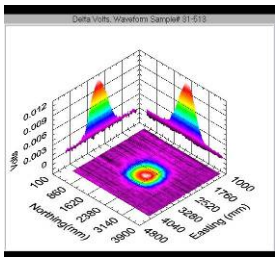
ZZM

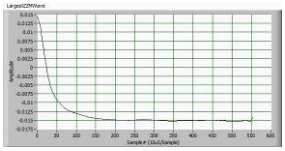
Largest ZZM waveform

# MK118 Rockeye

Table A.3.32. DiskOne 2007-08-08 MK118RockeyeAz0Inc45Td73

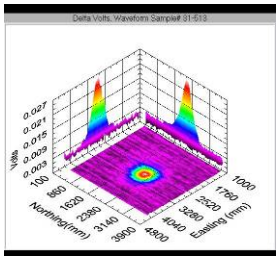
XZE

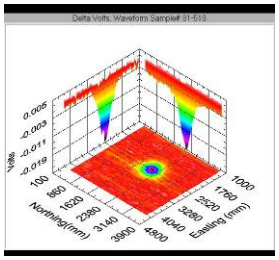
XZF

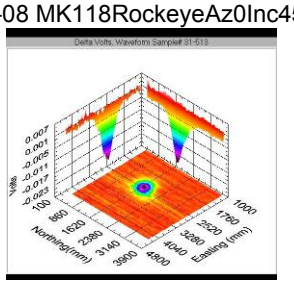
XZG

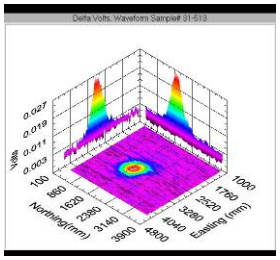
XZH

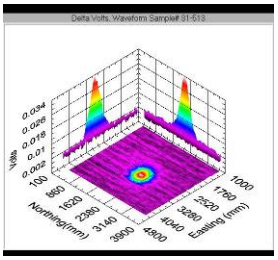
YZE

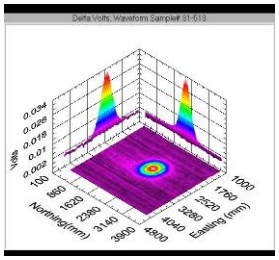
YZF

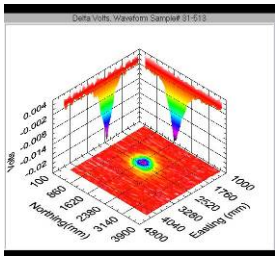
YZG

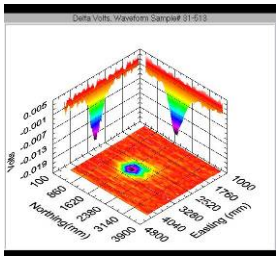
YZH

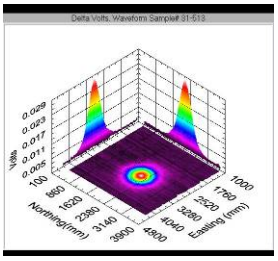
ZZE

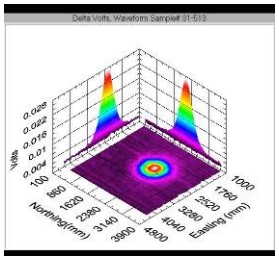
ZZF

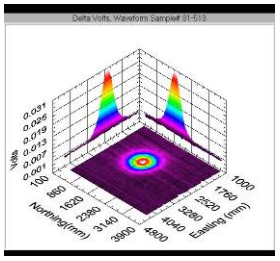
ZZG

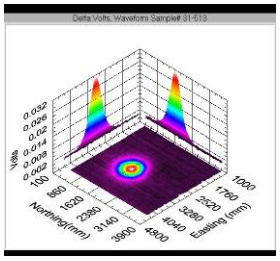
ZZH

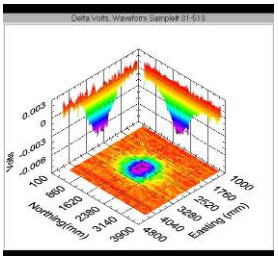
ZX1

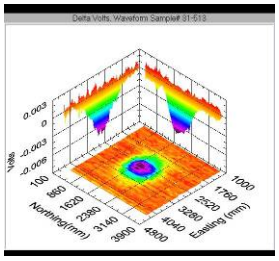
ZY1

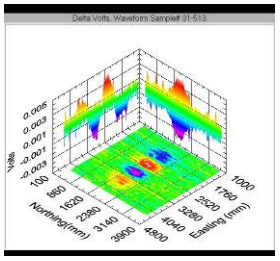
XX1

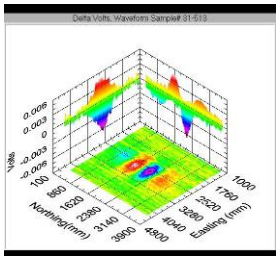
YY1

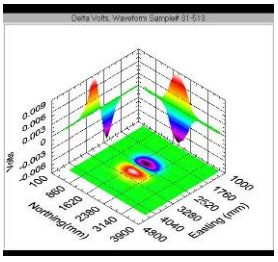
XZM

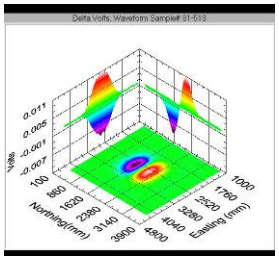
YZM

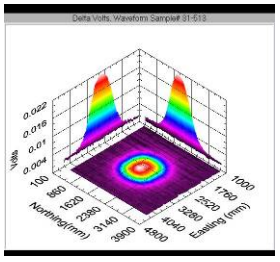
ZZM

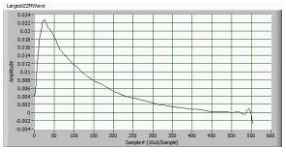
Largest ZZM waveform

Table A.3.33. DiskOne 2007-08-08 MK118RockeyeAz45Inc45Td73

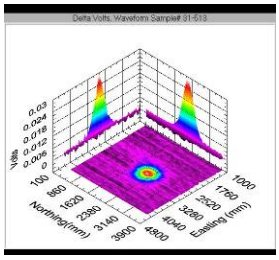
XZE

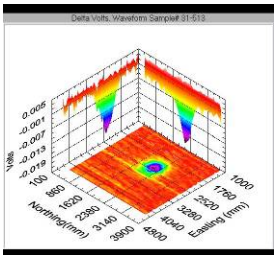
XZF

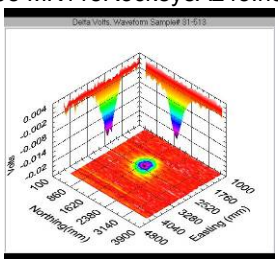
XZG

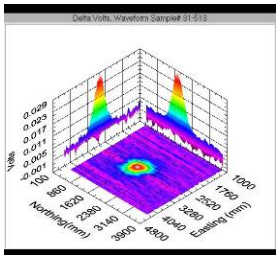
XZH

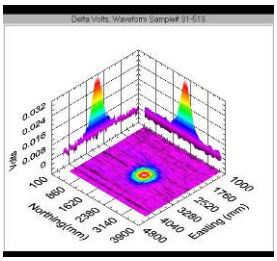
YZE

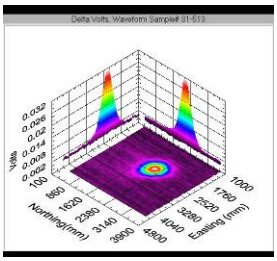
YZF

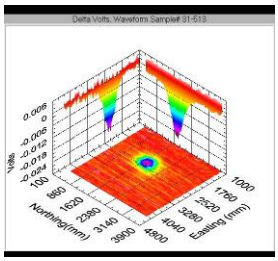
YZG

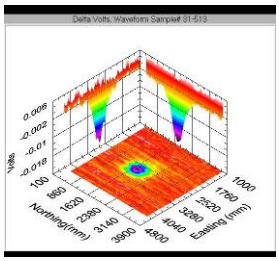
YZH

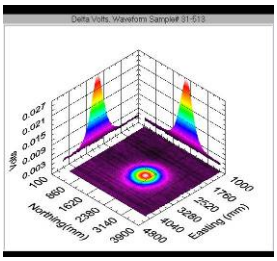
ZZE

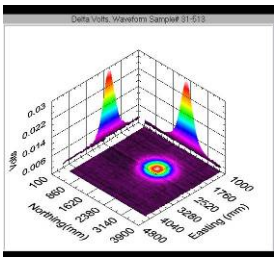
ZZF

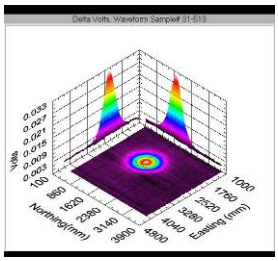
ZZG

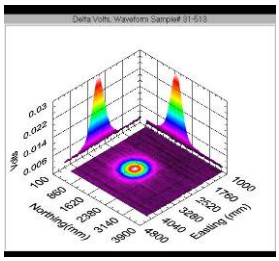
ZZH

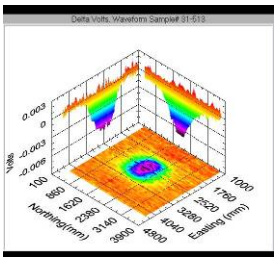
ZX1

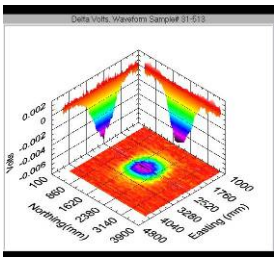
ZY1

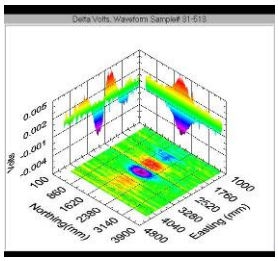
XX1

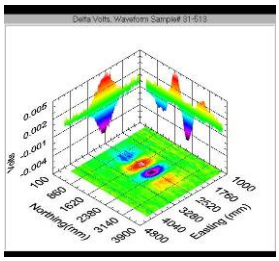
YY1

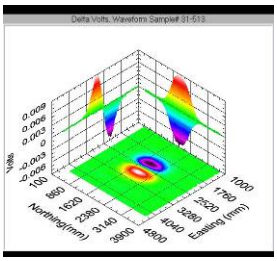
XZM

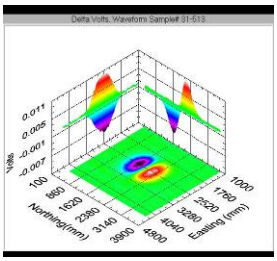
YZM

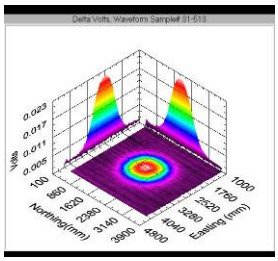
ZZM

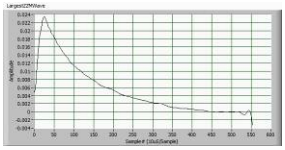
Largest ZZM waveform

# 81 mm

Table A.3.34. DiskTwo 2007-07-25 81mmAz0Inc0Td73

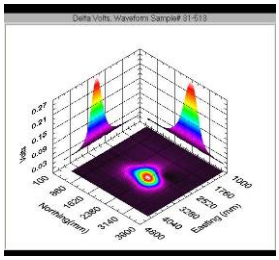
XZE

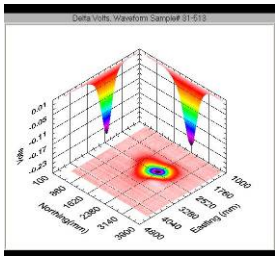
XZF

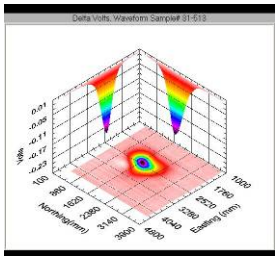
XZG

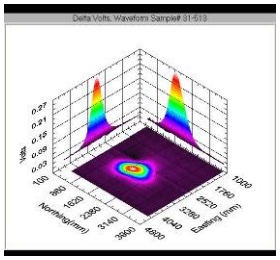
XZH

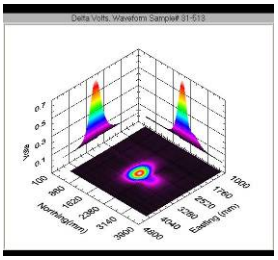
YZE

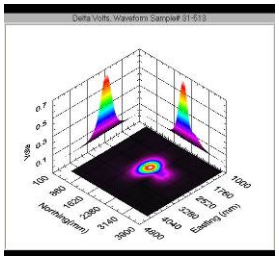
YZF

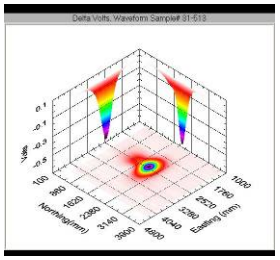
YZG

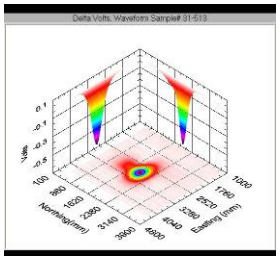
YZH

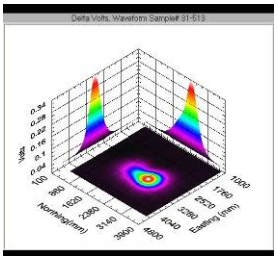
ZZE

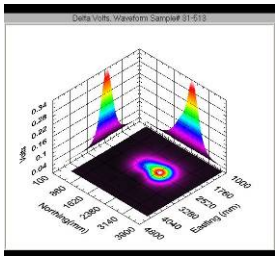
ZZF

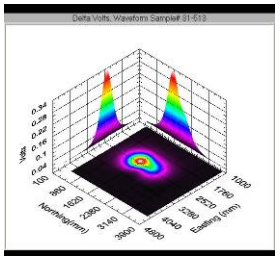
ZZG

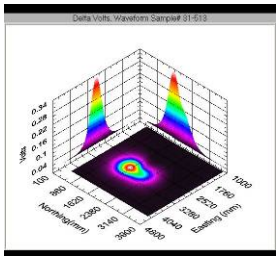
ZZH

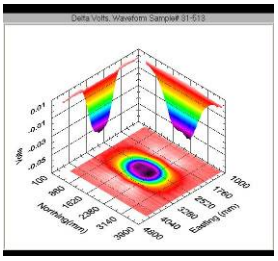
ZX1

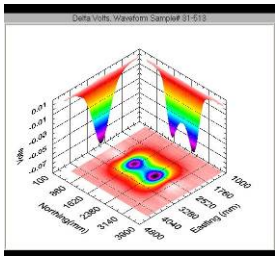
ZY1

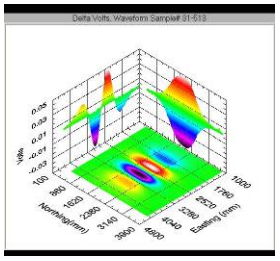
XX1

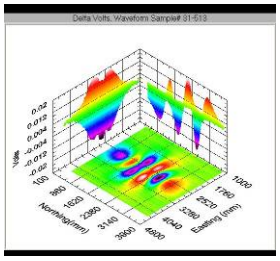
YY1

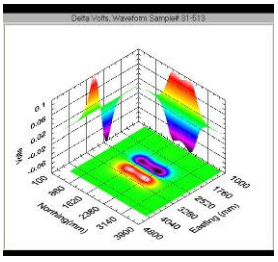
XZM

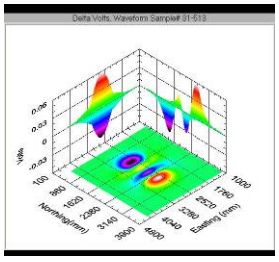
YZM

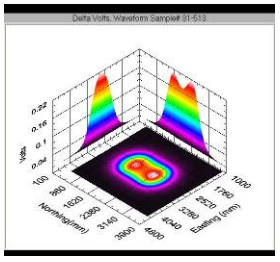
ZZM

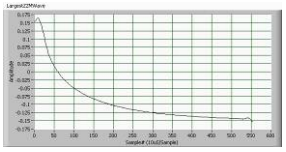
Largest ZZM waveform

Table A.3.35. DiskTwo 2007-07-25 81mmAz90Inc0Td73

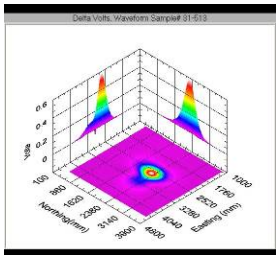
XZE

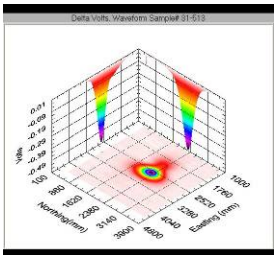
XZF

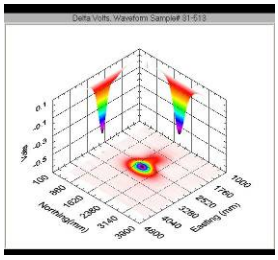
XZG

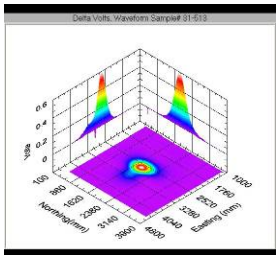
XZH

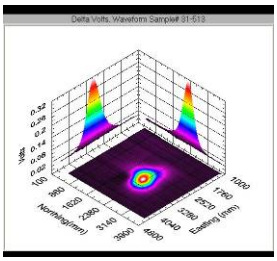
YZE

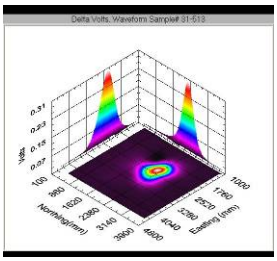
YZF

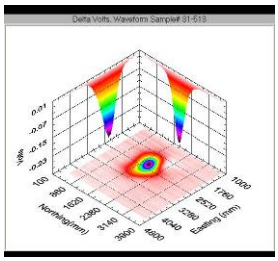
YZG

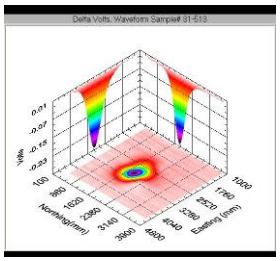
YZH

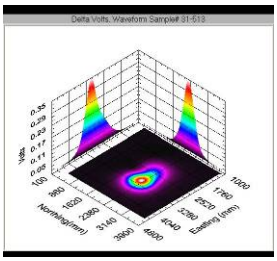
ZZE

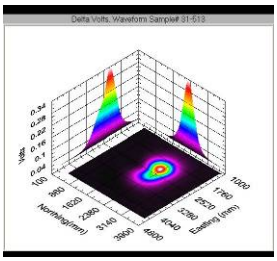
ZZF

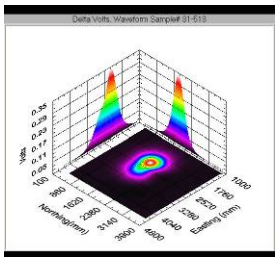
ZZG

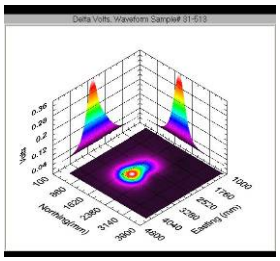
ZZH

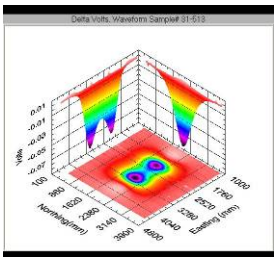
ZX1

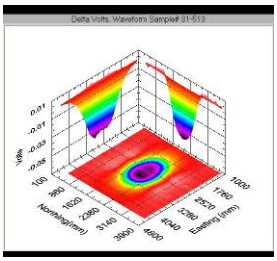
ZY1

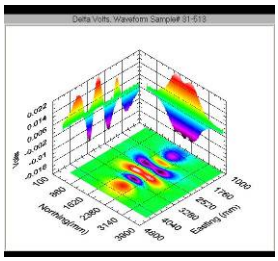
XX1

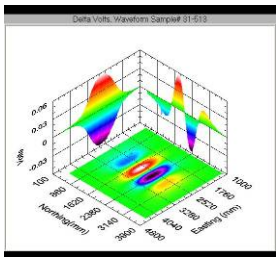
YY1

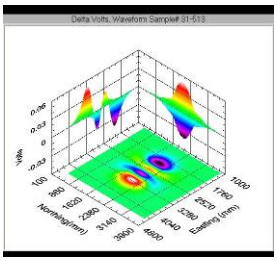
XZM

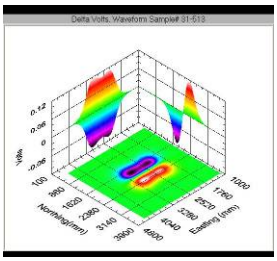
YZM

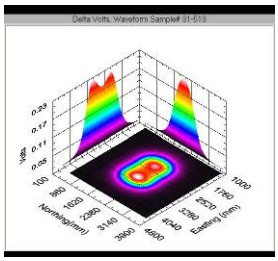
ZZM

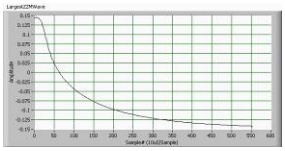
Largest ZZM waveform

Table A.3.36. DiskTwo 2007-07-26 81mmAz0Inc45Td73

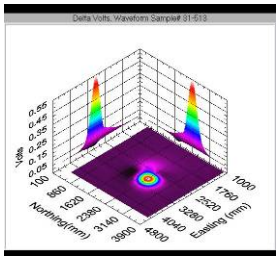
XZE

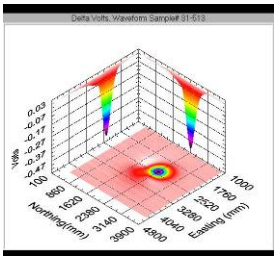
XZF

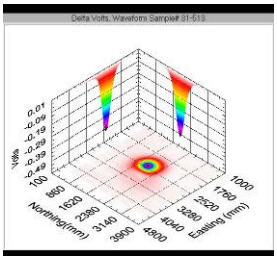
XZG

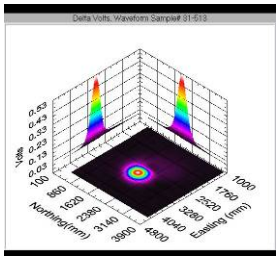
XZH

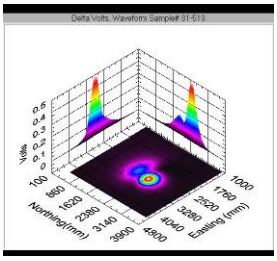
YZE

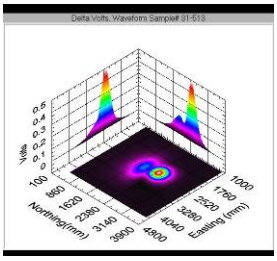
YZF

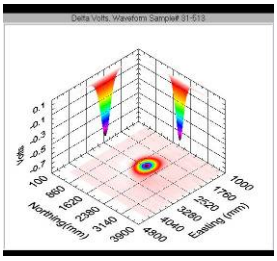
YZG

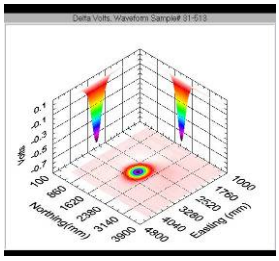
YZH

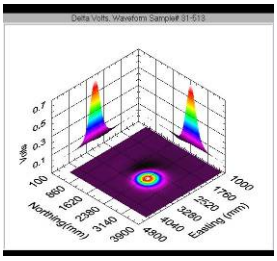
ZZE

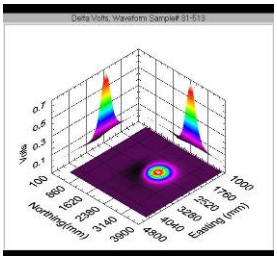
ZZF

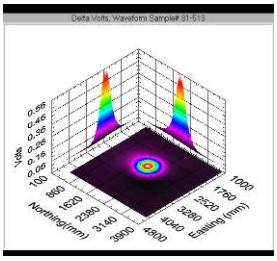
ZZG

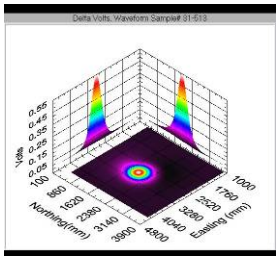
ZZH

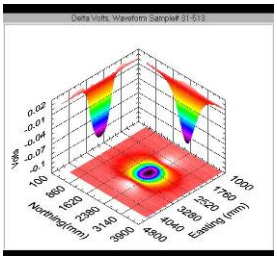
ZX1

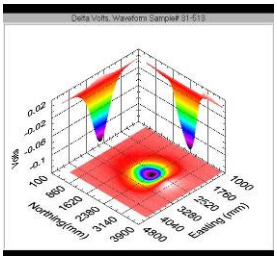
ZY1

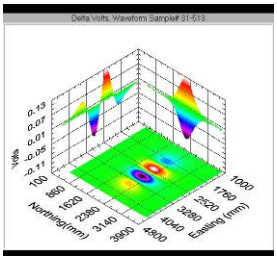
XX1

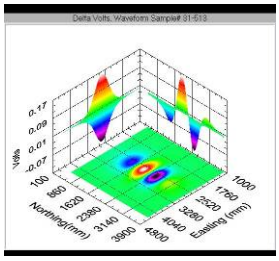
YY1

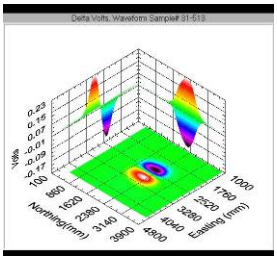
XZM

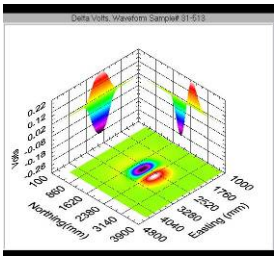
YZM

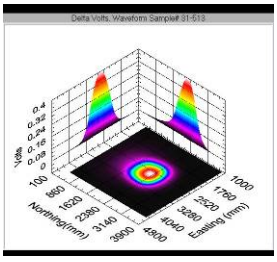
ZZM

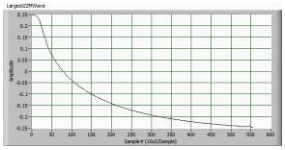
Largest ZZM waveform

Table A.3.37. DiskTwo 2007-07-26 81mmAz0Inc90Td73

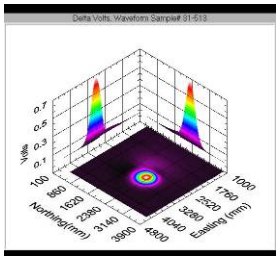
XZE

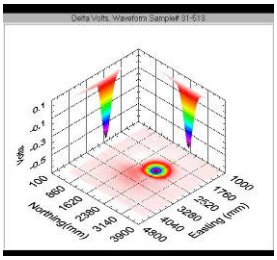
XZF

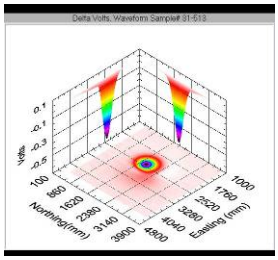
XZG

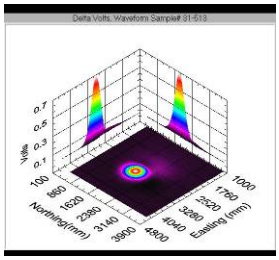
XZH

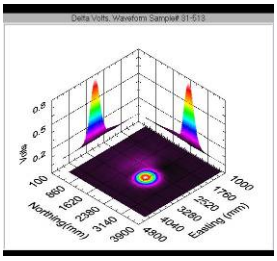
YZE

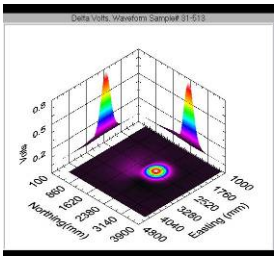
YZF

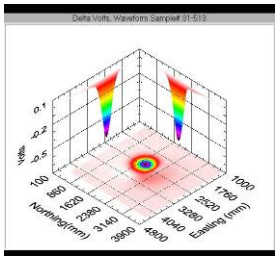
YZG

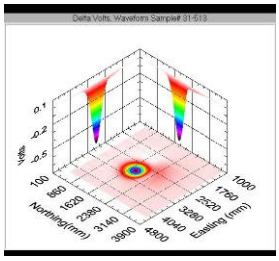
YZH

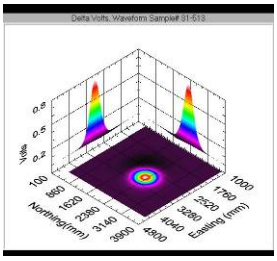
ZZE

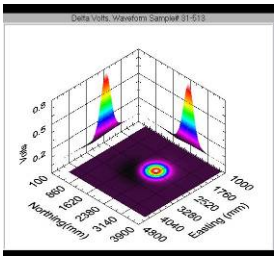
ZZF

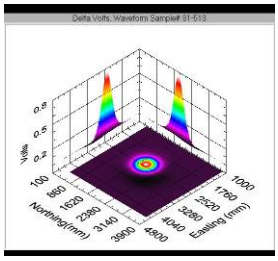
ZZG

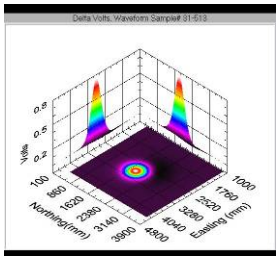
ZZH

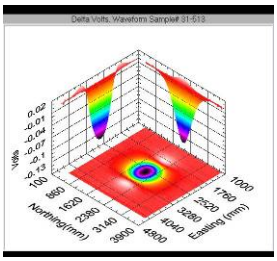
ZX1

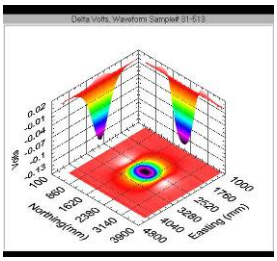
ZY1

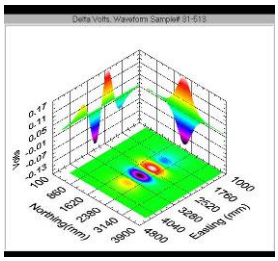
XX1

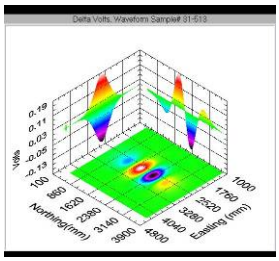
YY1

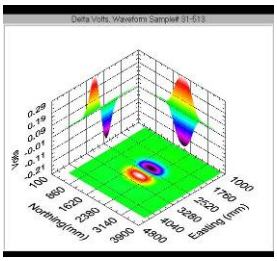
XZM

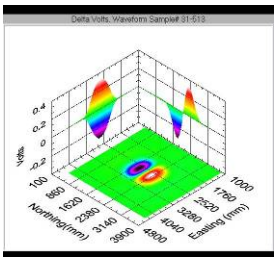
YZM

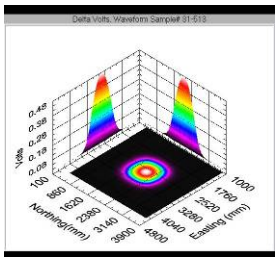
ZZM

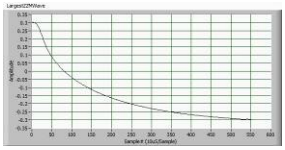
Largest ZZM waveform

Table A.3.38. DiskTwo 2007-07-26 81mmAz45Inc45Td73

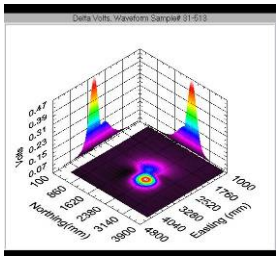
XZE

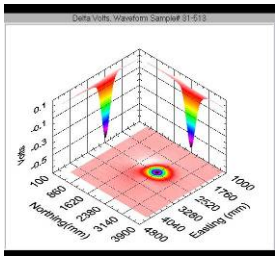
XZF

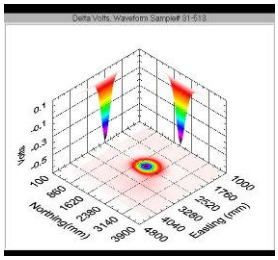
XZG

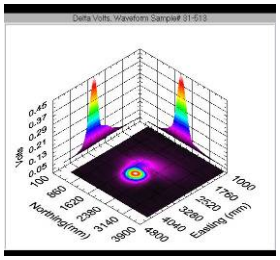
XZH

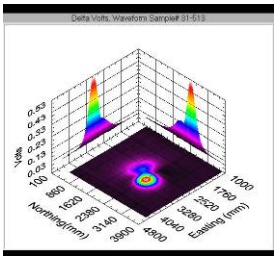
YZE

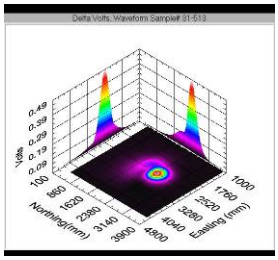
YZF

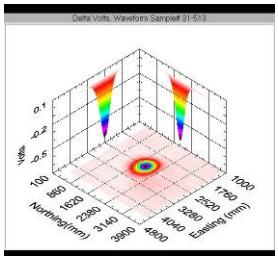
YZG

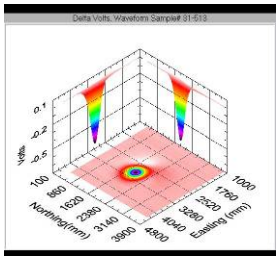
YZH

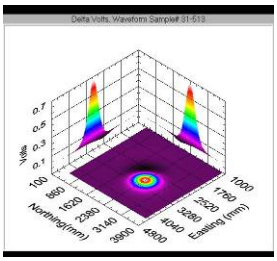
ZZE

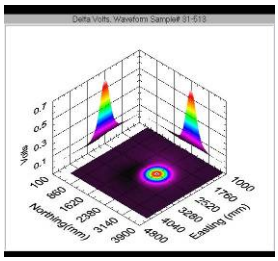
ZZF

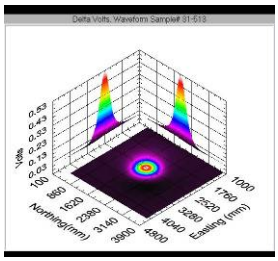
ZZG

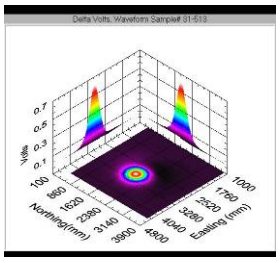
ZZH

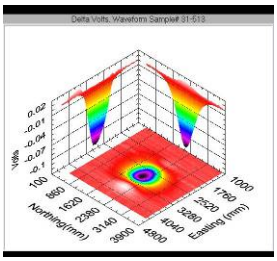
ZX1

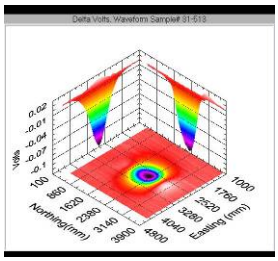
ZY1

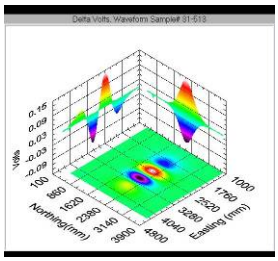
XX1

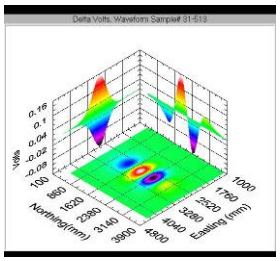
YY1

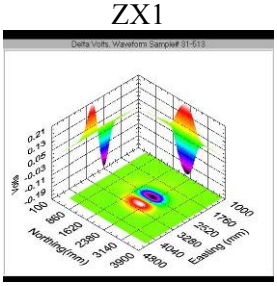
XZM

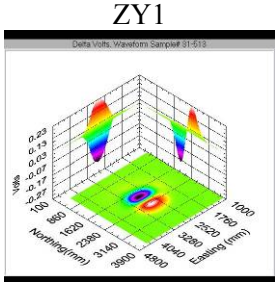
YZM

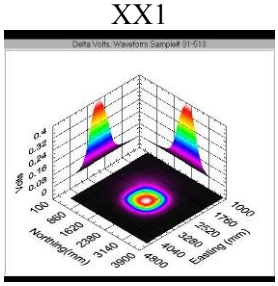
ZZM

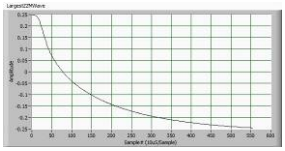
Largest ZZM waveform

Table A.3.39. DiskTwo 2007-08-20 81mmAz0Inc0Td103

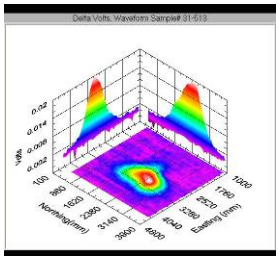
XZE

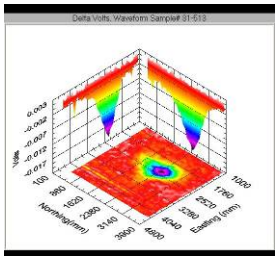
XZF

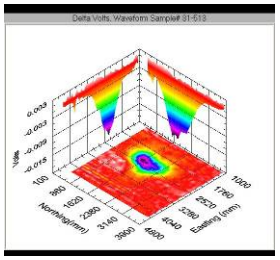
XZG

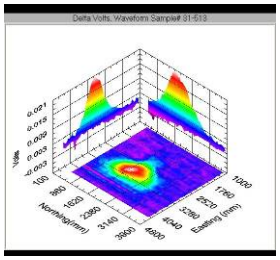
XZH

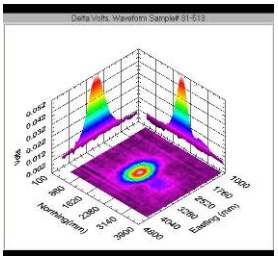
YZE

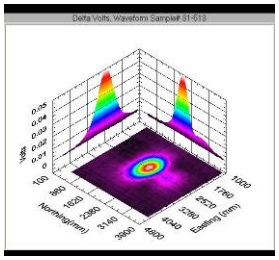
YZF

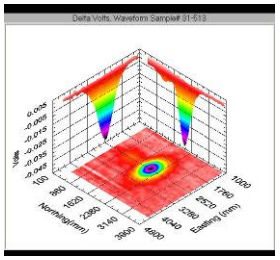
YZG

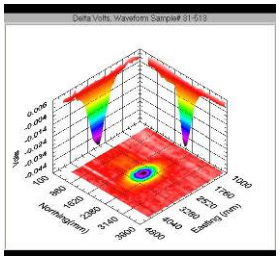
YZH

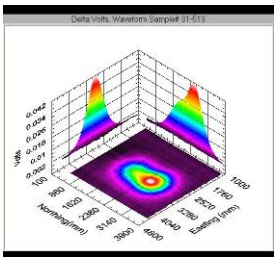
ZZE

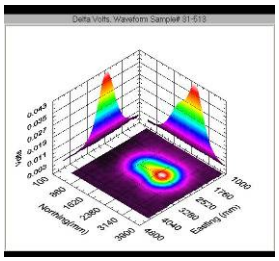
ZZF

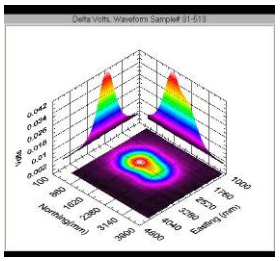
ZZG

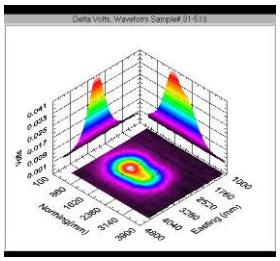
ZZH

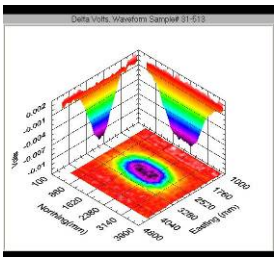
ZX1

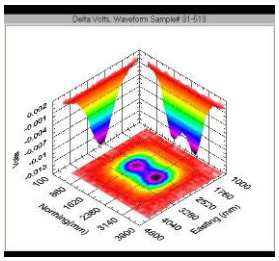
ZY1

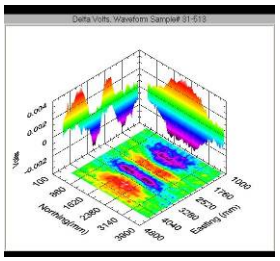
XX1

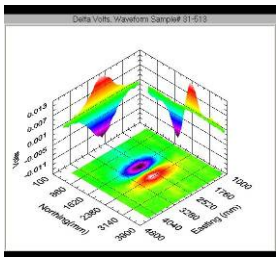
YY1

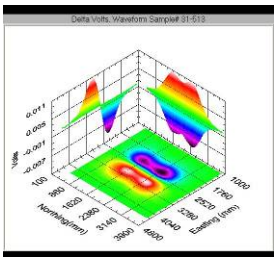
XZM

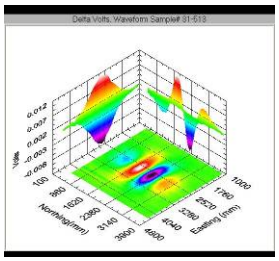
YZM

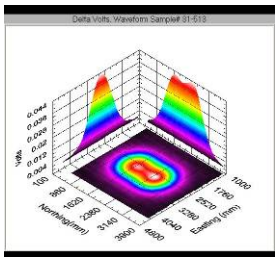
ZZM

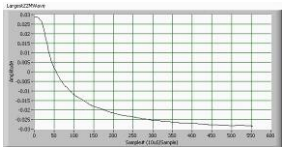
Largest ZZM waveform

Table A.3.40. DiskTwo 2007-08-21 81mmAz45Inc45Td103

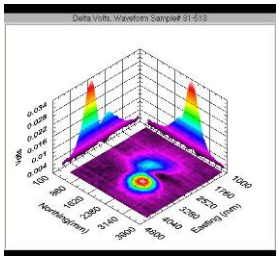
XZE

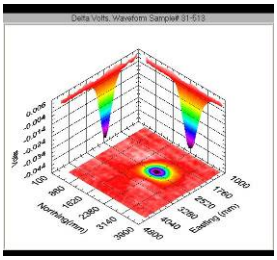
XZF

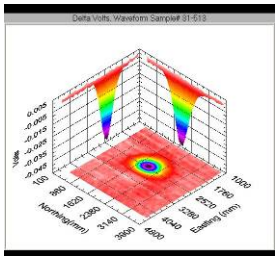
XZG

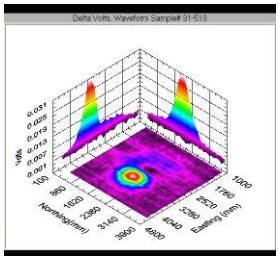
XZH

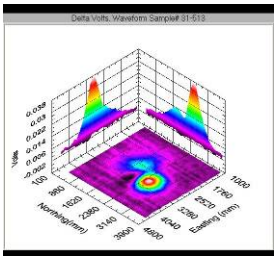
YZE

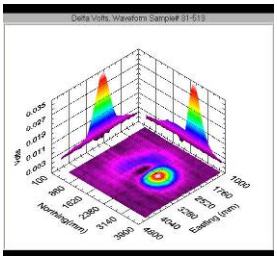
YZF

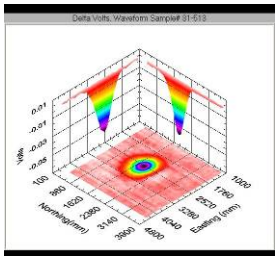
YZG

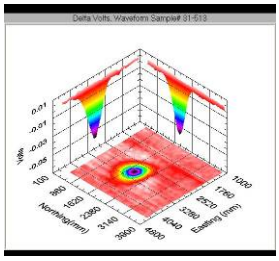
YZH

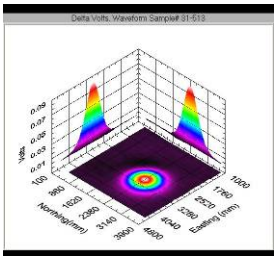
ZZE

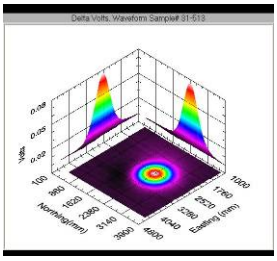
ZZF

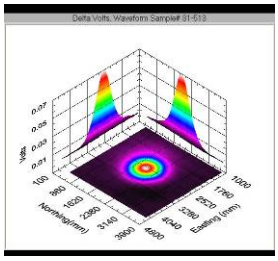
ZZG

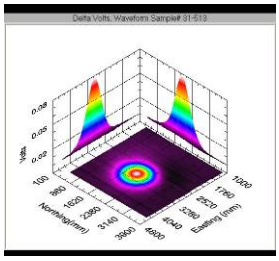
ZZH

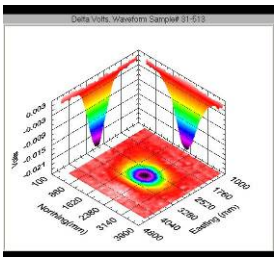
ZX1

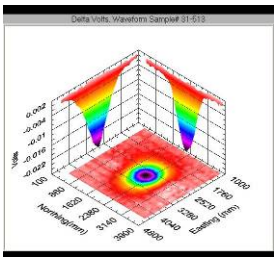
ZY1

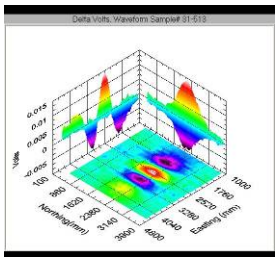
XX1

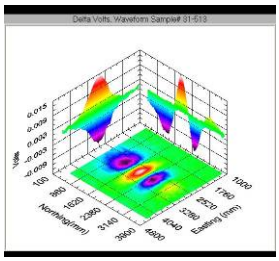
YY1

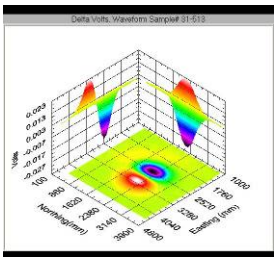
XZM

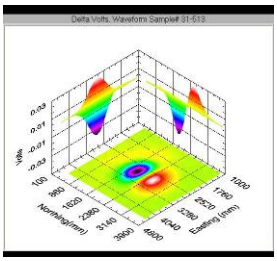
YZM

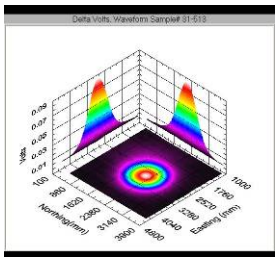
ZZM

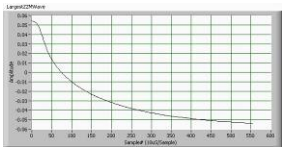
Largest ZZM waveform

Table A.3.41. DiskTwo 2007-08-20 81mmAz90Inc0Td103

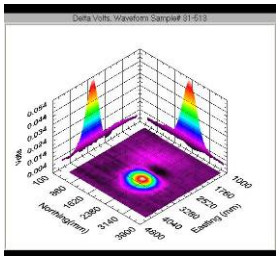
XZE

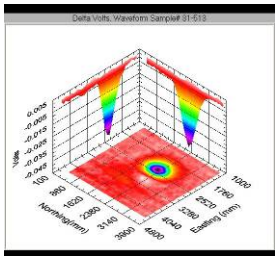
XZF

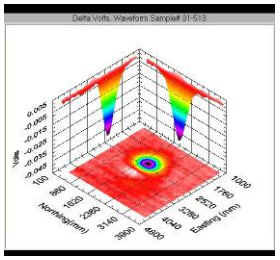
XZG

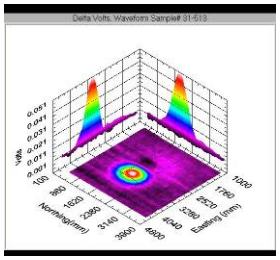
XZH

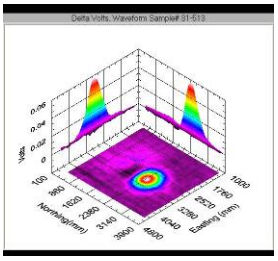
YZE

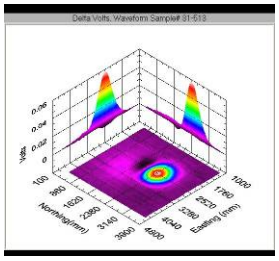
YZF

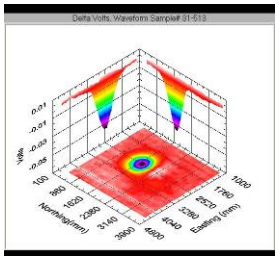
YZG

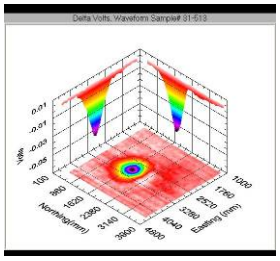
YZH

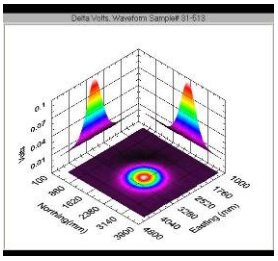
ZZE

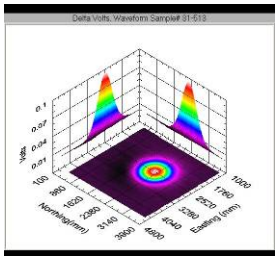
ZZF

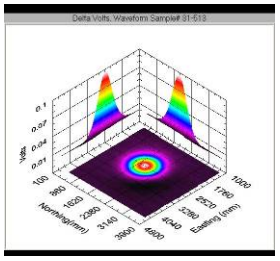
ZZG

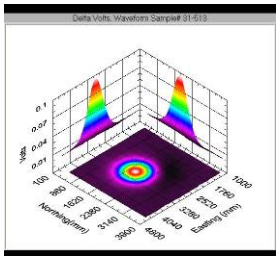
ZZH

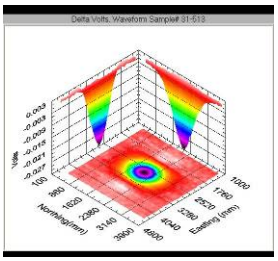
ZX1

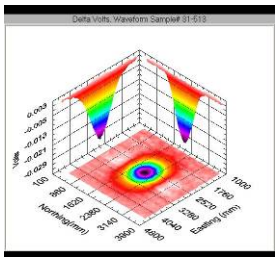
ZY1

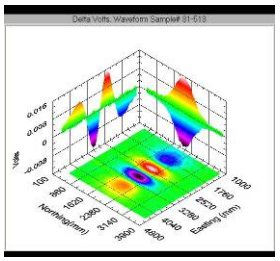
XX1

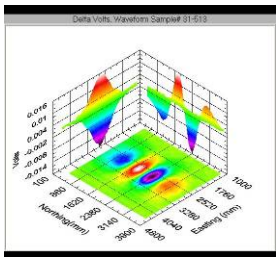
YY1

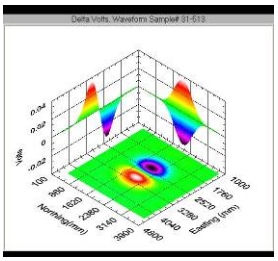
XZM

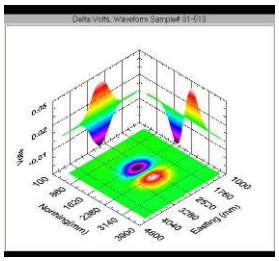
YZM

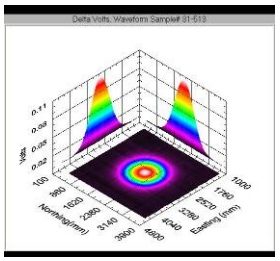
ZZM

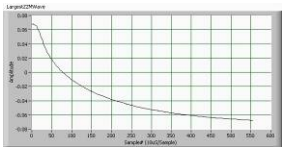
Largest ZZM waveform

Table A.3.42. DiskTwo 2007-08-21 81mmAz90Inc0Td103

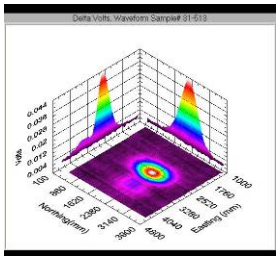
XZE

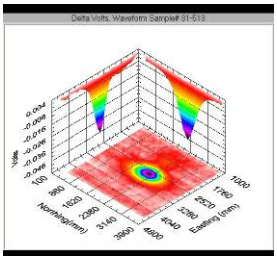
XZF

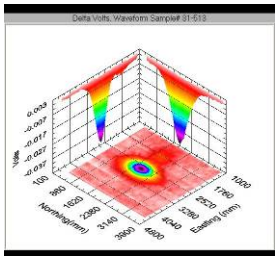
XZG

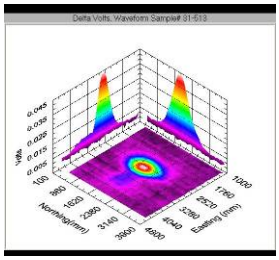
XZH

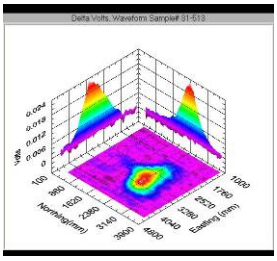
YZE

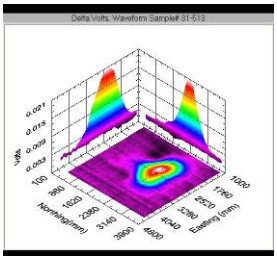
YZF

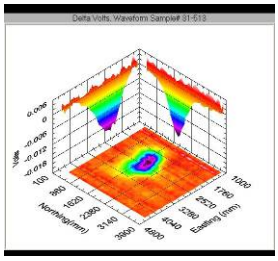
YZG

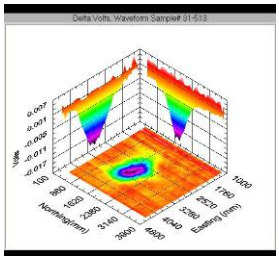
YZH

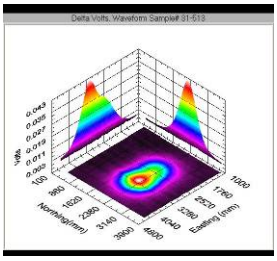
ZZE

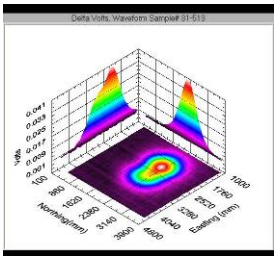
ZZF

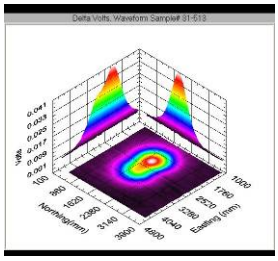
ZZG

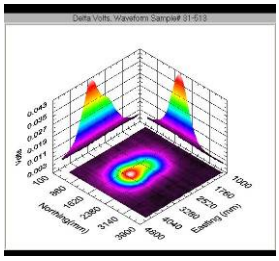
ZZH

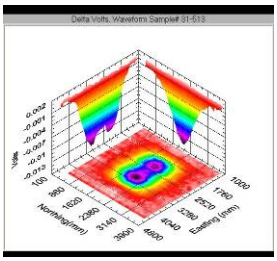
ZX1

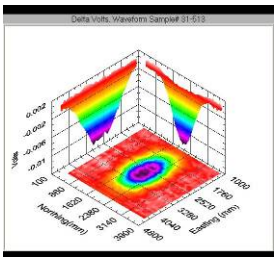
ZY1

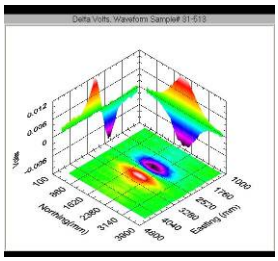
XX1

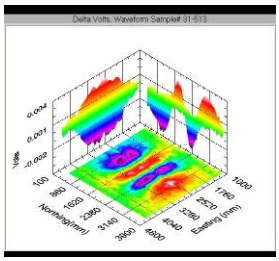
YY1

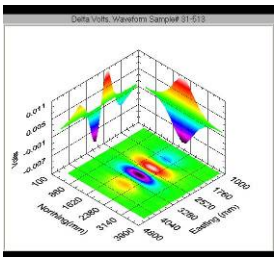
XZM

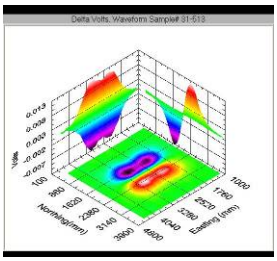
YZM

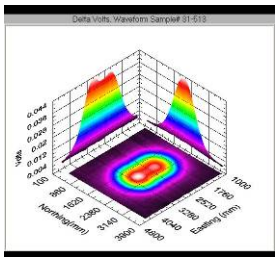
ZZM

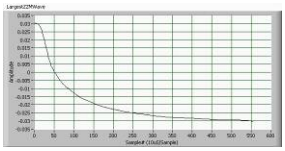
Largest ZZM waveform

# Clutter Angle Short

Table A.3.43. DiskTwo 2007-08-02 AngleShrtAz0Inc90Td73

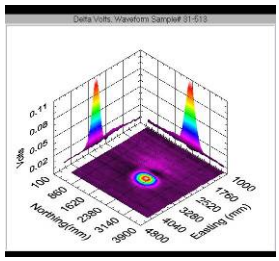
XZE

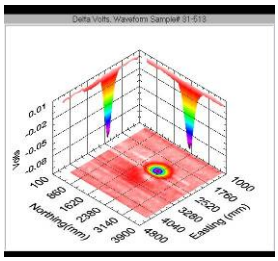
XZF

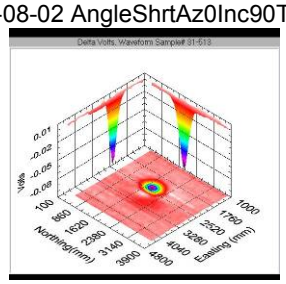
XZG

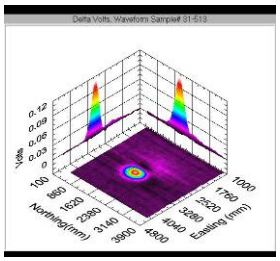
XZH

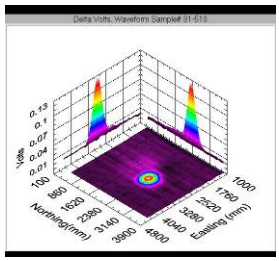
YZE

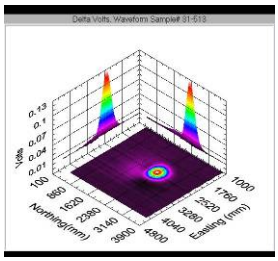
YZF

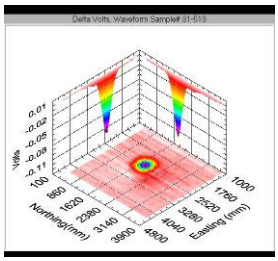
YZG

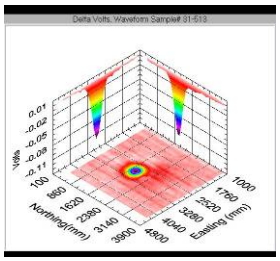
YZH

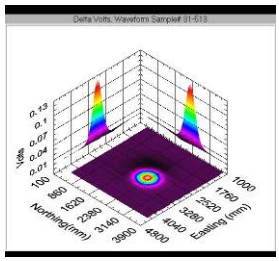
ZZE

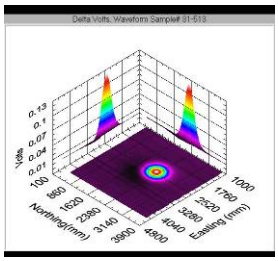
ZZF

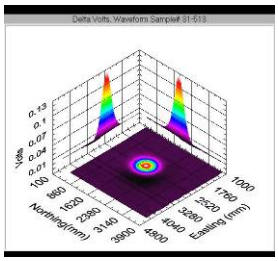
ZZG

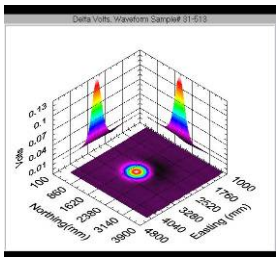
ZZH

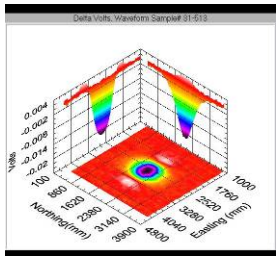
ZX1

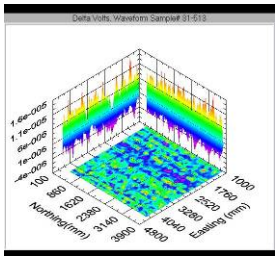
ZY1

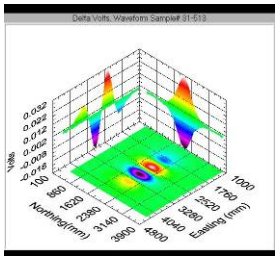
XX1

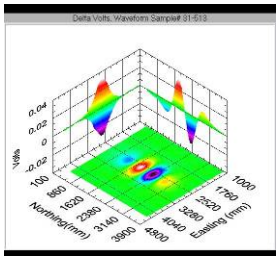
YY1

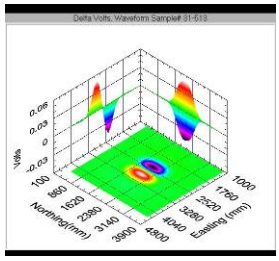
XZM

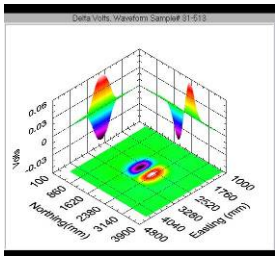
YZM

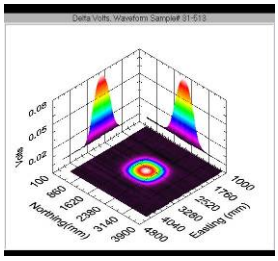
ZZM

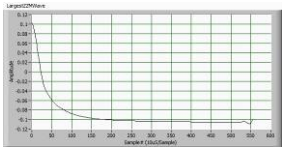
Largest ZZM waveform

Table A.3.44. DiskTwo 2007-08-03 AngleShrtAz0Inc45Td73Three

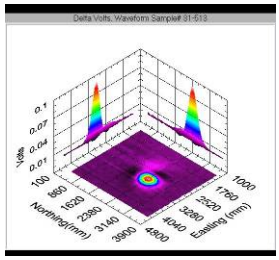
XZE

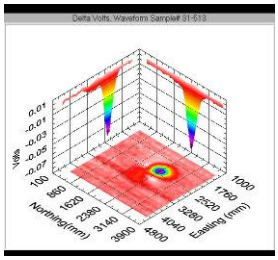
XZF

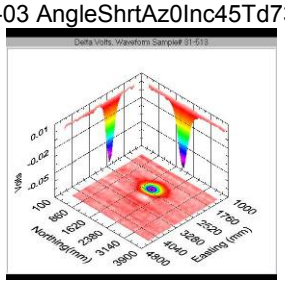
XZG

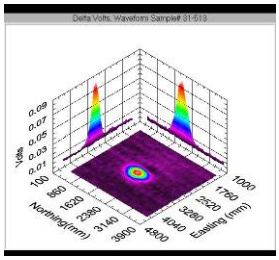
XZH

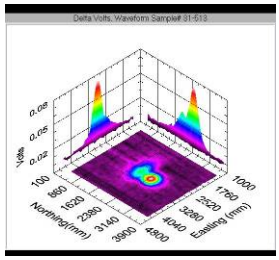
YZE

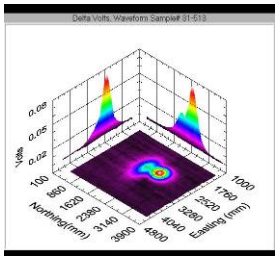
YZF

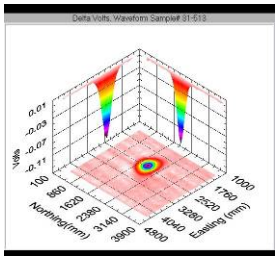
YZG

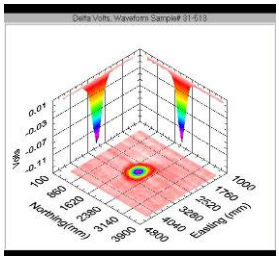
YZH

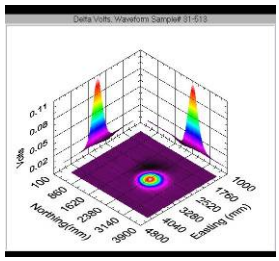
ZZE

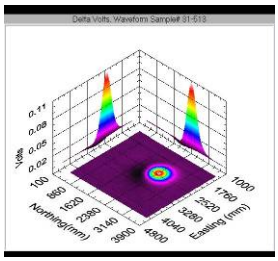
ZZF

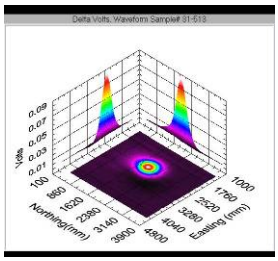
ZZG

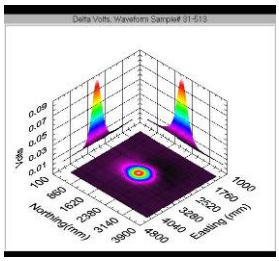
ZZH

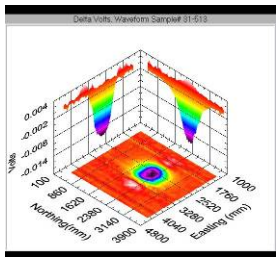
ZX1

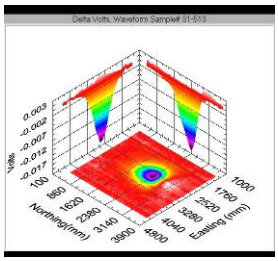
ZY1

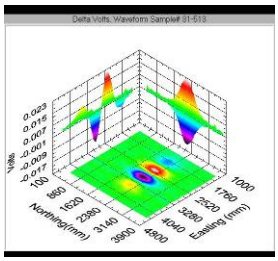
XX1

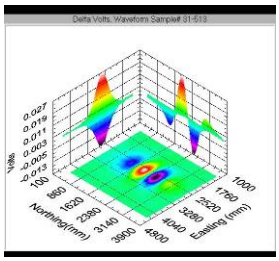
YY1

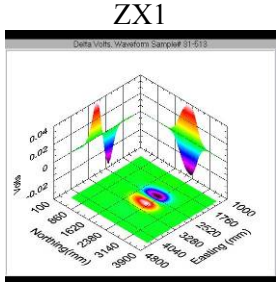
XZM

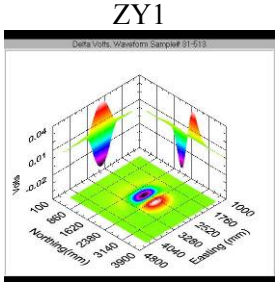
YZM

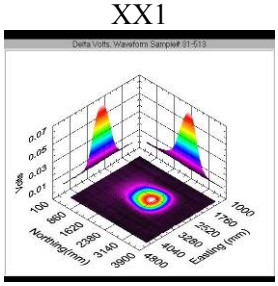
ZZM

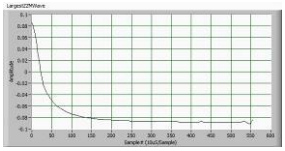
Largest ZZM waveform

Table A.3.45. DiskTwo 2007-08-03 AngleShrtAz90Inc0Td73

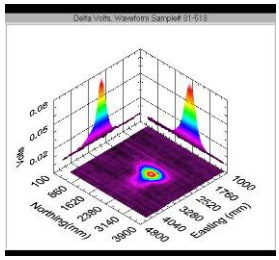
XZE

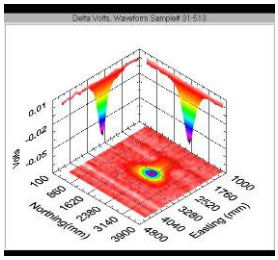
XZF

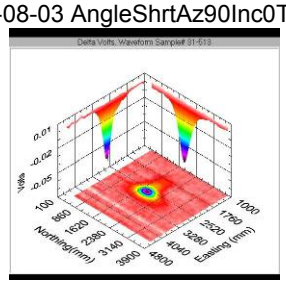
XZG

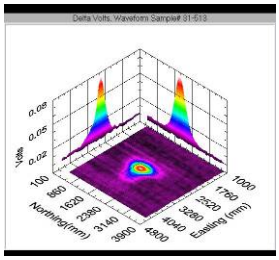
XZH

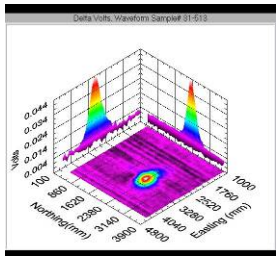
YZE

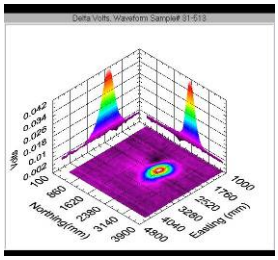
YZF

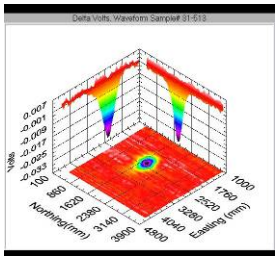
YZG

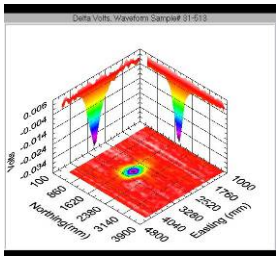
YZH

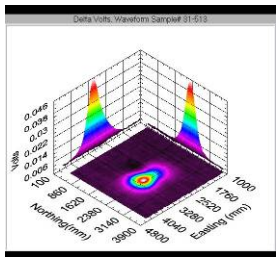
ZZE

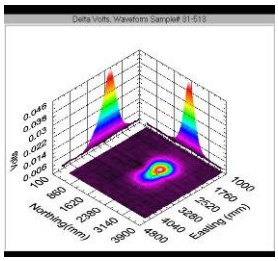
ZZF

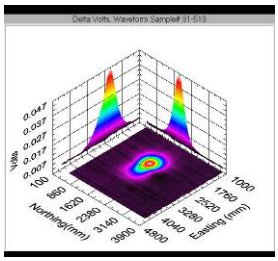
ZZG

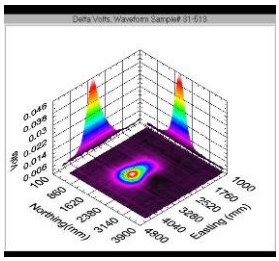
ZZH

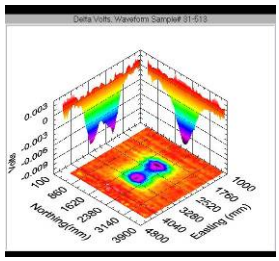
ZX1

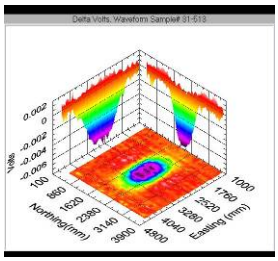
ZY1

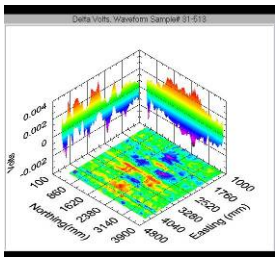
XX1

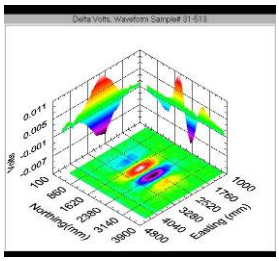
YY1

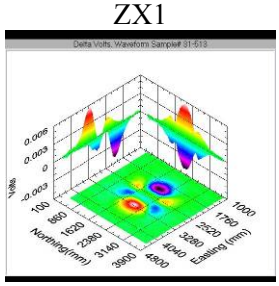
XZM

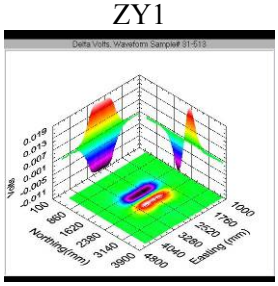
YZM

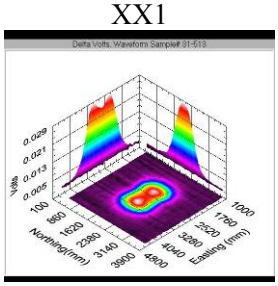
ZZM

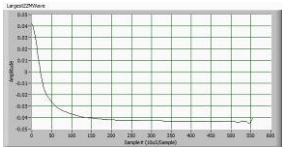
Largest ZZM waveform

Table A.3.46. DiskTwo 2007-08-28 AngleShrtAz0Inc0Td103

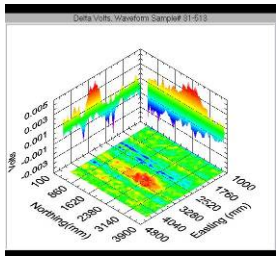
XZE

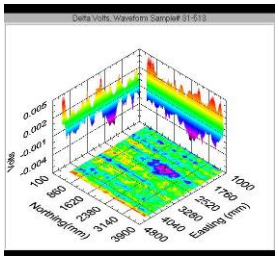
XZF

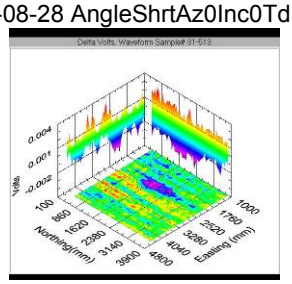
XZG

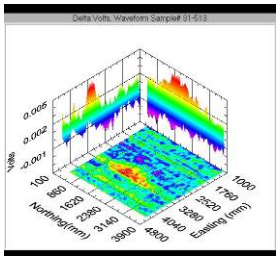
XZH

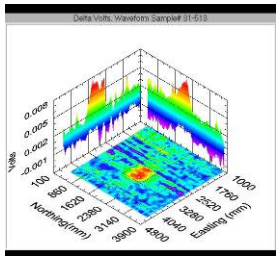
YZE

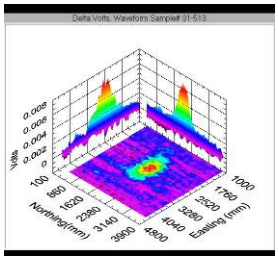
YZF

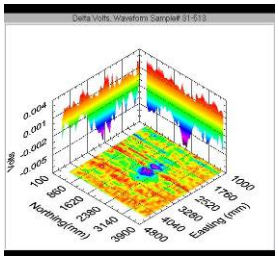
YZG

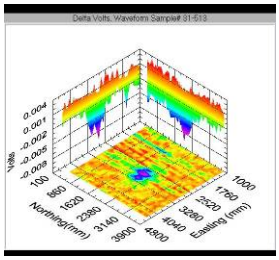
YZH

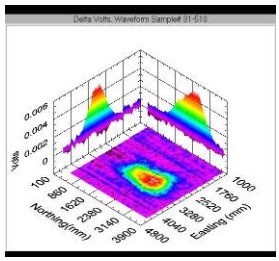
ZZE

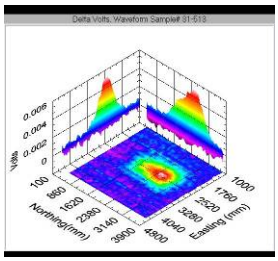
ZZF

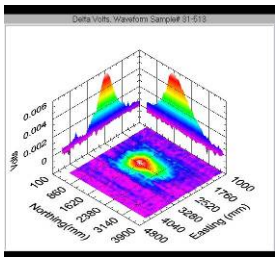
ZZG

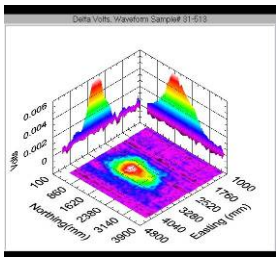
ZZH

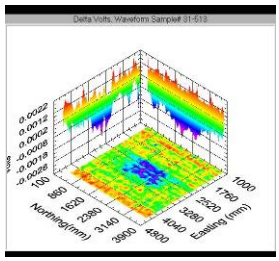
ZX1

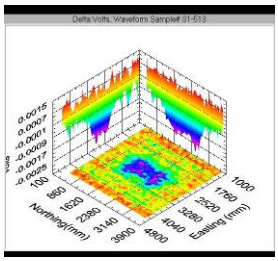
ZY1

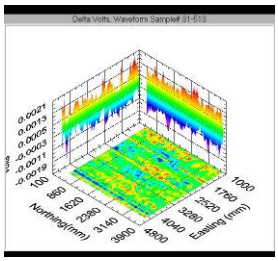
XX1

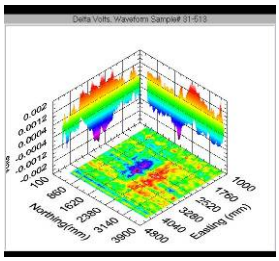
YY1

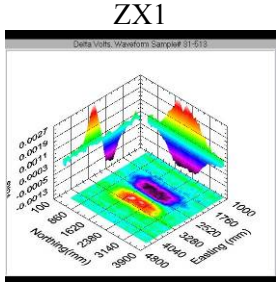
XZM

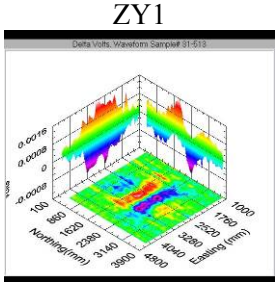
YZM

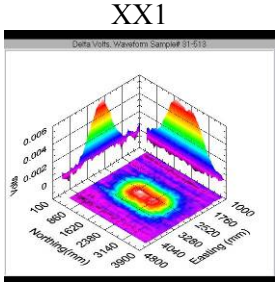
ZZM

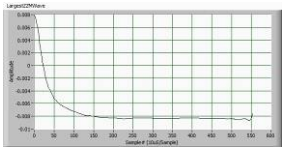
Largest ZZM waveform

# Clutter Angle Long

Table A.3.47. DiskTwo 2007-08-27 AngleLongAz0Inc0Td103Two

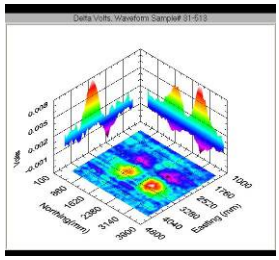
XZE

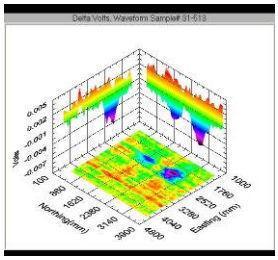
XZF

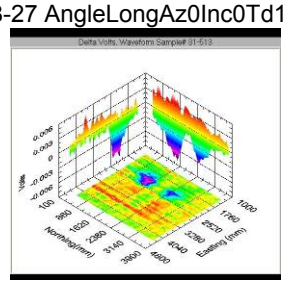
XZG

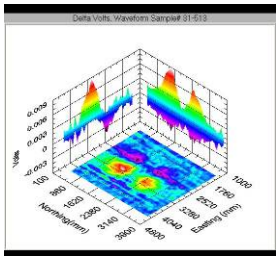
XZH

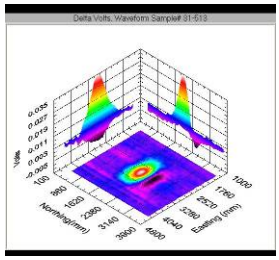
YZE

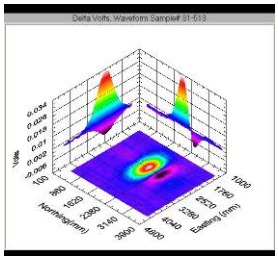
YZF

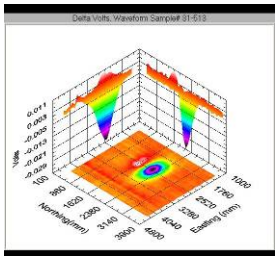
YZG

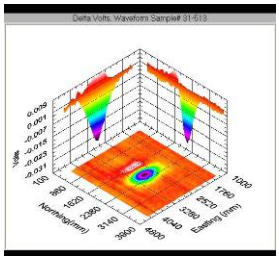
YZH

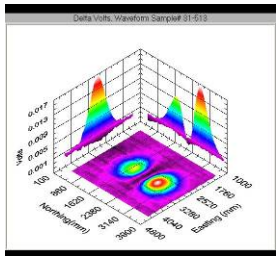
ZZE

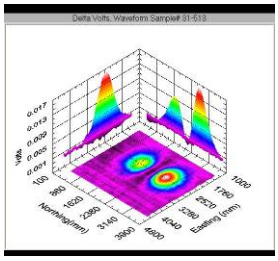
ZZF

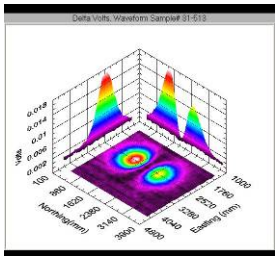
ZZG

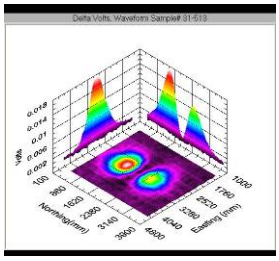
ZZH

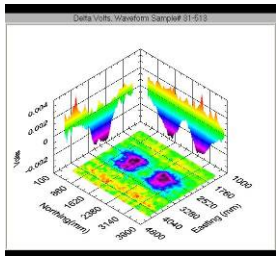
ZX1

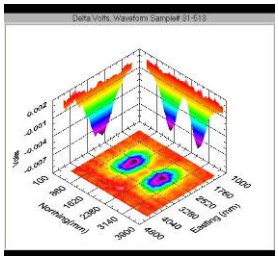
ZY1

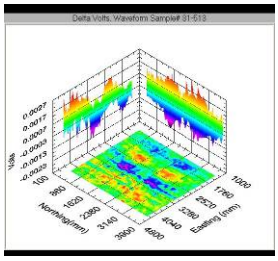
XX1

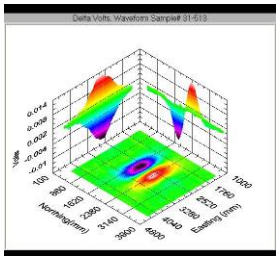
YY1

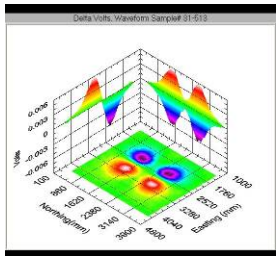
XZM

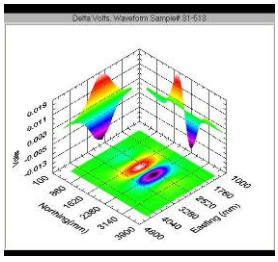
YZM

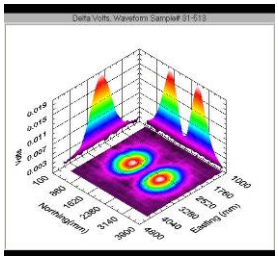
ZZM

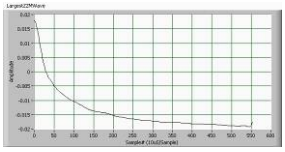
Largest ZZM waveform

Table A.3.48. DiskTwo 2007-08-27 AngleLongAz0Inc90Td103

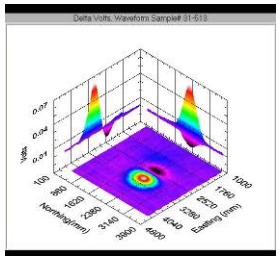
XZE

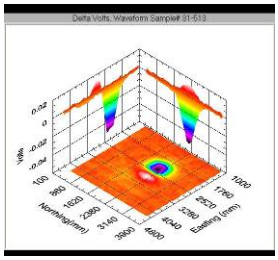
XZF

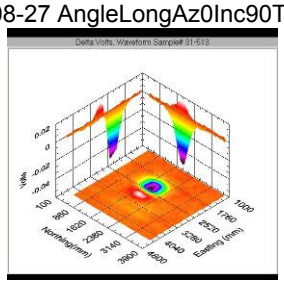
XZG

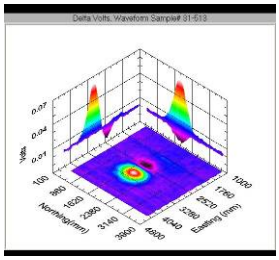
XZH

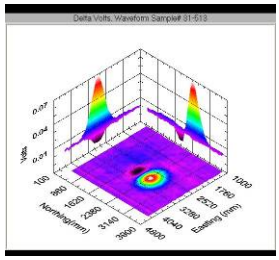
YZE

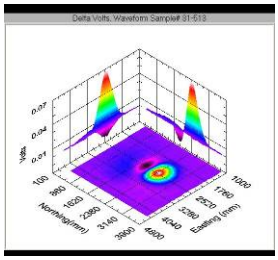
YZF

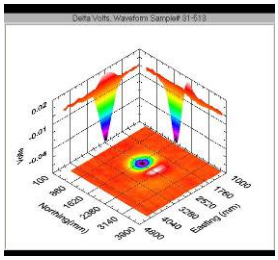
YZG

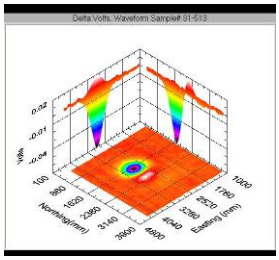
YZH

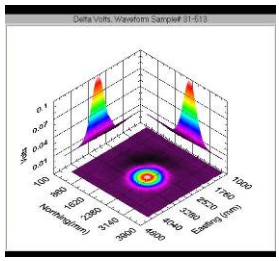
ZZE

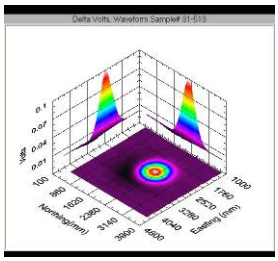
ZZF

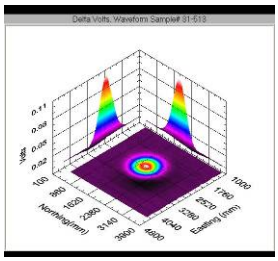
ZZG

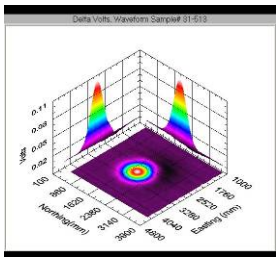
ZZH

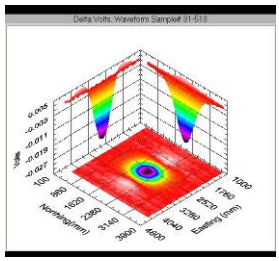
ZX1

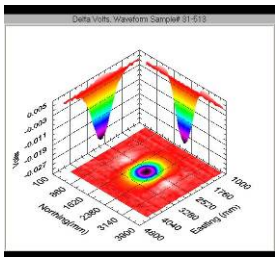
ZY1

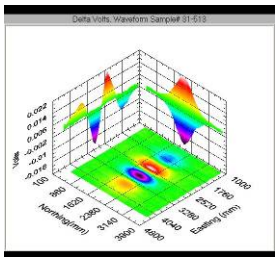
XX1

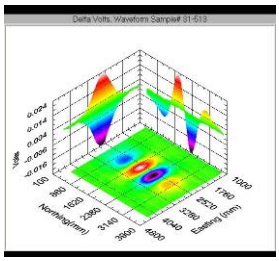
YY1

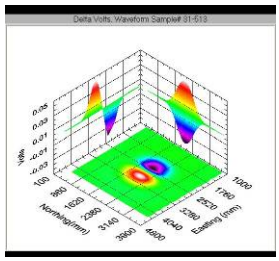
XZM

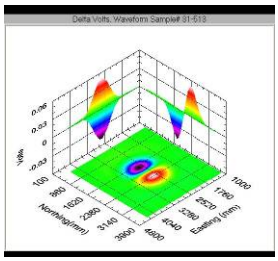
YZM

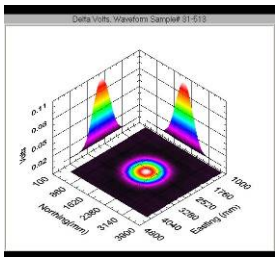
ZZM

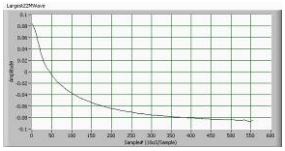
Largest ZZM waveform

Table A.3.49. DiskTwo 2007-08-27 AngleLongAz45Inc45Td103

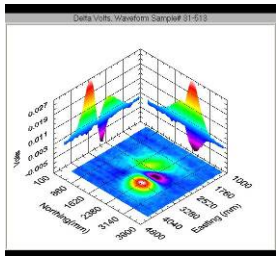
XZE

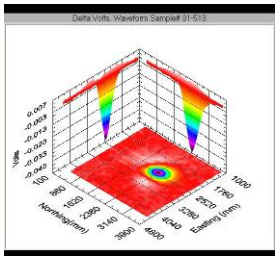
XZF

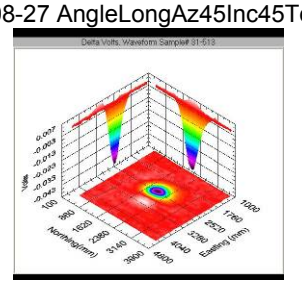
XZG

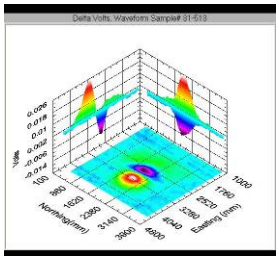
XZH

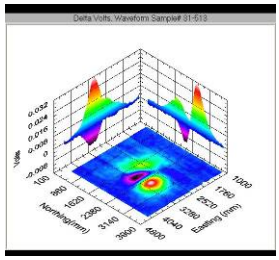
YZE

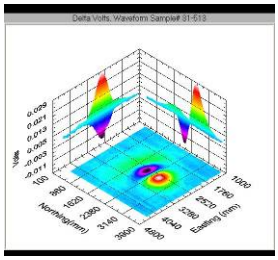
YZF

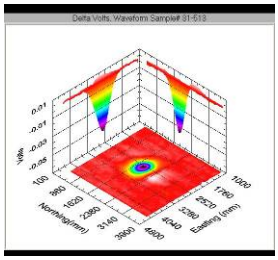
YZG

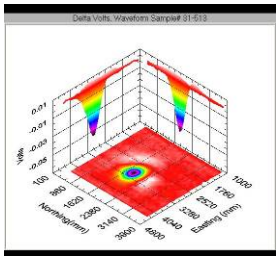
YZH

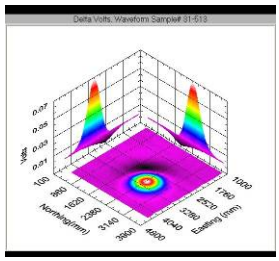
ZZE

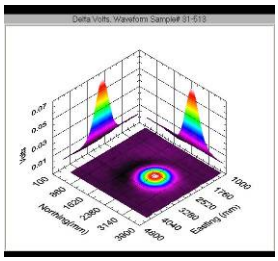
ZZF

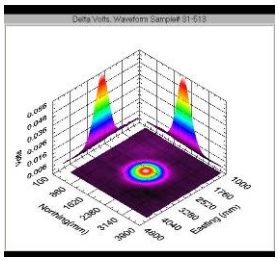
ZZG

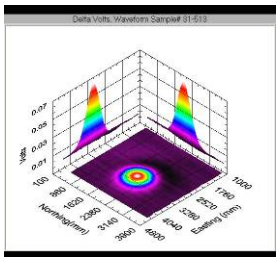
ZZH

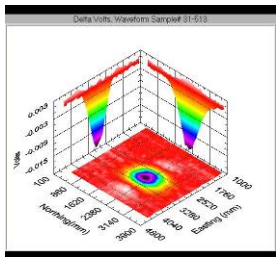
ZX1

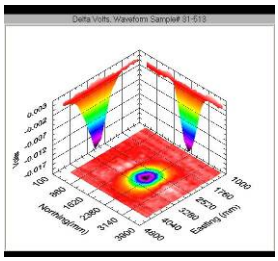
ZY1

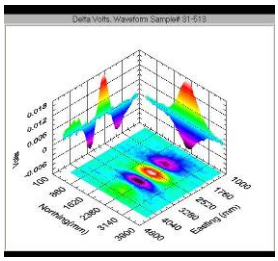
XX1

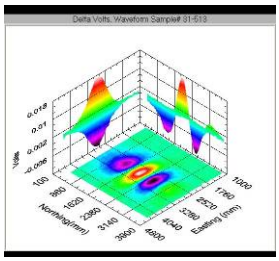
YY1

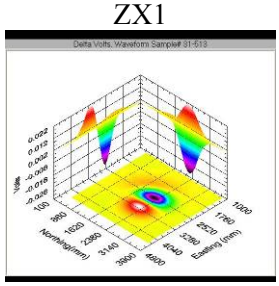
XZM

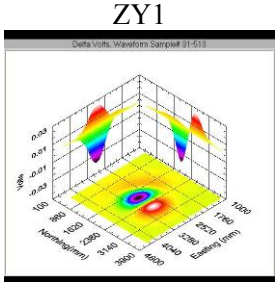
YZM

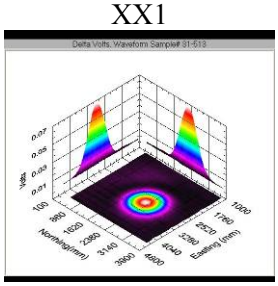
ZZM

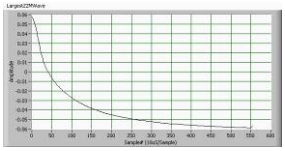
Largest ZZM waveform

Table A.3.50. DiskTwo 2007-08-27 AngleLongAz90Inc0Td103Two

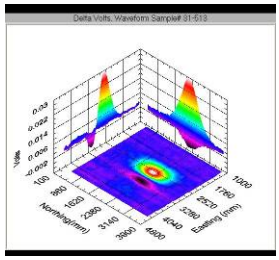
XZE

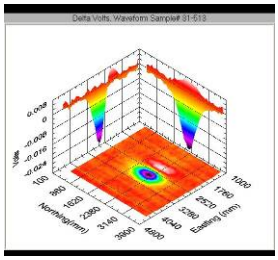
XZF

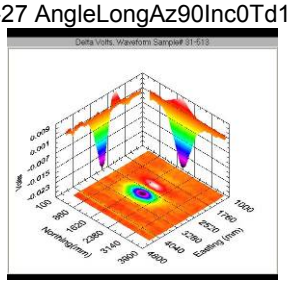
XZG

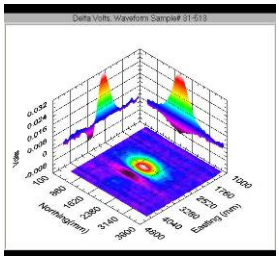
XZH

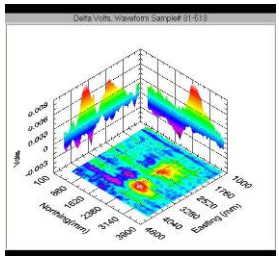
YZE

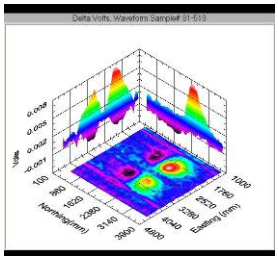
YZF

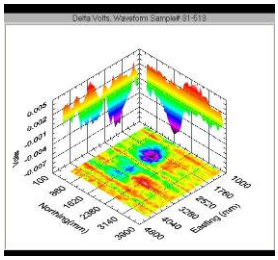
YZG

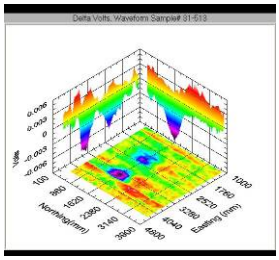
YZH

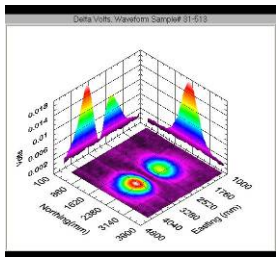
ZZE

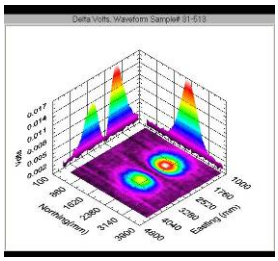
ZZF

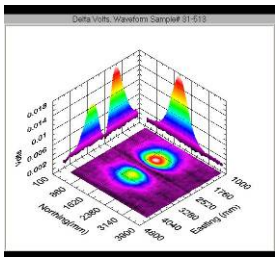
ZZG

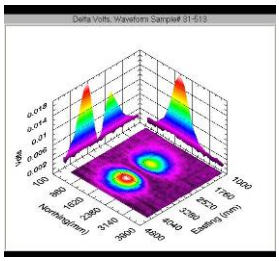
ZZH

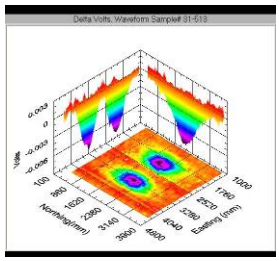
ZX1

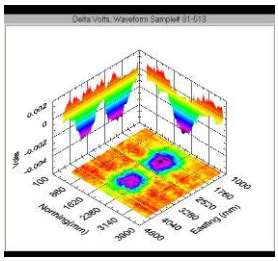
ZY1

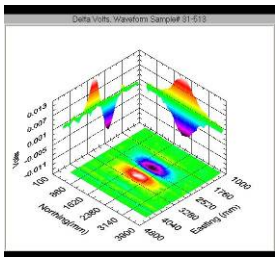
XX1

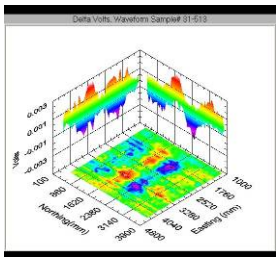
YY1

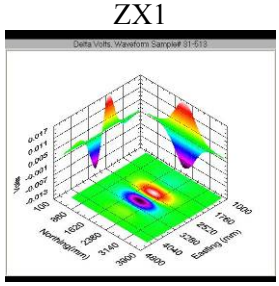
XZM

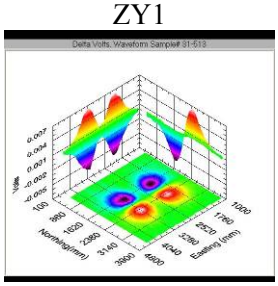
YZM

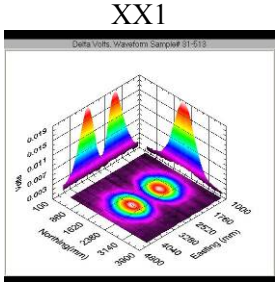
ZZM

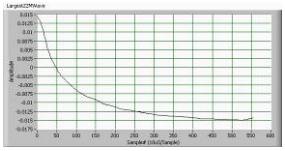
Largest ZZM waveform

# Clutter Ball Stainless

Table A.3.51. DiskTwo 2007-08-28 BallStainlessTd103RepeatTwo

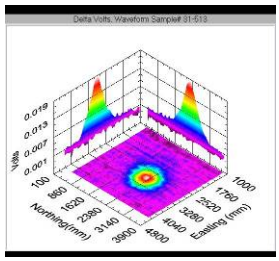
XZE

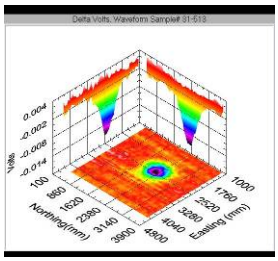
XZF

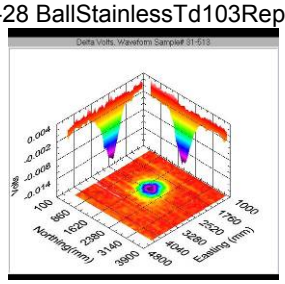
XZG

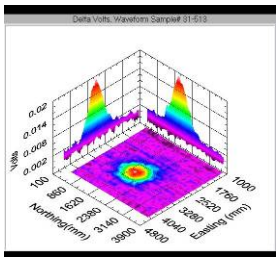
XZH

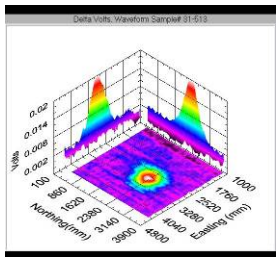
YZE

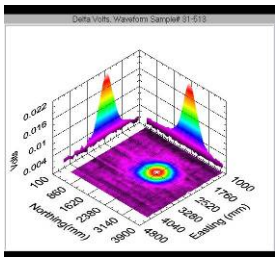
YZF

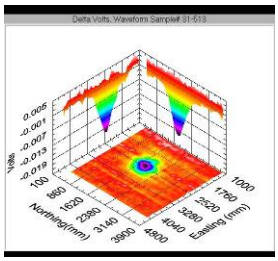
YZG

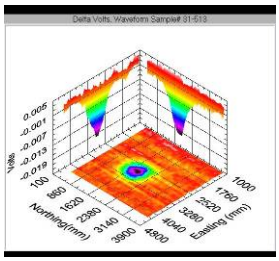
YZH

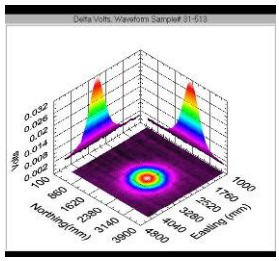
ZZE

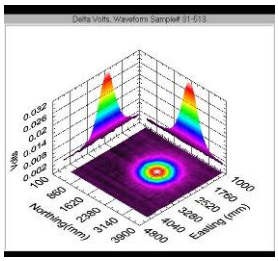
ZZF

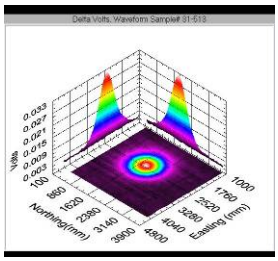
ZZG

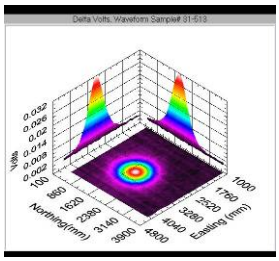
ZZH

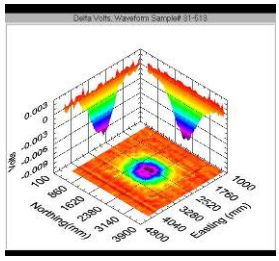
ZX1

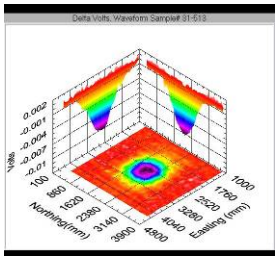
ZY1

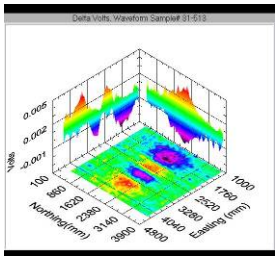
XX1

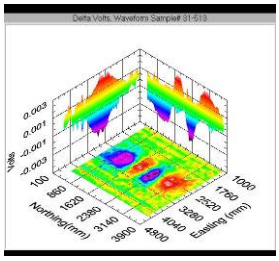
YY1

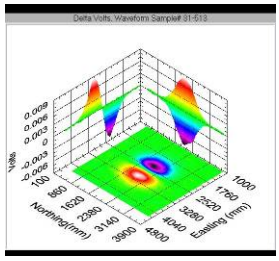
XZM

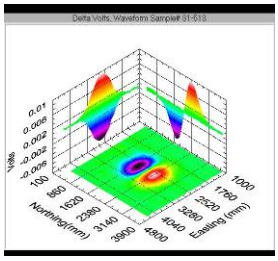
YZM

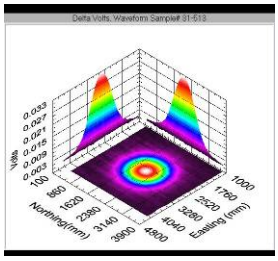
ZZM

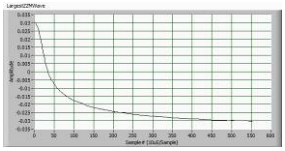
Largest ZZM waveform

# Clutter Chain

Table A.3.52. DiskTwo 2007-08-01 ChainAz0Inc0Td73

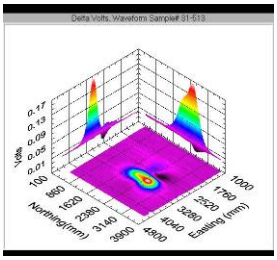
XZE

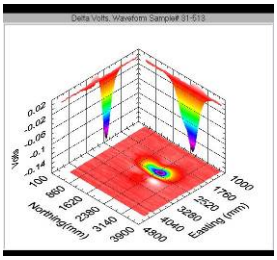
XZF

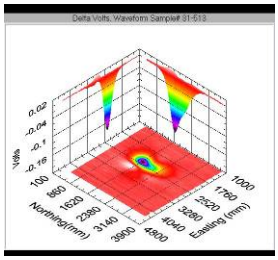
XZG

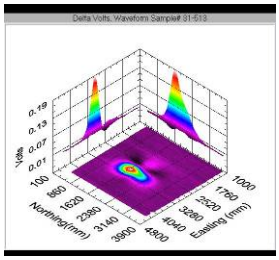
XZH

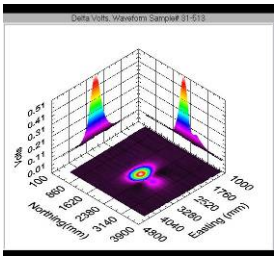
YZE

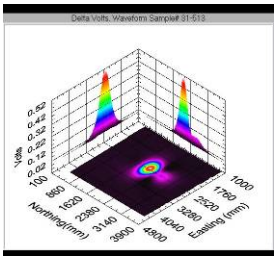
YZF

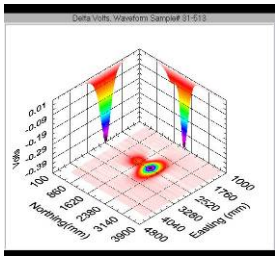
YZG

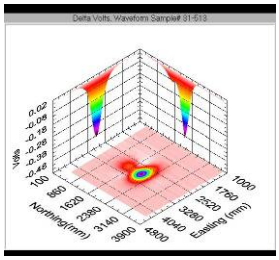
YZH

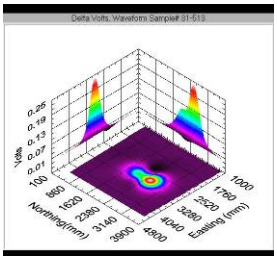
ZZE

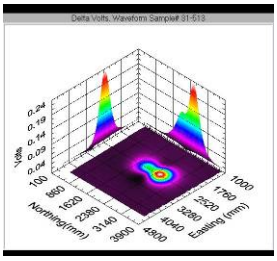
ZZF

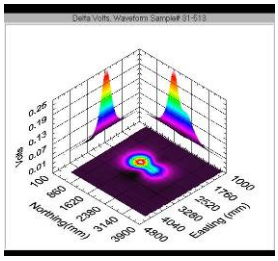
ZZG

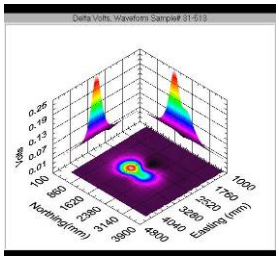
ZZH

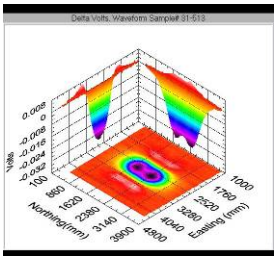
ZX1

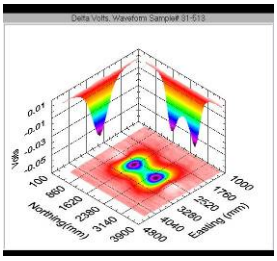
ZY1

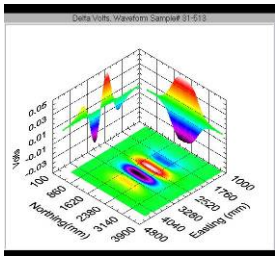
XX1

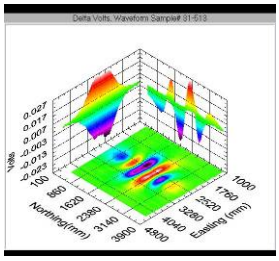
YY1

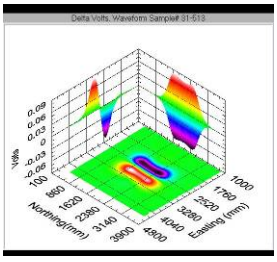
XZM

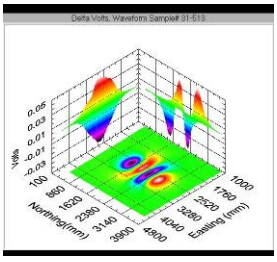
YZM

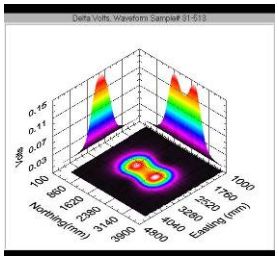
ZZM

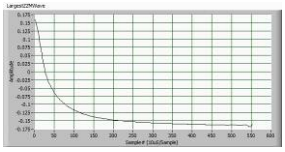
Largest ZZM waveform

Table A.3.53. DiskTwo 2007-08-01 ChainAz0Inc90Td73

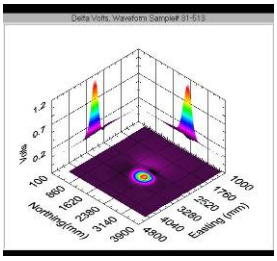
XZE

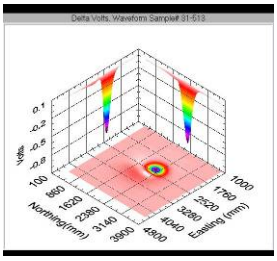
XZF

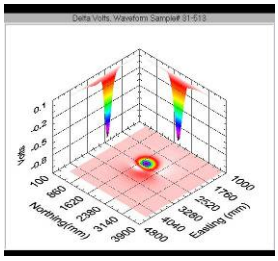
XZG

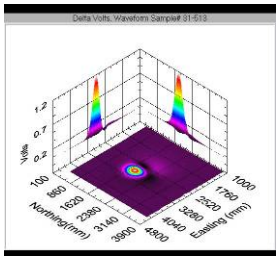
XZH

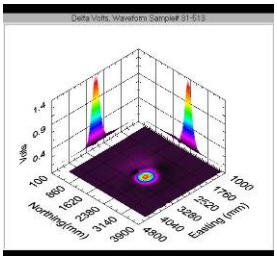
YZE

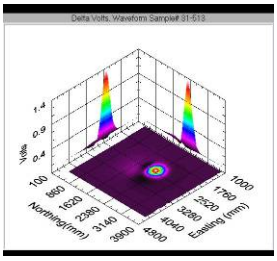
YZF

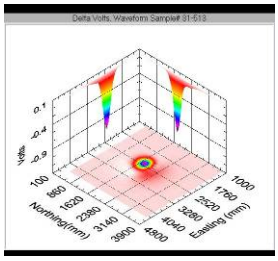
YZG

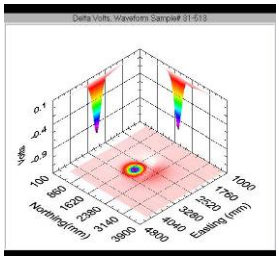
YZH

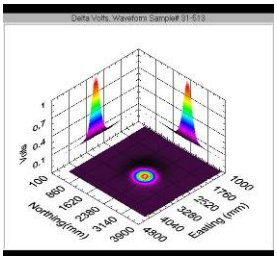
ZZE

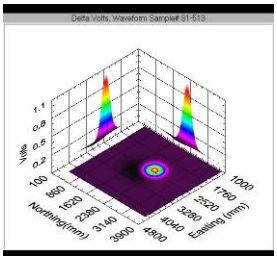
ZZF

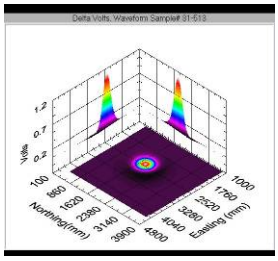
ZZG

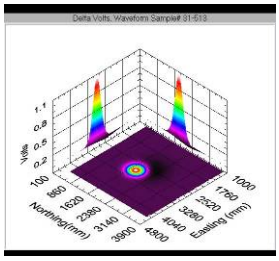
ZZH

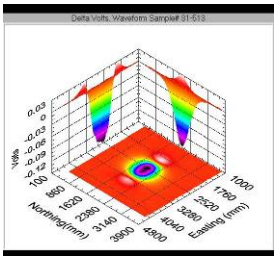
ZX1

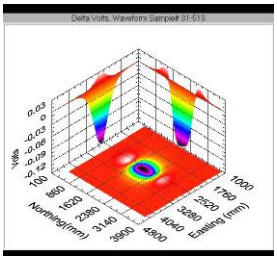
ZY1

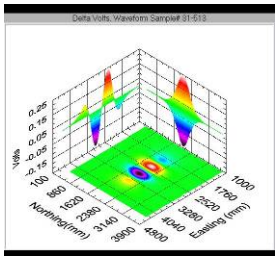
XX1

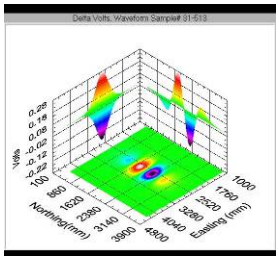
YY1

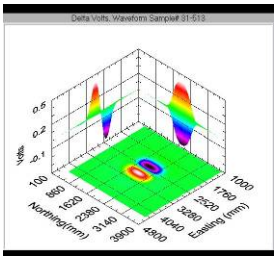
XZM

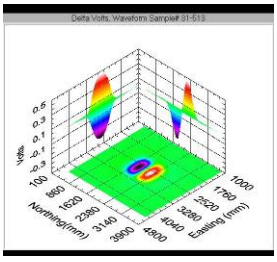
YZM

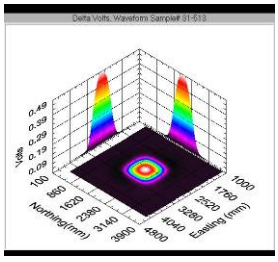
ZZM

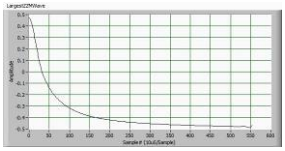
Largest ZZM waveform

Table A.3.54. DiskTwo 2007-08-01 ChainAz45Inc45Td73

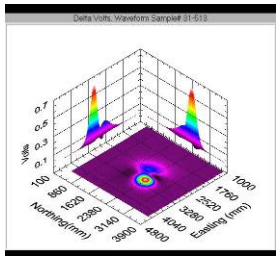
XZE

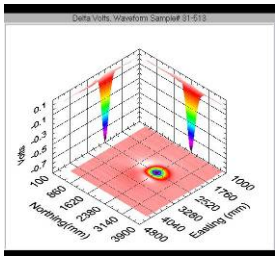
XZF

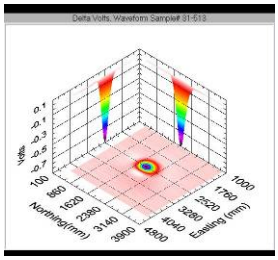
XZG

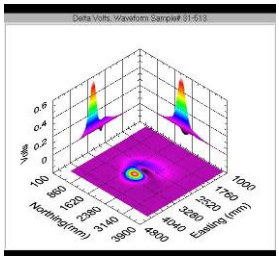
XZH

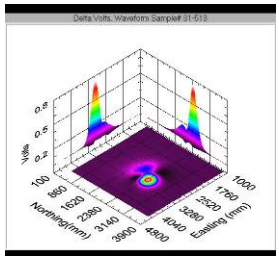
YZE

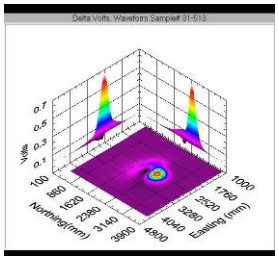
YZF

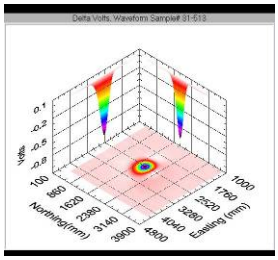
YZG

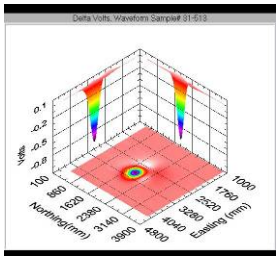
YZH

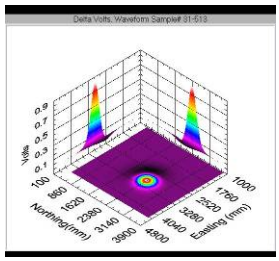
ZZE

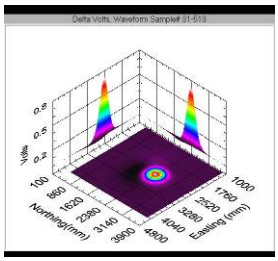
ZZF

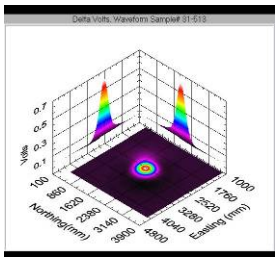
ZZG

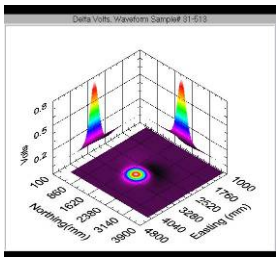
ZZH

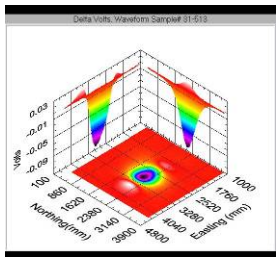
ZX1

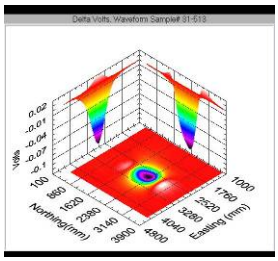
ZY1

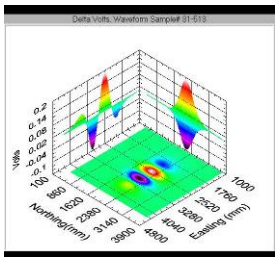
XX1

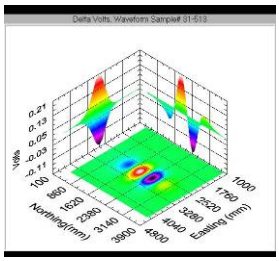
YY1

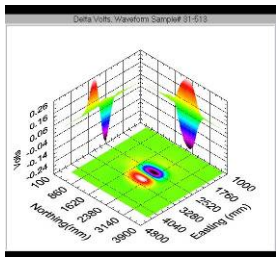
XZM

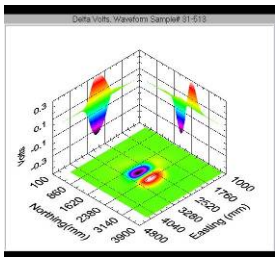
YZM

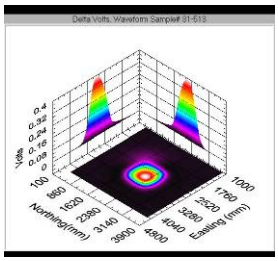
ZZM

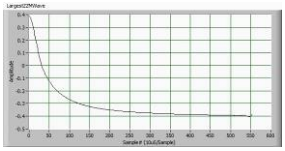
Largest ZZM waveform

Table A.3.55. DiskTwo 2007-08-27 ChainAz0Inc0Td103

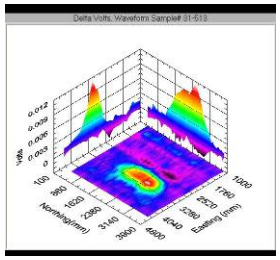
XZE

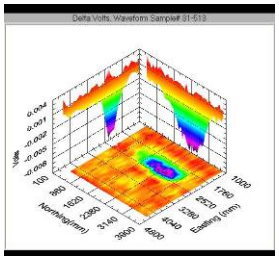
XZF

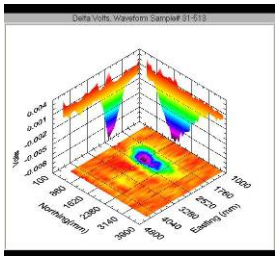
XZG

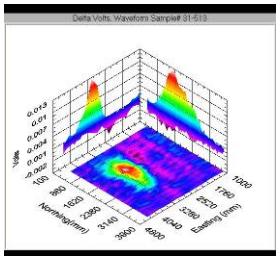
XZH

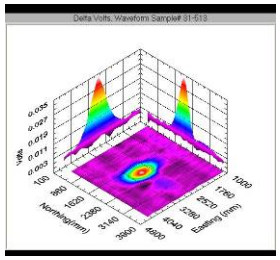
YZE

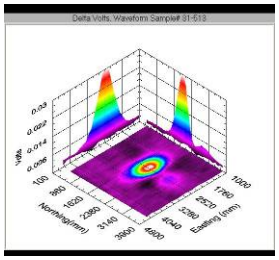
YZF

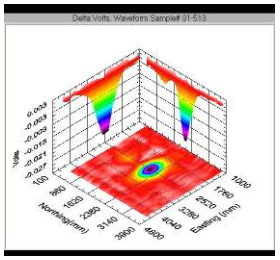
YZG

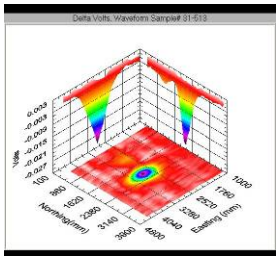
YZH

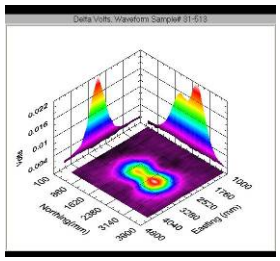
ZZE

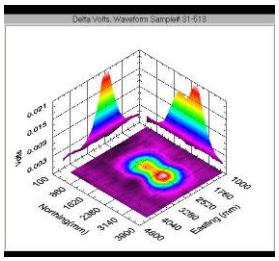
ZZF

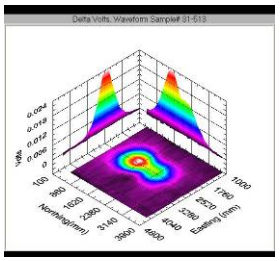
ZZG

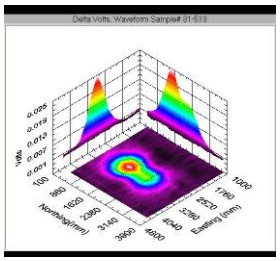
ZZH

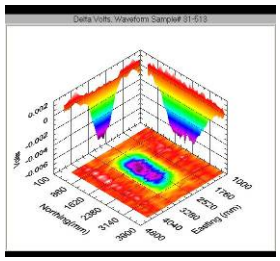
ZX1

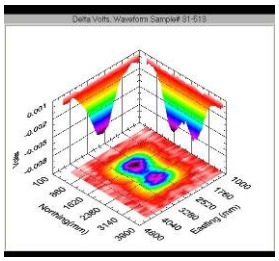
ZY1

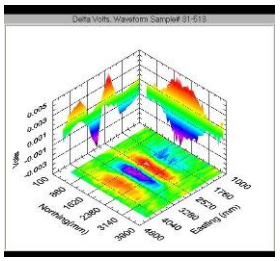
XX1

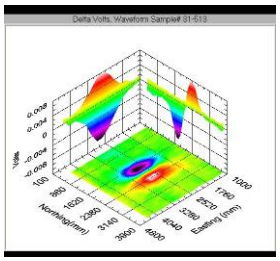
YY1

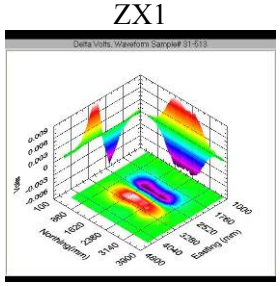
XZM

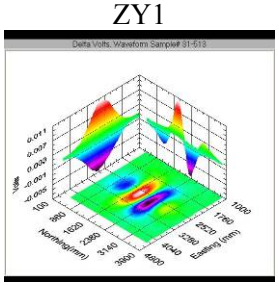
YZM

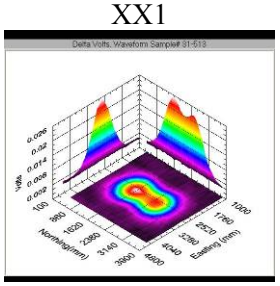
ZZM

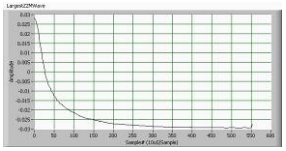
Largest ZZM waveform

Table A.3.56. DiskTwo 2007-08-27 ChainAz0Inc0Td103

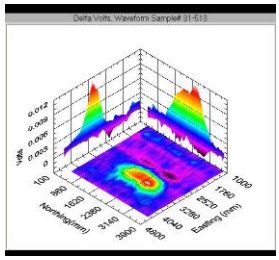
XZE

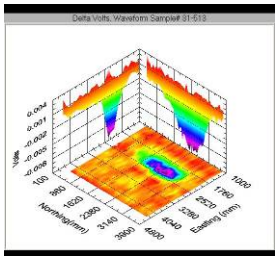
XZF

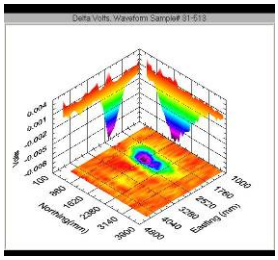
XZG

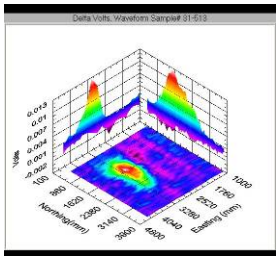
XZH

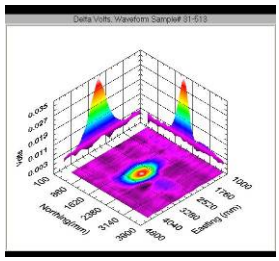
YZE

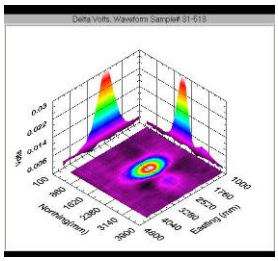
YZF

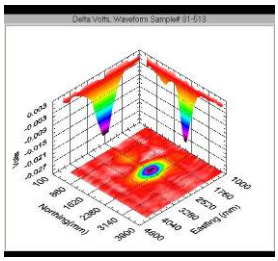
YZG

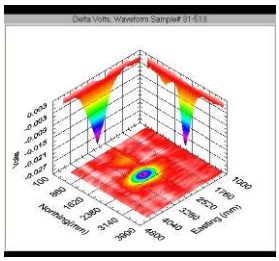
YZH

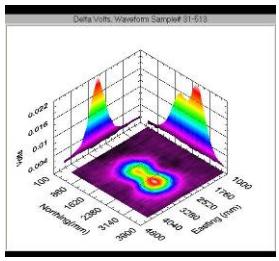
ZZE

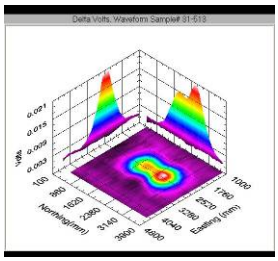
ZZF

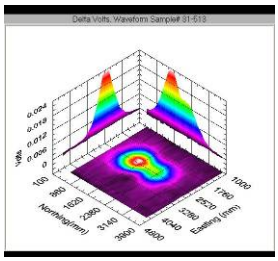
ZZG

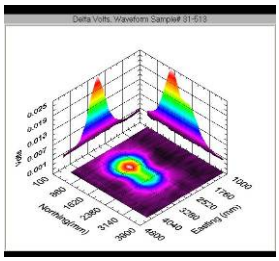
ZZH

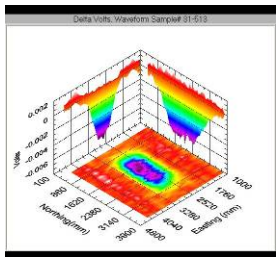
ZX1

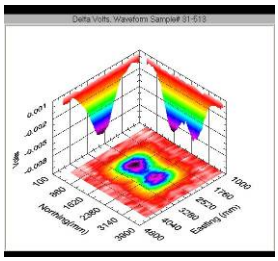
ZY1

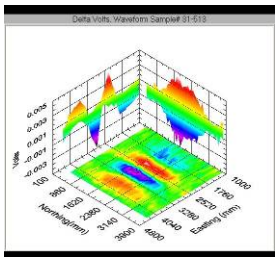
XX1

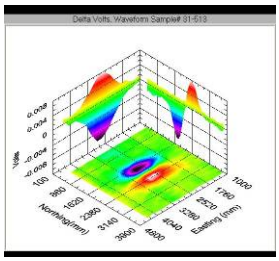
YY1

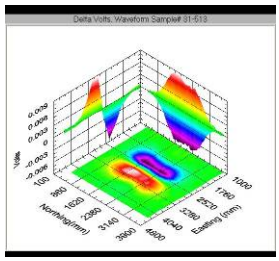
XZM

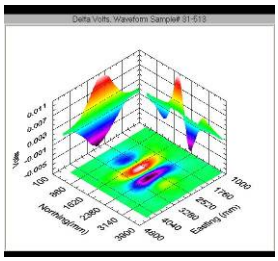
YZM

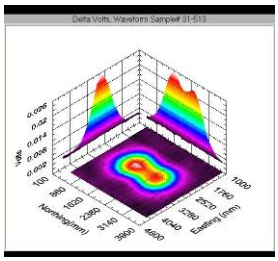
ZZM

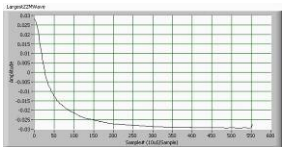
Largest ZZM waveform

## Clutter Disk Large

This larger disk was only surveyed at the deep depth.

Table A.3.57. DiskTwo 2007-08-24 DiskLargeHorzTd103

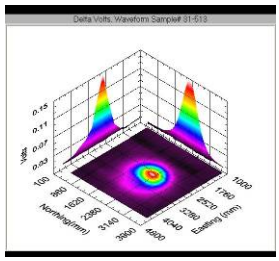
XZE

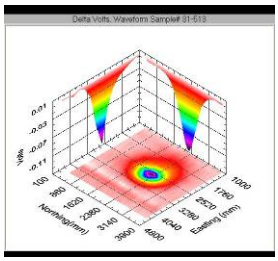
XZF

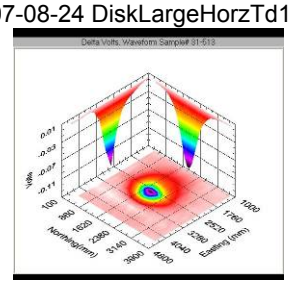
XZG

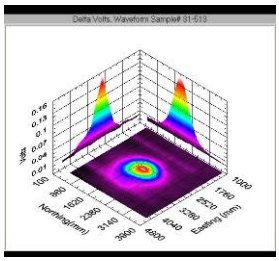
XZH

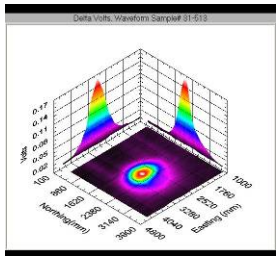
YZE

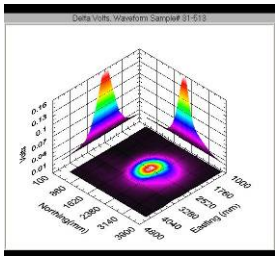
YZF

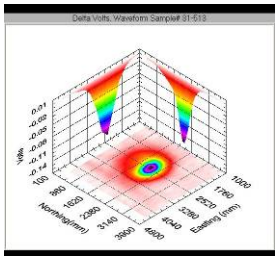
YZG

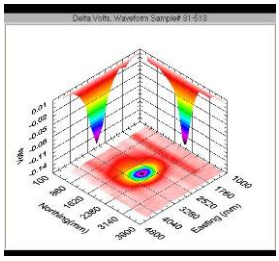
YZH

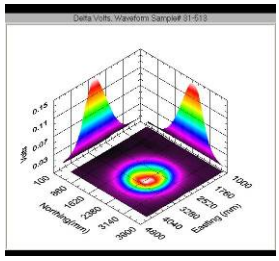
ZZE

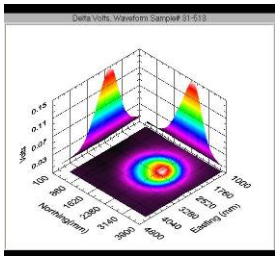
ZZF

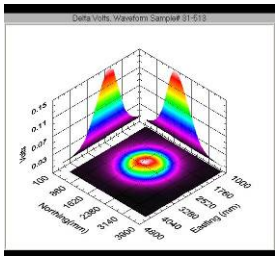
ZZG

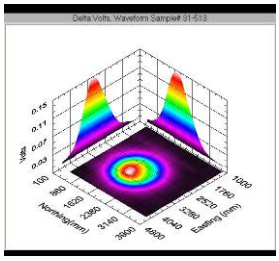
ZZH

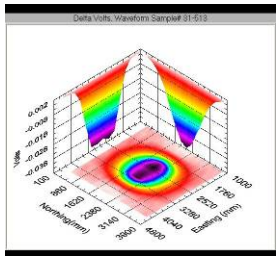
ZX1

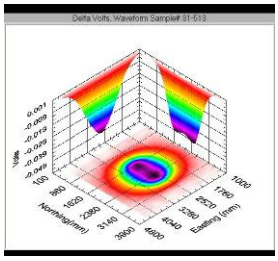
ZY1

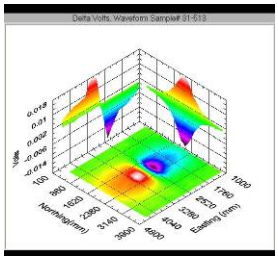
XX1

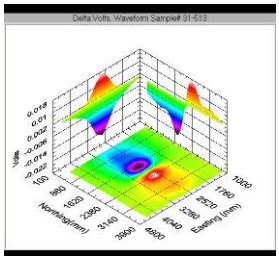
YY1

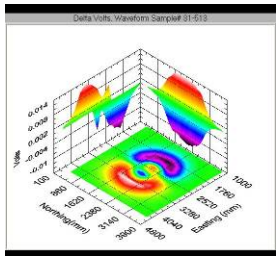
XZM

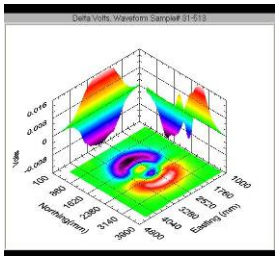
YZM

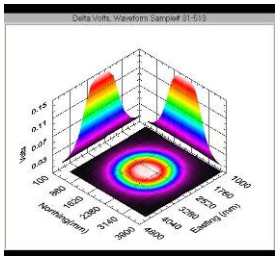
ZZM

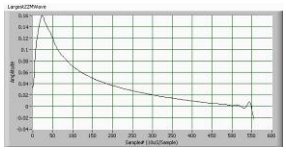
Largest ZZM waveform

Table A.3.58. DiskTwo 2007-08-24 DiskLargeVertTd103Two

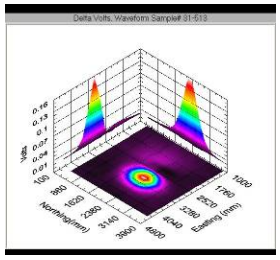
XZE

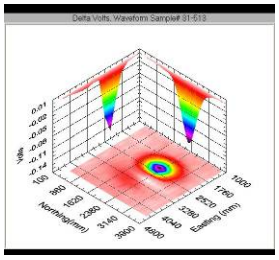
XZF

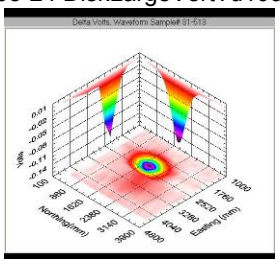
XZG

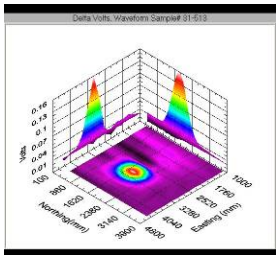
XZH

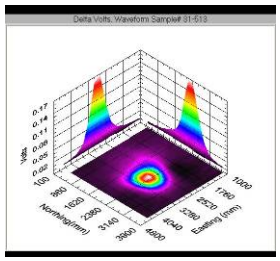
YZE

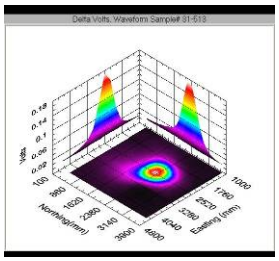
YZF

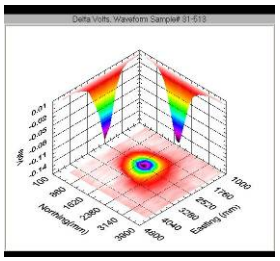
YZG

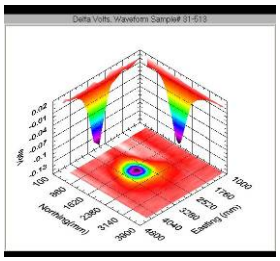
YZH

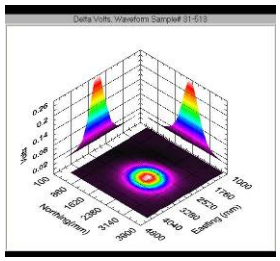
ZZE

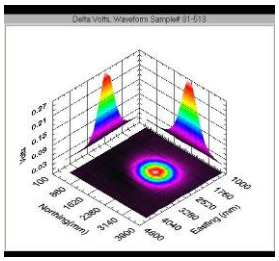
ZZF

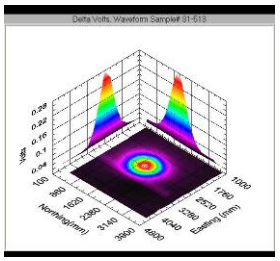
ZZG

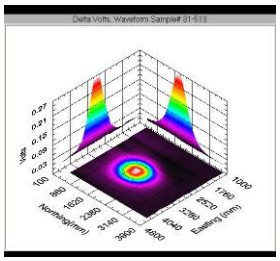
ZZH

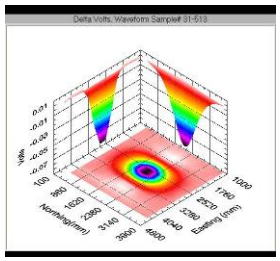
ZX1

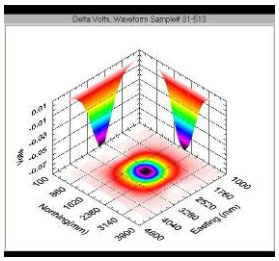
ZY1

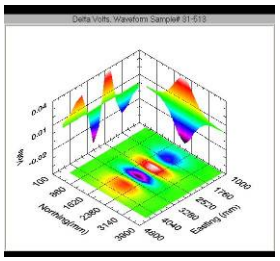
XX1

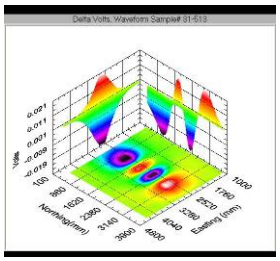
YY1

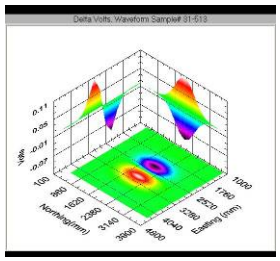
XZM

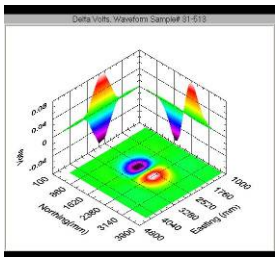
YZM

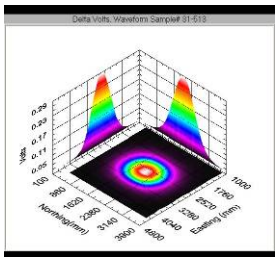
ZZM

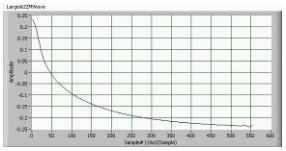
Largest ZZM waveform

# Clutter Disk Small

Table A.3.59. DiskTwo 2007-08-13 DiskSmallHorzTd73

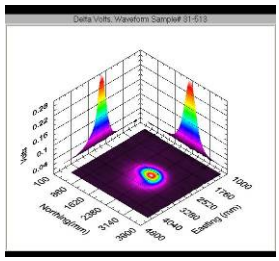
XZE

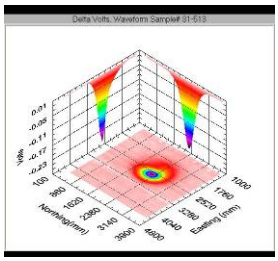
XZF

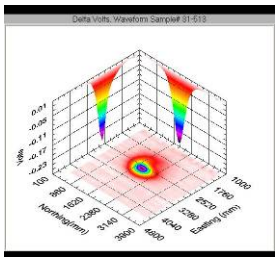
XZG

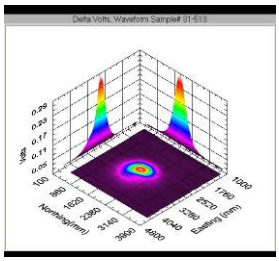
XZH

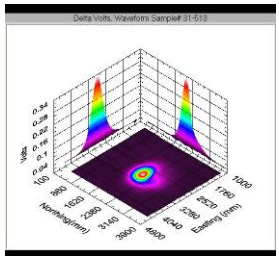
YZE

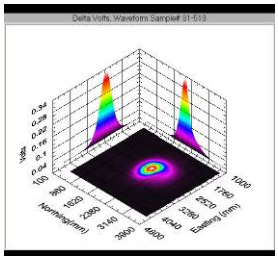
YZF

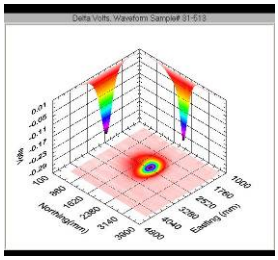
YZG

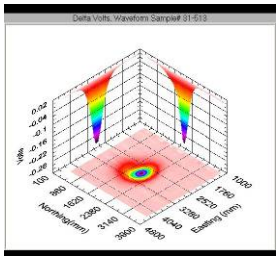
YZH

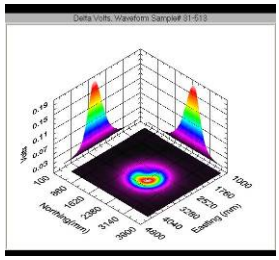
ZZE

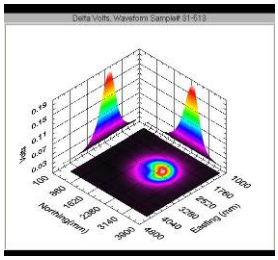
ZZF

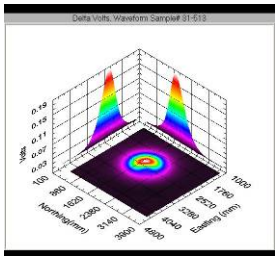
ZZG

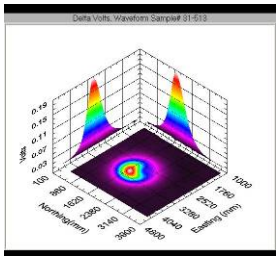
ZZH

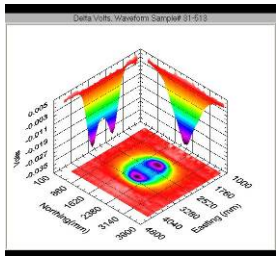
ZX1

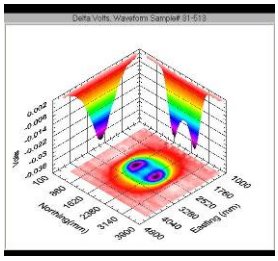
ZY1

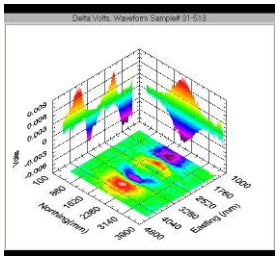
XX1

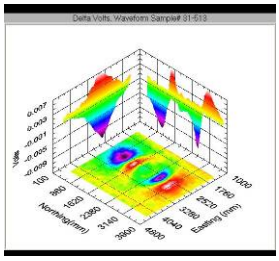
YY1

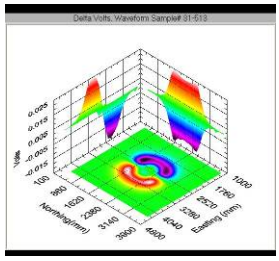
XZM

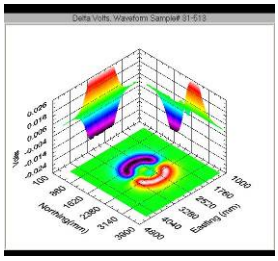
YZM

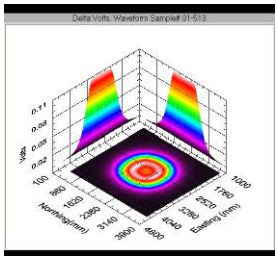
ZZM

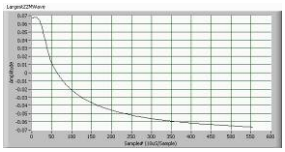
Largest ZZM waveform

Table A.3.60. DiskTwo 2007-08-13 DiskSmallVertTd73

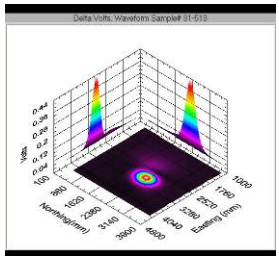
XZE

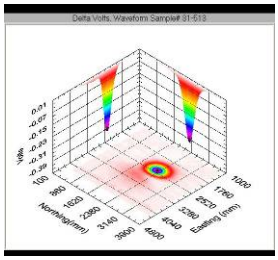
XZF

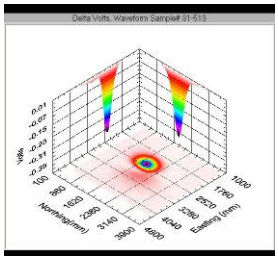
XZG

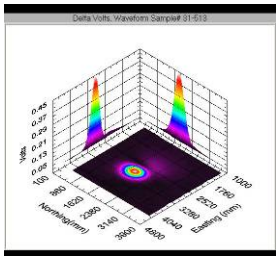
XZH

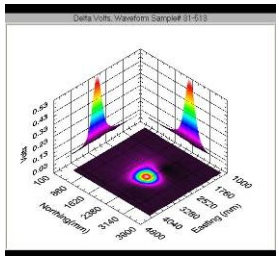
YZE

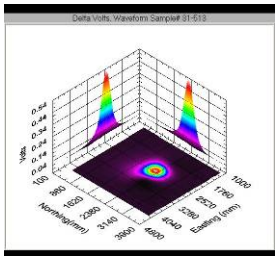
YZF

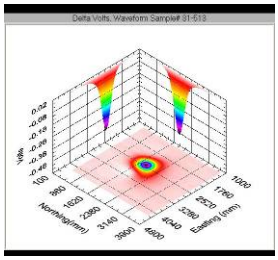
YZG

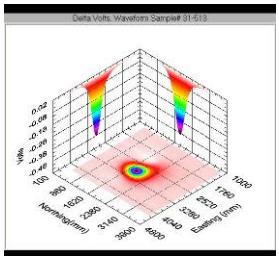
YZH

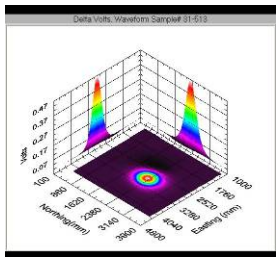
ZZE

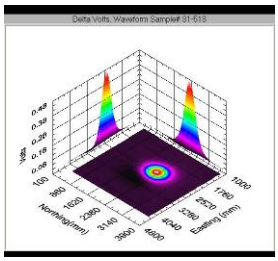
ZZF

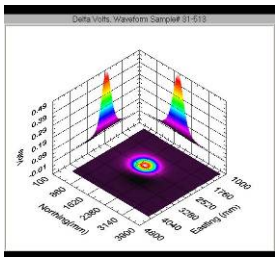
ZZG

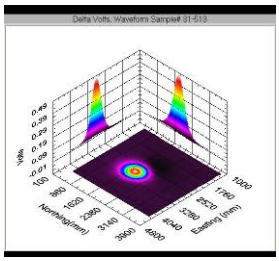
ZZH

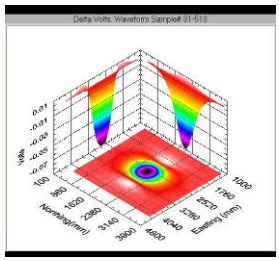
ZX1

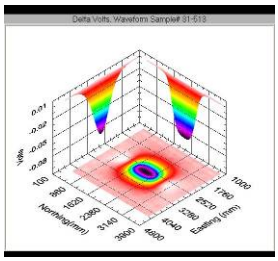
ZY1

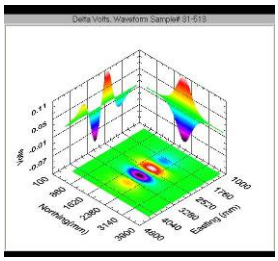
XX1

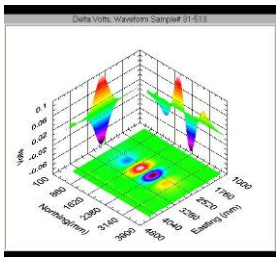
YY1

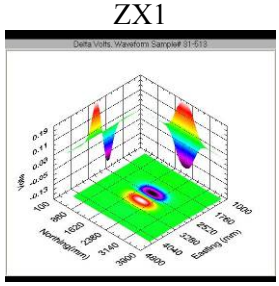
XZM

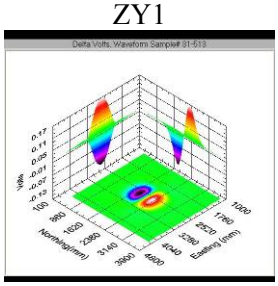
YZM

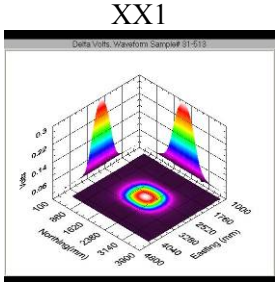
ZZM

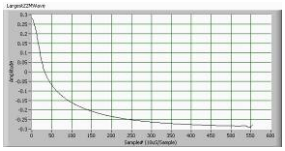
Largest ZZM waveform

Table A.3.61. DiskTwo 2007-08-24 DiskSmallHorzTd103

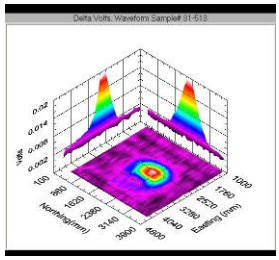
XZE

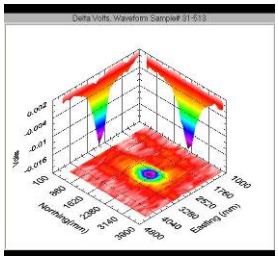
XZF

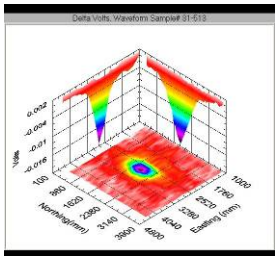
XZG

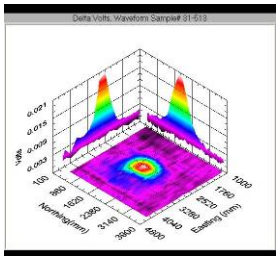
XZH

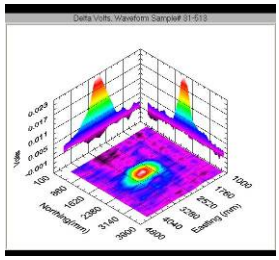
YZE

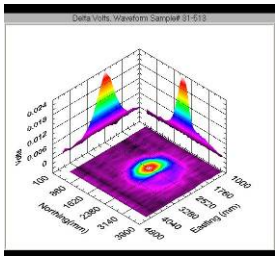
YZF

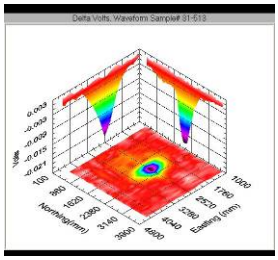
YZG

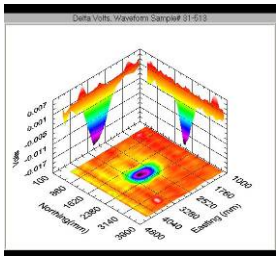
YZH

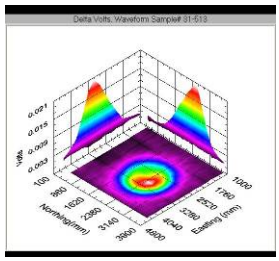
ZZE

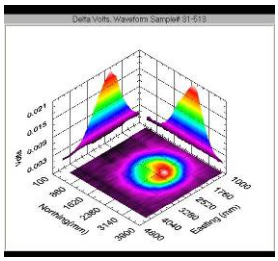
ZZF

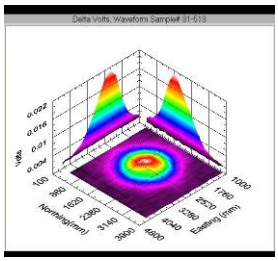
ZZG

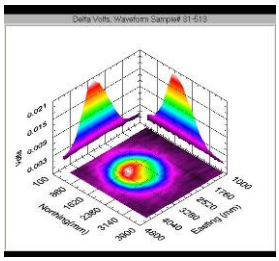
ZZH

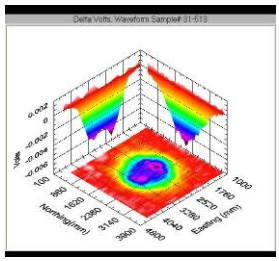
ZX1

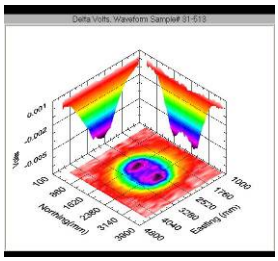
ZY1

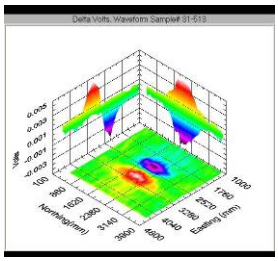
XX1

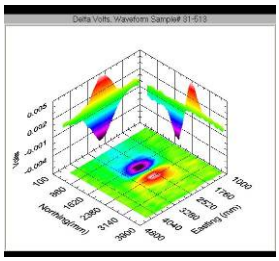
YY1

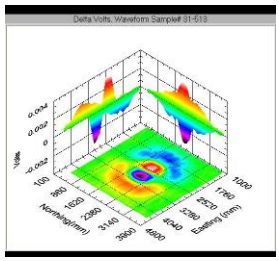
XZM

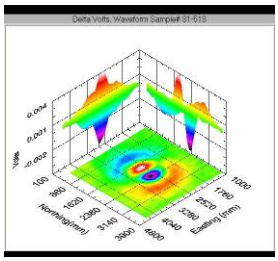
YZM

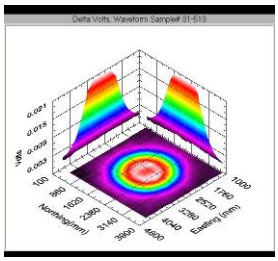
ZZM

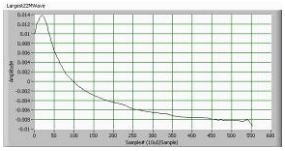
Largest ZZM waveform

Table A.3.62. DiskTwo 2007-08-27 DiskSmallVertTd103

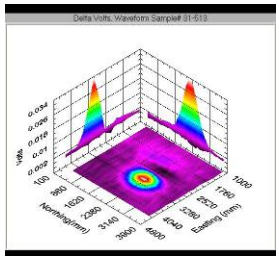
XZE

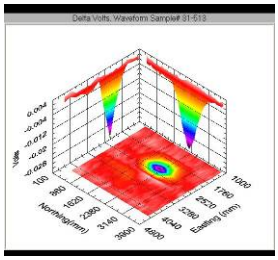
XZF

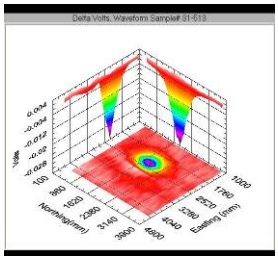
XZG

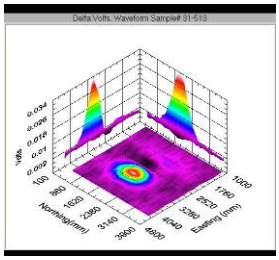
XZH

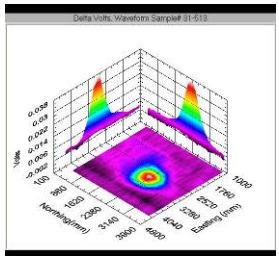
YZE

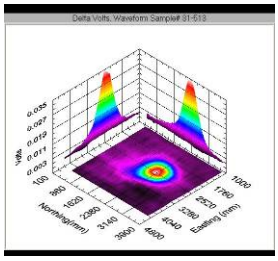
YZF

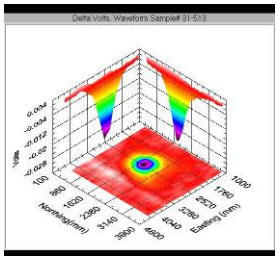
YZG

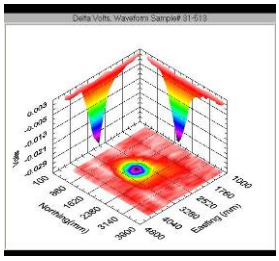
YZH

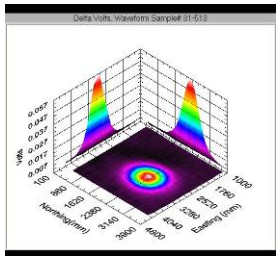
ZZE

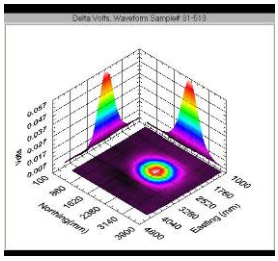
ZZF

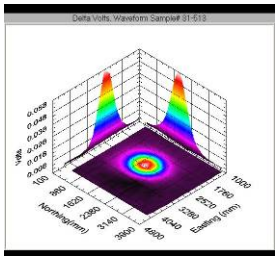
ZZG

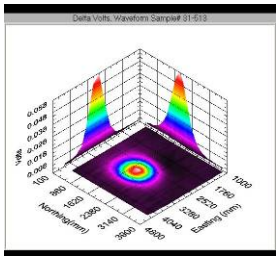
ZZH

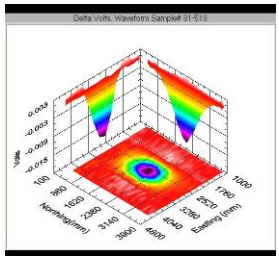
ZX1

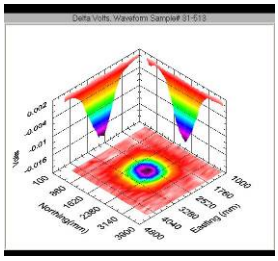
ZY1

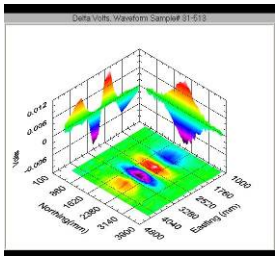
XX1

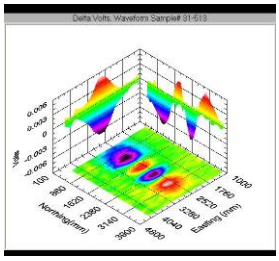
YY1

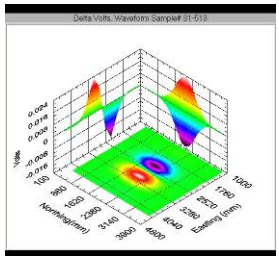
XZM

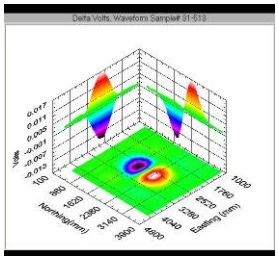
YZM

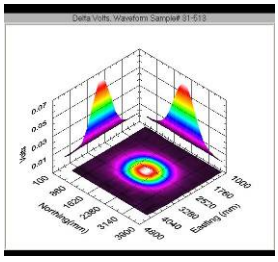
ZZM

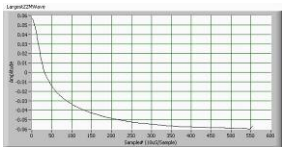
Largest ZZM waveform

# Clutter Plate Alum

Table A.3.63. DiskTwo 2007-08-13 PlateAlumHorzTd73

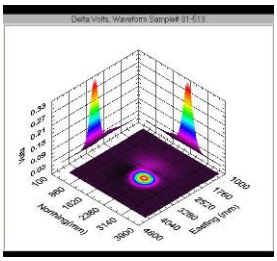
XZE

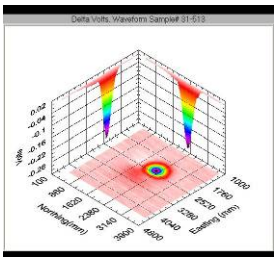
XZF

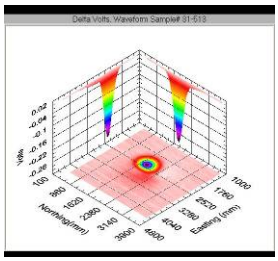
XZG

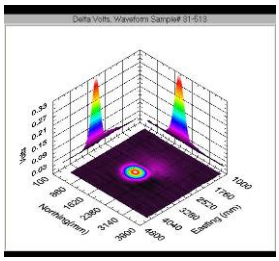
XZH

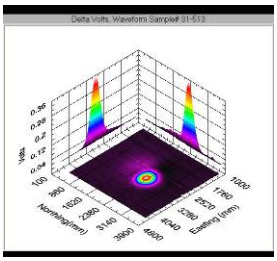
YZE

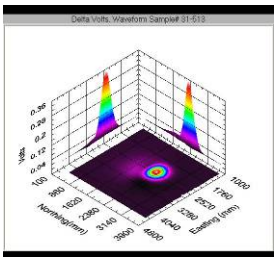
YZF

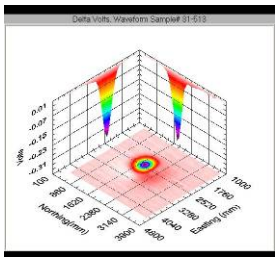
YZG

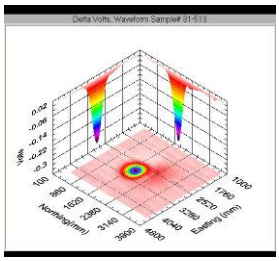
YZH

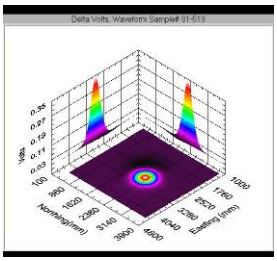
ZZE

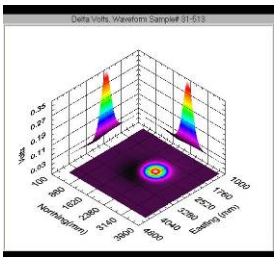
ZZF

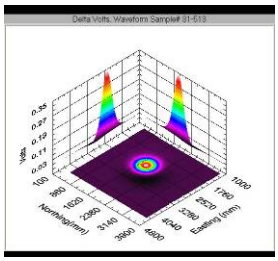
ZZG

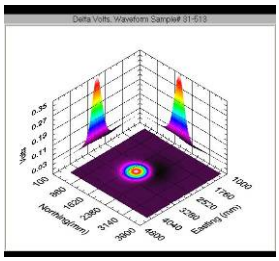
ZZH

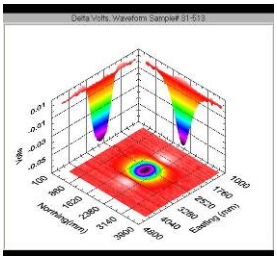
ZX1

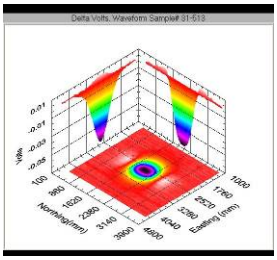
ZY1

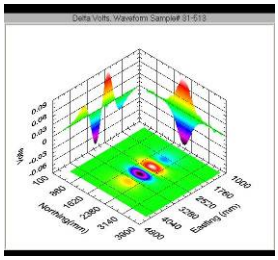
XX1

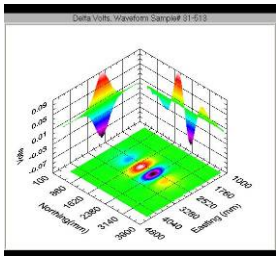
YY1

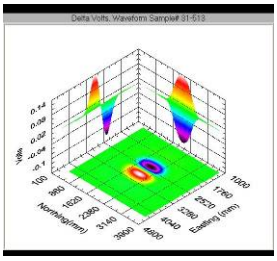
XZM

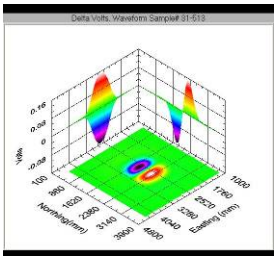
YZM

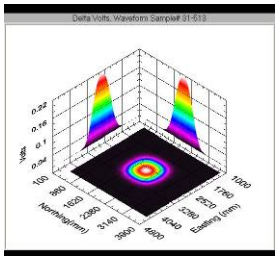
ZZM

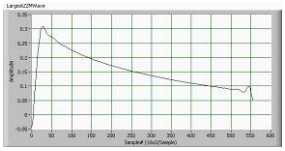
Largest ZZM waveform

Table A.3.64. DiskTwo 2007-08-13 PlateAlumVertTd73

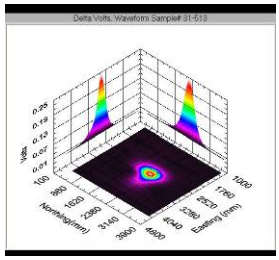
XZE

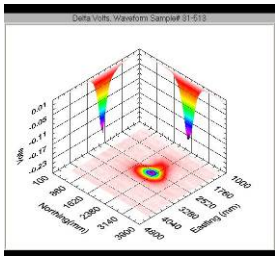
XZF

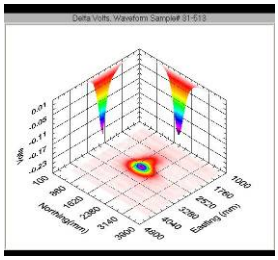
XZG

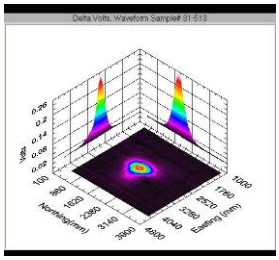
XZH

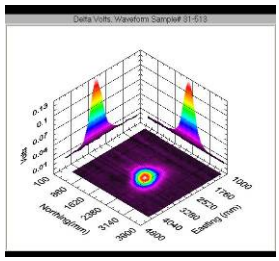
YZE

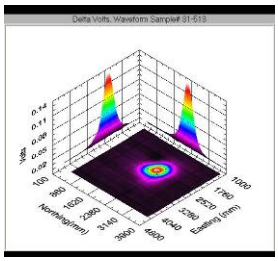
YZF

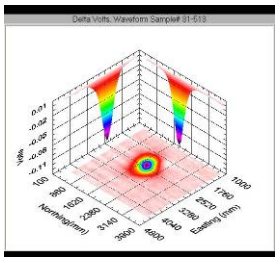
YZG

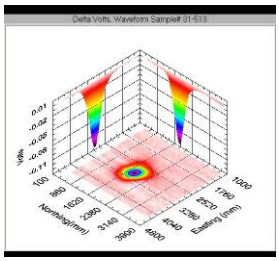
YZH

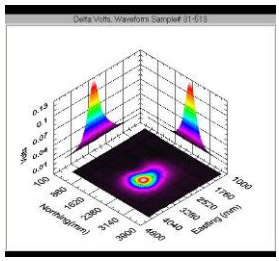
ZZE

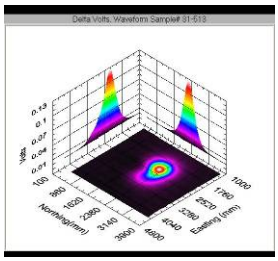
ZZF

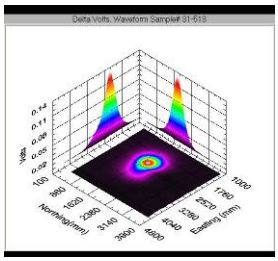
ZZG

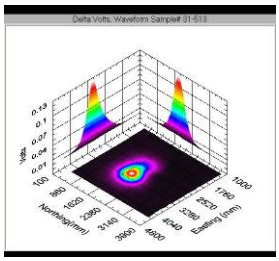
ZZH

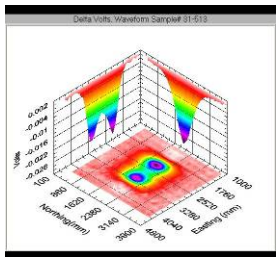
ZX1

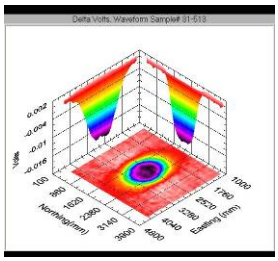
ZY1

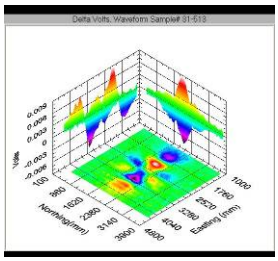
XX1

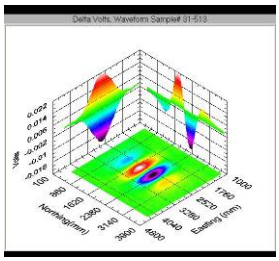
YY1

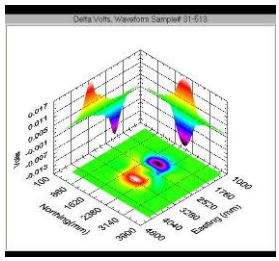
XZM

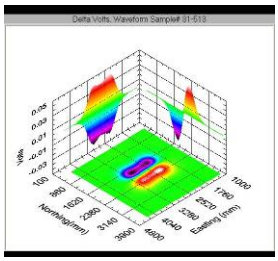
YZM

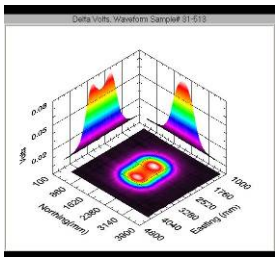
ZZM

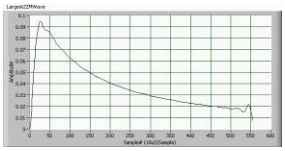
Largest ZZM waveform

Table A.3.65. DiskTwo 2007-08-24 PlateAlumHorzTd103

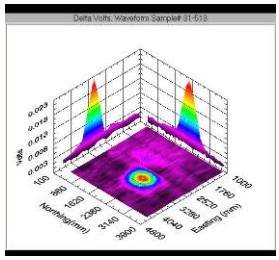
XZE

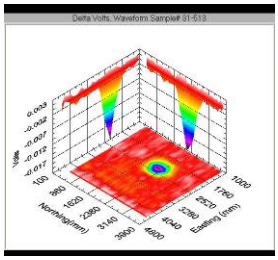
XZF

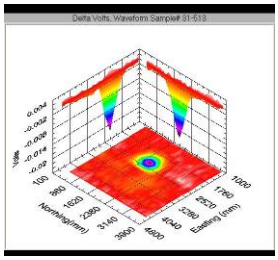
XZG

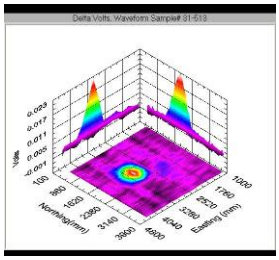
XZH

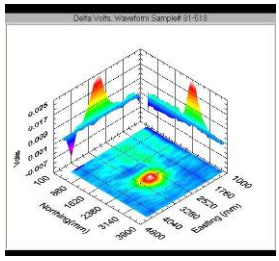
YZE

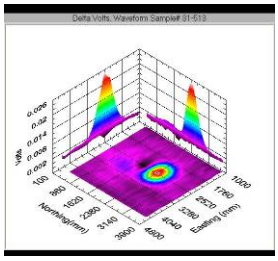
YZF

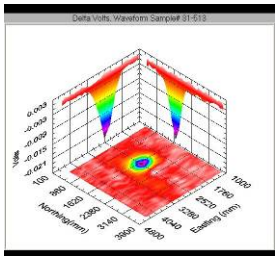
YZG

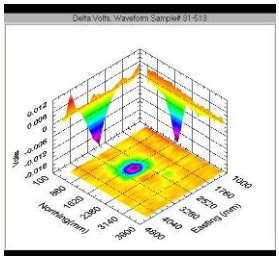
YZH

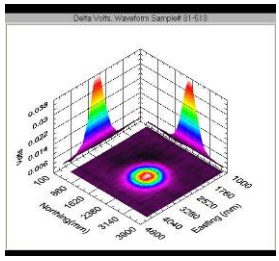
ZZE

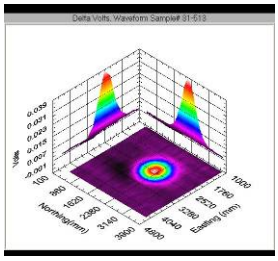
ZZF

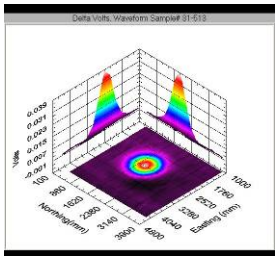
ZZG

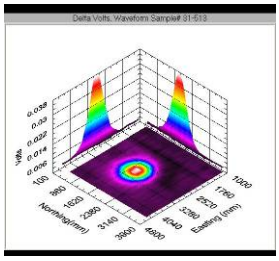
ZZH

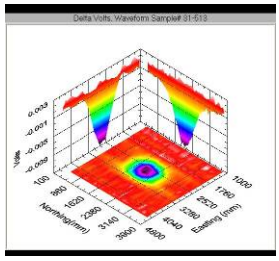
ZX1

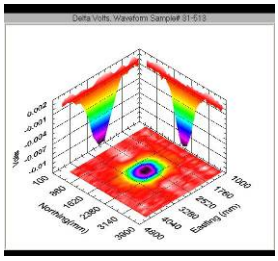
ZY1

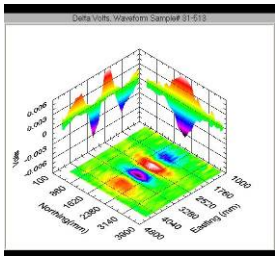
XX1

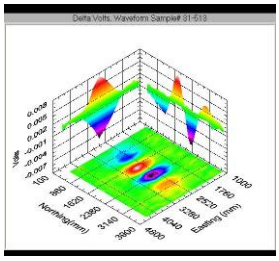
YY1

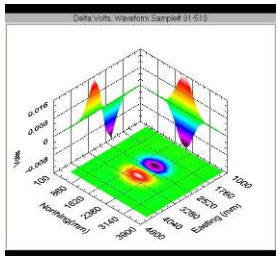
XZM

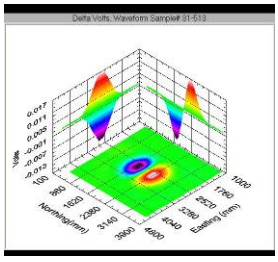
YZM

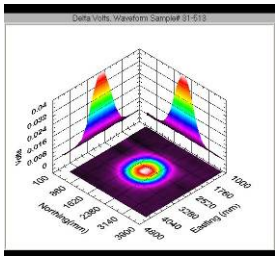
ZZM

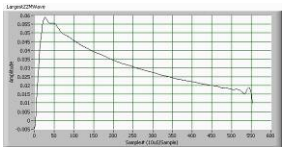
Largest ZZM waveform

Table A.3.66. DiskTwo 2007-08-23 PlateAlumVertTd103

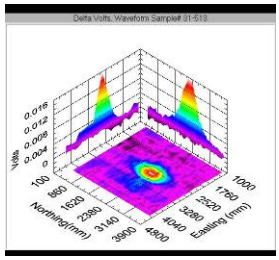
XZE

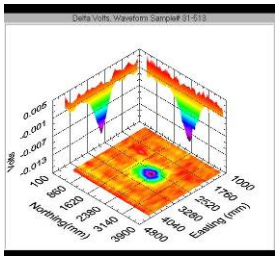
XZF

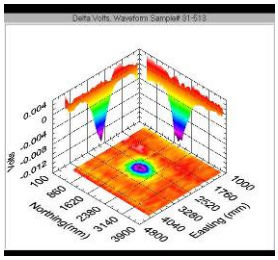
XZG

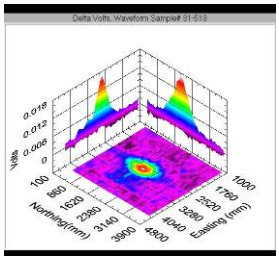
XZH

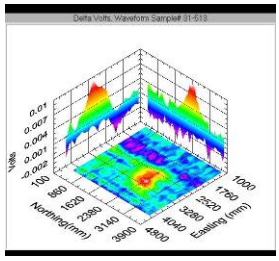
YZE

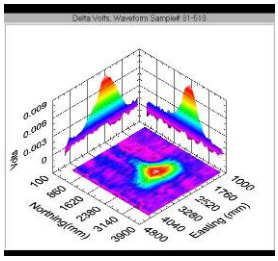
YZF

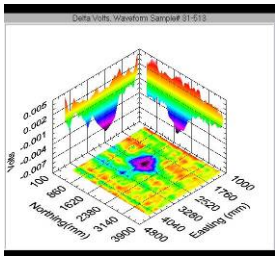
YZG

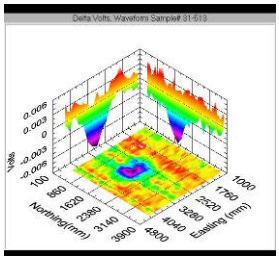
YZH

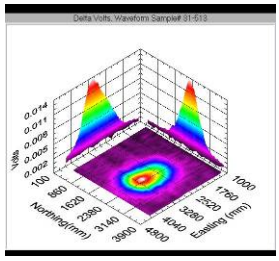
ZZE

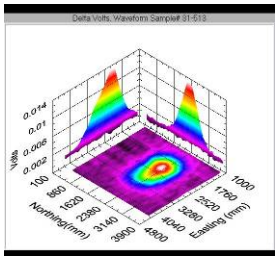
ZZF

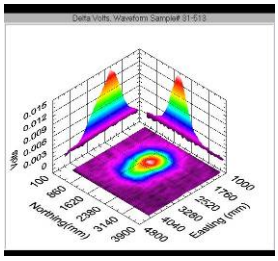
ZZG

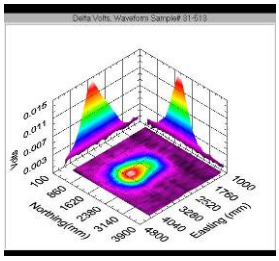
ZZH

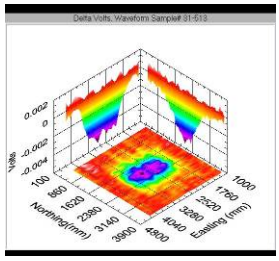
ZX1

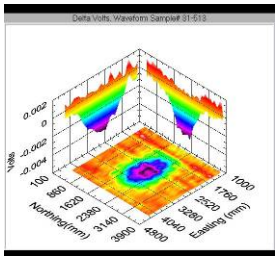
ZY1

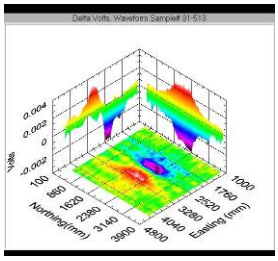
XX1

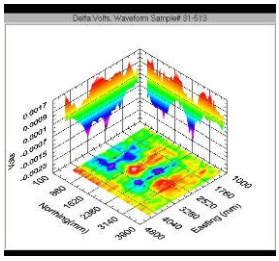
YY1

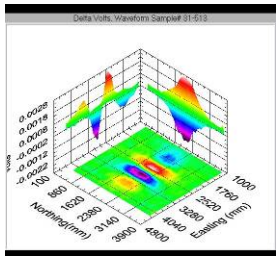
XZM

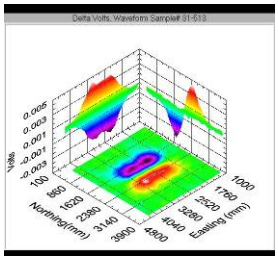
YZM

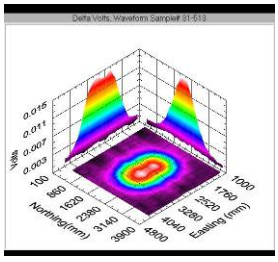
ZZM

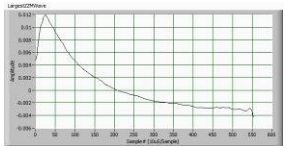
Largest ZZM waveform

## Clutter Rod

Table A.3.67. DiskTwo 2007-08-02 RodAz0Inc0Td73

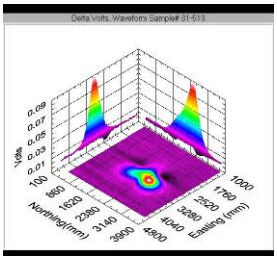
XZE

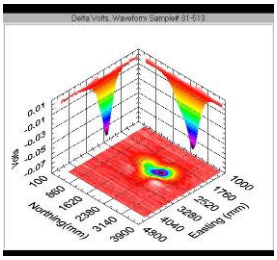
XZF

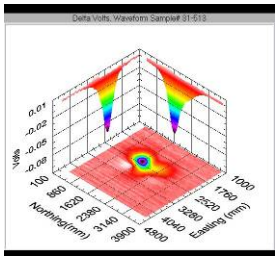
XZG

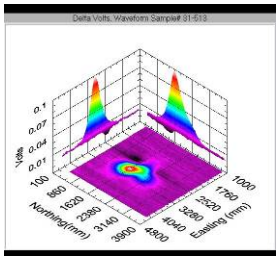
XZH

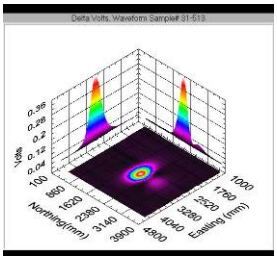
YZE

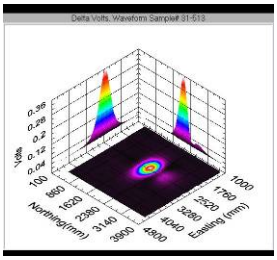
YZF

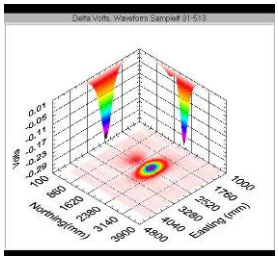
YZG

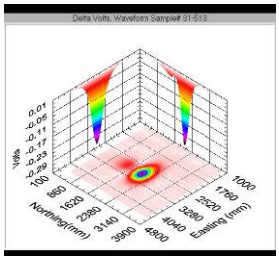
YZH

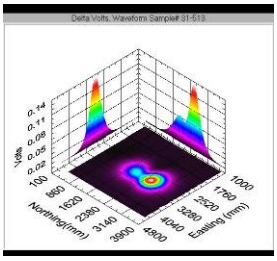
ZZE

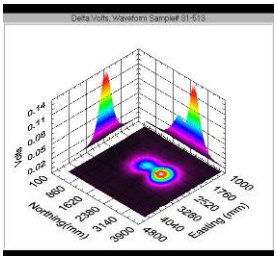
ZZF

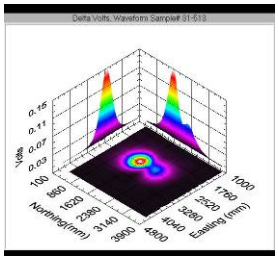
ZZG

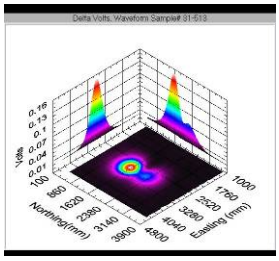
ZZH

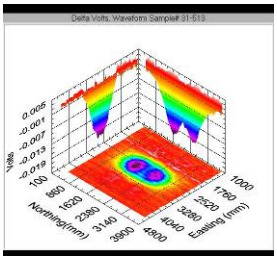
ZX1

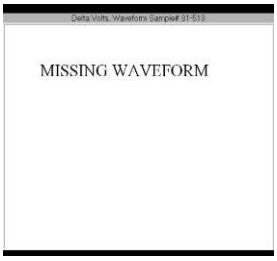

ZY1

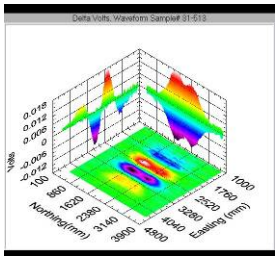
XX1

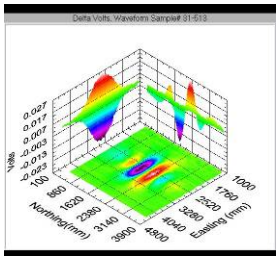
YY1

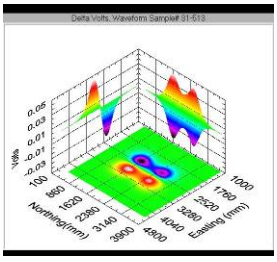
XZM

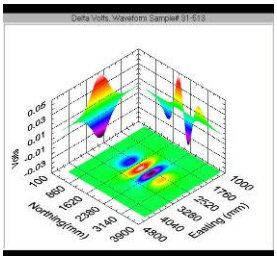
YZM

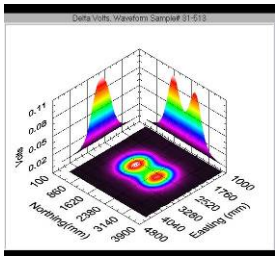
ZZM

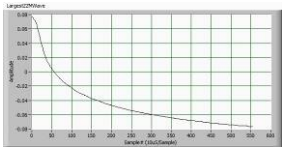
Largest ZZM waveform

Table A.3.68. DiskTwo 2007-08-02 RodAz0Inc45Td73

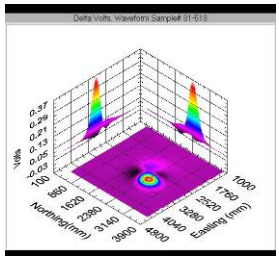
XZE

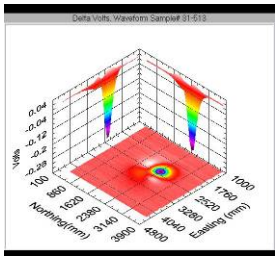
XZF

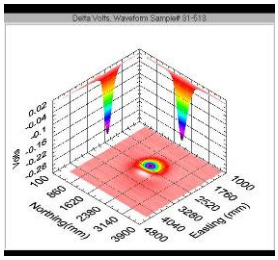
XZG

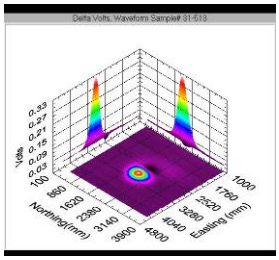
XZH

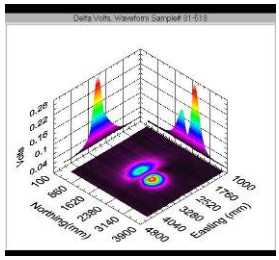
YZE

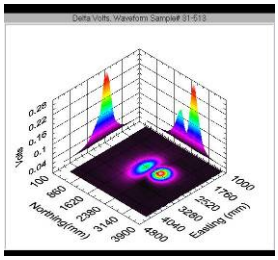
YZF

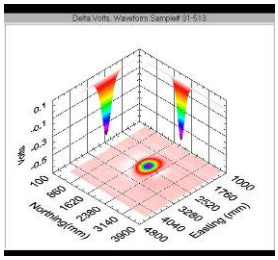
YZG

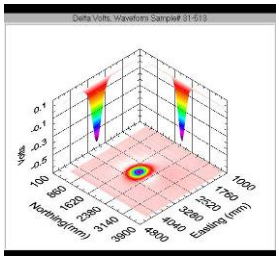
YZH

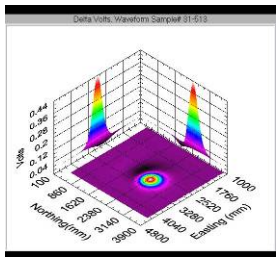
ZZE

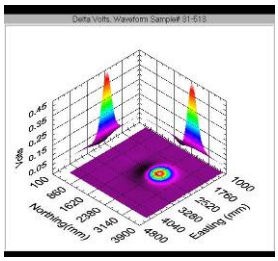
ZZF

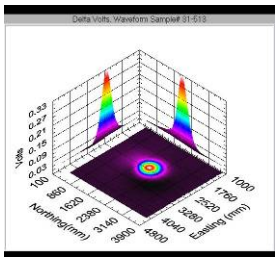
ZZG

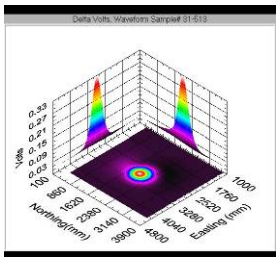
ZZH

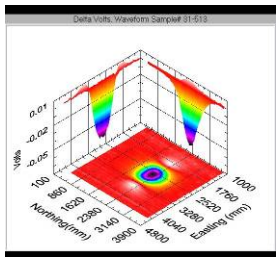
ZX1

MISSING WAVEFORM
ZY1

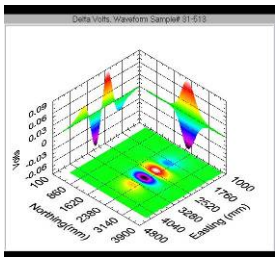
XX1

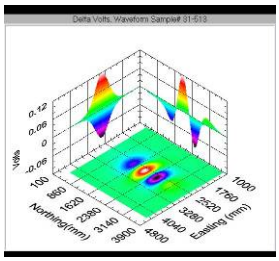
YY1

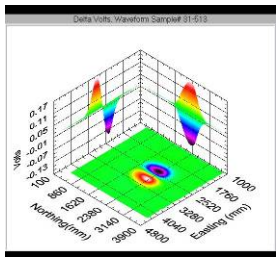
XZM

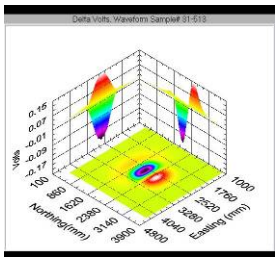
YZM

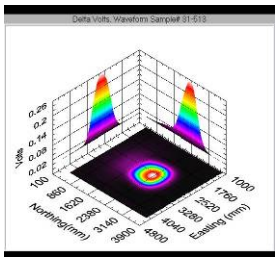
ZZM

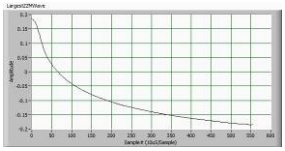
Largest ZZM waveform

Table A.3.69. DiskTwo 2007-08-02 RodAz0Inc90Td73

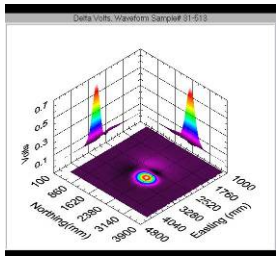
XZE

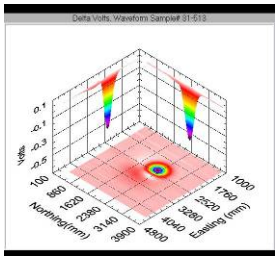
XZF

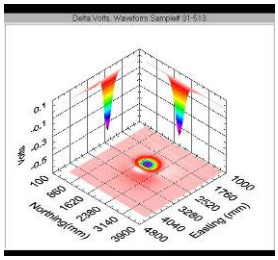
XZG

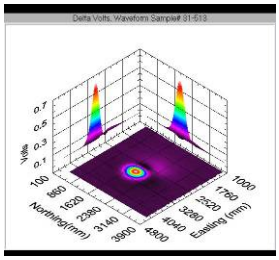
XZH

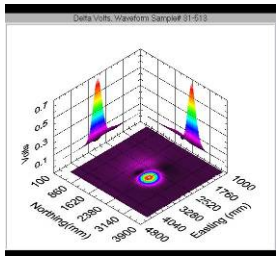
YZE

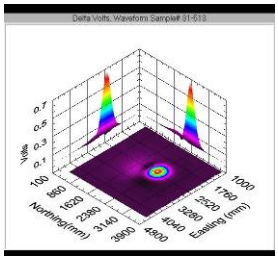
YZF

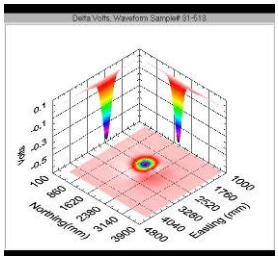
YZG

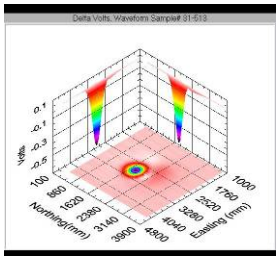
YZH

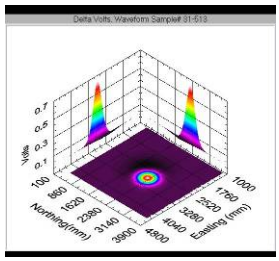
ZZE

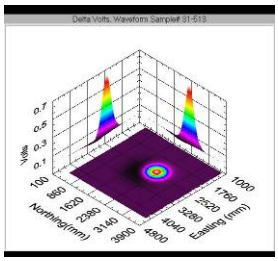
ZZF

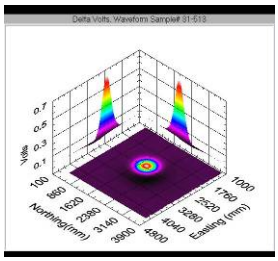
ZZG

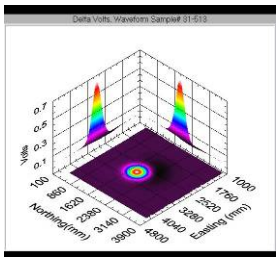
ZZH

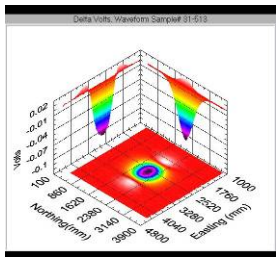
ZX1

MISSING WAVEFORM
ZY1

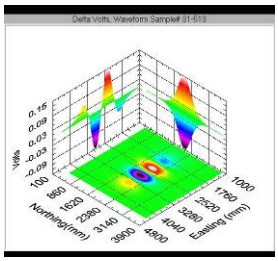
XX1

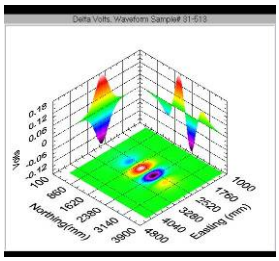
YY1

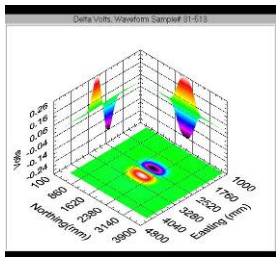
XZM

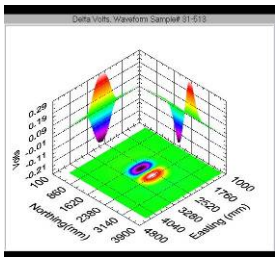
YZM

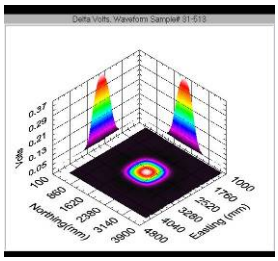
ZZM

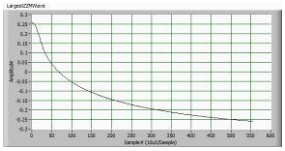
Largest ZZM waveform

Table A.3.70. DiskTwo 2007-08-02 RodAz45Inc45Td73

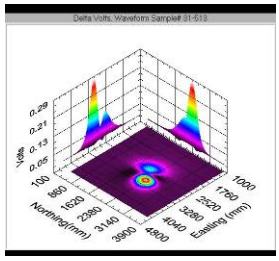
XZE

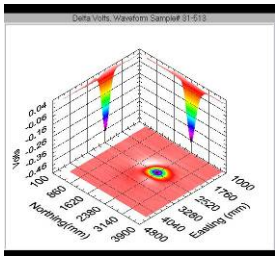
XZF

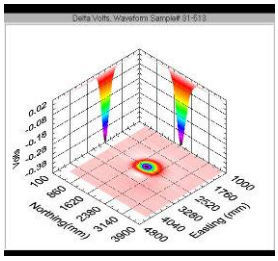
XZG

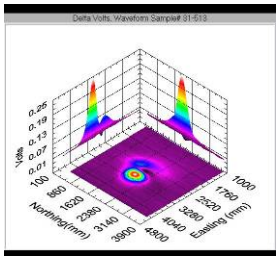
XZH

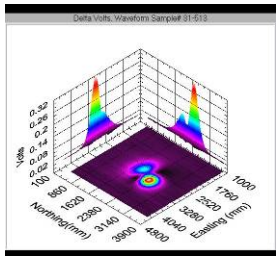
YZE

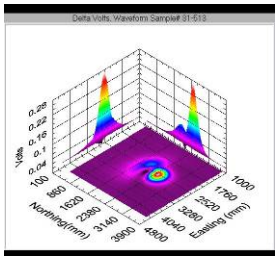
YZF

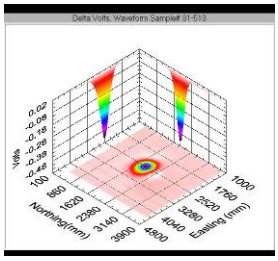
YZG

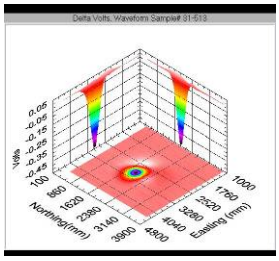
YZH

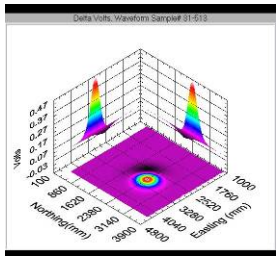
ZZE

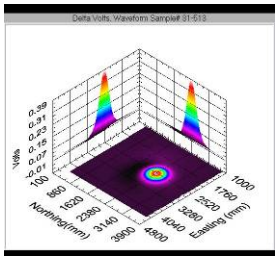
ZZF

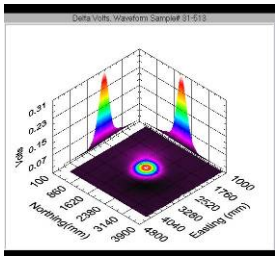
ZZG

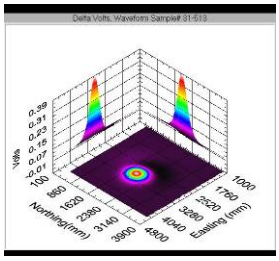
ZZH

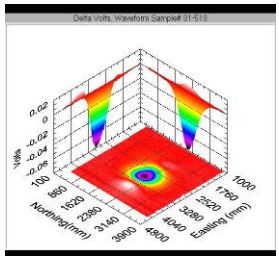
ZX1

MISSING WAVEFORM
ZY1

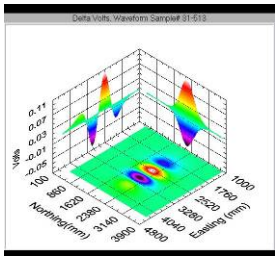
XX1

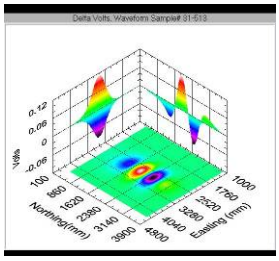
YY1

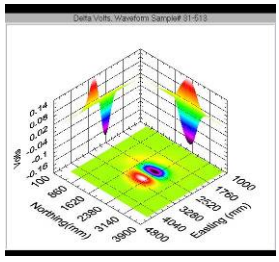
XZM

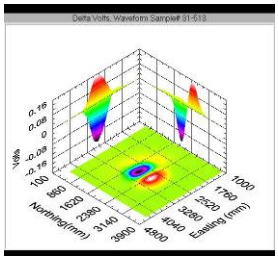
YZM

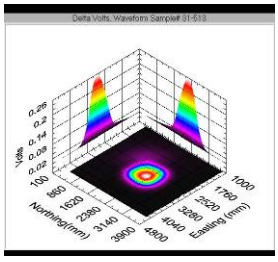
ZZM

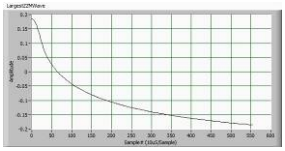
Largest ZZM waveform

Table A.3.71. DiskTwo 2007-08-02 RodAz90Inc0Td73

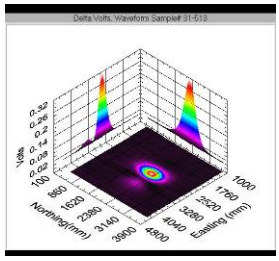
XZE

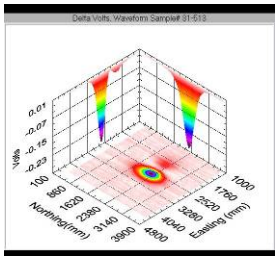
XZF

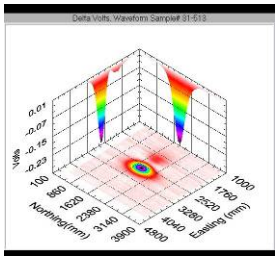
XZG

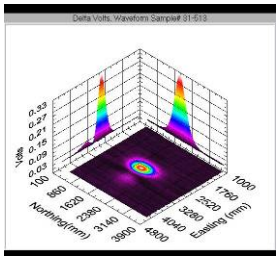
XZH

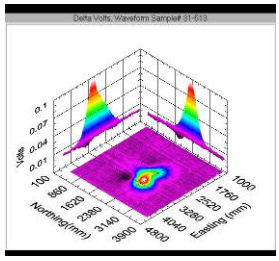
YZE

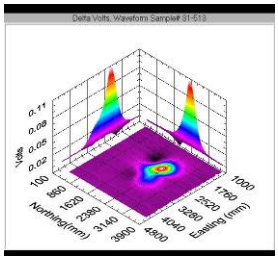
YZF

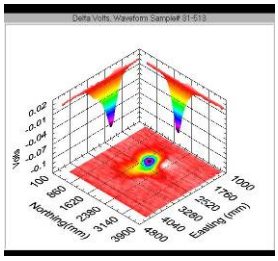
YZG

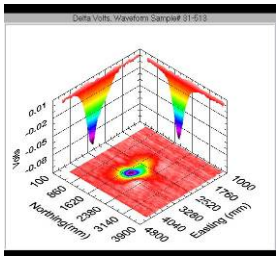
YZH

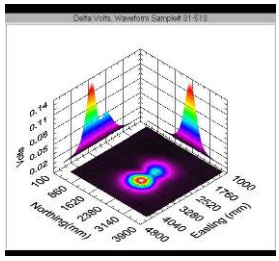
ZZE

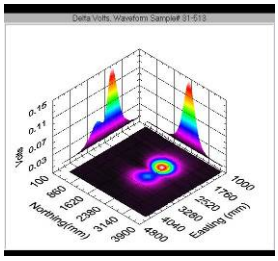
ZZF

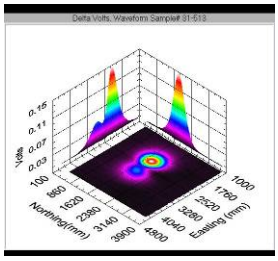
ZZG

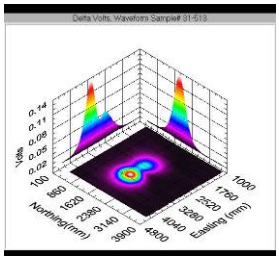
ZZH

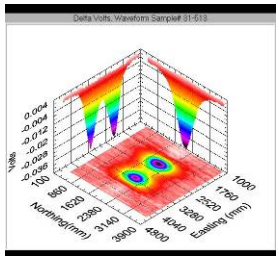
ZX1

MISSING WAVEFORM
ZY1

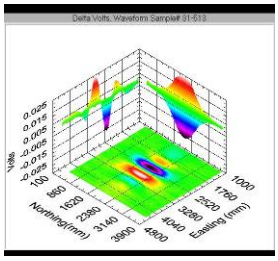
XX1

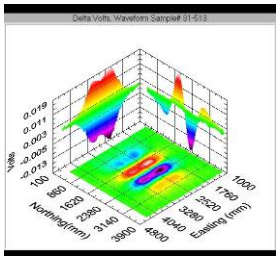
YY1

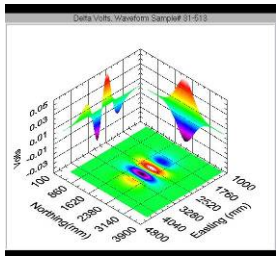
XZM

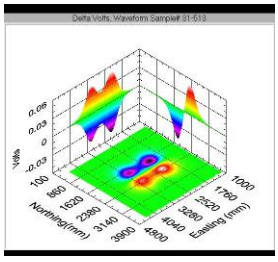
YZM

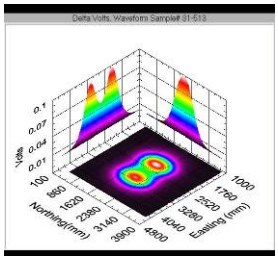
ZZM

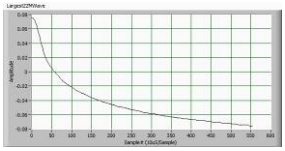
Largest ZZM waveform

# AA. Cube and Coil Geometry

Figures AAA.1.2 and AAA.1 display schematic drawings of the ALLTEM cube and its drive coils from top, bottom and side perspectives.

## AA.1 Sense coil dimensions and geometries

- The large top and bottom Rx loops are wound in four groups of 50 turns each.
    - They are combined electronically to make a 200 turn coil.
    - These are used for the ZZM, XZM, and YZM polarities
    - The inner windings are about 90.7 cm square and the outer windings are about 97.7 cm square.
    - Each coil is nominally 51.3 cm above and below the cube center.
- The smaller Rx loops are printed circuit boards with approximately square spiral-wound turns in 50 turn groups.
    - These are used for the ZZE, ZZF, ZZG, ZZH, XZE, XZF, XZG, XZH, YZE, YZF, YZG, and YZH polarities
    - Each small Rx loop consists of 4 each, 50 turn coils, on either side of a printed circuit board. On each side, the 50 turn coils are connected in series, making a 100 turn coil. The 100 turn coils are combined electronically to make a 200 turn coil.
    - The outer edge of the outer 50 turn spiral measures about 34.5 cm, and is  2.5 cm wide.
    - The outer edge of the inner 50 turn spiral measures about 26.9 cm, and is  2.5 cm wide.
    - The four top, and four mirror image bottom, horizontally mounted Rx loops are on 50 cm centers.
    - Each thin ( 1.524 mm) coil is nominally 50 cm above and below the cube center.
- The four vertically mounted Rx loops are mounted with their centers approximately 29.2 cm down from the cube center.
    - These are used for the XX1, and YY1 polarities and the bottom half of the ZX1 and ZY1 polarities
    - Each loop is placed on the vertical centerline of the face on which it is placed.
    - Each thin (1.524 mm) coil is nominally 52.3 cm from the cube center.
    - The coils are the same printed circuit board configuration as the ZZE type coils.
- The four vertically mounted Rx loops are mounted with their centers approximately 29.2 cm up from the cube center
    - These are used for the top half of the ZX1 and ZY1 polarities.
    - The top-left ZX1 is electronically subtracted from the bottom-left ZX1 coil electronically.
    - This signal is then differenced from the electronically subtracted top, right ZX1 and left ZX1 coil to get the final ZX1 signal.
    - Similar description applies to the generation of the final ZY1 signal.

- Each loop is placed on the vertical centerline of the face of the cube on which it is placed.
- The coils are thin (1.524 mm), each coil is nominally 52.3 cm from the cube center.
- The coils are the same printed circuit board configuration as the ZZE type coils.

## AA.2 Drive coils

- Number of turns: 63 for each Tx coil (X, Y, and Z) (3 layers of 21 turns for each of the X,Y, and Z coils)
- Width of winding: 5 cm
- Coil Shape: 100 cm square

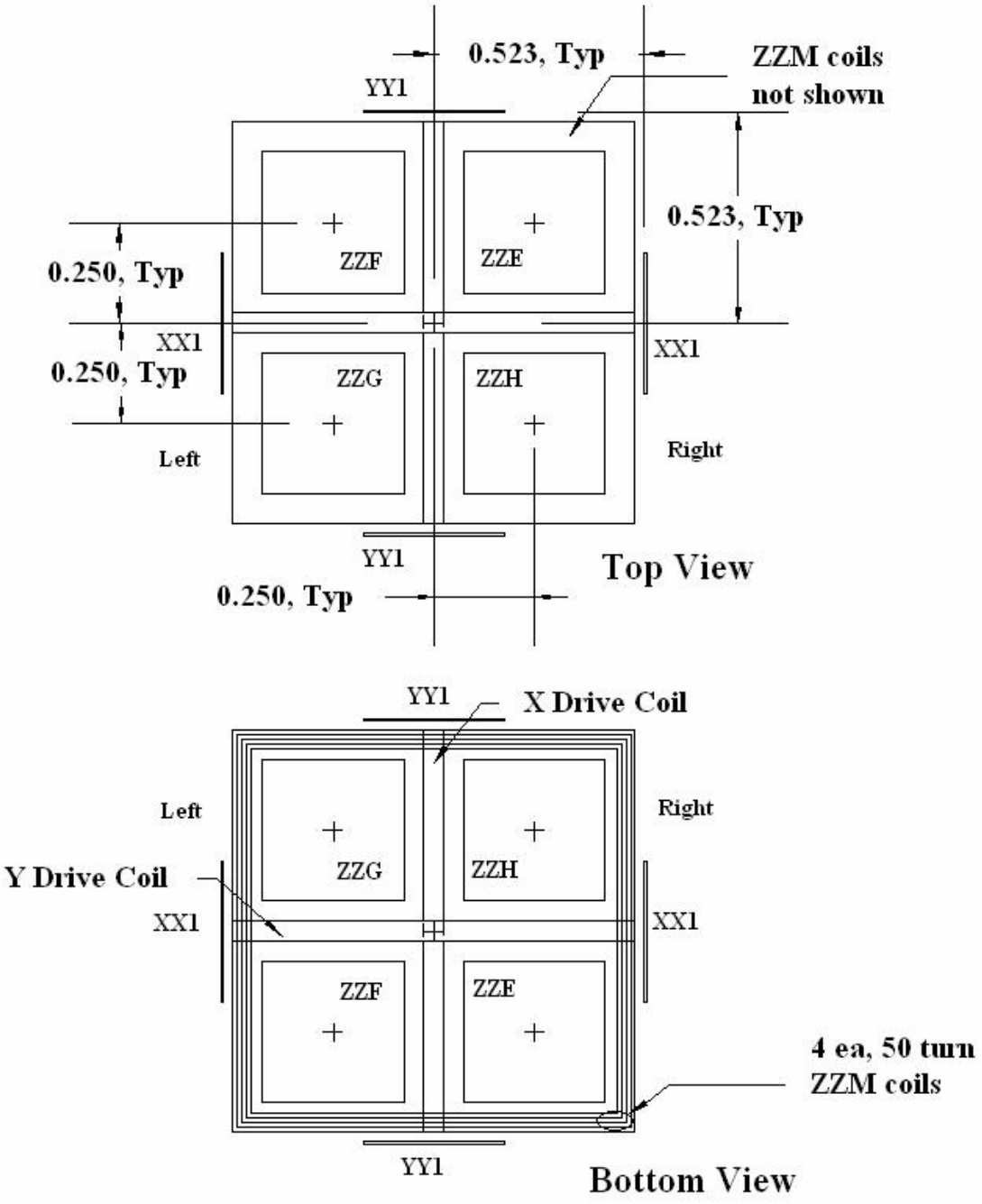


**Figure AA.1.1**. A top and bottom view of the ALLTEM cube including its drive and sense coils.

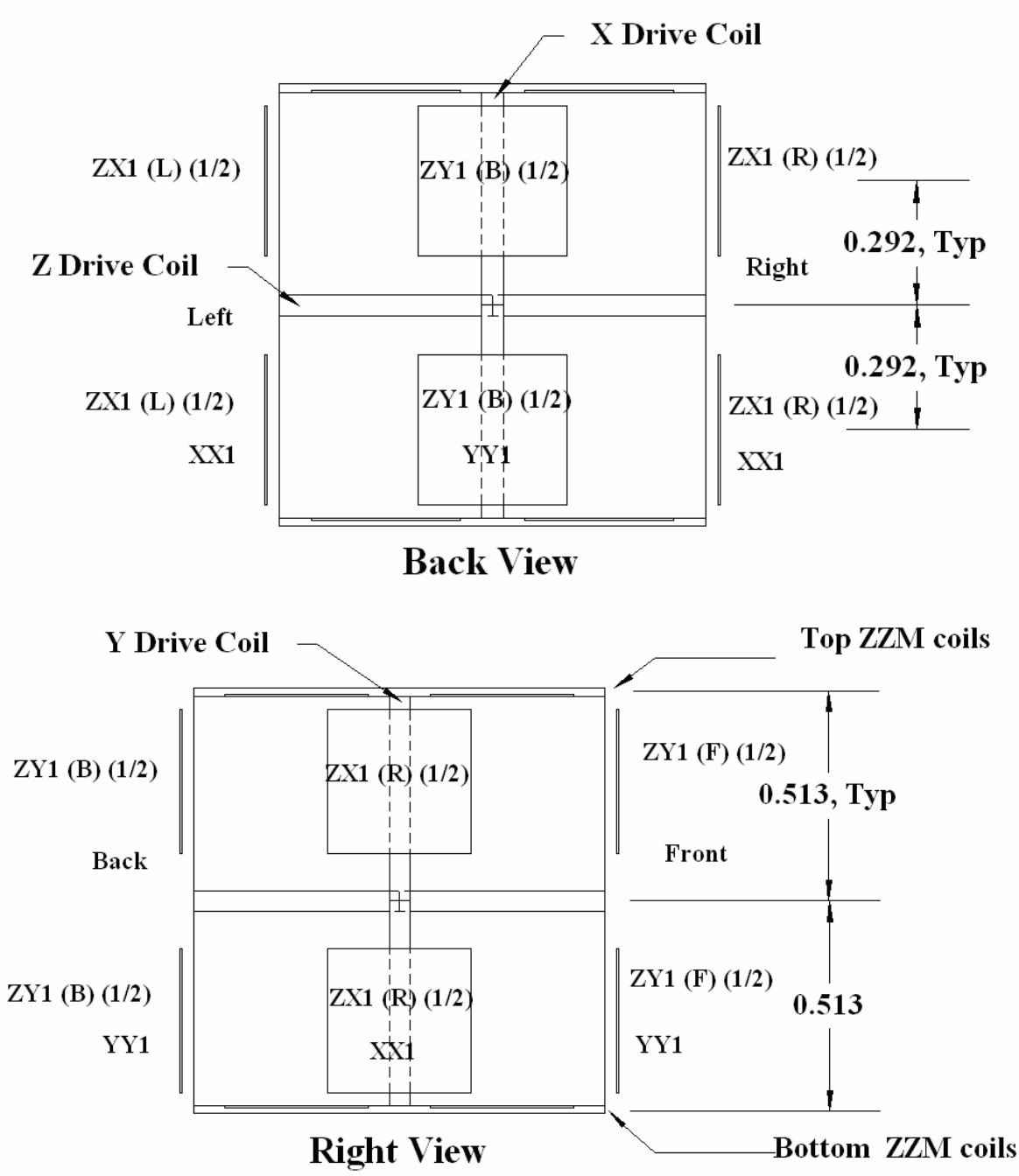


**Figure AA.1.2**. A back (top) and right (lower) view of the ALLTEM cube including its drive and sense coils.

## AA.3 ALLTEM coil patterns for down and diagonal gradiometer pairs

Figure AA.3.1 shows a representation of surveys over an ordnance item, and the predicted patterns in the antenna responses, for two different gradiometer configurations of the ALLTEM cube.

For the first case, with the straight down gradiometer pairs, (i.e. ZZE top subtracted from ZZE bottom, ZZF top subtracted from ZZF bottom, and so forth), the cube diagram on the left is meant to show the location of the ZZE, ZZF, ZZG, and ZZH coils at an instant of time when the cube is to the right of the ordnance. The typical survey would move the cube in the 'Along Line Direction' shown. The next line would move the cube over to the right in the 'Next Line Direction' shown. After a number of lines and cube motions to the right, if the responses from the four coils were plotted onto contours, the patterns shown on the right would result. Notice that the ZZE response pattern is diagonally opposite to the location of the ZZE coil on the cube. The response pattern location of the gradiometer pair is actually responsive to the location of the bottom gradiometer pair coil, as it is closest to the ordnance when to cube goes over it. The top gradiometer coil mainly acts as a reference. In this case, the top and bottom gradiometer coils have the same name, i.e. ZZE top - ZZE bottom.

For the second case, with the diagonal gradiometer pairs, (i.e. ZZE top subtracted from ZZG bottom, ZZF top subtracted from ZZH bottom, and so forth), the pattern locations will end up being essentially the same as the straight down gradiometer case, because the response is driven by the bottom coil location. The ALLTEM waveforms recorded for the survey were named according to the top coil location, thus the ZZE top - ZZG bottom pair response was named as ZZE. This naming convention essentially undoes the diagonal reversal shown in the patterns, thus the blue pattern named ZZG in the figure is named ZZE in the waveform files. The diagonal gradiometer configuration for the coils was used for all of the ALLTEM Test Stand data collection.

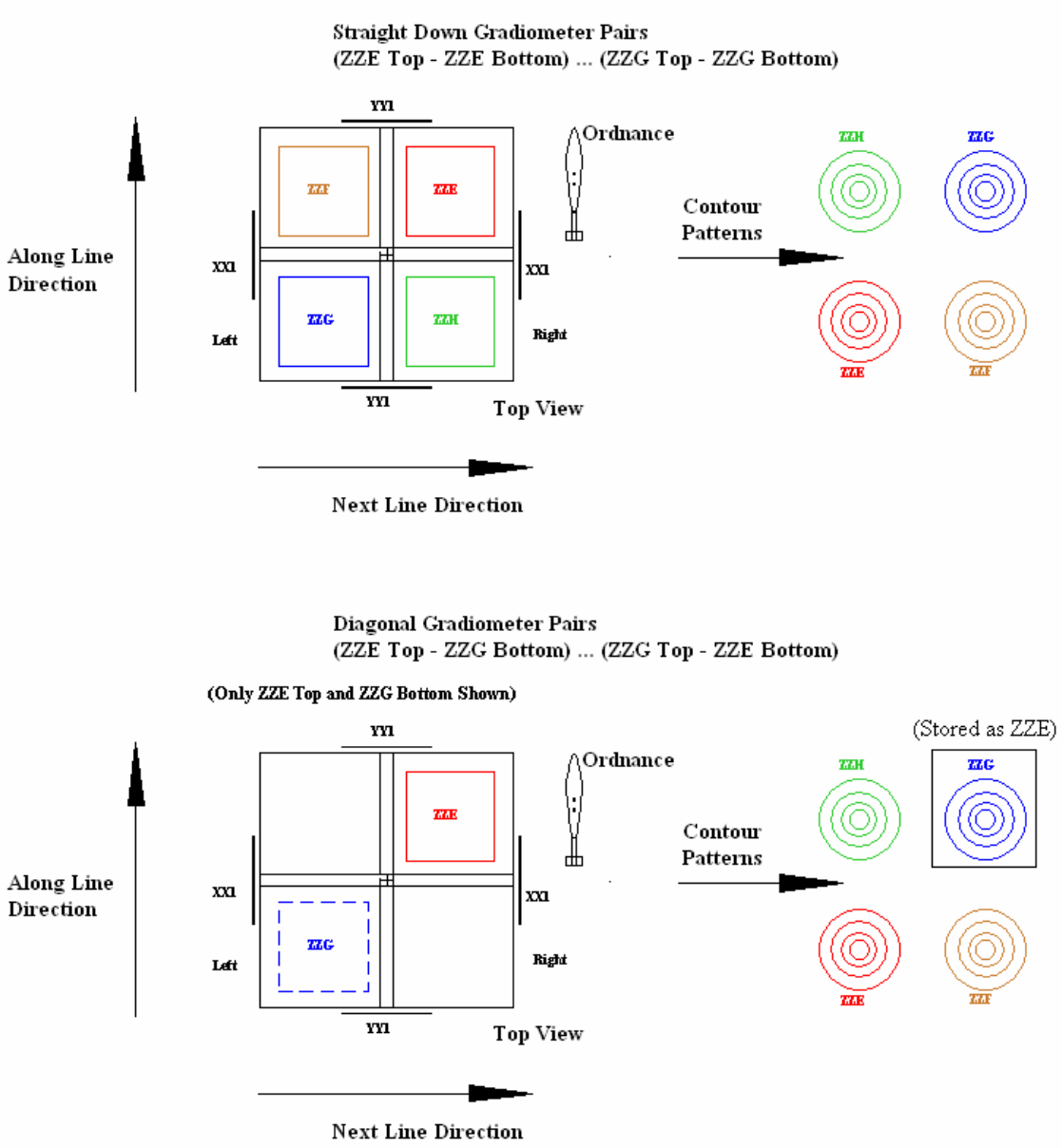


**Figure AA.3.1.** The ALLTEM coil patterns used for straight down and diagonal vertical gradiometer pairs.

# AB. ALLTEM SU Data Format Description

Following is a description of the data format of the .SU (Seismic Unix *http://cwp.mines.edu*) files used to store the waveform information. [3]

[3]The SU format is a widely used data file convention which was selected for use in an inversion program that has been developed at the USGS. SU files contain a header that is used to store information about waveform data before the actual data. In this case, the Northing and Easting locations of the waveform are the only items of interest in the header.

Figure AB.1 is an example of the data comprising the first waveform at the beginning of a .SU file. The file shown in this example is named:
`2007-08-01_Clutter_ChainAz0Inc0Td73_STDc_Ln28_all.XZF.SU_Ln28.XZF.SU`
Which is Line 28, Polarity XZF of the
`2007-08-01_Clutter_ChainAz0Inc0Td73_STDc survey`.

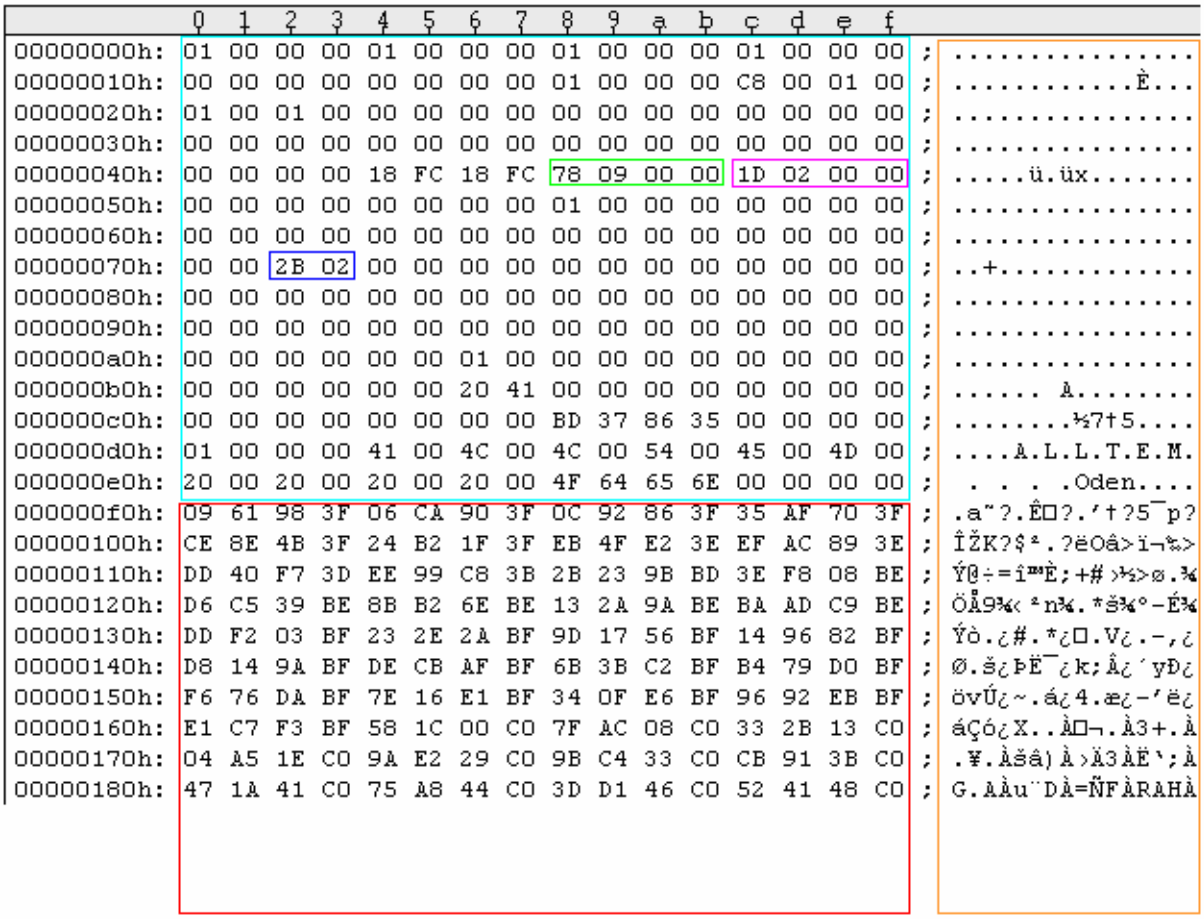


**Figure AB.1**. Output from a hexadecimal editor showing an SU header as used by ALLTEM data files in this distribution. The entire header is shown. The ASCII representation is displayed in tan at the right. Points of interest include: the easting position (in the green box), the northing position (in the magenta box), and the number of data points in each waveform (in the blue box).

Preceding each waveform is a 240-byte SU header. Consider 3 example fields of interest.

The first field, in the green box, is the Easting position for the following waveform. If the data are read as 4-byte single precision values, then the Easting is at location 19. In this case the Easting is stored as two 2-byte words 78 09 00 00. To convert it to a position in millimeters (mm), first swap the first and last words to get 00 00 78 09. Then swap the 2 bytes within the words to get 00 00 09 78. This is in hexadecimal format. Converting to decimal format gives 2424, or 2424 mm. The Northing and Easting are stored as integer values in the header, even

though the data waveform values later in the record are stored as single precision float values. By storing the waveform as binary data, as opposed to ASCII, the file size was reduced considerably.

The second field of interest, in the magenta box, is the Northing position for the following waveform. It is at location 20 (using 4 Bytes/Single Precision Value) Using the same procedure gives a word swapped and byte swapped hex value of 00 00 02 1D. This converts to a decimal value of 541 mm.

The third field of interest is in a blue box and is the number of points in the following waveform. The byte swapped hex value is 02 2B, which converts to a decimal value of 555. This value will not change.

Following the header, the waveform is stored as red 555 data points. Only a portion of the 555 points is shown. The delta time between each of the 555 waveform point is 10 μS. Each data point is stored as a 4-byte, single-precision, floating point number. The numbers are stored in the little-endian format (least significant digits first). The waveform values are in volts. The 24-bit digitizer used to acquire the data has a range of +/- 10 V.

The second header and waveform would start at 240 + (555*4) = 2460 bytes later in the record. For the typical ordnance surveys performed on the test stand there will be approximately 43 or 84 waveforms/line for each of the 19 polarities recorded (ZZM, ZZE, ZZF, and so forth). When the number is about 43, the ordnance shuttle was moved at 0.2 m/sec and when about 84 the speed was 0.1 m/sec. A few surveys were run at a shuttle speed of 0.5m/sec (approximately the survey speed used in the field at Yuma). These are labeled with 'Vel500' in the normal file nomenclature.

The area in the tan box to the right of the data area is the ASCII representation of the data to the left.

## AB.1 Order of polarities

The ALLTEM system drive and sense digitizers were never stopped during the acquisition of waveforms on the test stand. This was done, for one reason, to keep the drive coils at a stable temperature to minimize drift in the system. The three orthogonal drive coils, X, Y, and Z were being sequentially driven by the system. The beginning of travel of the shuttle holding the ordnance could start at any independent time relative to which drive coil was being driven. One implication of this is that the recording of waveforms along each line can start or end at any one of the three axis drive polarities (X, Y, or Z). The recorded waveforms were later processed to insure that the number of X, Y and Z axis cycles (a record packet) was equal for each line. The individual lines in a survey can have different number of record packets from other lines. Typically the number of record packets on each line will not vary by more than a few for the entire survey in the case of nearly equal line lengths.

# AC. Waveform Processing Performed on ALLTEM YPG 06 and Test Stand Data

The following discussion pertains to ALLTEM waveforms collected at the Yuma Proving Ground in 2006. The filtering methods applied to that data set were also used in the ALLTEM Test Stand data set collected in July-August of 2007. For the Test Stand data, an additional de-spiking, modified median filter was applied to the waveforms after the background subtraction and waveform half averaging filters. Figures for the median filter effects are not included in this discussion. In addition, the Test Stand waveforms were reduced to 555 points before storage as .SU files, instead of the 1111 points in the original collected data. This is because the waveform half-averaging filter averages the two 555 point half waveforms.

## AC.1 Typical raw waveforms

These waveforms (figure AAC.1.1) have been rolled 2.36 ms to the left so that the response to the triangle corner occurs near t=0. For an example of the unrolled waveform, see the band-stop filter section.

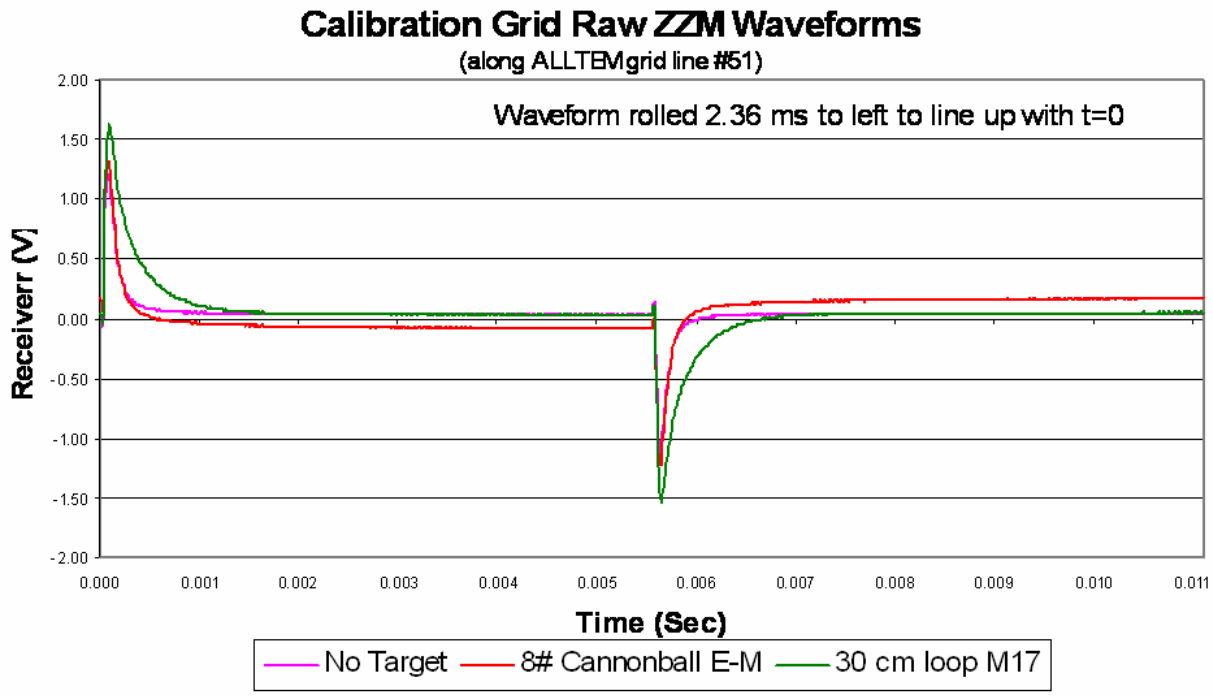


**Figure AC.1.1**. Example raw ALLTEM waveforms. The magenta line represents a waveform with no target beneath the cube. The red line was the response from an 8-lb shot while the green line was recorded over a 30-cm loop in Calibration Grid cell M17 at Yuma.

## AC.2 Software filters applied

### *AC.2.1 Background subtraction*

The first waveform in the Test Stand survey was taken with the ordnance far from the ALLTEM cube. If it was determined to be a good waveform ("good" meaning free of noise and containing no target

response), that waveform was subtracted from all the subsequent waveforms along that line. If it was not a good waveform, the nearest good first waveform from a previous line was used. Performing this task before the filters were applied helped to minimize the Gibbs effects because the large transitions around the triangle corners were not as large. Figure AC.2.1.1 shows an example of background subtracted data from the YPG Calibration Grid.

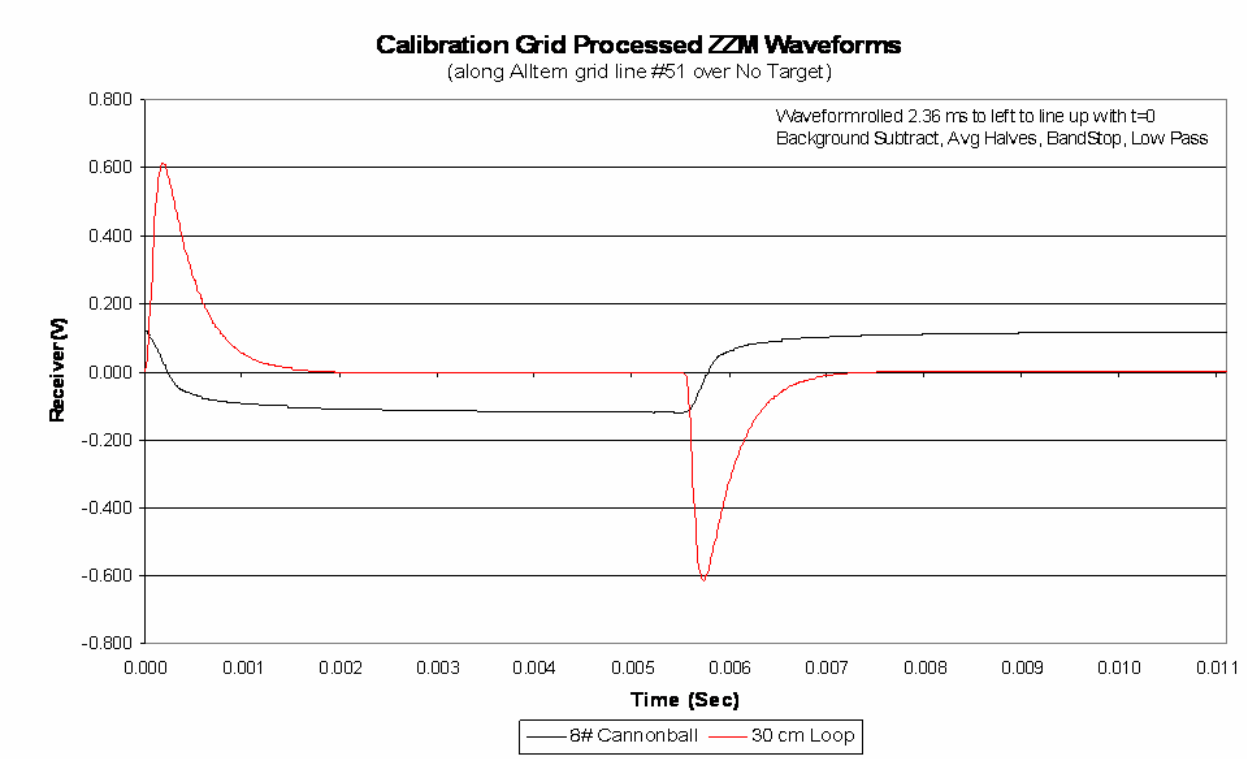


**Figure AC.2.1.1**. Background subtracted waveform.

## *AC.2.2 Waveform halves stacking*

The observed recorded waveforms from YPG and the Test Stand had a component of 180 Hz, synchronous, system noise which was relatively small, but for small targets, could reduce the signal-noise ratio appreciably. Each record of 1111 samples contains two complete, reciprocal, responses to the corners of the triangle wave used to drive the field producing coils. By splitting the 1111 samples in half, inverting the second half reciprocal response, adding it to the first half, and dividing the sum by 2, the 180 Hz component could be reduced significantly. To reconstruct an entire 1111 sample waveform, the half-waveform produced by the averaging was inverted and added onto the end of the half-waveform. This filter significantly reduced this noise source. Non-synchronous noise is also attenuated by this technique.

## *AC.2.3 Band-stop filter*

A component of noise was visible in all the waveforms at around 4.3 kHz. By applying a LabVIEW® zero phase, band-stop Filter, with low-stop = 3.3 kHz and high-stop = 5.3 kHz, the 4.3 kHz component was reduced somewhat. Figure AC.2.3.1 shows the reduction of noise when

waveform-halves stacking plus the band-stop filter are applied to the data. Filter orders higher than two introduce excessive Gibbs peaking around large transitions in the waveforms. Figure AC.2.3.2 illustrates the small Gibbs distortion introduced at fast transitions by the 2nd-order band-stop filter.

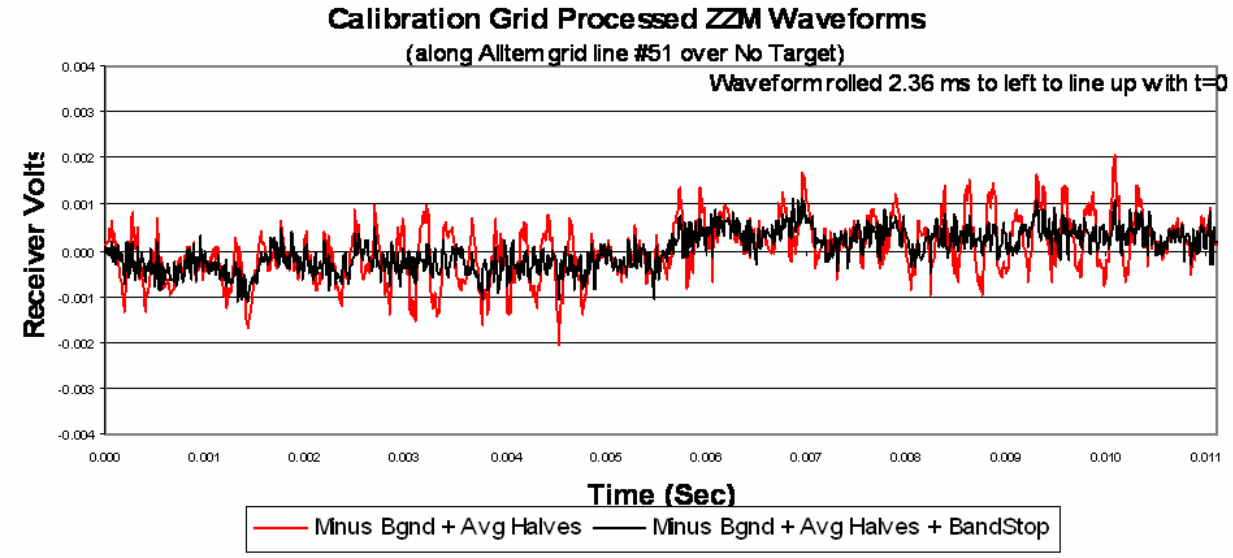


**Figure AC.2.3.1**. Effect of waveform-halves stacking and band-stop filter.

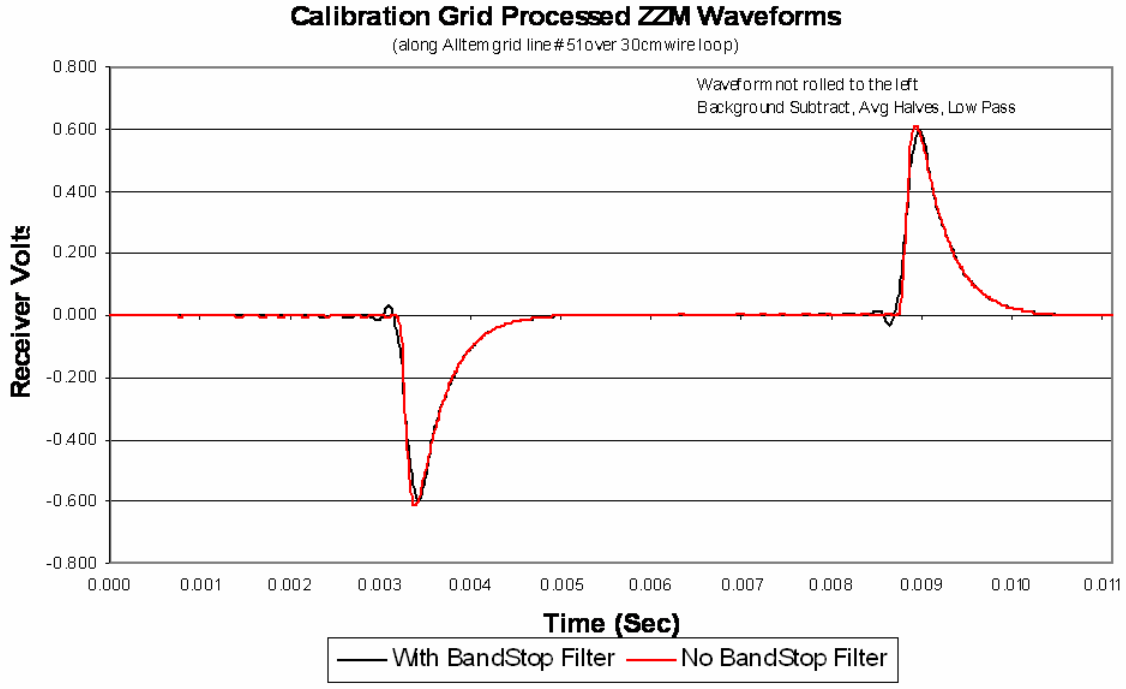


**Figure AC.2.3.2**. Band-stop filter and Gibbs effect.

## *AC.2.4 Low-pass filter*

A LabVIEW®, zero-phase, eighth-order, low-pass filter was applied to roll off any higher frequency noise that might be in the recorded data from VLF stations. The filter was placed at 15 kHz, which was

far enough from any frequencies of interest from the targets that any Gibbs effects were not significant. Figure AC.2.4.1 illustrates the reduction in noise gained from application of the 15 kHz low-pass filter.

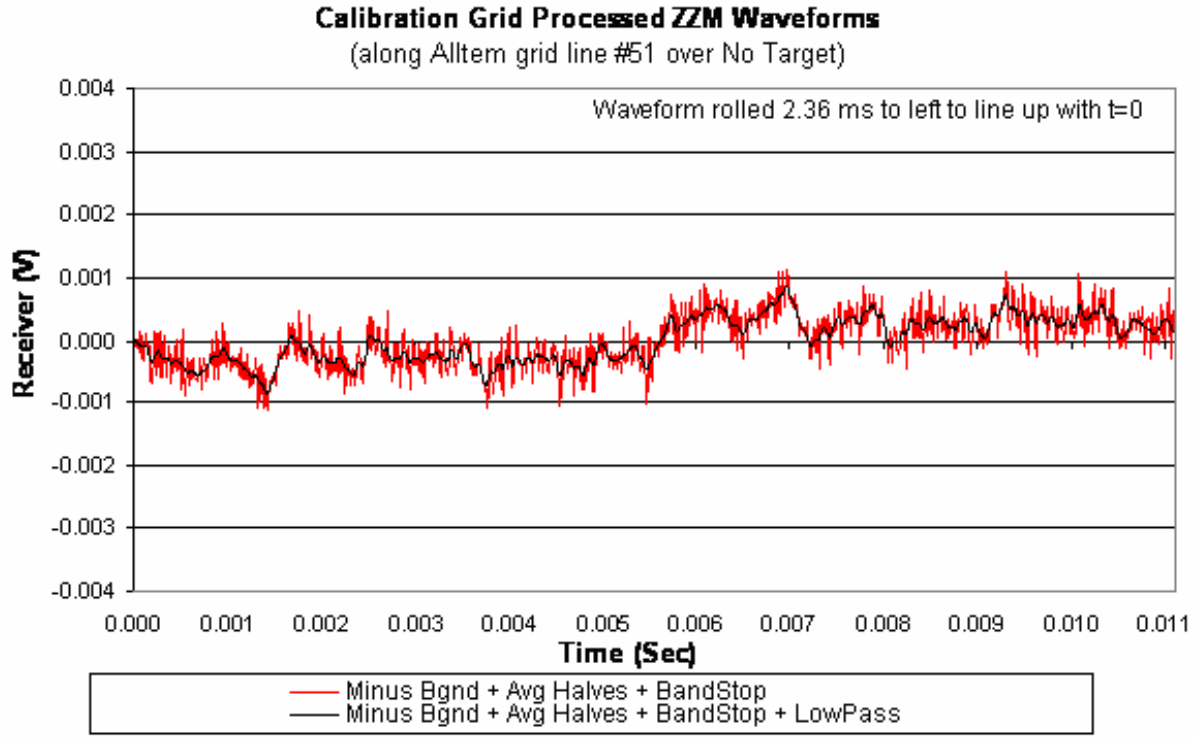


**Figure AC.2.4.1.** Low-pass filter noise reduction.

## AC.3 Summary View of all Filters (excluding Median)

Figure AC.3.1 shows a comparison of a waveform (red) where only the background has been removed. The noise level is almost 4 mV peak to peak. After application of all the filters described above the noise level is slightly less than 1 mV peak to peak. This is an SNR improvement of about 12 dB.

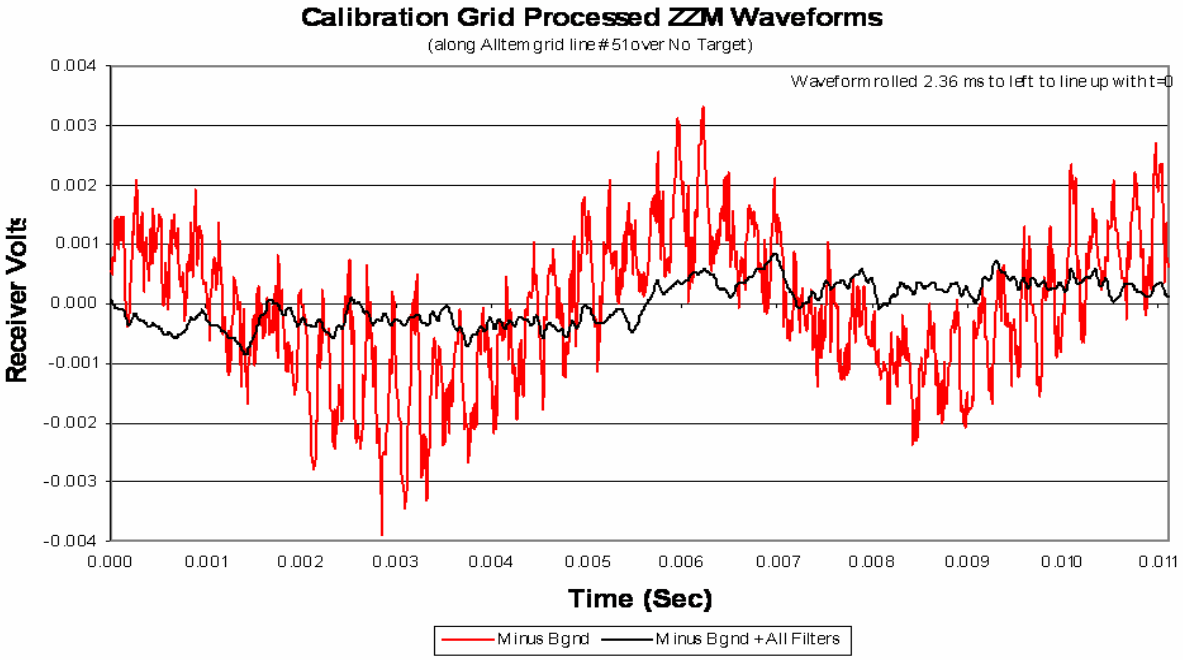


**Figure AC.3.1**. Example noise reduction when all filters are applied.

## AD. Voltage transfer function between the Rx coils and the digitizer

The voltage at the input to the digitizer, $V_{dig}$, is:

$$V_{dig} = \left[V_{coil1} \times G_{diff1} - V_{coil2} \times G_{diff2}\right] \times (N_c) \times G_{sub} \times G_{lp} \quad \text{(AD.1)}$$

where:

$V_{coil1}$=*Voltage across coil* 1 *of the gradiometer pair*
$V_{coil2}$=*Voltage across coil* 2 *of the gradiometer pair*
$G_{diff1}$=*Gain from coil* 1 *voltage output to differential amplifier* 1 *output*

For the large, 1-m coils:

$$G_{diff1} = G_{diff2} = (49.4K / 45.3K) + 1 = 2.09 \quad \text{(AD.2)}$$

For the small, 0.35m coils:

$$G_{diff1} = G_{diff2} = (49.4K / 7.5K) + 1 = 7.58$$

$G_{diff2}$= *Gain from coil* 2 *voltage output to differential amplifier* 2 *output*
$N_c$ = *Number of individual sense coils that make up each gradiometer coil*
$G_{sub}$ = *Gain in the subtraction stage of the differential coil voltages*
$G_{lp}$ = *Gain of the low–pass filter stage*

After the transients from the low pass filter and any potential transient from the differential amplifier (diff amp) low-pass pole mismatch have died out (≈100 to 300$\mu s$) we have:

$$\begin{aligned} V_{dig} &= (V_{coil1} \times G_{diff1} - V_{coil2} \times G_{diff2}) \times G_{sub} \times G_{lp} \quad \text{(AD.3)} \\ &= \left(V_{coil1} \times G_{diff1} - V_{coil2} \times G_{diff2}\right) \times \left(N_c \times \frac{60.4K + 50K}{5K}\right) \times 1.2 \\ &= \left(V_{coil1} \times G_{diff1} - V_{coil2} \times G_{diff2}\right) \times \left(N_c \times 26.4\right) \end{aligned}$$

For the 0.35m, circuit board coils, (2 Rx coils) this becomes:

$$\begin{aligned} V_{dig} &= (V_{coil1} \times 7.58 - V_{coil2} \times 7.58) \times 2 \times 26.4 \quad \text{(AD.4)} \\ &= (V_{coil1} \times 7.58 - V_{coil2} \times 7.58) \times 52.8 \\ &= (V_{coil1} - V_{coil2}) \times 400.2 \end{aligned}$$

For the 1-m coils (four Rx coils) this becomes:

$$\begin{aligned} V_{dig} &= (V_{coil1} \times 2.09 - V_{coil2} \times 2.09) \times 4 \times 26.4 \quad \text{(AD.5)} \\ &= (V_{coil1} - V_{coil2}) \times 220.7 \end{aligned}$$

## AD.1 Notes

$G_{diff1}$ and $G_{diff2}$ contain a DC component and a low-pass (LP) filter component. The LP filter is ≈100 kHz and is used to remove any RF noise that is picked up on the coils and wiring bringing the coil voltages to the circuit boards. The 100 kHz filters are 1st order with a pole defined by $1/2\pi RC$. The resistors (R's) are 1 percent tolerance and the capacitors (C's) are typically 5 percent tolerance. The mismatch of the RC product can lead to a difference in the rise times of the square waves coming out of the differential amplifier stage. The rise time difference, after the subtraction stage with its large gain, can lead to a short pulse on the output of the subtraction stage during the time that the coil square waves are transitioning from low to high or high to low. The width of this pulse is in the order of 100-200 μs. From testing, this effect only comes into play when the rise time of the input to the differential amplifier stage is < 20 μs. Measured values of the rise times of the voltage coming from the small Rx coils is in the order of 60 μs, so in theory the mismatch in time constants should not be contributing much. The 60 μs is determined by how fast the triangle current wave turns the corner. The feedback control circuit which drives the triangle current to the drive loop is damped slightly to prevent oscillations in this loop. This damping is what limits the sharpness of the triangle wave when it turns the corner.

$V_{coil1}$ is the average voltage out of the four individual coils that make up the 1-meter Rx coil 1. Each of the coils contain 50 turns of wire and are individually buffered by differential amps before being summed together electronically. The resonant frequency of a single 200-turn coil was too low, thus requiring the breakup into smaller coils. The four coils are physically nested within each other such that they have slightly different square areas and correspondingly different output voltages. Similar comments apply to $V_{coil2}$ as well. For the 0.35-m circuit board Rx coils, there are two, 100-turn coils. They are not nested, but are on opposite sides of a 1.5875-mm (1/16 inch) circuit board. Their outputs should be much more closely matched than the 1-m, four individual coils.

$G_{sub}$ is controlled by a jumper configurable, resistor. For the YPG 06 and Test Stand data, the resistor was 60.4 kohm. Each of the coil voltages is fed into the subtraction stage through a 4.99 kohm resistor, so $G_{sub}$=60.4/4.99=12.1.

$G_{lp}$ is a 2nd order, low pass Bessel-like filter with a pole frequency at:

$$\frac{1}{FSF}2\pi RC=1/2\pi(1.274)(17.8K)(1nF)=7.02KHz. \qquad \text{(AD 1.1)}$$

FSF is the Frequency Scaling Factor for a Bessel filter. The actual filter values give a filter that is slightly 'softer' than a Bessel filter, but is close enough for this model. The actual s domain transfer function is:

$$\frac{1.2}{s^2(713\times10^{-12})+s(-64.1\times10^{-12})+1} \qquad \text{(AD 1.2)}$$

The 1.2 dc factor has been verified experimentally in recent testing.

# AE. ALLTEM File name extension key

As an example, consider a file name with the extension <*filename*>.ZZM.SU. The 'ZZM', in this example, represents the polarization of the field producing coils and receiving antennas used to record the waveform. The three characters in the 'ZZM' have the following meanings (see figure AE.1):

- First letter: Direction of B field produced by drive coils:
  - X is perpendicular to the cube motion
  - Y is in the direction of the cube motion
  - Z is vertical, pointing up from the ground
- Second letter: Axis that gradiometer sense coils are measuring:
  - X field (gradiometer sense coils on Left-Right (LR) of cube)
  - Y field (gradiometer sense coils on Front-Back (FB) of cube)
  - Z field (gradiometer sense coils on Top-Bottom (TB) of cube)
- Third letter or character: Orientation of gradiometer sense coils:
  For small (0.35 m) sense coils measuring Z axis fields:
  (i.e ZZE, ZZF, ZZG, ZZH, XZE, XZF, XZG, XZH, YZE, YZF, YZG, YZG)
  - Straight-Down Gradiometer:
    1 = 1st quad of XY plane (Front Right (FR) position) FR top - FR bottom
    2 = 2nd quad of XY plane (Front Left (FL) position) FL top - FL bottom
    3 = 3rd quad of XY plane (Back Left (BL) position) BL top - BL bottom
    4 = 4th quad of XY plane (Back Right (BR) position) BR top - BR bottom
  - Front-Back Gradiometer:
    a = 1st quad of XY plane (FR position) FR top - BR bottom
    b = 2nd quad of XY plane (FL position) FL top - BL bottom
    c = 3rd quad of XY plane (BL position) BL top - FL bottom
    d = 4th quad of XY plane (BR position) BR top - FR bottom
    red
  - Diagonal Gradiometer : (Normal configuration for ALLTEM)
    e = 1st quad of XY plane (FR position) FR top - BL bottom
    f = 2nd quad of XY plane (FL position) FL top - BR bottom
    g = 3rd quad of XY plane (BL position) BL top - FR bottom
    h = 4th quad of XY plane (BR position) BR top - FL bottom
  - Left-Right Gradiometer:
    i = 1st quad of XY plane (FR position) FR top - FL bottom
    j = 2nd quad of XY plane (FL position) FL top - FR bottom
    k = 3rd quad of XY plane (BL position) BL top - BR bottom
    l = 4th quad of XY plane (BR position) BR top - BL bottom

<u>For large (1-m) Rx coils measuring Z axis fields: (i.e. ZZM, XZM, YZM, ZX1, ZY1)</u>
m = 1 meter coil
1 = normal gradiometer across cube using the small 0.35 m Rx coils above and below the Z field drive coil. The coil outputs above and below the Z field drive coils on one side are subtracted from each other before subtracting that output from the complementary pair on the opposite side of the cube.

<u>For Rx coils measuring X and Y axis fields: (i.e. XX1 and YY1)</u>

1= normal gradiometer across cube (small (0.35m) Rx coils)
Examples:

- ZZM = Z axis B field, Z axis sense gradiometer coils, 1-m Rx coils
- ZX1 = Z axis B field, X axis sense gradiometer coils, 1-m Rx coils
- zxe = Z axis B field, X axis sense gradiometer coils, 0.35-m Rx coils diagonal gradiometer, 1st quadrant
- XZM = X axis B field, Z axis sense gradiometer coils, 1-m Rx coils
- XX1 = X axis B field, X axis sense gradiometer coils, 0.35-m Rx coils
- YY1 = Y axis B field, Y axis sense gradiometer coils, 0.35-m Rx coils

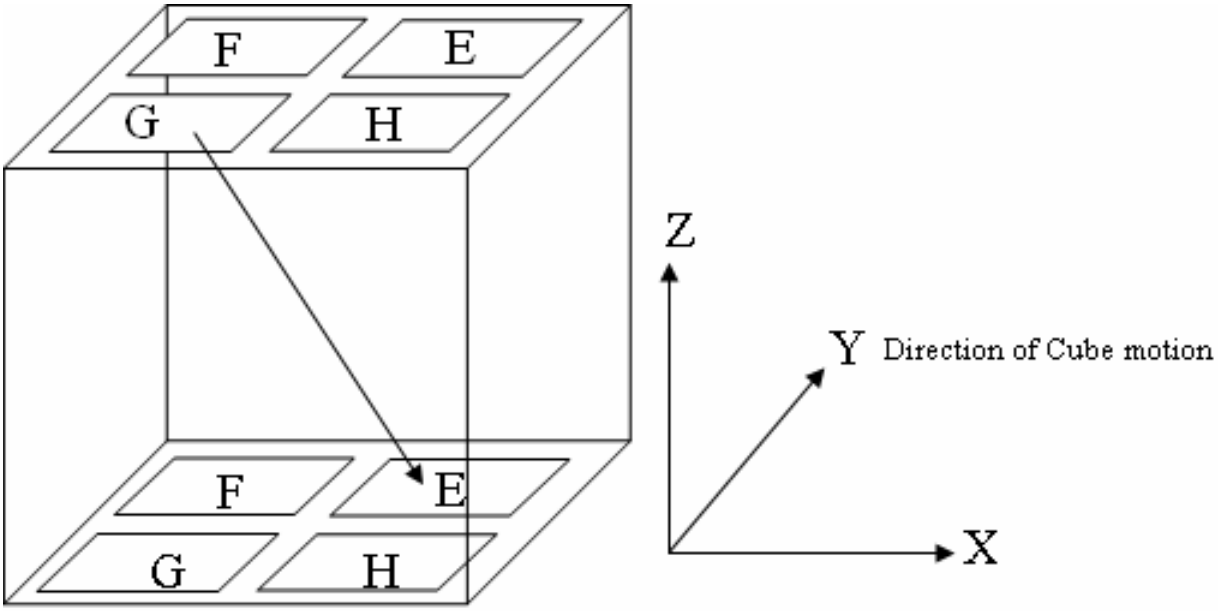


**Figure AE.1.** Figure showing diagonal gradiometer configuration with small coils.

Note: Files are named according to the location of the top antenna pair. (i.e. ZZG file is the top (G) antenna minus the bottom (E) antenna)

# AF. Test Stand Position Analysis

## AF.1 Northing Correction

Figure AAF.1.1 shows the trolley and shuttle with an exaggerated angle of $20^{o}$ on the trolley, for illustrative purposes. In actual use, the angles are much less than $1^{o}$. The term 'Disto' refers to the Leica Disto A6 laser measuring device.

### *AF.1.1 Legend*

$N_{meas}$= Distance measured by the String Pot. The String Pot value stored in the data acquisition program is initialized to the value read by the Shuttle Disto when the Shuttle is at the far north position. So, in essence, the String Pot value is the distance that would have been measured by the Shuttle Disto in this diagram.

$Off_{Shtl}$= Offset distance between the Shuttle Disto measuring point and RC (the azmuthal rotation center for the ordnance). This distance is 260.4 mm.

$W$= Angle of the trolley. W is calculated from the difference between the north and south trolley Disto measurements ($D_{TrolN}$, $D_{TrolS}$), and the distance along the trolley between their measurement points (4419.6 mm). For $D_{TrolN}-D_{TrolS}=20mm$ (a worst case value), the value for W would be: $W=tan^{-1}(20/4419.6)=.259^{o}$.

$N_{True}$=True distance of the ordnance from the Shuttle Disto. $N_{True}$ is calculated by:

$$N_{True}=(N_{Meas}+Off_{Shtl})*\cos(W) \qquad \text{(AF.1)}$$

### *AF.1.2 Calculating* $\mathbf{N_{True}}$ *with some trolley angles*

For the case shown, $W=20^{o}$. *Cosine*(20)=.9396, so the $N_{True}$ would be 94 percent of the measured value.

For the $0.259^{o}$ case (≈20-mm difference between $D_{TrolN}$ and $D_{TrolS}$), cosign(0.216)=0.99998976.

For $N_{Meas}+OffShtl$= the entire beam length (4419.6 mm), the true length would be 4419.6×0.99998976/4419.55 mm. This is a 0.05-mm error, and can realistically be ignored, given the tolerance band of ±5 mm for the positional error.

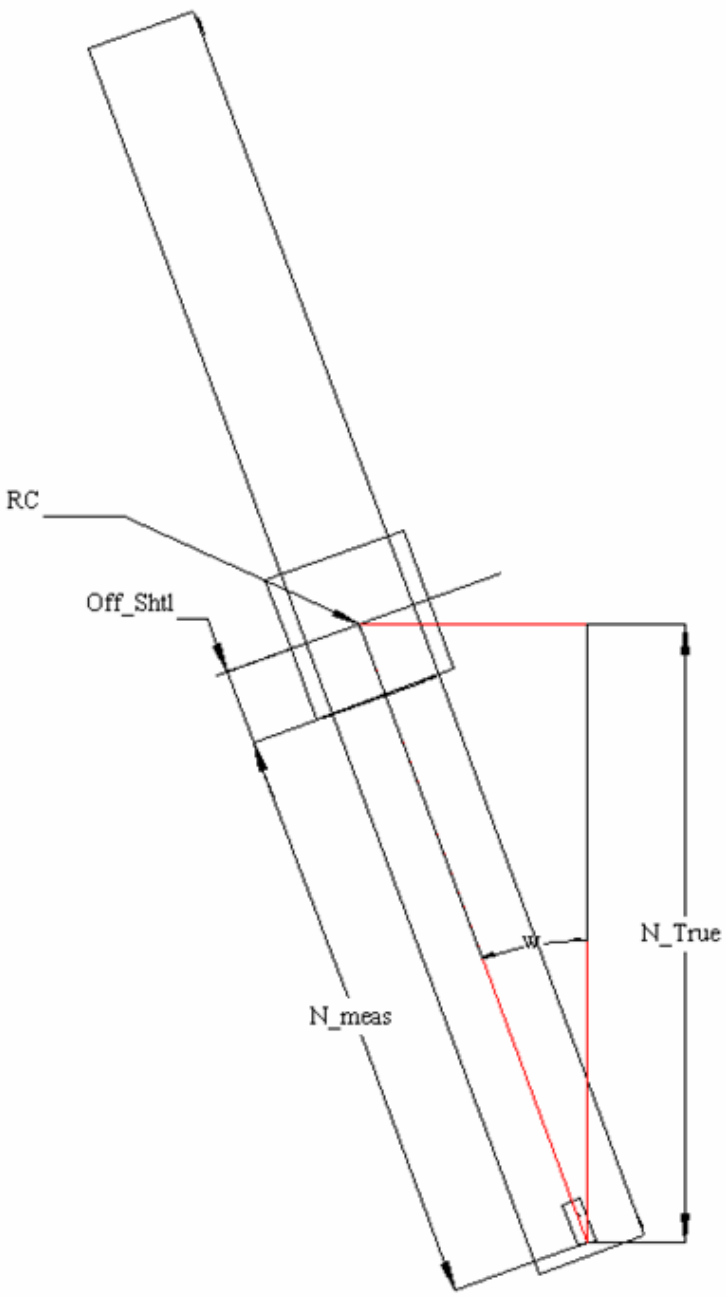


**Figure AF.1.1.** Northing correction diagram.

## AF.2 Easting correction

Figure AF.2.1 below is a diagram of the trolley and shuttle with an exaggerated angle of $20^{O}$ on the trolley, for illustrative purposes. In actual use, the angles are much less than $1^{O}$.

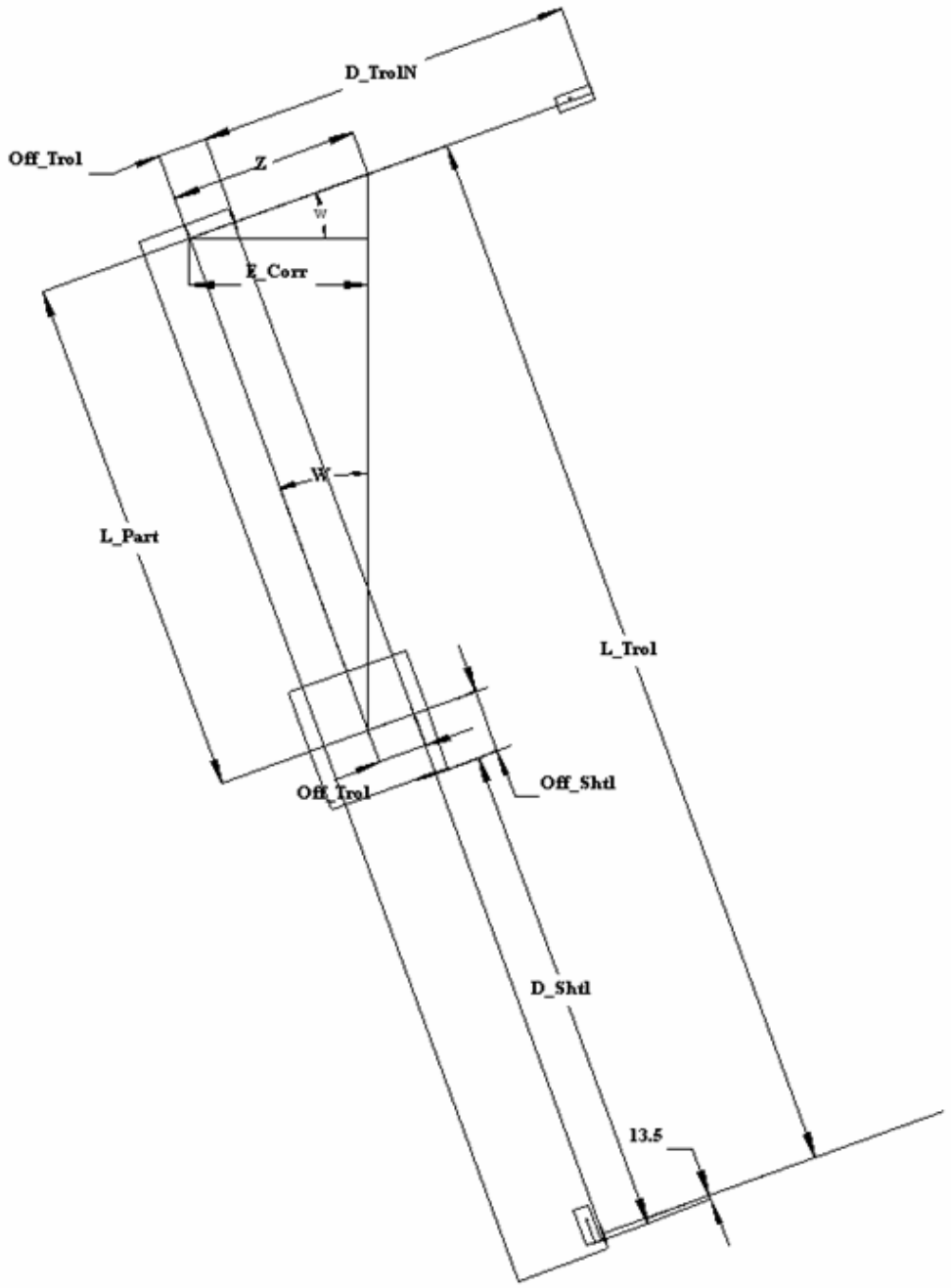


**Figure AF.2.1**. Easting correction diagram.

## *AF.2.1 Legend*

$L_{Trol}$= Length of trolley between the north and south Disto measurement points. This value is 4419.6 mm.

$L_{Part}$= Partial distance of the trolley between RC (the azmuthal rotation center of the shuttle) and NTMP (the north Disto measurement point) This value is:

$$L_{Part}=L_{Trol}-(D_{Shtl}+Off_{Shtl}+13.5) \quad \text{(AF.2)}$$

Note, the 13.5 mm is the small offset between the $D_{Shtl}$ reference plane and the South Disto measurement point.

$Off_{Trol}$= Offset distance between NTMP and RC. This value is 197.64 mm.

$W$= angle of the trolley beam with respect to north

$Z$= Length used for trig analysis

$E_{Corr}$= correction to the Easting value measured by the north trolley Disto.

$D_{TrolN}$= Distance measured by the north trolley Disto to the NTMP

### *AF.2.2 Derivation of* $\mathbf{E_{Corr}}$

From right triangle with sides $L_{Part}$ and $Z$:

$$Z=L_{Part}\times\tan(W) \quad \text{(AF.3)}$$

From right triangle with hypotenuse $Z$ and side $E_{Corr}$:

$$Z=\frac{E_{Corr}}{\cos(W)} \quad \text{(AF.4)}$$

Equating (AF.3) and (AF.4) and solving for $E_{Corr}$ gives:

$$E_{Corr}=\left[\tan(W)\times L_{Part}\right]\times\cos(W) \quad \text{(AF.5)}$$

### *AF.2.3 Calculating* $\mathbf{E_{Corr}}$ *for some angles and L Part values*

For the case in the diagram ($W$=20$^{o}$) and $D_{Shtl}+Off_{Shtl}+13.5$=2289.44, and $L_{Trol}$=4419.6 mm.

Then from (AF.2):

$$L_{Part}=4419.6-(2\ 015.54+260.4+13.5)=4\ 419.6-2\ 289.44=2\ 130.16 \quad \text{(AF.6)}$$

From (AF.5):

$$E_{Corr}=\left[\tan(20)\times 2\ 130.16\right]\times\cos(20)=728.55 \quad \text{(AF.7)}$$

A value of 728.49 *mm* was measured off of the scaled drawing for $E_{Corr}$, which is close enough.

The $D_{TrolN}$ and $D_{TrolS}$ measurements from the test stand vary no more than ≈20 mm (worst case). This corresponds to a trolley angle of ≈0.216$^{o}$. Repeating the calculation with this angle, and the same $D_{Shtl}$ value (2015.54) gives:

$$E_{Corr}=\left[\tan(0.216)\times 2\ 130.16\right]\times\cos(0.216)=8.03 \quad \text{(AF.8)}$$

So, at this shuttle position, the correction to the Easting value of $D_{TrolN}+Off_{Trol}$ would be 8.03 mm less.

## AF.3 Transformation to make it appear as if the ALLTEM cube was moving

The Test Stand data were collected by moving the ordnance underneath a stationary ALLTEM cube. This is not the way that data would be gathered in an actual field survey. To make the data look as if the ALLTEM cube was moving and the ordnance was stationary, the positions attached to each waveform gathered on the Test Stand were transformed. Figure AF.3.1 shows a top view of the Test Stand survey area. The black ALLTEM cube is at the center, and the ordnance is shown on the shuttle at two different positions along the trolley. The ordnance shown represents an 81 mm motor at an azimuth of 45 degrees. With the ordnance center of mass at the red position and the ALLTEM cube in the black position, the waveforms gathered are equivalent to the black ordnance and the red ALLTEM cube positions. Similarly, with the ordnance center of mass at the green position, the waveforms are equivalent to the black ordnance and the green ALLTEM cube positions.

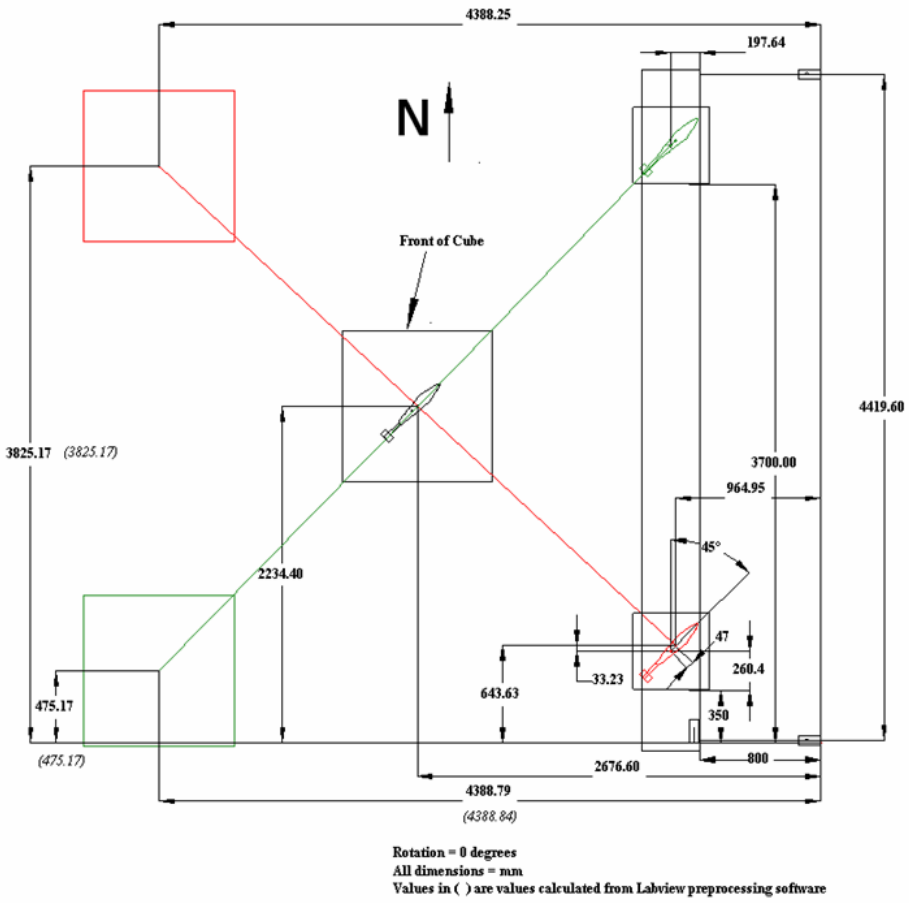


**Figure AF.3.1.** Test stand survey area.

The formulas used to transform the X (Easting) and Y (Northing) for a particular ordnance and ALLTEM Cube location are shown in Figure AF.3.2.

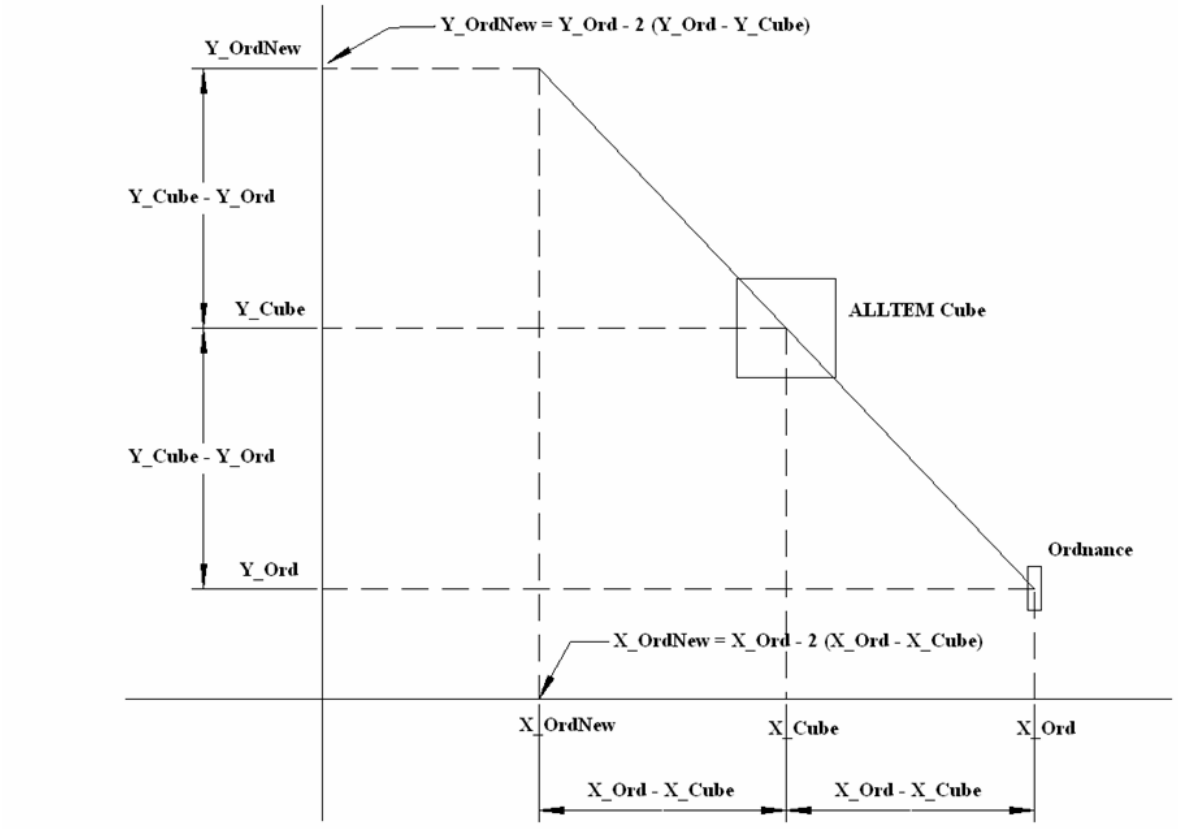


**Figure AF.3.2**. Coordinate transform equations

A further correction was made to the Northing values after the transformation for the moving cube and fixed ordnance. This was to done in part to allow the measured data to work with the USGS developed inversion program which requires that the cube front (E and F antennas) be oriented to the North when data is gathered in a moving cube type survey. Because of constraints in positioning the cube on the Test Stand, the E and F antennas had to be placed facing south. To accomplish moving the E and F antenna to North facing in the data set, the transformed Northing positions were inverted and then added to a value of 4300 mm. The 4300 mm value was chosen to make all of the Northing positions positive after the inversion. The actual value is not important. This operation modifies the Northing location of the center of the cube shown in Figure AF.3 from 2234.4 mm to –(2234.4)+4300=2065.6 mm.

*Therefore, inversions performed on the data sets should show a target Northing value of 2065.6 mm and an Easting value of 2676.6 mm*

## AF.4 Locating the ALLTEM Cube within the measurement grid

The ALLTEM Cube was placed in a 35.56-cm (14-inch) deep well on top of the Test Stand. It was placed in the well to allow ordnance items to get closer to the bottom of the cube, without

hitting the deck support joists. The bottom of the well was made level, to be parallel to the plane of the ordnance. A fixture was made that allowed a plum bob to hang directly beneath the corners of the Cube. With the plum bob hanging from the Cube SW corner, the shuttle and trolley were adjusted until the plum bob was just over the ordnance rotation center (RC) of the shuttle. Measurements were then taken with the Distos on the shuttle, and the north and south trolley. The plum bob fixture was then moved to the NW corner of the Cube and measurements were taken. The cube's position was adjusted slightly to try and get the same north and south trolley readings at the two corners. The setup and values recorded are shown in figure AF.4.1. Note that the south Disto reading at the NW and SW corners are identical (2977 and 2977 mm) and the north Disto reading at the NW and SW corners are within a mm (2983, 2982). The fact that they are 5-6 mm apart would suggest that the trolley was at a small angle compared to the point where the north and south Distos were initially placed and zeroed. The difference between the values was averaged and a cube center of 2979 mm was used in the location calculations. It should be noted that at the time the measurements were made the thin (4.76 mm) masonite Disto laser target blocks were not installed on the trolley beam. Later on, for the ordnance surveys, the blocks were used. The 4.76 mm value was compensated for in the value of the location of the ALLTEM cube.

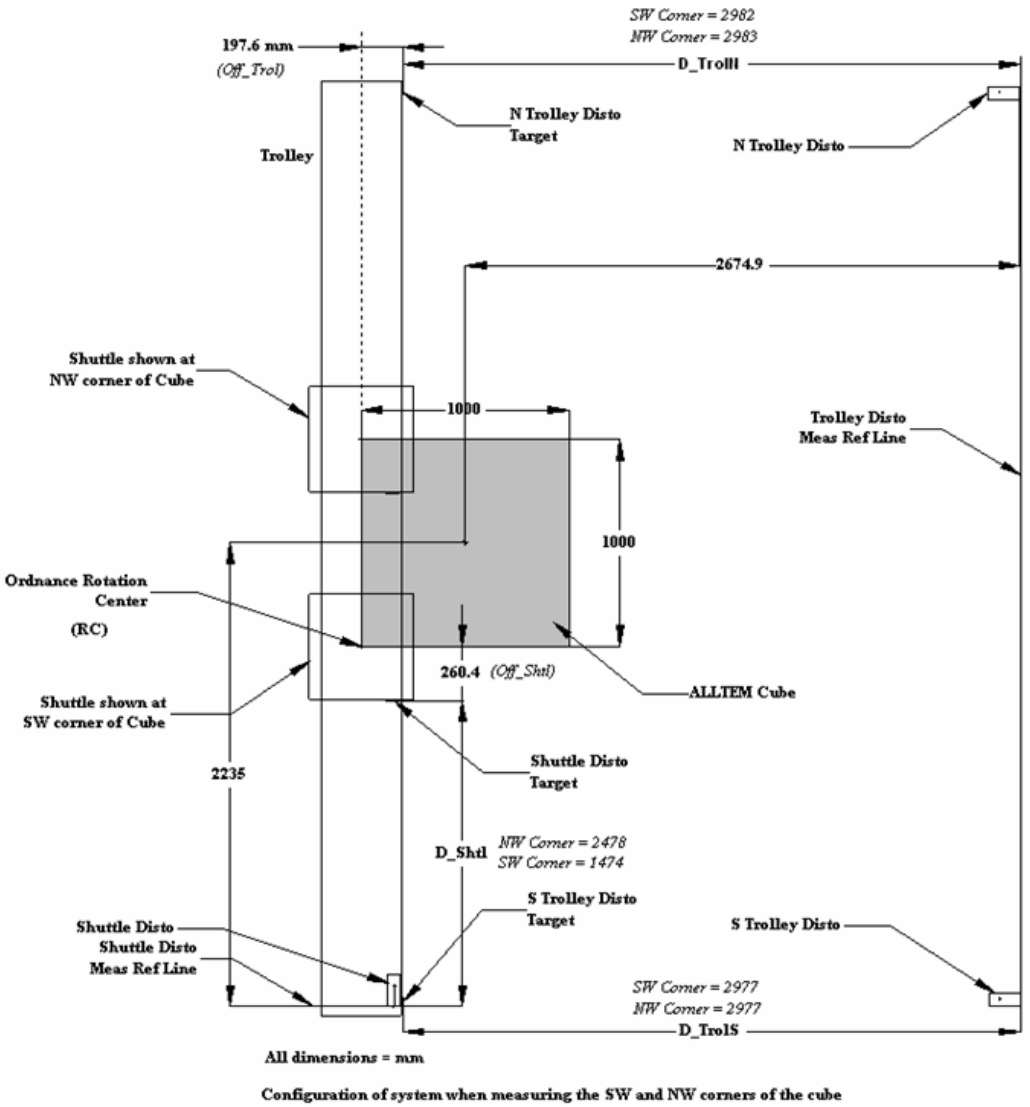


**Figure AF.4.1**. ALLTEM setup in test stand.

## AF.5 Initial placement of the north and south trolley Distos

The initial positioning of the north and south Distos was performed by placing the trolley near the middle of its east-west travel. The south trolley Disto had previously been attached to the extension of the south trolley beam with nylon screws. A south trolley Disto measurement was then made. The north Disto was then slid along the extension of the north trolley beam until the measurement made for the north trolley Disto was the same as the south trolley Disto. The measurements were repeated a number of times to ensure repeatability. A variation of ±1 mm was considered acceptable. When the north trolley Disto position was settled on, it was attached to the beam with nylon screws, so that it could be repeatable positioned each day. In order to check that the trolley was not significantly cocked when the north trolley Disto was being positioned, the trolley was moved back and forth a few times from the initial placement by

pushing and pulling from the middle. The measurements were repeated and compared for the north and south trolley Distos. The measurements typically agreed within a couple of mm.

## AF.6 Leveling adjustment of the north and south trolley beams

Before the ordnance measurements were made at the initial depth, the north and south trolley beams were leveled. The south trolley beam was placed at the initial height. The East-West slope of the beam was set as close to zero as possible by fine adjustments of the height adjustment sub-assemblies mounted to the deck corner posts. A 60.96-cm (2-foot) level was used for checking the level. During measurements, the level was flipped end for end to insure that the bubble was accurate. Once the level was deemed adequate, the leveling sub-assemblies were permanently attached to the deck outer posts. The sub-assemblies were also shimmed as necessary to insure that they hung vertical. To adjust the other two sub-assemblies that support the north trolley beam, string levels were used. A Kevlar string was used for the string levels, so that a lot of tension could be used. The string was strung across the top of the trolley PVC pipe rails to perpendicular points on the opposite trolley beam, and across the diagonals. Adjustments were made until both the perpendiculars and diagonals were deemed level. Again, shimming was added to ensure that the north trolley sub-assemblies hung vertically. When the trolley beams were later moved to the lower positions, it was important that the north and south trolley Distos remain in the same relative positions to the center of the ALLTEM cube. This was done by making a mark on the beams near the north and south trolley Distos. A plum bob was used to drop a vertical from that mark to a point in the concrete footing below the corner deck posts. A small hole was drilled in the concrete at that point to serve as a permanent reference. When the beams were repositioned, the marks on the beams were adjusted until they were at the same horizontal location over the marking holes in the concrete.

## AF.7 Corrections for ordnance azimuth and inclination

The decision was made to use the center of mass of the ordnance for its location. Because of the fixtures used to hold the various ordnances during the surveys on the test stand, the center of mass was not always at the center of rotation when the ordnance was placed at the various azimuths and inclinations. For each ordnance the distance from the center of mass to the center of rotation was measured (*DCmCr*). The distance was considered positive if it placed the center of mass further north of the center of rotation, when the ordnance was in the azimuth=0, inclination=0 orientation. The *DCmCr* distance and the particular azimuth (*Az*) setting were set to modify the reported Northing and Easting values according to the following formulas:

$$Easting\ correction = \sin(Az) \times DCmCr \tag{AF.9}$$

$$Northing\ correction = \cos(Az) \times DCmCr \tag{AF.10}$$

The inclination (*Inc*) value does not affect the Northing and Easting, but does affect the apparent depth of the ordnance below the ALLTEM cube according to the following formula:

$$\textit{Apparent Depth} = \textit{Depth to Center of Rotation} + \sin(\textit{Inc}) \times \textit{DCmCr} \quad \text{(AF.11)}$$

## AF.8 Correction for catenary droop of the string pot measuring string

The Celesco string pot (PT9150-0400-231-1110) used for measuring the Northing position of the ordnance, was purchased with 2 coil springs. One of the springs was disabled in order for the shuttle motor to have enough torque to pull the shuttle north, when it is pulling against the string pot spring tension. The droop (catenary curve) of the string between the shuttle and the pulley at the south end of the trolley cause a small error in the shuttle position measured by the string pot. The error in the position from this droop was calculated with the use of an on-line catenary calculator at the following web address:

`http://www.spaceagecontrol.com/calccabm.htm?F=1&a=5&q=0.001&g=9.81&Submit+Button=Calculate`

The force of the coil spring was measured with an Ohaus force-measuring scale as 0.5 kg (4.55 newtons). A 3-m section of the string pot string was measured with a Sunbeam electronic scale (model SP5). The weight was 4 g. This gave a weight per unit length of 0.0013 kg/m The span used for the calculation was 4.0 m. With these inputs the calculator gave the following results:

- The displacement cable length will be 4.00002095 m.
- The displacement cable will sag 0.00561 m.
- This cable sag adds ±0.000524 percent to the transducer's inherent measurement error.

This means that the extra length due to the catenary curve is 4.0 m – 4.00002095 m ≈ .021 mm extra length. This is small enough, compared to the desired positional accuracy of ±5 mm, that it can be ignored.

## AF.9 Variations in the trolley angle on each line in a survey

The $D_{TrolN}$ and $D_{TrolS}$ values were recorded on each line. These were recorded after the shuttle had finished its north-to-south traverse while waveforms were being recorded. It was observed that the trolley would cock slightly, due to shuttle pull string tension, at the moment that the shuttle began its north-to-south traverse. The trolley did not move during the time that the shuttle was moving during waveform recording. Figure AF.9.1 displays plots of the differences between the $D_{TrolN}$ and $D_{TrolS}$ for two different surveys. As can be seen, there are similarities in the shapes and trends of the data, but the data do not perfectly repeat. Therefore each survey is individually corrected for position errors due to the varying trolley angle.

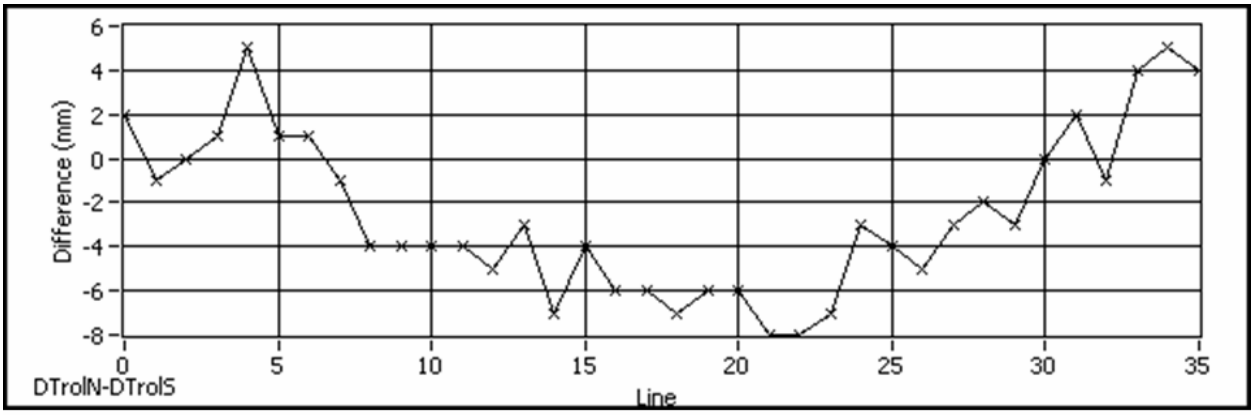


(A)

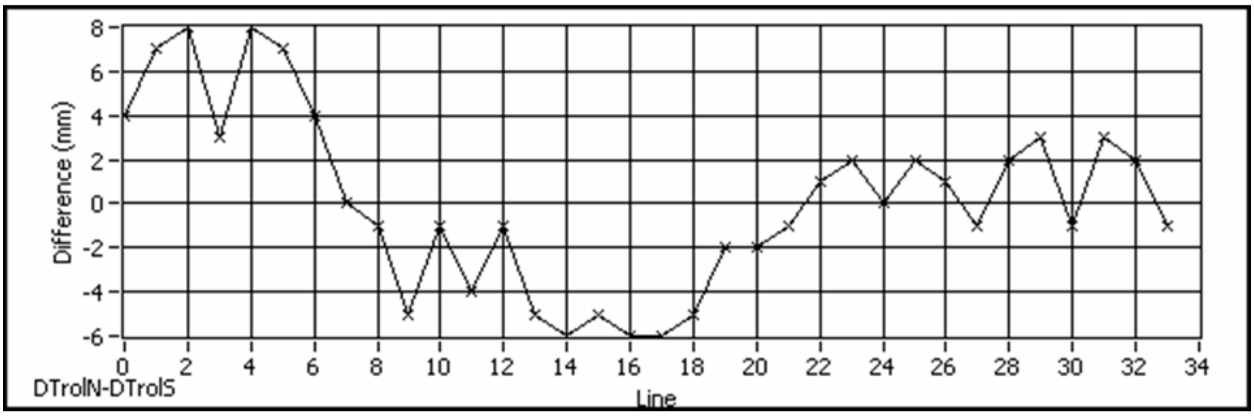


(B)

**Figure AF.9.1.** Changes in the trolley angle along two survey lines. The patterns are similar but not precisely the same.

The trolley angle can be calculated from:

$$Trolley\ Angle = \tan^{-1}\left[(DTrolN - DTrolS)/TrolleyLength\right] \quad \text{(AF.12)}$$

where: *TrolleyLength* = Distance between their measurement points on the trolley (4419.6 mm).

For $D_{TrolN} - D_{TrolS} = 8mm$, the angle is $tan^{-1}\ (8/4419.6) = 0.1037^{o}$.

## AF.10 Accuracy of the string pot measurement of the shuttle position

The Celesco string pot was used to record the shuttle positions during waveform recording. A variable in the data acquisition software (*SPot*) was set equal to the $D_{Shtl}$ measurement when the shuttle was at the north end, just before the shuttle was commanded to move south. Also, at that time, the hardware counters keeping track of the string pot encoder output were reset to zero. The readings from the hardware counter were then subtracted from the initialized software variable to calculate the position of the shuttle. This was performed every 33.33 ms, which was the waveform digitizer measurement period. After three of these measurement windows (stacking three), the latest SPot measured was tagged with the stored ordnance waveform. At the end of the north to south traverse of the shuttle, the shuttle position $D_{ShtlEnd}$, was measured with the Disto,

along with the final string pot position $SPot_{End}$. Usually, these values agreed with each other to within ±3 mm. A plot of the difference between the values is shown in figure AF.10.1 for a typical survey of 35 lines.

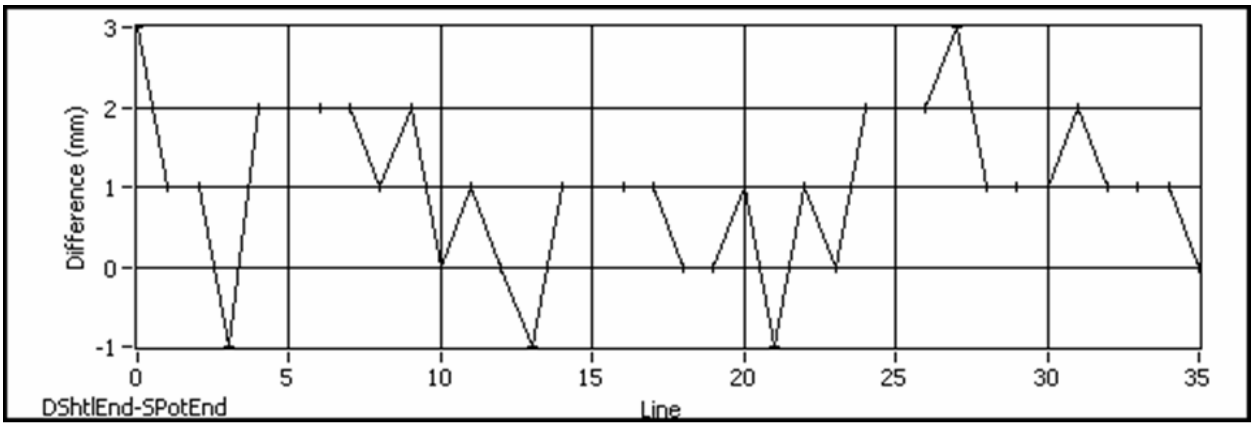


**Figure AF.10.1**. String-Pot/disto discrepancy over 35 lines.

## Appendix B. Technical Publications

### Technical Reports:


Bracken, R.E., Brown, P.J., 2005, Reducing Tensor Magnetic Gradiometer Data for Unexploded Ordnance Detection: U.S. Geological Survey Scientific Investigations Report 2005-5046, 03/03/2005, (Available on line at:: http://pubs.usgs.gov/sir/2005/5046.)

Bracken, R.E., Smith, D.V., Brown, P.J., 2005, Calibrating a Tensor Magnetic Gradiometer Using Spin Data: U.S. Geological Survey Scientific Investigations Report 2005-5045, (Available on line at: http://pubs.usgs.gov/sir/2005/5045.)

Oden, C.P., and Moulton, C.W., 2006, GP Workbench Manual: Technical Manual, User's Guide, and Software Guide: U. S. Geological Survey Open-File Report 2006-1365. (available on line at: http://pubs.usgs.gov/of/2006/1365. Includes source code.) 87p.

Wright, D.L., Smith, D.V., Li, Y., Nabighian, M.N., 2003, SERDP Project UX1328 2003 Annual Report (revised), 47p.

Wright, D.L., Smith, D.V., Bracken, R.E., Asch, T.H., Moulton, C.W., Hutton, S.R., Brown, P.J., Wallin, E., Horton, R.J., Li, Y., Nabighian, M.N., 2003, Tests of Three USGS Prototype Geophysical Instruments at the SERDP Standardized UXO Test Area at Yuma Proving Ground: Yuma Phase I Report, 250p.

Wright, D.L., Smith, D.V., Li, Y., Nabighian, M.N., 2005, On-Time 3D Time-Domain EMI and Tensor Magnetic Gradiometry for UXO Detection and Discrimination: 2005 Annual Report, 36p.

Wright, D.L., Smith, D.V., Li, Y., Nabighian, M.N., 2004, On-Time 3D Time-Domain EMI and Tensor Magnetic Gradiometer for UXO Detection and Discrimination: 2004 Annual Report, 77p.

Wright, D.L., Smith, D.V., Li, Y., Nabighian, M.N., 2005, SERDP Project MM-1328 - On-Time 3D Time-Domain EMI and Tensor Magnetic Gradiometry for UXO Detection and Discrimination: 2005 Annual Report, 84p.

Wright, D.L., Smith, D.V., Moulton, C.W., Asch, T.H., Brown, P.J., Hutton, R.E., Bracken, R.E., Li, Y., Nabighian, M.N., Sanchez, V., 2006, ALLTEM and TMGS May, 2006 Tests at the Standardized UXO Test Area at the Yuma Proving Ground: 2006 Annual Report, 238p.

**Conference/Symposium Proceedings:**


Bracken, R.E., Brown, P.J., 2005, Reducing tensor magnetic gradiometer data for unexploded ordnance detection: First Break, v. 23, 08/2005, European Association of Geoscientists and Engineers (EAGE), p. 63-66.

Sanchez, V., Sinex, D., Li, Y., Nabighian, M., Wright, D., and Smith, D., 2005, Processing and inversion of magnetic gradient tensor data for UXO applications: Proceedings of the 18th Annual Symposium on the Application of Geophysics to Engineering and Environmental Problems, Atlanta, GA, 04/06/2005, p. 1193-1202.

Smith, D.V. and Bracken, R.E., 2004, Field Experiments with the Tensor Magnetic Gradiometer System at Yuma Proving Ground, Arizona: Proceedings of the 17th Annual Symposium on the Application of Geophysics to Engineering and Environmental Problems (SAGEEP) 2004, 02/26/2004, Colorado Springs, CO, p. 1675-1691.

Wright, D.L. Smith, D. V., Moulton, C.W., Hutton, S.R., Bracken, R.E., Wallin, E.L., Brown, P.J., Stoddard, C.E., Kibler, J.D., Nabighian, M.N., Li, Y, 2003, Laboratory evaluation of three prototype geophysical instruments for UXO applications: Symposium on the Application of Geophysics to Engineering and Environmental Problems (SAGEEP 2003), Proceedings CD, p. 1431-1444, San Antonio, TX, 05/06/2003.

Wright, D.L., Moulton, C.W., Asch, T.H., Brown, P.J., Hutton, S.R., Nabighian, M.N., Li, Y. 2006, ALLTEM For UXO Applications - First Field Tests: Proceedings of the 19th Annual Symposium on the Application of Geophysics to Engineering and Environmental Problems, Seattle, Washington, 04/05/2006, p. 1761-1775.

Wright, D.L., Moulton, C.W., Asch, T.H., Hutton, S.R., Brown, P.J., Nabighian. M.N. and Li, Y., 2005, ALLTEM, a triangle wave on-time time-domain system for UXO applications: Proceedings of the 18th Annual Symposium on the Application of Geophysics to Engineering and Environmental Problems, 04/05/2005, Atlanta, GA, p. 1357-1367.

Wright, D.L., Moulton, C.W., Asch, T.H., Hutton, S.R., Brown, P.J., Nabighian. M.N., Li, Y., 2007, ALLTEM UXO Detection Sensitivity and Inversions for Target Parameters from Yuma Proving Ground Test Data: Proceedings of the 20th Annual Symposium on the Applications of Geophysics to Engineering and Environmental Problems, Denver, CO, p. 1422-1435. (Voted one of the 10 best papers of the Symposium).

Wright, D.L., Asch, T.H., Moulton, C.W., Smith, D.V., Hutton, S.R., Wallin, E., Brown, P.J., Nabighian, M.N., 2004, Test results from two prototype electromagnetic systems at the SERDP Standardized UXO Test Site at Yuma Proving Ground, Arizona: Proceedings of the 17th Annual Symposium on the Application of Geophysics to Engineering and Environmental Problems, 02/26/2004, Colorado Springs, CO, p. 1702-1713.

**Published Papers and Technical Abstracts:**

Brown, P.J. II, Bracken, R.E., Smith, D.V., 2004, A case study of magnetic gradient tensor invariants applied to the UXO problem: Society of Exploration Geophysicists (SEG) International Exposition and Seventy Fourth Annual Meeting Technical Program Expanded Abstracts CD, Denver, CO, 10/14/2004 Paper GM 3.3.

Smith, D.V., Bracken, R.E., 2004, Field experiments with the tensor magnetic gradiometer system for UXO surveys: a case history: Society of Exploration Geophysics (SEG) International Exposition and Seventy-Fourth Annual Meeting. Technical Program Expanded Abstracts CD, Denver, CO, 10/14/2004, Paper GM 3.6.

Wright, D.L., Smith, D.V., Li, Y., and Nabighian, M.N., 2002, Assessment of three prototype geophysical instruments for UXO applications: Partners in Environmental Technology Technical Symposium & Workshop, Washington D.C., 12/05/2002, Poster No. 219.

Wright, D.L., Smith, D.V., Bracken, R.E., Moulton, C.W., Hutton, S.R., Brown, P.J., Wallin, E.L., Li, Y., Nabighian, M.N., 2002, Field Tests of Three Prototype Systems at the Yuma Proving Ground SERDP Standardized UXO Calibration Area: Partners in Environmental Technology Technical Symposium & Workshop, Washington, D.C., 12/05/2002, Poster No. 45.

Wright, D.L., Smith, D.V., Moulton, C.W., Asch, T.H., Brown, P.J., Bracken, R.E., Hutton, S.R., Li, Y., Nabihian, M.N., 2005, Recent progress on the ALLTEM System and a Tensor Magnetic Gradiometer System (TMGS) for UXO Detection and Discrimination: Partners in Environmental Technology Technical Symposium and Workshop, Washington, D.C., 11/29/2005, Poster No. 145T.